MIRCEA RADEŞ

Mechanical Vibrations

II

Structural Dynamic Modeling

Preface

The second part of *Mechanical Vibrations* covers advanced topics on Structural Dynamic Modeling at postgraduate level. It is based on lecture notes prepared for the postgraduate and master courses organized at the Strength of Materials Chair, University Politehnica of Bucharest.

The first volume, published in 2006, treats vibrations in linear and nonlinear single degree of freedom systems, vibrations in systems with two and/or several degrees of freedom and lateral vibrations of beams. Its content was limited to what can be taught in a one-semester (28 hours) lecture course, supported by 28 hours of tutorial and laboratory.

The second volume is about modal analysis, computational methods for large eigenvalue problems, analysis of frequency response data by nonparametric methods, identification of dynamic structural parameters, dynamic model reduction and test-analysis correlation.

This book could be used as a textbook for a second course in Mechanical Vibrations or for a course at master level on Test-Analysis Correlation in Engineering Dynamics. For full comprehension of the mathematics employed, the reader should be familiar with matrix algebra and basic eigenvalue computations.

It addresses to students pursuing their master or doctorate studies, to postdoc students and research scientists working in the field of Structural Dynamics and Mechanical Vibrations, being a prerequisite for those interested in finite element model updating and experimental modal analysis.

The course reflects the author's experience and presents results from his publications. Some advanced methods, currently used in experimental modal analysis and parameter estimation of mechanical and structural systems, are not treated and can be found in the comprehensive bibliography at the end of each chapter.

Related not treated topics include: sensitivity analysis, modal analysis using operating deflection shapes, real normalization of complex modes, structural dynamics modification, automated finite element model updating, error localization, structural damage detection and material identification. They are discussed in a separate book.

March 2010   Mircea Radeş

Prefaţă

Partea a doua a cursului de *Vibraţii mecanice* conţine elemente avansate de modelare dinamică a structurilor, la nivel postuniversitar. Ea se bazează pe cursurile predate la cursurile de studii aprofundate şi de master organizate la Catedra de Rezistenţa materialelor de la Universitatea Politehnica Bucureşti

În primul volum, publicat în 2006, s-au prezentat vibraţii în sisteme liniare şi neliniare cu un grad de libertate, vibraţii în sisteme cu două sau mai multe grade de libertate şi vibraţiile barelor drepte. Conţinutul primei părţi a fost limitat la ceea ce se poate preda într-un curs de un semestru (28 ore), însoţit de activităţi de laborator şi seminar de 28 ore.

În volumul al doilea se prezintă elemente de analiză modală a structurilor, metode de calcul pentru probleme de valori proprii de ordin mare, metode neparametrice pentru analiza funcţiilor răspunsului în frecvenţă, identificarea pametrilor sistemelor vibratoare, reducerea ordinului modelelor şi metode de corelare a modelelor analitice cu rezultatele experimentale.

Cartea poate fi utilizată ca suport pentru un al doilea curs de Vibraţii mecanice sau pentru un curs la nivel de master privind Corelarea analiză-experiment în Dinamica structurilor. Pentru înţelegerea deplină a suportului matematic, cititorul trebuie să aibă cunoştinţe de algebră matricială şi rezolvarea problemelor de valori proprii.

Cursul se adresează studenţilor de la studii de masterat sau doctorat, studenţilor postdoc şi cercetătorilor ştiinţifici în domeniile Dinamicii structurilor şi Vibraţiilor mecanice, fiind util celor interesaţi în verificarea şi validarea modelelor cu elemente finite şi analiza modală experimentală.

Cursul reflectă experienţa autorului şi prezintă rezultate din propriile lucrări. O serie de metode moderne utilizate în prezent în analiza modală experimentală şi estimarea parametrilor sistemelor mecanice şi structurale nu sunt tratate şi pot fi consultate în referinţele bibliografice incluse la sfârşitul fiecărui capitol.

Nu se tratează analiza senzitivităţii, analiza modală fără excitaţie controlată, echivalarea reală a modurilor complexe de vibraţie, analiza modificării structurilor, updatarea automată a modelelor cu elemente finite, localizarea erorilor, detectarea defectelor structurale şi identificarea materialelor, acestea fiind studiate într-un volum aparte.

Martie 2010   Mircea Radeş

Contents

7.

MODAL ANALYSIS

The dynamic behavior of a mechanical vibratory system is usually studied by one of two methods: the mode superposition method or the direct integration method. The former involves calculating the response in each mode separately and then summing the response in all modes of interest to obtain the overall response. The latter involves computing the response of the system by step-by-step numerical integration. For many problems, the mode superposition offers greater insight into the dynamic behavior and parameter dependence of the system being studied.

The major obstacle in the solution of the differential equations of motion of a vibratory system, for a given set of forcing functions and initial conditions, is the coupling between equations. This is represented by non-zero off-diagonal elements in the system matrices. If the equations of motion could be uncoupled, i.e. for diagonal mass, stiffness (and damping) matrices, then each equation could be solved independent of the other equations. In this case, each uncoupled equation would look just like the equation for a single degree of freedom, whose solution can very easily be obtained.

The *analytical modal analysis* is such a procedure, based on a linear transformation of coordinates, which decouples the equations of motion. This coordinate transformation is done by a matrix comprised of the system modal vectors, determined from the solution of the system's eigenvalue problem. After solving for the modal coordinates, the displacements in the configuration space are expressed as linear combinations of the modal coordinates.

7.1 Modes of vibration

A mode of vibration can be defined as a way of vibrating, or a pattern of vibration, when applied to a system or structure that has several points with different amplitudes of deflection [7.1].

A mode of vibration is defined by two distinct elements: a) a time variation of the vibration; and b) a spatial variation of the amplitude of motion

across the structure. The time variation defines the frequency of oscillation together with any associated rate of decay or growth. The spatial variation defines the different vibration amplitudes from one point on the structure to the next.

For a discrete system, the expression that defines a vibration mode can be written as

$$\{x(t)\} = \{X\}e^{\lambda t},\qquad(7.1)$$

where λ represents the modal frequency, and the vector $\{X\}$ represents the mode shape (modal vector).

If λ is imaginary $(\lambda = i\omega)$, then the motion is purely oscillatory at frequency ω. If λ is complex, the motion is oscillatory with exponential decay or growth, depending on the sign of the real part of λ.

The elements of the modal vector may be real or complex quantities. In a *real mode* shape, all coordinates are vibrating exactly in or out of phase with each other. All points reach their maximum deflections at the same instants in time, and pass through their undeformed positions simultaneously (standing wave). In a *complex mode* shape, each coordinate vibrates with its own different phase angle. Each point of the structure reaches its own maximum excursion at different instants in time compared with its neighbors and, similarly, passes through its static equilibrium position at different instants to the other points (traveling wave).

There are basically two types of vibration modes: a) free vibration modes, and b) forced vibration modes. Modes of the first category are sometimes called 'normal' or 'natural' modes, while those of the second category are called 'forced modes'.

Substitution of (7.1) into the equations of motion of free vibrations leads to an eigenvalue problem. It turns out that the eigenvalues are connected to the modal frequencies and the eigenvectors are the modal vectors. Any modal decomposition is equivalent to solving the associate eigenproblem [7.2].

7.2 Real undamped natural modes

The normal modes are obtained from solution of the equations of motion for the case of zero external excitation, i.e. the solution to the homogeneous equations of motion. Undamped and proportionally damped systems have real modes of vibration. In the following only non-gyroscopic systems are considered. The analysis is restricted to systems with non-repeated natural frequencies. Unsupported (free-free) systems are discussed in a separate section.

7.2.1 Undamped non-gyroscopic systems

Consider the free vibrations of a discrete conservative system described by a linear system of ordinary differential equations with constant coefficients

$$\left[m \right]\{ \ddot{x} \} + \left[k \right]\{ x \} = \{ 0 \},\qquad(7.2)$$

where $\left[m \right]$ and $\left[k \right]$ are real mass and stiffness matrices, respectively, of order n, $\{ \ddot{x} \}$ and $\{ x \}$ are the n-dimensional vectors of accelerations and displacements.

It is of interest to find a special type of solution, in which all coordinates $x_j(t)$ execute synchronous motion. Physically, this implies a motion in which all the coordinates have the same time dependence. The general configuration of the system does not change, except for the amplitude, so that the ratio between any two coordinates $x_j(t)$ and $x_\ell(t)$ remains constant during the motion [7.3].

It is demonstrated that, if synchronous motion is possible, then the time dependence is harmonic

$$\{ x(t) \} = C\{ u \}\cos\left(\omega t - \phi \right),\qquad(7.3)$$

where C is an arbitrary constant, ω is the circular frequency of the harmonic motion, and ϕ is the initial phase shift.

Substitution of (7.3) into (7.2) yields

$$\left[k \right]\{ u \} = \omega^2 \left[m \right]\{ u \},\qquad(7.4)$$

which represents the symmetric generalized eigenvalue problem associated with matrices $\left[m \right]$ and $\left[k \right]$.

Equation (7.4) has non-trivial solutions if and only if ω satisfies the characteristic equation

$$\det\left(\left[k \right] - \omega^2 \left[m \right] \right) = 0,\qquad(7.5)$$

and the vector $\{ u \}$ satisfies the condition

$$\left(\left[k \right] - \omega^2 \left[m \right] \right)\{ u \} = \{ 0 \}.\qquad(7.6)$$

Equation (7.5) is of degree n in ω^2. It possesses in general n distinct roots, referred to as *eigenvalues*. The case of multiple roots is not considered herein. The square roots of the eigenvalues are the system *undamped natural frequencies*, ω_r, arranged in order of increasing magnitude. There are n eigenfrequencies ω_r in which harmonic motion of the type (7.3) is possible.

As matrices $[m]$ and $[k]$ are real and symmetric, the eigenvalues are real positive and the natural frequencies are real. Zero eigenvalues correspond to rigid body modes.

Associated with every one of the eigenfrequencies ω_r there is a certain non-trivial real vector $\{u\}_r$ which satisfies the equation

$$[k]\{u\}_r = \omega_r^2 [m]\{u\}_r. \qquad r = 1, 2, ..., n \qquad (7.7)$$

The *eigenvectors* $\{u\}_r$, also called *modal vectors*, represent physically the mode shapes, i.e. the spatial distribution of displacements during the motion in the respective mode of vibration. They are *undamped modes of vibration*, or *natural modes*, being intrinsic (natural) system properties, independent of the initial conditions of motion or the external forcing.

These vectors are unique, in the sense that the ratio between any two elements x_{ir} and x_{jr} is constant. The value of the elements themselves is arbitrary, because equations (7.7) are homogeneous.

Figure 7.1 illustrates the lowest three planar mode shapes of a cantilever beam. The modes are plotted at different time instants, revealing the *nodal points*, a characteristic of standing waves. For beams, there is a direct correlation between the mode index and the number of nodal points, a fact which helps in measurements.

Mode # 1

Mode # 2

Mode # 3
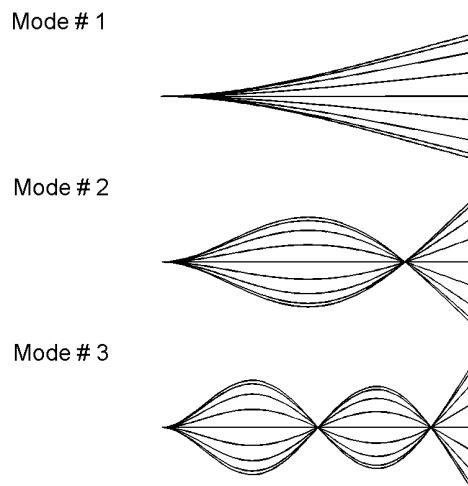
Fig. 7.1

In pseudo-animated displays, all points will reach maximum departures from their equilibrium positions or become zero at the same instants. The nodes are stationary. Hence, if stationary nodes are visible, then the modes are real.

7.2.1.1 Normalization of real modal vectors

The process of scaling the elements of the natural modes to render their amplitude unique is called *normalization*. The resulting vectors are referred to as *normal modes*.

1. Unity modal mass

A convenient normalization procedure consists of setting

$$\{u\}_r^T [m]\{u\}_r = 1. \qquad\qquad r = 1, 2,..., n \qquad (7.8)$$

This is called *mass normalization* and has the advantage of yielding

$$\{u\}_r^T [k]\{u\}_r = \omega_r^2. \qquad\qquad r = 1, 2,..., n \qquad (7.9)$$

2. Particular component of modal vector set to unity

Another normalization scheme consists of setting the value of the largest element of the modal vector $\{u\}_r$ equal to 1, which is useful for plotting the mode shapes.

3. Unity length of modal vector

This is a less recommended normalization, implying $\{u\}_r^T \{u\}_r = 1$.

The normalization process is just a convenience and is devoid of physical significance.

7.2.1.2 Orthogonality of real modal vectors

Pre-multiplying both sides of (7.7) by $\{u\}_s^T$ we obtain

$$\{u\}_s^T [k]\{u\}_r = \omega_r^2 \{u\}_s^T [m]\{u\}_r. \qquad\qquad (7.10)$$

Inverting indices and transposing yields

$$\{u\}_s^T [k]\{u\}_r = \omega_s^2 \{u\}_s^T [m]\{u\}_r. \qquad\qquad (7.11)$$

On subtracting (7.11) from (7.10) one finds, for $r \neq s$, if $\omega_r \neq \omega_s$ and assuming that matrices are symmetric, that the modal vectors satisfy the orthogonality conditions

$$\{u\}_s^T [m]\{u\}_r = 0, \qquad\qquad r \neq s \qquad (7.12)$$

$$\{u\}_s^T [k]\{u\}_r = 0. \qquad\qquad r \neq s \qquad (7.13)$$

Note that the orthogonality is with respect to either the mass matrix $[m]$ or the stiffness matrix $[k]$ which play the role of weighting matrices.

If the modes are mass-normalized, they satisfy the relation

$$\{u\}_r^T[m]\{u\}_s = \delta_{rs}, \qquad\qquad r,s=1,2,..,n \qquad (7.14)$$

where δ_{rs} is the Kronecker delta.

7.2.1.3 Modal matrix

The modal vectors can be arranged as columns of a square matrix of order n, known as the *modal matrix*

$$[u] = \Big[\ \{u\}_1\ \{u\}_2\ \cdots\ \{u\}_n\ \Big]. \qquad (7.15)$$

The modal analysis is based on a linear transformation

$$\{x\} = [u]\{q\} = \sum_{r=1}^{n} \{u\}_r q_r \qquad (7.16)$$

by which $\{x\}$ is expressed as a linear combination of the modal vectors $\{u\}_r$. The coefficients q_r are called *principal* or *modal coordinates*.

7.2.1.4 Free vibration solution

Inserting (7.16) into (7.2) and premultiplying the result by $\{u\}_r^T$, we obtain

$$\{u\}_r^T[m]\sum_{r=1}^{n}\{u\}_r \ddot{q}_r + \{u\}_r^T[k]\sum_{r=1}^{n}\{u\}_r q_r = 0. \qquad (7.17)$$

Considering the orthogonality conditions (7.12) and (7.13), we arrive at the equation of motion in the r-th mode of vibration

$$M_r\,\ddot{q}_r + K_r\,q_r = 0, \qquad (7.18)$$

where

$$M_r = \{u\}_r^T[m]\{u\}_r \quad K_r = \{u\}_r^T[k]\{u\}_r. \qquad (7.19)$$

By analogy with the single degree of freedom mass-spring system, M_r is a generalized or *modal mass*, K_r is a generalized or *modal stiffness*, and q_r is a

principal or *modal coordinate*. Modal masses and stiffnesses are functions of the scaling of modal vectors and are therefore themselves arbitrary in magnitude.

Inserting the first equation (7.16) into (7.2) and premultiplying by $\left[u\right]^T$ we obtain

$$\left[u\right]^T\left[m\right]\left[u\right]\{\ddot{q}\}+\left[u\right]^T\left[k\right]\left[u\right]\{q\}=\{0\},$$

or

$$\left[M\right]\{\ddot{q}\}+\left[K\right]\{q\}=\{0\}, \tag{7.20}$$

where the *modal mass matrix*

$$\left[M\right]=\left[u\right]^T\left[m\right]\left[u\right] \tag{7.21}$$

and the *modal stiffness matrix*

$$\left[K\right]=\left[u\right]^T\left[k\right]\left[u\right] \tag{7.22}$$

are diagonal matrices, due to the orthogonality of modal vectors.

It turns out that the linear transformation (7.16) uncouples the equations of motion (7.2). *The modal matrix (7.15) simultaneously diagonalizes the system mass and stiffness matrices.*

The *r*-th equation (7.18) has the same structure as that of an undamped single degree of freedom system. Its solution is a harmonic motion of the form

$$q_r(t)=C_r\cos\left(\omega_r t-\phi_r\right), \tag{7.23}$$

where

$$\omega_r^2=\frac{K_r}{M_r}=\frac{\{u\}_r^T\left[k\right]\{u\}_r}{\{u\}_r^T\left[m\right]\{u\}_r}\ . \tag{7.24}$$

The integration constants C_r and ϕ_r are determined from the initial conditions of the motion.

Inserting the modal coordinates (7.23) back into the transformation (7.16), we obtain the displacements in the configuration space

$$\{x\}=\sum_{r=1}^{n}C_r\{u\}_r\cos\left(\omega_r t-\phi_r\right). \tag{7.25}$$

Equation (7.25) indicates that the free vibration of a multi degree of freedom system consists of a superposition of *n* harmonic motions with frequencies equal to the system undamped natural frequencies.

It can be shown that, if the initial conditions are such that the mode $\{u\}_r$ is exclusively excited (e.g., zero initial velocity vector and initial displacement vector resembling the respective modal vector), the motion will resemble entirely that mode shape and the system will perform a synchronous harmonic motion of frequency ω_r.

7.2.1.5 Undamped forced vibration

In the case of forced vibrations, the equations of motion have the form

$$[m]\{\ddot{x}\}+[k]\{x\}=\{f\},\tag{7.26}$$

where $\{f\}$ is the forcing vector.

For harmonic excitation

$$\{f\}=\{\hat{f}\}\cos\omega t\tag{7.27}$$

the steady-state response is

$$\{x\}=\{\hat{x}\}\cos\omega t,\qquad \{q\}=\{\hat{q}\}\cos\omega t,\tag{7.28}$$

where a 'hat' above a letter denotes amplitude.

Substituting (7.27) and (7.28) into (7.26) we obtain

$$\left[-\omega^2[m]+[k]\right]\{\hat{x}\}=\{\hat{f}\}.\tag{7.29}$$

Using the coordinate transformation (7.16)

$$\{\hat{x}\}=[u]\{\hat{q}\}=\sum_{r=1}^{n}\{u\}_r\hat{q}_r\tag{7.30}$$

the *r*-th equation (7.29) becomes

$$\left(K_r-\omega^2 M_r\right)\hat{q}_r=\hat{F}_r\tag{7.31}$$

where the *modal force*

$$\hat{F}_r=\{u\}_r^{\mathrm{T}}\{\hat{f}\}.\tag{7.32}$$

The response in the modal space is

$$\hat{q}_r=\frac{\hat{F}_r}{K_r-\omega^2 M_r},\tag{7.33}$$

which substituted back into (7.30) gives the response in the configuration space

$$\{\hat{x}\} = \sum_{r=1}^{n} \{u\}_r \frac{\{u\}_r^T \{\hat{f}\}}{K_r - \omega^2 M_r} \tag{7.34}$$

or equivalently

$$\{\hat{x}\} = \sum_{r=1}^{n} \frac{\{u\}_r \{u\}_r^T}{\{u\}_r^T [k] \{u\}_r - \omega^2 \{u\}_r^T [m] \{u\}_r} \{\hat{f}\}. \tag{7.35}$$

The displacement at coordinate j produced by a harmonic force applied at coordinate ℓ is given by

$$\hat{x}_j = \sum_{r=1}^{n} \frac{u_{jr} u_{\ell r}}{K_r - \omega^2 M_r} \hat{f}_\ell \tag{7.36}$$

7.2.1.6 Excitation modal vectors

Although the response modal vectors $\{u\}_r$ are free vibration modes, i.e. they exist in the absence of any external forcing, it is possible to attach to each of them an *excitation modal vector* $\{\hat{\varXi}\}_r$, also called *principal mode of excitation*.

By definition, an *excitation modal vector* defines the distribution of external forcing able to maintain the vibration in an undamped natural mode at frequencies which are different from the corresponding natural frequency.

If an excitation $\{f\} = \{\hat{\varXi}\}_r e^{i\omega t}$ produces the response $\{x\} = \{u\}_r e^{i\omega t}$, then

$$\{\hat{\varXi}\}_r = \left([k] - \omega^2 [m] \right) \{u\}_r. \tag{7.37}$$

Premultiplying in (7.37) by $\{u\}_s^T$, and using (7.12) and (7.13), yields

$$\{u\}_s^T \{\hat{\varXi}\}_r = 0. \tag{7.38}$$

The work done by the forces from an excitation modal vector on the displacements of other modes of vibration is zero.

Equations (7.19) yield

$$\{u\}_r^T \{\hat{\varXi}\}_r = K_r - \omega^2 M_r = K_r \left(1 - \frac{\omega^2}{\omega_r^2} \right),$$

which for $\omega \neq \omega_r$ is different from zero.

7.2.2 Systems with proportional damping

The dynamic response of damped non-gyroscopic systems can be expressed in terms of the *real* normal modes of the associate conservative system if the damping is proportional to the system mass and/or stiffness matrix (Section 4.6), that is, if

$$[c] = \alpha[m] + \beta[k], \tag{7.39}$$

where α and β are constants. For this hypothetical form of damping, called *proportional damping* or *Rayleigh damping*, the coordinate transformation discussed previously, that diagonalizes the system mass and stiffness matrices, will also diagonalize the system damping matrix. Therefore we can transform the system coupled equations of motion into uncoupled equations describing single degree of freedom motions in modal coordinates.

There are also other conditions when the modal damping matrix becomes diagonal, e.g.

$$[c][m]^{-1}[k] = [k][m]^{-1}[c],$$

but they are only special cases which occur seldom [7.4, 7.5]. In practice the use of proportional damping is not based on the fulfilment of such a complicated condition, but on simply neglecting the off-diagonal elements of the modal damping matrix, i.e. neglecting the modal couplings due to the damping.

7.2.2.1 Viscous damping

Assume we have a viscously damped system, as represented by the following equation

$$[m]\{\ddot{x}\} + [c]\{\dot{x}\} + [k]\{x\} = \{f(t)\}, \tag{7.40}$$

where $[c]$ is the *damping matrix*, considered real, symmetric and positive definite, and $\{\dot{x}\}$ is the column *vector of velocities*.

We first solve the eigenvalue problem (7.4) associated with the undamped system. This gives the system's undamped natural frequencies and the real 'classical' mode shapes.

Then we apply the coordinate transformation (7.16) to equation (7.40) and premultiply by $[u]^T$ to obtain

$$[u]^T[m][u]\{\ddot{q}\} + [u]^T[c][u]\{\dot{q}\} + [u]^T[k][u]\{q\} = [u]^T\{f\}. \tag{7.41}$$

Due to the orthogonality properties of the real mode shapes, the *modal damping matrix*

$$[C] = [u]^T [c][u] = \alpha [u]^T [m][u] + \beta [u]^T [k][u] = \alpha [M] + \beta [K] \tag{7.42}$$

is diagonal.

The following orthogonality relations can be established (see 4.127)

$$\{u\}_s^T [c]\{u\}_r = 0. \qquad\qquad r \neq s \tag{7.43}$$

Equations (7.41) can be written

$$[M]\{\ddot{q}\} + [C]\{\dot{q}\} + [K]\{q\} = \{F\}, \tag{7.44}$$

where

$$\{F\} = [u]^T \{f\} \tag{7.45}$$

is the vector of *modal forces*.

The above equations are uncoupled. The *r*-th equation is

$$M_r \ddot{q}_r + C_r \dot{q}_r + K_r q_r = F_r, \tag{7.46}$$

where M_r and K_r are defined by (7.19) and

$$C_r = \{u\}_r^T [c]\{u\}_r, \qquad\qquad r = 1,2,...,n \tag{7.47}$$

are *modal damping* coefficients.

Equation (7.46) can be written

$$\ddot{q}_r + 2\zeta_r \omega_r \dot{q}_r + \omega_r^2 q_r = F_r / M_r, \tag{7.48}$$

where

$$\zeta_r = \frac{C_r}{2\sqrt{M_r K_r}} \tag{7.49}$$

is the *r*-th *modal damping ratio*, and ω_r is the *r*-th undamped natural frequency.

For free vibrations, equation (7.48) becomes

$$\ddot{q}_r + 2\zeta_r \omega_r \dot{q}_r + \omega_r^2 q_r = 0,$$

which, for $0 < \zeta_r < 1$, has solution of the form

$$q_r(t) = A_r e^{-\zeta_r \omega_r t} \cos\left(\sqrt{1-\zeta_r^2}\,\omega_r t - \phi_r\right). \tag{7.50}$$

For harmonic excitation and steady-state response (see Section 4.6.3.3), denote

$$\{f\}=\left\{\hat{f}\right\}e^{i\omega t}\,,\ \ \{x\}=\{\tilde{x}\}e^{i\omega t}\,, \tag{7.51}$$

$$\{F\}=\left\{\hat{F}\right\}e^{i\omega t}\,,\ \ \{q\}=\{\tilde{q}\}e^{i\omega t}\,, \tag{7.52}$$

$$\{\tilde{x}\}=\left[u\right]\{\tilde{q}\}=\sum_{r=1}^{n}\tilde{q}_{r}\{u\}_{r}\,, \tag{7.53}$$

where a 'hat' above a letter means real amplitude and a 'tilde' above a letter denotes complex amplitude.

Substitute (7.52) into equation (7.48) to obtain

$$\tilde{q}_{r}=\frac{\{u\}_{r}^{T}\left\{\hat{f}\right\}}{M_{r}\left(\omega_{r}^{2}-\omega^{2}+i\,2\zeta_{r}\omega\omega_{r}\right)} \tag{7.54}$$

then, from (7.53),

$$\{\tilde{x}\}=\sum_{r=1}^{n}\frac{\{u\}_{r}\{u\}_{r}^{T}}{M_{r}\left(\omega_{r}^{2}-\omega^{2}+i\,2\zeta_{r}\omega\,\omega_{r}\right)}\left\{\hat{f}\right\}. \tag{7.55}$$

Note that the dyadic product $\{u\}_{r}\{u\}_{r}^{\mathrm{T}}$ is a square matrix of order n.

7.2.2.2 Structural damping

The following discussion relates to the forced vibration of a system with structural (hysteretic) damping. The equation of motion to be considered is

$$\left[m\right]\{\ddot{x}\}+\frac{1}{\omega}\left[d\right]\{\dot{x}\}+\left[k\right]\{x\}=\left\{\hat{f}\right\}e^{i\omega t}\,, \tag{7.56}$$

where $\left[d\right]$ is the *structural damping matrix* (real, symmetric and positive definite).

For proportional structural damping, the following orthogonality relation holds

$$\{u\}_{s}^{T}\left[d\right]\{u\}_{r}=0\,. \qquad\qquad r\neq s \tag{7.57}$$

The modal structural damping coefficients are defined as

$$D_{r}=\{u\}_{r}^{T}\left[d\right]\{u\}_{r}\,. \qquad\qquad r=1,2,...,n \tag{7.58}$$

Assuming a solution of the form

$$\{x\}=\{\tilde{x}\}\mathrm{e}^{\mathrm{i}\omega t},\tag{7.59}$$

equation (7.56) becomes

$$\left[-\omega^2[m]+\mathrm{i}[d]+[k]\right]\{\tilde{x}\}=\{\hat{f}\}.\tag{7.60}$$

The coordinate transformation

$$\{\tilde{x}\}=[u]\{\tilde{p}\}=\sum_{r=1}^{n}\{u\}_r\,\tilde{p}_r\;,\tag{7.61}$$

where $\tilde{p}_r$ are *complex modal coordinates*, uncouples equations (7.60) which become

$$\left[-\omega^2[M]+\mathrm{i}[D]+[K]\right]\{\tilde{p}\}=[u]^T\{\hat{f}\}=\{\hat{F}\}\tag{7.62}$$

where

$$[D]=\mathrm{diag}\,[D_r].\tag{7.63}$$

The r-th equation is

$$\left(K_r-\omega^2 M_r+\mathrm{i}\,D_r\right)\tilde{p}_r=\hat{F}_r=\{u\}_r^T\{\hat{f}\}\tag{7.64}$$

with the solution

$$\tilde{p}_r=\frac{\{u\}_r^T\{\hat{f}\}}{K_r-\omega^2 M_r+\mathrm{i}\,D_r}\;.\tag{7.65}$$

Equation (7.61) gives the vector of complex displacement amplitudes

$$\{\tilde{x}\}=\sum_{r=1}^{n}\frac{\{u\}_r^T\{\hat{f}\}\{u\}_r}{K_r\left(1-\dfrac{\omega^2}{\omega_r^2}+\mathrm{i}\,g_r\right)}\tag{7.66}$$

where

$$g_r=\frac{D_r}{K_r},\qquad\qquad r=1,2,...,n\tag{7.67}$$

are the *modal structural damping factors*.

7.3 Complex damped natural modes

When a system contains non-proportional damping, i.e. when the damping matrix is no longer proportional to the mass and/or stiffness matrix, the previously used formulation of the eigenvalue problem will not yield mode shapes (eigenvectors) that decouple the system's equations of motion. In this case the system response can be expressed in terms of complex eigenvectors and complex eigenvalues [7.6].

7.3.1 Viscous damping

In the general case of viscous damping, the equations of motion can be decoupled irrespective of the type of external loading [7.7] but the derivation of the response equation is too long to be quoted here [7.8]. The corresponding eigenproblem is quadratic and its direct solution is rather complicated. Instead, a state space solution is generally adopted [7.9].

7.3.1.1 Quadratic eigenvalue problem

Consider again the equations of motion for the free vibrations of a viscously damped system

$$[m]\{\ddot{x}\}+[c]\{\dot{x}\}+[k]\{x\}=\{0\}, \qquad (7.68)$$

where $[m]$, $[c]$ and $[k]$ are symmetric mass, damping and stiffness matrices, respectively.

Seeking solutions of the form

$$\{x(t)\}=\{\psi\}e^{\lambda t}, \qquad (7.69)$$

we obtain a set of n homogeneous linear algebraic equations, representing the quadratic eigenvalue problem

$$\left(\lambda^{2}[m]+\lambda[c]+[k]\right)\{\psi\}=\{0\}. \qquad (7.70)$$

The condition to have non-trivial solutions

$$\det\left(\lambda^{2}[m]+\lambda[c]+[k]\right)=0 \qquad (7.71)$$

is the characteristic equation.

Equation (771) is an algebraic equation of order $2n$ in λ and its solution gives a set of $2n$ eigenvalues λ_r. Corresponding to each eigenvalue λ_r there exists an eigenvector $\{\psi\}_r$ having n components. They satisfy equation (7.70)

$$\left(\lambda_r^2 \left[m \right] + \lambda_r \left[c \right] + \left[k \right] \right) \{\psi\}_r = \{0\}. \qquad r = 1,...,2n \qquad (7.72)$$

The eigenvectors $\{\psi\}_r$ define the *complex* damped *modes of vibration*.

For a stable damped system, each of the eigenvalues will be either real and negative (for overdamped modes, i.e. modes for which an aperiodic decaying motion is obtained) or complex with a negative real part (for underdamped modes). If there are complex eigenvalues, they will occur in conjugate pairs

$$\lambda_r = -\sigma_r + \mathrm{i}\,\nu_r\,, \qquad\qquad \lambda_r^* = -\sigma_r - \mathrm{i}\,\nu_r\,. \qquad (7.73)$$

The imaginary part ν_r is called the *damped natural frequency* and the real part σ_r is called the *damping factor* (exponential decay rate).

For a pair of complex conjugate eigenvalues, the corresponding eigenvectors are also complex conjugates. The complex conjugates also satisfy equation (7.72). Therefore, if all $2n$ eigenvalues of an n-degree-of-freedom system are complex, which means that all modes are underdamped, these eigenvalues occur in conjugate pairs, and all eigenvectors will be complex and will also occur in conjugate pairs. This latter case will be considered in the following [7.10].

Premultiplying (7.72) by $\{\psi\}_s^T$ we obtain

$$\{\psi\}_s^T \left(\lambda_r^2 \left[m \right] + \lambda_r \left[c \right] + \left[k \right] \right) \{\psi\}_r = 0. \qquad\qquad r \neq s \quad (7.74)$$

Inverting indices and transposing we get

$$\{\psi\}_s^T \left(\lambda_s^2 \left[m \right] + \lambda_s \left[c \right] + \left[k \right] \right) \{\psi\}_r = 0. \qquad\qquad (7.75)$$

On subtracting (7.75) from (7.74) one finds, for $r \neq s$, if $\lambda_r \neq \lambda_s$,

$$\left(\lambda_r + \lambda_s \right) \{\psi\}_s^T \left[m \right] \{\psi\}_r + \{\psi\}_s^T \left[c \right] \{\psi\}_r = 0. \qquad\qquad (7.76,\ a)$$

Substituting the second term from (7.76, a) back in (7.72) we get

$$\lambda_r \lambda_s \{\psi\}_s^T \left[m \right] \{\psi\}_r - \{\psi\}_s^T \left[k \right] \{\psi\}_r = 0. \qquad\qquad (7.76,\ b)$$

The orthogonality conditions (7.76) are clearly more complicated than the previous set (7.12), (7.13) and (7.43). They only hold at the frequencies (eigenvalues) of the modes $\{\psi\}_r$ and $\{\psi\}_s$ to which they apply.

Once $\{\psi\}_r$ is known, λ_r can be obtained from equation (7.72) premultiplied by the transpose conjugate $\{\psi\}_r^H$

$$\lambda_r^2 \{\psi\}_r^H [m]\{\psi\}_r + \lambda_r \{\psi\}_r^H [c]\{\psi\}_r + \{\psi\}_r^H [k]\{\psi\}_r = 0 .$$

The matrix products in the above equation are entirely *real* and, by analogy with equations (7.19), (7.47) and (7.49), they may be denoted by $M_r^\Diamond$, $C_r^\Diamond$, and $K_r^\Diamond$, respectively. Hence

$$\lambda_r = -\frac{C_r^\Diamond}{2M_r^\Diamond} \pm \sqrt{\left(\frac{C_r^\Diamond}{2M_r^\Diamond}\right)^2 - \frac{K_r^\Diamond}{M_r^\Diamond}} = -\zeta_r \omega_r \pm i\,\omega_r \sqrt{1-\zeta_r^2} , \qquad (7.77)$$

where

$$\omega_r^2 = \frac{\{\psi\}_r^H [k]\{\psi\}_r}{\{\psi\}_r^H [m]\{\psi\}_r} , \qquad 2\zeta_r \omega_r = \frac{\{\psi\}_r^H [c]\{\psi\}_r}{\{\psi\}_r^H [m]\{\psi\}_r} .$$

After much tedious algebraic manipulation [7.8], the total response of the system can be expressed in the form

$$\{\tilde{x}\} = \sum_{r=1}^{n} \frac{[S_r + i\,\omega T_r]}{Z_r\left(\omega_r^2 - \omega^2 + i\,2\zeta_r \omega\,\omega_r\right)} \{\hat{f}\}, \qquad (7.78)$$

where $[S_r]$, $[T_r]$ and Z_r are real functions of $\{\psi\}_r$ and of the mass and damping. The terms of the series (7.78) are not quite the same as the usual single-degree-of-freedom frequency response function owing to the $i\,\omega[T_r]$ term in the numerator. Nevertheless, each term can be evaluated independently of all other terms, so the set of modes used in the analysis are uncoupled. Note that the frequency dependence in equation (7.78) is confined to the ω^2 and $i\,\omega$ terms. The $[S_r]$, $[T_r]$ and Z_r terms do not vary with frequency.

The analytical solution of the quadratic eigenvalue problem is not straightforward. A technique used to circumvent this is to reformulate the original second order equations of motion for an *n*-degree-of-freedom system into an equivalent set of 2*n* first order differential equations, known as 'Hamilton's canonical equations'. This method was introduced by W. J. Duncan in the 1930's [7.9] and more fully developed by K. A. Foss in 1958 [7.7].

7.3.1.2 State space formulation

In the terminology of control theory, the system response is defined by a 'state vector' of order 2*n*. In a typical mechanical system, its top *n* elements give

the displacements and its bottom n elements give the velocities at the n coordinates of the system (or vice-versa, depending how the equations are written).

The equations for the forced vibrations of a viscously damped system are

$$[m]\{\ddot{x}\}+[c]\{\dot{x}\}+[k]\{x\}=\{f(t)\}.\qquad(7.79)$$

If one adds to equation (7.79) the trivial equation

$$[m]\{\dot{x}\}-[m]\{\dot{x}\}=\{0\},$$

the resulting equations may be written in block matrix form

$$\begin{bmatrix}[c]&[m]\\[m]&[0]\end{bmatrix}\begin{Bmatrix}\{\dot{x}\}\\\{\ddot{x}\}\end{Bmatrix}+\begin{bmatrix}[k]&[0]\\[0]&-[m]\end{bmatrix}\begin{Bmatrix}\{x\}\\\{\dot{x}\}\end{Bmatrix}=\begin{Bmatrix}\{f\}\\\{0\}\end{Bmatrix}.$$

This matrix equation can also be written as

$$[A]\{\dot{y}\}+[B]\{y\}=\{N\},\qquad(7.80)$$

where

$$[A]=\begin{bmatrix}[c]&[m]\\[m]&[0]\end{bmatrix},\quad[B]=\begin{bmatrix}[k]&[0]\\[0]&-[m]\end{bmatrix},\quad\{N\}=\begin{Bmatrix}\{f\}\\\{0\}\end{Bmatrix}\qquad(7.81)$$

and

$$\{y\}=\begin{Bmatrix}\{x\}\\\{\dot{x}\}\end{Bmatrix}\qquad(7.82)$$

is called *state vector*.

The great advantage of this formulation lies in the fact that the matrices $[A]$ and $[B]$, both of order $2n$, are real and symmetric.

The solution of (7.80) by modal analysis follows closely the procedure used for undamped systems. Consider first the homogeneous equation where $\{N\}=\{0\}$:

$$[A]\{\dot{y}\}+[B]\{y\}=\{0\}.\qquad(7.83)$$

The solution of (7.83) is obtained by letting

$$\{y(t)\}=\{Y\}e^{\lambda t},\qquad(7.84)$$

where $\{Y\}$ is a vector consisting of $2n$ constant elements.

Equation (7.84), when introduced in (7.83), leads to the eigenvalue problem

$$-[B]\{Y\} = \lambda[A]\{Y\}, \tag{7.85}$$

which can be written in the standard form

$$[E]\{Y\} = \frac{1}{\lambda}\{Y\}, \tag{7.86}$$

where the *companion matrix*

$$[E] = -[B]^{-1}[A] = \begin{bmatrix} -[k]^{-1}[c] & -[k]^{-1}[m] \\ [I] & [0] \end{bmatrix}, \tag{7.87}$$

is real non-symmetric of order $2n$ and $[I]$ is the identity matrix of order n.

In general $[B]$ will have an inverse except when the stiffness matrix is singular, i.e. when rigid-body modes are present.

Equations (7.86) can be written

$$\left([E] - \frac{1}{\lambda}[I]\right)\{Y\} = \{0\}, \tag{7.88}$$

where $[I]$ is the identity matrix of order $2n$. They have non-trivial solutions if

$$\det\left([E] - \frac{1}{\lambda}[I]\right) = 0, \tag{7.89}$$

which is the characteristic equation.

Solution of equation (7.89) gives the $2n$ eigenvalues. Corresponding to each eigenvalue λ_r there is an eigenvector $\{Y\}_r$ having $2n$ components. There are $2n$ of these eigenvectors. They satisfy equation (7.85)

$$-[B]\{Y\}_r = \lambda_r[A]\{Y\}_r. \tag{7.90}$$

Consider the square complex matrix $[Y]$, constructed having the $2n$ eigenvectors $\{Y\}_r$ as columns, and the diagonal matrix $[\Lambda]$ whose diagonal elements are the complex eigenvalues

$$[Y] = \begin{bmatrix} \{Y\}_1 & \{Y\}_2 & \cdots & \{Y\}_{2n} \end{bmatrix}, \qquad [\Lambda] = \mathrm{diag}(\lambda_r). \tag{7.91}$$

Orthogonality of modes

The proof of the orthogonality of eigenvectors can proceed in the same way as for the undamped system.

Write equations (7.91) as

$$-[B][Y]=[A][Y][A]. \tag{7.92}$$

Premultiply equation (7.92) by $[Y]^T$ to obtain

$$-[Y]^T[B][Y]=[Y]^T[A][Y][A]. \tag{7.93}$$

Transpose both sides, remembering that $[A]$ and $[B]$ are symmetric and $[A]$ is diagonal, and obtain

$$-[Y]^T[B][Y]=[A][Y]^T[A][Y]. \tag{7.94}$$

From equations (7.93) and (7.94) it follows that

$$[Y]^T[A][Y][A]=[A][Y]^T[A][Y]. \tag{7.95}$$

Thus, if all the eigenvalues λ_r are different, then $[Y]^T[A][Y]$ is a diagonal matrix, and from equations (7.93) or (7.94) also $[Y]^T[B][Y]$ is diagonal.

We can denote

$$[Y]^T[A][Y]=[a], \quad [Y]^T[B][Y]=[b], \tag{7.96}$$

which means

$$\{Y\}_r^T[A]\{Y\}_r = a_r, \qquad \{Y\}_r^T[B]\{Y\}_r = b_r,$$

$$\{Y\}_s^T[A]\{Y\}_r = 0, \qquad \{Y\}_s^T[B]\{Y\}_r = 0, \quad r \neq s.$$

These orthogonality conditions state that both $[A]$ and $[B]$ are diagonalized by the same matrix $[Y]$. The diagonal matrices $[a]$ and $[b]$ can be viewed as normalization matrices related by

$$[A]=-[a]^{-1}[b]. \tag{7.97}$$

For a complex eigenvector only the relative magnitudes and the differences in phase angles are determined. The matrices $[a]$ and $[b]$ are complex. Hence the normalization of a complex eigenvector consists of not only

scaling all magnitudes proportionally, but rotating all components through the same angle in the complex plane as well.

The matrix $[Y]$ can be viewed as a transformation matrix which relates the system coordinates $\{y\}$ to a set of *modal coordinates* $\{z\}$

$$\{y\}=[Y]\{z\}. \tag{7.98}$$

Steady-state harmonic response

Consider now the non-homogeneous equations (7.80) and determine the steady-state response due to sinusoidal excitation $\{f\}=\{\hat{f}\}e^{i\omega t}$. For

$$\{N\}=\{\hat{N}\}e^{i\omega t},$$

$$\{y\}=\{\tilde{y}\}e^{i\omega t}, \qquad \{z\}=\{\tilde{z}\}e^{i\omega t}, \tag{7.99}$$

equation (7.80) can be written as

$$i\omega[A]\{\tilde{y}\}+[B]\{\tilde{y}\}=\{\hat{N}\}. \tag{7.100}$$

Substituting (7.98) into (7.100), premultiplying by $[Y]^T$ and taking into account the orthogonality properties (7.96), we obtain

$$\left(i\omega[a]+[b]\right)\{\tilde{z}\}=[Y]^T\{\hat{N}\}. \tag{7.101}$$

This is a set of $2n$ uncoupled equations, from which $\{\tilde{z}\}$ can be obtained as

$$\{\tilde{z}\}=\left(i\omega[a]+[b]\right)^{-1}[Y]^T\{\hat{N}\} \tag{7.102}$$

and $\{\tilde{y}\}$ from equation (7.98) as

$$\{\tilde{y}\}=[Y]\left(i\omega[a]+[b]\right)^{-1}[Y]^T\{\hat{N}\}. \tag{7.103}$$

Since in the underdamped case, in which we are primarily interested, all eigenvectors are complex and occur in conjugate pairs, based on (7.69) and (7.82), the matrix $[Y]$ can be partitioned as follows

$$[Y]=\begin{bmatrix}[\psi] & [\psi]^* \\ [\psi][\lambda] & [\psi]^*[\lambda]^*\end{bmatrix}, \tag{7.104}$$

where $[\lambda]$ is a diagonal matrix of order n, which contains the complex eigenvalues with positive imaginary part, and $[\psi]$ is called the *complex modal matrix* of order n, which contains the complex vectors of modal displacements, corresponding to the eigenvalues in $[\lambda]$. Matrices $[\psi]^*$ and $[\lambda]^*$ are the complex conjugates of $[\psi]$ and $[\lambda]$, respectively.

From equations (7.102), (7.103) and (7.104) it follows that the top n components of $\{\tilde{y}\}$ can be written as

$$\{\tilde{x}\} = \sum_{r=1}^{n} \left(\frac{\{\psi\}_r \{\psi\}_r^T}{i\omega\, a_r + b_r} + \frac{\{\psi\}_r^* \{\psi\}_r^H}{i\omega\, a_r^* + b_r^*} \right) \{\hat{f}\}, \qquad (7.105)$$

where a_r and a_r^* are respectively the top n and bottom n components of the diagonal matrix $[a]$, and b_r and b_r^* are respectively the top n and bottom n components of the diagonal matrix $[b]$.

As we know that

$$\lambda_r = -\frac{b_r}{a_r}, \qquad \lambda_r^* = -\frac{b_r^*}{a_r^*}, \qquad (7.106)$$

equation (7.105) can also be written

$$\{\tilde{x}\} = \sum_{r=1}^{n} \left(\frac{\{\psi\}_r \{\psi\}_r^T}{a_r \left(i\omega - \lambda_r\right)} + \frac{\{\psi\}_r^* \{\psi\}_r^H}{a_r^* \left(i\omega - \lambda_r^*\right)} \right) \{\hat{f}\}. \qquad (7.107)$$

Equation (7.107) represents the steady-state response to sinusoidal forces of amplitudes $\{\hat{f}\}$ in terms of the complex modes $\{\psi\}_r$ and $\{\psi\}_r^*$ $(r = 1, 2, .., n)$.

Comparison of complex and real modes

Complex modes $\{\psi\}_r$ can be represented in the complex plane by vector diagrams, in which each component of the modal vector is represented by a line of corresponding length and inclination, emanating from the origin. Figure 7.2 shows the 'compass plots' of two almost real modes
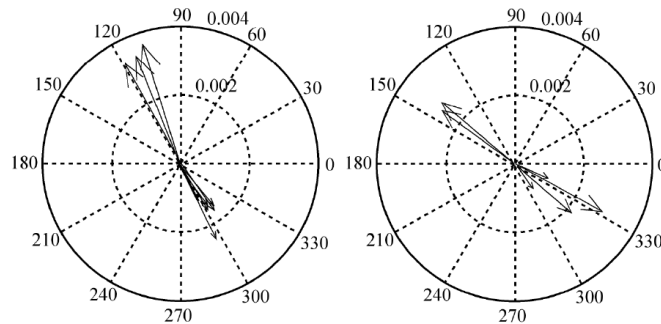
Fig. 7.2

In the case of non-proportional damping, the complex conjugate eigenvectors are of the form

$$\{\psi\}_r = \{\xi\}_r + \mathrm{i}\{\eta\}_r, \qquad \{\psi\}_r^* = \{\xi\}_r - \mathrm{i}\{\eta\}_r. \qquad (7.108)$$

The free vibration solution can be written as the sum of two complex eigensolutions associated with the pair of eigenvalues and eigenvectors

$$\{x(t)\}_r = \{\psi\}_r \mathrm{e}^{\lambda_r t} + \{\psi\}_r^* \mathrm{e}^{\lambda_r^* t} =$$
$$= \left(\{\xi\}_r + \mathrm{i}\{\eta\}_r\right)\mathrm{e}^{(-\sigma_r + \mathrm{i}\nu_r)t} + \left(\{\xi\}_r - \mathrm{i}\{\eta\}_r\right)\mathrm{e}^{(-\sigma_r - \mathrm{i}\nu_r)t}, \qquad (7.109)$$

$$\{x(t)\}_r = 2\mathrm{e}^{-\sigma_r t}\left(\{\xi\}_r \frac{\mathrm{e}^{\mathrm{i}\nu_r t} + \mathrm{e}^{-\mathrm{i}\nu_r t}}{2} + \mathrm{i}\{\eta\}_r \frac{\mathrm{e}^{\mathrm{i}\nu_r t} - \mathrm{e}^{-\mathrm{i}\nu_r t}}{2\mathrm{i}}\mathrm{i}\right) =$$
$$\qquad (7.109, a)$$
$$= 2\mathrm{e}^{-\sigma_r t}\left(\{\xi\}_r \cos \nu_r t - \{\eta\}_r \sin \nu_r t\right).$$

The motion is represented by the projection on the real axis of the components of rotating vectors. The contribution of the *r*-th mode to the motion of a point *j* can be expressed as

$$x_{jr}(t) = 2\mathrm{e}^{-\sigma_r t}\left(\xi_{jr} \cos \nu_r t - \eta_{jr} \sin \nu_r t\right), \qquad (7.110)$$

or

$$x_{jr}(t) = 2\mathrm{e}^{-\sigma_r t}\left|\psi_{jr}\right| \cos\left(\nu_r t - \phi_r - \theta_r\right), \qquad (7.110, a)$$

where

$$\theta_r = \tan^{-1}\frac{\eta_{jr}}{\xi_{jr}}.$$

The components of $\{x(t)\}_r$, plotted as vectors in the complex plane, rotate at the same angular velocity ν_r, and all decay in amplitude at the same rate σ_r, but each has a different phase angle in general, while the position relative to the other coordinates is preserved.

The motion is synchronous, but each coordinate reaches its maximum excursion at a different time than the others. However, the sequence in which the coordinates reach their maximum remains the same for each cycle. Furthermore, after one complete cycle, the coordinates are in the same position as at the beginning of the cycle. Therefore, the nodes (if they may be termed as such) continuously change their position during one cycle, but during the next cycle the pattern repeats itself. Of course, the maximum excursions decay exponentially from cycle to cycle.

Complex modes exhibit non-stationary zero-displacement points, at locations that change in space periodically, at the rate of vibration frequency.

In the case of proportional damping, the complex mode shape $\{\psi\}_r$ in equation (7.108) is replaced by a real mode $\{u\}_r$. The angle θ_r is either 0^0 or 180^0 depending on the sign of u_{jr}. The components of $\{x(t)\}_r$ in the complex plane rotate at the same angular velocity ν_r with amplitudes decaying exponentially with time and uniformly over the system, at a rate σ_r, but lie on the same line (they are in phase or 180^0 out of phase with each other). All points reach maximum departures from their equilibrium positions or become zero at the same instants.

Real modes exhibit stationary nodes.

7.3.2 Structural damping

Consider the equations of the forced harmonic motion of a system with structural damping

$$[m]\{\ddot{x}\}+([k]+i[d])\{x\}=\{\tilde{f}\}e^{i\omega t}, \qquad (7.111)$$

where $[m]$ and $[k+id]$ are symmetric matrices of order n, $\{\tilde{f}\}$ is a complex vector of excitation forces and

$$\{x\}=\{\tilde{x}\}e^{i\omega t}, \qquad (7.112)$$

where $\{\tilde{x}\}$ is the vector of complex displacement amplitudes.

Denoting $\omega^2=\lambda$, consider the homogeneous equation

$$[[k+id]-\lambda[m]]\{\tilde{x}\}=\{0\}. \qquad (7.113)$$

Equations of this sort for structural damping are usually regarded as being without physical meaning, because they are initially set up on the understanding that the motion they represent is forced harmonic. However, there is no objection [7.10] to defining *damped principal modes* $\{\phi\}_r$ of the system as being the eigenvectors of this equation, corresponding to which are complex eigenvalues λ_r satisfying the homogeneous equation

$$[[k+id]-\lambda_r[m]]\{\phi\}_r=\{0\}. \qquad (7.114)$$

In the following it is considered that the n eigenvalues are all distinct, and the corresponding modal vectors are linearly independent.

Mead [7.10] showed that such *complex damped modes* do have a clear physical significance if they are considered damped *forced* principal modes.

Indeed, let take $\{\tilde{f}\}$ to be a column of forces equal to $i g$ times the inertia forces corresponding to the harmonic vibration (7.112)

$$\{\tilde{f}\}=i g \omega^2 [m]\{\tilde{x}\}. \qquad (7.115)$$

Substituting (7.112) and (7.115) into equation (7.111) we find

$$\left[[k+i d]-\omega^2 (1+i g)[m]\right]\{\tilde{x}\}=\{0\}. \qquad (7.116)$$

Consider first the special case of proportional damping, in which $[d]=\beta[k]$. We then have

$$\left[(1+i\beta)[k]-\omega^2 (1+i g)[m]\right]\{\tilde{x}\}=\{0\} \qquad (7.117)$$

which is satisfied by $g=\beta$ and real vectors $\{\tilde{x}\}=\{u\}$.

By equating to zero both real and imaginary parts we have

$$\left([k]-\omega^2 [m]\right)\{u\}=\{0\} \qquad (7.118)$$

which yields the undamped principal modes and natural frequencies. Thus, if damping is distributed in proportion to the stiffness of the system, the undamped modes can be excited at their natural frequencies by forces which are equal to $i g$ times the inertia forces. The damped *forced* normal modes are then identical to the undamped normal modes.

When the damping matrix is *not* proportional to the stiffness matrix, there is no longer a unique value of β. Equation (7.117) must be retained in its general form, and the complex eigenvalues $\omega_r^2 (1+i g_r)$ and corresponding complex modal vectors $\{\phi\}_r$ satisfy the equation

$$\left[[k]-\omega_r^2 (1+i g_r)[m]+i[d]\right]\{\phi\}_r=\{0\}. \qquad (7.119)$$

It is easy to show that the modal vectors satisfy the orthogonality conditions

$$\begin{aligned} \{\phi\}_s^T [m]\{\phi\}_r &= 0, \\ \{\phi\}_s^T [k+i d]\{\phi\}_r &= 0, \end{aligned} \qquad r \neq s \qquad (7.120)$$

which do not contain the frequency of excitation or the natural frequencies of modes.

Equation (7.119) may be premultiplied by $\{\phi\}_r^T$ to show that

$$\overline{K}_r = \omega_r^2 \left(1 + i \, g_r\right) \overline{M}_r \, , \tag{7.121}$$

where

$$\begin{aligned}
\overline{M}_r &= \{\phi\}_r^T \left[m\right] \{\phi\}_r \, , \\
\overline{K}_r &= \{\phi\}_r^T \left[k + i \, d\right] \{\phi\}_r \, ,
\end{aligned} \qquad r = 1, 2, \dots, n \tag{7.122}$$

are the 'complex modal mass' and the 'complex modal stiffness', respectively.

As the n eigenvectors are linearly independent, any vector $\{\tilde{x}\}$ in their space can be expressed as linear combination of the eigenvectors

$$\{\tilde{x}\} = \left[\phi\right]\{w\} = \sum_{r=1}^{n} \{\phi\}_r w_r \, , \tag{7.123}$$

where w_r are *principal damped coordinates* and $\left[\phi\right]$ is a square matrix having the $\{\phi\}_r$'s as its columns.

Substituting (7.123) in (7.111) and using equations (7.120)-(7.122), we get

$$w_r = \frac{\{\phi\}_r^T \{\hat{f}\}}{\overline{K}_r - \omega^2 \overline{M}_r} \tag{7.124}$$

which has the form of a single degree of freedom frequency response function, resonating at the frequency ω_r with the loss factor g_r. The system vibrates in the complex mode $\{\phi\}_r$.

Hence, the solution of equation (7.111) is

$$\{\tilde{x}\} = \sum_{r=1}^{n} \frac{\{\phi\}_r^T \{\hat{f}\} \{\phi\}_r}{\overline{M}_r \left(\lambda_r - \omega^2\right)} \, , \tag{7.125}$$

in which

$$\lambda_r = \frac{\overline{K}_r}{\overline{M}_r} = \omega_r^2 \left(1 + i \, g_r\right). \tag{7.126}$$

The displacement at coordinate j produced by a harmonic force applied at coordinate ℓ is given by

$$\tilde{x}_j = \sum_{r=1}^{n} \frac{\phi_{jr} \phi_{\ell r}}{M_r \omega_r^2 \left(1 - \dfrac{\omega^2}{\omega_r^2} + i \, g_r\right)} \hat{f}_\ell \, . \tag{7.127}$$

Denoting the complex *modal constant*

$$A_{j\ell r} = \frac{\phi_{jr}\phi_{\ell r}}{M_r},$$

(7.128)

the complex displacement amplitude (7.127) becomes

$$\tilde{x}_j = \sum_{r=1}^{n} \frac{A_{j\ell r}}{\omega_r^2 - \omega^2 + \mathrm{i}\, g_r \omega_r^2}\, \hat{f}_\ell.$$

(7.129)

7.4 Forced monophase damped modes

Apart from the complex forced vibration modes discussed so far, there is another category of damped vibration modes defined as *real forced vibration modes*. These are described by real monophase vectors whose components are not constant, but frequency dependent, and represent the system response to certain monophase excitation forces. They are independent of the type of damping, viscous, structural, frequency dependent or a combination of these. At each undamped natural frequency, one of the monophase response vectors coincides with the corresponding real normal mode. The real forced vibration modes are particularly useful for the analysis of structures with frequency dependent stiffness and damping matrices. The existence of modes of this general type appears to have been pointed out first by Fraeijs de Veubeke [7.11], [7.12].

7.4.1 Analysis based on the dynamic stiffness matrix

For harmonic excitation, the equations of motion (7.40) and (7.56) of a system with combined viscous and structural damping can be written

$$[m]\{\ddot{x}\} + \left([c] + \frac{1}{\omega}[d]\right)\{\dot{x}\} + [k]\{x\} = \{\hat{f}\}e^{\mathrm{i}\omega t},$$

(7.130)

where the system square matrices are considered real, symmetric and positive definite, and $\{\hat{f}\}$ is a real forcing vector.

Assuming a steady-state response (7.112)

$$\{x(t)\} = \{\tilde{x}\}e^{\mathrm{i}\omega t},$$

where $\{\tilde{x}\}$ is a vector of complex displacement amplitudes, equation (7.130) becomes

$$\left[\left[k\right]-\omega^2\left[m\right]+\mathrm{i}\left(\omega\left[c\right]+\left[d\right]\right)\right]\{\tilde{x}\}=\{\hat{f}\}$$

or

$$\left[Z(\mathrm{i}\omega)\right]\{\tilde{x}\}=\{\hat{f}\}, \qquad (7.131)$$

where $\left[Z(\mathrm{i}\omega)\right]$ is referred to as the *dynamic stiffness matrix*.

This can be written

$$\left[Z(\mathrm{i}\omega)\right]=\left[Z_R(\omega)\right]+\mathrm{i}\left[Z_I(\omega)\right], \qquad (7.132)$$

where the real part and the imaginary part are given by

$$\left[Z_R(\omega)\right]=\left[k\right]-\omega^2\left[m\right], \qquad \left[Z_I(\omega)\right]=\omega\left[c\right]+\left[d\right].$$

The same formulation applies in the case of frequency dependent stiffness and damping matrices

$$\left[Z_R(\omega)\right]=\left[k(\omega)\right]-\omega^2\left[m\right], \quad \left[Z_I(\omega)\right]=\omega\left[c(\omega)\right]+\left[d\right],$$

and, in fact, is independent of the type of damping.

Following the development in [7.13], it will be enquired whether there are (real) forcing vectors $\{\hat{f}\}$ such that the complex displacements in $\{\tilde{x}\}$ are all in phase, though not necessarily in phase with the force. For such a set of displacements, the vector $\{\tilde{x}\}$ will be of the form

$$\{\tilde{x}\}=\{\hat{x}\}\mathrm{e}^{-\mathrm{i}\theta}, \qquad (7.133)$$

where $\{\hat{x}\}$ is an unknown vector of real amplitudes and θ is an unknown phase lag. Substitution of this trial solution into equation (7.131) yields

$$\left[Z_R+\mathrm{i}Z_I\right]\{\hat{x}\}(\cos\theta-\mathrm{i}\sin\theta)=\{\hat{f}\}.$$

Separating the real and imaginary parts, we obtain

$$\left(\left[Z_I\right]\cos\theta-\left[Z_R\right]\sin\theta\right)\{\hat{x}\}=\{0\},$$
$$\left(\left[Z_R\right]\cos\theta+\left[Z_I\right]\sin\theta\right)\{\hat{x}\}=\{\hat{f}\}, \qquad (7.134)$$

or

$$\left[Z_R\right]\{\hat{x}\}=\cos\theta\{\hat{f}\},$$
$$\left[Z_I\right]\{\hat{x}\}=\sin\theta\{\hat{f}\}. \qquad (7.135)$$

Denoting

$$\lambda = \frac{\cos\theta}{\sin\theta} = \tan^{-1}\theta\,, \tag{7.136}$$

equations (7.134) become

$$\left(\left[Z_R\right] - \lambda\left[Z_I\right]\right)\{\hat{x}\} = \{0\},$$
$$\left(\left[Z_R\right]\lambda + \left[Z_I\right]\right)\{\hat{x}\} = \frac{1}{\sin\theta}\{\hat{f}\}. \tag{7.137}$$

Denoting

$$\sin\theta = \frac{1}{\sqrt{1+\lambda^2}}\,, \qquad \cos\theta = \frac{\lambda}{\sqrt{1+\lambda^2}}\,, \tag{7.138}$$

we obtain

$$\left[Z_R\right]\{\hat{x}\} = \lambda\left[Z_I\right]\{\hat{x}\}\,, \tag{7.139}$$

$$\lambda\left[Z_R\right]\{\hat{x}\} + \left[Z_I\right]\{\hat{x}\} = \sqrt{1+\lambda^2}\{\hat{f}\}. \tag{7.140}$$

Provided that $\cos\theta \neq 0$, $\lambda \neq 0$, equation (7.139) has the form of a frequency-dependent generalized symmetric eigenvalue problem. The eigenvalues λ are solutions of the algebraic equation

$$\det\left(\left[Z_R\right] - \lambda\left[Z_I\right]\right) = 0\,. \tag{7.141}$$

For each root λ_r, there is a corresponding modal vector $\{\varphi\}_r$ satisfying the equation

$$\left(\left[Z_R\right] - \lambda_r\left[Z_I\right]\right)\{\varphi\}_r = \{0\}. \tag{7.142}$$

Both λ_r and $\{\varphi\}_r$ are real and frequency dependent.

Substituting λ_r and $\{\varphi\}_r$ into equation (7.140) we obtain

$$\lambda_r\left[Z_R\right]\{\varphi\}_r + \left[Z_I\right]\{\varphi\}_r = \sqrt{1+\lambda_r^2}\{\gamma\}_r\,. \tag{7.143}$$

where $\{\gamma\}_r$ is the corresponding force vector required to produce $\{\varphi\}_r$.

Vectors $\{\varphi\}_r$, referred to as *monophase response modal vectors*, represent a specific type of motion in which all coordinates execute synchronous motions, having the *same* phase shift θ_r with respect to the force vectors. Their spatial shape varies with the frequency. They are produced only by the external forcing defined by the *monophase excitation modal vectors* $\{\gamma\}_r$ derived from equation (7.143).

Mode labeling

Consider now the way in which the phase angles θ_r and the vectors $\{\varphi\}_r$ are labeled. When equation (7.141) was derived from equation (7.139), it was assumed that $\cos\theta \neq 0$. If, however, $\cos\theta = 0$, equation (7.139) becomes

$$[Z_R]\{\varphi\} = 0, \qquad \left([k] - \omega^2[m]\right)\{\varphi\} = \{0\}, \qquad (7.144)$$

and the condition for $\{\varphi\}$ to be non-trivial is that

$$\det\left([k] - \omega^2[m]\right) = 0. \qquad (7.145)$$

This means that ω must be an undamped natural frequency. If then $\omega = \omega_s$, the $\{\varphi\}$ mode corresponding to this value of ω and the solution $\cos\theta = 0$ may be identified with the *s*-th real normal mode $\{u\}_s$. If the θ solution and the corresponding value of $\{\varphi\}$ are labeled θ_s and $\{\varphi\}_s$, respectively, then one may write

$$\theta_s = \frac{\pi}{2}, \qquad \{\varphi\}_s = \{u\}_s, \quad \text{when} \quad \omega = \omega_s. \qquad (7.146)$$

For this value of ω there will also be $n-1$ other $\{\varphi\}_r$ modes corresponding to the remaining $n-1$ roots λ_r of equation (7.141).

Equation (7.146) may be used to give a consistent way of labeling the θ and the $\{\varphi\}$ for values of ω other than the undamped natural frequencies [7.13]. Each of the roots λ of equation (7.141) is a continuous function of ω, so that $\lambda = \lambda(\omega)$, and $\theta = \theta(\omega)$. Equation (7.142) shows that

$$\lambda_r = \tan^{-1}\theta_r = \frac{\{\varphi\}_r^T[Z_R]\{\varphi\}_r}{\{\varphi\}_r^T[Z_I]\{\varphi\}_r}. \qquad (7.147)$$

When $\omega = 0$, θ_r is a small positive angle. As ω grows and approaches ω_1, one of the roots $\lambda(\omega)$ will tend to zero, and $\theta(\omega)$ will approach the value $\pi/2$; let this angle be labeled $\theta_1(\omega)$.

As ω is increased, $\theta_1(\omega)$ grows larger than $\pi/2$ and when it is increased indefinitely, $\theta_1(\omega)$ will approach the value π. The remaining $n-1$ angles $\theta_s(\omega)$ may be labeled in a similar way: $\theta_s(\omega)$ is that phase shift which has the value $\pi/2$ when $\omega = \omega_s$. The angles θ_r are referred to as *characteristic phase lags*.

The forced modes are labeled accordingly. At any frequency ω_s, the shape of the *s*-th forced mode is given by the solution $\{\varphi(\omega)\}_s$ of

$$\left(\left[Z_R \right] - \tan^{-1}\theta_s \left[Z_I \right] \right)\{\varphi\}_s = \{0\}. \qquad (7.148)$$

Thus, $\{\varphi\}_s$ is the forced mode which coincides with $\{u\}_s$ when $\omega = \omega_s$.

Orthogonality

It may be shown that the modal vectors satisfy the orthogonality conditions

$$\{\varphi\}_s^T \left[Z_R \right] \{\varphi\}_r = 0,$$
$$\{\varphi\}_s^T \left[Z_I \right] \{\varphi\}_r = 0. \qquad r \neq s \qquad (7.149)$$

These conditions imply that

$$\{\varphi\}_s^T \{\gamma\}_r = \{\varphi\}_r^T \{\gamma\}_s = 0, \qquad r \neq s \qquad (7.150)$$

hence an excitation modal vector $\{\gamma\}_r$ introduces energy into the system only in the corresponding response modal vector $\{\varphi\}_r$.

Damped modal coordinates

If a square matrix $\left[\varphi \right]$ is introduced, which has the monophase response modal vectors as columns

$$\left[\varphi \right] = \left[\{\varphi\}_1 \ \{\varphi\}_2 \ \cdots \ \{\varphi\}_n \right], \qquad (7.151)$$

then the motion of the system can be expressed in terms of the component motions in each of the forced modes $\{\varphi\}_r$. Thus the vector of complex displacements $\{\tilde{x}\}$ may be written

$$\{\tilde{x}\} = \left[\varphi \right]\{\tilde{p}\} = \sum_{r=1}^{n}\{\varphi\}_r \tilde{p}_r, \qquad (7.152)$$

where the multipliers $\tilde{p}_r$ are the *damped modal coordinates*. The linear transformation (7.152) is used to uncouple the equations of motion (7.130).

Steady state response

Substituting (7.152) into (7.131) and premultiplying by $\left[\varphi \right]^T$ we obtain

$$\left[\varphi \right]^T \left[Z(i\omega) \right] \left[\varphi \right]\{\tilde{p}\} = \left[\varphi \right]^T \{\hat{f}\}, \qquad (7.153)$$

or

$$\left(\left[z_R(\omega) \right] + i\left[z_I(\omega) \right] \right) \left[\varphi \right]\{\tilde{p}\} = \left[\varphi \right]^T \{\hat{f}\}, \qquad (7.154)$$

where, due to the orthogonality relations (7.149),

$$[z_R(\omega)] = [\varphi]^T [Z_R][\varphi], \quad [z_I(\omega)] = [\varphi]^T [Z_I][\varphi], \qquad (7.155)$$

are both diagonal matrices.

The solution of the *r*-th uncoupled equation (7.154) is

$$\tilde{p}_r = \frac{\{\varphi\}_r^T \{\hat{f}\}}{z_{R_r} + \mathrm{i}\, z_{I_r}} . \qquad (7.156)$$

Substituting the damped modal coordinates (7.156) into (7.152) we obtain the solution in terms of the monophase response modal vectors

$$\{\tilde{x}\} = \sum_{r=1}^{n} \frac{\{\varphi\}_r^T \{\hat{f}\}\{\varphi\}_r}{\{\varphi\}_r^T \left([k] - \omega^2[m]\right)\{\varphi\}_r + \mathrm{i}\,\{\varphi\}_r^T \left(\omega[c] + [d]\right)\{\varphi\}_r} . \qquad (7.157)$$

Normalization

The response modal vectors $\{\varphi\}_r$ can be normalized to unit length

$$\{\varphi\}_r^T \{\varphi\}_r = 1. \qquad (7.158)$$

It is convenient to normalize also the excitation modal vectors $\{\gamma\}_r$ to unit length

$$\{\gamma\}_r^T \{\gamma\}_r = 1. \qquad (7.159)$$

Next, a new set of 'phi' vectors $\{\Phi\}_r$ is introduced,

$$\{\Phi\}_r = \sqrt{Q_r}\,\{\varphi\}_r \qquad (7.160)$$

using the frequency dependent scaling factors [7.14]

$$Q_r = \frac{\sin\theta_r}{\{\varphi\}_r^T [Z_I]\{\varphi\}_r} , \qquad (7.161)$$

and a new set of 'gamma' vectors $\{\Gamma\}_r$

$$\{\Gamma\}_r = \sqrt{Q_r}\,\{\gamma\}_r , \qquad (7.162)$$

so that

$$\{\Gamma\}_s^T \{\Phi\}_r = \{\Phi\}_s^T \{\Gamma\}_r = \delta_{rs} , \qquad (7.163)$$

where δ_{rs} is the Kronecker delta. The two sets of frequency dependent monophase modal vectors form a bi-orthogonal system. While the response vectors are right

eigenvectors of the matrix pencil $\left(\left[Z_R \right], \left[Z_I \right] \right)$, the excitation vectors are left eigenvectors of that pencil.

Equation (7.163) implies

$$\{\gamma\}_r^T \{\varphi\}_r = \frac{1}{Q_r} . \qquad (7.164)$$

Equations (7.135) become

$$\left[Z_R \right] \{\Phi\}_r = \cos \theta_r \{\Gamma\}_r ,$$
$$\left[Z_I \right] \{\Phi\}_r = \sin \theta_r \{\Gamma\}_r . \qquad (7.165)$$

which, using (7.163), can be written

$$\{\Phi\}_r^T \left[Z_R \right] \{\Phi\}_r = \cos \theta_r ,$$
$$\{\Phi\}_r^T \left[Z_I \right] \{\Phi\}_r = \sin \theta_r . \qquad (7.166)$$

Introducing the square modal matrix $\left[\Phi \right]$, which has the normalized monophase response modal vectors as columns

$$\left[\Phi \right] = \left[\{\Phi\}_1 \ \{\Phi\}_2 \ \cdots \ \{\Phi\}_n \right], \qquad (7.167)$$

equations (7.166) yield

$$\left[\Phi \right]^T \left[Z_R \right] \left[\Phi \right] = \left[\cos\theta_r \right], \qquad (7.168, a)$$

$$\left[\Phi \right]^T \left[Z_I \right] \left[\Phi \right] = \left[\sin\theta_r \right], \qquad (7.168, b)$$

and

$$\left[\Phi \right]^T \left[Z \right] \left[\Phi \right] = \left[e^{i\theta_r} \right]. \qquad (7.169)$$

The dynamic stiffness matrix is given by

$$\left[Z \right] = \left[\Phi \right]^{-T} \left[e^{i\theta_r} \right] \left[\Phi \right]^{-1} . \qquad (7.170)$$

Its inverse, the *dynamic flexibility* or *frequency response function* (FRF) matrix, is

$$\left[Z \right]^{-1} = \left[H \right] = \left[\Phi \right] \left[e^{-i\theta_r} \right] \left[\Phi \right]^T . \qquad (7.171)$$

The FRF matrix has the following modal decomposition

$$\left[H \right] = \sum_{r=1}^{n} e^{-i\theta_r} \{\Phi\}_r \{\Phi\}_r^T \qquad (7.172)$$

or, in terms of the unscaled vectors

$$[H] = \sum_{r=1}^{n} Q_r \, \mathrm{e}^{-\mathrm{i}\theta_r} \{\varphi\}_r \{\varphi\}_r^T .$$ (7.173)

Example 7.1

The four degree-of-freedom lumped parameter system from Fig. 7.3 is used to illustrate some of the concepts presented so far. The system parameters are given in appropriate units $\left(\mathrm{kg},\ \mathrm{N/m},\ \mathrm{Ns/m}\right)$.

The mass, stiffness and viscous damping matrices are [7.15], respectively,

$$[m] = \mathrm{diag}\begin{pmatrix} 3 & 2 & 1 & 2 \end{pmatrix},$$

$$[k] = \begin{bmatrix} 200 & -60 & -80 & -40 \\ & 340 & -120 & -50 \\ & & 800 & -200 \\ \mathrm{sym} & & & 1300 \end{bmatrix}, \ [c] = \begin{bmatrix} 3 & -0.9 & -0.6 & -1.0 \\ & 3 & -0.8 & -0.5 \\ & & 3 & -0.6 \\ \mathrm{sym} & & & 2.5 \end{bmatrix}.$$

The system has non-proportional damping.
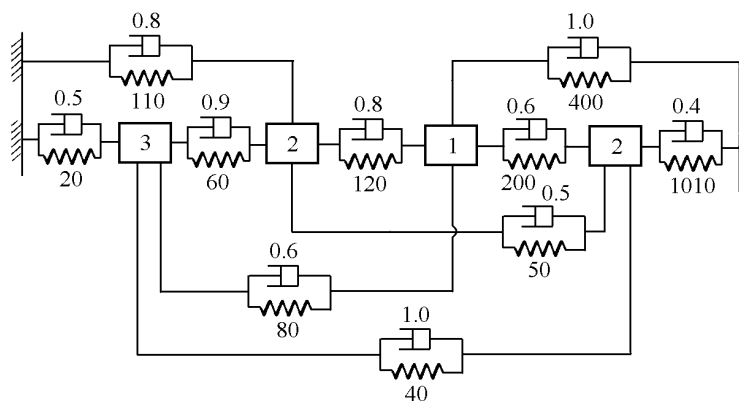
Fig. 7.3

The undamped natural frequencies $\omega_r/2\pi$ and the real normal modes $\{u\}_r$ (of the associated conservative system) are given in Table 7.1.

Table 7.1. Modal data of the 4-DOF undamped system

Mode	1	2	3	4
ω_r , Hz	1.1604	2.0450	3.8236	4.7512
Modal vector	1 0.37067 0.18825 0.08058	-0.26262 1 0.18047 0.07794	-0.06027 -0.17236 0.78318 1	-0.02413 -0.06833 1 -0.40552

The real normal modes are illustrated in Fig. 7.4.
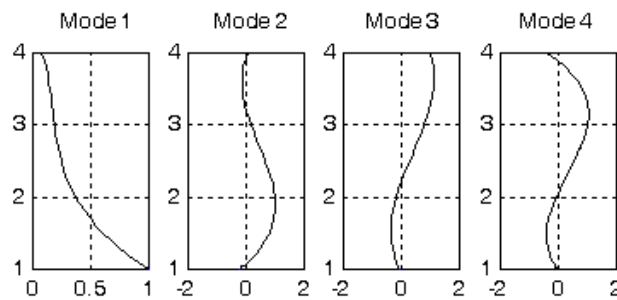
Fig. 7.4

The damped natural frequencies, the modal damping ratios and the magnitude and phase angle of the complex mode shapes are given in Table 7.2.

Table 7.2. Modal data of the 4-DOF damped system

Mode	1		2		3		4	
ω_r , Hz	1.1598		2.0407		3.8228		4.7423	
ζ_r	0.0479		0.0606		0.0313		0.0500	
Modal vector	1 0.37067 0.18825 0.08058	0 3.66 3.52 7.33	0.26473 1 0.18047 0.07794	-173.3 0 2.06 3.88	0.06210 0.17322 0.77950 1	-167.3 -174.4 -6.86 0	0.02378 0.06882 1 0.40241	-178.5 -171.9 0 172.29
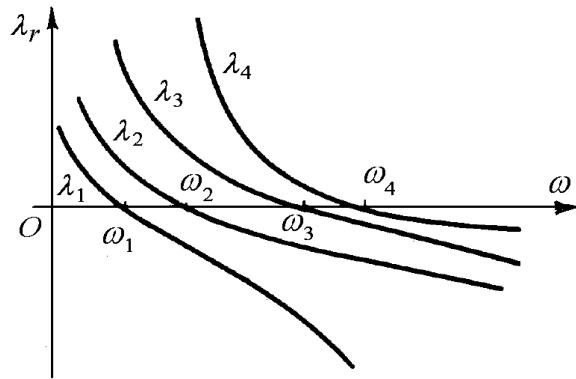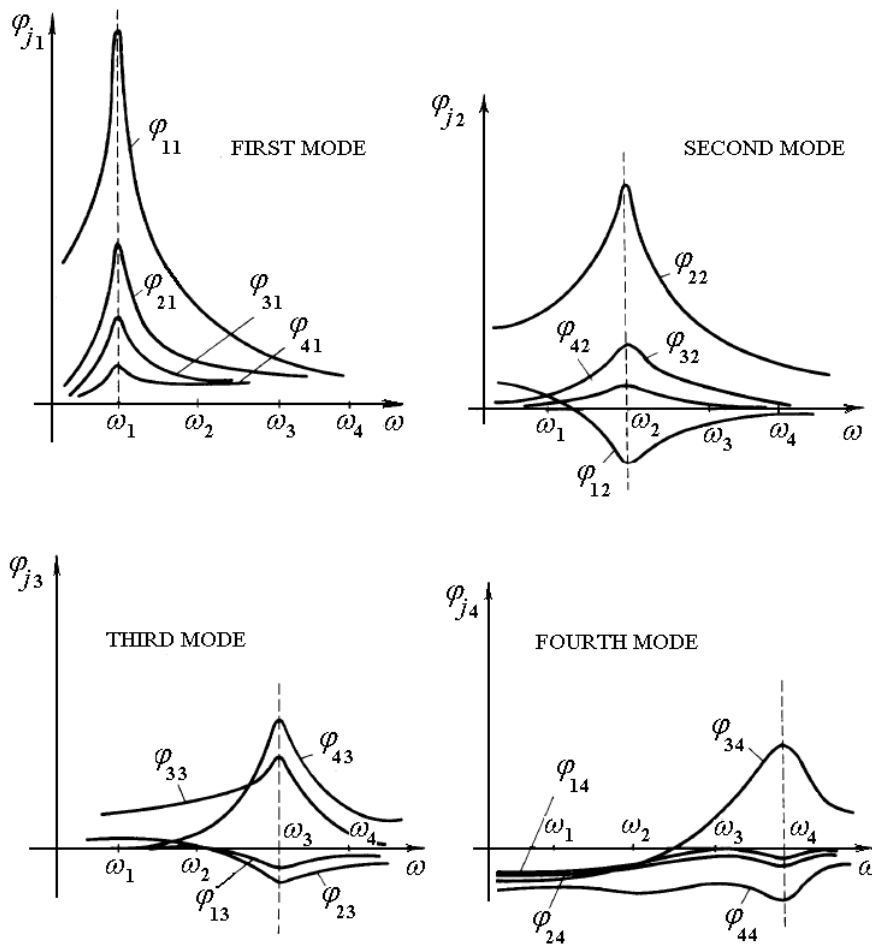
Fig. 7.5

Fig. 7.6 (from [7.16])
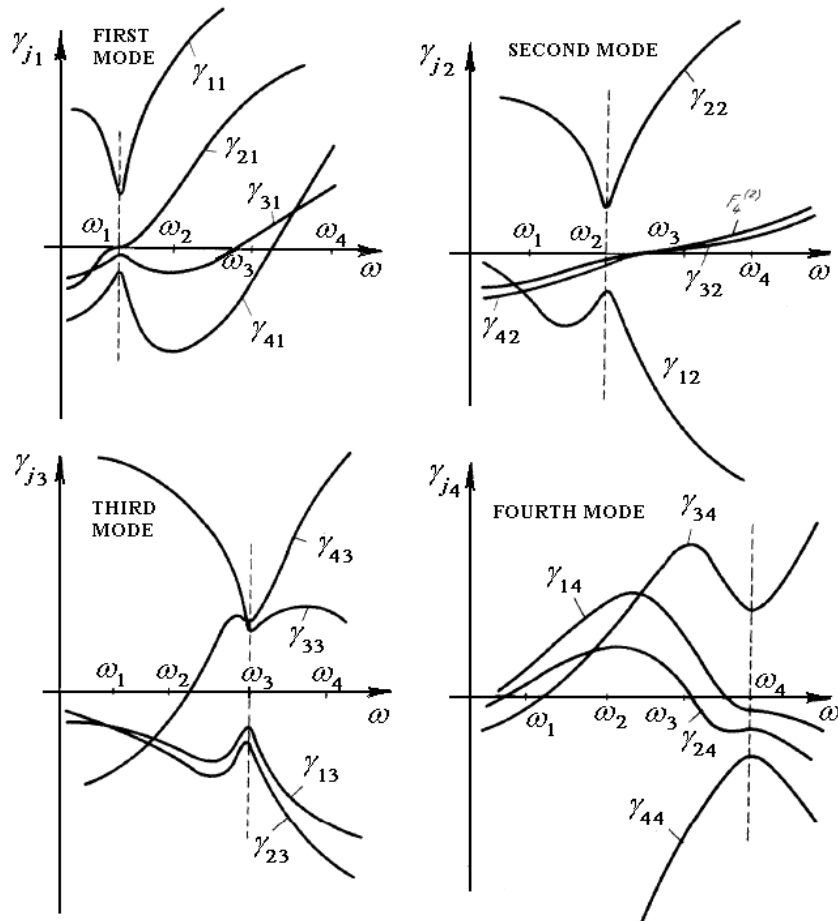
Fig. 7.7 (from [7.16])
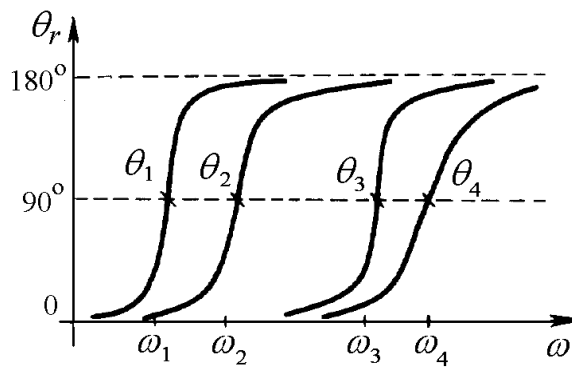
Fig. 7.8

The real eigenvalues of the generalized eigenproblem (7.142) are plotted versus frequency in Fig. 7.5. The monophase modal *response* vectors are illustrated in Fig. 7.6. The monophase modal *excitation* vectors are presented in Fig. 7.7. The characteristic phase lags are shown as a function of frequency in Fig. 7.8.

7.4.2 Analysis based on the dynamic flexibility matrix

The steady state response to harmonic excitation (7.131) has the form

$$\{\tilde{x}\} = \left[H(\mathrm{i}\omega)\right]\{\hat{f}\}, \tag{7.174}$$

where the *frequency response function* (FRF) *matrix* $\left[H(\mathrm{i}\omega)\right]$, also called the *dynamic flexibility matrix*, is the inverse of the dynamic stiffness matrix

$$\left[H(\mathrm{i}\omega)\right] = \left[Z(\mathrm{i}\omega)\right]^{-1} = \left[H_R(\omega)\right] + \mathrm{i}\left[H_I(\omega)\right]. \tag{7.175}$$

The elements of the FRF matrix are measurable quantities. The element $h_{j\ell}$ is the dynamic influence coefficient, defining the response at coordinate j due to unit harmonic excitation applied at coordinate ℓ.

The complex displacement amplitude can be written as

$$\{\tilde{x}\} = \{x_R\} + \mathrm{i}\{x_I\}, \tag{7.176}$$

where the in-phase portion of the response is

$$\{x_R\} = \left[H_R\right]\{\hat{f}\}, \tag{7.177}$$

and the out-of-phase portion is

$$\{x_I\} = \left[H_I\right]\{\hat{f}\}. \tag{7.178}$$

The following useful relationships can be established between the dynamic stiffness matrix and the FRF matrix

$$\begin{aligned}
\left[Z_R(\omega)\right] &= \left[H^*(\mathrm{i}\omega)\right]^{-1}\left[H_R(\omega)\right]\left[H(\mathrm{i}\omega)\right]^{-1}, \\
\left[Z_I(\omega)\right] &= -\left[H^*(\mathrm{i}\omega)\right]^{-1}\left[H_I(\omega)\right]\left[H(\mathrm{i}\omega)\right]^{-1}.
\end{aligned} \tag{7.179}$$

It has been shown that, at each forcing frequency ω, there are n monophase excitation vectors $\{\gamma\}_r$ which produce coherent-phase displacements of the form

$$\{\tilde{x}\} = \{\varphi\}_r\, \mathrm{e}^{-\mathrm{i}\theta_r}, \tag{7.180}$$

having the same phase lag θ_r with respect to the excitation, defining real monophase response vectors $\{\varphi\}_r$.

To see whether such a property may hold, a trial solution of equation (7.174) is sought of the form (7.133)

$$\{\tilde{x}\} = \{\hat{x}\} e^{-i\theta},\tag{7.181}$$

where $\{\hat{x}\}$ has real elements and the phase shift θ is common to all coordinates. This is equivalent to considering that the in-phase portion of response $\{x_R\}$ is proportional to the out-of-phase portion $\{x_I\}$, i.e.

$$\{x_R\} = -\lambda\{x_I\},\tag{7.182}$$

where

$$\lambda = \tan^{-1}\theta.\tag{7.183}$$

Substitution of (7.181) into (7.174) yields

$$\{\hat{x}\} = [H_R + iH_I](\cos\theta + i\sin\theta)\{\hat{f}\}.\tag{7.184}$$

Considering the real and imaginary parts separately, one finds

$$\begin{aligned}([H_R]\cos\theta - [H_I]\sin\theta)\{\hat{f}\} &= \{\hat{x}\},\\ ([H_I]\cos\theta + [H_R]\sin\theta)\{\hat{f}\} &= \{0\},\end{aligned}\tag{7.185}$$

or

$$\begin{aligned}[H_R]\{\hat{f}\} &= \cos\theta\{\hat{x}\},\\ [-H_I]\{\hat{f}\} &= \sin\theta\{\hat{x}\}.\end{aligned}\tag{7.186}$$

Dividing by $\sin\theta$ we obtain

$$\begin{aligned}[H_R]\{\hat{f}\} &= \lambda[-H_I]\{\hat{f}\},\\ ([H_R]\lambda - [H_I])\{\hat{f}\} &= \sqrt{1+\lambda^2}\{\hat{x}\},\end{aligned}\tag{7.187}$$

where

$$\lambda = \frac{\cos\theta}{\sin\theta} = \tan^{-1}\theta,\quad \sin\theta = \frac{1}{\sqrt{1+\lambda^2}},\quad \cos\theta = \frac{\lambda}{\sqrt{1+\lambda^2}}.\tag{7.188}$$

The first equation (7.187) is homogeneous. Provided that $\cos\theta \neq 0$, $\lambda \neq 0$, this equation has the form of a frequency-dependent generalized symmetric eigenvalue problem.

The condition for $\{\hat{f}\}$ to be non-trivial is

$$\det([H_R] - \lambda[-H_I]) = 0.$$

There are n eigenvalues $\lambda_r(\omega)$, solutions of the above algebraic equation. For each root λ_r there is an *excitation modal vector* $\{\gamma\}_r$ satisfying the equation

$$\left([H_R] - \lambda_r [-H_I]\right)\{\gamma\}_r = \{0\}. \tag{7.189}$$

The eigenvalues are given by

$$\lambda_r = \tan^{-1}\theta_r = \frac{\{\gamma\}_r^T [H_R]\{\gamma\}_r}{\{\gamma\}_r^T [-H_I]\{\gamma\}_r}. \tag{7.190}$$

Both the eigenvalues λ_r and the excitation eigenvectors $\{\gamma\}_r$ are real and frequency dependent. Different sets of λ_r's and $\{\gamma\}_r$'s are obtained for each frequency ω.

Substituting λ_r and $\{\gamma\}_r$ into the second equation (7.187), the *response modal vectors* $\{\varphi\}_r$ are obtained from

$$\lambda [H_R]\{\gamma\}_r + [-H_I]\{\gamma\}_r = \sqrt{1+\lambda_r^2}\,\{\varphi\}_r, \tag{7.191}$$

where $\{\varphi\}_r$ is the response vector produced by the monophase excitation $\{\gamma\}_r$.

Equations (7.186) can also be written

$$\begin{aligned}[H_R]\{\gamma\}_r &= \cos\theta_r\,\{\varphi\}_r,\\ [-H_I]\{\gamma\}_r &= \sin\theta_r\,\{\varphi\}_r\,.\end{aligned} \tag{7.192}$$

The excitation modal vectors satisfy the orthogonality relations

$$\begin{aligned}\{\gamma\}_s^T [H_R]\{\gamma\}_r &= 0,\\ \{\gamma\}_s^T [H_I]\{\gamma\}_r &= 0.\end{aligned} \qquad r \neq s \tag{7.193}$$

These conditions imply that

$$\{\varphi\}_s^T \{\gamma\}_r = \{\varphi\}_r^T \{\gamma\}_s = 0, \qquad\qquad r \neq s \tag{7.194}$$

hence an excitation modal vector $\{\gamma\}_r$ develops energy only in the corresponding response modal vector $\{\varphi\}_r$.

Response at the undamped natural frequencies

If $\lambda = 0$, then $\cos\theta = 0$, $\theta = 90^0$ and the response is in quadrature with the excitation. The first equation (7.137) becomes

$$\left[H_R(\omega)\right]\left\{\hat{f}\right\}=\left\{0\right\}. \tag{7.195}$$

The condition to have non-trivial solutions is

$$\det\left(\left[H_R(\omega)\right]\right)=0. \tag{7.196}$$

The roots of the determinantal equation (7.196) are the undamped natural frequencies ω_r $(r=1,...,n)$. The latent vectors of the matrix $\left[H_R(\omega_r)\right]$ are the vectors of the *forced modes of excitation* $\left\{\varXi\right\}_r$ so that

$$\left[H_R(\omega_r)\right]\left\{\varXi\right\}_r=\left\{0\right\}. \tag{7.197}$$

Premultiplying in (7.195) by $\left[Z^*(\mathrm{i}\omega)\right]$, and using (7.179), one obtains

$$\left[Z^*(\mathrm{i}\omega)\right]\left[H_R(\omega)\right]\left\{\hat{f}\right\}=\left[Z_R(\omega)\right]\left[H(\mathrm{i}\omega)\right]\left\{\hat{f}\right\}=\left[Z_R(\omega)\right]\left\{\tilde{x}\right\}=\left\{0\right\}$$

which, using notation (7.181), yields

$$\left[Z_R(\omega)\right]\left\{\hat{x}\right\}=\left\{0\right\}, \tag{7.198}$$

or

$$\left(\left[k\right]-\omega^2\left[m\right]\right)\left\{\hat{x}\right\}=\left\{0\right\}. \tag{7.199}$$

The only solution to equation (7.199) is the normal mode solution, i.e. ω must be a natural undamped frequency ω_r and $\left\{\hat{x}\right\}$ must be a normal mode vector $\left\{u\right\}_r$ satisfying the eigenvalue problem (7.7).

It follows that at $\omega=\omega_r$, the r-th eigenvalue $\lambda_r(\omega_r)=0$, the r-th characteristic phase lag $\theta_r(\omega_r)=90^0$, the r-th response modal vector becomes the r-th normal undamped mode $\left\{\varphi(\omega_r)\right\}_r\equiv\left\{u\right\}_r$ and the r-th excitation modal vector becomes the forcing vector appropriated to the r-th natural mode $\left\{\gamma(\omega_r)\right\}_r\equiv\left\{\varXi\right\}_r$.

The second equation (7.187) becomes

$$\left[-H_I(\omega_r)\right]\left\{\varXi\right\}_r=\left\{u\right\}_r \tag{7.200}$$

where the vectors $\left\{\varXi\right\}_r$ (different from those defined in Section 7.2.1.6) are

$$\left\{\varXi\right\}_r=\left[Z_I(\omega_r)\right]\left\{u\right\}_r=\left(\omega_r\left[c\right]+\left[d\right]\right)\left\{u\right\}_r. \tag{7.201}$$

Normalization

The excitation modal vectors $\left\{\gamma\right\}_r$ can be normalized to unit length

$$\left\{\gamma\right\}_r^T\left\{\gamma\right\}_r=1. \tag{7.202}$$

Next, a new set of 'gamma' vectors $\{\Gamma\}_r$ is introduced,

$$\{\Gamma\}_r = \sqrt{Q_r}\,\{\gamma\}_r, \tag{7.203}$$

using the frequency dependent scaling factors

$$Q_r = \frac{\sin\theta_r}{\{\gamma\}_r^{\mathrm{T}}[-H_I]\{\gamma\}_r} \tag{7.204}$$

and correspondingly a new set of 'phi' vectors $\{\Phi\}_r$

$$\{\Phi\}_r = \sqrt{Q_r}\,\{\varphi\}_r \tag{7.205}$$

which satisfy the bi-orthogonality conditions (7.163)

$$\{\Gamma\}_s^T\{\Phi\}_r = \{\Phi\}_s^T\{\Gamma\}_r = \delta_{rs}, \tag{7.206}$$

where δ_{rs} is the Kronecker delta. While the excitation vectors are right eigenvectors of the matrix pencil $\left([H_R],[-H_I]\right)$, the response vectors are left eigenvectors of that pencil.

Equation (7.206) implies

$$\{\gamma\}_r^T\{\varphi\}_r = \frac{1}{Q_r}. \tag{7.207}$$

Equations (7.192) become

$$\begin{aligned}[H_R]\{\Gamma\}_r &= \cos\theta_r\,\{\Phi\}_r,\\[-H_I]\{\Gamma\}_r &= \sin\theta_r\,\{\Phi\}_r.\end{aligned} \tag{7.208}$$

which, using (7.206), can be written

$$\begin{aligned}\{\Gamma\}_s^T[H_R]\{\Gamma\}_r &= \cos\theta_r,\\\{\Gamma\}_s^T[-H_I]\{\Gamma\}_r &= \sin\theta_r.\end{aligned} \tag{7.209}$$

Introducing the square modal matrix $[\Gamma]$, which has the normalized monophase excitation modal vectors as columns

$$[\Gamma] = \Big[\ \{\Gamma\}_1\ \{\Gamma\}_2\ \cdots\ \{\Gamma\}_n\ \Big], \tag{7.210}$$

equations (7.209) yield

$$[\Gamma]^{\mathrm{T}}[Z_R][\Gamma] = [\cos\theta_r], \tag{7.211}$$

$$[\Gamma]^{\mathrm{T}}[-H_I][\Gamma] = [\sin\theta_r], \tag{7.212}$$

and

$$[\Gamma]^T [H][\Gamma] = \left[e^{-i\theta_r} \right].$$ (7.213)

The FRF matrix is given by

$$[H] = [\Gamma]^{-T} \left[e^{-i\theta_r} \right][\Gamma]^{-1}.$$ (7.214)

Its inverse, the dynamic stiffness matrix, is

$$[H]^{-1} = [Z] = [\Gamma] \left[e^{i\theta_r} \right][\Gamma]^T.$$ (7.215)

The dynamic stiffness matrix has the following modal decomposition

$$[Z] = \sum_{r=1}^{n} e^{i\theta_r} \{\Gamma\}_r \{\Gamma\}_r^T$$ (7.216)

or, in terms of the unscaled vectors,

$$[Z] = \sum_{r=1}^{n} Q_r\, e^{i\theta_r} \{\gamma\}_r \{\gamma\}_r^T.$$ (7.217)

The bi-orthogonality conditions and (7.167) imply

$$[\Phi] = [\Gamma]^{-T}.$$ (7.218)

Energy considerations

During a cycle of vibration, the complex energy transmitted to the structure by the excitation $\{\Gamma\}_r e^{i\omega t}$ is

$$W(i\omega) = W_R(\omega) + i W_I(\omega) = i\,\pi\,\{\Gamma\}_r^T \{\Phi\}_r e^{-i\theta_r},$$ (7.219)

$$W(i\omega) = i\,\pi\,\{\Gamma\}_r^T [H(i\omega)]\{\Gamma\}_r.$$ (7.220)

The active energy, actually dissipated in the system, is

$$W_R(\omega) = -\pi\,\{\Gamma\}_r^T [H_I(\omega)]\{\Gamma\}_r = \pi \sin\theta_r > 0.$$ (7.221)

The reactive energy is

$$W_I(\omega) = \pi\,\{\Gamma\}_r^T [H_R(\omega)]\{\Gamma\}_r = \pi \cos\theta_r.$$ (7.222)

It follows that $\sin\theta_r$ is a measure of the relative modal active energy and $\cos\theta_r$ is a measure of the relative modal reactive energy [7.17]

$$\sin\theta_r = \frac{W_R}{\sqrt{W_R^2 + W_I^2}}, \quad \cos\theta_r = \frac{W_I}{\sqrt{W_R^2 + W_I^2}} . \tag{7.223}$$

7.4.3 Proportional damping

The *forced modes of excitation* $\{\varXi\}_r$ defined in equation (7.197)

$$[H_R(\omega_r)]\{\varXi\}_r = \{0\}$$

form a complete linearly independent set, or base, of the vectorial space. An expansion of $\{\hat{f}\}$ is thus always possible (and unique) of the form

$$\{\hat{f}\} = [\varXi]\{\hat{\chi}\} = \sum_{r=1}^{n}\{\varXi\}_r \hat{\chi}_r, \tag{7.224}$$

where $[\varXi]$ is the square matrix having the principal modes of excitation $\{\varXi\}_r$ as columns and $\{\hat{\chi}\}$ is a vector of scalar multipliers.

Substitution of (7.224) into the second equation (7.185) and premultiplication by $[\varXi]^T$, yields

$$\left([\tau]\cos\theta + [\sigma]\sin\theta\right)\{\hat{\chi}\} = \{0\}, \tag{7.225}$$

where, in the case of proportional damping,

$$[\varXi]^T[H_R][\varXi] = [\sigma], \tag{7.226}$$

$$[\varXi]^T[H_I][\varXi] = [\tau], \tag{7.227}$$

are diagonal matrices [7.18].

Indeed, the dynamic stiffness matrix can be written

$$[Z(\mathrm{i}\omega)] = [u]^{-T}[u]^T[Z(\mathrm{i}\omega)][u][u]^{-1}, \tag{7.228}$$

or

$$[Z(\mathrm{i}\omega)] = [u]^{-T}[z(\mathrm{i}\omega)][u]^{-1}, \tag{7.229}$$

where

$$[z(\mathrm{i}\omega)] = [u]^T[Z(\mathrm{i}\omega)][u], \tag{7.230}$$

$$[z(\mathrm{i}\omega)] = [u]^T\left[[k] - \omega^2[m] + \mathrm{i}\left(\omega[c] + [d]\right)\right][u], \tag{7.231}$$

or, using equations (7.12), (7.13), (7.43) and (7.57), for proportional damping

$$\left[z(\mathrm{i}\omega) \right] = \left[K \right] - \omega^2 \left[M \right] + \mathrm{i} \left(\omega \left[C \right] + \left[D \right] \right). \tag{7.232}$$

The FRF matrix can be written

$$\left[H(\mathrm{i}\omega) \right] = \left[Z(\mathrm{i}\omega) \right]^{-1} = \left[u \right] \left[h(\mathrm{i}\omega) \right] \left[u \right]^T \ , \tag{7.233}$$

where

$$\left[h(\mathrm{i}\omega) \right] = \left[z(\mathrm{i}\omega) \right]^{-1} = \mathrm{diag} \left(\frac{1}{K_r - \omega^2 M_r + \mathrm{i} \left(\omega C_r + D_r \right)} \right). \tag{7.234}$$

According to (7.201)

$$\left[\varXi \right]^T \left[u \right] = \left[u \right]^T \left[\varXi \right] = \mathrm{diag} \left(\omega_r C_r + D_r \right). \tag{7.235}$$

It follows that the matrix product

$$\left[\varXi \right]^T \left[H(\mathrm{i}\omega) \right] \left[\varXi \right] = \left[\varXi \right]^T \left[u \right] \left[h(\mathrm{i}\omega) \right] \left[u \right]^T \left[\varXi \right] = \left[\sigma \right] + \mathrm{i} \left[\tau \right] \tag{7.236}$$

is indeed a diagonal matrix.

If $\cos\theta \neq 0$, equation (7.225) becomes

$$\left(\left[\tau \right] \lambda_r + \left[\sigma \right] \right) \left\{ \hat{\chi} \right\}_r = \left\{ 0 \right\}, \tag{7.237}$$

where the eigenvectors are of the form

$$\left\{ \hat{\chi} \right\}_r = \left\{ I \right\}_r \hat{\chi}_{rr} \tag{7.238}$$

in which $\left\{ I \right\}_r$ is the *r*-th column of the identity matrix. Due to the diagonal form of the characteristic matrix, the only non-zero element in $\left\{ \hat{\chi} \right\}_r$ is the *r*-th element $\hat{\chi}_{rr}$.

Comparison with equation (7.189) shows that the excitation modal vector $\left\{ \gamma \right\}_r$ is a solution of equation (7.237), being proportional to the *r*-th principal mode of excitation

$$\left\{ \hat{f} \right\} = \left\{ \gamma \right\}_r = \left[\varXi \right] \left\{ \hat{\chi} \right\}_r = \left\{ \varXi \right\}_r \hat{\chi}_{rr}. \tag{7.239}$$

This way it has been demonstrated [7.18] that, in the case of proportional damping, the excitation modal vectors $\left\{ \gamma \right\}_r$ are no longer dependent on the excitation frequency ω. The same applies to the response modal vectors $\left\{ \varphi \right\}_r$ [7.13]. This property can be used as a criterion to identify whether the damping is proportional or non-proportional in an actual structure.

Example 7.2

The two-degree-of-freedom system from Fig. 7.9 will be used to illustrate the foregoing theoretical results. The mass and stiffness coefficients are $m_1 = m_2 = 0.0259\text{kg}$, $k_1 = k_3 = 100\text{N/m}$, and $k_2 = 50\text{N/m}$ [7.19].
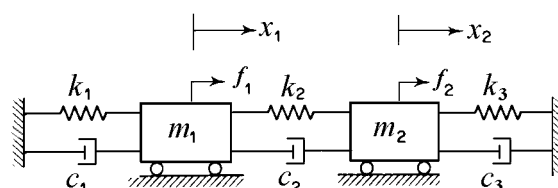
Fig. 7.9

The undamped natural frequencies are $\omega_1 = 62.128\,\text{rad/sec}$, $\omega_2 = 87.863\,\text{rad/sec}$ and the (orthonormalized) normal modal vectors are

$$\{u\}_1 = \left\{\frac{\sqrt{2}}{2}\quad\frac{\sqrt{2}}{2}\right\}^T, \quad \{u\}_2 = \left\{\frac{\sqrt{2}}{2}\quad-\frac{\sqrt{2}}{2}\right\}^T.$$

Case I. Nonproportional damping.

Consider the following damping coefficients: $c_1 = 3\,\text{Ns/m}$, $c_2 = 2\,\text{Ns/m}$, $c_3 = 1\,\text{Ns/m}$. The modal matrices are

$$[M] = \begin{bmatrix} 10/386 & 0 \\ 0 & 10/386 \end{bmatrix}, [K] = \begin{bmatrix} 100 & 0 \\ 0 & 200 \end{bmatrix}, [C] = \begin{bmatrix} 2 & 1 \\ 1 & 6 \end{bmatrix}.$$

a

b
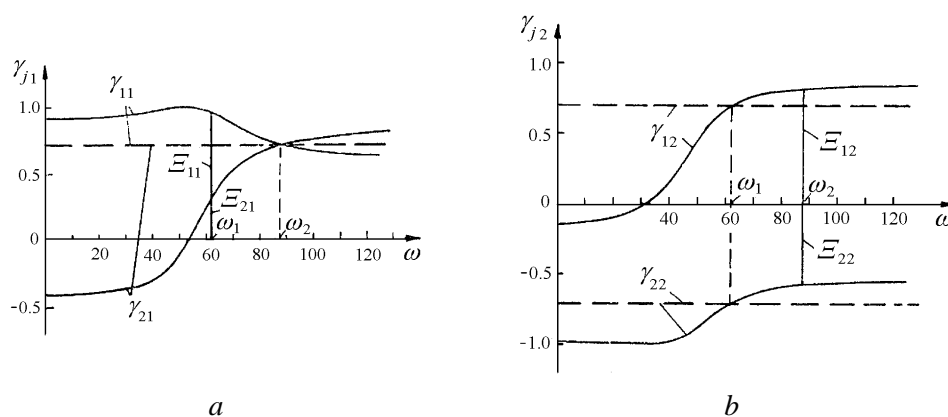
Fig. 7.10 (from [7.18])

The orthonormalized appropriated force vectors are

$$\{ \Xi \}_1 = \left\{ \frac{3}{\sqrt{10}} \quad \frac{1}{\sqrt{10}} \right\}^T , \quad \{ \Xi \}_2 = \left\{ \frac{7}{\sqrt{74}} \quad -\frac{5}{\sqrt{74}} \right\}^T .$$

The frequency dependence of the elements of excitation modal vectors is shown in Fig. 7.10 and that of the response modal vectors in Fig. 7.11. The strong variation with frequency of these components proves the existence of nonproportional damping.
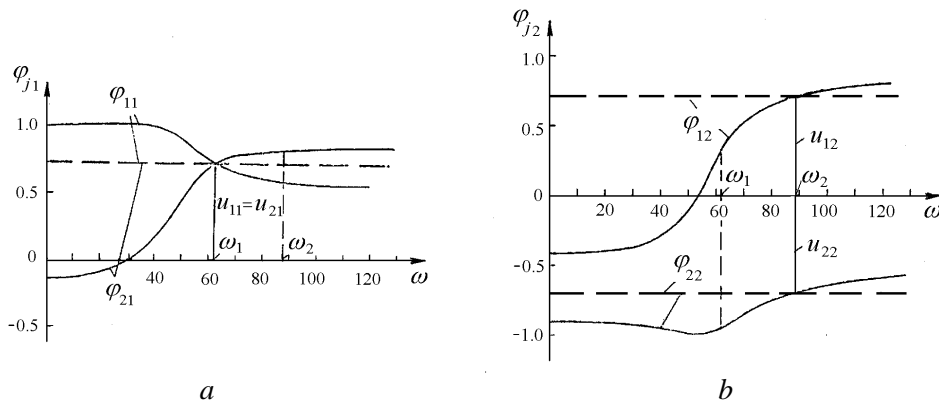
Fig. 7.11 (from [7.18])

Case II. Proportional damping.

If $c_1 = 2 \,\text{Ns/m}$, $c_2 = 1 \,\text{Ns/m}$, $c_3 = 2 \,\text{Ns/m}$, the modal damping matrix is diagonal

$$[C] = \begin{bmatrix} 2 & 0 \\ 0 & 4 \end{bmatrix} ,$$

denoting proportional damping.

The orthonormalized appropriated force vectors are

$$\{ \Xi \}_1 = \left\{ \frac{\sqrt{2}}{2} \quad \frac{\sqrt{2}}{2} \right\}^T , \quad \{ \Xi \}_2 = \left\{ \frac{\sqrt{2}}{2} \quad -\frac{\sqrt{2}}{2} \right\}^T .$$

The elements of the modal vectors $\{ \gamma \}_r$ and $\{ \varphi \}_r$ are plotted in Figs. 7.10 and 7.11 with dotted lines. Their graphs are horizontal straight lines. This independence of frequency proves the existence of proportional damping.

7.5 Rigid-body modes

Motion as a rigid body can occur in addition to elastic deformation in unsupported structures. Such systems have one or more *rigid-body modes*, that is, modes in which there is no structural deformation. This is true for aerospace vehicles in flight, like airplanes and rockets, whose structure is free to move as a rigid body without deformation.

The concept is extended in practice to elastically supported structures. These have a few lowest modes in which only the supporting springs deform and the structure is practically undeformed. They are not genuine rigid-body modes and are called like that only for convenience.

For unsupported structures, the stiffness matrix is singular (its determinant is zero) and the flexibility matrix is indeterminate (by nature of its definition, it must be found relative to supports). These difficulties can be overcome for the stiffness matrix, by a condensation process, and for the flexibility matrix, by introducing artificial supports. The two methods of analysis are presented in the following for undamped systems.

Rigid-body modes have a frequency of zero. An eigenvalue problem that results in one or more zero eigenvalues is called a *semidefinite eigenvalue problem* and the stiffness matrix is *semipositive definite*.

7.5.1 Flexibility method

Consider a vibratory system whose motion is defined by a set of n total degrees of freedom (DOFs) consisting of n_R rigid-body DOFs and n_E elastic DOFs

$$n = n_R + n_E. \tag{7.240}$$

The vector of total displacements $\{x\}$ can be expressed as

$$\{x\} = [A_R]\{q_R\} + [A_E]\{q_E\}, \tag{7.241}$$

where $\{q_R\}$ are rigid body displacements, $\{q_E\}$ are elastic displacements, and $[A_R]$ and $[A_E]$ are transformation matrices.

Example 7.3

A uniform flexible beam carries five equal equidistant lumped masses as in Fig. 7.12, *a*. Only the vertical displacements are considered as degrees of freedom.

The vector of displacements is

$$\{x\} = \lfloor x_1 \quad x_2 \quad x_3 \quad x_4 \quad x_5 \rfloor^T.$$

The two rigid-body modes are defined by the translation q_{R1} and the rotation q_{R2} (Fig. 7.12, *b*) with respect to the center of mass

$$\{q_R\} = \begin{Bmatrix} q_{R1} \\ q_{R2} \end{Bmatrix}.$$

The rigid body effects are defined by

$$\begin{Bmatrix} x_1 \\ x_2 \\ x_3 \\ x_4 \\ x_5 \end{Bmatrix}_R = \begin{bmatrix} A_R \end{bmatrix}\{q_R\} = \begin{bmatrix} 1 & -2\ell \\ 1 & -\ell \\ 1 & 0 \\ 1 & \ell \\ 1 & 2\ell \end{bmatrix} \begin{Bmatrix} q_{R1} \\ q_{R2} \end{Bmatrix}.$$

The system has three deformation modes. To eliminate the q_R's we introduce supports as in Fig. 7.12, *c* (one possibility).
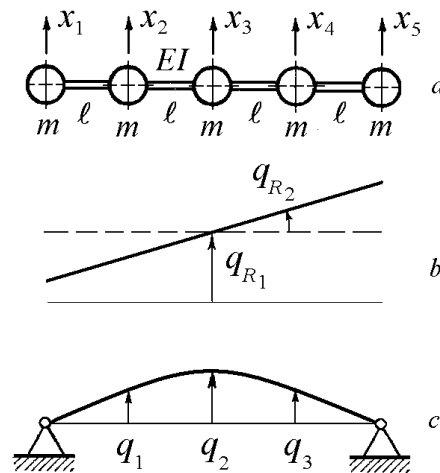
Fig. 7.12

The structural deformation effects are defined by

$$\begin{Bmatrix} x_1 \\ x_2 \\ x_3 \\ x_4 \\ x_5 \end{Bmatrix}_E = \begin{bmatrix} A_E \end{bmatrix} \{ q_E \} = \begin{bmatrix} 0 & 0 & 0 \\ 1 & 0 & 0 \\ 0 & 1 & 0 \\ 0 & 0 & 1 \\ 0 & 0 & 0 \end{bmatrix} \begin{Bmatrix} q_{E1} \\ q_{E2} \\ q_{E3} \end{Bmatrix}.$$

Rigid-body motion involves no deformation, so that no forces are required to produce it, i.e.

$$\{ f_R \} = [k] \{ x_R \} = [k][A_R] \{ q_R \} = \{ 0 \}. \qquad (7.242)$$

Since $\{ q_R \}$ is arbitrary, we get

$$[k][A_R] = \{ 0 \} \qquad (7.242, a)$$

or transposing

$$[A_R]^T [k] = \{ 0 \}. \qquad (7.243)$$

The equation of free vibrations of the undamped system is (7.2)

$$[m] \{ \ddot{x} \} + [k] \{ x \} = \{ 0 \}. \qquad (7.244)$$

Premultiplying by $[A_R]^T$ we get

$$[A_R]^T [m] \{ \ddot{x} \} + [A_R]^T [k] \{ x \} = \{ 0 \},$$

where the second term is zero according to (7.243).

The remaining equation is

$$[A_R]^T [m] \{ \ddot{x} \} = \{ 0 \},$$

expressing the overall equilibrium of the inertia forces. For simple harmonic motion, in which

$$\{ \ddot{x} \} = -\omega^2 \{ x \},$$

the above equation becomes

$$[A_R]^T [m] \{ x \} = \{ 0 \}. \qquad (7.245)$$

The elastic deformations are given by

$$\{ x_E \} = [A_E] \{ q_E \} = \{ x \} - [A_R] \{ q_R \} = [\delta] \{ f \},$$

where $[\delta]$ is the elastic flexibility matrix and $\{ f \}$ are the inertia forces.

Thus

$$\{x\}-[A_R]\{q_R\}=-[\delta][m]\{\ddot{x}\},$$

or

$$\{x\}-[A_R]\{q_R\}+[\delta][m]\{\ddot{x}\}=\{0\}. \tag{7.246}$$

For simple harmonic motion $\{\ddot{x}\}=-\omega^2\{x\}$, hence

$$\{x\}-[A_R]\{q_R\}-\omega^2[\delta][m]\{x\}=\{0\}. \tag{7.247}$$

Premultiplying by $[A_R]^T[m]$ we get

$$[A_R]^T[m]\{x\}-[A_R]^T[m][A_R]\{q_R\}-\omega^2[A_R]^T[m][\delta][m]\{x\}=\{0\}. \tag{7.248}$$

The first term is zero, according to (7.245) hence

$$\{q_R\}=-\omega^2[m_R]^{-1}[A_R]^T[m][\delta][m]\{x\}, \tag{7.249}$$

where

$$[m_R]=[A_R]^T[m][A_R] \tag{7.250}$$

is the mass matrix corresponding to the rigid-body freedoms. It is a diagonal matrix if $[A_R]$ is calculated with respect to the center of mass of the system.

Substituting for $\{q_R\}$ in (7.247) we obtain

$$\{x\}+\omega^2[A_R][m_R]^{-1}[A_R]^T[m][\delta][m]\{x\}-\omega^2[\delta][m]\{x\}=\{0\},$$

or

$$\left([I]-\omega^2[\Re][\delta][m]\right)\{x\}=\{0\}, \tag{7.251}$$

where

$$[\Re]=[I]-[A_R][m_R]^{-1}[A_R]^T[m] \tag{7.252}$$

is called the *release matrix*. It effectively releases the "supports".

Note that, for supported systems and harmonic solution, equation (7.244) is written

$$\left([I]-\omega^2[\delta][m]\right)\{x\}=\{0\}, \tag{7.253}$$

where

$$[\overline{D}]=[\delta][m] \tag{7.254}$$

is called the *dynamical matrix*.

By comparison with (7.251), for unsupported systems we can define a matrix with the same meaning

$$[D]=[\Re][\delta][m], \tag{7.255}$$

where $[\delta]$ is the flexibility matrix of the "supported" structure, obtained by putting n_R displacements equal to zero. It is singular and will contain rows and columns of zeros corresponding to the statically determinate constraints ("supports").

Example 7.4

Determine the natural modes of vibration in the vertical plane for the free-free beam with lumped masses from Fig. 7.13, a , taking as degrees of freedom only the vertical translations.
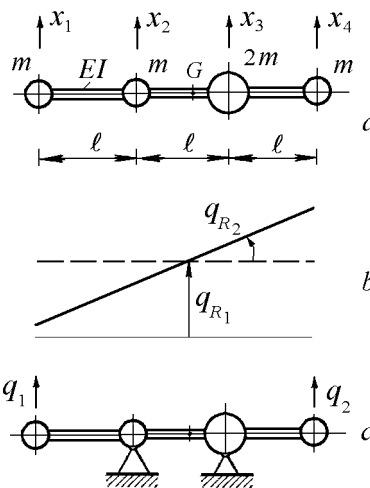
Fig. 7.13

Solution. The vector of displacements is

$$\{x\} = \lfloor x_1 \quad x_2 \quad x_3 \quad x_4 \rfloor^T .$$

Calculating moments about *1*, the position of the center of mass is

$$\bar{x} = \frac{m\ell + 2m \cdot 2\ell + m \cdot 3\ell}{5m} = \frac{8}{5}\ell .$$

The two rigid-body modes are defined by coordinates q_{R1} and q_{R2} (Fig. 7.13, b).

The transformation matrix for rigid body effects is

$$[A_R] = \begin{bmatrix} 1 & 8\ell/5 \\ 1 & 3\ell/5 \\ 1 & -2\ell/5 \\ 1 & -7\ell/5 \end{bmatrix}.$$

The mass matrix is

$$[m] = \mathrm{diag}\begin{pmatrix} m & m & 2m & m \end{pmatrix}.$$

The mass matrix corresponding to the rigid-body freedoms is

$$[m_R] = [A_R]^T [m] [A_R] = m \begin{bmatrix} 5 & 0 \\ 0 & \dfrac{26}{5}\ell^2 \end{bmatrix},$$

where $5m$ is the total mass and $\dfrac{26}{5}m\ell^2$ is the mass moment of inertia about the center of mass.

Its inverse is

$$[m_R]^{-1} = \frac{5}{m} \begin{bmatrix} 1/25 & 0 \\ 0 & 1/26\,\ell^2 \end{bmatrix}.$$

The matrix product

$$[A_R][m_R]^{-1}[A_R]^T[m] = \frac{1}{26} \begin{bmatrix} 18 & 10 & 4 & -6 \\ 10 & 7 & 8 & 1 \\ 2 & 4 & 12 & 8 \\ -6 & 1 & 16 & 15 \end{bmatrix}$$

and the release matrix

$$[\Re] = [I] - [A_R][m_R]^{-1}[A_R]^T[m] = \frac{1}{26} \begin{bmatrix} 8 & -10 & -4 & 6 \\ -10 & 19 & -8 & -1 \\ -2 & -4 & 14 & -8 \\ 6 & -1 & -16 & 11 \end{bmatrix}.$$

Now, consider the structure "supported" as in Fig. 7.13, *c*. The flexibility influence coefficients are

$$\delta_{11} = \delta_{44} = \frac{2}{3}\frac{\ell^3}{EI}, \quad \delta_{14} = \delta_{41} = \frac{1}{6}\frac{\ell^3}{EI}.$$

The singular flexibility matrix, with rows and columns of zeros corresponding to supports, is

$$[\delta] = \frac{\ell^3}{6EI} \begin{bmatrix} 4 & 0 & 0 & 1 \\ 0 & 0 & 0 & 0 \\ 0 & 0 & 0 & 0 \\ 1 & 0 & 0 & 4 \end{bmatrix}.$$

The dynamical matrix

$$[\delta][m] = \alpha \begin{bmatrix} 4 & 0 & 0 & 1 \\ 0 & 0 & 0 & 0 \\ 0 & 0 & 0 & 0 \\ 1 & 0 & 0 & 4 \end{bmatrix},$$

where $\alpha = \dfrac{\ell^3}{6EI}$.

For the unsupported system

$$[D] = [\Re][\delta][m] = \frac{m\alpha}{26} \begin{bmatrix} 38 & 0 & 0 & 32 \\ -41 & 0 & 0 & -14 \\ -46 & 0 & 0 & -34 \\ 35 & 0 & 0 & 50 \end{bmatrix}.$$

The eigenvalue problem

$$(\lambda[I] - [D])\{u\} = \{0\},$$

where $\lambda = 1/\omega^2$, has non-zero eigenvalues $\lambda_1 = 3\alpha m$ and $\lambda_2 = 10/26 \cdot \alpha m$. The eigenvectors, scaled with the first component equal to 1, are

$$\{u\}_1 = \lfloor 1 \quad -3/4 \quad -3/4 \quad 5/4 \rfloor^T, \quad \{u\}_2 = \lfloor 1 \quad -23/8 \quad 11/8 \quad -7/8 \rfloor^T$$

The non-zero natural frequencies are

$$\omega_1 = \sqrt{2}\sqrt{\frac{EI}{m\ell^3}}, \qquad \omega_2 = \sqrt{15.6}\sqrt{\frac{EI}{m\ell^3}}.$$

7.5.2 Stiffness method

In an analysis using the stiffness method, one would not obtain the dynamical matrix by using a directly assembled flexibility matrix and the problem must be re-formulated.

We start with the equation of motion (7.244)

$$[m]\{\ddot{x}\}+[k]\{x\}=\{0\} \tag{7.256}$$

and express the displacement vector as in (7.241)

$$\{x\}=[A_R]\{q_R\}+[A_E]\{q_E\}, \tag{7.257}$$

separating the rigid body effects, and the structural deformation effects.

In (7.256) the $n \times n$ stiffness matrix $[k]$ is singular. Substituting (7.257) into (7.256) we obtain

$$[m][A_R]\{\ddot{q}_R\}+[m][A_E]\{\ddot{q}_E\}+[k][A_R]\{q_R\}+[k][A_E]\{q_E\}=\{0\} \tag{7.258}$$

where, from (7.242, *a*), the third term is zero.

Premultiplying (7.258) by $[A_E]^T$ and separately by $[A_R]^T$ we get

$$[A_E]^T[m][A_R]\{\ddot{q}_R\}+[A_E]^T[m][A_E]\{\ddot{q}_E\}+[A_E]^T[k][A_E]\{q_E\}=\{0\} \tag{7.259}$$

and

$$[A_R]^T[m][A_R]\{\ddot{q}_R\}+[A_R]^T[m][A_E]\{\ddot{q}_E\}+[A_R]^T[k][A_E]\{q_E\}=\{0\}. \tag{7.260}$$

The third term in (7.260) is zero, according to (7.243), and the coefficient of the first term is $[m_R]$, from (7.250), so that

$$\{\ddot{q}_R\}=-[m_R]^{-1}[A_R]^T[m][A_E]\{\ddot{q}_E\}=\{0\}. \tag{7.261}$$

Substituting (7.261) into (7.259) and putting $\{\ddot{q}\}=-\omega^2\{q\}$, we get

$$[A_E]^T[m][A_R]\left(\omega^2[m_R]^{-1}[A_R]^T[m][A_E]\{q_E\}\right)-$$
$$-\omega^2[A_E]^T[m][A_E]\{q_E\}+[A_E]^T[k][A_E]\{q_E\}=\{0\}. \tag{7.262}$$

In the last term, the non-singular matrix

$$[k_R]=[A_E]^T[k][A_E] \tag{7.263}$$

is called the *reduced stiffness matrix*.

We can now reformulate the eigenvalue problem in terms of $\{q_E\}$, i.e.

$$\frac{1}{\omega^2}\{q_E\}+[k_R]^{-1}[A_E]^T[m][A_R][m_R]^{-1}[A_R]^T[m][A_E]\{q_E\}-$$
$$-[k_R]^{-1}[A_E]^T[m][A_E]\{q_E\}=\{0\}$$

or

$$\lambda\{q_E\}-[k_R]^{-1}[A_E]^T[m][\Re][A_E]\{q_E\}=\{0\}, \tag{7.264}$$

where $[\Re]$ is the release matrix (7.252).

The eigenvalue problem

$$\left(\lambda[I]-[k_R]^{-1}[A_E]^T[m][\Re][A_E]\right)\{q_E\}=\{0\}, \qquad (7.265)$$

will give the $n_E = n - n_R$ non-zero eigenvalues and the corresponding eigenvectors.

However, we need $\{x\}$. Returning to (7.257)

$$\{\ddot{x}\}=[A_R]\{\ddot{q}_R\}+[A_E]\{\ddot{q}_E\}. \qquad (7.266)$$

Substituting for $\{\ddot{q}_R\}$ from (7.261) and putting $\{\ddot{x}\}=-\omega^2\{x\}$, gives

$$-\omega^2\{x\}=[A_R]\omega^2[m_R]^{-1}[A_R]^T[m][A_E]\{q_E\}-\omega^2[A_E]\{q_E\}$$

or

$$\{x\}=\left([I]-[A_R][m_R]^{-1}[A_R]^T[m]\right)[A_E]\{q_E\}$$

and using (7.252)

$$\{x\}=[\Re][A_E]\{q_E\}, \qquad (7.267)$$

where $\{q_E\}$ is obtained from (7.265).

If we return to (7.264) and premultiply by $[\Re][A_E]$ we obtain

$$\lambda[\Re][A_E]\{q_E\}-[\Re][A_E][k_R]^{-1}[A_E]^T[m][\Re][A_E]\{q_E\}=\{0\}$$

or

$$\lambda\{x\}-[\Re][A_E][k_R]^{-1}[A_E]^T[m]\{x\}=\{0\},$$

and finally

$$\left(\lambda[I]-[\Re][\delta][m]\right)\{x\}=\{0\},$$

where

$$[\delta]=[A_E][k_R]^{-1}[A_E]^T=[A_E]\left([A_E]^T[k][A_E]\right)^{-1}[A_E]^T=[k]^{-1},$$

which is the same as (7.251).

Example 7.5

Solve the problem from Example 7.4 using the stiffness method.

Solution. The rigid-body modes are defined by q_{R1} and q_{R2} (Fig. 7.13, *b*) and the elastic displacements for the structure "supported" as in Fig. 7.13, *c* are $q_{E1} = x_1$ and $q_{E2} = x_4$.

It may be shown that the stiffness matrix is

$$[k] = \frac{EI}{5\ell^3} \begin{bmatrix} 8 & -18 & 12 & -2 \\ -18 & 48 & -42 & 12 \\ 12 & -42 & 48 & -18 \\ -2 & 12 & -18 & 8 \end{bmatrix}.$$

The transformation matrix for structural deformation effects is

$$[A_E] = \begin{bmatrix} 1 & 0 \\ 0 & 0 \\ 0 & 0 \\ 0 & 1 \end{bmatrix}$$

hence the reduced stiffness matrix is

$$[k_R] = [A_E]^T [k][A_E] = \frac{EI}{5\ell^3} \begin{bmatrix} 8 & -2 \\ -2 & 8 \end{bmatrix}.$$

Its inverse is

$$[k_R]^{-1} = \frac{5\ell^3}{60EI} \begin{bmatrix} 8 & 2 \\ 2 & 8 \end{bmatrix}.$$

Then the product

$$[k_R]^{-1}[A_E]^T[m][\Re][A_E] = \frac{m\alpha}{26} \begin{bmatrix} 38 & 35 \\ 35 & 50 \end{bmatrix},$$

where $\alpha = \dfrac{\ell^3}{6EI}$ and the release matrix $[\Re]$ is as in Example 7.5.

The characteristic equation is

$$\det\left(\beta[I] - \begin{bmatrix} 38 & 35 \\ 35 & 50 \end{bmatrix} \right) = 0,$$

where $\beta = \dfrac{26\lambda}{m\alpha}$, or

$$\lambda^2 - 88\lambda + 780 = 0,$$

with roots $\lambda_1 = 78$ and $\lambda_2 = 10$.

The eigenvectors are

$$\{q_E\}_1 = \lfloor 1 \quad 8/7 \rfloor^T, \qquad\qquad \{q_E\}_2 = \lfloor 1 \quad -4/5 \rfloor^T,$$

so that

$$\{u\}_1 = [\mathfrak{R}][A_E]\{q_E\}_1 = \lfloor 1 \quad -0.75 \quad -0.75 \quad 1.25 \rfloor^T,$$

$$\{u\}_2 = [\mathfrak{R}][A_E]\{q_E\}_2 = \lfloor 1 \quad -2.875 \quad 1.375 \quad -0.875 \rfloor^T,$$

as before.

7.6 Modal participation factors

When one of the matrices $[k]$ or $[c]$ is nonsymmetrical, as for rotors in fluid film bearings, the system matrix $\lambda^2[m] + \lambda[c] + [k]$ has both right and left eigenvectors. Left eigenvectors are solutions of the adjoint eigenvalue problem. The physical interpretation of their components is one of modal participation factors.

In the eigenproblem (7.72)

$$\left(\lambda_r^2[m] + \lambda_r[c] + [k] \right) \{\psi\}_r = \{0\}. \quad r = 1,...,2n \qquad (7.268)$$

the right eigenvectors $\{\psi\}_r$ define the *mode shapes*.

The adjoint eigenvalue problem admits the same eigenvalues, and adjoint eigenvectors $\{\ell\}_r$ which satisfy the equations

$$\left(\lambda_r^2[m]^T + \lambda_r[c]^T + [k]^T \right) \{\ell\}_r = \{0\}. \qquad r = 1,...,2n \qquad (7.269)$$

Because equation (7.269) can be written in the form

$$\lfloor \ell \rfloor_r \left(\lambda_r^2[m] + \lambda_r[c] + [k] \right) = \lfloor 0 \rfloor. \qquad (7.270)$$

where $\lfloor \ell \rfloor_r = \{\ell\}_r^T$, the adjoint eigenvectors are known as *left eigenvectors*.

It can be shown that, for nonsymmetric matrices, equation (7.107) becomes

$$\{\tilde{x}\} = \sum_{r=1}^{2n} \frac{\{\psi\}_r \lfloor \ell \rfloor_r}{a_r(\mathrm{i}\omega - \lambda_r)} \{\hat{f}\}, \qquad (7.271)$$

where

$$a_r = \lfloor \ell \rfloor_r [A]\{Y\}_r, \qquad \lambda_r = -\frac{\lfloor \ell \rfloor_r [B]\{Y\}_r}{\lfloor \ell \rfloor_r [A]\{Y\}_r} . \qquad (7.272)$$

The vectors of modal participation factors are defined as

$$\lfloor L \rfloor_r = \frac{1}{a_r} \lfloor \ell \rfloor_r . \qquad r = 1,...,2n . \qquad (7.273)$$

Equation (7.271) has the form

$$\{\tilde{x}\} = [H(\mathrm{i}\omega)]\{\hat{f}\}. \qquad (7.274)$$

Denoting

$$[\Psi] = \left[\{\psi\}_1 \ \{\psi\}_2 \ \cdots \ \{\psi\}_{2n} \right], \qquad (7.275)$$

$$[\ell] = \begin{bmatrix} \lfloor \ell \rfloor_1 \\ \lfloor \ell \rfloor_2 \\ \vdots \\ \lfloor \ell \rfloor_{2n} \end{bmatrix}, \qquad (7.276)$$

the frequency response function (FRF) matrix can be written

$$[H(\mathrm{i}\omega)] = [\Psi]\left(\mathrm{i}\,\omega\,[a] + [b]\right)^{-1}[\ell], \qquad (7.277)$$

or

$$[H(\mathrm{i}\omega)] = [\Psi]\left[\frac{1}{\mathrm{i}\,\omega - \lambda_r}\right][L] = \sum_{r=1}^{2n} \frac{\{\psi\}_r \lfloor L \rfloor_r}{\mathrm{i}\,\omega - \lambda_r} . \qquad (7.278)$$

In (7.278) the matrix of modal participation factors is

$$[L] = [a]^{-1}[\ell]. \qquad (7.279)$$

The *j*-th row of the FRF matrix is

$$\lfloor H \rfloor_j = \sum_{r=1}^{2n} \frac{\psi_{jr} \lfloor L \rfloor_r}{\mathrm{i}\,\omega - \lambda_r} . \qquad (7.280)$$

The ℓ - th - column of the FRF matrix

$$\{H\}_\ell = \sum_{r=1}^{2n} \frac{\{\psi\}_r \, \ell_{\ell r}}{\mathrm{i}\,\omega - \lambda_r} \, . \tag{7.281}$$

The elements of the left eigenvectors express the *participation* of the mode shapes to $[H]$, for input at the different coordinates. The components of the scaled matrix $[L]$ can therefore be called *modal participation factors*.

When all system matrices are symmetric, as considered so far in this text, the vectors of the modal participation factors are proportional to the corresponding modal vector transposed

$$\lfloor L \rfloor_r = \frac{1}{a_r} \{\psi\}_r^T \, . \qquad r = 1,...,2n \tag{7.282}$$

References

7.1 Ewins, D.J., *Mode of vibration*, in 'Encyclopedia of Vibration' (S. Braun, D. Ewins, S. S. Rao, eds.), Academic Press, London, pp 838-844, 2002.

7.2 Meirovitch, L., *Elements of Vibration Analysis*, McGraw-Hill Book Comp., New York, 1975.

7.3 Meirovitch, L., *Analytical Methods in Vibrations*, Macmillan, London, 1967.

7.4 Caughey, T.K., *Classical normal modes in damped linear dynamic systems*, Journal of Applied Mechanics, Trans. ASME, vol.27, pp 269-271, 1960.

7.5 Fawzy, I. and Bishop, R.E.D., *On the dynamics of linear non-conservative systems*, Proceedings Royal Society London, Series A, vol.352, pp 25-40, 1976.

7.6 Lancaster, P., *Lambda-Matrices and Vibrating Systems*, Pergamon Press, Oxford, 1966.

7.7 Foss, K.A., *Co-ordinates which uncouple the equations of motion of damped linear systems*, Journal of Applied Mechanics, Trans. ASME, vol.25, pp 361-364, 1958.

7.8 Crandall, S.H. and McCalley, R.B., Jr., *Numerical methods of analysis,* Ch.28 in 'Shock and Vibration Handbook' (C. M. Harris & Ch. E. Crede, eds.), McGraw-Hill, New York, 1961.

7.9 Frazer, R.A., Duncan, W.J. and Collar, A.R., *Elementary Matrices*, Macmillan, New York, 1946.

7.10 Mead, D.J., *The existence of normal modes of linear systems with arbitrary damping*, Proc. Symposium on Structural Dynamics, Loughborough University of Technology, Paper No. C5, 1970.

7.11 de Veubeke, B.F., *Déphasages caractéristiques et vibrations forcées d'un système amorti*, Acad. Royale de Belgique, Bulletin de la Classe des Sciences, 5e Série, vol.34, pp 626-641, 1948.

7.12 de Veubeke, B.F., *A variational approach to pure mode excitation based on characteristic phase lag theory*, AGARD Report No.39, April 1956 and Third Meeting of the AGARD Structures Panel, Washington D.C., April 9-17, 1956.

7.13 Bishop, R.E.D. and Gladwell, G.M.I., *An investigation into the theory of resonance testing*, Phil. Trans. Royal Society of London, Series A, vol.255, pp 241-280, 1963.

7.14 Radeş, M., *Modal analysis of structures with frequency dependent properties,* Proc. 17th International Modal Analysis Conference, Kissimmee, Florida, pp 349-355 1999.

7.15 Wei, M.L., Allemang, R.J., Brown, D.L., *Real-normalization of measured complex modes*, Proceedings 5th International Modal Analysis Conference, London, pp 708-712 1987.

7.16 Radeş, M., *Determination of undamped normal modes from measured real forced modes using frequency response data*, Proceedings 9th International Modal Analysis Conference, Florence, Italy, pp 596-602, 1991.

7.17 Radeş, M., *Metode dinamice pentru identificarea sistemelor mecanice*, Editura Academiei, Bucureşti, 1979.

7.18 Radeş, M., *A technique for assessing the existence of proportional damping*, Buletinul Institutului Politehnic Bucureşti, Seria Transporturi-Aeronave, vol.46-47, pp 88-96, 1984-1985.

7.19 Van Loon, P., *Modal Parameters of Mechanical Structures,* Ph.D. Thesis, Katholieke Universiteit Leuven, Belgium, 1974.

7.20 ∗∗∗ *User Manual for Modal Analysis*, Version 9.0, Structural Dynamics Research Corporation, 1985.

7.21 Heylen, W., Lammens, S. and Sas, P., *Modal Analysis Theory and Testing*, Katholieke Universiteit Leuven, Belgium, 1997.

7.22 Ewins, D.J., *Modal Testing: Theory, Practice and Application*, 2nd ed., Research Studies Press Ltd., Baldock, 2000.

8.

EIGENVALUE SOLVERS

This chapter is about eigenvalues and eigenvectors of matrices encountered in undamped structural systems. Computational algorithms for both dense, small or modest order, and sparse large matrices are shortly described. The aim of the presentation is to provide the analytical and computational background to select the algorithms most adequate to the solution of a specific problem. Excellent software is available nowadays on the Internet. Full descriptions can be found in the books quoted in the text.

8.1 Structural dynamics eigenproblem

Dynamic analyses of conservative non-gyroscopic structural systems lead to the generalized symmetric eigenproblem

$$[k]\{x\} = \lambda [m]\{x\},\tag{8.1}$$

where the stiffness and the mass matrices $[k]$ and $[m]$ are real and symmetric, λ are real eigenvalues and $\{x\}$ are real eigenvectors.

An obvious approach is to transform (8.1) to a standard eigenproblem

$$[A]\{x\} = \lambda \{x\},\tag{8.2}$$

where $[A]$ is an unsymmetric matrix.

This can be made by inverting either $[k]$ or $[m]$, or to work with more complicated transformations, such as the Cayley Transform $([k] - \sigma[m])^{-1}([k] - \tau[m])$ [8.1].

If $[m]$ is non-singular, equation (8.1) transforms to

$$[m]^{-1}[k]\{x\} = \lambda \{x\},\tag{8.3}$$

having the same eigenvalues.

If $[k]$ is non-singular, equation (8.1) yields

$$[k]^{-1}[m]\{x\}=\frac{1}{\lambda}\{x\}. \qquad (8.4)$$

The inverse matrix has inverse eigenvalues.

The forms (8.3) and (8.4) are used only for small system matrices. These approaches share the disadvantage that matrices $[k]$ and $[m]$ are not treated in the same way. This leads to problems if $[k]$ is singular or ill-conditioned.

8.2. Transformation to standard form

Two procedures can be used to transform the generalized eigenproblem (8.1) to the standard eigenproblem (8.2): a) the Cholesky factorization of $[m]$, which leads to a symmetric matrix having the same eigenvalues, and b) a shift-and-invert spectral transformation, which yields an unsymmetrical matrix having the same eigenvectors as (8.1).

8.2.1 Cholesky factorization of the mass matrix

When $[m]$ is positive-definite, it can be factored into

$$[m]=[L][L]^{T}, \qquad (8.5)$$

where $[L]$ is lower triangular. It follows that

$$[k]\{x\}=\lambda\,[L][L]^{T}\{x\}, \quad [L]^{-1}[k]\{x\}=\lambda\,[L]^{T}\{x\},$$
$$\left([L]^{-1}[k][L]^{-T}\right)\!\left([L]^{T}\{x\}\right)=\lambda\,\left([L]^{T}\{x\}\right), \qquad (8.6)$$

hence

$$[B]\{y\}=\lambda\,\{y\}, \qquad (8.7)$$

where

$$[B]=[L]^{-1}[k][L]^{-T} \qquad (8.8)$$

is a symmetric matrix with the same eigenvalues as those of the generalized problem and with eigenvectors

$$\{y\}=[L]^{T}\{x\}. \qquad (8.9)$$

If $[m]$ is positive-semidefinite, its Cholesky factors are singular and this transformation cannot be performed.

8.2.2 Shift-and-invert spectral transformation

When a shift of the origin σ is performed in (8.1) then

$$\left([k]-\sigma\,[m]\right)\{x\}=(\lambda-\sigma)\,[m]\{x\},$$

which can be written

$$\left([k]-\sigma\,[m]\right)^{-1}[m]\{x\}=\frac{1}{\lambda-\sigma}\,\{x\}, \qquad (8.10)$$

or

$$[A]\{x\}=\theta\,\{x\}, \qquad (8.11)$$

where

$$[A]=\left([k]-\sigma\,[m]\right)^{-1}[m]\,, \qquad (8.12)$$

and

$$\theta=\frac{1}{\lambda-\sigma}\,. \qquad (8.13)$$

The matrix $[A]$ is not symmetric but has the same eigenvectors as the original problem. The spectrum of $[A]$ is related to the original spectrum through (8.13). The eigenvalue of (8.1) that is closest to σ corresponds to the eigenvalue of largest magnitude of $[A]$, as shown in Fig. 8.1.
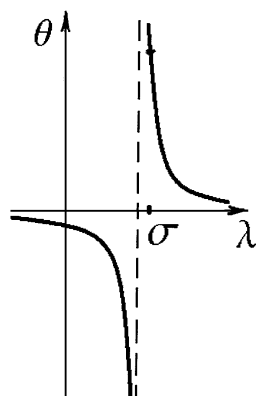
Fig. 8.1

The matrix $\left([k] - \sigma [m]\right)^{-1} [m]$ is *M*-symmetric, i.e. $[m][A]$ is symmetric. The spectral transformation leaves the eigenvectors unchanged. The eigenvalues of (8.1) close to the shift become the largest absolute of (8.9). In addition, they are relatively well separated, which improves the speed of convergence of iterative methods. The cost of the improved convergence rate is the necessity to solve a linear system of equations involving $[k] - \sigma [m]$. Denoting $[k_\sigma] = [k] - \sigma [m]$, in order to compute the matrix-vector product $\{y\} = [A]\{x\} = [k_\sigma]^{-1} [m]\{x\}$, one simply solves $[k_\sigma]\{y\} = [m]\{x\}$ by inverse iteration, using the LU factorization of $[k_\sigma]$:

$$\{y\} = [U] \backslash ([L] \backslash [m]\{x\}).$$

8.3. Determinant search method

Computation of the eigenvalues λ via the explicit construction of the characteristic equation

$$p(\lambda) = \det\left([A] - \lambda [I]\right) = 0 \qquad (8.14)$$

is, except for very special cases, not an option since the coefficients of the characteristic equation cannot be computed from determinant evaluations ("determinant search") in a numerically stable way.

Even if the characteristic equation could be determined accurately, the computation of its roots, in finite precision, may be highly unstable since small perturbations in the coefficients may lead to large perturbations of the roots. The numerical computation of the associated eigenvectors is even more delicate, in particular when the eigenvectors of $[A]$ make small angles with each other. This was already recognized by Jacobi who, in 1846, computed the eigenvalues of symmetric matrices by rotating the matrix to a strongly diagonally dominant one [8.2].

The so-called "determinant search method" is based on an iteration with the characteristic polynomial $p(\lambda)$ used in conjunction with the Sturm sequence and vector inverse iteration. The basic strategy is to calculate first an approximation to the unknown eigenvalue using a polynomial iteration scheme, and switch to inverse iteration only when a shift close to the required eigenvalue has been obtained [8.3].

Consider the iteration for the eigenpair $\left(\lambda_1, \{x\}_1\right)$. Let σ_{k-1} and σ_k be two approximations to λ_1, where $\sigma_{k-1} < \sigma_k \leq \lambda_1$.

The first aim is to obtain as economically as possible a shift near λ_1. This is accomplished by using an accelerated secant iteration in which the next shift σ_{k+1} is calculated using

$$\sigma_{k+1} = \sigma_k - \eta \frac{p(\sigma_k)}{p(\sigma_k) - p(\sigma_{k-1})}(\sigma_k - \sigma_{k-1}),$$

where η is a constant. Usually $\eta \geq 2$, because the iteration with $\eta = 2$ can only jump over one root, which would be detected by a sign change in *p*.

There are essentially two approaches to calculate eigenvalues, *transformation* and *iterative* methods.

8.4. Matrix transformation methods

The standard approach for the numerical solution of the eigenproblem is to reduce the matrix involved to some simpler form, which yields the eigenvalues and eigenvectors directly, for instance, for symmetric matrices, the diagonal form. The idea is to make the transformation with orthogonal operators as often as possible, in order to reduce the effect of perturbations [8.4].

Unsymmetric matrices do not in general have an orthonormal set of eigenvectors but they can be transformed to Schur form. Any matrix can be transformed to upper triangular form $[T]$ by a unitary similarity transformation

$$[U]^H [A][U] = [T]. \tag{8.15}$$

The diagonal elements of $[T]$ are the eigenvalues of $[A]$. The columns of $[U]$ are Schur vectors. If $[A]$ were symmetric, $[T]$ would be diagonal.

Matrices are usually first transformed to upper Hessenberg form or tridiagonal form, then the subdiagonal elements are zeroed by iteration methods.

Transformation methods can be used when it is possible to store the whole matrix in one array in the computer and when all eigenvalues are required. MATLAB [8.5] and LAPACK [8.6] give transformation methods as their primary choice and can handle dense matrices of not too large order.

The recognition that matrices could be reduced, by orthogonal transformations, in a finite number of steps, to some special reduced form that lends itself more efficiently to further computations was a very important step in the solution of eigenproblems [8.1]. In particular, a symmetric matrix can be reduced to tridiagonal form by Jacobi-rotations, provided that these rotations are

restricted to annihilate entries of $\begin{bmatrix} A \end{bmatrix}$ outside its tridiagonal part. This was suggested by Givens in 1954.

In 1958 Householder discovered that complete columns of $\begin{bmatrix} A \end{bmatrix}$ could be reduced to zero, outside the tridiagonal part, by the more efficient Householder reflections (section 8.4.2). His method has become the method of choice for the reduction of matrices to tridiagonal form on serial computers.

Thus for eigenproblems, a *symmetric* matrix can be reduced by a finite number of orthogonal similarity transformations to *tridiagonal* form, and *unsymmetric* matrices can be transformed to *upper Hessenberg* form (a matrix which is zero below the subdiagonal).

By 1960, the eigenvalue problem for a symmetric tridiagonal matrix was solved in ANSYS [8.7] by using the Sturm sequence property for successive subdeterminants. The corresponding eigenvectors were computed by inverse iteration. A complete and thorough analysis for the Givens and Householder reductions and for the use of Sturm sequences, is given in Wilkinson's book [8.8], which was the bible of numerical linear algebra for a long time.

A superior technique for determining the complete set of eigenvalues and eigenvectors is the QR method. It became the method of choice for symmetric problems after the publication of Parlett's book [8.9]. The key idea came from Rutishauser with his construction of a related algorithm, called LR, in 1958. After 1980, the Householder-QR-inverse iteration sequence of methods has been used for dense matrices of order up to a few thousands [8.1].

8.4.1 The eigenvalue decomposition

Let $\lambda_1, \lambda_2, ..., \lambda_n$ be the eigenvalues of a matrix $\begin{bmatrix} A \end{bmatrix}$, let $\{x\}_1, \{x\}_2, ..., \{x\}_n$ be a set of corresponding eigenvectors, let $\begin{bmatrix} \Lambda \end{bmatrix}$ denote the $n \times n$ diagonal matrix with the λ_s on the diagonal, and let $\begin{bmatrix} X \end{bmatrix}$ denote the $n \times n$ matrix whose j-th column is $\{x\}_j$. Then

$$\begin{bmatrix} A \end{bmatrix}\begin{bmatrix} X \end{bmatrix} = \begin{bmatrix} X \end{bmatrix}\begin{bmatrix} \Lambda \end{bmatrix} \qquad (8.16)$$

and, if the eigenvectors are linearly independent, $\begin{bmatrix} X \end{bmatrix}^{-1}$ exists, and

$$\begin{bmatrix} A \end{bmatrix} = \begin{bmatrix} X \end{bmatrix}\begin{bmatrix} \Lambda \end{bmatrix}\begin{bmatrix} X \end{bmatrix}^{-1}. \qquad (8.17)$$

This is known as the *eigenvalue decomposition* of the matrix $\begin{bmatrix} A \end{bmatrix}$.

With non-singular $\begin{bmatrix} X \end{bmatrix}$, equation (8.16) becomes

$$[X]^{-1}[A][X] = [\Lambda], \qquad (8.18)$$

known as a *similarity transformation*.

So $[A]$ is transformed to diagonal form by a similarity transformation. Usually this cannot be made in a single step. Transforming techniques for symmetric matrices make a sequence of similarity transformations until a diagonal form (8.18) is reached, showing all the eigenvalues and eigenvectors.

8.4.2 Householder reflections

Formally, a Householder reflection is a matrix of the form

$$[H] = [I] - \{u\}\{u\}^T / h, \qquad (8.19)$$

where $\{u\}$ is any nonzero vector and $h = \{u\}^T \{u\}/2$. The resulting matrix is both symmetric, $[H]^T = [H]$, and orthogonal, $[H]^T[H] = [I]$. Hence $[H]^{-1} = [H]^T = [H]$.

The matrix $[H]$ is called a *reflection matrix*, because the vector $[H]\{w\}$ is the reflection of the vector $\{w\}$ in the plane to which $\{u\}$ is orthogonal.

The real symmetric matrix $[B]$ in equation (8.7) is reduced to a symmetric tridiagonal matrix $[A]$ using orthogonal similarity transformations:

$$\{y\} = [H]\{z\}, \qquad (8.20)$$

$$[B][H]\{z\} = \lambda[H]\{z\},$$

$$[H]^{-1}[B][H]\{z\} = \lambda\{z\},$$

$$[A]\{z\} = \lambda\{z\}, \qquad (8.21)$$

where

$$[A] = [H]^{-1}[B][H] = [H][B][H]. \qquad (8.22)$$

The similarity transformation $[H][B][H]$ eliminates the elements in the j-th row of $[B]$ to the left of the subdiagonal and the symmetrical elements in the j-th column.

This was the basis of the subroutine TRED1 in EISPACK [8.10].

8.4.3 Sturm sequence and bisection

For the eigenproblem (8.21), the characteristic equation in determinantal form is

$$\begin{vmatrix} a_{11}-\lambda & a_{12} & 0 & 0 & \cdots \\ a_{21} & a_{22}-\lambda & a_{23} & 0 & \cdots \\ 0 & a_{32} & a_{33}-\lambda & a_{34} & \cdots \\ 0 & 0 & a_{43} & a_{44}-\lambda & \cdots \\ \cdots & \cdots & \cdots & \cdots & \cdots \end{vmatrix} = 0 \, . \quad (8.23)$$

Let $\det_0 = 1$ and consider the determinants marked off by dotted lines

$$\det_1 = a_{11} - \lambda \, ,$$

$$\det_2 = \left(a_{22} - \lambda \right) \det_1 - a_{21}^2 \det_0 \, ,$$

$$\det_3 = \left(a_{33} - \lambda \right) \det_2 - a_{32}^2 \det_1 \, ,$$

$$\det_4 = \left(a_{44} - \lambda \right) \det_3 - a_{43}^2 \det_2 \, ,$$

and

$$\det_r = \left(a_{rr} - \lambda \right) \det_{r-1} - a_{r,r-1}^2 \det_{r-2} \, . \quad (8.24)$$

For a given value of λ (say $\lambda = b$) the sequence $\det_0, \det_1, ..., \det_n$ may be evaluated easily by the recurrence relationship (8.24). This is known as a *Sturm sequence* and has the property that the number of distinct real roots of $\det_n$ with an algebraic value less than b is equal to the number of changes of sign in it.

If, for $\lambda = b$, we have

$\det_0$	$\det_1$	$\det_2$	$\det_3$	$\det_4$
+	+	−	−	+

then below b there are two eigenfrequencies.

When one of the determinants has a value of zero, it is given the sign of the previous determinant in the sequence.

For a tridiagonal symmetric matrix it is thus possible to determine the number of eigenvalues with an algebraic value less than *LB* and *UB*, respectively. Their difference is the number of eigenvalues in the interval (*LB*, *UB*).

Given the number, they may be located by a systematic search procedure. Each subinterval enclosing an eigenvalue in (*LB*, *UB*) is shrunk using a bisection process until the endpoints are close enough to be accepted as an eigenvalue. The result is an ordered set of eigenvalues within (*LB*, *UB*). The corresponding eigenvectors are determined using inverse iteration.

Identical eigenvalues are perturbed slightly in an attempt to obtain independent eigenvectors. These perturbations are not recorded in the eigenvalue array [8.11].

8.4.4 Partial Schur decomposition

The problem of finding the eigenvectors of a matrix $[A]$ can be reduced to computing the eigenvectors of a triangular matrix using a Schur decomposition.

Denoting $[X_k] = [\{x\}_1, \{x\}_2, ..., \{x\}_k]$ and $[\Theta_k] = \mathrm{diag}(\theta_1, \theta_2, ..., \theta_k)$, the individual relations $[A]\{x\}_k = \theta_k \{x\}_k$ can be combined in

$$[A][X_k] = [X_k][\Theta_k]. \tag{8.25}$$

For a selected set of k (e.g.: largest) eigenvalues of $[A]$, there is a partial Schur decomposition [8.12]

$$[A][U_k] = [U_k][T_k], \tag{8.26}$$

where $[T_k]$ is upper triangular. $[U_k]$ is orthogonal and its columns are *Schur vectors* of $[A]$. The diagonal elements of $[T_k]$ are eigenvalues of $[A]$. By appropriate choice of $[U_k]$ they may be made to appear in any specified order. The Schur matrix $[T_k]$ has an eigendecomposition

$$[T_k][S_k] = [S_k][\Theta_k], \tag{8.27}$$

where $[S_k]$ is the upper triangular matrix of the eigenvectors of $[T_k]$, and $[\Theta_k]$ is the diagonal matrix of the eigenvalues from equation (8.25). It turns out that the eigenvector matrix $[X_k]$ is given by

$$[X_k] = [U_k][S_k], \tag{8.28}$$

so that the eigenvectors of $[A]$ are linear combinations of the orthogonal Schur vectors corresponding to the selected eigenvalues

$$\{x\}_i = \sum_{j=1}^{k} s_{ji}\{u\}_j. \tag{8.29}$$

Thus, the eigenvectors of the original matrix $[A]$ can be found by computing the eigenvectors of the Schur form $[T_k]$ and transforming them back using the orthogonal transformation $[U_k]$ as shown in Fig. 8.2.
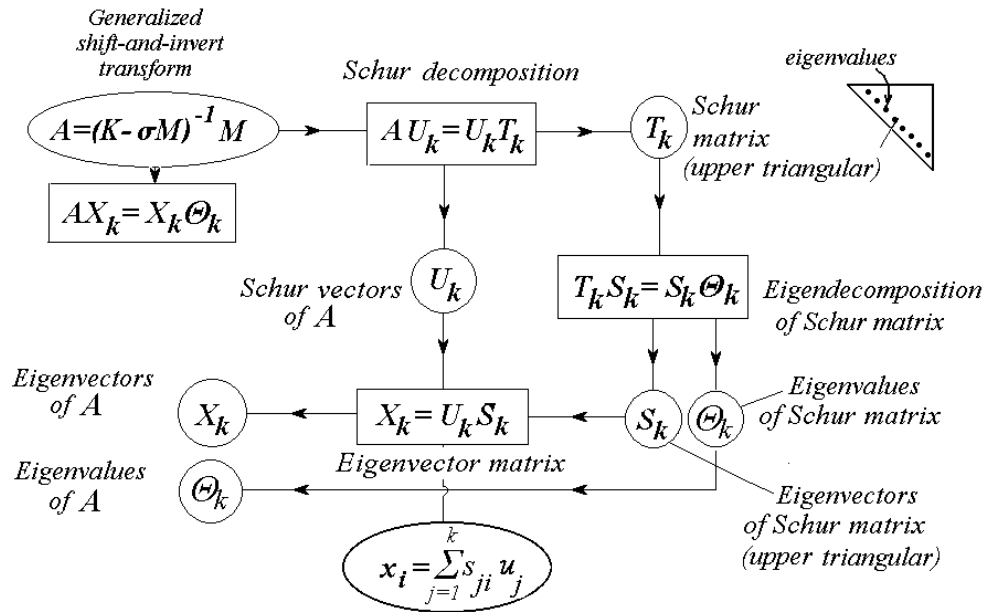
Fig. 8.2 (from [8.13])

If the Schur vectors are M-orthonormal, then $[U_k]^T[m][U_k]=[I_k]$. Because matrices $[k]$ and $[m]$ are symmetric, the product $[m][A]$ is symmetric. Then $[U_k]^T[m][A][U_k]=[T_k]$ is a Schur form of $[m][A]$, $[T_k]^T=[T_k]$, so that $[T_k]$ itself is symmetric, hence is diagonal. Its elements are eigenvalues of $[A]$ and the Schur vectors are eigenvectors of $[A]$ $([S_k]=[I_k])$.

For large order systems, it is better to solve the generalized Hermitian eigenproblem (8.1) without transformation to a standard eigenproblem. For stability reasons, it is more appropriate to work with orthogonal transformations and to compute Schur vectors for the pencil $[k]-\lambda[m]$ rather than eigenvectors.

A partial generalized Schur form of dimension k for the matrix pair $([k],[m])$ is the decomposition

$$[k][Z_k]=[Q_k][T_k^K], \qquad [m][Z_k]=[Q_k][T_k^M], \qquad (8.30)$$

where $[Z_k]$ and $[Q_k]$ are orthonormal $n \times k$ matrices, and $[T_k^K]$ and $[T_k^M]$ are upper triangular $k \times k$ matrices. The columns of $[Z_k]$ (and $[Q_k]$) are referred to as *generalized Schur vectors*. Eigenvalues are computed from the ratio of the diagonals of the triangular forms [8.1].

8.5. Iteration methods

All general purpose eigenvalue algorithms are necessarily iterative. This is a consequence of Abel's proof that there is no algebraic formula for the roots of a general polynomial of degree greater than four. Hence, there is no method of computing the eigenvalues of an *n*-th order matrix in a finite number of computations.

An algorithm for a matrix with a general structure (that is, neither diagonal nor triangular or alike) is necessarily iterative. The problem is to identify iterative algorithms which have a fast rate of convergence and lead to accurate results.

In an iterative method, a sequence of vectors is computed

$$\left\{ x^{(1)} \right\}, \left\{ x^{(2)} \right\}, \ldots, \left\{ x^{(k)} \right\} \quad \Rightarrow \quad \left\{ x \right\}_j,$$

hopefully converging toward an eigenvector $\left\{ x \right\}_j$.

8.5.1 Single vector iterations

Single vector iteration techniques include the power method, the shifted power method, the inverse iteration and the Rayleigh quotient iteration.

The *power method* is based on the observation [8.1] that if we multiply a given vector $\{v\}$ by the matrix $[A]$, then each eigenvector component in $\{v\}$ is multiplied by the corresponding eigenvalue of $[A]$. In other words, if a given vector is repeatedly applied to a matrix, and is properly normalized, then ultimately it will lie in the direction of the eigenvector associated with the eigenvalue which is largest in absolute value. In the iteration process, the component of the starting vector in the direction of the eigenvector with largest eigenvalue is magnified relative to the other components. Householder called this Simple Iteration [8.2] and attributed the first treatment of it to Müntz (1913).

An effective variant is the *inverse power method* proposed by Wielandt (1944) in which one works with the matrix $([A] - \mu[I])^{-1}$. Wielandt also

proposed continuing the process after the largest eigenvalue has converged, by working with the deflated matrix $[A] - \lambda_1 \{x\}_1 \{x\}_1^T$, for which $\lambda_1, \{x\}_1$ is the computed eigenpair (with $\{x\}_1^T \{x\}_1 = 1$), associated with the largest eigenvalue in magnitude.

Another possibility is working with properly updated shifts in the inverse process and, in particular, if one takes the Rayleigh quotient with the most recent vector as a shift, then one obtains the *Rayleigh quotient iteration.*

The power method and the inverse power method, in their pure form, are no longer competitive methods even for the computation of a few eigenpairs. They are still of interest since they are explicitly or implicitly part of most modern methods such as the QR method, and the methods of Lanczos and Arnoldi.

8.5.1.1 The power method

Assume $[A]$ has real eigenvalues and a complete set of eigenvectors

$$[A]\{x\}_r = \lambda_r \{x\}_r, \quad (r = 1, 2, \dots, n). \tag{8.31}$$

We further assume that the largest eigenvalue in modulus is single and that

$$\lambda_1 > \lambda_2 \geq \dots > \lambda_n.$$

Now suppose we are given a vector $\{v\}_1$ which can be expressed in terms of the eigenvectors (expansion theorem) as

$$\{v\}_1 = \gamma_1 \{x\}_1 + \gamma_2 \{x\}_2 + \dots + \gamma_n \{x\}_n = \sum_{r=1}^{n} \gamma_r \{x\}_r. \tag{8.32}$$

We assume that $\gamma_1 \neq 0$. This means that $\{v\}_1$ has a nonzero component in the direction of the largest eigenvector.

If the arbitrary vector $\{v\}_1$ is premultiplied by $[A]$, we obtain

$$\{v\}_2 = [A]\{v\}_1 = \sum_{r=1}^{n} \gamma_r [A]\{x\}_r = \lambda_1 \sum_{r=1}^{n} \gamma_r \frac{\lambda_r}{\lambda_1} \{x\}_r. \tag{8.33}$$

In contrast to $\{v\}_1$, in which the eigenvectors $\{x\}_r$ are multiplied by the constants γ_r, the eigenvectors $\{x\}_r$ in the vector $\{v\}_2$ are multiplied by $\gamma_r \dfrac{\lambda_r}{\lambda_1}$.

Because $\dfrac{\lambda_r}{\lambda_1} < 1$ and the ratios decrease with increasing r, the participation of the higher modes in $\{v\}_2$ tends to decrease, as opposed to their participation in $\{v\}_1$. If $\{v\}_1$ is regarded as a trial vector toward obtaining the eigenvector $\{x\}_1$, then $\{v\}_2$ must be regarded as an improved trial vector.

The procedure can be repeated

$$\{v\}_3 = \frac{1}{\lambda_1}[A]\{v\}_2 = \frac{1}{\lambda_1}[A]^2\{v\}_1 = \sum_{r=1}^{n} \gamma_r \frac{\lambda_r}{\lambda_1}[A]\{x\}_r = \lambda_1 \sum_{r=1}^{n} \gamma_r \left(\frac{\lambda_r}{\lambda_1}\right)^2 \{x\}_r.$$

It comes out that $\{v\}_3$ is a better trial vector for $\{x\}_1$ than $\{v\}_2$.

By premultiplying the newly obtained vectors repeatedly by $[A]$ we are establishing an iteration procedure converging to the first eigenvalue and eigenvector.

In general, we have

$$\{v\}_p = \frac{1}{\lambda_1}[A]\{v\}_{p-1} = \dots = \frac{1}{\lambda_1^{p-2}}[A]^{p-1}\{v\}_1 = \lambda_1 \sum_{r=1}^{n} \gamma_r \left(\frac{\lambda_r}{\lambda_1}\right)^{p-1} \{x\}_r \quad (8.34)$$

so, for a sufficiently large integer p, the first term in the series becomes the dominant one

$$\lim_{p\to\infty} \frac{1}{\lambda_1}\{v\}_p = \lim_{p\to\infty} \frac{1}{\lambda_1^{p-1}}[A]^{p-1}\{v\}_1 = \gamma_1 \{x\}_1. \qquad (8.35)$$

In practice only a finite number of iterations will suffice to reach a desired level of accuracy. The rate of convergence depends on the ratio of the second largest eigenvalue to the largest eigenvalue.

When convergence is achieved, the vectors $\{v\}_{p-1}$ and $\{v\}_p$ satisfy equation (8.31) because they can be both regarded as $\{x\}_1$. Denoting $\{w\}_p = [A]^{p-1}\{v\}_1$, the Rayleigh quotient of these vectors is equal to the eigenvalue

$$\lim_{p\to\infty} \frac{\{w\}_p^T[A]\{w\}_p}{\{w\}_p^T\{w\}_p} = \lambda_1. \qquad (8.36)$$

The question remains as how to obtain the higher modes.

8.5.1.2 Wielandt deflation

If $\{x\}_1$ is mass-normalized

$$\{x\}_1^T [m] \{x\}_1 = 1, \tag{8.37}$$

then the matrix

$$[A]_2 = [A] - \lambda_1 \{x\}_1 \{x\}_1^T [m] \tag{8.38}$$

has the same eigenvalues as $[A]$ except that λ_1 is replaced by zero.

The vector

$$[A]_2 \{v\}_1 = \sum_{r=2}^{n} \gamma_r \lambda_r \{x\}_r$$

is free from $\{x\}_1$. In (8.38) $[A]_2$ is called the *deflated matrix* corresponding to the second eigenvalue.

The power method applied to the matrix

$$[A]_3 = [A]_2 - \lambda_2 \{x\}_2 \{x\}_2^T [m] \tag{8.39}$$

converges to the eigenpair λ_3, $\{x\}_3$.

In order to prevent over- or underflow, the iteration vectors are scaled.

8.5.1.3 Inverse iteration

The inverse power method can be used to determine an eigenvector corresponding to an eigenvalue that has already been determined with reasonable accuracy by some method.

Let α be an approximation to the eigenvalue λ of $[A]$ so that $\alpha [I] - [A]$ is nearly singular. The scaled *inverse power method* for an initial vector $\{x\}_0$ defines the sequence of vectors $\{v\}_k$ and $\{x\}_k$ recursively as follows

$$\left(\alpha [I] - [A] \right) \{v\}_{k+1} = \{x\}_k,$$

$$\{x\}_{k+1} = \{v\}_{k+1} \big/ \left\| \{v\}_{k+1} \right\|. \qquad k = 0, 1, 2, \dots$$

At each stage of this iterative process, a linear system is solved with the same coefficient matrix but a different right-hand side. Thus first the LU-decomposition of $\alpha[I]-[A]$ is formed, and at successive steps the system is solved using only a forward and back substitution. For a good approximation α of λ, the method may be expected to converge quite rapidly.

Example 8.1

Calculate the first natural frequency and mode shape of torsional vibration for the three-disk system of Fig. 8.3, where $J_1 = 3J$, $J_2 = 2J$, $J_3 = J$, $K_1 = K_2 = K_3 = K$.
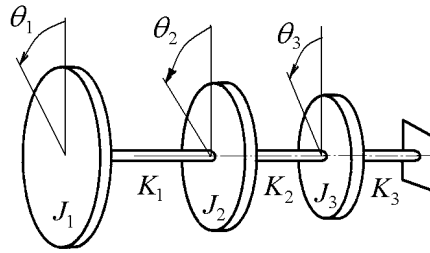
Fig. 8.3

Solution. The equations of motion are

$$J_1 \ddot{\theta}_1 + K_1 \theta_1 - K_1 \theta_2 = 0,$$

$$J_2 \ddot{\theta}_2 - K_1 \theta_1 + \left(K_1 + K_2\right)\theta_2 - K_2 \theta_3 = 0,$$

$$J_3 \ddot{\theta}_3 - K_2 \theta_2 + \left(K_2 + K_3\right)\theta_3 = 0.$$

In matrix form

$$\begin{bmatrix} J_1 & 0 & 0 \\ 0 & J_2 & 0 \\ 0 & 0 & J_3 \end{bmatrix} \begin{Bmatrix} \ddot{\theta}_1 \\ \ddot{\theta}_2 \\ \ddot{\theta}_3 \end{Bmatrix} + \begin{bmatrix} K_1 & -K_1 & 0 \\ -K_1 & K_1 + K_2 & -K_2 \\ 0 & -K_2 & K_2 + K_3 \end{bmatrix} \begin{Bmatrix} \theta_1 \\ \theta_2 \\ \theta_3 \end{Bmatrix} = \begin{Bmatrix} 0 \\ 0 \\ 0 \end{Bmatrix}.$$

For the given disk inertia and shaft stiffness parameters, the mass and stiffness matrices are

$$[m] = J\begin{bmatrix} 3 & 0 & 0 \\ 0 & 2 & 0 \\ 0 & 0 & 1 \end{bmatrix}, \qquad [k] = K\begin{bmatrix} 1 & -1 & 0 \\ -1 & 2 & -1 \\ 0 & -1 & 2 \end{bmatrix}.$$

The flexibility matrix is

$$[k]^{-1} = [\delta] = \frac{1}{K}\begin{bmatrix} 3 & 2 & 1 \\ 2 & 2 & 1 \\ 1 & 1 & 1 \end{bmatrix}.$$

The working matrix for iteration is

$$[b] = [\delta][m] = \frac{J}{K}\begin{bmatrix} 3 & 2 & 1 \\ 2 & 2 & 1 \\ 1 & 1 & 1 \end{bmatrix}\begin{bmatrix} 3 & 0 & 0 \\ 0 & 2 & 0 \\ 0 & 0 & 1 \end{bmatrix} = \frac{J}{K}\begin{bmatrix} 9 & 4 & 1 \\ 6 & 4 & 1 \\ 3 & 2 & 1 \end{bmatrix}.$$

The starting vector is taken proportional to the first column of matrix $[b]$

$$\{v\}_1 = \begin{Bmatrix} 1 \\ 2/3 \\ 1/3 \end{Bmatrix}.$$

The first iteration

$$[b]\{v\}_1 = \frac{J}{K}\begin{bmatrix} 9 & 4 & 1 \\ 6 & 4 & 1 \\ 3 & 2 & 1 \end{bmatrix}\begin{Bmatrix} 1 \\ 0.667 \\ 0.333 \end{Bmatrix} = \frac{J}{K}\begin{Bmatrix} 12 \\ 9 \\ 4.667 \end{Bmatrix} = 12\frac{J}{K}\begin{Bmatrix} 1 \\ 0.750 \\ 0.389 \end{Bmatrix} = 12\frac{J}{K}\{v\}_2.$$

The second iteration

$$[b]\{v\}_2 = \frac{J}{K}\begin{bmatrix} 9 & 4 & 1 \\ 6 & 4 & 1 \\ 3 & 2 & 1 \end{bmatrix}\begin{Bmatrix} 1 \\ 0.750 \\ 0.389 \end{Bmatrix} = \frac{J}{K}\begin{Bmatrix} 12.389 \\ 9.389 \\ 4.889 \end{Bmatrix} = 12.389\frac{J}{K}\begin{Bmatrix} 1 \\ 0.758 \\ 0.395 \end{Bmatrix} = 12.389\frac{J}{K}\{v\}_3$$

The third iteration

$$[b]\{v\}_3 = \frac{J}{K}\begin{bmatrix} 9 & 4 & 1 \\ 6 & 4 & 1 \\ 3 & 2 & 1 \end{bmatrix}\begin{Bmatrix} 1 \\ 0.758 \\ 0.395 \end{Bmatrix} = \frac{J}{K}\begin{Bmatrix} 12.427 \\ 9.427 \\ 4.911 \end{Bmatrix} = 12.427\frac{J}{K}\begin{Bmatrix} 1 \\ 0.758 \\ 0.395 \end{Bmatrix} = 12.427\frac{J}{K}\{v\}_3$$

The first mode of vibration is defined by

$$\{x\}_1 = \begin{Bmatrix} 1 \\ 0.758 \\ 0.395 \end{Bmatrix}, \quad \omega_1^2 = \frac{1}{12,427}\frac{K}{J} = 0.0805\frac{K}{J}, \quad \omega_1 = 0.2836\sqrt{\frac{K}{J}}.$$

8.5.2 The QR method

The QR algorithm is based on the repeated use of the QR factorization, which factors any matrix into the product of a matrix $[Q]$ with orthonormal columns and a matrix $[R]$ that is nonzero only in its upper, or right, triangle.

The simplest variant, known as the *single-shift algorithm*, is implemented in MATLAB as the **qr** function [8.5].

First, the QR factorization makes the matrix triangular

$$[A] - \sigma [I] = [Q][R], \tag{8.40}$$

where $\sigma = A(n,n)$ is the shift and $[I]$ is the identity matrix.

Then, the reverse order multiplication, RQ, restores the eigenvalues because

$$[R][Q] + \sigma [I] = [Q]^T ([A] - \sigma [I])[Q] + \sigma [I] = [Q]^T [A][Q], \tag{8.41}$$

so the new $[A]$ is orthogonally similar to the original $[A]$. Each iteration effectively transfers some information from the lower to the upper triangle while preserving the eigenvalues. As iterations are repeated, the matrix often approaches an upper triangular matrix with the eigenvalues conveniently displayed on the diagonal.

The QR algorithm is always preceded by a reduction to Hessenberg form, in which all the elements below the subdiagonal are zero. This reduced form is preserved by the iteration and the factorizations can be done much more quickly. The QR algorithm introduces zeros in the first subdiagonal.

The simplest variant involves real, symmetric matrices. The reduced form in this case is tridiagonal.

The basic QR method is described as follows [8.15]:

Denote the $n \times n$ matrix $[A]$ by $[A_0]$. The QR factorization of $[A_0]$ is

$$[A_0] = [Q_0][R_0] \ .$$

Define

$$[A_1] = [R_0][Q_0] \ .$$

Perform the QR-factorization of $[A_1]$

$$[A_1] = [Q_1][R_1] \ .$$

Define

$$[A_2] = [R_1][Q_1] \ .$$

In general, obtain the QR-factorization of $[A_{k-1}]$

$$\left[A_{k-1}\right] = \left[Q_{k-1}\right]\left[R_{k-1}\right] \ , \tag{8.42}$$

then define

$$\left[A_k\right] = \left[R_{k-1}\right]\left[Q_{k-1}\right] \ , \qquad k \geq 1 . \tag{8.43}$$

To form $\left[A_k\right]$ we take the product of the QR-factors from the previous step in reverse order. This simple process yields a sequence of matrices $\left[A_0\right], \left[A_1\right], \ \dots .$ It can be shown that the $\left[A_k\right]$ are orthogonally similar to $\left[A_0\right] = \left[A\right]$:

$$\left[A_k\right] = \left(\left[Q_0\right]\left[Q_1\right]\cdots\left[Q_{k-1}\right]\right)^T \left[A_0\right]\left(\left[Q_0\right]\left[Q_1\right]\cdots\left[Q_{k-1}\right]\right) \tag{8.44}$$

and that $\lim_{k \to \infty} \left[A_k\right]$ is an upper triangular matrix. Its diagonal elements are the eigenvalues.

8.5.3 Simultaneous iteration

Assume that we start with a set of independent vectors

$$\left[U_k^{(0)}\right] = \left[\ \{u\}_1, \{u\}_2, \dots, \{u\}_k\ \right] \ , \tag{8.45}$$

and that we carry out the power method with $\left[U_k^{(0)}\right]$, which leads to the computation of

$$\left[U_k^{(i)}\right] = \left[A\right]\left[U_k^{(i-1)}\right] \tag{8.46}$$

per iteration.

If we do this in a straightforward manner, then this will lead to unsatisfactory results because each of the columns of $\left[U_k^{(0)}\right]$ is effectively used as a starting vector for a single vector power method, and all these single vector processes will tend to converge towards the dominant vector. This will make the columns of $\left[U_k^{(i)}\right]$ highly dependent in the course of the iteration.

It is therefore a good idea to try to maintain better numerical independence between these columns and the most common technique for this is to make them orthonormal after each multiplication with $\left[A\right]$. This leads to the *orthogonal iteration method*, as represented in the following template [8.1]:

start with orthonormal $\left[U_k^{(1)} \right]$

for i = 1, …, **until convergence**

$$\left[V_k \right] = \left[A \right] \left[U_k^{(i)} \right],$$

orthonormalize the columns of $\left[V_k \right]$

$$\left[V_k \right] = \left[Q_k \right] \left[R_k \right],$$

$$\left[U_k^{(i+1)} \right] = \left[Q_k \right],$$

end

The columns of $\left[U_k^{(i)} \right]$ converge to a basis of an invariant subspace of dimension k, under the assumption that the largest k eigenvalues (counted according to multiplicity) are separated from the remainder of the spectrum. This can be easily seen from the same arguments as for the power method. The eigenvalues appear along the diagonal of $\left[R \right]$.

8.5.4 The QZ method

A stable method for the solution of the generalized problem (8.1) is the QZ method proposed by Moler and Stewart (1973) and implemented in the **eig.m** subroutine in MATLAB. Though more general, we are interested in its application in the case when $\left[k \right]$ and $\left[m \right]$ are symmetric with the latter positive definite.

The symmetric-definite problem can be solved using a method that utilizes both the Cholesky factorization $\left[m \right] = \left[L \right] \left[L \right]^T$ and the symmetric QR algorithm applied to $\left[B \right] = \left[L \right]^{-1} \left[k \right] \left[L \right]^{-T}$. This computes the Schur decomposition $\left[Q \right]^T \left[B \right] \left[Q \right] = \mathrm{diag}\left(\theta_1, ..., \theta_n \right)$ to obtain a nonsingular $\left[X \right] = \left[L \right]^{-1} \left[Q \right]$ such that $\left[X \right]^T \left[m \right] \left[X \right] = \left[I_n \right]$ and $\left[X \right]^T \left[k \right] \left[X \right] = \mathrm{diag}\left(\theta_1, ..., \theta_n \right)$, where $\theta_1, ..., \theta_n$ are the eigenvalues.

The QZ method for real matrices is based on the generalized real Schur decomposition. If $\left[k \right]$ and $\left[m \right]$ are real $n \times n$ matrices, then there exist orthogonal matrices $\left[Q \right]$ and $\left[Z \right]$ such that

$$\left[Q \right]^T \left[k \right] \left[Z \right] = \left[T^K \right] \text{ and } \left[Q \right]^T \left[m \right] \left[Z \right] = \left[T^M \right] \quad (8.47)$$

are upper triangular.

The computation of this decomposition is made in two steps. The first step is to reduce $[k]$ to upper Hessenberg form and $[m]$ to upper triangular form via orthogonal transformations. Then, by applying a sequence of QZ steps to the Hessenberg-triangular pencil $[k] - \lambda [m]$, it is possible to reduce $[k]$ to (quasi-) triangular form. The ratio of diagonal elements of $[T^K]$ and $[T^M]$ define the eigenvalues λ. Eigenvectors are computed by a back substitution algorithm.

8.6. Subspace iteration methods

Subspace iteration was originally introduced by Bauer (1957), who called the method *Treppeniteration* (staircase iteration). In the modern iterative subspace methods, like Arnoldi's method for unsymmetric matrices, Lanczos' method for symmetric matrices, and Davidson's method, the given large problem is reduced to a much smaller one. This smaller problem can then be solved by the, by now, standard techniques for dense matrices.

8.6.1 The Rayleigh-Ritz approximation

The Rayleigh-Ritz method is used for extracting an approximate low-dimensional eigenspace from a larger subspace. It is possible to construct k approximate eigenvectors of $[A]$, $[X_k] = [\{x\}_1, \{x\}_2, ..., \{x\}_k]$, as linear combinations of some trial vectors $[V_m] = [\{v\}_1, \{v\}_2, ..., \{v\}_m]$:

$$[X_k] = [V_m][Y_k], \qquad \{x\}_i = \sum_{j=1}^{m} y_{ji} \{v\}_j , \qquad (8.48)$$

where $[Y_k] = [\{y\}_1, \{y\}_2, ..., \{y\}_k]$, and $k << n$. In reference [8.16], the number of trial vectors $m=2k$.

Any pair $\{x\}_i, \theta_i$ that satisfies the orthogonality condition for residuals

$$[V_m]^T \left([A]\{x\}_i - \theta_i \{x\}_i \right) = \{0\} \qquad (8.49)$$

is called a *Ritz pair*. For k eigenpairs, equation (8.49) can be written

$$[V_m]^T \left([A][X_k] - [X_k][\Theta_k] \right) = [0] \qquad (8.50)$$

where $\left[\Theta_k\right] = \mathrm{diag}\left(\theta_1, \theta_2, ..., \theta_k\right)$. Substituting (8.48) in equation (8.50), one obtains the reduced eigensystem

$$\left[H_m\right]\left[Y_k\right] = \left[Y_k\right]\left[\Theta_k\right], \tag{8.51}$$

where

$$\left[H_m\right] = \left[V_m\right]^T\left[A\right]\left[V_m\right] \tag{8.52}$$

has the form of a Rayleigh quotient matrix, and $\left[V_m\right]^T\left[V_m\right] = \left[I_m\right]$.
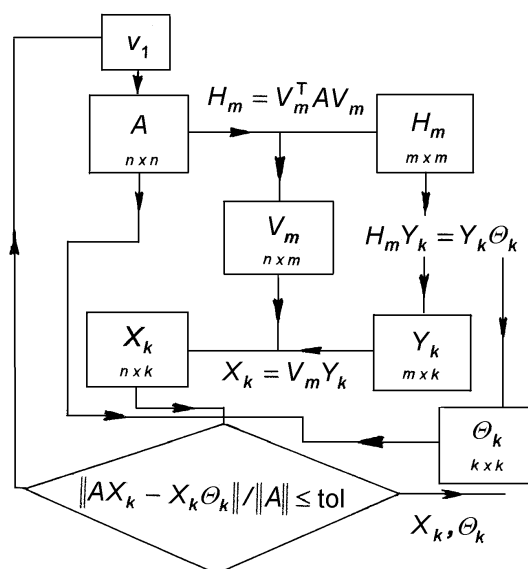
Fig 8.4 (from [8.13])

The columns of $\left[X_k\right]$ are called the *Ritz vectors*, and the elements of $\left[\Theta_k\right]$ are the *Ritz values*. The columns of $\left[Y_k\right]$ are referred to as *primitive Ritz vectors*.

The Rayleigh-Ritz approximation (8.48) allows constructing eigenpairs $\{x\}_i, \theta_i$ of the large matrix $\left[A\right]$, from the eigenpairs $\{y\}_i, \theta_i$ of the small matrix $\left[H_m\right]$. If $m \ll n$, the eigensystem of $\left[H_m\right]$ can be computed by conventional (dense) means. An appropriate form of $\left[H_m\right]$ for the QR iteration is the Hessenberg form. This can be obtained using the Arnoldi factorization [8.17], i.e. selecting the columns of $\left[V_m\right]$ as orthonormal Arnoldi vectors.

Figure 8.4 shows the relationships between the quantities involved in computation.

Using *M*-orthogonal Arnoldi vectors, $\left[V_m\right]^T\left[m\right]\left[V_m\right]=\left[I_m\right]$, the matrix $\left[H_m\right]$ is symmetric (tridiagonal) and the Arnoldi process reduces to the more simple Lanczos process for the symmetric problem.

8.6.2 Krylov subspaces

Given $\left\{v\right\}_1$, in the power method we compute

$$\left[A\right]\left\{v\right\}_1,\ \left[A\right]\left(\left[A\right]\left\{v\right\}_1\right),\ \ldots\ldots,\ \left[A\right]^{p-1}\left\{v\right\}_1.$$

At each step, the power method considers only the single vector $\left[A\right]^{p-1}\left\{v\right\}_1$ which amounts to throwing away the information contained in the previously generated vectors. However, it turns out that this information is valuable.

Generally, the sequence

$$\left\{v\right\}_1,\ \left[A\right]\left\{v\right\}_1,\ \left[A\right]^2\left\{v\right\}_1,\ \left[A\right]^3\left\{v\right\}_1,\ \ldots.$$

is a *Krylov sequence* based on $\left[A\right]$ and $\left\{v\right\}_1$.

A *Krylov subspace* is defined by

$$K_p\left(\left[A\right];\left\{v\right\}_1\right)\equiv\text{span}\left\{\left\{v\right\}_1,\left[A\right]\left\{v\right\}_1,\ldots\left[A\right]^{p-1}\left\{v\right\}_1\right\}. \qquad (8.53)$$

Krylov subspaces play a central role in iterative methods for eigenvalue computations. The methods of Lanczos and Arnoldi exploit the whole Krylov subspace.

8.6.3 The Arnoldi method

Arnoldi's method can be thought of as an effective way of constructing an orthogonal set of vectors, referred to as Arnoldi vectors, for use in the Rayleigh-Ritz approximation procedure to reduce the dimension of the equations of motion.

The original algorithm [8.18] was designed to reduce a dense non-Hermitian matrix to upper Hessenberg form by an orthogonal projection onto the subspace spanned by the Arnoldi vectors. The symmetric version is the Lanczos method [8.19] which reduces a Hermitian matrix to tridiagonal form.

The value of Arnoldi's method as a technique for approximating a few eigenvalues and their matching eigenvectors was recognized later [8.20]. More than two decades of fruitful research efforts, to solve the various problems raised by its numerical implementation, resulted in ARPACK [8.21], a well-coded and

well documented software package, claiming to become the standard for large non-Hermitian eigenproblems. ARPACK is written in Fortran 77 and is based on the Implicitly Restarted Arnoldi (IRA) iteration [8.17]. There is also a MATLAB implementation [8.16].

The basic idea behind the Arnoldi reduction is to use orthogonalized Krylov vectors as trial vectors $[V_m]$ in equation (8.48).

8.6.3.1 Arnoldi's algorithm

The basic algorithm consists of the following five steps:

1 - build an orthogonal basis for the subspace spanned by the columns of the Krylov matrix

$$[K_m] = \left[\{v\}_1 \ [A]\{v\}_1 \ [A]^2\{v\}_1 \cdots [A]^{m-1}\{v\}_1 \right] \ ;$$

2 – form the matrix

$$[V_m] = \left[\{v\}_1 \ \{v\}_2 \ \{v\}_3 \cdots \{v\}_m \right] \ , \quad \text{where} \quad \{v\}_k = [A]^{k-1}\{v\}_1 ;$$

3 - compute the Rayleigh matrix

$$[H_m] = [V_m]^T [A][V_m];$$

4 - eigensolution

$$[H_m]\{y\} = \theta\{y\};$$

5 – compute Ritz vectors

$$\{x\} = [V_m]\{y\}.$$

As *m* increases, extremal well-separated eigenvalues of $[A]$ are well approximated by a subset of the eigenvalues of $[H_m]$.

8.6.3.2 Generation of Arnoldi vectors

Arnoldi vectors $\{v\}_j$ represent orthogonal unit directions in an *n*-dimensional basis subspace.

Initial vector

The unit vector $\{v\}_1$ is along $\{\bar{v}\}_1$, determined solving

$$([k] - \sigma[m])\{\bar{v}\}_1 = [m]\{v\}_0 ,$$

where

$$\{v\}_0 = \{\bar{v}\}_0 / \|\bar{v}_0\|_2, \quad \{\bar{v}\}_0 = \text{randn}\,(n,1) - 0.5,$$

then normalized to unit length

$$\{v\}_1 = \{\bar{v}\}_1 / \|\bar{v}_1\|_2.$$

Second vector

Premultiplication by $[A]$ yields the vector

$$\{\bar{v}\}_2 = [A]\{v\}_1,$$

rotated with respect to $\{v\}_1$.

The component of $\{\bar{v}\}_2$ along $\{v\}_1$ is the projection $\left(\{v\}_1\{v\}_1^T\right)\{\bar{v}\}_2$. The component orthogonal to $\{v\}_1$ is

$$\beta_2\,\{v\}_2 = \left([I] - \{v\}_1\{v\}_1^T\right)\{\bar{v}\}_2,$$

where $\{v\}_2$ has unit length, $\|v_2\|_2 = 1$ and β_2 is the amplitude.

Third vector

Premultiplication of $\{v\}_2$ by $[A]$ yields

$$\{\bar{v}\}_3 = [A]\{v\}_2,$$

rotated out of the plane of $\{v\}_1$ and $\{v\}_2$.

The component of $\{\bar{v}\}_3$ along $\{v\}_1$ is $\left(\{v\}_1\{v\}_1^T\right)\{\bar{v}\}_3$, the component along $\{v\}_2$ is $\left(\{v\}_2\{v\}_2^T\right)\{\bar{v}\}_3$ and the component orthogonal to both $\{v\}_1$ and $\{v\}_2$ is

$$\beta_3\,\{v\}_3 = \left([I] - \{v\}_1\{v\}_1^T - \{v\}_2\{v\}_2^T\right)\{\bar{v}\}_3,$$

where $\{v\}_3$ has unit length, $\|v_3\|_2 = 1$ and β_3 is the amplitude.

The $(m+1)$-th vector

In general, premultiplication of $\{v\}_m$ by $[A]$ yields

$$\{\bar{v}\}_{m+1} = [A]\{v\}_m.$$

The component of $\{\bar{v}\}_{m+1}$, orthogonal to all previous unit vectors in the sequence, is

$$\beta_{m+1}\{v\}_{m+1} = \left([I] - [V]_m[V]_m^T\right)\{\bar{v}\}_{m+1}, \qquad \|v_{m+1}\|_2 = 1$$

or

$$\beta_{m+1}\{v\}_{m+1} = [A]\{v\}_m - \sum_{j=1}^{m} h_{jm}\{v\}_j, \tag{8.54}$$

where

$$h_{jm} = \{v\}_j^T[A]\{v\}_m. \tag{8.55}$$

The recurrence equations can be written in matrix form

$$[A][V_m] = [V_m][H_m] + \beta_{m+1}\{v\}_{m+1}\{e\}_m^T$$

where $\{e\}_m^T = \lfloor 0, ..., 0, 1 \rfloor$ has m elements.

8.6.3.3 The Arnoldi factorization

In exact arithmetic, the matrix $[A] \in \mathfrak{R}^{n \times n}$ can be reduced to upper Hessenberg form $[H_n]$ by a congruence transformation

$$[V_n]^T[A][V_n] = [H],$$

where $[V_n] = \left[\{v\}_1, \{v\}_2, ..., \{v\}_n\right]$ is orthogonal.

The Hessenberg decomposition of $[A]$:

$$[A][V_n] = [V_n][H_n],$$

can also be written in the form

$$
[A]\left[\{v\}_1, \{v\}_2, ..., \{v\}_n\right] =
$$

$$
= \left[\{v\}_1, \{v\}_2, ..., \{v\}_n\right]
\begin{bmatrix}
h_{11} & h_{12} & \cdots & h_{1m} & \cdots & h_{1,n-1} & h_{1n} \\
\beta_2 & h_{22} & \cdots & h_{2m} & \cdots & h_{2,n-1} & h_{2n} \\
 & \beta_3 & \ddots & \cdots & \cdots & \cdots & \cdots \\
 & & \ddots & \cdots & \cdots & \cdots & \cdots \\
 & & & \beta_{m+1} & \ddots & \cdots & \cdots \\
 & 0 & & & \ddots & h_{n-1,n-1} & \cdots \\
 & & & & & \beta_n & h_{nn}
\end{bmatrix}. \tag{8.56}
$$

In equation (8.56), the subdiagonals

$$\beta_{m+1} = h_{m+1,m} \ \left(m = 1, ..., n-1 \right), \qquad \beta_{n+1} = 0 . \qquad (8.57)$$

After *m* steps, the Arnoldi method computes what is called *a length m Arnoldi factorization of* $\left[A \right]$:

$$\left[A \right] \left[\{v\}_1, \{v\}_2, ..., \{v\}_m \right] =$$

$$= \left[\{v\}_1, \{v\}_2, ..., \{v\}_{m+1} \right] \begin{bmatrix} h_{11} & h_{12} & \cdots & \cdots & h_{1m} \\ \beta_2 & h_{22} & & & h_{2m} \\ & \beta_3 & \ddots & & \cdots \\ & & \ddots & \ddots & \cdots \\ 0 & & & \ddots & h_{mm} \\ & & & & \beta_{m+1} \end{bmatrix} . \qquad (8.58)$$

Denoting $\left[V_m \right] = \left[\{v\}_1, \{v\}_2, ..., \{v\}_m \right]$, $m < n$, equation (8.58) can be written compactly as

$$\left[A \right] \left[V_m \right] = \left[V_m \right] \left[H_m \right] + \{r\}_m \{e\}_m^T . \qquad (8.59)$$

In equation (8.59), the residual

$$\{r\}_m = \{v\}_{m+1} \beta_{m+1} \qquad (8.60)$$

forms the last column in the last term matrix (Fig. 8.5). Since $\{r\}_m$ is a multiple of $\{v\}_{m+1}$, it must be orthogonal to all previous Arnoldi vectors $\{v\}_j$ ($j = 1, ..., m$), hence $\left[V_m \right]^T \{r\}_m = \{0\}$.


Fig. 8.5

Suppose that $\left[V_m \right]$ is known, i.e. *m* columns of $\left[V_n \right]$ have been determined. Write the *m*-th column of (8.56) in the form

$$[A]\{v\}_m = [V_m]\{h\}_m + \{v\}_{m+1}\beta_{m+1}, \qquad (8.61)$$

where $\{h\}_m = \lfloor h_{1m}, ..., h_{mm} \rfloor^T$.

Denoting the residual (8.61)

$$\{r\}_m = [A]\{v\}_m - [V_m]\{h\}_m = \{v\}_{m+1}\beta_{m+1}, \qquad (8.62)$$

the Arnoldi algorithm forces $[V_m]^T\{r\}_m = \{0\}$ via the choice of the elements of $\{h\}_m$:

$$\{h\}_m = [V_m]^T[A]\{v\}_m, \qquad (8.63)$$

and normalizes then $\{r\}_m$ to get β_{m+1} and $\{v\}_{m+1}$:

$$\beta_{m+1} = \|r_m\|_2, \qquad (8.64)$$

$$\{v\}_{m+1} = \{r\}_m / \|r_m\|_2. \qquad (8.65)$$

Cancellation in equation (8.62) can cause the Arnoldi process to fail producing orthogonal vectors. The cure is reorthogonalization and accumulation of changes in $\{h\}_m$:

$$\{h\}_m \leftarrow \{h\}_m + [V_m]^T\{r\}_m, \qquad (8.66)$$

$$\{r\}_m \leftarrow \left([I_m] - [V_m][V_m]^T\right)\{r\}_m. \qquad (8.67)$$

This is known as the DGKS correction [8.22].

If $\{r\}_m = 0$, then β_{m+1} is undefined and

$$[A][V_m] = [V_m][H_m]. \qquad (8.68)$$

The subspace spanned by the columns of $[V_m]$ is invariant with respect to $[A]$, i.e. it is an eigenspace of $[A]$, and one can determine its eigenelements [8.12].

In order to compute the other eigenelements, the algorithm is restarted choosing $\{v\}_{m+1}$ orthogonal to $[V_m]$. The eigenvalues of $[H_m]$ are a subset of those of $[A]$. The initial vector $\{v\}_1 = [V_m]\{e\}_1$ is a linear combination of vectors spanning an invariant subspace of $[A]$.

It is better to use *M*-orthogonal Arnoldi vectors:

$$[V_m]^T[m][V_m] = [I_m].$$

Premultiplying equation (8.68) by $\left[V_m\right]^T\left[m\right]$ one obtains, instead of equation (8.52),

$$\left[V_m\right]^T\left[m\right]\left[k\right]^{-1}\left[m\right]\left[V_m\right]=\left[H_m\right],\qquad(8.69)$$

and $\left\{r\right\}_m$ is *M*-orthogonal to $\left[V_m\right]$. In this case, the Hessenberg matrix is symmetric (tridiagonal) and the Arnoldi process reduces to the more simple Lanczos process for the symmetric problem.

Using the *M*-Arnoldi process, equations (8.63) to (8.65) become

$$\left\{h\right\}_m=\left[V_m\right]^T\left[m\right]\left\{\bar{r}\right\}_m\,,\qquad\left[k\right]\left\{\bar{r}\right\}_m=\left[m\right]\left\{v\right\}_m\,,\qquad(8.70)$$

$$\left\{v\right\}_{m+1}=\left\{r\right\}_m/\beta_{m+1}\,,\qquad\beta_{m+1}=\left(\left\{r\right\}_m^T\left[m\right]\left\{r\right\}_m\right)^{1/2}.\qquad(8.71)$$

Again, reorthogonalization is necessary.

8.6.3.4 Eigenpair approximation

Once the matrix of Arnoldi vectors, $\left[V_m\right]$, and the Ritz matrix, $\left[H_m\right]$, are constructed, the focus is to extract information about the eigensystem of the matrix $\left[A\right]$.

Equation (8.59) shows that, for a given *m* and $\left\{v\right\}_1$

$$\left[A\right]\left[V_m\right]-\left[V_m\right]\left[H_m\right]=\beta_{m+1}\left\{v\right\}_{m+1}\left\{e\right\}_m^T=\left\{R\right\}_m\neq0.\qquad(8.72)$$

In order to obtain equation (8.68) it seems that it is sufficient to make $\left\{R\right\}_m=\left\{0\right\}$. Obviously, $\left\|R_m\right\|\rightarrow0$ when $\beta_{m+1}\rightarrow0$.

If $\beta_{m+1}=0$, then $\text{span}\left(\left[V_m\right]\right)$ is an invariant subspace, and $\left[H_m\right]$ is the restriction of $\left[A\right]$ to it. Nevertheless, in practical applications $\beta_{m+1}=0$ never happens. However, some of the eigenvalues of $\left[A\right]$ are often much more accurately approximated than indicated by the size of the subdiagonal element β_{m+1} .

The strategy for obtaining $\left[A\right]\left[V_m\right]=\left[V_m\right]\left[H_m\right]$ is to find an appropriate initial vector which forces $\left\{r\right\}_m$ to vanish. It makes $\left\{v\right\}_1$ be a linear combination of *m* eigenvectors of $\left[A\right]$. If *m* is fixed, then the initial vector is updated while repeatedly doing *m* Arnoldi steps, until a subdiagonal element of the Hessenberg matrix is less than a prescribed tolerance.

In exact arithmetic, $\{R\}_m$ has all its elements concentrated in the last column. If $[H_m]\{y\}_i = \theta_i\{y\}_i$, then $\{x\}_i = [V_m]\{y\}_i$. satisfies the relation

$$\left\| [A]\{x\}_i - \theta_i\{x\}_i \right\| = \beta_{m+1}\left| \{e\}_m^T\{y\}_i \right|. \qquad (8.73)$$

The last term in equation (8.73), called the *Ritz estimate* of the eigenpair $\left(\{y\}_i, \theta_i\right)$, describes the goodness of the eigenpair approximation. As β_{m+1} is multiplied by the last element of $\{y\}_i$, all eigenvalues of $[H_m]$, whose vectors have small last elements, have smaller errors than expected from β_{m+1}.

Computations performed in finite-precision arithmetic complicate the picture. In fact, all columns of $\{R\}_m$ contain round off, so its elements are not concentrated in the last column.

In [8.16], the Ritz estimates are first used to assess the convergence. When the Ritz estimates become too small, the convergence tolerance is computed using the 1-norm of the matrix of errors

$$\text{tol} = \left\| [A][X_k] - [X_k][\Theta_k] \right\|_1 / \|A\|_1. \qquad (8.74)$$

The Arnoldi algorithm is used with repeated, carefully chosen restarts, to keep small the storage space, and a controlled iteration maximum.
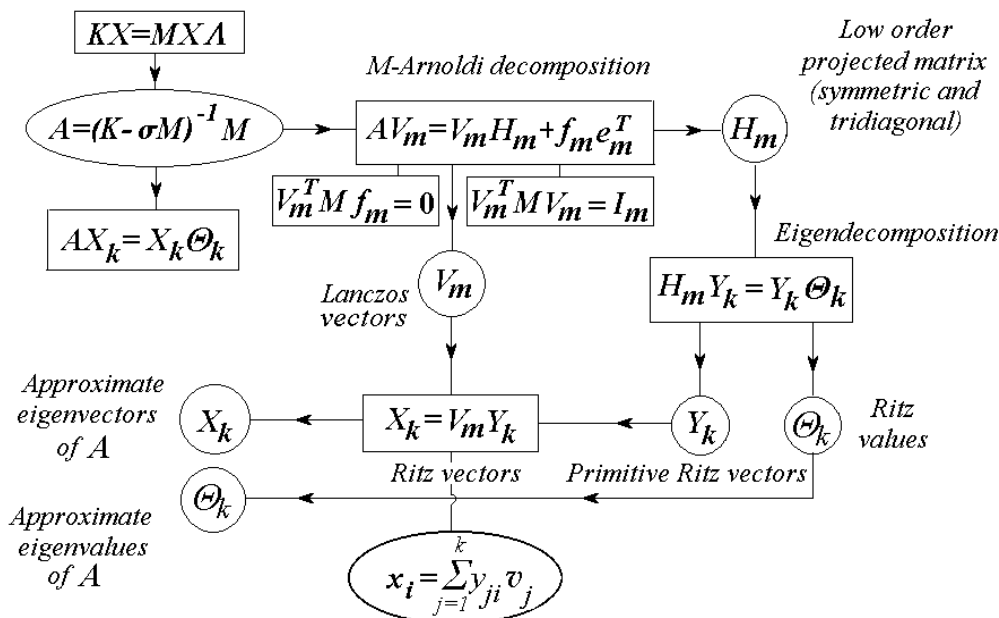

Fig. 8.6 (from [8.13])

Apart from the desired convergence tolerance, other quantities to be decided are: the starting vector, the number of desired eigenpairs, the dimension of the Arnoldi basis necessary to ensure the prescribed accuracy, the stagnation tolerance and the maximum number of Arnoldi iterations.

In [8.16], the starting vector is randomly generated, $\{\bar{v}\}_0 = \text{randn}(n,1) - 0.5$, then it is normalized to unit length $\{v\}_0 = \{\bar{v}\}_0 / \|\bar{v}_o\|_2$. One power iteration is performed before starting the iterative process, using the initial vector $\{\bar{v}\}_1 = [A]\{v\}_0$ instead of $\{v\}_1 = \{\bar{v}\}_0$.

8.6.3.5 Implementation details

Krylov subspace methods encompass three main steps: a) matrix preparation, b) subspace generation, and c) eigenvalue approximation. If $m \ll n$, the eigensystem of $[H_m]$ can be computed by conventional (dense) means. An appropriate form of $[H_m]$ for the QR iteration is the Hessenberg form. This can be obtained using the Arnoldi factorization [8.12], i.e. selecting the columns of $[V_m]$ as orthonormal Arnoldi vectors.

Arnoldi vectors are orthogonal Krylov vectors, generated by repeated multiplication of a starting vector with the working matrix and reorthogonalization [8.23]. The subspace is generated by adding one vector at a time and orthogonalizing. Vectors already converged are locked, fake vectors are purged from the basis, the others are used for further computation in implicit restart.

The result of the *M*-Arnoldi decomposition is a set of Lanczos vectors collected in $[V_m]$ and the low-order projected matrix $[H_m] = [V_m]^T [m][A][V_m]$, which is symmetric and tridiagonal.

One way further is to directly use the eigendecomposition of $[H_m]$. Its eigenvalues are used to approximate some of the eigenvalues of the data matrix. The eigenvectors of the operating matrix are expressed as linear combinations of the Lanczos vectors, with the multiplying factors as elements of the eigenvectors of $[H_m]$ (Fig. 8.6). The power of the method consists in the fact that excellent approximations to a few eigenvalues can be obtained after a number of iterations significantly smaller than the order of the working matrix.

Another general approach (Fig. 8.7) is to first compute a partial Schur form of $[H_m]$, then to use its eigendecomposition to obtain approximate eigenvalues of $[A]$. The matrix of primitive Ritz vectors $[Y_k]$ can be obtained premultiplying the eigenmatrix of $[R_k]$ by the matrix of Schur vectors of $[H_m]$. Approximate eigenvectors of $[A]$ are then obtained as before using the Lanczos vectors.

Alternatively, approximate Schur vectors of $[A]$ are first obtained multiplying the matrix of Lanczos vectors by the matrix of Schur vectors of $[H_m]$. Then, Ritz vectors of $[A]$ are obtained multiplying $[U_k]$ by the eigenmatrix of $[R_k]$.
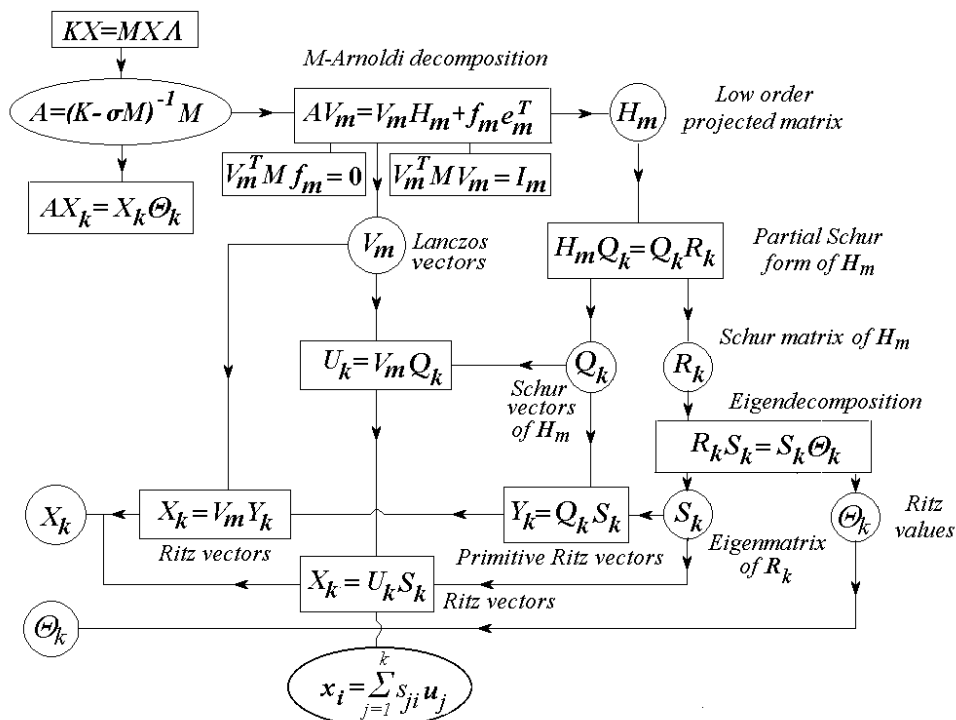

Fig. 8.7 (from [8.13])

For the *M*-Arnoldi process, the eigendecomposition of $[R_k]$ is not necessary. It is mentioned here because it is implemented in existing codes.

8.6.4 The Lanczos method

Simple processes, like the *power method*, require, in principle, an infinite number of expensive matrix-vector products to converge to an eigenvector. The method of *minimized iterations*, proposed by Lanczos in 1950, expands each eigenvector in a converged series with at most *n* terms. For eigenvectors belonging to extreme eigenvalues the convergence is usually very quick. However, Lanczos' method was first used only as a process to tridiagonalize a symmetric matrix.

To compete in accuracy with the Givens and Householder method, the Lanczos process has to be supplemented with the explicit orthogonalization of the

Lanczos vectors which, in exact arithmetic, would be orthogonal automatically. One advantage is that the only way the matrix $[A]$ enters the Lanczos algorithm is through a subprogram which computes a matrix-vector product.

In the following we present a Krylov-Lanczos method in exact arithmetic. The use of finite precision arithmetic provokes significant departures from the exact version, especially the loss of orthogonality among the Lanczos vectors. Left to itself, a simple Lanczos program will run forever, finding more and more copies of the outer eigenvalues for each new inner eigenvalue it discovers. So it has to be stopped after a number of steps, then restarted with a new starting vector [8.24].

One simplification with respect to the Arnoldi vectors is that each Lanczos vector is made orthogonal to the previous *two* Lanczos vectors, and this makes the present Lanczos vector (theoretically) orthogonal to *all* prior vectors.

The following algorithm presents the Lanczos method (in exact arithmetic) with emphasis on the physical meaning of Lanczos vectors when the starting vector is load dependent [8.25]. While closely related to the powerful and popular Lanczos eigensolvers, the procedure discussed here does not employ an eigenvector subspace and avoids the computational expense of reorthogonalization.

The starting vector $\{r\}_1$ can be the static deflection of the structure due to the load distribution vector $\{f\}$, given by

$$[k]\{r\}_1 = \{f\}. \tag{8.75}$$

This vector is mass normalized to form the first Lanczos vector

$$\{v\}_1 = \frac{1}{\beta_1}\{r\}_1 \tag{8.76}$$

where the normalizing factor is

$$\beta_1 = \sqrt{\{r\}_1^T [m]\{r\}_1}. \tag{8.77}$$

The second Lanczos vector is obtained by first solving for the static deflection $\{\bar{r}\}_2$ of the structure subjected to inertia loading due to the first vector deflection

$$[k]\{\bar{r}\}_2 = [m]\{v\}_1. \tag{8.78}$$

Then, the Gram-Schmidt orthogonalization is used to remove the starting vector component $\{v\}_1$ of this iterate

$$\{r\}_2 = \{\bar{r}\}_2 - \alpha_1\{v\}_1, \tag{8.79}$$

where

$$\alpha_1 = \{v\}_1^T [m]\{\bar{r}\}_2 \tag{8.80}$$

is the amplitude of $\{v\}_1$ along $\{\bar{r}\}_2$.

Finally, the vector $\{r\}_2$ is mass normalized to form the second Lanczos vector

$$\{v\}_2 = \frac{1}{\beta_2}\{r\}_2 \ , \tag{8.81}$$

where the normalizing factor is

$$\beta_2 = \sqrt{\{r\}_2^T [m]\{r\}_2} \ . \tag{8.82}$$

The general Lanczos vector, $\{v\}_j$, $j = 3, 4, \ldots$, is obtained by the following steps:

First, solve the equation

$$[k]\{\bar{r}\}_{j+1} = [m]\{v\}_j \tag{8.83}$$

for the static deflection $\{\bar{r}\}_{j+1}$.

Use the Gram-Schmidt procedure to remove both the $\{v\}_j$ component and the $\{v\}_{j-1}$ component of this iterate

$$\{r\}_{j+1} = \{\bar{r}\}_{j+1} - \alpha_j \{v\}_j - \beta_j \{v\}_{j-1} \tag{8.84}$$

where

$$\alpha_j = \{v\}_j^T [m]\{\bar{r}\}_{j+1} \tag{8.85}$$

and

$$\beta_j = \{v\}_{j-1}^T [m]\{\bar{r}\}_{j+1} \tag{8.86}$$

which can be shown to be just the preceding normalizing factor.

Finally, mass normalize the vector $\{r\}_{j+1}$ to form the $(j+1)$st Lanczos vector

$$\{v\}_{j+1} = \frac{1}{\beta_{j+1}}\{r\}_{j+1} \ , \tag{8.87}$$

where the normalizing factor is

$$\beta_{j+1} = \sqrt{\{r\}_{j+1}^T [m]\{r\}_{j+1}} \ . \tag{8.88}$$

Let $[V_m]$ contain the first m Lanczos vectors as columns

$$[V_m] = \left[\{v\}_1, \{v\}_2, ..., \{v\}_m \right],$$ (8.89)

and let the corresponding tridiagonal matrix containing the coefficients α_i and β_i be

$$[T_m] = \begin{bmatrix} \alpha_1 & \beta_2 & 0 & \cdots & 0 & 0 \\ \beta_2 & \alpha_2 & \beta_3 & \cdots & 0 & 0 \\ 0 & \beta_3 & \alpha_3 & \cdots & 0 & 0 \\ \vdots & \vdots & \vdots & \ddots & \vdots & \vdots \\ 0 & 0 & 0 & \cdots & \alpha_{m-1} & \beta_m \\ 0 & 0 & 0 & \cdots & \beta_m & \alpha_m \end{bmatrix}.$$ (8.90)

The matrix $[T_m]$ can be expressed in terms of the Lanczos vectors as

$$[T_m] = [V_m]^T [m][k]^{-1}[m][V_m],$$ (8.91)

where

$$[V_m]^T [m][V_m] = [I_m].$$ (8.92)

It can be shown that the differential equation of motion

$$[m]\{\ddot{x}\} + [k]\{x\} = \{f\},$$ (8.93)

where $\{f\}$ is the column vector of external forcing, can be reduced using a Ritz-type coordinate transformation

$$\{x\} = [V_m]\{x_m\},$$ (8.94)

to the following form

$$[T_m]\{\ddot{x}_m\} + [I_m]\{x_m\} = \lfloor \beta_1 \quad 0 \quad \cdots \quad 0 \rfloor^T.$$ (8.95)

Note that the transformed mass matrix is the tridiagonal matrix of orthogonalization coefficients, while the transformed stiffness matrix is the identity matrix. Also note that the only nonzero forcing term acts on the first Lanczos coordinate. The remaining coordinates are only coupled through the off-diagonal terms of the transformed mass matrix in equation (8.95).

There are several improvements of the basic Lanczos method such as the shifted Lanczos, the block Lanczos, the two-sided Lanczos, and the implicitly restarted Lanczos algorithms [8.12], [8.23]. Their presentation is beyond the aim of this lecture course.

8.7. Software

Numerous codes for solving eigenproblems can be found in the software repository *Netlib* on the Internet at `http://www.netlib.org/`. They are also available by anonymous **ftp**.

Reliable high quality software for linear algebra was first published in the book edited by Wilkinson and Reinsch [8.26] as Algol 60 subroutines. In the early 1970s most of these were transcripted in FORTRAN and included in the software package EISPACK [8.27] and later in NAG, IMSL and MATLAB packages. The Jacobi method was not included in EISPACK and at that time the Lanczos and Arnoldi methods were not even considered as candidates.

EISPACK was superseded in 1995 by LAPACK [8.6]. The authors of LAPACK developed new routines and restructured the EISPACK software to achieve much greater efficiency, where possible, on modern high-performance computers. This was accomplished by writing routines that call all three levels of the BLAS (Basic Linear Algebra Subprograms) [8.28].

In 1970 there were few robust and well-understood iterative methods available, and mainly for this reason, these methods were not included in the packages constructed then. Since 1998 MATLAB has had iterative methods for eigenproblems available and the **eigs.m** function [8.16] was available in source code.

Improvements made to the Arnoldi method, in particular the implicit restart technique [8.17], lead to the ARPACK software [8.21] which seems to be the default choice for large sparse eigenproblems. ARPACK makes extensive use of BLAS and LAPACK.

MATLAB files that implement the Lanczos method for finding eigenvalues of a symmetric matrix, written by J. Demmel, are available on the Internet for the applications in his book [8.29]. The LANSEL eigenpackage based on the Lanczos algorithm with selective orthogonalization is presented in [8.30].

The subspace iteration code SRRIT [8.31] computes an orthonormal basis for the invariant subspace corresponding to the eigenvalues of largest modulus.

The code LOPSI [8.32] uses a subspace iteration combined with a *lopsided* oblique projection to compute the eigenvalues of largest modulus together with the corresponding eigenvectors.

The JDQZ and JDQR algorithms, described in the paper [8.33], have MATLAB 5.1 and FORTRAN 77 implementations available on the Internet. They are based on the Jacobi-Davidson method [8.34]. This is an iterative subspace method incorporating an effective restart strategy for computing one or more eigenvalues and eigenvectors of an eigenproblem. The MATLAB implementation is based on algorithms presented in [8.23].

A black-box implementation of the inverse free preconditioned Krylov subspace method [8.35] is the **eigifp.m** MATLAB program that computes a few (algebraically) smallest or largest eigenvalues of large symmetric matrices.

irbleigs.m [8.36] is a MATLAB program for computing a few eigenvalues and associated eigenvectors of a sparse Hermitian matrix of large order. This program implements a restarted block-Lanczos method with judiciously chosen acceleration polynomials. **ahbeigs.m** is for non-symmetric matrices.

A unified overview of theory, algorithms, and practical software for engineering eigenvalue problems is presented in the book [8.23]. Numerical recipes and "black box" methods are given for Hermitian and non-Hermitian eigenvalue problems, generalized Hermitian and non-Hermitian eigenvalue problems and nonlinear eigenvalue problems.

References

8.1 Van der Vorst, H.A., *Computational Methods for Large Eigenvalue Problems*, Springer, Berlin, 1988.

8.2 Golub, G.H. and Van der Vorst, H.A., *Eigenvalue computation in the 20th century,* Journal of Computational and Applied Mathematics, vol.123, no.1-2, pp 35-65, Nov 2000.

8.3 Bathe, K.-J. and Wilson, E.L., *Numerical Methods in Finite Element Analysis*, Prentice-Hall, Englewood Cliffs, New Jersey, 1976.

8.4 Moler, C., *Numerical Computing with MATLAB*, SIAM, Philadelphia, PA, 2004.

8.5 *** *Using MATLAB* (Version 5), The MathWorks Inc., Dec. 1996.

8.6 Anderson, E., Bai, Z., Bischof, C., Demmel, J., Dongarra, J., Du Croz, J., Greenbaum, A., Hammarling, S., McKenney, A., Ostrouchov, S. and Sorensen, D., *LAPACK Users' Guide*, SIAM, Philadelphia, 2nd ed, 1995.

8.7 Kohnke, C. (ed.), *ANSYS Engineering Analysis System, Theoretical Manual*, Rev 4.3, Swanson Analysis Systems Inc., Houston, PA, 1987.

8.8 Wilkinson, J.H., *The Algebraic Eigenvalue Problem*, Clarendon Press, Oxford, 1965.

8.9 Parlett, B.N., *The Symmetric Eigenvalue Problem*, Prentice-Hall, Englewood Cliffs, N.J., 1980.

8.10 Garbow, B.S., Boyle, J.M., Dongarra, J.J. and Moler, C.B., *Matrix eigensystem routines – EISPACK Guide extension*, in Lecture Notes in Computer Science, Springer, N.Y., 1977.

8.11 Meirovitch, L., *Elements of Vibration Analysis*, 2nd ed., McGraw Hill Book Comp., New York, 1986.

8.12 Stewart, G.W., *Matrix Algorithms II: Eigensystems*, SIAM, Philadelphia, 2001.

8.13 Radeş, M., *Application of Lanczos and Schur vectors in structural dynamics*, Shock and Vibration Journal, vol.15, no.3-4, pp 459-466, June 2008.

8.14 Radeş, M. and Ewins, D.J., *Some applications of Arnoldi vectors in modal testing*, Proceedings of IMAC 21 Conference on Structural Dynamics, Kissimmee, Florida, Paper S11P06, 2003.

8.15 Hill, D.R. and Moler, C.B., *Experiments in Computational Matrix Algebra*, Random House, N.Y., 1988.

8.16 Radke, R.J., *A Matlab Implementation of the Implicitly Restarted Arnoldi Method for Solving Large-Scale Eigenvalue Problems*, M.A. Thesis, Rice University, Houston, Texas, 1996.

8.17 Sorensen, D.C., *Implicit application of polynomial filters in a k-step Arnoldi method*, SIAM Journal of Matrix Analysis and Applications, vol.13, pp 357-385, 1992.

8.18 Arnoldi, W.E., *The principle of minimized iterations in the solution of the matrix-eigenvalue problem*, Quarterly of Applied Mathematics, vol.9, pp 17-29, 1951.

8.19 Lanczos, C., *An iteration method for the solution of the eigenvalue problem of linear differential and integral operators,* Journal of Research of the National Bureau of Standards, vol.45, no.4, pp 255-282, 1950.

8.20 Saad, Y., *Variations on Arnoldi's method for computing eigenelements of large unsymmetric matrices*, SIAM Journal of Numerical Analysis, vol.17, pp 687-706, 1980.

8.21 Lehoucq, R.B., Sorensen, D.C. and Yang, C., *ARPACK Users' Guide: Solution of Large Scale Eigenvalue Problems by Implicitly Restarted Arnoldi Methods*, SIAM, Philadelphia, 1998.

8.22 Daniel, J., Gragg, W.B., Kaufman, L. and Stewart, G.W., *Reorthogonalization and stable algorithms for updating the Gram-Schmidt QR factorization*, Mathematics of Computation, vol.30, pp 772-795, 1976.

8.23 Bai, Z., Demmel, J., Dongara, J., Ruhe, A. and Van der Vorst, H., *Templates for the Solution of Algebraic Eigenvalue Problems: A Practical Guide*, SIAM, Philadelphia, PA, 2000.

8.24 Parlett, B.N. and Scott, D.S., *The Lanczos algorithm with selective orthogonalization*, Mathematics of Computation, vol.33, no.145, pp 217-238, 1979.

8.25 Craig, R.R. Jr., *Krylov-Lanczos methods*, in 'Encyclopedia of Vibration' (S. Braun, D. Ewins, S.S. Rao, eds.), Academic Press, London, pp 691-698, 2002.

8.26 Wilkinson, J.H. and Reinsch, C. (eds.), *Handbook for Automatic Computation,* vol.2, *Linear Algebra*, Springer, Heidelberg, 1971.

8.27 Smith, T., Boyle, J.M., Dongarra, J.J., Garbow, B.S., Ikebe, Y., Klema, V.C. and Moler, C.B., *EISPACK Guide*, 2nd ed., Springer, Berlin, 1976.

8.28 Lawson, C.L., Hanson, R.J., Kincaid, D.R. and Krogh, F.T., *Basic linear algebra subprograms for FORTRAN usage*, ACM Transactions on Mathematical Software, vol.5, no.3, pp 308-323, 1979.

8.29 Demmel, J., *Applied Numerical Linear Algebra*, U. C. Berkeley, 1993.

8.30 Hughes, T.J.R., *The Finite Element Method. Linear Static and Dynamic Finite Element Analysis*, Prentice-Hall, Englewood Cliffs, N.J., 1987.

8.31 Bai, Z. and Stewart, G.W., *SRRIT – A FORTRAN subroutine to calculate the dominant invariant subspace of a nonsymmetric matrix*. Technical Report 2908, Department of Computer Science, University of Maryland, 1992.

8.32 Stewart, W.J. and Jennings, A., *ALGORITHM 570: LOPSI a simultaneous iteration method for real matrices,* ACM Transactions of Mathematical Software, vol.7, no.2, pp 230-232, 1981.

8.33 Fokkema, D.R., Sleijpen, G.L.G. and Van der Vorst, H.A., *Jacobi-Davidson style QR and QZ algorithms for the reduction of matrix pencils*, SIAM Journal on Scientific Computing, vol.20, no.1, pp 94-125, 1998.

8.34 Sleijpen, G.L.G. and Van der Vorst, H.A., *The Jacobi-Davidson iteration method for linear eigenvalue problems*, SIAM Journal on Matrix Analysis and Applications, vol.17, pp 401-425, 1996.

8.35 Golub, G. and Ye, Q., *An inverse free preconditioned Krylov subspace method for symmetric generalized eigenvalue problems*, SIAM Journal on Scientific Computing, vol.24, pp 312-334, 2002.

8.36 Baglama, J., Calvetti, D. and Reichel, L., ***irbleigs***: *A MATLAB program for computing a few eigenpairs of a large sparse Hermitian matrix*, ACM Transactions of Mathematical Software, vol.29, no.5, pp 337-348, 2003.

9.

FREQUENCY RESPONSE NONPARAMETRIC ANALYSIS

The dynamic characteristics of a structure are conveniently described by Frequency Response Functions (FRF). In the following, only receptances and inertances will be considered, though measured FRFs include mobilities as well.

FRFs can be expressed in terms of modal parameters. This is the basis of parameter identification methods presented in the next chapter.

This chapter is devoted to the non-parametric analysis of the FRFs. Elimination of noise and redundant information from a set of measured FRFs is one topic of interest. Evaluation of the number of modes active in the measured frequency range is necessary for model building. Determination of optimal response measurement and excitation locations is also performed in the pre-test phase of experimental modal analysis. All ensuing methods are based on an eigenvalue problem, the singular value decomposition or the pivotal QR decomposition of FRF matrices.

9.1 Frequency response function matrices

FRFs are complex response/excitation ratios measured at discrete frequencies. Modal testing procedures in current use are based on response functions measured at N_o output coordinates, due to excitation applied at N_i input coordinates and N_f frequencies. A 'complete' data set consists of $N = N_o N_i$ FRFs sampled at N_f frequencies.

Apart from controllability and observability requirements, N_o is set by the desired spatial resolution of mode shapes, while N_i is most often dictated by the multiplicity of natural frequencies. The primary basis for the selection of input/output locations is the adequate definition of all modes of interest.

9.1.1 Frequency response functions

For single point harmonic excitation

$$f_q(t) = \hat{f}_q \, e^{\,\mathrm{i}\omega t} \tag{9.1}$$

and steady-state single point response

$$x_p(t) = \tilde{x}_p \, e^{\,\mathrm{i}\omega t} = \hat{x}_p \, e^{\,\mathrm{i}(\omega t + \theta)} \tag{9.2}$$

the displacement frequency response function (receptance) is defined as

$$H_{pq}(\mathrm{i}\omega) = \frac{x_p(t)}{f_q(t)} = \frac{\hat{x}_p}{\hat{f}_q} \, e^{\,\mathrm{i}\theta} \tag{9.3}$$

or

$$H_{pq}(\mathrm{i}\omega) = \frac{\hat{x}_p}{\hat{f}_q} \cos\theta + \mathrm{i} \frac{\hat{x}_p}{\hat{f}_q} \sin\theta . \tag{9.4}$$

Generally, for excitation $f(t)$ and response $x(t)$, the FRF is defined as

$$H(\mathrm{i}\omega) = \frac{X(\mathrm{i}\omega)}{F(\mathrm{i}\omega)} = \frac{X(\mathrm{i}\omega)\cdot F^*(\mathrm{i}\omega)}{F(\mathrm{i}\omega)\cdot F^*(\mathrm{i}\omega)} = \frac{S_{fx}(\mathrm{i}\omega)}{S_{ff}(\omega)} \tag{9.5}$$

where $F(\mathrm{i}\omega)$ and $X(\mathrm{i}\omega)$ are the Fourier transforms of $f(t)$ and $x(t)$, $F^*(\mathrm{i}\omega)$ is the complex conjugate of $F(\mathrm{i}\omega)$, $S_{fx}(\mathrm{i}\omega)$ is the cross-spectral density of $f(t)$ and $x(t)$, and $S_{ff}(\omega)$ is the power spectral density of $f(t)$. For random or pseudo-random excitation, the spectral densities can be calculated as Fourier transforms of the corresponding correlation functions.

For multivariate systems, the input-output relationship is defined by an FRF matrix

$$\{X\}_{N_o \times 1} = [H(\mathrm{i}\omega)]_{N_o \times N_i} \{F\}_{N_i \times 1} \tag{9.6}$$

or

$$\begin{Bmatrix} X_1 \\ X_2 \\ \vdots \\ X_p \\ \vdots \\ X_{N_o} \end{Bmatrix} = \begin{bmatrix} H_{11} & H_{12} & \cdots & H_{1q} & \ldots & H_{1,N_i} \\ H_{21} & H_{22} & \cdots & H_{2q} & \cdots & H_{2,N_i} \\ \vdots & \vdots & & \vdots & & \vdots \\ H_{p1} & H_{p2} & \cdots & H_{pq} & \cdots & H_{p,N_i} \\ \vdots & \vdots & & \vdots & & \vdots \\ H_{N_o,1} & H_{N_o,2} & \cdots & H_{N_o,q} & \cdots & H_{N_o,N_i} \end{bmatrix} \begin{Bmatrix} F_1 \\ F_2 \\ \vdots \\ F_q \\ \vdots \\ F_{N_i} \end{Bmatrix} . \tag{9.6, a}$$

An element H_{pq} of the matrix $[H]$ represents the response at coordinate p due to an excitation applied at coordinate q

$$H_{pq} = \frac{X_p}{F_q}.$$ (9.7)

FRFs can be analyzed either simultaneously, at all frequencies, or in turn, at each frequency [9.1]. In the first case, the FRF test data can be arranged in a 2D matrix encompassing all FRFs (Fig. 9.1). In the second case, the FRF matrices measured at different frequencies can be visualized as arranged in a 3D matrix (Fig. 9.2).
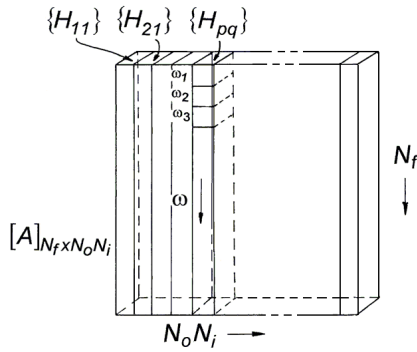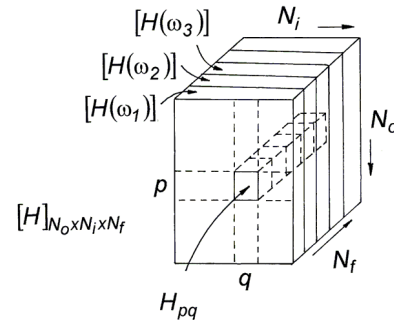
Fig. 9.1   Fig. 9.2

9.1.2 2D FRF matrices

The two-dimensional Compound Frequency Response Function (CFRF) matrix (Fig. 9.1) is a multi-frequency matrix containing the whole FRF information. It has the form

$$\left[A\right]_{N_f x N_o N_i} = \left[\left\{H_{11}\right\} \ \left\{H_{21}\right\} \ ... \ \left\{H_{pq}\right\} \ ...\right],$$ (9.8)

where $\left\{H_{pq}\right\}$ is an N_f dimensional FRF column vector, with response at location p due to input at q. Thus, each column corresponds to a different input/output location combination for all frequencies. Each row corresponds to different individual FRFs all measured at the same frequency.

The CFRF matrix can be constructed by first concatenating the columns of the rectangular $\left[H\right]_{N_o x N_i}$ matrices into $N_o \times N_i$ dimensional column vectors, then transposing these column vectors to transform them in rows of the CFRF matrix.

A reduced-rank FRF matrix $\left[\tilde{A}\right]_{N_f x N_r}$, where $N_r = \mathrm{rank}\left[A\right]$, referred to as the Aggregate FRF (AFRF) matrix, can be constructed by Principal Component Analysis of the CFRF matrix. It provides a condensed representation of FRFs, free

of redundant information and with reduced noise. Its row dimension is equal to the rank of the CFRF matrix, i.e. the number of modes represented by the test data.

Simultaneous analysis of the whole FRF information of CFRF-type matrices proved to be useful in the estimation of system order and the optimal location of sensors and exciters for modal testing.

However, in many practical applications the original CFRF matrix is apparently of full rank due to noise and non-linear effects. Its effective rank can hardly be estimated from the decrease of singular values or from the separation of the principal response functions.

One problem of interest can be stated as follows: given a set of $N_o \times N_i$ FRFs (which is redundant, at least owing to reciprocity), find the smallest subset of linearly independent FRFs that correctly describe the dynamics of the tested structure. This is strongly connected with the choice of measurement coordinates.

9.1.3 3D FRF matrices

An alternative is the stepwise analysis of rectangular $N_o \times N_i$ FRF matrices, at one frequency at a time. The data set can be visualized as a 3D matrix consisting of N_f rectangular $N_o \times N_i$ FRF matrices (Fig. 9.2). Each horizontal line along the frequency axis represents an H_{pq} FRF measured at a given combination of output/input coordinates. Usually $N_i < N_o$ and N_f is dictated by the required frequency resolution of FRFs.

9.2 Principal response analysis of CFRF matrices

The singular value decomposition (SVD) of the CFRF multi-frequency matrices helps separating the frequency dependence from the spatial dependence of FRF data. The analysis of SVD-related quantities calculated for CFRF matrices can be used to determine the number of modes present in a given frequency range, to identify (quasi-) repeated natural frequencies and to pre-process the FRF data to make them more amenable to the modal analysis.

9.2.1 The singular value decomposition

Let $[A]$ be a complex m by n matrix, and assume without loss of generality that $m \geq n$. There exist a unitary m by m matrix $[U]$ and a unitary n by n matrix $[V]$, such that [9.2]

$$[U]^H [A][V]=[\Sigma],\qquad\qquad (9.9)$$

where $[\Sigma]$ is the *m* by *n* matrix whose top *n* rows contain $\mathrm{diag}(\sigma_1,\sigma_2,...,\sigma_n)$ and whose bottom $m-n$ rows are zero. The nonnegative elements σ_i are the *singular values*, and are sorted so that $\sigma_1 \geq \sigma_2 \geq \cdots \geq \sigma_n \geq 0$. The columns $\{v\}_i$ of $[V]$ are the *right singular vectors* and the columns $\{u\}_i$ of $[U]$ are the *left singular vectors* of $[A]$. For unitary matrices $[U]^H [U]=[U][U]^H =[I_m]$, $[V]^H [V]=[V][V]^H =[I_n]$. The factorization

$$[A]=[U][\Sigma][V]^H ,\qquad\qquad (9.10)$$

is called the *singular value decomposition* (SVD) of $[A]$.

In (9.10), the last $m-n$ columns of $[U]$ are "extra"; they are not needed to reconstruct $[A]$. There is an *economy* version of the SVD, that saves computer memory, in which only the first *n* columns of $[U]$ and first *n* rows of $[\Sigma]$ are computed.

Singular values are fairly insensitive to perturbations in the matrix elements. The number of nonzero singular values is equal to the rank of the matrix $[A]$. In finite precision arithmetic it rarely happens that singular values are equal to zero, even if they should have been in exact arithmetic. Therefore, one also uses the notation of *numerical rank* of a matrix. If for some $\varepsilon > 0$ the singular values can be ordered as

$$\sigma_1 \geq \sigma_2 \geq \cdots \geq \sigma_r \geq \varepsilon \geq \sigma_{r+1} \geq \cdots \geq \sigma_n \geq 0,$$

then we say that $[A]$ has numerical rank *r* (with respect to ε), $\mathrm{rank}[A]=r$. The matrix $[A]$ is nearly singular when its singular values fall below the limit of numerical precision, ε, which is often taken to be a multiple of the floating point precision.

The closest matrix to $[A]$ that has rank *r* is

$$[A_r]=\sum_{i=1}^{r} \sigma_i \{u\}_i \{v\}_i^H .\qquad\qquad (9.11)$$

Replacing $[A]$ by $[A_r]$ amounts to filtering the small singular values.

The SVD of $[A]$ is

$$[A]=[U]\begin{bmatrix}[\Sigma_r] & 0 \\ 0 & 0\end{bmatrix}[V]^H ,\qquad\qquad (9.10, a)$$

where $\left[\Sigma_r \right] = \mathrm{diag}\left(\sigma_1, \sigma_2, ..., \sigma_r \right)$.

The parallel with eigenpairs of a square matrix $\left[A \right]$ is made visible through writing out (9.9) for the i-th column of $\left[A \right]\left[V \right]$, and for the i-th column of $\left[A \right]^H \left[U \right]$:

$$[A]\{v\}_i = \sigma_i \{u\}_i, \qquad (9.12, a)$$

$$[A]^H \{u\}_i = \sigma_i \{v\}_i. \qquad (9.12, b)$$

Together, these equations can be expressed as a true eigenvalue problem for an auxiliary matrix

$$\begin{bmatrix} 0 & [A] \\ [A]^H & 0 \end{bmatrix} \begin{Bmatrix} \{u\}_i \\ \{v\}_i \end{Bmatrix} = \sigma_i \begin{Bmatrix} \{u\}_i \\ \{v\}_i \end{Bmatrix}. \qquad (9.13)$$

Other relations, which are of interest in order to understand properties of the singular values and singular vectors, are

$$[A]^H [A]\{v\}_i = \sigma_i^2 \{v\}_i, \qquad (9.14)$$

$$[A][A]^H \{u\}_i = \sigma_i^2 \{u\}_i. \qquad (9.15)$$

The rectangular m by n matrix $\left[A \right]$ has n singular values, which are the square roots of the eigenvalues of $\left[A \right]^H \left[A \right]$. The matrix $\left[A \right]^H$ has m singular values, which are the square roots of the eigenvalues of $\left[A \right]\left[A \right]^H$. The left singular vectors $\{u\}_i$ of $\left[A \right]$ are the eigenvectors of $\left[A \right]\left[A \right]^H$. The right singular vectors $\{v\}_i$ are the eigenvectors of $\left[A \right]^H \left[A \right]$.

Note that equations (9.14) and (9.15) are not always adequate for the computation of accurate singular vectors and singular values, because of the matrix products $\left[A \right]^H \left[A \right]$ and $\left[A \right]\left[A \right]^H$, which may lead to significantly larger perturbations.

9.2.2 Principal response functions

The SVD of the CFRF matrix is of the form

$$[A]_{N_f \times N} = [U]_{N_f \times N} [\Sigma]_{N \times N} [V]_{N \times N}^H \qquad (9.16)$$

where $N \leq N_o N_i$.

The SVD decomposes the CFRF matrix into a sum of rank-one matrices $[A_i] = \sigma_i \{u\}_i \{v\}_i^H$ of the same size as $[A]$ (Fig. 9.3). Each singular value is equal to the Frobenius norm of the associated $[A_i]$ matrix

$$\sigma_i = \left\| A_i \right\|_F \qquad (9.17)$$

and can be considered as a measure of its energy content [9.3].
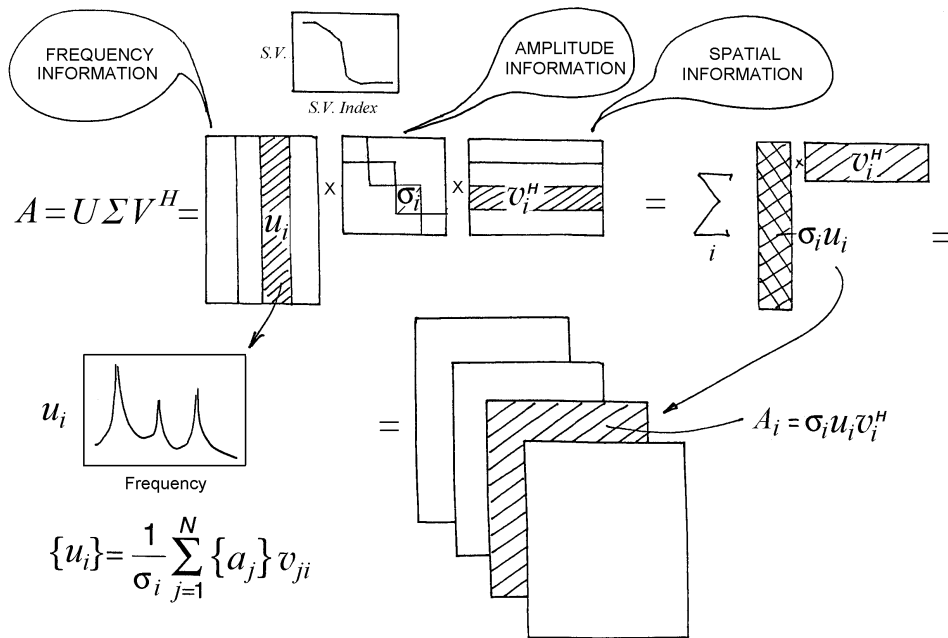
Fig. 9.3

The columns of the matrix $[U]$ are the left singular vectors (LSV), sometimes referred to as *principal components* [9.4]

$$\{u\}_i = \frac{1}{\sigma_i} \sum_{j=1}^{N} \{a\}_j \, v_{ji} \, . \qquad (i = 1, ..., N) \qquad (9.18)$$

They contain the frequency distribution of the energy, being linear combinations of the original FRFs that form the columns of $[A]$. The LSV are mutually (pairwise) orthogonal vectors, so they are linearly independent. In equation (9.18), the multiplying factors v_{ji} are the complex valued elements of the right singular vectors.

Because the left and right singular vectors have unit length, the amplitude information is contained in the singular values from the diagonal matrix $[\Sigma]$, arranged in descending order from the upper left. The columns of the matrix $[V]$ are the right singular vectors (RSV). They describe the spatial distribution of the energy contained in the FRF set (Fig. 9.4).
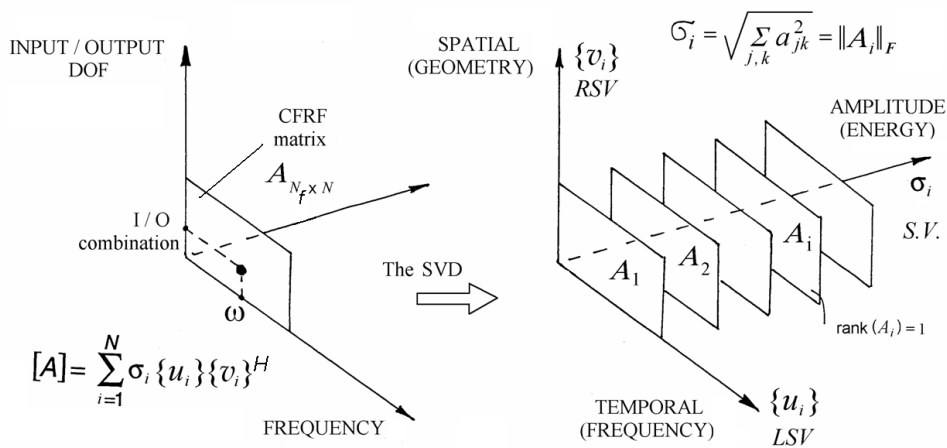
Fig. 9.4

The Principal Response Functions (PRF), $\{P\}_i$, defined as the LSVs scaled by the respective singular values [9.5], are linear combinations of the original FRFs, $\{a\}_i$:

$$\{P\}_i = \sigma_i \{u\}_i = [A]\{v_i\} = \sum_{j=1}^{N} v_{ji} \{a\}_j . \qquad (9.19)$$

The matrix of Principal Response Functions is

$$[P] = [U][\Sigma]. \qquad (9.20)$$

Transforming the original FRFs to PRFs amounts to a rotation of coordinate axes to a new coordinate system that has inherent energy properties. The PRFs give a new set of linearly combined measurements. PRFs are orthogonal vectors, each one representing the frequency distribution of an amount of energy equal to the square of the related singular value.

Algebraically, Principal Response Functions are particular linear combinations of the $N \le N_o N_i$ initial (measured) FRFs.

Geometrically, these linear combinations represent the selection of a new coordinate system, obtained by rotating the original system, with $\{A_j\} = \{H_{pq}\}$ as the coordinate axes. The unit vectors along these directions are the LSVs which are orthonormal.

Physically, the new axes represent the directions with maximum power (energy) and provide a simpler and more parsimonious description of the FRF data.

Indeed, if $[C] = [A][A]^H$ is the cross-power matrix (power spectrum matrix), its spectral decomposition is

$$[A][A]^H [U] = [U][\Sigma]^2 . \tag{9.21}$$

One can think of

$$\int_{t_1}^{t_2} \| x(t) \|^2 \, \mathrm{d}t \tag{9.22}$$

as the total energy in the response set $\{x(t)\}$ over the interval $[t_1 \ t_2]$.

The Frobenius norm of the CFRF matrix is

$$\| A \|_F = \left(\sum_{i=1}^{N} \sum_{j=1}^{N} | c_{ij} |^2 \right)^{1/2} . \tag{9.23}$$

The trace of $[C] = [A][A]^H$ is related to the total power

$$\| A \|_F^2 = \mathrm{trace}\left([A][A]^H \right) = \mathrm{trace}\left([U][\Sigma]^2 [U]^H \right) =$$
$$= \mathrm{trace}\left([U]^H [U][\Sigma]^2 \right) = \mathrm{trace}\left([\Sigma]^2 \right) = \sum_{i=1}^{N} \sigma_i^2 . \tag{9.24}$$

Because by definition, $\sigma_1 \ge \sigma_2 \ge ...... \ge \sigma_r$, the SVD decomposes the CFRF matrix $[A]$ into a sum of principal component matrices containing decreasing levels of energy. So, one can say that, for example, the first LSV is the normalized linear combination of original FRFs (columns of the CFRF matrix) with maximum energy (power) content [9.6].

In terms of the matrix of PRFs

$$[A][A]^H = [U][\Sigma]^2[U]^H = [U][\Sigma][\Sigma][U]^H = [P][P]^H \quad (9.25)$$

so that

$$\text{trace}\left([A][A]^H\right) = \text{trace}\left([P][P]^H\right) = \sum_{i=1}^{N_r} \sigma_i^2 . \qquad (9.26)$$

In many cases, the number of measured FRFs is too large and the FRF data set contains redundant information, FRFs being not linearly independent. A way of reducing the number of FRFs to be analyzed is to discard the linear combinations of FRFs which have small energy and study only those with large energies.

Otherwise stated, the cross-product matrix of the uncorrelated PRFs should be diagonal, representing autopower. Indeed

$$[P]^H[P] = ([A][V])^H[A][V] = [V]^H\left([A]^H[A]\right)[V] = [\Sigma]^2, \quad (9.27)$$

so that the cross-power off-diagonal elements are zero.

The columns of $[P]$ form a set of orthogonal response functions, each one representing an amount of energy equal to the square of the related singular value. The first PRF, corresponding to the largest singular value, is the uncorrelated response function with the largest autopower. The second PRF has the second largest autopower, and so on [9.7].

PRFs have peaks at the natural frequencies, as have the FRFs. The modes whose shape is similar to the weighting RSV are enhanced, while the other are attenuated. For an adequate selection of input/output coordinate combinations, each PRF is dominated by a single mode of vibration. Single degree of freedom identification techniques can be used to determine the corresponding modal parameters [9.8]. For a non-optimal location of sensors and excitation coordinates, resulting in an insufficient spatial independence of the modal vectors, and for limited spatial resolution, a PRF can have multiple peaks, especially when this is backed by insufficient frequency resolution.

The plot of left singular vectors versus frequency helps locating the natural frequencies, but it is rather confusing for noise polluted data. A similar plot of PRFs is more useful. PRFs with low energy level are LSVs multiplied by small singular values, so the respective curves are shifted down. A gap in the singular values produces a marked separation of PRFs containing useful information from those with negligible energy content and polluted by noise. If the first N_r PRFs are separated from the others in the upper part of the PRF plot, then N_r can be chosen as the effective rank of the CFRF matrix. However, the vertical shifting of the PRF

curves, due to the multiplication of LSVs by the singular values, can obscure the highest peaks, if not located by distinctive marks.

9.2.3 The reduced-rank AFRF matrix

If $N_r = \text{rank}\,(A)$, then, setting the singular values $\sigma_i = 0$ for $i = N_r + 1$ to N, equation (9.16) becomes

$$\left[\tilde{A}\right]_{N_f x N_r} = \left[\,\left[U_r\right]\,\left[U_s\right]\,\right]\begin{bmatrix}\left[\Sigma_r\right] & \\ & \left[0\right]\end{bmatrix}\begin{bmatrix}\left[V_r\right] \\ \left[V_s\right]\end{bmatrix}^H, \qquad (9.28)$$

where $\left[\tilde{A}\right]$ is referred to as the Aggregate FRF (AFRF) matrix.
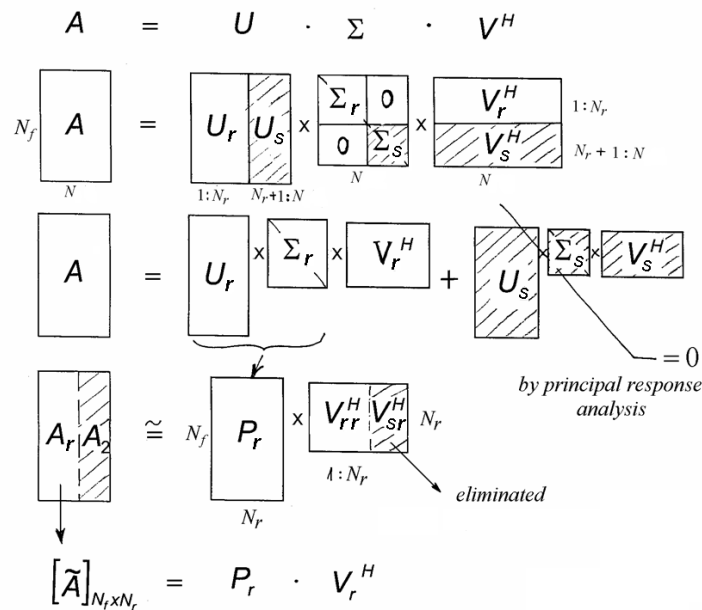
Fig. 9.5

The columns of the AFRF matrix $\left[\tilde{A}\right]$ represent a condensed set of FRFs. In the case of orthogonal noise, the original CFRF matrix $\left[A\right]$ can be approximated by the reduced-rank reconstructed AFRF matrix (Fig. 9.5)

$$\left[\tilde{A}\right]_{N_f x N_r} = \left[P_r\right]_{N_f x N_r}\left[V_r\right]_{N_r x N_r}^H. \qquad (9.29)$$

The reduced-rank matrix of Principal Response Functions is

$$\left[P_r \right]_{N_f x N_r} = \left[U_r \right]_{N_f x N_r} \left[\mathit{\Sigma}_r \right]_{N_r x N_r} = \left[\tilde{A} \right]_{N_f x N_r} \left[V_r \right]_{N_r x N_r}^{-H} . \quad (9.30)$$

Example 9.1

Figure 9.6 shows the 15-DOF lumped parameter system of Example 5.8 and its physical parameters [9.9]. Table 9.1 lists the system damped natural frequencies and damping ratios.


Masses:
0.001295 kg   3, 6, 9, 12, 15
0.0259 kg   the other

Stiffnesses:
1000 N/m   1-18
1100 N/m   19
 900 N/m   20
1200 N/m   21
 800 N/m   22

Damping coefficients:
0.10 Ns/m   1-12
0.01 Ns/m   13-22
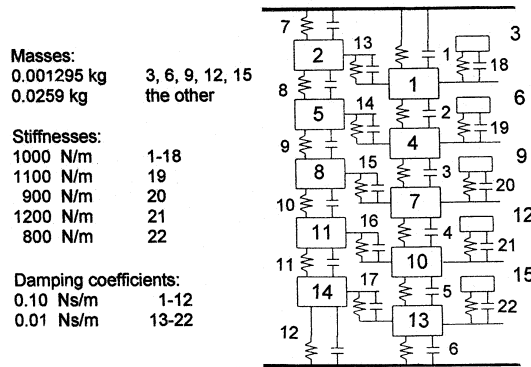
Fig. 9.6

Table 9.1   Natural frequencies and damping ratios of 15-DOF system

Mode	Natural frequency Hz	Damping ratio, %	Mode	Natural frequency Hz	Damping ratio, %
1	15.98	0.50	9	68.88	1.38
2	30.86	0.97	10	73.72	1.58
3	43.60	1.36	11	128.87	0.54
4	46.47	0.30	12	136.59	0.51
5	53.35	1.67	13	143.89	0.48
6	53.42	0.67	14	150.87	0.46
7	59.45	1.85	15	157.52	0.44
8	61.62	1.06			

The analytical data set is constructed such that there are 10 modes of vibration in the frequency range 10-100 Hz and 5 modes between 120-160 Hz, with a quasi-repeated mode at about 53.4 Hz.

Receptance FRFs were computed at 1024 frequencies between 10-180 Hz for different input/output combinations. Both additive noise and multiplicative noise was added to theoretical data, as in reference [9.5]. The noise level is scaled

such that its mean deviation was the stated percentage of the mean magnitude of the CFRF matrix.

In the following, two cases will be considered [9.1]. In *Case I,* the system is 'tested' by excitation applied on masses 5 and 11, and the response is 'measured' at masses 3, 5, 9, 11, 15. The CFRF matrix, of size 1024x10, polluted with 5% multiplicative noise, is used as the test data. In *Case II*, the input points are on masses 5, 9, 11 and the output points are on masses 3, 5, 9, 11, 15. The additional input point at 9 is on a small mass, introducing local modes. In this case, the CFRF matrix is of size 512x15 and is polluted with 0.5% additive noise.

9.2.4 SVD plots

Because the singular values are a weighting factor for the corresponding singular vectors, the number of significant singular values presents an estimate of the number of mode shapes that comprise the $\begin{bmatrix} A \end{bmatrix}$ matrix. In the case of ideal, noise-free data, all non-significant singular values will be zero. In the case of real data, the non-significant singular values will not be zero. As singular values are indexed in descending order, a gap in the singular values indicates a rank-deficient matrix.
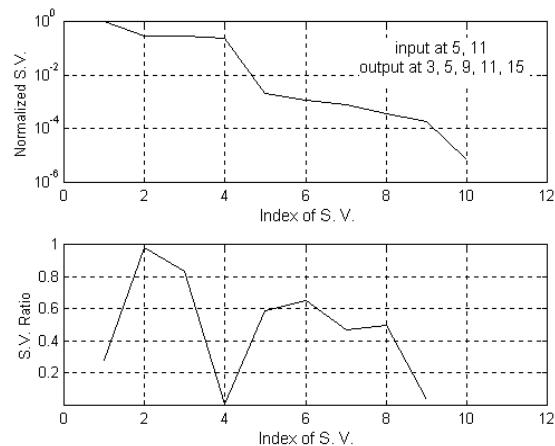
Fig. 9.7

The significant singular values can be separated from the unimportant ones. One way to do this is to plot the magnitudes of the singular values as a function of their index. A steep drop (large negative slope) will appear at the index which defines the useable rank of test data. Another way is to plot the ratio of successive singular values. A distinct through in the diagram indicates the numerical rank of FRF data. Both of these methods are illustrated in Fig. 9.7, computed for Case I.

In the upper plot in Fig. 9.7, magnitudes of the singular values are plotted on a logarithmic scale, normalized to the largest singular value. The sudden drop in the curve after the fourth singular value indicates that there are four significant singular values, or four modes in the frequency band. This conclusion is supported by the second of the two plots, which shows a distinct minimum at the index 4. The plots of singular values give a clear indication of rank $N_r = 4$.
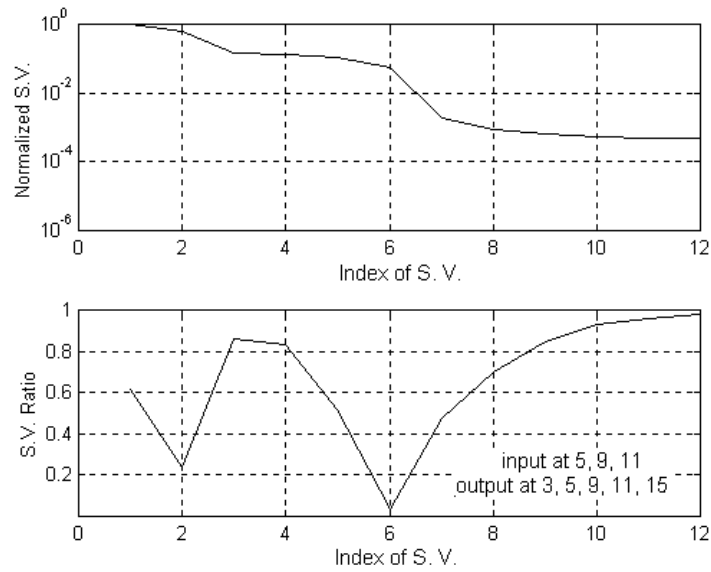
Fig. 9.8

In Case II, the plots of singular values (Fig. 9.8) indicate a rank $N_r = 6$.

9.2.5 PRF plots

It is reasonably to expect that the numerical limit for the test data is due to noise and errors in the measured data, rather than due to the limits of floating point representation [9.5]. A matrix of test data contains noise.

The rank-limited matrix $\left[\tilde{A} \right]$ contains data separated from the noise. The original matrix $[A]$ can be approximated by $\left[\tilde{A} \right] = \left[P_r \right] \left[V_r \right]^H$ using only the first N_r columns of $\left[P_r \right]$ and $\left[V_r \right]$. The inspection of the columns of $[P]$ is helpful in estimating the useable rank of $[A]$ when noise is present. The separation of the data space from the noise space in the measured data is expected to be evidenced by an abrupt change in the shape of the columns of $[P]$ beyond the N_r-th column.
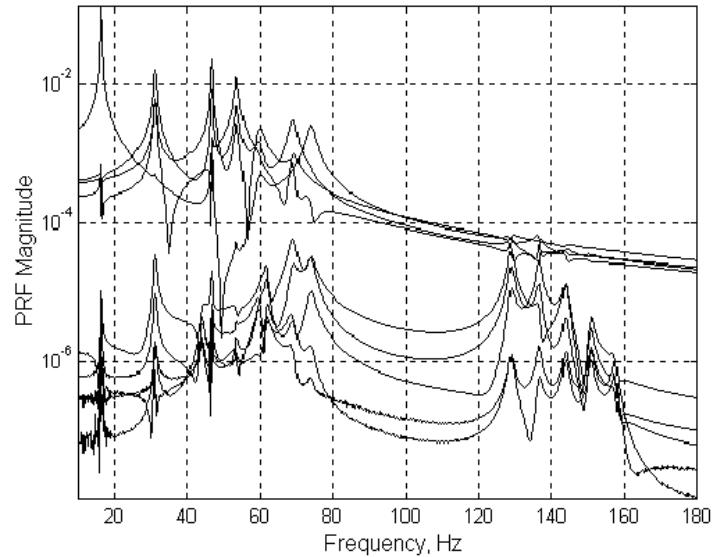
Fig. 9.9

Figure 9.9 shows nine PRFs computed for *Case I* over the whole frequency band. Only four PRFs have higher magnitude, confirming the rank 4 of data. The lower five PRFs correspond to the five local modes due to masses 3, 6, 9, 12, 15.
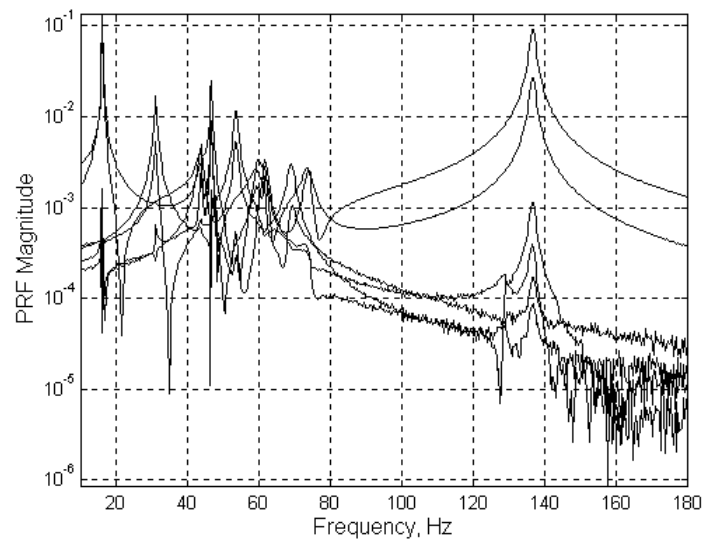

Fig. 9.10

Figure 9.10 shows six PRFs for *Case II*, two of them having high magnitude due to the local modes between 100-180 Hz. The scaling of PRFs by the singular values makes them less appropriate for use as modal indicators.

9.2.6 Mode indicator functions

Mode Indicator Functions (MIFs) are real-valued frequency-dependent scalars that exhibit local minima or maxima at the modal frequencies of the system. The left singular vectors of the CFRF matrix contain the frequency information and are used to construct MIFs. The number of curves in such a MIF plot is equal to the effective rank of the CFRF matrix. If this is lower than the number of response coordinates, a single point excitation can locate even double modes.

9.2.6.1 The UMIF

The left singular vectors $\{u\}_i$ of the CFRF matrix $[A]$ contain the frequency distribution of energy and are linear combinations of the measured FRFs (9.18). Their plot versus frequency is the *U-Mode Indicator Function* (UMIF) [9.10]. The UMIF has peaks at the damped natural frequencies. The UMIF shown in Fig. 9.11 is computed for the 15-DOF system from Fig. 9.6. It locates all 15 modes.
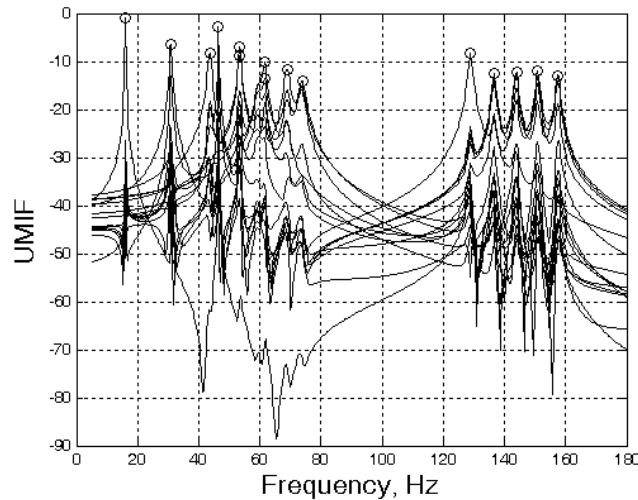
Fig. 9.11

9.2.6.2 The CoMIF

The Componentwise Mode Indicator Function (CoMIF) is defined [9.11] by vectors of the form

$$\{CoMIF\}_i = \{1\} - \{u\}_i \otimes \{u\}_i^*, \qquad (9.31)$$

computed as the difference between a column vector of ones and the Hadamard product of the left singular vectors. In equation (9.31) the star superscript denotes the complex conjugate.

        In the CoMIF plot, the number of curves is equal to the estimated effective rank of the CFRF matrix. Each curve has local minima at the damped natural frequencies, with the deepest trough at the natural frequency of the corresponding dominant mode.
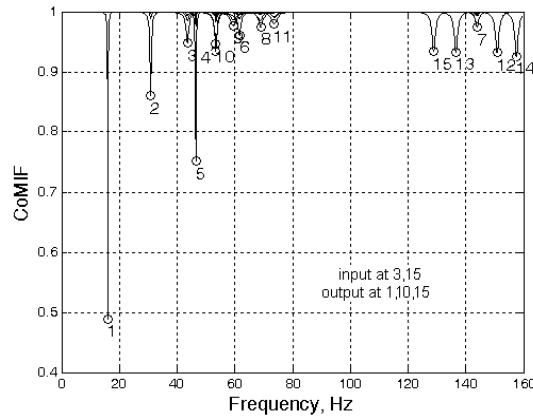

Fig. 9.12

        The CoMIF shown in Fig. 9.12 is computed for the 15-DOF system, using noise free FRFs for excitation at points 3 and 15, and response at points 1, 10 and 15. The estimated rank of the CFRF matrix is 15, so it contains 15 overlaid curves which locate all 15 modes of vibration. Again, in order to better locate the natural frequencies, the lowest trough of each curve is marked by circles.
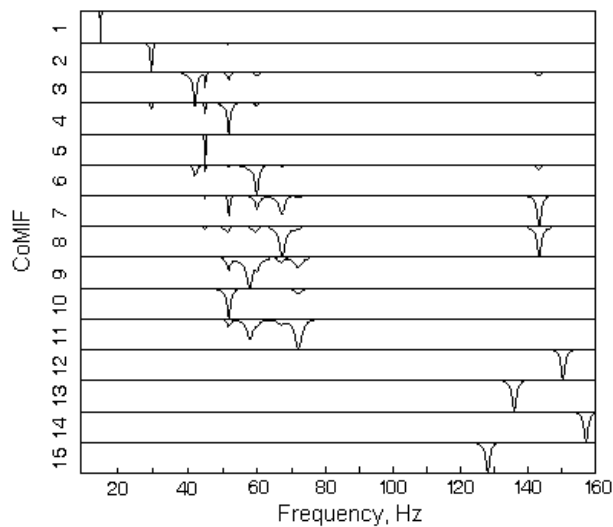
Fig. 9.13

Sometimes it is better to plot each CoMIF curve separately like in Fig. 9.13 [9.6]. Subplots correspond to individual CoMIFs with the index shown on the left. The deepest trough in each subplot locates a mode of vibration. Use of cursors (not shown) enables a more accurate location of damped natural frequencies.

9.2.6.3 The AMIF

The *Aggregate Mode Indicator Function* (AMIF) is defined as [9.1]

$$AMIF = \text{diag}\left([A][A]^+ \right), \tag{9.32}$$

where $^+$ denotes the pseudoinverse.

It is seen that $[A][A]^+$ is the orthogonal projector onto the column space of $[A]$. Each diagonal element of $[A][A]^+$ represents the fractional contribution of the respective frequency to the rank of $[A]$ and hence to the independence of its columns.

The AMIF is a plot of the diagonal elements of $[A][A]^+$, on a log magnitude scale, as a function of the respective frequency. The peaks detected in the AMIF plot locate natural frequencies to the nearest frequency line. Sometimes, troughs in the 1-AMIF plot allow better location of the dominant modes of vibration. It must also be noted that since AMIF is a single curve plot, it cannot locate nearly coincident natural frequencies or double modes.

AMIF is influenced by noise in data. In order to minimize the influence of noise, the AMIF applied to the rank-limited reconstructed AFRF matrix is:

$$\widetilde{AMIF} = \text{diag}\left(\left[\tilde{A}\right]\left[\tilde{A}\right]^+ \right). \tag{9.33}$$

Peaks detected in this AMIF locate the modes of vibration that effectively contribute to the AFRF matrix. Their number is usually equal to the number of significant singular values of $[A]$. Since the columns of $\left[\tilde{A}\right]$ are linear combinations of PRFs, the AMIF applied to $\left[\tilde{A}\right]$ exhibits low values between resonances and high values at the natural frequencies of the dominant modes.

If the first N_r columns of the $[U]$ matrix form an orthogonal basis for the column space of the CFRF matrix, the orthogonal projector onto the column space of $[A]$ is equal to the orthogonal projector onto the subspace of left singular vectors

$$AMIF = \text{diag}\left(\sum_{i=1}^{N_r} \{u\}_i \{u\}_i^H \right). \tag{9.34}$$

For *Case I*, the AMIF plot from Fig. 9.14, based on the original data (CFRF matrix) exhibits nine peaks in the range 10-100 Hz and five peaks between 100-180 Hz, missing only the double mode at 53.4 Hz.

The AMIF based on reduced-rank data (AFRF matrix) exhibits only six peaks, while the 1-AMIF plot exhibits four marked troughs, indicating the four dominant modes of vibration.

The AMIF computed from the original test data indicates the local modes, while the AMIF computed from reduced-rank data locates only the dominant modes.

The AMIF cannot show a double mode.
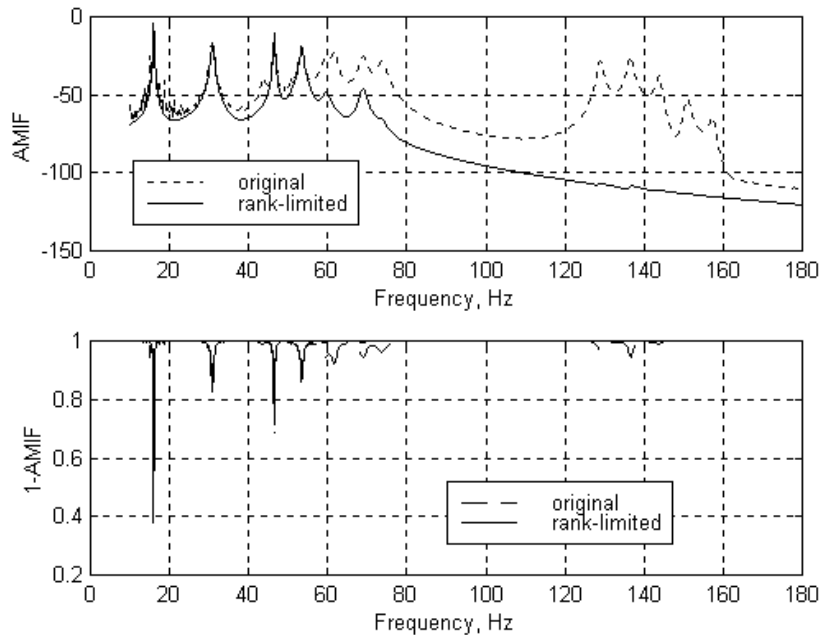
Fig. 9.14

For *Case II*, the AMIF plot from Fig. 9.15, based on original data, shows only two peaks between 100-180 Hz, as well as the close modes at 43.6 and 46.5 Hz. An AMIF computed for 0.5% multiplicative noise (Fig. 9.16) locates 14 modes (only the double mode missing).

At the same time, the AMIF plot from Fig. 9.17, based on the AFRF matrix, shows only one peak between 100-180 Hz.

The 1-AMIF plot from Fig. 9.18 clearly shows six dominant modes corresponding to a rank $N_r = 6$.
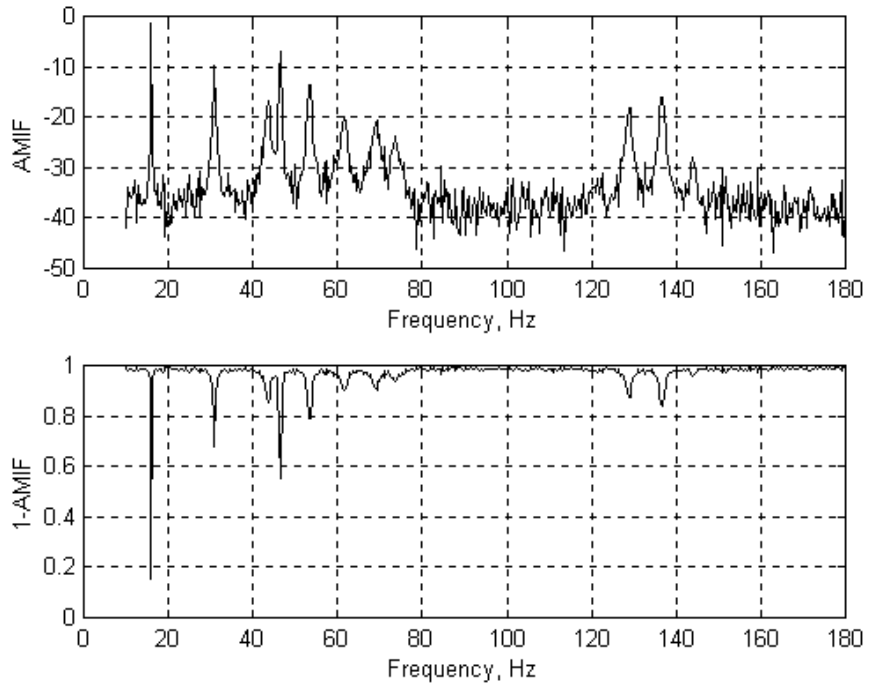
Fig. 9.15
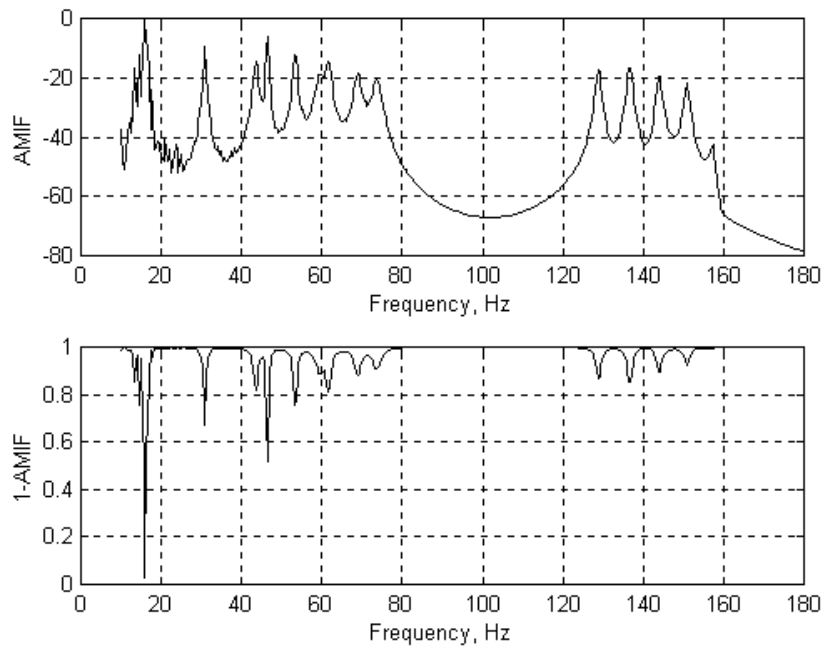
Fig. 9.16
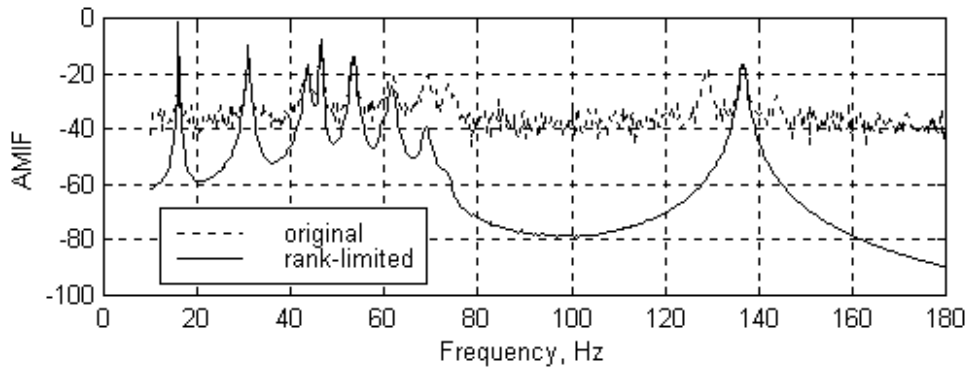
Fig. 9.17
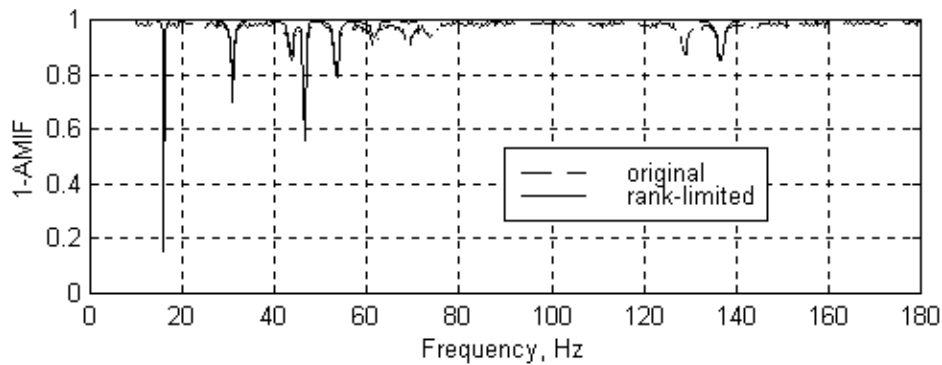
Fig. 9.18

9.2.7 Numerical simulations

Two more numerical simulation examples are considered in the following: an 11-DOF lumped parameter system with structural damping and a 7-DOF system with viscous damping.

9.2.7.1 11-DOF system

Consider the 11-DOF system with structural damping of Example 5.7 shown in Fig. 9.19. Its physical parameters and the modal parameters are given in Table 9.2 [9.12]. Due to mass and stiffness symmetry, the system has five pairs of complex modes with close natural frequencies. In each pair, one mode is predominantly symmetrical while the other mode is predominantly anti-symmetrical. The right hand branch (masses 6 to 11) has higher damping values than the left hand branch.
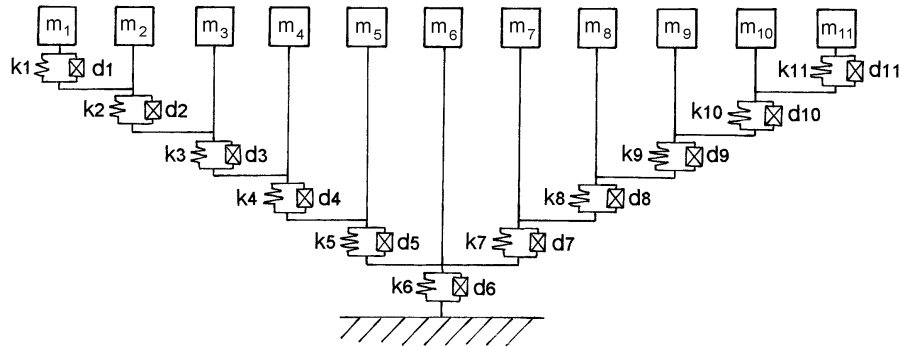
Fig. 9.19

Table 9.2: Physical and modal parameters of the 11-DOF system

i	Mass	Stiffness	Structural damping	Natural frequency	Damping factor	Mode
	m_i	k_i	d_i	ω_r	g_r	r
	kg	N/m	N/m	Hz	%	
1	1	2421	96.8	2.74	8.93	1
2	1	2989	149.5	2.95	9.05	2
3	1	3691	221.4	7.27	8.86	3
4	1	4556	318.9	7.78	9.12	4
5	1	5625	450.0	11.54	8.77	5
6	1	18000	1620.0	12.08	9.20	6
7	1	5625	562.5	15.12	8.64	7
8	1	4556	501.2	15.51	9.34	8
9	1	3691	442.9	18.54	8.89	9
10	1	2989	388.6	19.27	9.11	10
11	1	2421	339.0	28.58	9.00	11

Receptance FRFs were computed at 1024 frequencies between 10-180 Hz, for different input/output combinations. Additive noise or multiplicative noise was added to theoretical data, as in reference [9.1]. The noise level was scaled such that its mean deviation was the stated percentage of the mean magnitude of the CFRF matrix.

The plots of singular values shown in Fig. 9.20 give a clear indication of rank $N_r = 11$.
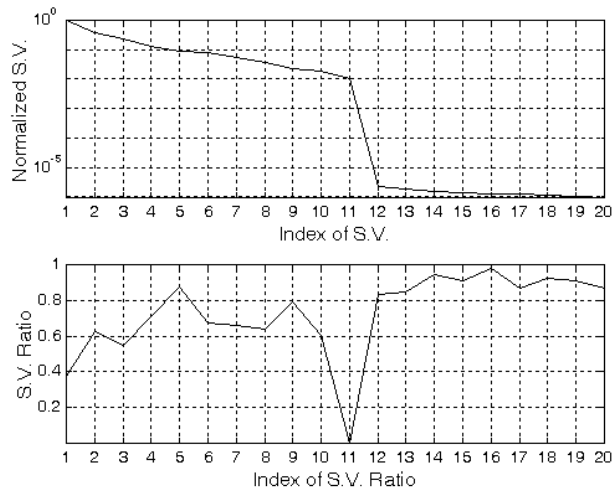
Fig. 9.20

In Fig. 9.21 are shown PRFs computed with 5 percent multiplicative noise. It is easy to see that the first eleven stand out as looking like FRFs, while the remaining functions define a "noise floor", below 10^{-5}. It means that the entire FRF matrix, which is of rank 11, can be represented by these first 11 PRFs, together with the first 11 columns of $\left[V\right]$.
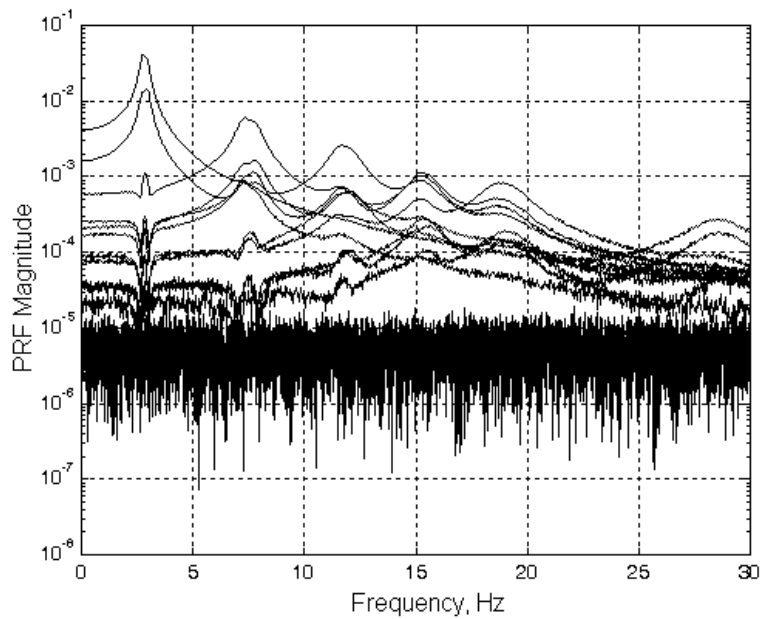

Fig. 9.21

The UMIF shown in Fig. 9.22 is based on FRFs calculated for excitation at only one point and response measurement at all 11 points, with noise free data. It clearly locates all 11 modes of vibration.
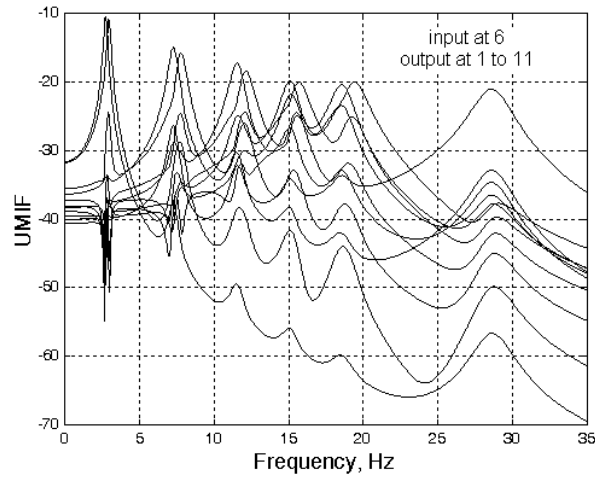
Fig. 9.22

The UMIF shown in Fig. 9.23, computed for excitation at points 1 and 11, and response at only six points 1, 3, 5, 7, 9, and 11, also locates all 11 modes. In order to better locate the natural frequencies, the peaks are marked by small circles.
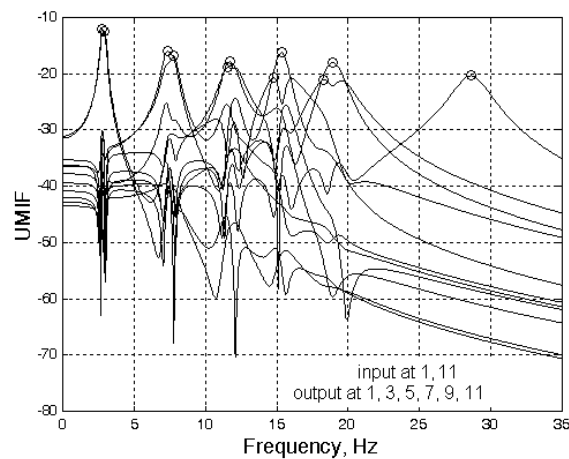

Fig. 9.23

The AMIF and 1-AMIF plots shown in Fig. 9.24 are calculated using FRFs for excitation at points 1 and 11, and response at points 1, 3, 5, 7, 9 and 11. As expected, they cannot locate relatively close natural frequencies.
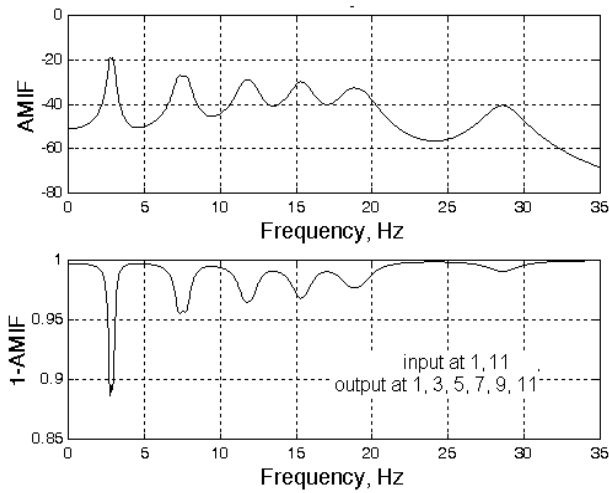
Fig. 9.24

The CoMIF shown in Fig. 9.25 is computed using FRFs for excitation at points 1 and 11, and response at points 1, 3, 5, 7, 9 and 11. The estimated rank of the CFRF matrix is 11, so it contains 11 overlaid curves which locate all 11 modes of vibration. Again, in order to better locate the natural frequencies, the lowest trough of each curve is marked by a circle.
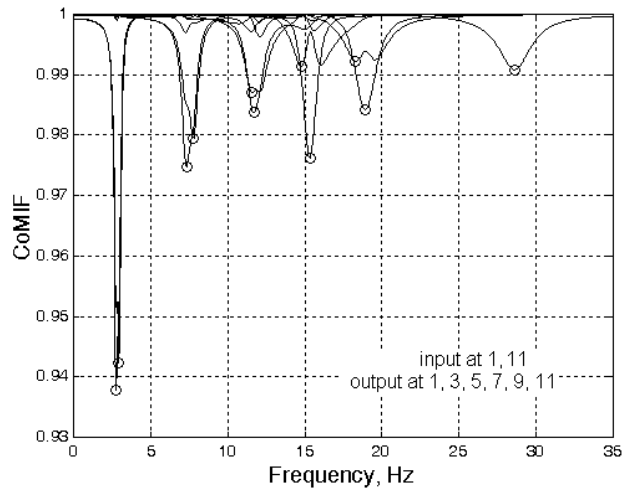
Fig. 9.25

The same CoMIF is presented in Fig. 9.26 with each curve plotted separately. Subplots correspond to individual CoMIFs with the index shown on the left. The deepest trough in each subplot locates a mode of vibration.
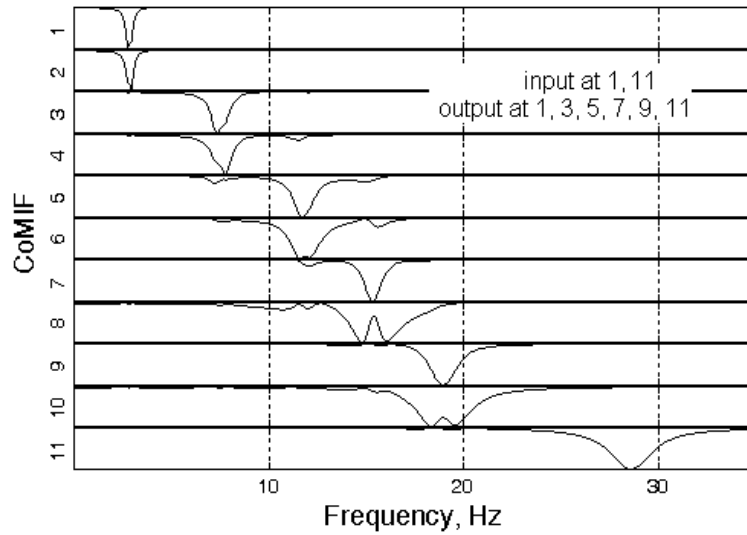
Fig. 9.26

The CoMIF with overlaid curves from Fig. 9.27 is computed for the same system, using FRFs for excitation at point 6 and response measurement at all 11 points. It clearly locates all 11 modes of vibration, despite the single point excitation in a system with pairs of close natural frequencies and relatively high damping.
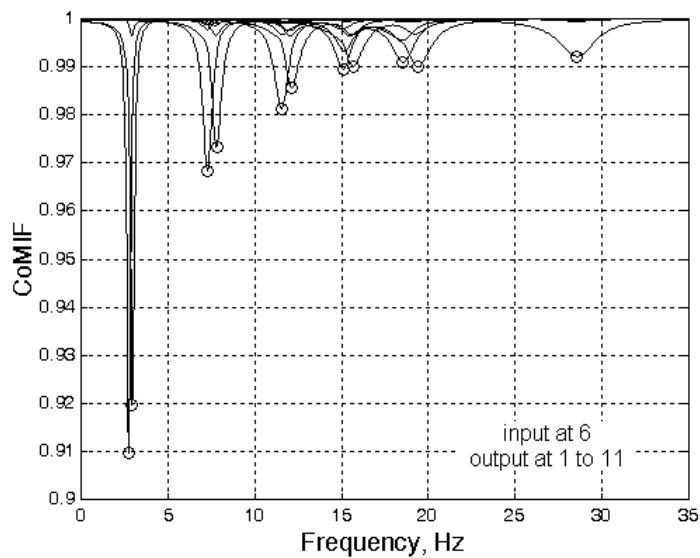

Fig. 9.27
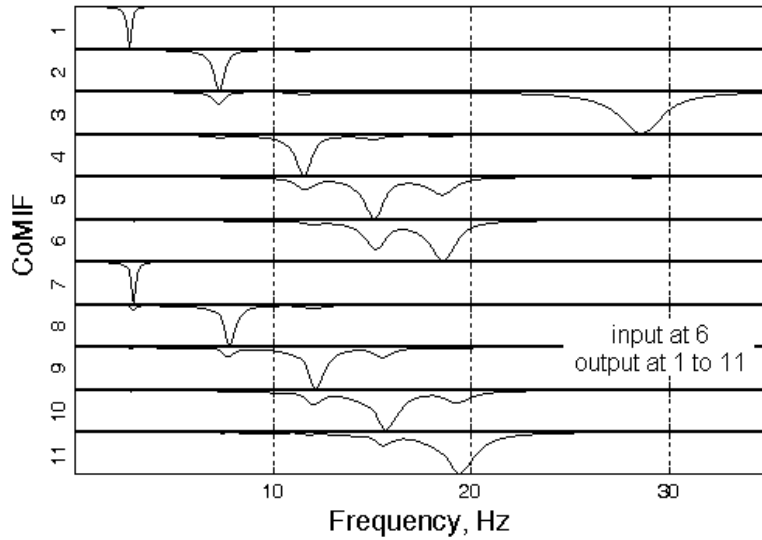
Fig. 9.28

The same CoMIF with individual curves displayed separately in subplots is shown in Fig. 9.28.

9.2.7.2 7-DOF system

Figure 9.29 shows a 7-DOF system [9.13] and its physical parameters.
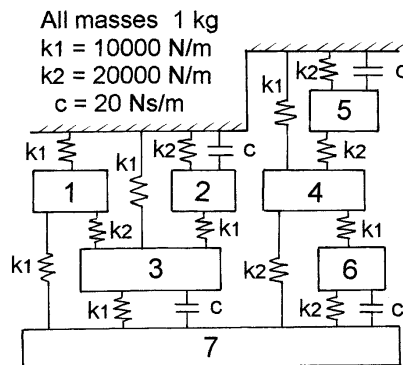

Fig. 9.29

Using only 7 receptance FRFs as 'test' data, calculated for excitation at mass #7 and response at all 7 masses, then polluted with 1% additive noise, the PRF plot from Fig. 9.30, *a* shows that the mode which is resonant at 28.12 Hz is buried in noise. The same plot is shown in Fig. 9.30, *b* for noise free data.
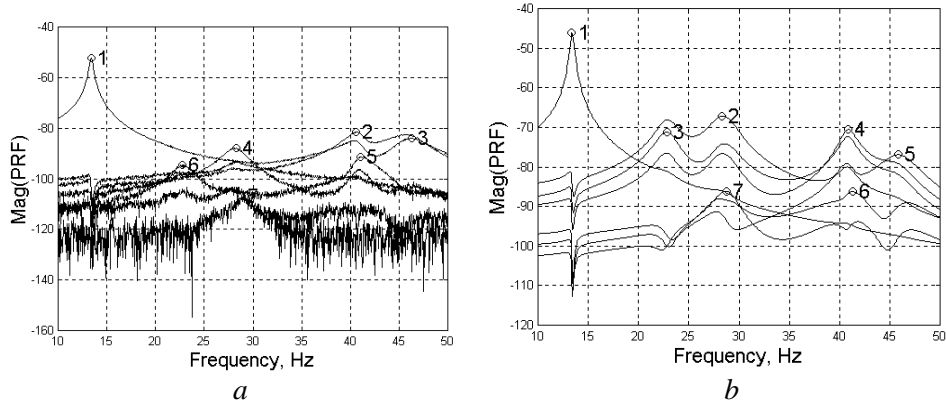
Fig. 9.30

The plot of left singular vectors from Fig. 9.31, *a* shows that the UMIF becomes difficult to be interpreted in the case of noisy data. The same plot is shown in Fig. 9.31, *b* for noise free data.
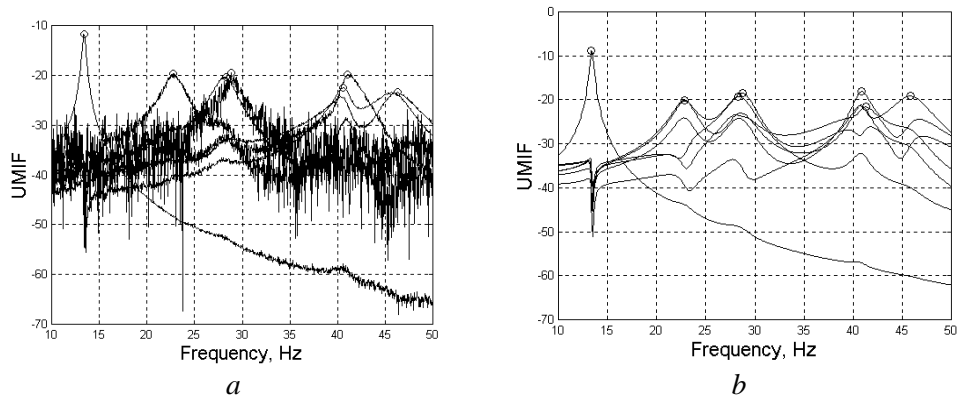
Fig. 9.31
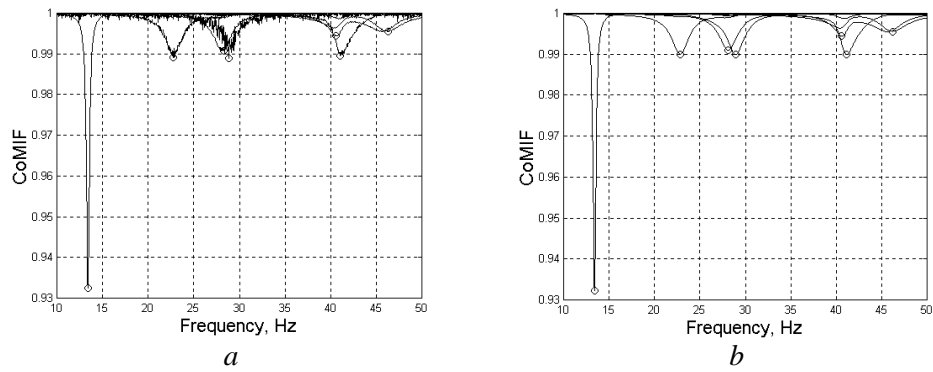
Fig. 9.32

The CoMIF plot from Fig. 9.32, *a* turns out to be a better modal indicator even when a weak mode makes the associate curve highly influenced by noise. Again, the same plot is shown in Fig. 9.32, *b* for noise free data.
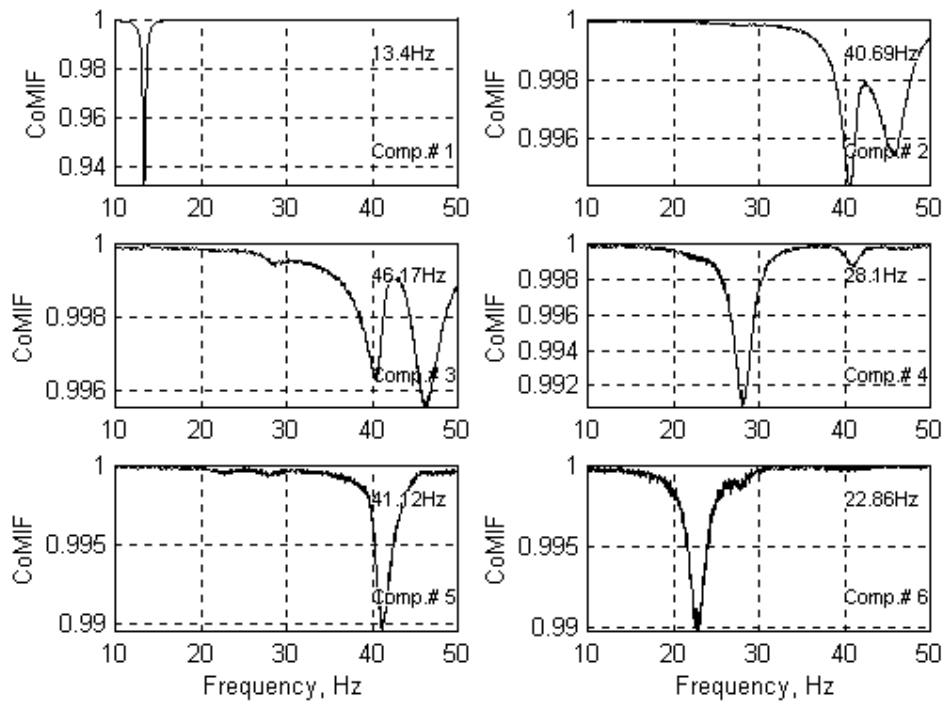

Fig. 9.33

Figure 9.33 illustrates individual CoMIF plots for the first six principal components of the CFRF matrix. The accuracy in locating natural frequencies is influenced, apart from the frequency resolution, by the noise in data.

9.2.8 Test data example 1

The inertance FRFs in this example were measured on the fan case shown in Fig. 9.34, at 12 locations around the lower rim, from each of the three force input locations 2, 3 and 50, in the frequency range 24 to 224 Hz. The frequency resolution was 0.25 Hz [9.1].

Each FRF contains 801 frequency points. The CFRF matrix is of size 801×36. The inputs were not a strict subset of the outputs and only one column of the CFRF matrix was redundant due to reciprocity.
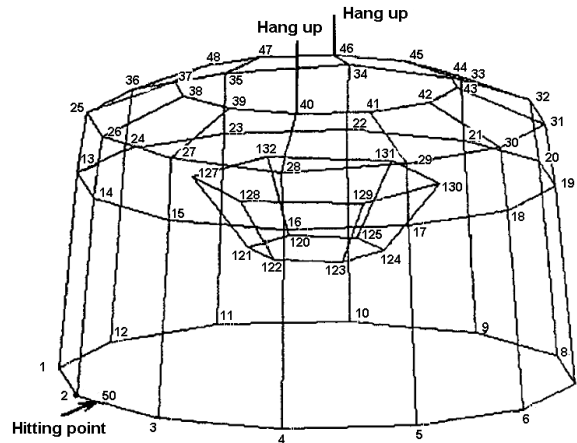
Fig. 9.34

The singular value plots (Fig. 9.35) of the CFRF matrix indicate a rank $N_r = 6$.
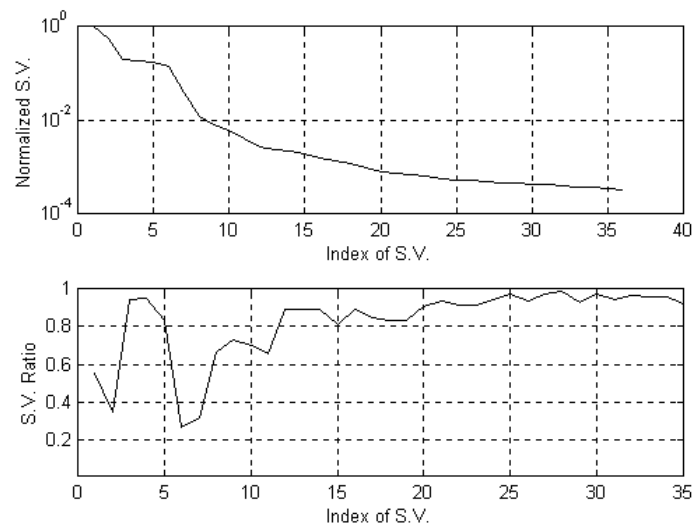
Fig. 9.35

The first six PRFs are shown in Fig. 9.36, calculated based on only 12 FRFs obtained with excitation at point 50. This plot reveals only the six most observable modes of vibration, i.e. two pairs of quasi-repeated eigenfrequencies at 103.1 and 177.9 Hz, and other two dominant modes at 45.75 and 75.7 Hz.

The AMIF is shown in Fig. 9.37. Applied to the original data, it reveals as many modes as the PRF plot, but applied to the reduced-rank data, it indicates only

four dominant modes. The difference is the number of double modes that cannot be shown by a single-curve MIF.
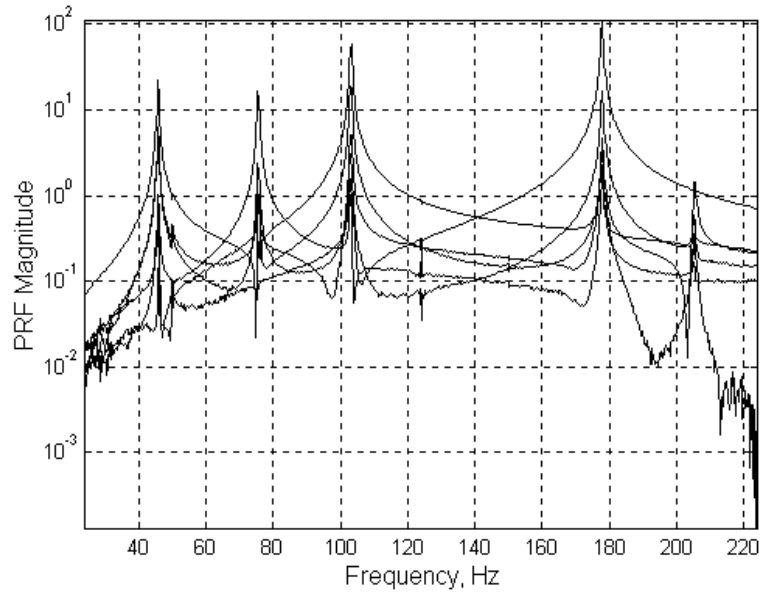
Fig. 9.36
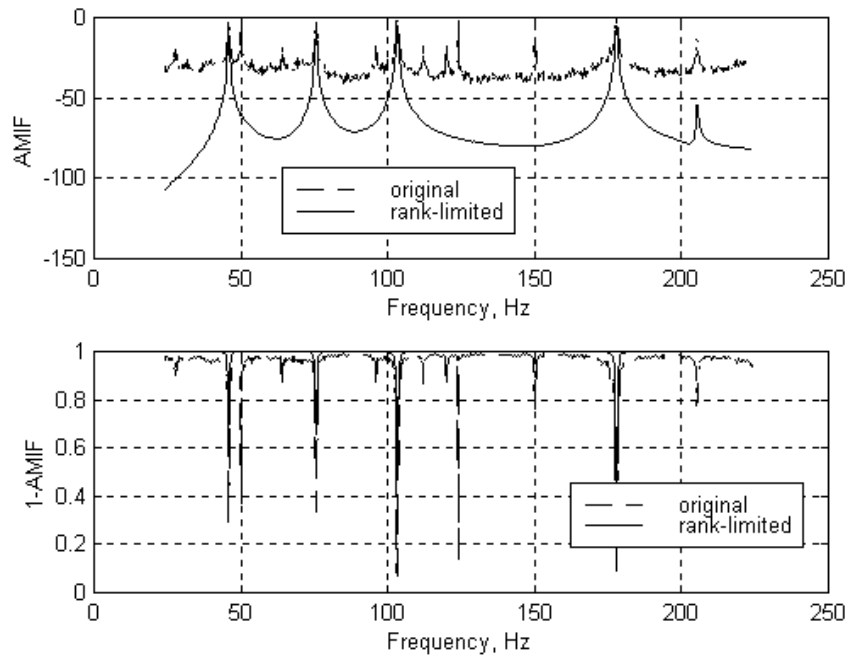
Fig. 9.37
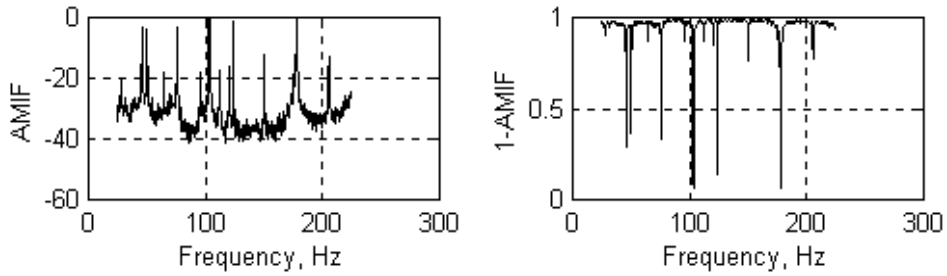
Fig. 9.38
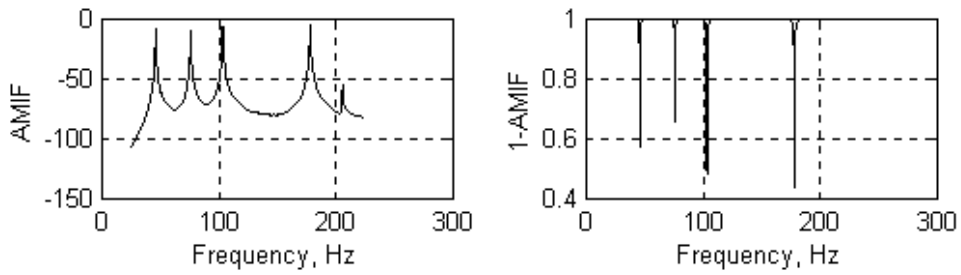
Fig. 9.39

Figure 9.38 is a presentation of the AMIF and 1-AMIF plots based on original data, while figure 9.39 shows the same plots for rank-limited data.
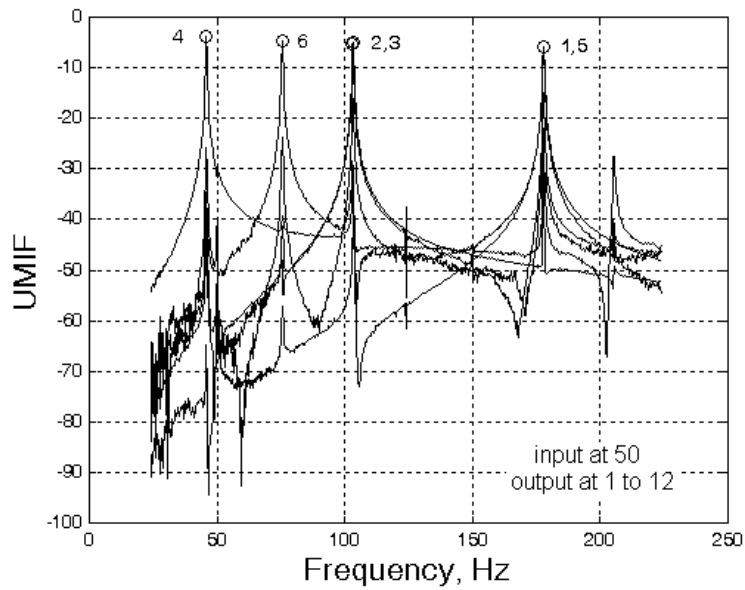

Fig. 9.40

Figure 9.40 shows the first six left singular vectors of the CFRF matrix. This plot is used as the *U-Mode Indicator Function* (UMIF), to reveal repeated modes. Indeed, at 103.1 and 177.9 Hz, two pairs of curves are superimposed. They should be differently colored to be distinguished from each other.
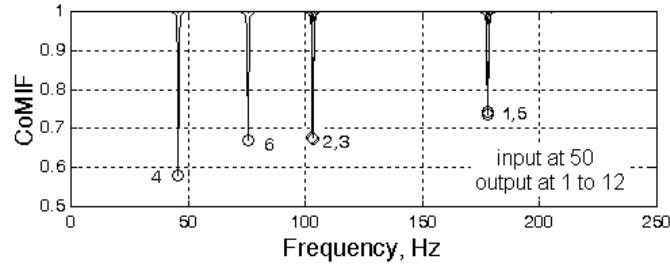
Fig. 9.41

The CoMIF with overlapped curves is presented in Fig. 9.41.

9.3 Analysis of the 3D FRF matrices

When the FRFs can be analyzed in turn, at each frequency, the data set can be visualized as a 3D matrix consisting of N_f rectangular $N_o \times N_i$ FRF matrices (Fig. 9.2). Various MIFs have been developed based on either the singular value decomposition (SVD) of each $[H]_{N_o \times N_i}$ matrix or on an eigenproblem involving the real and imaginary parts of the $[H(\omega)]$ matrices. Examples are the CMIF [9.14], the MMIF [9.15] and the related MRMIF, ImMIF and ReMIF [9.16]. There are as many curves in a plot as the number of references.

9.3.1 The CMIF

The economical SVD of the FRF matrix at each spectral line is defined as

$$[H]_{N_o \times N_i} = [U]_{N_o \times N_i} [\varSigma]_{N_i \times N_i} [V]_{N_i \times N_i}^H, \qquad (9.35)$$

where $[\varSigma]$ is the diagonal matrix of singular values, $[U]$ is the matrix of left singular vectors and $[V]$ is the matrix of right singular vectors. Matrices $[U]$ and $[V]$ have orthonormal columns.

The *Complex Mode Indicator Function* (CMIF) is defined [9.14] by the singular values plotted as a function of frequency on a logarithmic magnitude scale. The number of CMIF curves is equal to the number of driving points. The

largest singular values have peaks at the *damped* natural frequencies. The frequencies where more than one curve has a peak are likely to be repeated natural frequencies.

Early versions used the square of the singular values, calculated as the eigenvalues of the normal matrix $[H]^H[H]$. The left singular vectors are proportional to the mode shape vectors, and the right singular vectors relate to the modal participation factors.

It is recommended to plot 'tracked' CMIFs, connecting points which belong to the same modal vector, instead of 'sorted' CMIFs, in which points are connected simply based on magnitude. A detailed review of the CMIF and enhanced FRF concepts is given in [9.17]. Use of the $[H_I]$ matrix instead of $[H]$ has some advantages in the location of modes.

The CMIF performance declines for structures with very close frequencies and high damping levels. In such cases, two different curves exhibit flat peaks at very close frequencies which have to be located by cursors. The high damping merges the otherwise distinct close peaks.
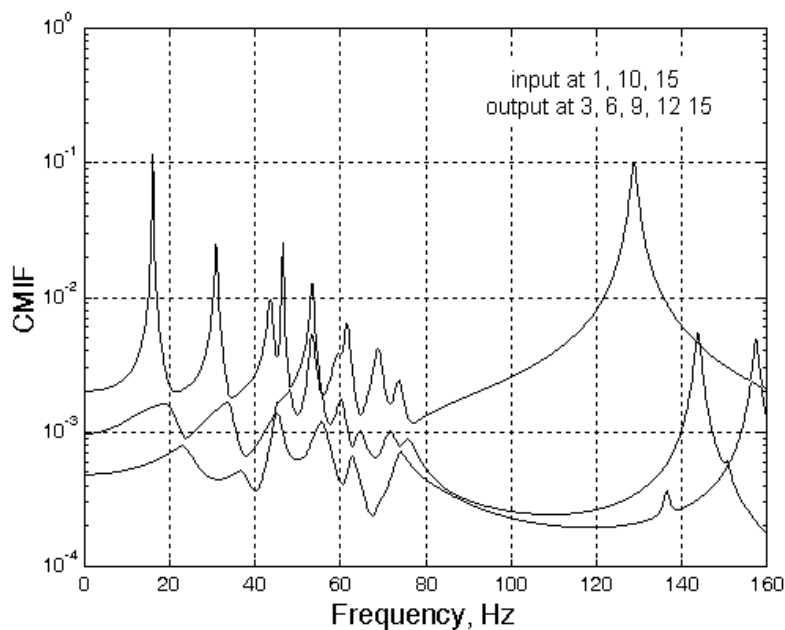

Fig. 9.42

Figure 9.42 presents the CMIF plot computed for the 15-DOF system of Fig. 9.6, using 5×3 FRF matrices for excitation at 1, 10, 15 and response at 3, 6, 9, 12 and 15. It clearly locates the close modes at 53.35 and 53.42 Hz.
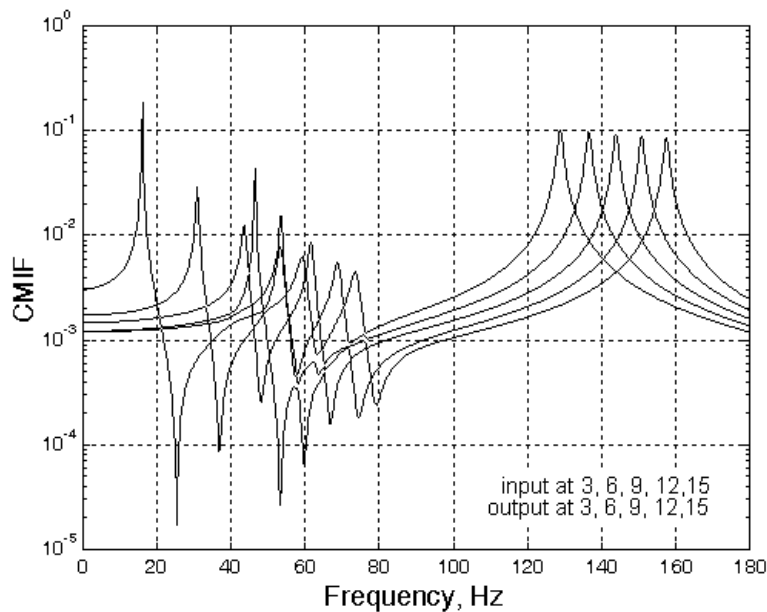
Fig. 9.43

The CMIF from Fig. 9.43 is computed for 5 by 5 FRF matrices, using the same input and output points at the small masses 3, 6, 9, 12, and 15.

9.3.2 Eigenvalue-based MIFs

In the definition of these MIFs, a cost function is first defined as the ratio of some norms of either the real, the imaginary or the total response. Expressing response vectors in terms of force vectors and the FRF matrix, the mini(maxi)mization problem takes the form of a Rayleigh quotient. This is equivalent to a frequency-dependent eigenvalue formulation, involving normal matrices, formed from the FRF matrix or its real and imaginary components. MIFs are defined by the eigenvalues of these matrix products, plotted against frequency. The existence of a mode of vibration is indicated by distinct troughs, peaks or zero crossings in the MIF plot.

9.3.2.1 The MMIF

For a linear time-invariant structure, at each frequency, the relationship between the complex vector of steady-state response, $\{\tilde{x}\}$, and the real force vector, $\{f\}$, is given by

$$\{\tilde{x}\} = \{x_R\} + i\,\{x_I\} = [H(i\omega)]\{f\} = [[H_R(\omega)] + i\,[H_I(\omega)]]\{f\}, \quad (9.36)$$

where $[H]_{N_o \times N_i}$ is the displacement FRF matrix. Usually, the number of input (excitation) points, N_i, is less than the number of output (response) points, N_o. In a given frequency band, the number of dominant modes (effective degrees of freedom) N_r is less or equal to the smallest dimension of the FRF matrix.

The *Multivariate Mode Indicator Function* (MMIF) is defined [9.15] by the eigenvalues of the generalized problem

$$[H_R]^T[H_R]\{f\} = \alpha\left([H_R]^T[H_R] + [H_I]^T[H_I]\right)\{f\}, \quad (9.37)$$

plotted against frequency.

The matrix products in (9.37) are of order N_i so that there are as many MMIF curves as driving points. The curve of the smallest eigenvalue exhibits troughs at the *undamped* natural frequencies (UNFs). These minima correspond to minima of the cost function given by the ratio of the Euclidian norm of the in-phase response vector to the norm of the total vector response

$$\min \frac{\|x_R\|^2}{\|x_R + i\,x_I\|^2} = \alpha\,. \quad (9.38)$$

The minimization problem (9.38) can be written in the form of a Rayleigh quotient

$$\min \frac{\{f\}^T[H_R]^T[H_R]\{f\}}{\{f\}^T\left([H_R]^T[H_R] + [H_I]^T[H_I]\right)\{f\}} = \alpha, \quad (9.39)$$

which is equivalent to the frequency-dependent eigenproblem (9.37).

Small MMIFs at troughs is a measure of the purity of mode isolation by the applied forcing vector. Higher MMIF values at minima indicate poorly excited modes. The frequencies where more than one curve has a minimum are likely to indicate multiple natural frequencies. Sometimes, not all troughs in the MMIF indicate modes.

Usually, MMIF curves are plotted as a function of magnitude, based on sorted eigenvalues. Points representing the smallest eigenvalue, the second smallest eigenvalue, etc. are connected separately. This gives rise to the 'cross-eigenvalue effect' at frequencies where at least two curves cross each other. Cross-over troughs occur, which have to be carefully analyzed. They prevent the use of an automatic through detector to locate eigenfrequencies. The problem is alleviated by the use of tracked MMIFs, plotted by connecting points corresponding to the same modal vector.

Apart from cross-eigenvalue effects, antiresonances can produce fallacious troughs. Hence, it is recommended to use the MMIF not on its own but together with other MIFs or with the composite response spectrum to confirm the validity of its minima.
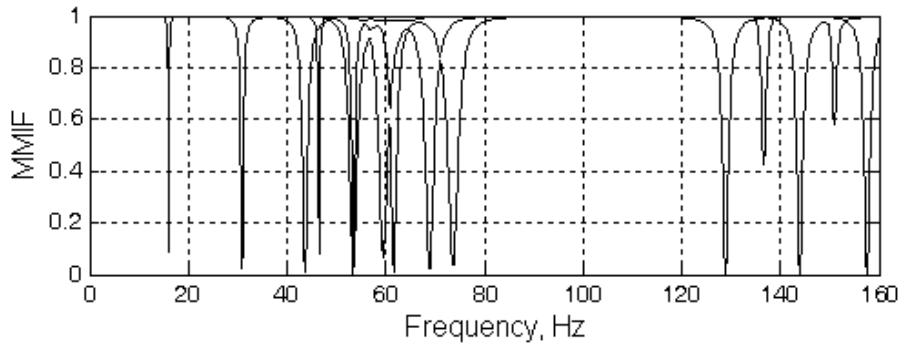

Fig. 9.44

Figure 9.44 presents the MMIF plot computed for the 15-DOF system of Fig. 9.6, using the same FRFs as for Fig. 9.42. The plot locates all 15 modes.

The inverted MMIF [9.18] is defined by the eigenvalues of the spectral problem

$$[H_I]^T[H_I]\{f\} = \beta \left([H_R]^T[H_R] + [H_I]^T[H_I]\right)\{f\}, \qquad (9.40)$$

where $\beta = 1 - \alpha$. Undamped natural frequencies occur at maxima of the largest eigenvalue, with multiple eigenfrequencies indicated by peaks in the next highest eigenvalues.

In fact, the undamped natural frequencies indicated by the MMIF are frequencies at which the closest approximation to an undamped normal mode can be excited from the forcing points available. The corresponding eigenvector calculated at this frequency gives the appropriate force distribution.

9.3.2.2 The MRMIF

The modified real mode indicator function (MRMIF) is defined by the frequency dependence of the eigenvalues of the generalized problem

$$[H_R]^T[H_R]\{f\} = \mu [H_I]^T[H_I]\{f\}. \qquad (9.41)$$

Like the MMIF concept, this is based on a Rayleigh quotient

$$\min \frac{\{f\}^T[H_R]^T[H_R]\{f\}}{\{f\}^T[H_I]^T[H_I]\{f\}} = \mu, \qquad (9.42)$$

but is generated by minimizing the ratio of the Euclidian norm of the in-phase response vector to the norm of the quadrature response vector only [9.19]

$$\min \frac{\| x_R \|^2}{\| x_I \|^2} = \mu \,.$$ (9.43)

MRMIF eigenvalues are plotted on a log magnitude scale (to reduce the difference between dips) as a function of frequency, having similar shapes as the MMIF curves. Undamped natural frequencies are located at the minima in the MRMIF curves. Interpretation of dips in higher order MRMIFs is rather difficult on sorted curves and prevents the use of an automatic mode detector.
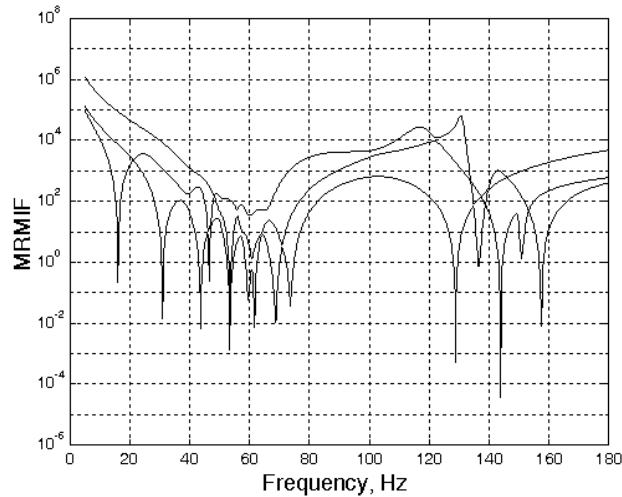
Fig. 9.45

Figure 9.45 shows the MRMIF plot computed for the 15-DOF system of Fig. 9.6, using the same data as for the MMIF from Fig. 9.44.

The inverted MRMIF is defined by the eigenvalues of the spectral problem

$$[H_I]^T[H_I]\{f\} = \nu\,[H_R]^T[H_R]\{f\}.$$ (9.44)

The undamped natural frequencies occur at maxima of eigenvalues. The shape of curves resembles the inverted MMIF.

Use of the quotient singular value decomposition (QSVD) is recommended to solve the spectral problem (9.41). This avoids formation of the matrix products, which causes loss of half of the numerical relative accuracy. QSVD implies the simultaneous SVD of matrices $[H_R]$ and $[H_I]$, using the same orthonormalized right singular vectors [9.20].

9.3.2.3 The ImMIF

The imaginary mode indicator function (ImMIF) is defined as the eigenvalues of the spectral problem

$$[H_I]^T[H_I]\{f\} = \gamma\{f\} \qquad\qquad (9.45)$$

plotted against frequency [9.21]. The equivalent Rayleigh quotient formulation is

$$\min \frac{\{f\}^T[H_I]^T[H_I]\{f\}}{\{f\}^T\{f\}} = \gamma. \qquad\qquad (9.46)$$

Local peaks of the largest eigenvalues define the undamped natural frequencies. The singular values of the $[H_I]$ matrix can be used to avoid loss of numerical accuracy due to the squaring in the Gram matrix. This is equivalent to using the $[H_I]$ matrix instead of $[H]$ in the CMIF.
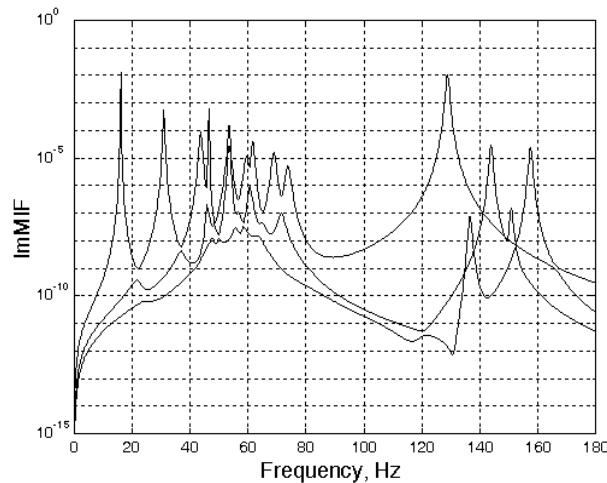
Fig. 9.46

Figure 9.46 shows the ImMIF plot computed for the 15-DOF system of Fig. 9.6, using the same data as for the CMIF from Fig. 9.42.

9.3.2.4 The RMIF

The RMIF is defined by the frequency dependence of the eigenvalues of the matrix product $[H_I]^+[H_R]$, where $^+$ denotes the Moore-Penrose pseudoinverse [9.22]. They are a measure of the ratio of reactive energy to the active energy transmitted to the structure during a cycle of forced vibrations.

There are as many RMIF curves as points of excitation, N_i. Each curve can cross the frequency axis several times. Only zero crossings with positive slope indicate *undamped* natural frequencies. Multiple (or closely spaced) eigenfrequencies can be revealed by several curves crossing the frequency axis (almost) at the same frequency. Appropriated force vectors are obtained from the eigenvectors calculated at the undamped natural frequencies. For a given scaling of force vectors [9.23], the slopes at zero crossings are proportional to the modal masses. Diagonal modal damping coefficients are proportional to the inverses of the undamped natural frequencies.

The theoretical background of the RMIF is different from that of other MIFs. Instead of looking directly for a real normal mode, by minimizing the ratio of out-of-phase energy to total energy, the concept of monophase forced modes of vibration is used. The monophase condition, implying proportionality between the real part and the imaginary part of the response vector (minus sign omitted),

$$\{x_R\} = \lambda \{x_I\},$$

yields the frequency dependent spectral problem of a rectangular matrix pencil

$$[H_R(\omega)]\{f(\omega)\} = \lambda(\omega)[H_I(\omega)]\{f(\omega)\}. \tag{9.47}$$

At a given frequency ω, a monophase excitation vector $\{f\}$ gives the force distribution that can produce the closest approximation to a (real) monophase response vector. The two real vectors are not in phase with one another. Monophase excitation vectors are modal filters developing energy only in the corresponding reduced response modal vector. The theory of monophase modal vectors (Section 7.4) explains why only positive zero crossings indicate undamped natural frequencies.

Because the matrices in equation (9.47) are rectangular, the spectral problem can be solved only approximately. A pure monophase mode cannot be excited because the number of exciters is not sufficient to cancel, at each reference point, the damping forces and the reactive forces, so as to ensure the equiphase condition. Mathematically, the number of equations N_o is larger than the number of unknowns N_i. The solution is to find a scalar λ and a force vector $\{f\}$ to minimize

$$\{x_R\} - \lambda \{x_I\} = \{\varepsilon\},$$

i.e., the residual formed by the difference of the two members of equation (9.47).

The best procedure is to form the quadratic residual $\{\varepsilon\}^T\{\varepsilon\}$ and to divide it by the Euclidian norm of the displacement amplitude, and to minimize the scalar function

$$\delta = \frac{\{\varepsilon\}^T \{\varepsilon\}}{\|x_R\|^2 + \|x_I\|^2}, \tag{9.48}$$

or

$$\delta = \frac{\{f\}^T \left([H_R]^T - \lambda[H_I]^T\right)\left([H_R] - \lambda[H_I]\right)\{f\}}{\{f\}^T \left([H_R]^T[H_R] + [H_I]^T[H_I]\right)\{f\}}. \tag{9.49}$$

This is independent of the scaling of forcing vectors [9.24].

The conditions of minimum are

$$\frac{\partial \delta}{\partial \{f\}} = 0 \qquad \text{and} \qquad \frac{\partial \delta}{\partial \lambda} = 0. \tag{9.50}$$

The first condition yields the eigenvalue problem

$$[E]\{f\} = \delta \left([A] + [B]\right)\{f\}. \tag{9.51}$$

The second condition gives the quotient

$$\lambda = \frac{\{x_I\}^T \{x_R\}}{\{x_I\}^T \{x_I\}} = \frac{\{f\}^T [C]\{f\}}{\{f\}^T [B]\{f\}}, \tag{9.52}$$

where

$$[E] = [A] - \lambda \left([C] + [D]\right) + \lambda^2 [B],$$

$$[A] = [H_R]^T [H_R], \quad [C] = [H_I]^T [H_R], \tag{9.53}$$

$$[B] = [H_I]^T [H_I], \quad [D] = [H_R]^T [H_I].$$

The eigenvalue form of (9.52) is

$$[C]\{f\} = \lambda [B]\{f\}.$$

or

$$[H_I]^T [H_R]\{f\} = \lambda [H_I]^T [H_I]\{f\}. \tag{9.54}$$

If $[H_I]$ has full column rank, equation (9.51) can be written

$$\left([H_I]^T [H_I]\right)^{-1} [H_I]^T [H_R]\{f\} = \lambda \{f\} \tag{9.55}$$

or

$$[H_I]^+ [H_R]\{f\} = \lambda \{f\}. \tag{9.55, a}$$

The eigenvalues λ vanish at the undamped natural frequencies of the system. The pseudoinverse of the matrix $\left[H_I \right]$ can be calculated in a principal component sense, performing its singular value decomposition and cancelling the negligible singular values before inversion. This diminishes the sensitivity to the rank-deficiency of the FRF matrix and noise encountered with the standard formulation [9.23], which can give spurious zero crossings. Unlike other methods, the RMIF offers no assessment of mode purity.
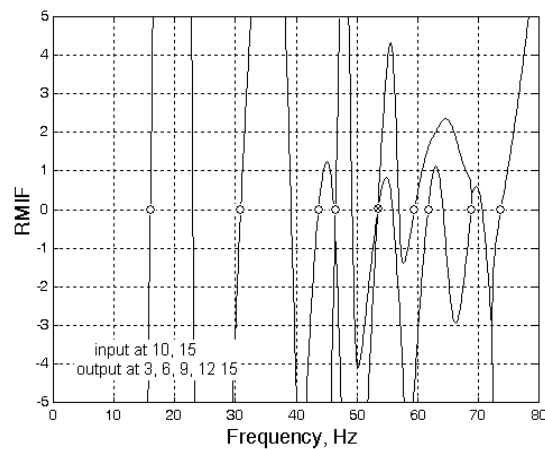
Fig. 9.47

Figure 9.47 shows the RMIF plot computed for the 15-DOF system of Fig. 9.6, for a frequency range encompassing only the first ten modes.

9.3.3 Single-curve MIFs

The first single-curve MIF was developed by Breitbach in 1973 [9.25] at DFVLR (German Aerospace Research Establishment) for the modal survey of complex aircraft structures. It helped in the selection of optimal force vectors to isolate normal modes of a structure. In the following it is denoted *MIF1*.

At each frequency the *MIF1* is defined as

$$MIF1_i = 1 - \frac{\sum\limits_{j=1}^{N} \left| \mathrm{Re}\left(a_{ij} \right) \right| \left| a_{ij} \right|}{\sum\limits_{j=1}^{N} \left| a_{ij} \right|^2} \; , \qquad (9.56)$$

where the sums extend over $N \leq N_o \times N_i$ FRF functions. Note that $1 - MIF1$ has dips instead of peaks [9.26].

The somewhat complementary *MIF2* is defined [9.27] as

$$MIF2_i = 1 - \frac{\sum\limits_{j=1}^{N} \left| \mathrm{Im}\left(a_{ij}\right) \right| \left| a_{ij} \right|}{\sum\limits_{j=1}^{N} \left| a_{ij} \right|^2} \quad . \tag{9.57}$$

They both locate the frequencies where the forced response is closest to the monophase condition.
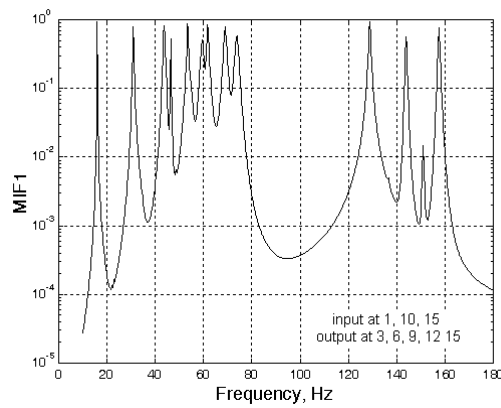
Fig. 9.48

Figure 9.48 shows the *MIF1* plot computed for the 15-DOF system of Fig. 9.6, using 15 FRFs for excitation at 1, 10, 15 and response at 3, 6, 9, 12 and 15. It locates only 13 modes.
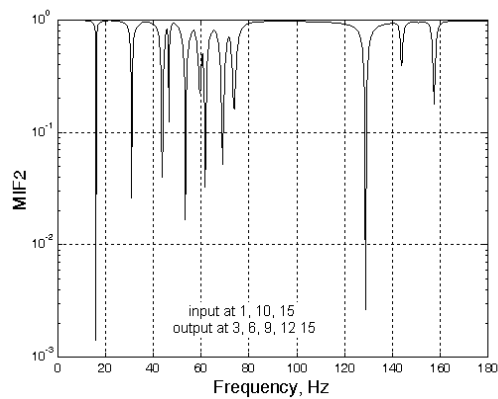
Fig. 9.49

Figure 9.49 shows the *MIF2* plot computed for the same data as Fig. 9.48. It locates only 12 modes of vibration.

9.3.4 Numerical simulations

The numerical simulation examples presented in the following are calculated for the 11-DOF lumped parameter system used in Section 9.2.7.1 and for a 5-DOF system with hysteretic damping.

9.3.4.1 11-DOF system

For the 11-DOF system with hysteretic damping of Fig. 9.19, a typical CMIF plot is shown in Fig. 9.50. It exhibits 6 peaks in the upper curve and 4 peaks in the lower curve, failing to locate one mode. Cursors are necessary to locate the *damped* natural frequencies. Figure 9.51 shows the MMIF plot computed for the same 7×2 FRF matrices as the CMIF. It locates all 11 modes.
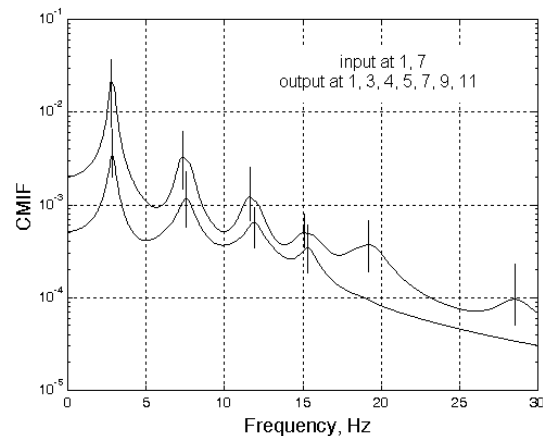
Fig. 9.50
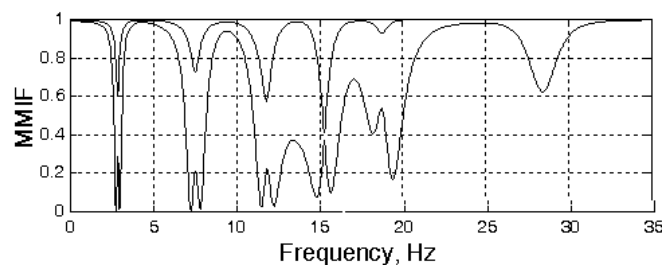
Fig. 9.51

The CMIF performance declines for structures with relatively close frequencies and high damping levels. When two curves exhibit flat peaks at very close frequencies these have to be located by cursors. The high damping merges the otherwise distinct close peaks. In such cases the MMIF performs better because it locates the *undamped* natural frequencies, which are more distant from one another than the corresponding *damped* natural frequencies indicated by the CMIF.
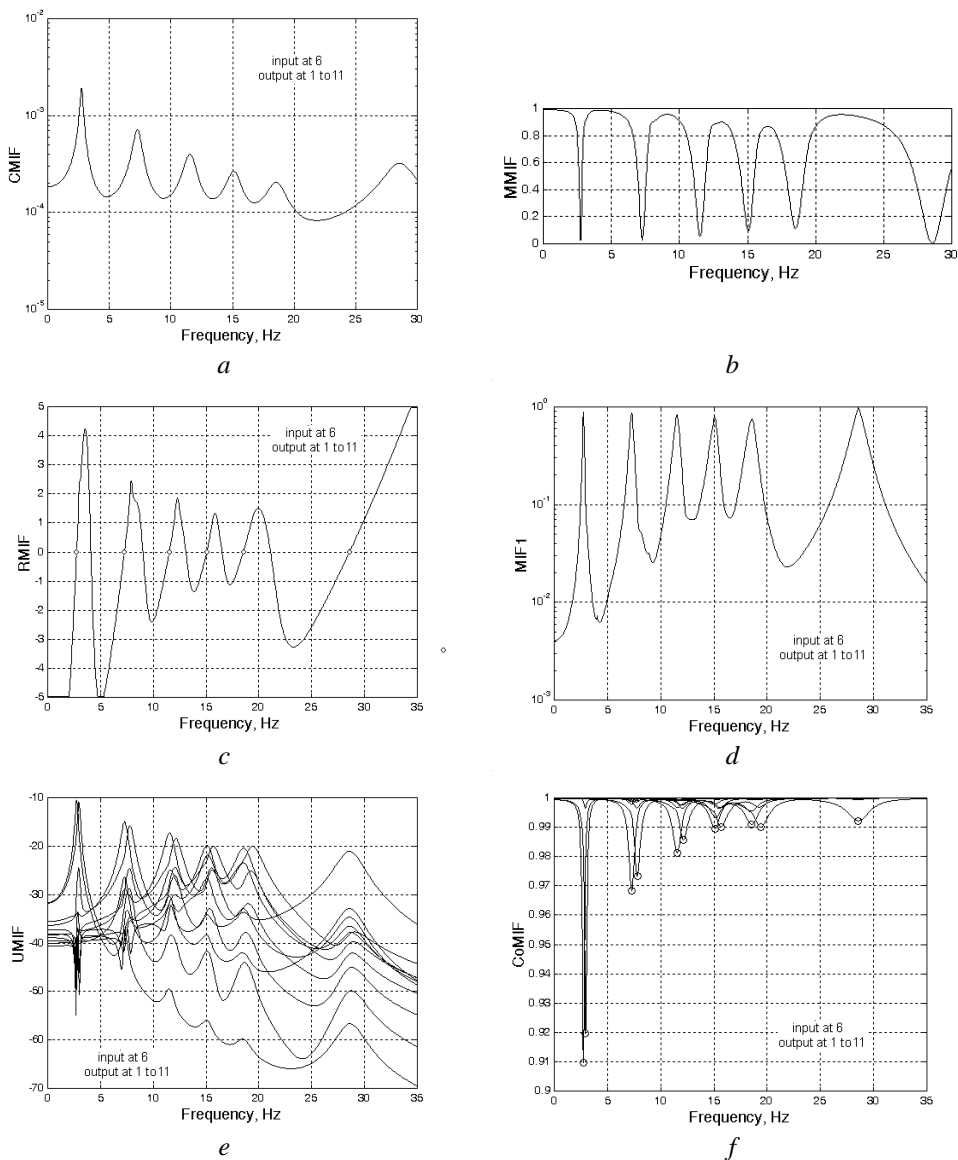
Fig. 9.52

Six different MIFs are compared in Fig. 9.52, for excitation at mass 6 and response measurement at all 11 masses. The UMIF and CoMIF plots locate all 11 modes, while the other MIFs fail to locate the quasi-double modes. The CMIF, MMIF and RMIF plots have been expected not to locate all of them from single point excitation, because the number of curves is equal to the number of inputs, while MIF1 is a basically a single curve MIF.

9.3.4.2 5-DOF system

The five degrees of freedom system with structural damping from Fig. 9.53 [9.28] will be used for a comparison of MIFs. Two different FRF data sets (free of noise) will be used in the simulation: case 1 - excitation at points 1, 4 and response measurement at points 1, 2, 4; case 2 - excitation at 1, 2 and response measurement at 1, 2, 4.
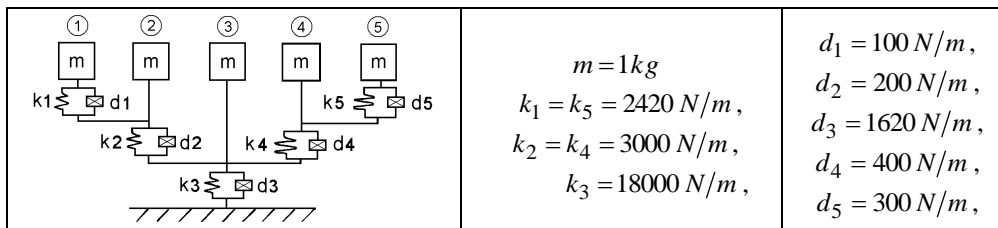
Fig. 9.53

The *undamped* natural frequencies are 4.689, 5.213, 12.366, 13.092 and 25.131 Hz. Depending on the FRF data used, the MMIFs can be erroneous indicators. The MMIF plot in Fig. 9.54, *a* has a fallacious trough at 7.8 Hz, produced by an antiresonance, while the MMIF in Fig. 9.54, *b* does not indicate all modes.
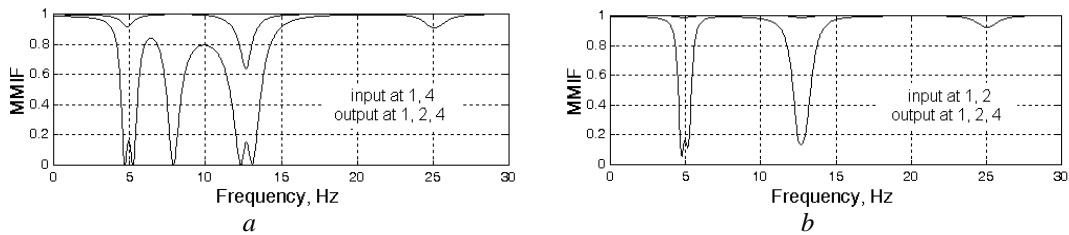
Fig. 9.54

The *damped* natural frequencies are 4.702, 5.202, 12.449, 13.015 and 25.131 Hz. The CMIF plot in Fig. 9.55 indicates all five modes and performs better than the MMIF from Fig. 9.53, but the CMIF in Fig. 9.56 fails to indicate one mode, having only four peaks. This is due to the particular selection of input points.
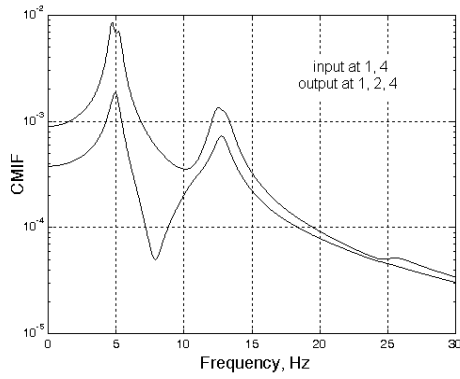
Fig. 9.55
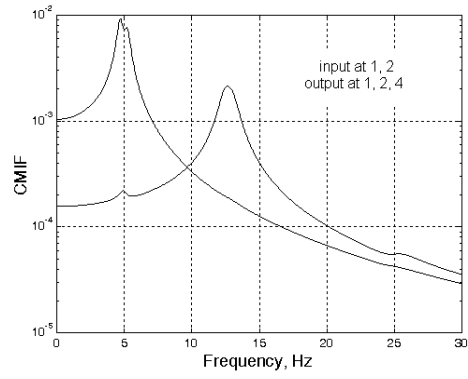
Fig. 9.56
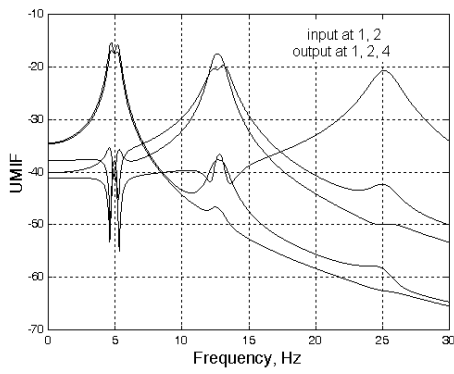
Fig. 9.57
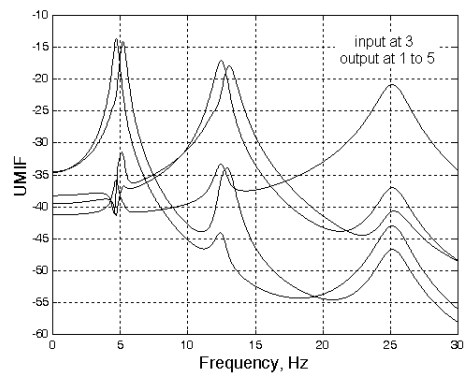
Fig. 9.58
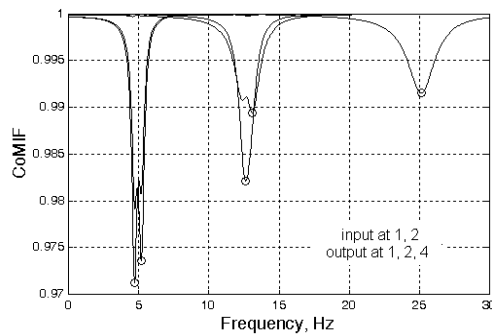
Fig. 9.59

It is interesting to compare the MMIFs and CMIFs with the UMIFs. The UMIF in Fig. 9.57 locates all five modes and outperforms the MMIF and CMIF plotted for the same FRF data set (case 2) which failed to locate one mode. Using

FRFs from a single input point results in an UMIF plot (Fig. 9.58) which locates all 5 modes. The CoMIF with overlapped curves is shown in Fig. 9.59. It also locates all 5 modes.

9.3.5 Test data example 1

Figures 9.60 and 9.61 show the CMIF and MMIF plots calculated based on FRFs from 12 locations (1 to 12 along the lower rim), and 3 force input locations (2, 3 and 50) measured on the fan case shown in Fig. 9.34.
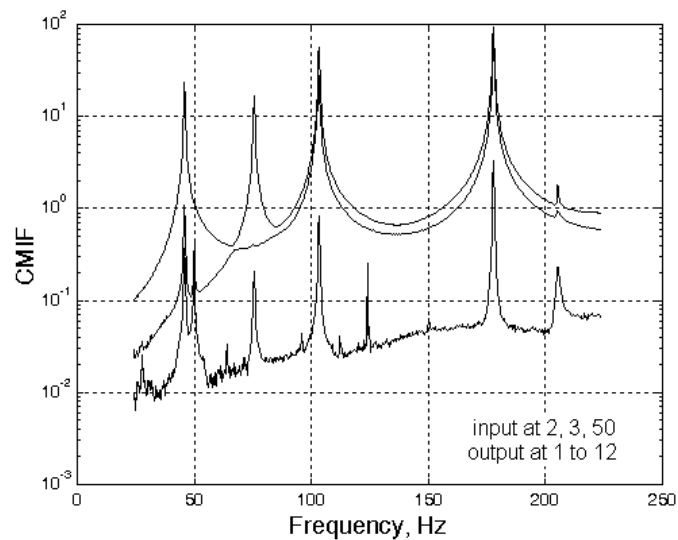
Fig. 9.60
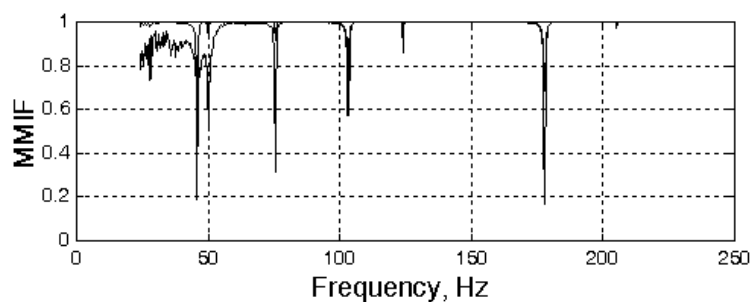
Fig. 9.61

They detect two pairs of quasi-repeated eigenfrequencies at 103.1 and 177.9 Hz, other dominant modes at 45.75 and 75.7 Hz and some local modes. They

perform well for lightly damped structures, but the overlapped MMIF curves should be differently coloured to be distinguished from each other.
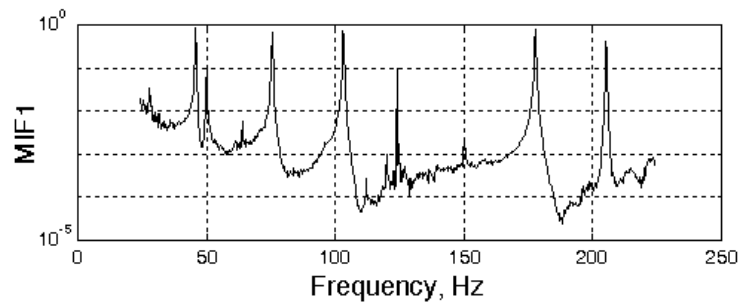
Fig. 9.62
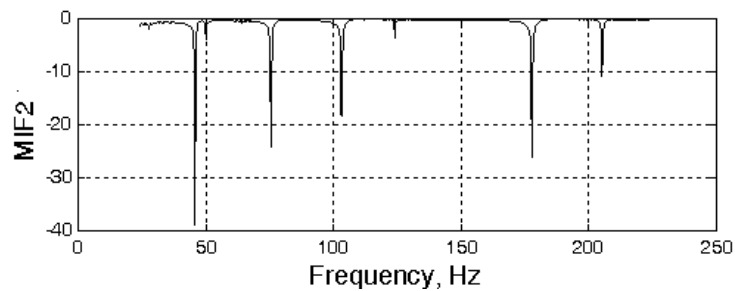
Fig. 9.63

The single-curve MIF plots from Figs. 9.62 and 9.63 are calculated based on the same FRF data. They fail to indicate the existence of double modes, but show some local modes which appear also in the CMIF plot, on the curve corresponding to excitation at point 50.

9.4 QR decomposition of the CFRF matrices

Applied to measured Frequency Response Functions, the *pivoted orthogonal triangularization* provides an alternative parsimonious description of frequency response data, being less expensive and more straightforward than the *singular value decomposition*. The main objective is to replace the measured set of FRFs by a reduced set of uncorrelated *Q-Response Functions* (QRFs) containing (almost) as much information as the original FRFs. The *pivoted QLP decomposition* [9.29] is an extension of the *pivoted QR decomposition* with better rank-revealing properties.

9.4.1 Pivoted QR factorization of the CFRF matrix

The pivoted QR factorization [9.30] decomposes the CFRF matrix into a sum of rank-one matrices, $\left[\hat{A}_i\right]$. The column-permuted version of $[A]$ is

$$\left[\hat{A}\right]=[A]\left[\Pi_R\right]=[Q][R]=\sum_{i=1}^{N}\{q\}_i\lfloor r\rfloor_i=\sum_{i=1}^{N}\left[\hat{A}_i\right]. \qquad (9.58)$$

In (9.58), $[Q]$ is an $N_f \times N$ rectangular matrix with orthonormal columns, $\{q\}_i$, $[R]$ is upper triangular of order *N*, with rows $\lfloor r\rfloor_i$, and $\left[\Pi_R\right]$ is a permutation matrix. The diagonal entries of $[R]$ are arranged in the descending order of their absolute values. Moreover, the diagonal of the $[R]$ matrix contains the maximum entry for each row, $r_{jj}=\max(\lfloor r\rfloor_j)$.

The columns of $[Q]$ represent orthogonal unit directions in an *N*-dimensional identification space, i.e. a new set of linearly independent frequency response functions, sometimes referred to as QRFs (*Q Response Functions*).

Algebraically, the *Q*-vectors, $\{q\}_k$, are particular linear combinations of the measured FRFs, i.e. of the columns $\{a\}_j$ of the CFRF matrix

$$\{q\}_k=\sum_{j=1}^{k}s_{jk}\{a\}_j. \qquad (9.59)$$

In (9.59), the multiplying factors s_{jk} are complex-valued elements of the upper triangular matrix $[S]=[R]^{-1}$ (for $[A]$ full rank).

Geometrically, the transformation from FRFs to *Q*-vectors amounts to a rotation of the coordinate axes represented by the original FRFs, to a new coordinate system with mutually orthogonal axes, represented by the uncorrelated *Q*-vectors. Thus $\{q\}_1$ is along $\{a\}_1$, $\{q\}_1$ and $\{q\}_2$ are coplanar with $\{a\}_1$ and $\{a\}_2$, $\{q\}_3$ is orthogonal to $\{q\}_1$ and $\{q\}_2$ and so on. The *Q*-vectors form an orthonormal basis for the column space of the CFRF matrix. The coordinate system defined by the *Q*-vectors is different from the one defined by the left singular vectors of $[A]$, that represent the principal axes of inertia of the data in the measurement space (directions with extremal autopower properties).

Each component matrix, $\left[\hat{A}_i\right]$, is connected to one of the observable modes of vibration in the test data. It is expected that a componentwise analysis of the CFRF matrix will yield the system modal characteristics.

Because the Q-vectors have unit length, the amplitude information is contained in the $[R]$ matrix. Generally, $r_{ij} = \{q\}_i^H \{a\}_j$ if $i \leq j$, and $r_{ij} = 0$ if $i > j$. The j-th column of $[R]$ contains the components of $\{a\}_j$ along the directions $\{q\}_1$ to $\{q\}_j$, i.e.: $\{q\}_1^H \{a\}_j$, $\{q\}_2^H \{a\}_j$,....., $\{q\}_j^H \{a\}_j$. The diagonal entries of $[R]$ are projections of the column from $[\hat{A}]$ onto the direction from $[Q]$.

The non-zero columns in each matrix $[\hat{A}_i]$ represent the projection of the columns $\{a\}_j$ $(j = i : N)$ onto the direction of $\{q\}_i$ (i.e. the product of the column $\{a\}_i$, for $i = j : N$, with the projection matrix $\{q\}_i \{q\}_i^H$).

If $\text{rank}[A] = N_r < N$, one can write

$$[Q]^H [A][\Pi_R] = [R] = \begin{bmatrix} [R_{11}] & [R_{12}] \\ [0] & [R_{22}] \end{bmatrix} \cdot \begin{matrix} N_r \\ N - N_r \end{matrix} \quad (9.60)$$
$$\begin{matrix} N_r & N - N_r \end{matrix}$$

The leading block $[R_{11}]$ is upper triangular and non-singular. In order to determine the rank N_r of the matrix $[A]$, one has to carry out correctly the truncation of $[R]$, setting $[R_{22}] = 0$. Determination of N_r consists in deciding which is the first negligible entry down the diagonal of $[R]$. The magnitude of an element r_{jj} can be considered as an indicator for the linear independence of the previous columns of $[A]$.

Practically, N_r is determined by tracking the changes in magnitude of the diagonal elements of $[R]$. Using the plot of the ratio of successive diagonal entries of $[R]$, the rank of $[R]$, hence of $[A]$, is set to the index of the diagonal entry for which the ratio is a minimum.

Partitioning

$$[Q] = [[Q_1] \ [Q_2]],$$
$$\begin{matrix} N_r & N - N_r \end{matrix}$$

the column permuted version of $[A]$ becomes

$$[\tilde{A}] = [A][\Pi_R] = [Q_1] [[R_{11}] [R_{12}]]. \quad (9.61)$$

9.4.2 Pivoted QLP decomposition of the CFRF matrix

It has been found that diagrams of the diagonal entries r_{jj} of $[R]$ are not entirely reliable for detecting the rank N_r. The solution is a subsequent processing of the pivoted QR decomposition that yields the so-called "pivoted QLP decomposition", which has better rank revealing properties [9.29].

The algorithm of the *pivoted QLP decomposition* consists of two applications of the *pivoted QR decomposition*, first to the matrix $[A]$ as in (9.58)

$$[A][\Pi_R]=[Q][R],$$

then to the conjugate transpose of the upper triangular matrix $[R]$

$$[R]^H [\Pi_L]=[P][L]^H, \qquad (9.62)$$

where $[P]$, of order N, has orthonormal columns and $[L]$, of order N, is lower triangular (hence $[L]^H$ is upper triangular). The pivots $[\Pi_R]$ and $[\Pi_L]$ are permutations to order the diagonal elements of $[R]$ and $[L]^H$, respectively, in the descending order of their absolute value.

Substituting $[R]=[\Pi_L][L][P]^H$ into $[A]=[Q][R][\Pi_R]^H$, one obtains

$$[A]=[\hat{Q}][L][\hat{P}]^H, \qquad (9.63)$$

where

$$[\hat{Q}]=[Q][\Pi_L] \quad \text{and} \quad [\hat{P}]=[\Pi_R][P]. \qquad (9.64)$$

This is a pivoted orthogonal triangularization of $[A]$, of the form

$$[A] = (\text{orthogonal}) \times (\text{lower triangular}) \times (\text{orthogonal}),$$

which is cheap to compute and tends to isolate independent columns of $[A]$.

The diagram of the diagonal entries ℓ_{jj} of $[L]$ versus their index resembles quite well the plot of singular values of $[A]$. In comparison with the diagonal entries of $[R]$, the ℓ_{jj} values track the singular values with remarkable fidelity, having better rank-revealing capability.

If $\text{rank}[A]=N_r$ and matrices $[\hat{P}]$ and $[\hat{Q}]$ are partitioned accordingly

$$[\Pi_R][P]=[\hat{P}]=[[\hat{P}_1][\hat{P}_2]] , \qquad (9.65)$$
$$N_r \quad N-N_r$$

$$[Q][\Pi_L]=[\hat{Q}]=[[\hat{Q}_1][\hat{Q}_2]] , \qquad (9.66)$$
$$N_r \quad N-N_r$$

then the pivoted QLP decomposition can be written in the partitioned form

$$[A]=[[\hat{Q}_1][\hat{Q}_2]]\begin{bmatrix}[L_{11}] & [0] \\ [L_{21}] & [L_{22}]\end{bmatrix}\begin{bmatrix}[\hat{P}_1]^H \\ [\hat{P}_2]^H\end{bmatrix}, \qquad (9.67)$$

where $[L_{11}]$ is of order N_r.

The full-rank approximation of $[A]$, of rank N_r, is

$$[\tilde{A}]=[\hat{Q}_1][L_{11}][\hat{P}_1]^H . \qquad (9.68)$$

In general, the pivoting mixes up the columns of $[Q]$ so that $[\hat{Q}_1]$ cannot be associated with a set of columns of $[A]$.

For $[\hat{A}]=[A][\Pi_R]=[Q][R]$ full rank, if $[S]=[R]^{-1}$, the columns of $[Q]$ are

$$\{q\}_k = \sum_{j=1}^{k} s_{jk}\{a\}_j , \qquad (9.69)$$

where $\{a\}_j$ are the columns of $[\hat{A}]$.

The *L*-values tend to track the singular values of $[A]$, so they can be used to reveal gaps in the latter. If the singular values of $[A]$ have a gap at σ_{N_r}, the diagonal entries of $[L]$ will generally exhibit a well-marked gap at $\ell_{N_r N_r}$. Practically, N_r is determined by tracking the variation in magnitude of the *L*-values. Plotting the ratio of the magnitudes of successive *L*-values, the rank of $[L]$, hence of $[A]$, is set to the index of the diagonal entry for which this ratio is a minimum.

The pivoted QLP algorithm performs also better than the pivoted QR decomposition, where the associated *R*-values (diagonal entries of $[R]$) tend to underestimate the large singular values and overestimate the small ones.

9.4.3 The QCoMIF

For each component $\left[\hat{A}_i \right]$ of the CFRF matrix, the diagonal elements of the orthogonal projector onto the null space of $\left[\hat{A}_i \right]^H$ exhibit minima at the natural frequencies.

The *Q*-vector componentwise mode indicator function (QCoMIF) is defined [9.31] by vectors of the form:

$$\left\{ QCoMIF \right\}_i = \mathrm{diag} \left(\left[I_{N_f} \right] - \left[\hat{A}_i \right] \left[\hat{A}_i \right]^+ \right), \qquad (9.70,\, a)$$

$$\left\{ QCoMIF \right\}_i = \mathrm{diag} \left(\left[I_{N_f} \right] - \left\{ q \right\}_i \left\{ q \right\}_i^H \right), \qquad (9.70,\, b)$$

where $^+$ denotes the pseudoinverse and $\left[I_{N_f} \right]$ is the identity matrix of order N_f. It can be computed as the difference between a column vector of ones and the Hadamard product of the *Q*-vectors

$$\left\{ QCoMIF \right\}_i = \left\{ 1 \right\} - \left\{ q \right\}_i \otimes \left\{ q \right\}_i^*. \qquad (9.71)$$

In (9.71) the star superscript denotes the complex conjugate and $\otimes$ denotes element-by-element vector product.
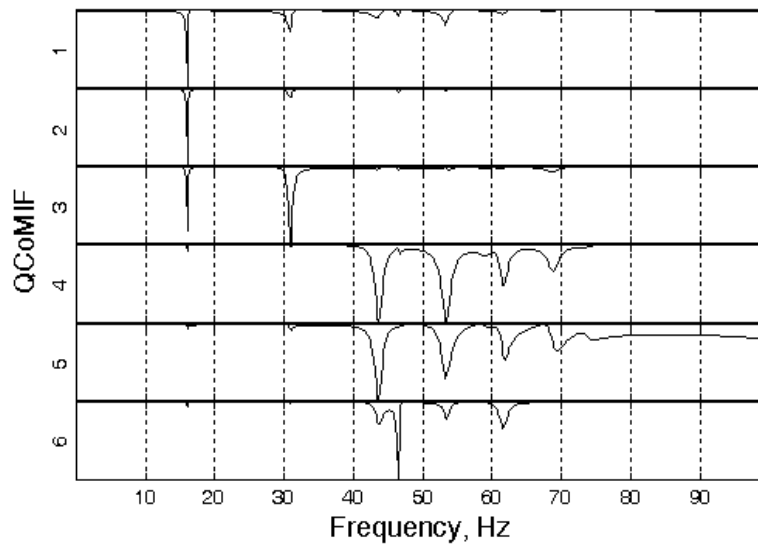
Fig. 9.64

In the QCoMIF plot, the number of curves is equal to the estimated effective rank of the CFRF matrix, i.e. to the truncated number of its rank-one components. Each curve has local minima at the natural frequencies, with the deepest trough at the natural frequency of the corresponding dominant mode.

Visual inspection of QCoMIF curves reveals the number of modes active in a given frequency band and the dominant mode in each QCoMIF curve. The componentwise analysis allows a better understanding of the contribution of each mode to the dynamics of the system.

For noisy data and for structures with high modal density, an overlay of the QCoMIF curves becomes hard to interpret, so that a single-curve mode indicator function has been developed.

The QCoMIF shown in Fig. 9.64 is computed for the 15-DOF system, using noise free FRFs for excitation at points 3 and 15, and response at points 1, 10 and 15. The plot is for frequencies in the range $0 - 100$ Hz. The deepest trough in each subplot locates a damped natural frequency.

9.4.4 The QRMIF

The *QR Mode Indicator Function* (QRMIF) is an aggregate indicator, defined [9.31] as:

$$\text{QRMIF} = \text{diag}\left(\left[\hat{A} \right]\left[\hat{A} \right]^+ \right) \cong \text{diag}\left(\sum_{i=1}^{N_r} \{q\}_i \{q\}_i^H \right), \quad (9.72)$$

where $\{q\}_i \{q\}_i^H$ is the projection matrix onto the direction of $\{q\}_i$ and the sum extends over a number of Q-vectors equal to the estimated rank of $[A]$.

Different QRMIF curves can be plotted for different values of N_r. From equation (9.72) it is seen that the QRMIF is an aggregate of vectors of the form

$$\{QRMIF\}_i = \text{diag}\left(\left[\hat{A}_i \right]\left[\hat{A}_i \right]^+ \right) = \text{diag}\left(\{q\}_i \{q\}_i^H \right) = \{q\}_i \otimes \{q\}_i^*. \quad (9.73)$$

Note that

$$\left\| \left[\hat{A}_i \right]\left[\hat{A}_i \right]^+ \right\|_F = \text{rank}\left(\{q\}_i \{q\}_i^H \right) = \text{trace}\left(\{q\}_i \{q\}_i^H \right) = 1. \quad (9.74)$$

It comes out that the QRMIF is an AMIF calculated using a different set of orthogonal vectors. Similarly, the QCoMIF is a CoMIF based on Q-vectors instead of left singular vectors [9.32].
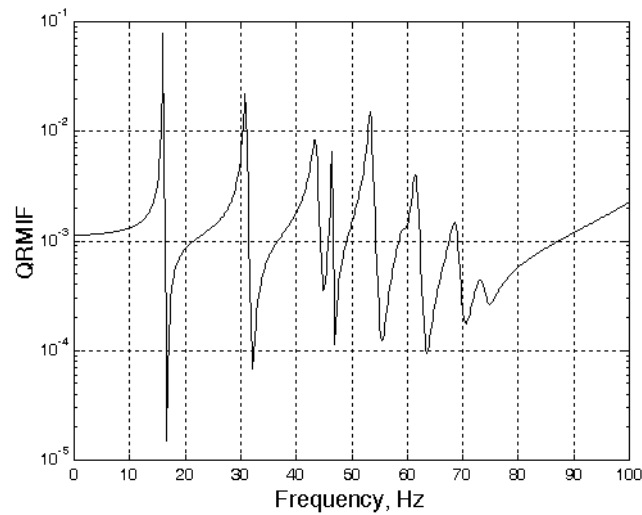
Fig. 9.65

The QRMIF shown in Fig. 9.65 is computed for the 15-DOF system, using noise free FRFs for excitation at points 3 and 15, and response at points 1, 10 and 15. The plot is for frequencies in the range 0 – 100 Hz.

9.4.5 Test data example 2

The experimental data used in this example have been obtained for the GARTEUR SM-AG-19 testbed, designed and manufactured by ONERA, and used as a benchmark by the COST F3 working group on model updating [9.33].
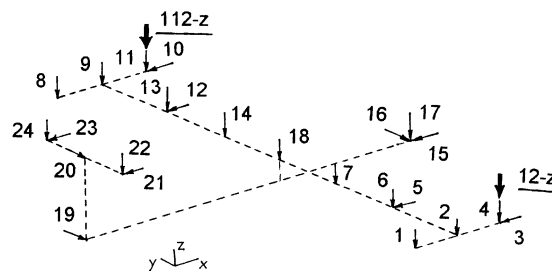
Fig. 9.66

The testbed represents a typical aircraft design with fuselage, wings and tail. Realistic damping levels are achieved by the application of a viscoelastic tape bonded to the upper surface of the wings and covered by a thin aluminium constraining layer. The overall dimensions of the testbed are: 2 m wingspan and

1.5 m fuselage. The locations and directions of the 24 measurement degrees of freedom are shown in Fig. 9.66.

The experimental data-base, measured for the structure modified by a mass added to the tail (referred to as MOD1), using single point hammer excitation at the right wing tip, consists of 24 complex valued inertance FRFs. They span a frequency range from about 0 to 100 Hz, with 0.125 Hz frequency resolution, for which a CFRF matrix of size 801×24 has been constructed.
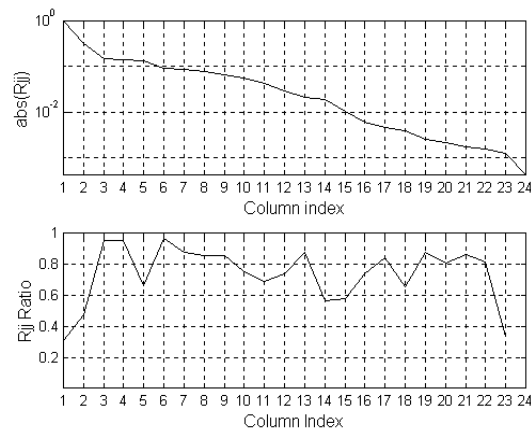
Fig. 9.67
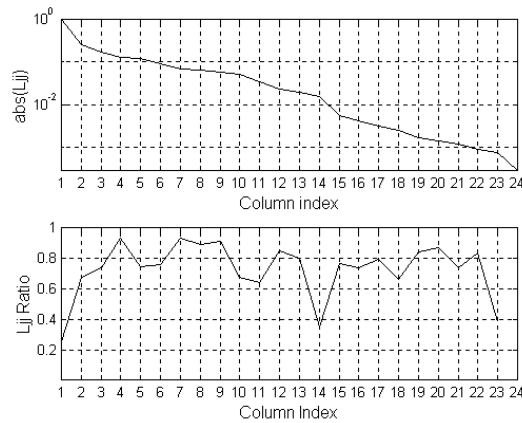
Fig. 9.68

By performing a pivoted QR decomposition of the CFRF matrix, the diagonal values of the $\begin{bmatrix} R \end{bmatrix}$ matrix, referred to as *R*-values, are indexed in descending order. The upper part of Fig. 9.67 is a plot of magnitudes of the *R*-values versus their index, normalized to the first one. There is no sudden drop in

the curve to estimate an effective rank of the CFRF matrix. The lower plot shows the ratio of successive R-values. Again there is no distinct trough.

From the pivoted QLP decomposition of the CFRF matrix, the diagonal entries of the $[L]$ matrix, referred to as *L*-values, are computed and plotted in Fig. 9.68. The distinct minimum in the lower diagram indicates a rank $N_r = 14$.
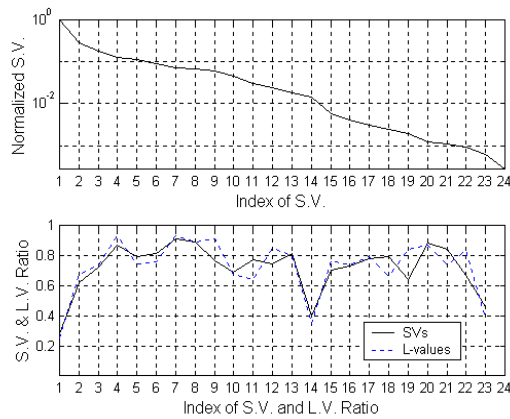
Fig. 9.69

For comparison, the plot of the singular values of the CFRF matrix is presented in Fig. 9.69. The lower plot is an overlaid of the curves giving the singular value ratio (solid line) and *L*-value ratio (broken line). The *L*-values track the singular values remarkably well.
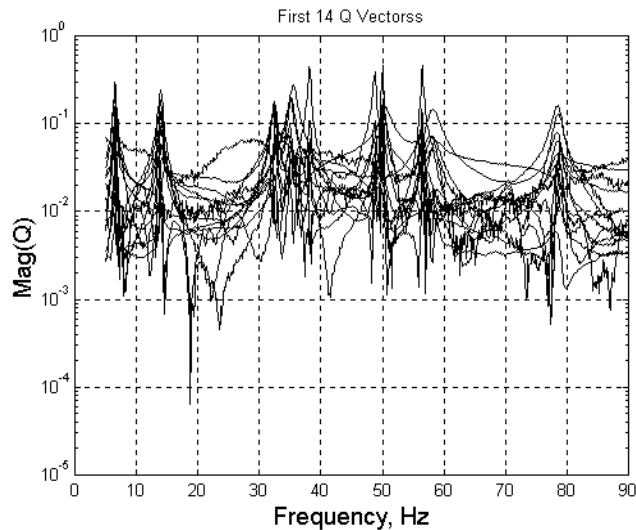
Fig. 9.70

The first 14 *Q*-vectors are shown in Fig. 9.70 and the overlaid QCoMIF curves are presented in Fig. 9.71.
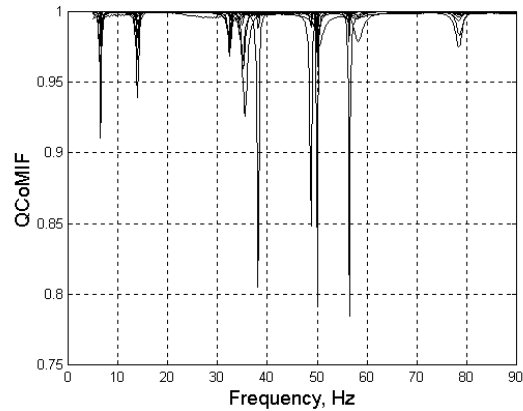
Fig. 9.71

The individual QCoMIF curves are displayed in Fig. 9.72, revealing at least eleven modes between 5 and 80 Hz. Subplots correspond to separate QCoMIFs with the index shown on the left. Each detected mode is marked by a local minimum at the associated frequency. The deepest minimum indicates the dominant mode.
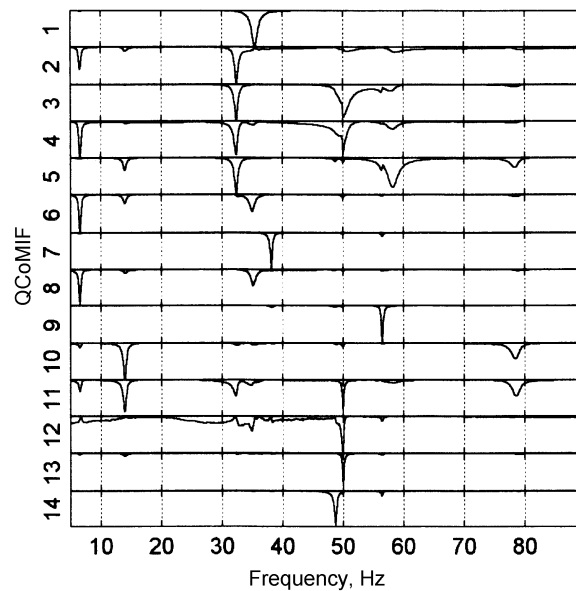
Fig. 9.72

The aggregate QRMIF and its complement 1-QRMIF are shown in Fig. 9.73, computed for $N_r = 14$. For comparison, the MIF1 and MIF2 plots are presented in Fig. 9.74. Both fail locating mode 7 at about 49 Hz and mode 4 at 35 Hz. On the contrary, mode 7 is clearly indicated in the QCoMIF overlay in Fig. 9.71 and in both QRMIF and 1-QRMIF plots from Fig. 9.73. Mode 4 at 35 Hz can also be located in Fig. 9.71 by a small trough overlaid on the deeper next mode trough at 35.5 Hz.
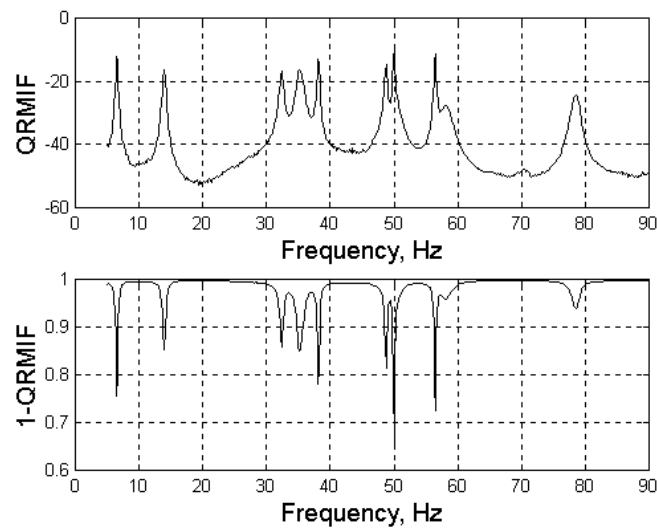
Fig. 9.73
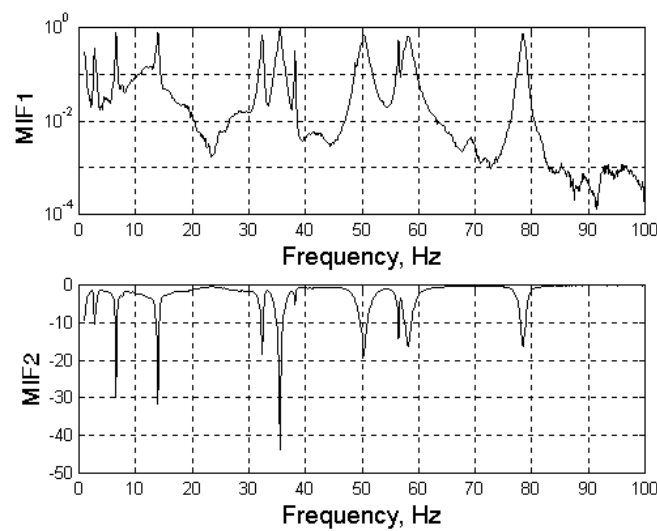
Fig. 9.74

Figure 9.75 shows the overlaid CoMIF curves. The plot resembles the QCoMIF presented in Fig. 9.71.
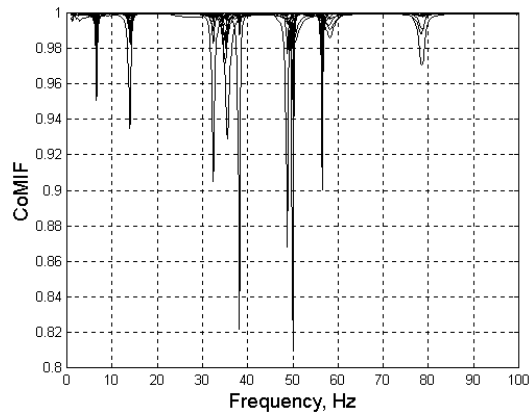
Fig. 9.75

The individual CoMIF curves are displayed in Fig. 9.76.
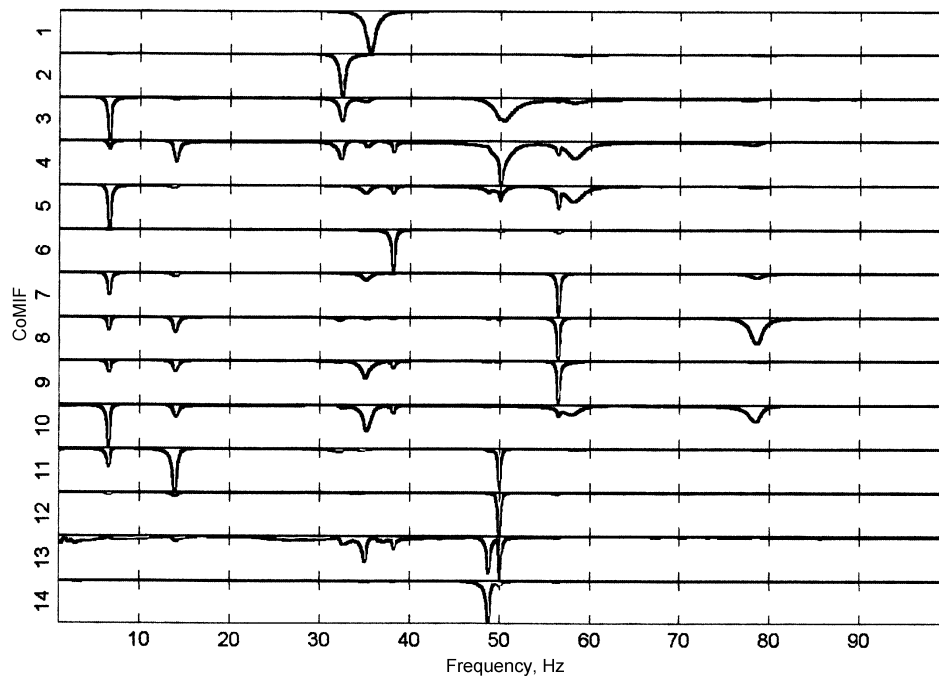
Fig. 9.76

Table 9.3 lists the description of the modes, their natural frequencies and damping ratios determined by SDOF circle-fit analysis of the QRF diagrams around the dominant resonance.

Table 9.3. Eigenfrequencies and damping ratios for MOD1

Mode	Natural frequency, Hz	Damping ratio, %	Description
1	6.55	2.52	2N wing bending
2	13.95	1.85	Fuselage rotation
3	32.40	0.97	3N wing bending
4	35.17	0.80	Symmetric wing torsion
5	35.54	1.58	Skewsymmetric wing torsion
6	38.17	0.49	Tail torsion
7	48.78	0.44	In-plane wing vs. fuselage
8	49.92	1.97	4N wing bending
9	56.46	0.25	Symmetric in-plane bending
10	58.25	1.73	Fuselage bending
11	78.59	0.97	5N wing bending

An example of circle fit modal analysis is illustrated in Fig. 9.77, *a*, using the Nyquist plot of the highest peak from Fig. 9.77, *b*, which is a diagram of the first *Q*-vector versus frequency. The almost circular shape of the plot in the neighborhood of resonance indicates good mode isolation for single degree of freedom analysis.

a   *b*
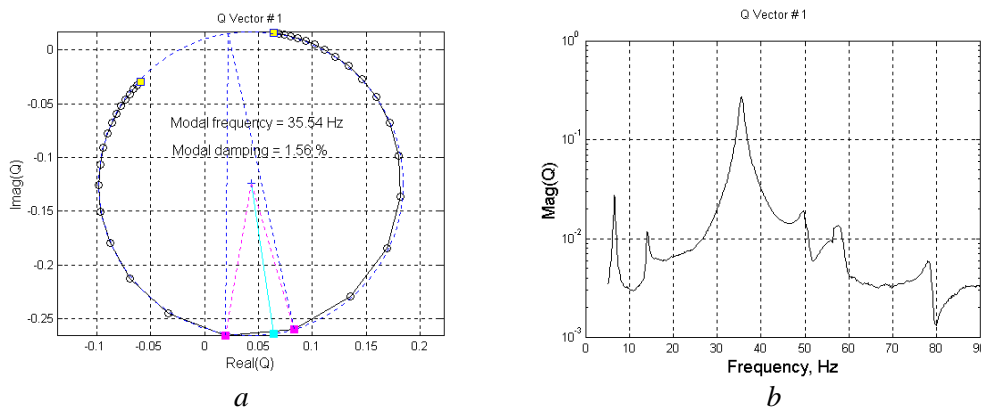
Fig. 9.77

9.4.6 Concluding remarks

Mode indicator functions locate the observable modes in the test data and their natural frequencies, sometimes used together with interference diagrams and singular value ratio plots. Their performance is determined by the selection of input and output locations for the adequate definition of all modes of interest.

Eigenvalue based MIFs and the CMIF use rectangular FRF matrices calculated in turn at each excitation frequency. Their plots have as many curves as the number of references. The number of input points should be equal to the multiplicity of modal frequencies.

Other MIFs do the simultaneous analysis of all FRF information organized in a compound FRF matrix. They have a different physical basis and outperform the eigenvalue based MIFs developed to locate frequencies where the response is closest to the monophase condition.

The left singular vectors (*U*-vectors) or the *Q*-vectors obtained from the pivoted QLP decomposition of the CFRF matrix contain the frequency information and are used to construct MIFs. They are based on projections onto an orthogonal base of the subspace of measured FRFs. These orthogonal response functions are calculated as linear combinations of the measured FRFs and represent a response dominated by a single mode with a major contribution to the dynamics of the test structure in the given frequency band.

The number of curves in a CoMIF or QCoMIF plot is equal to the effective rank of the CFRF matrix. If this is lower than the number of response coordinates, a single point excitation can locate even double modes. The condition to use as many input points as the multiplicity of modal frequencies is no more imposed. They have been used with good results for complex structures with high modal density.

References

9.1 Radeş, M. and Ewins, D.J., *The aggregate mode indicator function*, Proceedings of 18th International Modal Analysis Conference, San Antonio, Texas, pp 201-207, 2000.

9.2 Stewart, G.W., *On the early history of the singular value decomposition*, SIAM Review, vol.35, no.4, pp 551-566, 1993.

9.3 Jolliffe, I.T., *Principal Component Analysis*, Springer, Berlin, 1986.

9.4 Moore B.C., *Principal component analysis in linear systems, controllability, observability and model reduction*, IEEE Transactions on Automatic Control, vol. AC-26, no.1, pp 17-32, 1981.

9.5 Pickrel, C.R., *Estimating the rank of measured response data using SVD and principal response functions*, Second International Conference on Structural Dynamics Modelling, Test Analysis and Correlation, Cumbria, UK, pp 89-99, 1996.

9.6 Radeş, M. and Ewins, D.J., *Principal response analysis in structural dynamics*, ICATS Imperial College Consultants, London, UK, www.icats.co.uk/pubs/principal.pdf.

9.7 Radeş, M. and Ewins, D. J., *Principal component analysis of the GARTEUR SM-AG-19 Testbed data,* Proceedings of the European COST-3 Conference on Structural System Identification, University of Kassel, Germany, pp 127-134, 2001.

9.8 Radeş, M., *Metode dinamice pentru identificarea sistemelor mecanice*, Editura Academiei, Bucureşti, 1979.

9.9 Yang, M., and Brown, D., *An Improved Procedure for Handling Damping During Finite Element Model Updating*, Proceedings of 14th International Modal Analysis Conference, Dearborn, Michigan, pp 576-584, 1996.

9.10 Radeş, M., *Displays of vibration properties*, in Encyclopedia of Vibration (S. Braun, D. Ewins and S.S. Rao, eds.), vol. 1, pp 413-431, 2001.

9.11 Radeş, M. and Ewins, D.J., *The componentwise mode indicator function*, Proceedings of IMAC-19 Conference on Structural Dynamics, Kissimmee, Florida, pp 903-908, 2001.

9.12 Breitbach, E.J., *Recent developments in multiple input modal analysis*, ASME Journal of Vibration, Acoustics, Stress and Reliability in Design, vol.110, pp 478-484, 1988.

9.13 Lembregts, F., *Frequency Domain Identification Techniques for Experimental Multiple Input Modal Analysis*, Ph.D. Thesis, Katholieke Universiteit Leuven, Belgium, 1988.

9.14 Shih, C.Y., Tsuei, Y.G., Allemang, R.J. and Brown, D.L., *Complex Mode Indication Function and Its Applications to Spatial Domain Parameter Estimation*, Proceedings of 7th International Modal Analysis Conference, pp 533-540, 1989; and Journal of Mechanical Systems and Signal Processing, vol.2, no.4, 1988.

9.15 Hunt, D.L., Vold, H., Peterson, E.L. and Williams, R., *Optimal selection of excitation methods for enhanced modal testing*, AIAA Paper no.84-1068, 1984.

9.16 Radeş, M., *A Comparison of Some Mode Indicator Functions,* Mechanical Systems and Signal Processing, vol.8, no.4, pp 459-474, 1994.

9.17 Allemang, R.J. and Brown, D.L., *A complete review of the complex mode indicator function (CMIF) with applications*, Proceedings of ISMA-2006 International Conference on Noise and Vibration Engineering, K. U. Leuven, Belgium, pp. 3209-3246, Sept 2006.

9.18 Nash, M., *Use of the multivariate mode indicator function for normal mode determination*, Proceedings of 6th International Modal Analysis Conference, Kissimmee, Florida, pp 740-744, 1988.

9.19 Clerc, D., *Méthode de recherche des modes propres par calcul de l'excitation harmonique optimum d'apres les resultats bruts d'essais de vibrations*, Note Technique ONERA No.119, 1976.

9.20 De Moor, B., Swevers, J. and Van Brussel, H., *Stepped sine system identification, errors in variables and the quotient singular value decomposition,* Proceedings of 15th International Seminar on Modal Analysis, K. U. Leuven, Belgium, pp 59-76, 1990.

9.21 Rost, R.W., *Investigation of Multiple Input Frequency Response Function Estimation Techniques for Experimental Modal Analysis*, Ph.D. Thesis, University of Cincinnati, 1985.

9.22 Radeş, M., *Use of monophase forced modes of vibration in experimental modal analysis*, Proceedings of the Florence Modal Analysis Conference, Italy, pp 347-352, 1991.

9.23 Radeş, M., *Determination of undamped normal modes from measured real forced modes using frequency response data*, Proceedings of 9th International Modal Analysis Conference, Florence, Italy, pp 596-602, 1991.

9.24 Fillod, R. and Piranda, J., *Etude d'une méthode d'appropriation des systèmes lineaires*, Proceedings of 8th Conference on Dynamics of Machines, Prague, pp 129-138, 1973.

9.25 Breitbach, E.J., *A semi-automatic modal survey test technique for complex aircraft and spacecraft structures*, Proceedings of 3rd ESA Testing Symposium, pp. 519-528, 1973.

9.26 Crowley, J.R., Rocklin, G.T., Hunt, D.L. and Vold, H., *The practical use of the polyreference modal parameter estimation method,* Proceedings of 2nd International Modal Analysis Conference, Orlando, Florida, pp 126-133, 1984.

9.27 Balmes, E., Chapelier, C., Lubrina, P. and Fargette, P., *An evaluation of modal testing results based on the force appropriation method*, Proceedings of 13th International Modal Analysis Conference, Nashville, Tennessee, pp 47-53, 1995.

9.28 Radeş, M., *Performance of various mode indicator functions*, Proceedings of the ICEDyn2009 Conference, Ericeira, Portugal, 2009.

9.29 Stewart, G.W., *Matrix Algorithms*, vol.1: *Basic Decompositions*, SIAM, Philadelphia, 1998.

9.30 Golub, G.H. and Van Loan, Ch.F., *Matrix Computations*, 3rd ed, The Johns Hopkins University Press, Baltimore, 1996.

9.31 Radeş, M. and Ewins, D.J., *MIFs and MACs in modal testing*, Proceedings of the IMAC-20 Conference on Structural Dynamics, Los Angeles, Ca., pp 771-778, 2002.

9.32 Radeş, M. and Ewins, D.J., *Analysis of FRF test data using the pivoted QLP decomposition*, International Conference on Structural Dynamics Modelling, Funchal, Madeira, Portugal, pp 509-516, 2002.

9.33 Degener, M. and Hermes, M., *Ground Vibration Test and Finite Element Analysis of the GARTEUR SM-AG19 Testbed*, D.F.L.R. e. V. Institut für Aeroelastik-23200, 1996.

10.

STRUCTURAL PARAMETER
IDENTIFICATION

In this chapter a brief description is presented of approaches to build mathematical models using test data, to assist in the analysis of structures and to help in determining responses to loads and the effects of modifications.

The *experimental modal analysis,* also called *modal testing,* is such a procedure. Its aim is the determination of a structure's vibration properties, described in terms of its modes of vibration, from test data. The following presentation is limited to the extraction of system model's modal parameters from measured frequency response data under controled excitation, which is applied in most practical cases.

10.1 Models of a vibrating structure

Some of the major reasons for structural dynamic testing are [10.1]:

– to obtain a description of a structure's properties for comparison with values predicted by a theoretical model, perhaps in order to refine that model;

– to obtain a mathematical description of one particular component which forms part of a complete assembled structure and which may not be amenable to theoretical analysis, in order that its contribution to the vibration of the assembly may be fully accounted for in an analysis of the complete structure;

– to develop a mathematical model of a test structure or system which can then be used to predict, for example, a) the effects of modifications to the structure; b) the response of the structure to various excitation conditions, and c) the forces which are causing a machine or system to vibrate with an observed response.

In all cases, the aim is to construct a mathematical model from test data, which is capable of describing the observed behavior of the test structure.

Conventionally, there are three types of mathematical models: a) spatial (physical) models; b) modal models, and c) response models (Fig.10.1). Each of these is capable of describing the required structural dynamic behavior, but each formulating the model in a different way, based on different fundamental features [10.1].
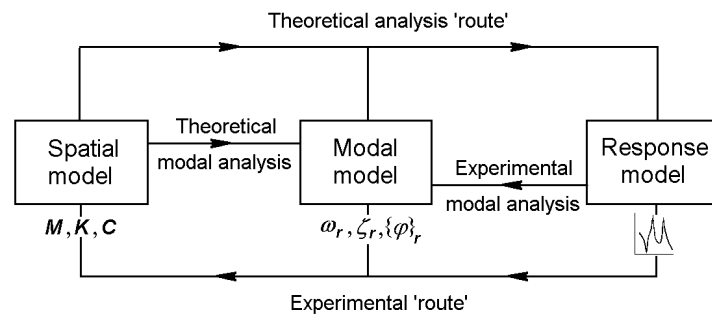
Fig. 10.1

The *spatial model* describes the distribution in space of the essential physical features of the structure – its mass or inertia, its stiffness and its damping properties. It is defined by the mass, stiffness and damping elements or matrices which are used in describing equations of motion for the system.

In a finite element or lumped parameter representation of a structure, the quantities which are obtained directly from the structure geometry and material properties are 'intuitive'. The values of mass, stiffness and damping elements depend on the specific formulation of the analytical model and cannot be measured. For instance, the element k_{ij} of the stiffness matrix, defined as the internal force at coordinate i due to a unit displacement at coordinate j when all coordinates except j are constrained from motion, is not directly measurable.

The *modal model* comprises the natural frequencies, modal damping ratios and the mode shapes.

The *response model* consists of response functions (usually, but not exclusively FRFs) that relate the input/output relationships for all the degrees of freedom of the structure. The typical individual FRF from which this model is built is $H_{jk}(\omega)$ and is defined as the harmonic response in DOF j due to a unit harmonic excitation applied in DOF k at frequency ω. The response functions are non-parametric descriptors of the structural dynamic response, defined by dynamic influence coefficients (flexibilities) which are observable or measurable parameters. Their values are independent of the formulation of the analytical model.

Because modal parameters conform to the response characteristics, they could also be considered as measurable. Thus, one cannot measure the parameters that can be modeled and one cannot directly model what can be measured [10.2].

In Fig. 10.1, the *theoretical analysis 'route'* to vibration analysis is from the left to the right. Starting from the system's equations of motion written in terms of the mass, stiffness and damping matrices, the scope of the *theoretical modal analysis* is the prediction of the structure's modes of vibration. Prediction of response characteristics is usually made using the modal properties already obtained, as shown in Chapter 7.

The experimental analysis 'route' is from the right to the left. Given the actual structure, what can be measured directly is its response to a particular excitation – equivalent to the last part of the theoretical analysis procedure. The modal properties have to be extracted from the response characteristics which are measurable quantities, and this process is defined as *modal testing* or *experimental modal analysis*. Spatial properties can be further obtained either directly from response functions or from knowledge of all the modal properties. But this process encounters several difficulties due to frequency and spatial truncations.

Thus the experimental 'route' appears as the reverse of the theoretical one.

Though comparisons between experiment and theory could be made using any of the three kinds of models, they are usually made using the modal properties. This chapter is devoted to the extraction of modal parameters from FRF measurement data.

10.2 Single-mode parameter extraction methods

There exist a number of parameter identification methods based on the assumption that in the vicinity of a resonance the total response is dominated by the contribution of the mode whose natural frequency is closest. A detailed presentation is given in [10.3]. In the following, some of the most frequently used methods are presented, based on measured FRFs. SDOF techniques perform an independent fit of each resonance peak (or loop), one mode at a time. They are utilized for systems with low modal density and light damping, in troubleshooting applications or in the second stage of MDOF fitting processes for determining mode shape coefficients.

10.2.1 Analysis of receptance data

FRF receptance data are conveniently analyzed using a hysteretic damping model which yields circular Nyquist plots for SDOF systems.

10.2.1.1 Peak-amplitude method

The 'peak-amplitude' or 'peak-picking' method requires the measurement of only the response amplitude (not also the phase) as a function of

frequency. It works adequately for structures whose FRFs exhibit well-separated modes. These should be neither so lightly damped that accurate measurements at resonance are difficult to be obtained, nor so heavily damped that the response at a resonance is strongly influenced by more than one mode.

The steps in this simple, single mode approach, based on the analysis of a basic single-degree-of-freedom system, as described in Sections 2.4.4 and 2.4.7, are the following:

1 – individual resonance peaks are detected on the FRF plot of magnitude versus frequency (Fig. 10.2, *a*) and the frequency of the maximum response is taken as the natural frequency of that mode, ω_r ;

2 – the maximum value of the FRF is noted, α_{res} , and the frequencies for a response level of $(1/R)\alpha_{res}$ are determined, if possible for several values of R. The two points thus identified, B_R and C_R , have frequencies ω_{1R} and ω_{2R} , respectively (Fig. 10.2, *b*);
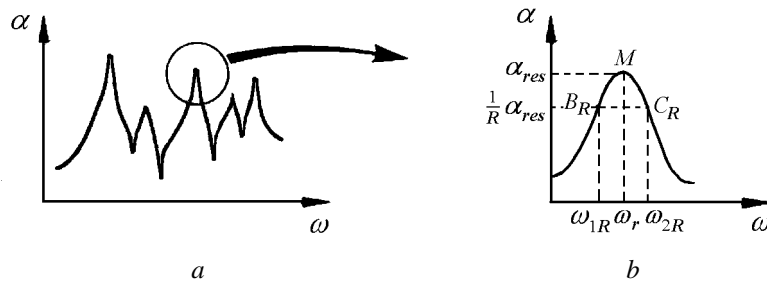
Fig. 10.2

3 – assuming hysteretic damping, the loss factor of the mode in question is given by [10.4]

$$g_r = \frac{1}{\sqrt{R^2-1}} \frac{\omega_{2R}^2 - \omega_{1R}^2}{2\omega_r^2} , \qquad (10.1)$$

which, for lightly-damped systems, becomes [10.5]

$$g_r = \frac{1}{\sqrt{R^2-1}} \frac{\omega_{2R} - \omega_{1R}}{\omega_r} . \qquad (10.2)$$

For $R = \sqrt{2}$, B_R and C_R are the 'half-power points' B and C , of frequencies (see Section 2.4.4)

$$\omega_{1,2} = \omega_r \sqrt{1 \mp g_r} \qquad (10.3)$$

and the hysteretic damping factor is [10.6]

$$g_r = \frac{\omega_2^2 - \omega_1^2}{\omega_2^2 + \omega_1^2} = \frac{\omega_2^2 - \omega_1^2}{2\omega_r^2} \ . \tag{10.4}$$

For light damping equation (10.4) becomes

$$g_r \cong \frac{\omega_2 - \omega_1}{\omega_r} \ . \tag{10.5}$$

4 – the modal constant of the mode being analyzed can be obtained assuming that the total response in this resonant region is attributed to a single term in the general FRF series (equation (7.129))

$$\alpha_{res} \cong \frac{A_r}{g_r \omega_r^2} \ ,$$

or

$$A_r \cong \alpha_{res} \, g_r \, \omega_r^2 \tag{10.6}$$

which is proportional to the inverse of the modal mass M_r.

It is obvious that only real modal constants – and that means real modes, or proportionally damped structures – can be deduced by this method.

Also, it is clear that the estimates of both damping and modal constant depend heavily on the accuracy of the maximum FRF value, α_{res}. This quantity cannot be measured with great accuracy due to the contribution of the neighboring modes to the total response at the resonance of the mode being analyzed.

10.2.1.2 Circle-fit method

The 'circle-fit' method requires the measurement of both the response amplitude and phase as a function of frequency, or equivalently of the real (in-phase, coincident) and imaginary (in-quadrature) components. It works adequately for structures whose FRFs exhibit well separated modes, to render the assumptions of the SDOF approach to be applicable, and for proportional damping, i.e. no damping coupling between the normal modes.

As mentioned, a basic assumption is that in the neighborhood of a resonance the response of a MDOF system is dominated by a single mode. Algebraically, this means that the magnitude of the FRF is effectively controlled by one of the terms in the series (7.129), namely the one relating to the mode whose resonance is being observed.

Equation (7.129) can be rewritten as

$$\alpha\left(\omega\right) = \frac{A_r}{\omega_r^2 - \omega^2 + \mathrm{i}\, g_r \omega_r^2} + \sum_{\substack{s=1 \\ s \neq r}}^{N} \frac{A_s}{\omega_s^2 - \omega^2 + \mathrm{i}\, g_s \omega_s^2} \,. \tag{10.7}$$

The circle-fit procedure is based on the assumption that at frequencies very close to ω_r, the second term in (10.7) is approximately independent of frequency and the expression for the receptance can be written as

$$\alpha\left(\omega\right) \cong C_r\, e^{\,\mathrm{i}\beta_r}\, \frac{1}{\omega_r^2 - \omega^2 + \mathrm{i}\, g_r \omega_r^2} + B_r \,, \tag{10.8}$$

where $B_r = const.$ and the complex quantity $C_r\, e^{\,\mathrm{i}\beta_r}$ represents an effective modal flexibility.

Now, consider the Nyquist plot of this receptance FRF, building up the total plot by considering one element of the expression (10.8) at a time.

First, consider just the frequency-dependent term which results in a simple upright circle of diameter $1\big/ g_r \omega_r^2$ (Fig. 10.3, *a*), as shown in Section 2.4.7.
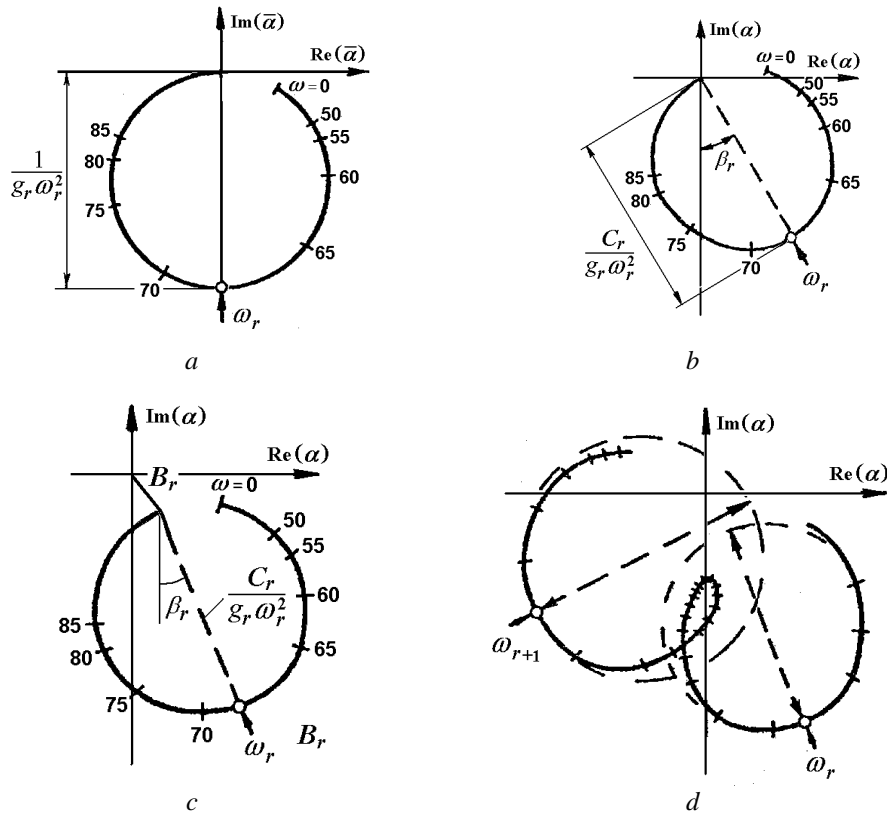
Fig. 10.3

Next, the effect of multiplying this term by the complex constant $C_r\, e^{\,i\beta_r}$ is to rotate the circle through β_r, and to scale its diameter by C_r (Fig. 10.3, *b*) [10.7]. Then, by adding the complex constant B_r, the circle is displaced bodily by an amount B_r (Fig. 10.3, *c*).

Finally, we can deduce the general case, as shown in Fig. 10.3, *d*. The Nyquist plot of the complete FRF consists of loops. In the vicinity of a resonance, each loop can be approximated by a modal circle. Each modal circle is the scaled, rotated and displaced version of the essential circle defining the response of a SDOF system.

Circle fit

The circle fit can be most accurately obtained using a least squares circular curve fitting technique as follows. The general equation of a circle is

$$x^2 + y^2 + ax + by + c = 0 \,.$$

Let the above equation be equal to an error function, ε, then square the error and sum it over the N_f excitation frequencies

$$\sum_{f=1}^{N_f} \varepsilon^2 = \sum_{f=1}^{N_f} \left(x_f^2 + y_f^2 + ax_f + by_f + c \right)^2 \,.$$

Now differentiate with respect to *a*, *b*, and *c*, and set the result to zero. Dropping the index *f*

$$\frac{\partial \sum \varepsilon^2}{\partial a} = 2\sum \left(x^2 + y^2 + ax + by + c \right) x = 0 \,,$$

$$\frac{\partial \sum \varepsilon^2}{\partial b} = 2\sum \left(x^2 + y^2 + ax + by + c \right) y = 0 \,,$$

$$\frac{\partial \sum \varepsilon^2}{\partial c} = 2\sum \left(x^2 + y^2 + ax + by + c \right) = 0 \,.$$

In matrix form, the above equations become

$$\begin{bmatrix} \sum x & \sum y & N_f \\ \sum xy & \sum y^2 & \sum y \\ \sum x^2 & \sum xy & \sum x \end{bmatrix} \begin{Bmatrix} a \\ b \\ c \end{Bmatrix} = \begin{Bmatrix} -\sum (x^2 + y^2) \\ -\sum (x^2 y + y^3) \\ -\sum (x^3 + x y^2) \end{Bmatrix} \,.$$

Therefore, the parameters a, b, and c can be determined from the above set of equations. The radius and center of the modal circle are easily determined from a, b, and c as follows:

$$x_{center} = -\frac{1}{2}a, \qquad y_{center} = -\frac{1}{2}b,$$

$$radius = \sqrt{\frac{a^2}{4} + \frac{b^2}{4} - c}.$$

It is useful to present the properties of the modal circle used in the extraction of modal parameters. The basic function with which we are dealing is

$$\overline{\alpha} = \frac{1}{\omega_r^2 - \omega^2 + i\, g_r \omega_r^2}. \tag{10.9}$$

Location of resonance frequency

A plot of the quantity $\overline{\alpha}$ in the Argand plane is given in Fig. 10.4, *a*. The length of the arc on the curve is the radius times the angle subtended

$$ds = \frac{1}{g_r \omega_r^2}\, d\theta. \tag{10.10}$$
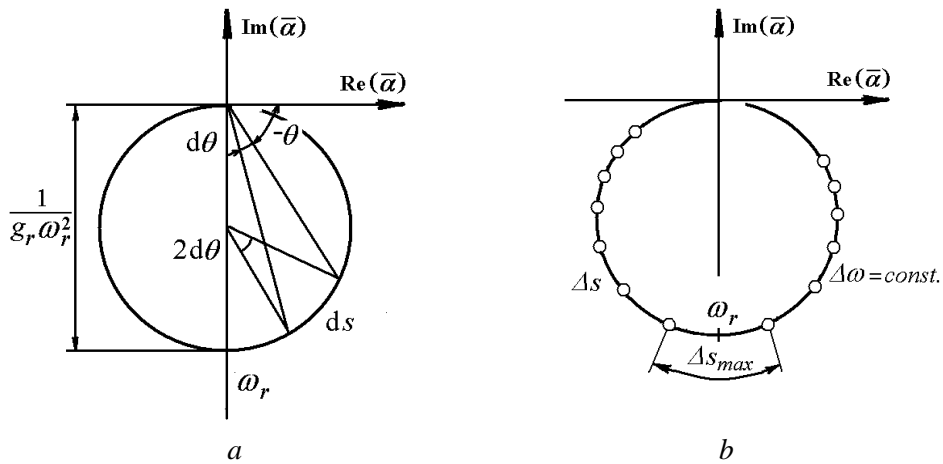
Fig. 10.4

The derivative with respect to ω^2/ω_r^2 is

$$\frac{\mathrm{d}s}{\mathrm{d}\left(\dfrac{\omega^2}{\omega_r^2}\right)} = -\frac{1}{g_r\omega_r^2}\frac{\mathrm{d}\theta}{\mathrm{d}\left(\dfrac{\omega^2}{\omega_r^2}\right)} = -\frac{1}{g_r\omega_r^2}\frac{\mathrm{d}}{\mathrm{d}\left(\dfrac{\omega^2}{\omega_r^2}\right)}\left[\tan^{-1}\left(\frac{-g_r}{1-\dfrac{\omega^2}{\omega_r^2}}\right)\right] = \omega_r^2\alpha^2 . \quad (10.11)$$

The rate of change of the arc length with respect to frequency (squared) attains a maximum value at resonance, where $\overline{\alpha}$ is maximum. This property is the basis of a method for locating natural frequencies developed by Kennedy and Pancu in 1947 [10.8].

If the system is excited by a harmonic force and $\overline{\alpha}$ is plotted point by point in the Argand plane, at equal frequency increments $\varDelta\omega$, then the arc length $\varDelta s$ between two successive points is a maximum at resonance (Fig. 10.4, *b*).

Estimation of the damping factor

For determining the hysteretic damping factor, g_r, we can use just three points on the circle: the resonant point *M*, one below it and one above it, as shown in Fig. 10.5.
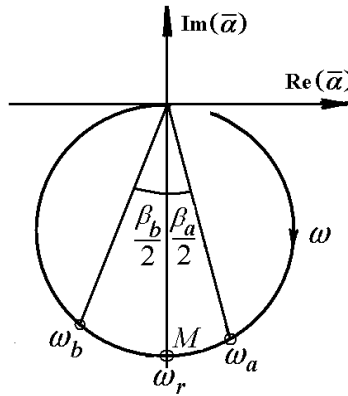
Fig. 10.5

Based on the circle geometry

$$\tan\frac{1}{2}\beta_a = \frac{1}{g_r}\left(1-\frac{\omega_a^2}{\omega_r^2}\right), \qquad \tan\frac{1}{2}\beta_b = \frac{1}{g_r}\left(\frac{\omega_b^2}{\omega_r^2}-1\right),$$

from which we have [10.9]

$$g_r = \left(\frac{\omega_b^2 - \omega_a^2}{\omega_r^2} \right) \left(\frac{1}{\tan \frac{1}{2} \beta_a + \tan \frac{1}{2} \beta_b} \right), \qquad (10.12)$$

or, if g_r is small,

$$g_r \cong \left(\frac{\omega_b - \omega_a}{\omega_r} \right) \left(\frac{2}{\tan \frac{1}{2} \beta_a + \tan \frac{1}{2} \beta_b} \right). \qquad (10.13)$$

This is seen to reduce to the half power points formula (10.5) when $\beta_a = \beta_b = 90^0$, but usually these have to be located by interpolation between the points actually measured, which is a source of error.

The formula (10.12) permits multiple estimates of the damping factor to be made, since there will generally be several points which could be used for ω_a, and several others which can be used for ω_b, the net effect being that a whole set of damping estimates are obtained, all of which should be identical.

If the level of damping is low and the natural frequencies are well spaced, each loop will be nearly circular in the immediate vicinity of a resonance, where the curve is swept out most rapidly with respect to the variation in ω, though none of the loops will be a full circle.

Steps of SDOF circle-fit parameter identification

A single mode analysis can be carried out for each loop, with the following steps [10.1]:

a) identify those FRF points which lie close to a resonance (generally, those surrounding a local maximum in the modulus plot) and plot them in the Argand plane;

b) fit a circle through the selected points (Fig. 10.6, *a*);

c) by examination of the spacing of the points around the circle, plotted at equal frequency increments, $\Delta\omega$, locate the natural frequency within the small range covered, at the point where the circle radius is sweeping most rapidly with frequency (Fig. 10.6, *b*).

This is achieved using Stirling's interpolation formula [10.10]. Four successive points are selected, the pair most widely spaced (maximum chord length) and other two points, one at either side. If the chord length $z = \sqrt{(\Delta x)^2 + (\Delta y)^2}$ (instead of the arc length) is plotted as a function of the mean

frequency, ω, of each interval (which is not at the middle of the interval), then a quadratic which passes through the three ordinates (Fig. 10.6, *c*) is described by the equation

$$z = z_i + u\,\frac{z_{i+1} - z_{i-1}}{2} + \frac{u^2}{2}\left(z_{i+1} - 2z_i + z_{i-1}\right),$$

where

$$u = \frac{\omega - \omega_i}{\Delta\omega}, \qquad \Delta\omega = \omega_{i+1} - \omega_i = \omega_i - \omega_{i-1}.$$

The first derivative

$$\frac{\mathrm{d}z}{\mathrm{d}u} = \frac{z_{i+1} - z_{i-1}}{2} + u\left(z_{i+1} - 2z_i + z_{i-1}\right)$$

cancels for

$$u_{max} = -\frac{z_{i+1} - z_{i-1}}{2\left(z_{i+1} - 2z_i + z_{i-1}\right)}$$

so that the natural frequency is approximately

$$\omega_r = \omega_i + u_{max}\,\Delta\omega.$$

d) determine the damping factor from a measurement of the sweep rate of the radial vector (above) or from application of formula (10.13) (Fig. 10.6, *d*);
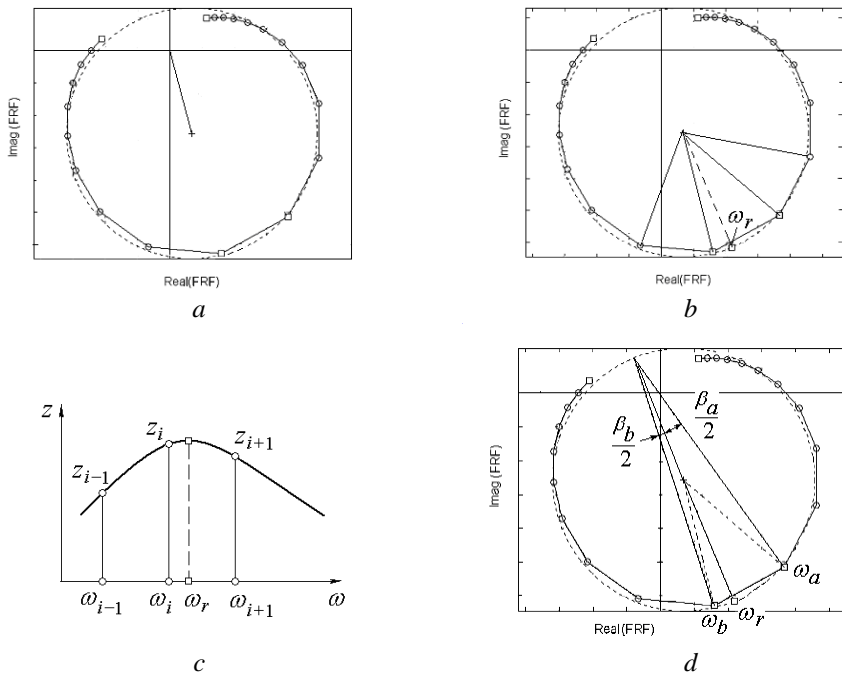

Fig. 10.6

e) determine the modal constant from the property that the diameter of the modal circle gives its modulus (multiplied by $g_r \omega_r^2$) and the angular rotation of the circle from the vertical gives its argument.

In the case of proportional damping, the modal constant is real, hence the circle is not rotated from the vertical and the diameter at resonance is parallel with the imaginary axis. The extent to which the modal circle is displaced from the origin (i.e. that the top of the diameter at resonance is away from the origin) is a measure of the sum contribution of all other modes of vibration.

Note that if viscous damping is assumed, then the modal damping ratio, ζ_r, would be equal to $g_r/2$. The exact formulas are given in reference [10.3]. In fact, where $g_r < 0.1$, which covers virtually all practical cases, the response of a viscously damped system in the vicinity of resonance is virtually identical with that of an equivalent hysteretically damped system.

The approach described here for hysteretic damping can equally be applied to viscous damping, simply by using mobility data instead of receptances. In this case, the Nyquist diagrams are rotated by 90^0 counterclockwise, but are otherwise very similar in appearance.

Example 10.1

Consider the 11-DOF system with hysteretic damping of Fig. 9.19. Its physical parameters as well as the damped natural frequencies and hysteretic damping factors are given in Table 9.2. FRFs obtained from randomly 'polluted' mass, stiffness and damping data have been used in the numerical simulation study.

a   *b*
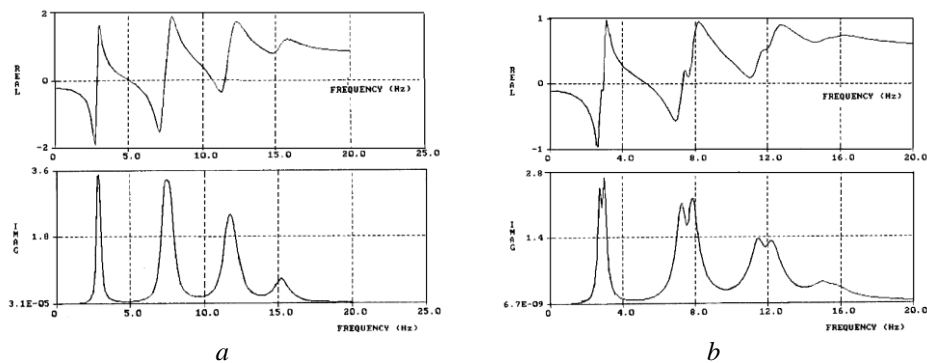
Fig. 10.7

Driving point inertance curves are shown in Fig. 10.7, *a* for mass m_1 and in Fig. 10.7, *b* for mass m_{11}. Despite the symmetric location of these two masses, owing to the lower damping values in the left-hand side of the system, the FRF

curves from Fig. 10.7, *a* do not exhibit pairs of closely spaced peaks as expected. FRF curves determined for mass points located in the right-hand side of the system give more information.

a   b
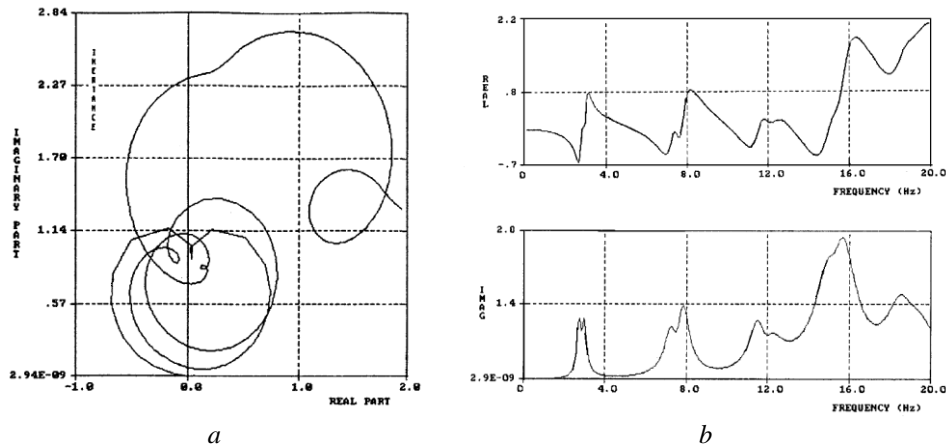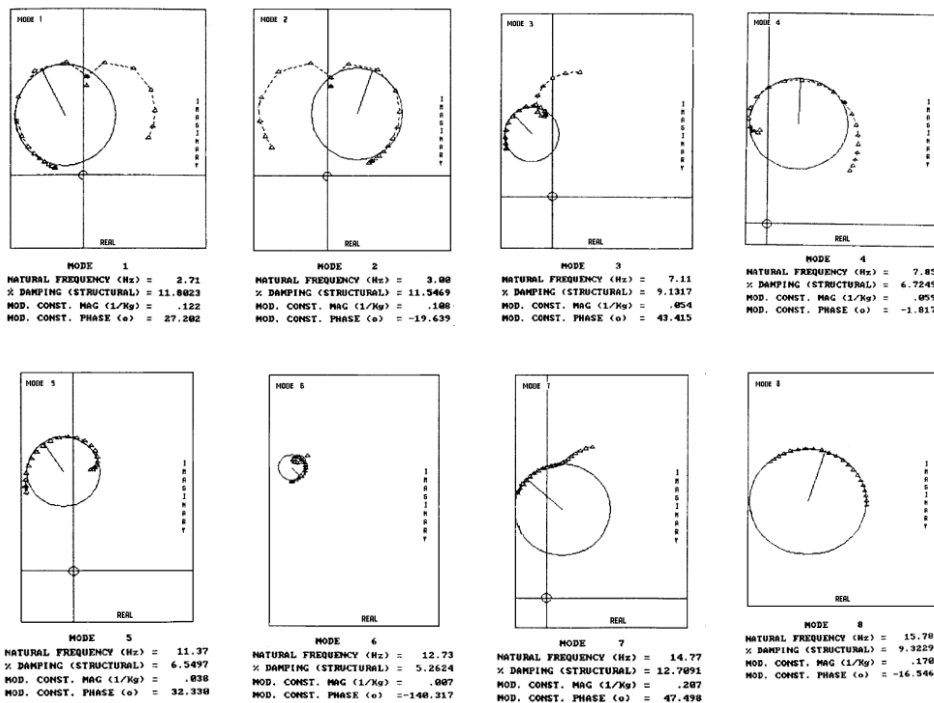
Fig. 10.8

Fig. 10.9

Figure 10.8, *a* shows the Nyquist plot of the drive-point inertance for mass m_9. The diagrams of the real and imaginary components are given in Fig. 10.8, *b*. At least 9 peaks can be seen on the plot of the imaginary component.

The circle-fit method is used to illustrate a single FRF based SDOF modal analysis procedure carried out using the program MODENT [10.11]. For each loop of the Nyquist plot of Fig. 10.8, *a*, a circle is fitted to the data points, the maximum frequency spacing criterion is used to locate the resonance, and the modal damping is calculated from equation (10.13). Results of the analysis of the first eight modes are shown in Fig. 10.9. A comparison of 'theoretical' and simulated 'experimental' modal data is given in Table 10.1.

Table 10.1. Modal parameters of the 11-DOF system

Mode No	Theoretical data		'Experimental' data	
	Frequency, Hz	Damping Factor,%	Frequency, Hz	Damping Factor,%
1	2.74	8.93	2.71	11.8
2	2.95	9.05	3.00	11.54
3	7.27	8.86	7.11	9.13
4	7.78	9.12	7.85	6.72
5	11.54	8.77	11.37	6.54
6	12.08	9.20	12.73	5.26
7	15.12	8.64	14.77	12.71
8	15.51	9.34	15.78	9.32

The drawbacks of a single FRF analysis are obvious. Modal parameters extracted by SDOF modal analysis for a system with relatively close modes are not accurate. However, the circle-fit method can extract modal parameters where the peak amplitude method may fail.

Example 10.2

The experimental data used in this example have been obtained for the GARTEUR SM-AG-19 testbed, as described in Section 9.4.5. It consists of 24 complex valued inertance FRFs, measured using single point hammer excitation at 24 arbitrarily selected locations (Fig. 10.10) and acceleration measured at the right wing tip. QRFs obtained from the pivoted QLP decomposition of the CFRF matrix, as explained in Section 9.4.5, have been used for modal parameter identification.

Table 10.2 lists the natural frequencies and damping ratios for the unmodified structure. The index of the QRF used for modal parameter identification in each case is given in column 2.

Table 10.2. Natural frequencies and damping ratios of the UNMOD structure

Mode	QRF	Natural frequency, Hz	Damping ratio, %	Description
1	8	6.55	4.04	2N wing bending
2	10	16.60	2.63	Fuselage rotation
3	4	35.01	0.9	Antisymmetric wing torsion
4	1	35.29	1.97	Symmetric wing torsion
5	6	36.52	1.24	3N wing bending
6	5	49.49	2.16	4N wing bending
7	11	50.78	0.57	In-plane wing vs. fuselage
8	9	56.42	0.45	Symmetric in-plane wing bending
9	4	65.03	2.21	5N wing bending
10	7	69.72	0.57	Tail torsion

Examples of circle fit parameter identification from QRF Nyquist plots are shown in Fig. 10.11. Because mode 4 is clearly marked by a minimum in the *first* subplot from the QCoMIF (Fig. 9.72), its modal parameters are determined from the diagrams of the *first* QRF. Indeed, the magnitude versus frequency plot (first row, first column) exhibits a prominent peak at about 35 Hz. The Nyquist plot for the frequencies in the neighbourhood of the resonance peak (first row, second column) is almost circular, indicating good mode isolation for single-degree-of-freedom circle fit analysis. The natural frequency is located at maximum rate of change of arc length with frequency. The modal viscous damping value is calculated as the arithmetic mean of two values, one determined using the two measured points chosen next to resonance, indicated in figure, and the other determined using the next close points below and above resonance, using equation (10.13).
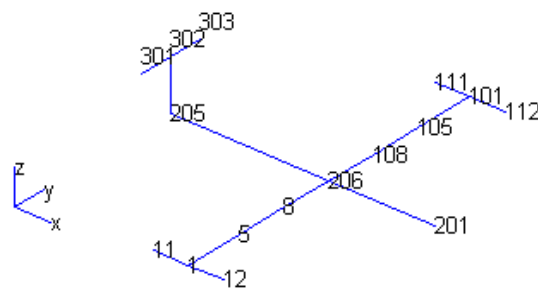
Fig. 10.10

Mode 1 is clearly marked in the *eighth* subplot in Fig. 9.72, so that its modal parameters are determined using the eighth QRF (second row in Fig. 10.11). Analogously, mode 8 is analyzed based on the 9th QRF, while modal parameters of mode 10 are determined from the 7th QRF. In all cases, the decision on what QRF to choose for analysis is based on the inspection of the QCoMIF plot (Fig. 9.72).
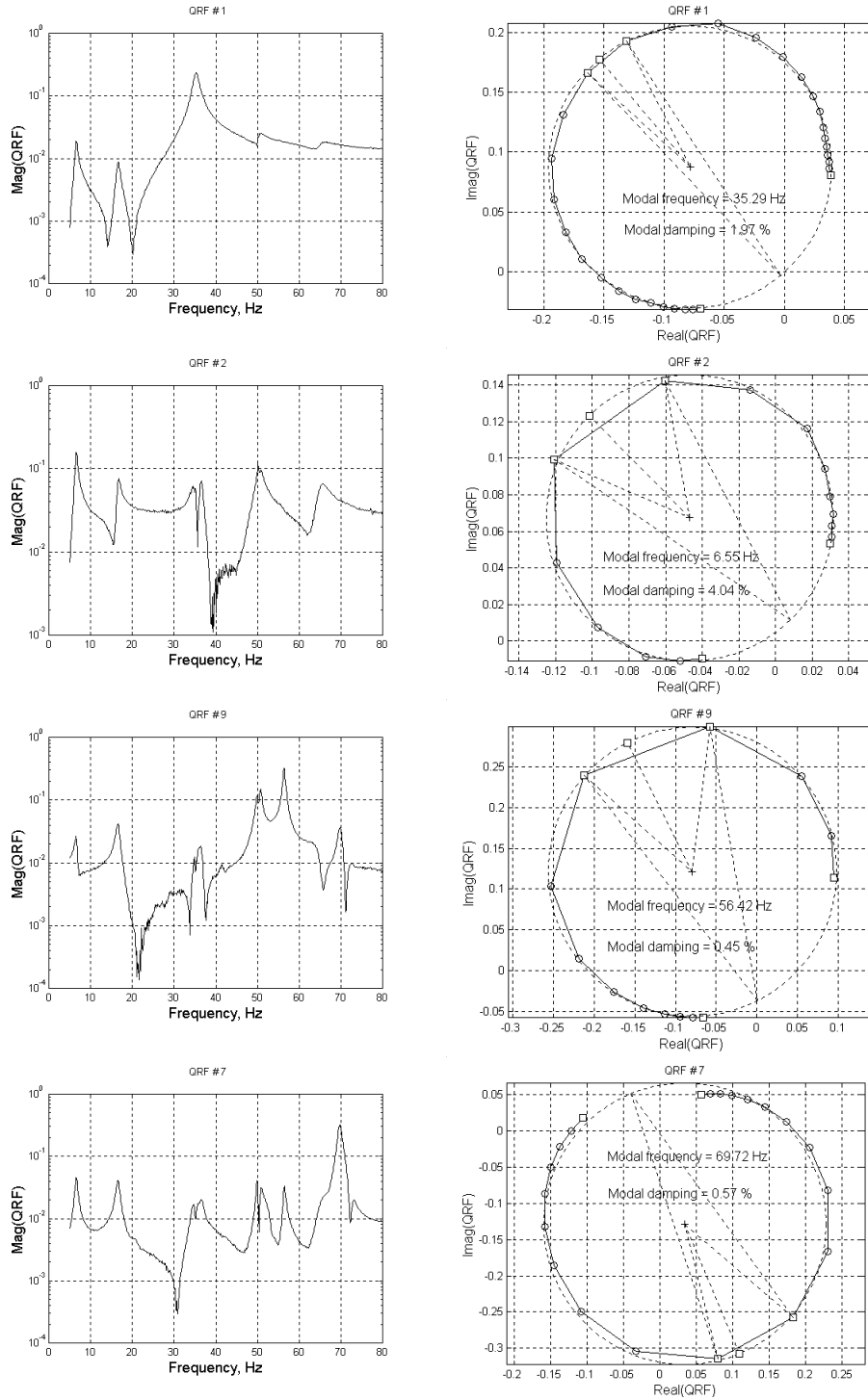
Fig. 10.11 (from [10.12])

10.2.1.3 Co-quad components method

Measurement of the real (in-phase) and imaginary (quadrature) components of the harmonic response and separate use of their diagrams had preceded [10.13] the use of Nyquist plots. These diagrams can also be used for modal parameter identification, especially for systems with proportional damping.
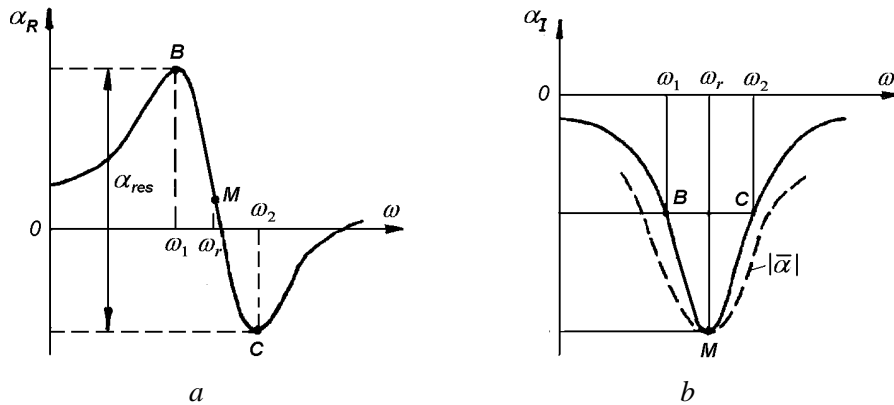
Fig. 10.12

Resonances are located at the frequencies where α_I has extreme values and α_R has inflection points, or $d\alpha_R/d\omega$ is a maximum. Use of the diagram of the quadrature component is justified by the fact that α_I peaks more sharply than the total response. The half-power points B and C correspond to extreme values of α_R (Fig. 10.12) and the difference (vertical distance) between their ordinates is a good measure for the modal response at resonance. Equation (10.4) can once again be used for evaluating the damping factor.

When the coupling of modes cannot be neglected, alternative formulae are [10.14]

$$g_r = \frac{2\alpha_{res}}{\omega_r \left| -\dfrac{d\alpha_R}{d\omega} \right|_{\omega_r}} \qquad (10.14)$$

and

$$\frac{\omega_2^2 - \omega_1^2}{\omega_2^2 + \omega_1^2} = g_r \sqrt{1 + \left(\frac{\alpha_R}{\alpha_I}\right)^2_{\omega_r}} \,, \qquad (10.14, a)$$

where ω_1 and ω_2 are the frequencies of the points of local minimum and maximum in the diagram of the in-phase component.

10.2.1.4 Phase angle method

For the SDOF system, the variation of the phase angle with frequency is shown in Fig. 10.13, *a*. The "phase resonance" occurs at the frequency ω_r where $\theta = -90^0$. The half-power points *B* and *C,* defined by frequencies ω_1 and ω_2, correspond to phase angles of -45^0 and -135^0, respectively; thus, the damping factor can be evaluated using equation (10.4). This will be affected somewhat by the coupling of the modes and the presence of motion in off-resonant modes.

a   *b*
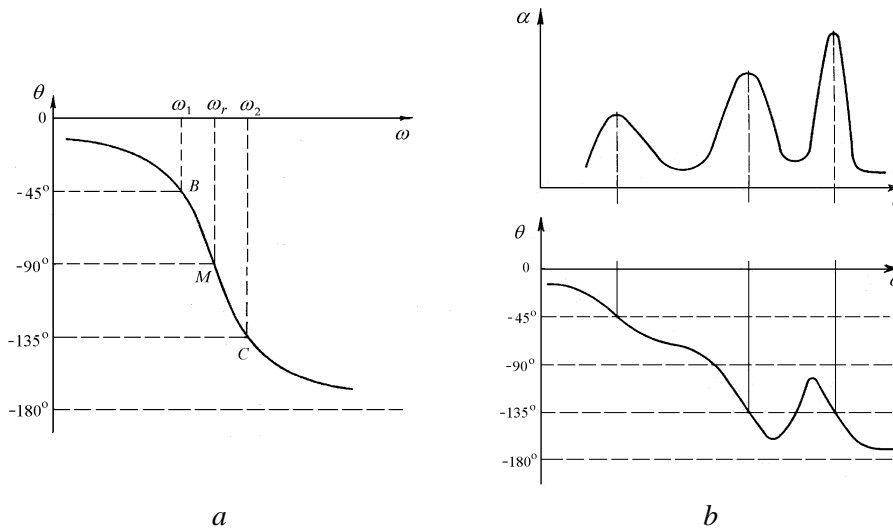
Fig. 10.13

For MDOF systems it is better to locate the resonance at the point at which the phase angle curve has an inflection point, $\mathrm{d}^2\theta/\mathrm{d}\omega^2 = 0$ (Fig. 10.13, *b*). The damping factor can then be calculated from the slope of the tangent to the curve at that point [10.15]

$$g_r = \frac{2}{\omega_r \left| \dfrac{\mathrm{d}\theta}{\mathrm{d}\omega} \right|_{\omega_r}} = \frac{2}{\omega_r} \frac{1}{(\text{- slope at } \omega_r)}. \qquad (10.15)$$

For a pure mode, therefore, the natural frequency may be calculated by the intersection of the phase-angle curve with the line $\theta = -90^0$ (or $\theta = -135^0$), and the damping factor may then be calculated from the slope of the curve at this point. Thus it is only necessary to plot the phase-angle curve over a small frequency range around each resonance in order to obtain both pieces of information.

10.2.2 Analysis of mobility data

The hysteretic damping model is conveniently used with receptance- or inertance-type FRF data because the SDOF Nyquist plots are circles. Apparently, use of a linear viscous damping model would be beneficial with mobility-type FRF data, for which the SDOF Nyquist plots are circles. In the following, modal parameter identification methods based on measured *mobility* data are presented in some detail, to understand the approximations involved in their practical use.

10.2.2.1 Skeleton method

The skeleton technique [10.16] is a direct spatial parameter identification method, different from those described above, in that the model derived is not based on the modal parameters of the structure. The method is best suited to lightly damped systems with relatively few degrees of freedom (typically, less than four), and can be summarized as consisting of the following steps [10.17]:

a) measuring a point mobility on the test structure;

b) deciding upon a suitable and plausible mathematical model for the system (i.e. a suitable configuration of masses and springs);

c) direct identification of the mass and stiffness parameters in the chosen model from the mass and stiffness lines which make up the skeleton of the measured curve.

The skeleton technique is based on the properties of the graph of mobility (i.e. velocity at constant force amplitude) against frequency. If the two rectangular coordinates are scaled logarithmically to a common scale-modulus, a straight line with a slope -1 implies constant inertance, i.e. a mass-like response, $\left| M \right|_m = 1/m\omega$, while a straight line with a slope $+1$ implies constant receptance (displacement), i.e. a spring-like response, $\left| M \right|_k = \omega/k$. The cross-over frequency of a mass-line and a spring-line corresponds to an *antiresonance*, and the cross-over frequency of a spring-line and a mass-line corresponds to a *resonance*.

For a free-free system, the very low frequency response is mass-like and the corresponding part of the drive-point mobility curve will follow a mass-line, which on log-log plot is a straight line of -1 slope. Extended down to the first antiresonant frequency, this constitutes the first 'arm' of the skeleton. At the first antiresonant frequency, the skeleton changes direction and follows a stiffness line, of $+1$ slope, being that which intersects the previous mass line at the antiresonant frequency. Then, at the first resonance frequency, the skeleton changes back to another mass line, followed at the second antiresonant frequency by a further reversal to a stiffness line. At very high frequencies the skeleton ends with a mass line, the mass at the driving point.

Certain information regarding the damping of the system may also be deduced from an extension to the skeleton construction outlined above [10.16].

The values of mass and stiffness corresponding to each arm of the skeleton can be related to the distribution of mass and stiffness in the structure. The lowest and highest arms provide direct information concerning the total mass of the structure and the mass of the element at the driving point, respectively.
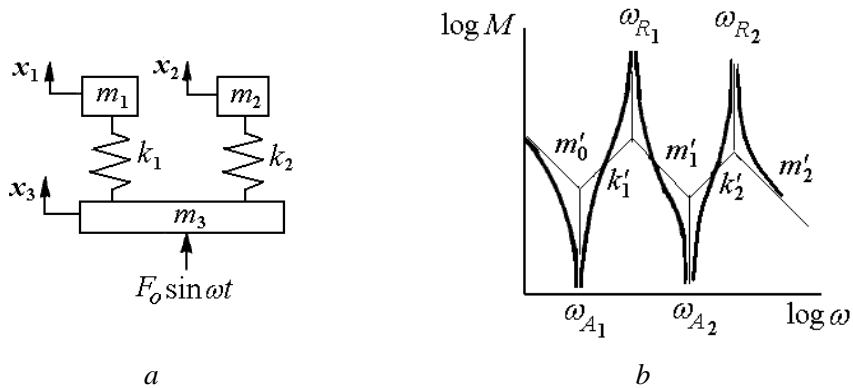
Fig. 10.14

An example of the method is illustrated in Fig. 10.14 where the drive-point mobility of an ungrounded three-mass system is shown alongside a suitable (though not unique) spatial model.

From the skeleton curve (Fig. 10.14, *b*) it is possible to deduce: two resonant frequencies, ω_{R1} and ω_{R2}, two antiresonant frequencies, ω_{A1} and ω_{A2}, three mass lines, m_0', m_1' and m_2', and two stiffness lines, k_1' and k_2'.

For the model it is necessary to specify three mass elements, m_1, m_2 and m_3, and two stiffness elements, k_1 and k_2. These five parameters may be calculated directly from the properties of the skeleton [10.3] as

$$k_1 = m_2' \frac{\left(\omega_{R1}^2 - \omega_{A1}^2\right)\left(\omega_{R2}^2 - \omega_{A1}^2\right)}{\omega_{A2}^2 - \omega_{A1}^2}, \; k_2 = m_2' \frac{\left(\omega_{A2}^2 - \omega_{R1}^2\right)\left(\omega_{R2}^2 - \omega_{A2}^2\right)}{\omega_{A2}^2 - \omega_{A1}^2},$$

$$m_1 = \frac{k_1}{\omega_{A1}^2}, \; m_2 = \frac{k_2}{\omega_{A2}^2}, \; m_3 = m_2'. \tag{10.16}$$

In fact, all skeleton links may be determined from one single arm plus all the resonant and antiresonant frequencies. A full description of the method together with tabulated formulae for the identification of a range of similar systems are given in [10.3] based on [10.16].

Example 10.3

The skeleton technique has been applied to a free-free uniform beam, whose drive-point mobility can be readily calculated and compared with measured values.

The test beam, shown in Fig. 10.15, has length $\ell = 2610\,\text{mm}$ and hexagonal cross section with $d = 50\,\text{mm}$, Young's modulus $E = 210\,\text{GPa}$ and mass density $\rho = 7850\,\text{kg}\big/\text{m}^3$. The cross section area is $A = 0.866\,d^2 = 2.165 \cdot 10^{-3}\,\text{m}^2$, and the second moment of area is $I_z = 0.06\,d^4 = 3.75 \cdot 10^{-7}\,\text{m}^4$.
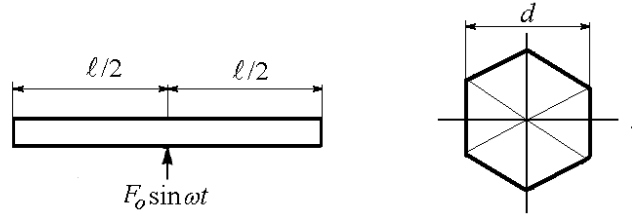
Fig. 10.15

The drive-point mobility is

$$\left| M \right| = \frac{\omega Y\!\left(\dfrac{\ell}{2}\right)}{F_0} = \frac{\ell^3}{2\,EI_z}\,\frac{\omega}{(\alpha\ell)^3}\,\frac{1 + \cos\dfrac{\alpha\ell}{2}\cosh\dfrac{\alpha\ell}{2}}{\cosh\dfrac{\alpha\ell}{2}\sin\dfrac{\alpha\ell}{2} + \cos\dfrac{\alpha\ell}{2}\sinh\dfrac{\alpha\ell}{2}},$$

where $Y(\ell/2)$ is the dynamic deflection at the beam midpoint (6.42).

In Fig. 10.16, the theoretical drive-point mobility curve is drawn with broken line, and the measured curve with solid line. The lack of coincidence in the very low frequency range is due to the beam suspension by chords of finite stiffness which makes the rigid body response to influence the response near the first antiresonance.

Using the above presented skeleton procedure one obtains

$$m_0' = 44.04\,\text{kg}, \; m_1' = 17.3\,\text{kg}, \; m_2' = 9.25\,\text{kg},$$

$$f_{A1} = 22.37\,\text{Hz}, \; f_{A2} = 140.17\,\text{Hz}, \; f_{R1} = 35.58\,\text{Hz}, \; f_{R2} = 192.3\,\text{Hz}.$$

Equations (10.16) yield the following physical parameters

$$k_1 = 5.326 \cdot 10^5\,\text{N}\big/\text{m}, \; k_2 = 6.076 \cdot 10^6\,\text{N}\big/\text{m},$$

$$m_1 = 26.96\,\text{kg}, \; m_2 = 7.83\,\text{kg}, \; m_3 = 9.25\,\text{kg},$$

of the associated lumped parameter model of Fig. 10.14, *a*.
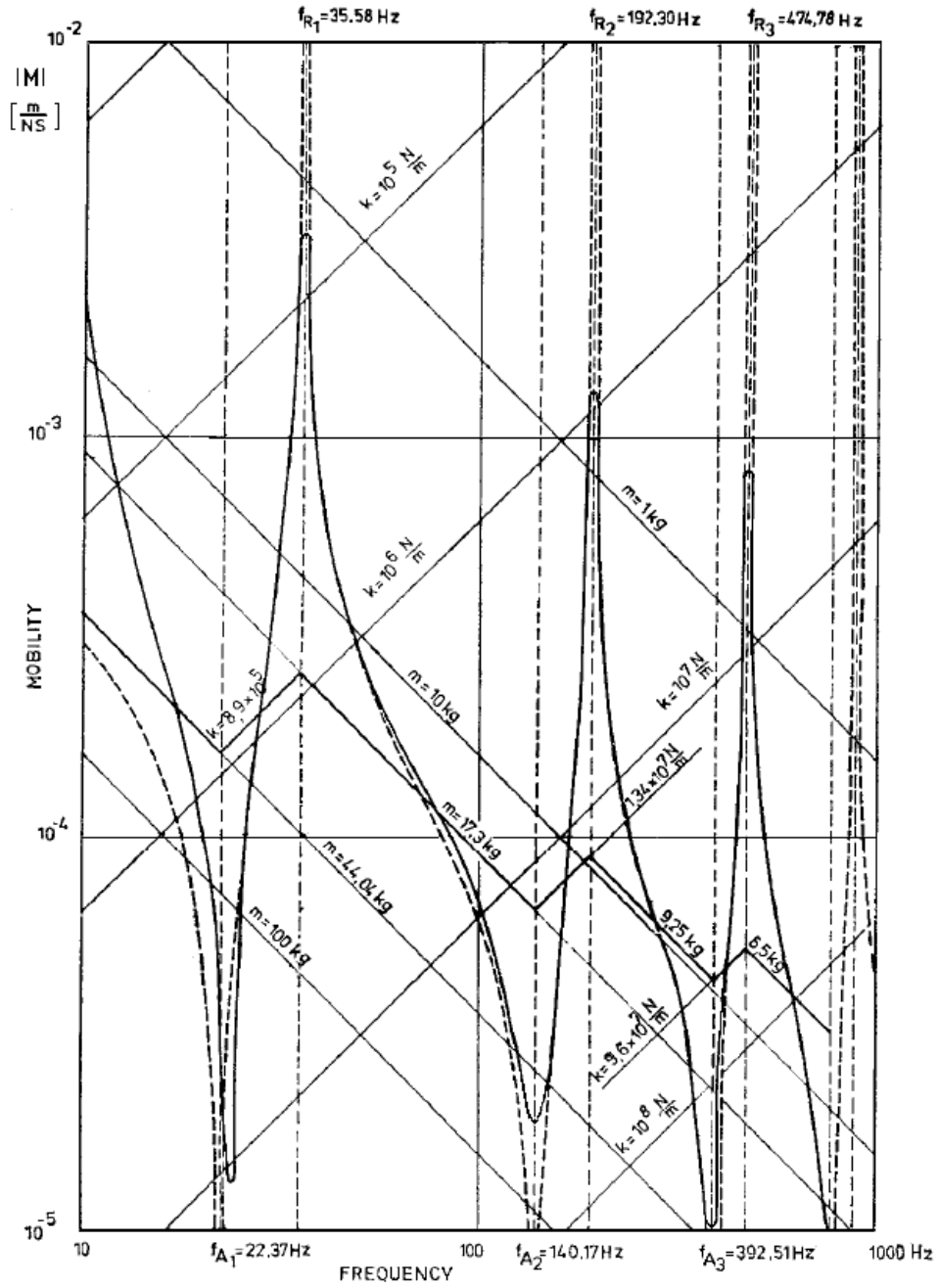
Fig. 10.16 (from [10.18])

It can be checked that the drive-point mobility curve of the equivalent system coincides with that of the beam over the frequency range up to the second resonant frequency.

10.2.2.2 SDOF mobility data

For harmonic excitation $f(t) = F_0 e^{i\omega t}$ and steady-state response $x(t) = \tilde{X} e^{i\omega t}$, the velocity is $v(t) = v_0 e^{i\omega t} = i\omega \tilde{X} e^{i\omega t}$.

The complex mobility is

$$\overline{M} = \frac{v}{f} = \frac{v_0}{F_0} = \frac{1}{c + i\left(m\omega - \dfrac{k}{\omega}\right)}, \tag{10.17}$$

or

$$\overline{M} = \frac{1}{\sqrt{km}\left[2\zeta + i\left(\Omega - \dfrac{1}{\Omega}\right)\right]}, \tag{10.17, a}$$

where

$$\Omega = \frac{\omega}{\omega_n}, \quad \omega_n = \sqrt{\frac{k}{m}}, \quad \zeta = \frac{c}{2\sqrt{km}}. \tag{10.18}$$

It can also be expressed as

$$\overline{M} = M_R + i M_I = |M| e^{i\theta_v}, \tag{10.19}$$

where the in-phase and quadrature components are

$$M_R = \frac{1}{\sqrt{km}} \frac{2\zeta\Omega^2}{\left(1-\Omega^2\right)^2 + 4\zeta^2\Omega^2}, \quad M_I = \frac{1}{\sqrt{km}} \frac{\left(1-\Omega^2\right)\Omega}{\left(1-\Omega^2\right)^2 + 4\zeta^2\Omega^2}, \tag{10.20}$$

and the magnitude and phase angle are given by

$$|M| = \frac{1}{\sqrt{km}} \frac{\Omega}{\sqrt{\left(1-\Omega^2\right)^2 + 4\zeta^2\Omega^2}}, \tag{10.21}$$

$$\theta_v = \tan^{-1}\frac{1-\Omega^2}{2\zeta\Omega}. \tag{10.22}$$

10.2.2.3 Peak amplitude method

A plot of the magnitude of the complex mobility (10.21) as a function of frequency is shown in Fig. 10.17. Amplitude resonance occurs at $\omega_n = \sqrt{k/m}$ where the peak response is

$$M_{max} = \frac{1}{\sqrt{km}} \frac{1}{2\zeta} = \frac{1}{c}. \qquad (10.23)$$

The frequencies for a response level of $\left(1/\varepsilon\right)M_{max}$ are determined, if possible for several values of ε. The two points thus identified, B_ε and C_ε, have frequencies $\omega_{1\varepsilon}$ and $\omega_{2\varepsilon}$, respectively:

$$\omega_{1\varepsilon,2\varepsilon} = \omega_n \left(\sqrt{\zeta^2\left(\varepsilon^2 - 1\right) + 1} \mp \zeta\sqrt{\varepsilon^2 - 1} \right). \qquad (10.24)$$
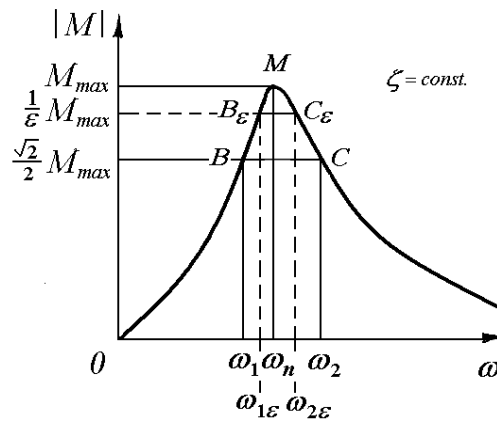
Fig. 10.17

The damping ratio is given by the exact formula [10.3]

$$\zeta = \frac{1}{\sqrt{\varepsilon^2 - 1}} \frac{\omega_{2\varepsilon} - \omega_{1\varepsilon}}{2\omega_n}, \qquad (10.25)$$

which, substituting $\omega_n^2 = \omega_{1\varepsilon}\omega_{2\varepsilon}$, becomes

$$\zeta = \frac{1}{\sqrt{\varepsilon^2 - 1}} \frac{\omega_{2\varepsilon} - \omega_{1\varepsilon}}{2\sqrt{\omega_{1\varepsilon}\omega_{2\varepsilon}}}. \qquad (10.26)$$

For $\varepsilon = \sqrt{2}$, B_ε and C_ε are the 'half-power points' B and C, of frequencies

$$\omega_{1,2} = \omega_n \left(\sqrt{\zeta^2 + 1} \mp \zeta \right) \tag{10.27}$$

and the damping ratio is given by the exact formula

$$\zeta = \frac{\omega_2 - \omega_1}{2\omega_n} \tag{10.28}$$

or, because $\omega_n^2 = \omega_1 \omega_2$, by

$$\zeta = \frac{\omega_2 - \omega_1}{2\sqrt{\omega_1 \omega_2}} = \frac{1}{2} \left(\sqrt{\frac{\omega_2}{\omega_1}} - \sqrt{\frac{\omega_1}{\omega_2}} \right). \tag{10.29}$$

In log-log coordinates, the resonant curve from Fig. 10.17 becomes symmetrical.

10.2.2.4 Circle-fit method

In the circle-fit method, each loop of the Nyquist plot of the mobility FRF is approximated by a circle in the vicinity of a resonance.

For a SDOF system with viscous damping, the Nyquist plot of the complex mobility is a circle (Fig. 10.18) of equation

$$\left(M_R - \frac{1}{4\zeta\sqrt{km}} \right)^2 + M_I^2 = \left(\frac{1}{4\zeta\sqrt{km}} \right)^2. \tag{10.30}$$
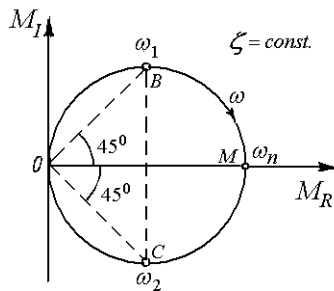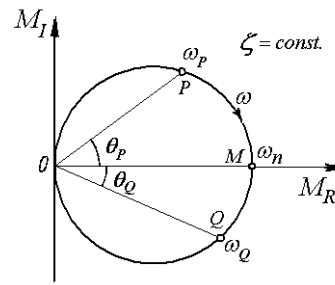
Fig. 10.18   Fig. 10.19

The center of the mobility circle in on the real axis, so that the diameter at resonance $\overline{OM}$ is no more rotated as for hysteretic damping (Fig. 2.35, *a*). The half-power points lie at the ends of the perpendicular diameter $\overline{BC}$.

The arc length is

$$ds = \frac{1}{2c}\,d\theta_v,$$

and the derivative with respect to Ω is

$$\frac{ds}{d\Omega} = -\frac{1}{2c}\frac{d\theta_v}{d\Omega} = \frac{1}{2c}\frac{d}{d\Omega}\left[\tan^{-1}\left(\frac{\Omega^2 - 1}{2\zeta\Omega}\right)\right] = \frac{1}{2\sqrt{km}}\frac{1 + \Omega^2}{\left(1 - \Omega^2\right)^2 + 4\zeta^2\Omega^2}.$$

The rate of change of the arc length with respect to frequency, $\dfrac{ds}{d\omega}$, is a maximum at the frequency $\omega_n\sqrt{-1 + 2\sqrt{1 - \zeta^2}}$ which is less than the resonant frequency ω_n. For $\zeta \ll 1$, the difference is negligible and the Kennedy and Pancu criterion can be used for the location of the natural frequency.

For determining the damping ratio, ζ, we can use three points on the circle: the resonant point M, one below it, P, and one above it, Q, as shown in Fig. 10.19.

Using equation (10.22) we obtain

$$\tan\theta_P = \frac{1 - \Omega_P^2}{2\zeta\Omega_P}, \quad \tan\theta_Q = \frac{\Omega_Q^2 - 1}{2\zeta\Omega_Q},$$

from which we have [10.3]

$$\zeta = \frac{\omega_Q - \omega_P}{2\omega_n}\left(1 + \frac{\omega_n^2}{\omega_P\omega_Q}\right)\frac{1}{\tan\theta_P + \tan\theta_Q}. \tag{10.31}$$

If $\theta_P = \theta_Q = \theta$, then $\omega_n^2 = \omega_P\omega_Q$ and equation (10.31) becomes

$$\zeta = \frac{\omega_Q - \omega_P}{2\omega_n}\,\cot\theta. \tag{10.32}$$

10.2.3 Base-excited systems

Base excited configurations are used in test rigs for determining the dynamic properties of anti-vibration mountings and materials used in vibration isolation.

Consider the base-excited mass–damped spring–mass system with hysteretic damping from Fig. 10.20.

A harmonic force $f(t) = F_0 \, e^{i\omega t}$ is applied to the bottom mass. The steady-state response of the two masses is $x_1(t) = \tilde{X}_1 \, e^{i\omega t}$ and $x_2(t) = \tilde{X}_2 e^{i\omega t}$. The complex dimensionless displacement amplitudes are given by

$$\frac{\tilde{X}_1}{F_0/k} = -\frac{1}{(1+\gamma)\Omega^2} \, \frac{1 - \Omega^2 + i\,g}{1 - \dfrac{\gamma}{1+\gamma}\Omega^2 + i\,g} \,, \tag{10.33}$$

$$\frac{\tilde{X}_2}{F_0/k} = -\frac{1}{(1+\gamma)\Omega^2} \, \frac{1 + i\,g}{1 - \dfrac{\gamma}{1+\gamma}\Omega^2 + i\,g} \,. \tag{10.34}$$

The relative displacement between the two masses is

$$\frac{\tilde{X}_1 - \tilde{X}_2}{F_0/k} = \frac{1}{1+\gamma} \, \frac{1}{1 - \dfrac{\gamma}{1+\gamma}\Omega^2 + i\,g} \,, \tag{10.35}$$

and the motion transmissibility is

$$\overline{T} = \frac{\tilde{X}_2}{\tilde{X}_1} = \frac{1 + i\,g}{1 - \Omega^2 + i\,g} \,, \tag{10.36}$$

where

$$\Omega = \frac{\omega}{\omega_2}, \quad \omega_2 = \sqrt{\frac{k}{m_2}}, \quad g = \frac{h}{k}, \quad \gamma = \frac{m_1}{m_2}. \tag{10.37}$$
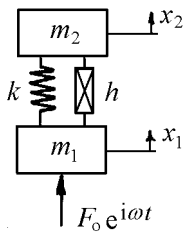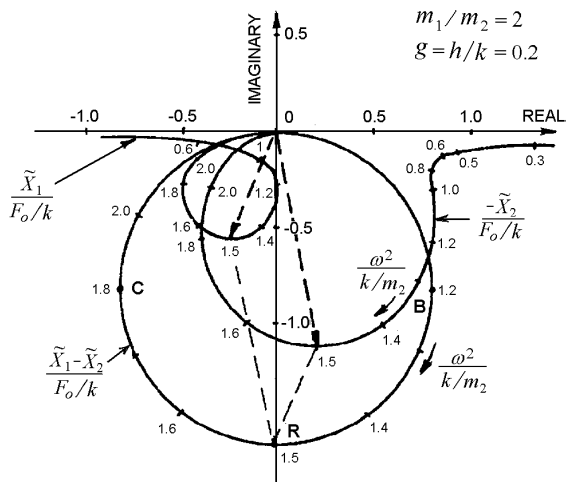
Fig. 10.20   Fig. 10.21

Equations (10.33)-(10.35) are plotted in Fig. 10.21 for $g = 0.2$ and $\gamma = 2$ [10.19]. The frequency parameter along the polar plots is Ω^2.

Resonance occurs at $\Omega^2_{res} = \dfrac{\gamma + 1}{\gamma}$, hence at the frequency

$$\omega_{res} = \sqrt{k\left(\frac{1}{m_1} + \frac{1}{m_2}\right)} \tag{10.38}$$

where a minimum of force produces a maximum of relative motion between the two masses. This occurs at point M on the diagram of $\left(\tilde{X}_1 - \tilde{X}_2\right)$, which is a circle. It can be located using the Kennedy and Pancu criterion, where the rate of change of the arc length (or phase angle) with frequency is a maximum.

On the diagrams of $\tilde{X}_1$ and $\tilde{X}_2$, the resonant frequency corresponds to the points where the quadrature component is a maximum.

At the half-power points B and C, the dimensionless frequencies are given by

$$\Omega^2_{1,2} = \frac{\gamma + 1}{\gamma}\left(1 \mp g\right),$$

so that the hysteretic damping factor is

$$g = \frac{\gamma}{\gamma + 1} \frac{\Omega^2_2 - \Omega^2_1}{2} = \frac{\Omega^2_2 - \Omega^2_1}{2\Omega^2_{res}} = \frac{\omega^2_2 - \omega^2_1}{2\omega^2_{res}}. \tag{10.39}$$
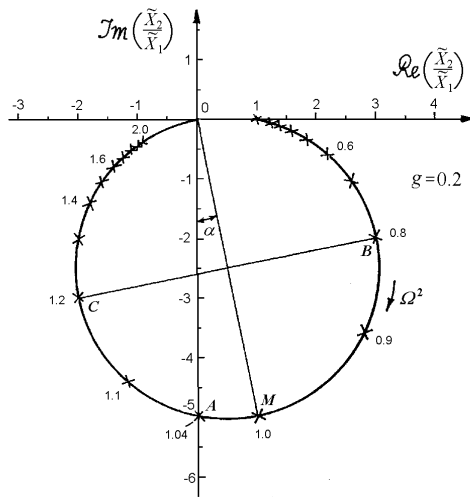
Fig. 10.22

Equation (10.36) is plotted in Fig. 10.22 for $g = 0.2$. The frequency parameter along the polar plot is Ω^2. The Nyquist plot of the complex transmissibility $\bar{T} = T_R + iT_I$ is a circle of equation

$$\left(T_R - \frac{1}{2} \right)^2 + \left(T_I + \frac{1}{2g} \right)^2 = \frac{1+g^2}{4g^2} . \tag{10.40}$$

Resonance occurs at $\Omega_M^2 = 1$, hence at the frequency $\omega_M = \sqrt{\dfrac{k}{m_2}}$ which can be located using the Kennedy and Pancu criterion. The diameter *OM* at resonance is inclined an angle $\alpha = \tan^{-1} g$ with respect to the negative imaginary semiaxis. At the ends of the diameter AB, perpendicular to OM, the half-power points have frequencies

$$\Omega_{B,C}^2 = \sqrt{1 \mp g} ,$$

so that the hysteretic damping factor can be calculated from

$$g = \frac{\Omega_C^2 - \Omega_B^2}{2} = \frac{\Omega_C^2 - \Omega_B^2}{2\Omega_M^2} = \frac{\omega_C^2 - \omega_B^2}{2\omega_M^2} . \tag{10.41}$$
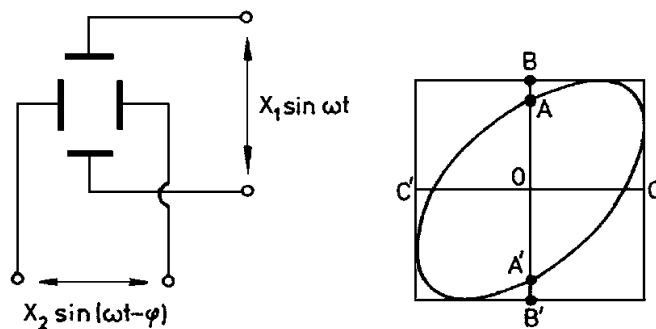
Fig. 10.23

If the damped spring from Fig. 10.20 is a test specimen from a material modeled by a complex stiffness $k^* = k(1+ig)$, the bottom mass has a harmonic motion $x_1(t) = X_1 e^{i\omega t}$ and the top mass has a motion $x_2(t) = X_2 e^{i(\omega t - \varphi)}$, lagging with an angle φ the input displacement of the bottom mass, then the dynamic stiffness k and the equivalent hysteretic damping factor g are given by [10.20]

$$k = m_2 \omega^2 \frac{1 - \dfrac{X_1}{X_2}\cos\varphi}{1 + \dfrac{X_1^2}{X_2^2} - 2\dfrac{X_1}{X_2}\cos\varphi} \,, \qquad g = \frac{\sin\varphi}{\dfrac{X_2}{X_1} - \cos\varphi} \,. \qquad (10.42)$$

If two identical accelerometers are installed on the two masses and their output signals are fed to the X and Y plates of an oscilloscope, an ellipse is traced on the screen (Fig. 10.23). The quantities $\dfrac{X_1}{X_2} = \dfrac{OC}{OB}$ and $\sin\varphi = \dfrac{OA}{OB}$ can be determined using the elliptical-pattern measuring technique.

10.3 Multiple-mode parameter extraction methods

Multi-degree-of-freedom (MDOF) parameter identification methods perform a simultaneous fit of several resonance peaks (or loops), often for curves from all response stations, but with the same excitation location (single reference multi-curve algorithms). These techniques are utilized for systems with high modal density (overlapping of half-power bandwidths of two adjacent modes) or high damping (resonance loops or peaks not visible in the FRF plots), when the modes are not separated, so that their shapes cannot be determined from the response measured at resonance. Sometimes, modal frequencies and modal damping factors are first estimated using SDOF techniques, and special separation methods are then used to determine the individual modal responses. In the following, only single point excitation techniques are presented, based on measured FRFs.

10.3.1 Phase-separation method

With the assumption of proportional hysteretic damping, the vector of complex displacement amplitudes is (7.66)

$$\{\tilde{x}\} = \sum_{r=1}^{N} \frac{\{u\}_r^{\mathrm{T}}\{\hat{f}\}\{u\}_r}{K_r\left(1 - \dfrac{\omega^2}{\omega_r^2} + \mathrm{i}\,g_r\right)} \,, \qquad (10.43)$$

where

$$g_r = \frac{D_r}{K_r} \,, \qquad\qquad r = 1, 2, ..., N \qquad (10.44)$$

are the *modal structural damping factors*.

The steady-state complex displacement at coordinate *j,* produced by a harmonic force applied at coordinate ℓ, is given by

$$\tilde{x}_j = \sum_{r=1}^{N} \frac{u_{jr} u_{\ell r}}{K_r \left(1 - \dfrac{\omega^2}{\omega_r^2} + i\, g_r \right)} \hat{f}_\ell, \tag{10.45}$$

so that the complex transfer receptance is

$$\alpha_{j\ell} = \alpha_{j\ell R} + i\, \alpha_{j\ell I} = \frac{\tilde{x}_j}{\hat{f}_\ell} = \sum_{r=1}^{N} \chi_{j\ell r} \left[a_r(\omega) + i b_r(\omega) \right], \tag{10.46}$$

where

$$\chi_{j\ell r} = \frac{u_{jr} u_{\ell r}}{K_r g_r}, \quad a_r(\omega) = \frac{\left(1 - \dfrac{\omega^2}{\omega_r^2}\right) g_r}{\left(1 - \dfrac{\omega^2}{\omega_r^2}\right)^2 + g_r^2}, \quad b_r(\omega) = \frac{-g_r^2}{\left(1 - \dfrac{\omega^2}{\omega_r^2}\right)^2 + g_r^2}. \tag{10.47}$$

The quadrature component in all coordinates, due to a force applied at coordinate ℓ, is

$$\left\{ \alpha_{\ell I}(\omega) \right\} = \sum_{r=1}^{n} \left\{ \chi_\ell \right\}_r b_r(\omega) = \left[\chi \right] \left\{ b(\omega) \right\}, \tag{10.48}$$

where

$$\left\{ \alpha_{\ell I}(\omega) \right\} = \left\{ \alpha_{1\ell I} \;\; \alpha_{2\ell I} \;\; \cdots \;\; \alpha_{j\ell I} \;\; \cdots \;\; \alpha_{N\ell I} \right\}^T,$$

$$\left\{ b(\omega) \right\} = \left\{ b_1(\omega) \;\; b_2(\omega) \;\; \cdots \;\; b_N(\omega) \right\}^T, \tag{10.49}$$

$$\left[\chi \right] = \left[\left\{ \chi_\ell \right\}_1 \;\; \left\{ \chi_\ell \right\}_2 \;\; \cdots \;\; \left\{ \chi_\ell \right\}_N \right] = \left[\left\{ u \right\}_1 \frac{u_{\ell 1}}{K_1 g_1} \;\; \left\{ u \right\}_2 \frac{u_{\ell 2}}{K_2 g_2} \;\; \cdots \;\; \left\{ u \right\}_N \frac{u_{\ell N}}{K_N g_N} \right].$$

This can be evaluated at N_f excitation frequencies $\overline{\omega}_1, \overline{\omega}_2, \cdots, \overline{\omega}_{N_f}$, and written under the form

$$\left[\alpha_{\ell I} \right] = \left[\chi \right] \left[b \right], \tag{10.50}$$

where

$$\left[\alpha_{\ell I} \right] = \left[\left\{ \alpha_{\ell I}(\overline{\omega}_1) \right\} \left\{ \alpha_{\ell I}(\overline{\omega}_2) \right\} \cdots \left\{ \alpha_{\ell I}(\overline{\omega}_{N_f}) \right\} \right],$$

$$\left[b \right] = \left[\left\{ b(\overline{\omega}_1) \right\} \left\{ b(\overline{\omega}_2) \right\} \cdots \left\{ b(\overline{\omega}_{N_f}) \right\} \right]. \tag{10.51}$$

Equation (10.50) has the form [10.21]

$$
\begin{bmatrix}
\alpha_{1\ell I}(\overline{\omega}_1) & \alpha_{1\ell I}(\overline{\omega}_2) & \cdots & \alpha_{1\ell I}(\overline{\omega}_{N_f}) \\
\alpha_{2\ell I}(\overline{\omega}_1) & \alpha_{2\ell I}(\overline{\omega}_2) & \cdots & \alpha_{2\ell I}(\overline{\omega}_{N_f}) \\
\vdots & \vdots & \ddots & \vdots \\
\alpha_{N\ell I}(\overline{\omega}_1) & \alpha_{N\ell I}(\overline{\omega}_2) & \cdots & \alpha_{N\ell I}(\overline{\omega}_{N_f})
\end{bmatrix}
=
\begin{bmatrix}
\chi_{1\ell 1} & \chi_{1\ell 2} & \cdots & \chi_{1\ell N} \\
\chi_{2\ell 1} & \chi_{2\ell 2} & \cdots & \chi_{2\ell N} \\
\vdots & \vdots & \ddots & \vdots \\
\chi_{N\ell 1} & \chi_{N\ell 2} & \cdots & \chi_{N\ell N}
\end{bmatrix}
\cdot
$$

$$
\cdot
\begin{bmatrix}
\dfrac{-g_1^2}{\left(1-\dfrac{\overline{\omega}_1^2}{\omega_1^2}\right)^2 + g_1^2} & \dfrac{-g_1^2}{\left(1-\dfrac{\overline{\omega}_2^2}{\omega_1^2}\right)^2 + g_1^2} & \cdots & \dfrac{-g_1^2}{\left(1-\dfrac{\overline{\omega}_{N_f}^2}{\omega_1^2}\right)^2 + g_1^2} \\[2em]
\dfrac{-g_2^2}{\left(1-\dfrac{\overline{\omega}_1^2}{\omega_2^2}\right)^2 + g_2^2} & \dfrac{-g_2^2}{\left(1-\dfrac{\overline{\omega}_2^2}{\omega_2^2}\right)^2 + g_2^2} & \cdots & \dfrac{-g_2^2}{\left(1-\dfrac{\overline{\omega}_{N_f}^2}{\omega_2^2}\right)^2 + g_2^2} \\[2em]
\vdots & \vdots & \ddots & \vdots \\[1em]
\dfrac{-g_N^2}{\left(1-\dfrac{\overline{\omega}_1^2}{\omega_N^2}\right)^2 + g_N^2} & \dfrac{-g_N^2}{\left(1-\dfrac{\overline{\omega}_2^2}{\omega_N^2}\right)^2 + g_N^2} & \cdots & \dfrac{-g_N^2}{\left(1-\dfrac{\overline{\omega}_{N_f}^2}{\omega_N^2}\right)^2 + g_N^2}
\end{bmatrix}
\cdot
$$

$$ \text{(10.52)} $$

If $N_f = N$ and the matrix $[b]$ is non-singular, equation (10.50) can be solved for the normal modes

$$
[\chi] = [\alpha_{\ell I}][b]^{-1}, \tag{10.53}
$$

where starting estimates of g_r and ω_r are used.

This yields terms of the form

$$
\chi_{j\ell r} = \frac{u_{jr} u_{\ell r}}{K_r g_r}, \tag{10.47, a}
$$

or, if the normal modes are normalized to unit modal mass, $M_r = 1$, of the form

$$
\chi_{j\ell r} = \frac{u_{jr} u_{\ell r}}{\omega_r^2 g_r}. \tag{10.47, b}
$$

It will be noted that this method of separation is not tenable when two modes have coincident or very nearly coincident natural frequencies and have similar damping factors.

Although all measured modes could be used in equation (10.53), it is only necessary to include those modes which are sufficiently close to cause modal interaction in the measured quadrature response. It will seldom be necessary to include more than four modes in the equation. Thus, the number of estimated modes is smaller than the number of structural degrees of freedom and much smaller then the number of degrees of freedom of the identification model.

When the number of modal parameters is smaller than the number of experimental data available, no exact solution to the above equation can be found. Optimal values of the modal parameters are found minimizing the square error between calculated and experimental data (least squares method). When the model order is larger than the system order, there are more determined modes than structural modes, the remainder being called *computational* or noise *modes*. The latter are readily identified as they cannot be repeatedly obtained by a choice of a different set of effective DOFs. To sort out the physically meaningful modes, the concept of *modal confidence factor* was introduced [10.22].

Multi-mode curve fitting procedures using single point excitation require at least one column of the FRF matrix to completely define the mode shapes. But analyzing one FRF curve at a time, different estimates of the natural frequency and modal damping are derived for each mode, though these are 'global' properties.

In many cases it is not possible to identify the complete modal vector due to near-zero modal coefficients obtained as a result of the poor choice of excitation and response points. The solution is to change their location. Improved frequency and damping estimates can be extracted from *multiple single-point* or *multi-point* surveys. When more than one column of the FRF matrix is available (redundant data) multiple estimates for the modal parameters are obtained, which are generally not consistent. Inconsistencies involve frequency shifts, non-reciprocity and non-stationarity in the data. These errors in the measured FRFs are partly due to structural nonlinearities, to environmental effects and to exciter and transducer attachment.

10.3.2 Residues

The effect of out-of-band modes can be compensated using either additional residual terms in the FRF mathematical expressions or extra modes in the identification model.

The expression of the receptance FRF (10.45) can be written

$$\alpha_{j\ell} = \frac{1}{K_{j\ell}^R} + \sum_{r=N'}^{N''} \frac{u_{jr} u_{\ell r}}{M_r \left(\omega_r^2 - \omega^2 + \mathrm{i}\, g_r \omega_r^2 \right)} - \frac{1}{\omega^2 M_{j\ell}^R} \,, \quad (10.54)$$

where the quantities $K_{j\ell}^R$ and $M_{j\ell}^R$ are the *residual stiffness* and *residual mass* for the considered FRF in the frequency range of the measurements.
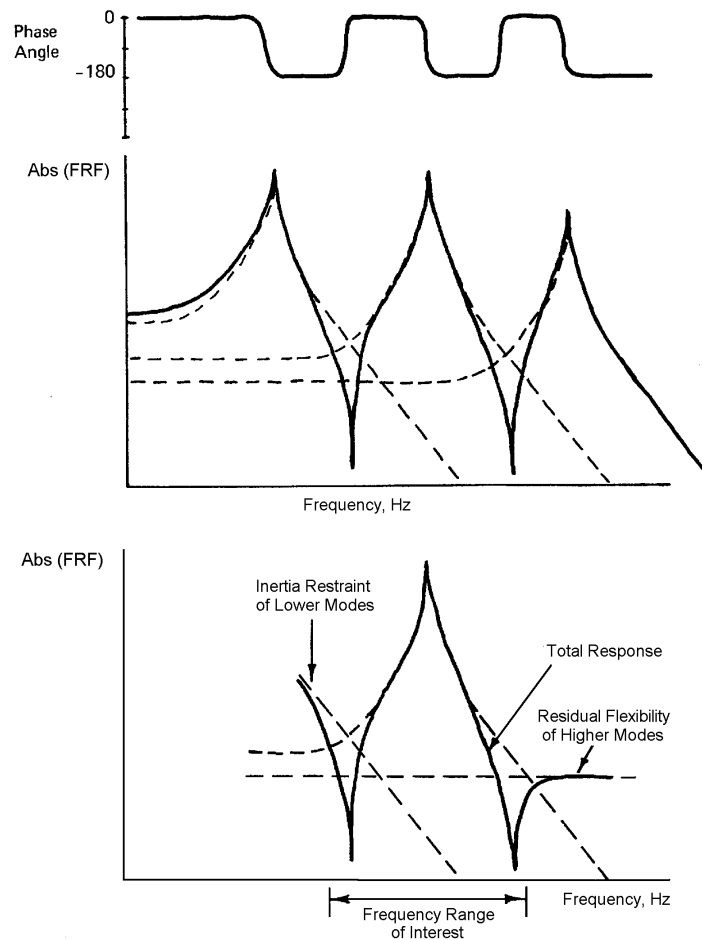
Fig. 10.24 (from [10.23])

  This equation indicates that the response in a certain frequency range can be approximately described in terms of the "inertia restraint" of the lower modes of vibration, the modes of vibration which are resonant in that frequency range and the "residual flexibility" of the higher frequency modes.

  It should be noticed that residual terms are not global modal properties. It is not possible to predict the residues of a direct FRF from those of another direct FRF and the cross FRF corresponding to the pair of points where direct FRFs are measured. Moreover, determination on the number of DOFs in the data is critical for most algorithms.

10.3.3 Modal separation by least squares curve fit

The modal parameters can be extracted by least squares curve fitting equation (10.54) to the receptance FRF data measured at N_f excitation frequencies $\overline{\omega}_1,\ \overline{\omega}_2,\ \cdots,\ \overline{\omega}_{N_f}$ [10.24].

Setting up an equation at each excitation frequency, the following set of equations is obtained

$$
\left\{
\begin{array}{c}
\alpha_{j\ell}(\overline{\omega}_1) \\
\alpha_{j\ell}(\overline{\omega}_2) \\
\vdots \\
\vdots \\
\alpha_{j\ell}(\overline{\omega}_{N_f})
\end{array}
\right\} =
$$

$$
=
\begin{bmatrix}
1 & \dfrac{1}{\omega_{N'}^2 - \overline{\omega}_1^2 + \mathrm{i}\, g_{N'}\omega_{N'}^2} & \cdots & \dfrac{1}{\omega_{N''}^2 - \overline{\omega}_1^2 + \mathrm{i}\, g_{N''}\omega_{N''}^2} & -\dfrac{1}{\overline{\omega}_1^2} \\
1 & \vdots & \cdots & \vdots & -\dfrac{1}{\overline{\omega}_2^2} \\
\vdots & \vdots & \cdots & \vdots & \vdots \\
\vdots & \vdots & \cdots & \vdots & \vdots \\
1 & \dfrac{1}{\omega_{N'}^2 - \overline{\omega}_{N_f}^2 + \mathrm{i}\, g_{N'}\omega_{N'}^2} & \cdots & \dfrac{1}{\omega_{N''}^2 - \overline{\omega}_{N_f}^2 + \mathrm{i}\, g_{N''}\omega_{N''}^2} & -\dfrac{1}{\overline{\omega}_{N_f}^2}
\end{bmatrix}
\left\{
\begin{array}{c}
\dfrac{1}{K_{j\ell}^R} \\
\dfrac{u_{jN'}u_{\ell N'}}{M_{N'}} \\
\vdots \\
\dfrac{u_{jN''}u_{\ell N''}}{M_{N''}} \\
\dfrac{1}{M_{j\ell}^R}
\end{array}
\right\}
$$

or

$$
\{\alpha\}=[T]\{\beta\}.
$$

It is assumed that estimates of the values g_r and ω_r are known so that $[T]$ can be calculated. In the case when there are more FRF values measured in $\{\alpha\}$ than parameters of interest in $\{\beta\}$, an error function is introduced

$$
\{e\}=\{\alpha\}-[T]\{\beta\}
$$

and the sum of the error squared can be written as

$$
\{e\}^T\{e\}=\{\{\alpha\}-[T]\{\beta\}\}^T\{\{\alpha\}-[T]\{\beta\}\}. \tag{10.55}
$$

In equation (10.55) it is implied that the total error should be dependent on the magnitude squared of the measured FRF data. In general, this is not wanted, since the FRF data near the antiresonances is frequently of just as much or more importance that the data taken near the resonances. Therefore, it is recommended to introduce a weighting function into equation (10.55) to modify the importance of the data. Thus, define a diagonal matrix $[W]$ having elements proportional to the significance of the data measured at that frequency (i.e. often taken as the inverse of the magnitude squared):

$$\{e\}^T[W]\{e\} = \{\{\alpha\}-[T]\{\beta\}\}^T[W]\{\{\alpha\}-[T]\{\beta\}\}.$$

The product $\{e\}^T[W]\{e\}$ is minimized by taking its derivative with respect to the vector $\{\beta\}$ and setting the result equal to zero

$$\frac{\partial\left(\{e\}^T[W]\{e\}\right)}{\partial\{\beta\}} = 0 = 2[T]^T[W][T]\{\{\beta\}-[T]\{\alpha\}\}.$$

This yields the "weighted" least squares solution

$$\{\beta\} = \left[[T]^T[W][T]\right]^{-1}\left\{[T]^T[W]\{\alpha\}\right\}. \qquad (10.56)$$

Using estimates of the elements of $\{\beta\}$, the total error can be evaluated. Each value of the natural frequency can be changed successively to determine the minimum error and then each damping coefficient can be changed to determine the damping factor for minimum error. After new values for the natural frequencies and damping factors are found, equation (10.56) can be used again and the procedure repeated as many times as necessary to reduce the error to an acceptable level [10.23]. The goodness-of-fit check is made synthesizing an FRF using the estimated values of the modal parameters and overlaying this function on the original test data.

10.3.4 Elimination of the modal matrix

A method which is not based on initial estimates of g_r and ω_r starts with the elimination of the matrix containing the mode shape coefficients [10.25]. It is assumed that the number of response measurement points, N_o, is larger the number of modes of vibration, *n*.

Using equations (10.47), the in-phase component in all coordinates, due to a force applied at coordinate ℓ, can be written as

$$\{\alpha_{\ell R}(\omega)\} = \sum_{r=1}^{n}\{\chi_\ell\}_r\, a_r(\omega) = [\chi]\{a(\omega)\}, \qquad (10.57)$$

where

$$\{\alpha_{\ell R}(\omega)\} = \lfloor \alpha_{1\ell R} \quad \alpha_{2\ell R} \quad \cdots \quad \alpha_{j\ell R} \quad \cdots \quad \alpha_{N\ell R} \rfloor^T,$$

$$\{a(\omega)\} = \lfloor a_1(\omega) \quad a_2(\omega) \quad \cdots \quad a_N(\omega) \rfloor^T, \tag{10.58}$$

and $[\chi]$ is given by (10.49).

Evaluated at N_f excitation frequencies $\bar{\omega}_1, \bar{\omega}_2, \cdots, \bar{\omega}_{N_f}$, this can be written under the form

$$[\alpha_{\ell R}] = [\chi][a], \tag{10.59}$$

where

$$[\alpha_{\ell R}] = \left[\{\alpha_{\ell R}(\bar{\omega}_1)\} \ \{\alpha_{\ell R}(\bar{\omega}_2)\} \ \cdots \ \{\alpha_{\ell R}(\bar{\omega}_{N_f})\} \right],$$

$$[a] = \left[\{a(\bar{\omega}_1)\} \ \{a(\bar{\omega}_2)\} \ \cdots \ \{a(\bar{\omega}_{N_f})\} \right]. \tag{10.60}$$

Observe that in equations (10.50) and (10.59) $[\alpha_{\ell R}]$, $[\alpha_{\ell I}]$ and $[\chi]$ are rectangular $N_o \times N$ matrices, while $[a]$ and $[b]$ are square $N \times N$ matrices.

From equation (10.50)

$$[\chi] = [\alpha_{\ell I}][b]^{-1} \tag{10.61}$$

which substituted in (10.59) yields

$$[\alpha_{\ell R}] = [\alpha_{\ell I}][b]^{-1}[a] \tag{10.62}$$

and

$$[\alpha_{\ell I}]^+[\alpha_{\ell R}] = [b]^{-1}[a], \tag{10.63}$$

where

$$[\alpha_{\ell I}]^+ = \left[[\alpha_{\ell I}]^T[\alpha_{\ell I}]\right]^{-1}[\alpha_{\ell I}]^T. \tag{10.64}$$

Equation (10.63) can be written

$$[a] = [b][c], \tag{10.65}$$

where the matrix

$$[c] = [\alpha_{\ell I}]^+[\alpha_{\ell R}] \tag{10.66}$$

has measured elements.

As

$$a_r^2\left(\overline{\omega}_f\right)=-b_r\left(\overline{\omega}_f\right)\left[1+b_r\left(\overline{\omega}_f\right)\right], \qquad (10.67)$$

and from (10.65)

$$a_r\left(\overline{\omega}_f\right)=\sum_{e=1}^{N} b_r(\overline{\omega}_e)\,c_{ef}\;, \qquad (10.68)$$

where c_{ef} is a generic element of the matrix $[c]$, $a_r\left(\overline{\omega}_f\right)$ can be eliminated from equations (10.67) and (10.68). This results in n sets of n equations in $b_r\left(\overline{\omega}_f\right)$, hence n^2 equations of the form

$$b_r\left(\overline{\omega}_f\right)\left[1+b_r\left(\overline{\omega}_f\right)\right]+\left(\sum_{e=1}^{N} b_r(\overline{\omega}_e)\,c_{ef}\right)^2=0, \qquad (r,f=1,...,n) \quad (10.69)$$

wherefrom the n^2 elements of the matrix $[b]$ can be determined.

Denoting

$$\tau_r(\omega)=\frac{1-\dfrac{\omega^2}{\omega_r^2}}{g_r} \qquad (10.70)$$

we can write

$$b_r(\omega)=-\frac{1}{\tau_r^2(\omega)+1}, \qquad (10.71)$$

hence

$$\tau_r(\omega)=\pm\sqrt{-\left[1+\frac{1}{b_r(\omega)}\right]}. \qquad (10.72)$$

Evaluating (10.70) at two excitation frequencies, $\overline{\omega}_e$ and $\overline{\omega}_f$, the natural frequencies and modal damping factors are obtained as follows

$$g_r=\frac{\overline{\omega}_f^2-\overline{\omega}_e^2}{\overline{\omega}_f^2\,\tau_r(\overline{\omega}_e)-\overline{\omega}_e^2\,\tau_r(\overline{\omega}_f)}\,, \qquad (10.73)$$

$$\omega_r^2=\frac{\overline{\omega}_f^2\,\tau_r(\overline{\omega}_e)-\overline{\omega}_e^2\,\tau_r(\overline{\omega}_f)}{\tau_r(\overline{\omega}_e)-\tau_r(\overline{\omega}_f)}. \qquad (10.74)$$

Using the above values, the matrix $[b]$ is calculated and, if it is non-singular, equation (10.61) gives the matrix $[\chi]$ with elements of the form (10.47). The mode shape coefficients are determined as

$$u_{jr} = \omega_r \sqrt{g_r \chi_{jjr}} \, , \qquad u_{\ell r} = u_{jr} \frac{\chi_{j\ell r}}{\chi_{jjr}} \, . \qquad (10.75)$$

The main drawback of this method is the arbitrary selection of the frequencies $\overline{\omega}_e$ and $\overline{\omega}_f$ in (10.73) and (10.74).

10.3.5 Multipoint excitation methods

Natural frequencies and modal damping factors are *global properties*, i.e. intrinsic structural properties, independent of the input or response measurement locations, or both. Inclusion of data from multiple reference locations in the estimation of global properties dictates the need for consistency between measurement data. This goal is achieved by multipoint excitation and simultaneous recording of various FRFs.

Single-input multi-output (SIMO) methods can calculate global estimates only for natural frequencies and damping values. Multi-input multi-output (MIMO) methods can also calculate consistent modal vectors. Advantage is taken of the fact that mode shapes are independent of the input location, whereas modal participation factors are independent of the response location. Additionally, MIMO methods can handle symmetrical structures or structures with very high modal density, for which it is necessary to have data from as many independent exciter locations as the (pseudo-) multiplicity of the repeated roots.

Multiple reference simultaneous algorithms perform an ensemble MDOF fit of FRF curves from all response locations and several or all excitation locations. The theoretical basis of multiple input/output FRF analysis is documented in [10.26]. Their analysis is beyond the aim of this presentation. Surveys of frequency-domain parameter estimation techniques are given in [10.27]-[10.30].

The advantages of the multiple input FRF techniques include better energy distribution in the tested structure with a consequent decrease in the effect of nonlinearities, excitation of local modes, reduction in the test time, increased accuracy of results due to information redundancy.

It is necessary to make a distinction between *low order complete* and *large order incomplete* or truncated *models* [10.31]. Low order complete models describe the system response in terms of a reduced set of modes that are effectively observable in the frequency range of interest. The number of response locations used in the model is at most equal to this number. Large order incomplete models describe the response with many more modes (and use more response locations) than are observable. This leads to the identification of rank deficient dynamic matrices. The most obvious shortcoming of low order complete models is the loss of significance between the terms in the physical model matrices and the structural members.

In the context of multi-input methods, estimation of the model order and use of a minimum order solution is current practice. Principal component analysis (Section 9.2) is used to evaluate the rank of the measured FRF matrix. The singular value decomposition of this matrix offers an efficient order test. The trough in the graph of ratios of successive singular values helps in the selection of the number of modes of the low order complete model. Mode indicator functions (Section 9.2.6) can also be used to estimate the system order.

For heavily-damped systems, for which individual modes of vibration are not distinguishable, the frequency response is curve fitted by an FRF expressed in a rational fraction form (different from the partial fractions form), as a ratio of two frequency-dependent polynomials. Algorithms are developed for the evaluation of the polynomial coefficients [10.3]. If the considered error is simply the difference between the absolute magnitudes of the actual FRF and the polynomial ratio, minimizing the sum of the so defined errors at the experimental frequencies leads to a nonlinear least squares problem. In order to linearize the minimization problem, the above defined error is multiplied by a weighting function, usually the denominator polynomial.

10.3.6 Appropriated excitation techniques

The main objective of appropriated excitation techniques is to excite (tune) a pure undamped natural mode of a system using a set of synchronous and coherently phased forces. Mode shape vectors are determined by direct measurement of (total or quadrature) responses at phase resonances. Subsequent parameter identification is performed using either methods developed for single-degree-of-freedom systems or specific methods.

A special case of the multiple-excitation methods is referred to as *normal mode testing*. This is a form of modal test in which the excitation is multi-point and appropriated to produce a response which is directly proportional to one of the mode shapes of the structure.

In the testing phase, all the effort is to find a force distribution which cancels all modal components of the response except one, the desired modal vector. Furthermore, by measuring the variation in the response vector for the same excitation pattern, but applied at different frequencies in the vicinity of the resonance of the mode in question, the natural frequency and damping factor for that mode are extracted by simple SDOF analysis. This only really works well when the damping is proportional and the normal modes are real.

A *modal survey*, as it is sometimes referred to, can be performed by applying several exciters to a structure and driving it sinusoidally as a function of time at one of its natural frequencies (sinusoidal testing). But from a practical point of view it is difficult, if not impossible, to achieve pure resonance in a test. A pure

mode exists only if damping forces are in equilibrium with the applied forces at each point of the structure. Because in an actual structure the dissipative forces are distributed continuously throughout the structure, it is impossible to achieve a strict equilibrium between applied and damping forces everywhere in the structure using a finite number of exciters.

The conditions at resonance are given by equations (7.197) and (7.200)

$$\begin{aligned}
\left[H_R(\omega_r) \right] \{ \Xi \}_r &= \{ 0 \}, \\
-\left[H_I(\omega_r) \right] \{ \Xi \}_r &= \{ u \}_r,
\end{aligned} \tag{10.76}$$

which means that the coincident response is zero and the quadrature response is that of the normal mode shape of the excited mode.

The above conditions are true when the number of applied forces (number of exciters) is equal to the number of degrees of freedom and with the number of computed modes. However, in practical applications the number of degrees of freedom required to describe the system motion is larger then the number of exciters, which is limited to a relatively small number (maximum 24, but more commonly 4 or 6). If the number of exciters used is less than the number of degrees of freedom, the resulting response will differ from the true natural mode shapes. With this *incomplete modal excitation,* a pure mode cannot be excited even for a discrete system, because the number of exciters is not sufficient to suppress the contributions of all other modes and to cancel the damping forces. All that can be made is to obtain the *closest approximation to a normal mode*, consistent with the constraints imposed.

If an excitation

$$\{ f \} = \{ \Xi \}_r \mathrm{e}^{\mathrm{i}\omega_r t} \tag{10.77}$$

produces the quadrature response

$$\{ x \} = -\mathrm{i} \{ u \}_r \mathrm{e}^{\mathrm{i}\omega_r t}, \tag{10.78}$$

substituting (10.77) and (10.78) into the equations of motion (7.40), we obtain

$$\left([k] - \omega_r^2 [m] \right) \{ u \}_r = \{ 0 \}, \tag{10.79}$$

$$\{ \Xi \}_r = \omega_r [c] \{ u \}_r. \tag{10.80}$$

For proportional damping, equation (10.80) becomes

$$\{ \Xi \}_r = 2\zeta_r \omega_r^2 [m] \{ u \}_r,$$

where

$$\zeta_r = \frac{C_r}{2M_r \omega_r}, \qquad \omega_r^2 = \frac{K_r}{M_r},$$

so that the modal masses are given by

$$M_r = \frac{\{u\}_r^T \{\varXi\}_r}{2\zeta_r \omega_r^2} \,.$$

The numerator above is the energy introduced into the system and can be measured during the resonance test.

In order to determine the general form of the appropriated forces, able to excite a pure mode at any frequency, not only at resonance, consider the excitation vector

$$\{f\} = \{\hat{f}\}_r e^{i(\omega t + \varphi)}$$

which can produce a response

$$\{x\} = \{u\}_r e^{i\omega t} = [u]\{I\}_r e^{i\omega t},$$

where $\{I\}_r$ is the r-th column of the identity matrix.

Substituting $\{q\} = \{I\}_r e^{i\omega t}$ in (7.44) yields

$$([K] - \omega^2 [M])\{I\}_r = \{F\}\cos\varphi,$$

$$\omega[C]\{I\}_r = \{F\}\sin\varphi,$$

or

$$(\omega_r^2 - \omega^2)[u]^T[m]\{u\}_r = [u]^T\{f'\},$$

$$\omega[u]^T[c]\{u\}_r = [u]^T\{f''\},$$

where the real and imaginary components of the general force vector are

$$(\omega_r^2 - \omega^2)[m]\{u\}_r = \{f'\},$$

$$\omega[c]\{u\}_r = \{f''\}.$$

The in-phase component $\{f'\}$ balances the elastic and inertia forces, while the quadrature component $\{f''\}$ balances the damping forces.

It turns out that, in order to excite a structure in a real pure undamped normal mode of vibration, the vector of excitation forces should have the form

$$\{f\} = \{f' + i f''\}e^{i\omega t} = \left[(\omega_r^2 - \omega^2)[m] + i\omega[c]\right]\{u\}_r e^{i\omega t},$$

where the ratio between the coincident and quadrature components is frequency-dependent.

As the above distribution is hardly achievable, the solution is to use a real excitation vector, i.e. forces in phase with each other, of amplitudes

$$\{ \varXi \}_r = \sqrt{ \left(1 - \frac{\omega^2}{\omega_r^2} \right)^2 + \left(2\zeta_r \frac{\omega}{\omega_r} \right)^2 } \; \omega_r^2 \left[m \right] \{ u \}_r . \qquad (10.81)$$

This means that the appropriated forces should be proportional to the inertia forces corresponding to the modal displacements.

Undamped modes can be tuned by sinusoidal dwells or sweeps [10.32].

Tuned-dwell methods are experimental iterative processes that either minimize phase lags between discrete points along the tested structure or monitor the peaks and zeroes of real and imaginary components of response. They require rather complicated and expensive test equipment, being based on various strategies of adjusting force ratios, with the possibility of overlooking modes and limitations in the case of nonproportionally damped structures. Sine-dwell methods are inadequate for analyzing systems with very close natural frequencies. Their results are dependent on operator skill and experience.

Tuned-sweep methods combine the advantages of multi-driver tuning and curve-fitting techniques. Narrow-band sine sweeps are made close to the undamped natural frequencies with fixed force-amplitude distribution. Analysis of co-quad plots of the complex receptance or mobility FRFs provides good estimates of the mode shapes and the modal parameters of systems with proportional damping. The complex power method [10.33] and the complex energy admittance technique [10.34] are described in [10.3]. None of them can ensure adequate tuning. Difficulties are encountered in maintaining fixed amplitudes and phases of applied forces due to the interaction between vibrators and tested structure. Limits imposed on the excitation level and inaccessibility of key points produce untunable modes that affect the accuracy of any multi-exciter method.

Analytically aided tuning methods have been developed as well, that use information from non-appropriated excitation, even from single-vibrator tests.

In Asher's method [10.35], undamped natural frequencies are determined at the steep zero crossings of the determinant of the in-phase response matrix plotted versus frequency. Zero crossings that are not true natural frequencies can occur, mostly as a result of incomplete excitation. However, modes corresponding to these spurious frequencies exhibit large phase errors at some of the non-excited stations and can thus be readily identified. The method has been extended to rectangular FRF matrices [10.36]. The singular value decomposition of these matrices has been used to establish the system order, to locate undamped natural frequencies and to determine tuned forcing vectors and truncated normal vectors. The right singular vectors of the real part of the FRF matrix give the force distributions which minimize the singular values at the undamped natural frequencies.

Plots of eigenvalues of the real part of a square FRF matrix versus frequency permit a more accurate location of undamped natural frequencies than the determinantal plot used in the Asher method. Each curve crosses the frequency axis only once, so that modes having indefinitely close (or repeated) natural frequencies can be separated [10.37]. All modal parameters, including modal mass and damping coefficients, are calculated from data obtained by non-appropriate excitation.

If the FRF matrix is separated into the real and imaginary parts, characteristic phase lags and forced modes of excitation can be obtained by solving the generalized eigenvalue problem associated with these two matrices [10.38]. Plots of the cosine of the characteristic phase lag versus frequency allow location of undamped natural frequencies at zero crossings. The modal mass results from the slope at these points. The complete nondiagonal matrix of modal damping coefficients can be also estimated [10.39].

10.3.7 Real frequency-dependent modal characteristics

This section presents methods for the determination of normal modes, appropriated force vectors and the corresponding modal parameters, from identified frequency-dependent modal vectors, using non-appropriated harmonic excitation. All methods are based on the solution of an eigenvalue problem at a series of excitation frequencies and apply to systems with general nonproportional damping [10.40]. This implies the use of square FRF matrices. The approximations due to the use of rectangular FRF matrices are briefly mentioned.

10.3.7.1 Characteristic phase-lag modes

In section 7.4.2 it is shown that at any excitation frequency ω, there exist $r = 1,...,n$ independent monophase force distributions $\left\{ \hat{f} \right\} = \left\{ \gamma(\omega) \right\}_r$, eigenvectors of (7.189)

$$\left(\left[H_R \right] - \lambda_r \left[-H_I \right] \right) \left\{ \gamma \right\}_r = \left\{ 0 \right\}. \tag{10.82}$$

Each force vector excites a corresponding real valued monophase response mode $\left\{ \varphi(\omega) \right\}_r$ of forced vibration, given by (7.192)

$$\left\{ \varphi \right\}_r = \mathrm{e}^{\mathrm{i}\theta_r} \left[H \right] \left\{ \gamma \right\}_r, \tag{10.83}$$

in which all points of the system vibrate in phase with one another, at a characteristic phase lag $\theta_r(\omega)$ with respect to the excitation.

The eigenvalues in (10.82) are given by

$$\lambda_r = \tan^{-1}\theta_r = \frac{\{\gamma\}_r^T [H_R]\{\gamma\}_r}{\{\gamma\}_r^T [-H_I]\{\gamma\}_r} .$$

(10.84)

At an undamped natural frequency, when $\omega = \omega_r$, the r-th eigenvalue $\lambda_r(\omega_r) = 0$, the r-th characteristic phase lag $\theta_r(\omega_r) = 90^0$, the r-th response modal vector becomes the r-th normal undamped mode $\{\varphi(\omega_r)\}_r \equiv \{u\}_r$ and the r-th excitation modal vector becomes the forcing vector appropriated to the r-th natural mode $\{\gamma(\omega_r)\}_r \equiv \{\varXi\}_r$.

The graphs of $\lambda_r(\omega)$, $\cos\theta_r(\omega)$, $\sin\theta_r(\omega)$, and $\theta_r(\omega)$ can be used for extraction of modal parameters. Undamped natural frequencies are located at the zero crossings of the diagrams $\lambda_r(\omega)$, $\cos\theta_r(\omega)$, and $\theta_r(\omega)$.

Modal masses M_r of normal modes (7.19) are proportional to the slopes at the zero crossing points

$$M_r = -\frac{1}{2\omega_r}\left(\frac{d\lambda_r}{d\omega}\right)_{\omega_r} = \frac{1}{2\omega_r}\left(\frac{d\theta_r}{d\omega}\right)_{\omega_r} = \frac{1}{2\omega_r}\left(\frac{d\cos\theta_r}{d\omega}\right)_{\omega_r} .$$

(10.85)

The diagonal modal damping coefficients are given by

$$C_{rr} = \frac{1}{\omega_r}\{u\}_r^T\{\varXi\}_r = \frac{1}{\omega_r Q_r(\omega_r)} ,$$

(10.86)

where Q_r is a frequency-dependent scale factor.

The appropriated force vectors $\{\varXi\}_r$ are the latent vectors of the coincident FRF matrix evaluated at the respective natural frequency (10.76)

$$[H_R(\omega_r)]\{\varXi\}_r = \{0\}.$$

(10.87)

The normal vectors $\{u\}_r$ are given by (7.200)

$$\{u\}_r = -[H_I(\omega_r)]\{\varXi\}_r ,$$

(10.88)

where (10.80)

$$\{\varXi\}_r = \omega_r[c]\{u\}_r .$$

The non-diagonal damping coefficients C_{sr} are obtained from

$$C_{sr} = \frac{1}{\omega_r}\{u\}_s^T\{\varXi\}_r .$$

(10.89)

The identification methodology consists of the following steps:

1. Using matrices $[H_R(\omega)]$ and $[H_I(\omega)]$, measured at discrete values of the forcing frequency ω, the eigenvalue problem (10.82) is solved for each ω, yielding $\lambda_r(\omega)$, $\theta_r(\omega)$, and $\{\gamma\}_r$ for $r = 1,...,n$.

2. The response modal vectors $\{\varphi\}_r$ are calculated from equation (10.83) for $r = 1,...,n$.

3. The graphs of the following functions are plotted versus frequency: $\lambda_r(\omega)$, $\cos\theta_r(\omega)$, $\sin\theta_r(\omega)$, $\theta_r(\omega)$.

4. The undamped natural frequencies are determined at the zero crossings of the diagrams $\lambda_r(\omega)$ or $\cos\theta_r(\omega)$.

5. The slope of each curve $\lambda_r(\omega)$ is measured and the modal masses M_r are calculated from equations (10.85) and the diagonal modal damping coefficients C_{rr} from (10.86).

6. The matrices $[H_R(\omega_r)]$ and $[H_I(\omega_r)]$ are calculated by interpolation, based on existing experimental data or from a new series of measurements at ω_r $r = 1,...,n$.

7. The vectors $\{\varXi\}_r = \{\gamma(\omega_r)\}_r$ and $\{u\}_r = \{\varphi(\omega_r)\}_r$ are calculated from (10.87) and (10.88), then the non-diagonal modal damping coefficients are obtained from (10.89).

Note that the above procedure applies for square FRF matrices only, i.e. when the number of excitation points is equal to the number of response measurement points and to the number of active modes of vibration in the frequency range of interest.

Since $\{\varphi\}_r$ are unit vectors, the amplitude information in the spectral decomposition of $[H]$ (7.173) is contained in the scaling factors $Q_r(\omega)$ of the modal receptance matrix $\lfloor h \rceil = \lfloor Q e^{-i\theta} \rceil$. Each entry represents an enhanced FRF

$$h_r = Q_r e^{-i\theta_r} = Q_r^2 \{\gamma\}_r^T [H] \{\gamma\}_r \qquad (10.90)$$

due to the filtering effect of $\{\gamma\}_r$.

The functions $h_r(\omega)$ are called *Spatially Filtered Receptances* (SFR). Modal parameters of normal modes can be determined from the SFR plots, in the vicinity of UNFs, using SDOF curve fit formulae [10.41]. Since the response modal vectors $\{\varphi\}_r$ are not mutually orthogonal, the *r*-th mode in the function $h_r(\omega)$ is not completely decoupled.

Example 10.4

The 10 degree-of-freedom system shown in Fig. 10.25 [10.42], represented by the masses and stiffnesses listed in Table 3, is considered to illustrate the method. The system is grounded at spring #1. Viscous damping coefficients are equal to 0.002 of the stiffness values.
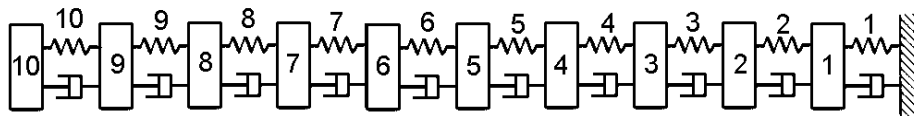

Fig. 10.25

FRFs were computed at 1024 frequencies between 0 and 10 Hz for the 10×10 elements of the FRF matrix. An additive uniformly distributed random noise of 5% of the mean magnitude of the FRF matrix was added to each FRF.

Table 10.3. Physical parameters of the 10-DOF system

DOF	1	2	3	4	5	6	7	8	9	10
m	4.00	3.61	3.24	2.89	2.56	2.25	1.96	1.69	1.44	1.21
k	2000	1900	1800	1700	1600	1500	1400	1300	1200	1100

Simulation started by selecting points 1, 8 and 10 as input and response measurement points. This is an arbitrary selection. Best location by the Improved Reduction System method [10.43] is at points 2, 6, 10, while location by the Effective Independence method [10.44] is at points 3, 6, 10. A monophase analysis of the 3×3 FRF matrix for DOFs 1, 8 and 10 has been carried out at each of the 1024 frequencies.
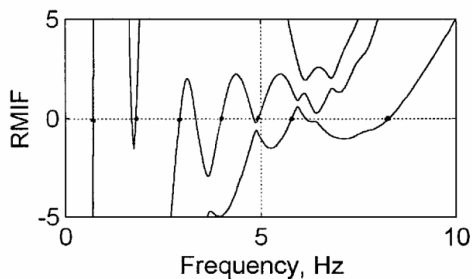

Fig. 10.26
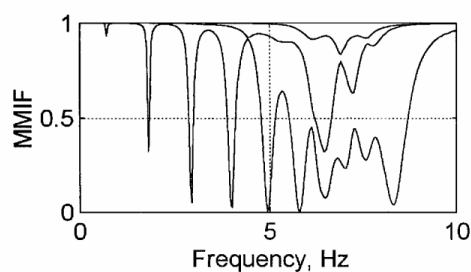
Fig. 10.27

The RMIF plot ($RMIF = -\lambda_r$) is shown in Fig. 10.26. Each of the three curves crosses several times the frequency axis, locating some of the UNFs. Thus λ_1 locates f_1 and f_2, λ_2 locates f_3, f_4 and f_5, while λ_3 locates f_6 and f_{10}. For comparison, the MMIF plot is given in Fig. 10.27.

Undamped natural frequencies (UNF) located by RMIF are compared to analytical FEM values in Table 10.4. Note that only the first three values are of interest for this part of analysis.

Table 10.4. Undamped natural frequencies of the 10-DOF system

Mode	1	2	3	4	5	6	10
Undamped natural frequency, Hz							
Analytical	0.7183	1.8192	2.9272	3.9799	4.9444	5.7937	8.3504
RMIF	0.7184	1.8174	2.9309	3.9844	4.9423	5.7807	8.2534

The plot of $\sin\theta_r$ vs. frequency is shown in Fig. 10.28. Comparison with the MMIF reveals some fake troughs so that it cannot be used as a mode indicator. This feature is due to the model incompleteness. For complete models, the number of curves equals the model order. Each curve has only one peak at the corresponding UNF.
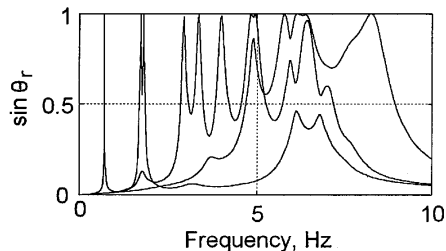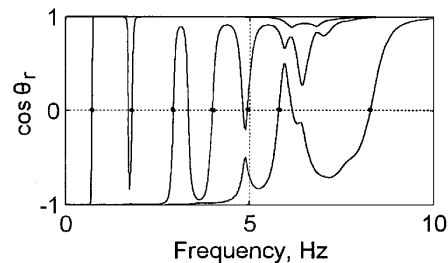
Fig. 10.28   Fig. 10.29

The $\cos\theta_r$ plot is shown in Fig. 10.29. Crossings of frequency axis with positive slope correspond to UNFs. Crossing points with negative slope correspond to peaks in the $\sin\theta_r$ plot that do not indicate UNFs. Again, this feature is due to the incompleteness of the reduced model. Instead of crossing only once the frequency axis, at the corresponding UNF, each curve has to cross several times the frequency axis to locate more than one UNF, so that fake crossings with negative slope appear.

The frequency dependence of the elements of the 'phi' vectors $\{\varphi\}_r$ is shown in Fig. 10.30 and that of the 'gamma' vectors $\{\gamma\}_r$ - in Fig. 10.31. Note that, even for a system with proportional damping, monophase modes of

incomplete models are frequency dependent. This contrasts with complete models, that exhibit frequency independent mode shapes in the case of proportional damping (Section 7.4.3).

At UNFs, gamma-vectors become the appropriated force distributions $\{\varXi\}_r$ able to isolate the corresponding normal mode.

At UNFs, phi-vectors become the real normal modes. Thus

$$\{\varphi(\omega_1)\}_1 = \{u\}_1, \quad \{\varphi(\omega_2)\}_1 = \{u\}_2, \quad \{\varphi(\omega_3)\}_2 = \{u\}_3, \quad \{\varphi(\omega_4)\}_2 = \{u\}_4,$$

$$\{\varphi(\omega_5)\}_3 = \{u\}_5, \quad \{\varphi(\omega_6)\}_3 = \{u\}_6, \quad \ldots\ldots$$

While $\{u\}_1$, $\{u\}_2$ and $\{u\}_3$ are 'exact', the others are approximations. The number of 'exact' mode shapes is equal to the number of input points.
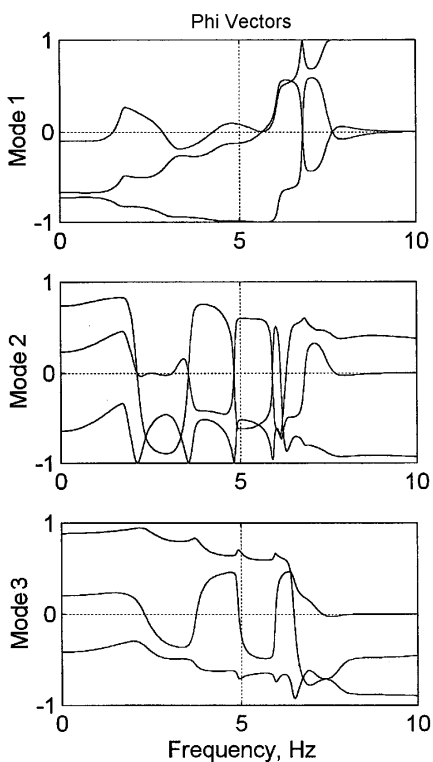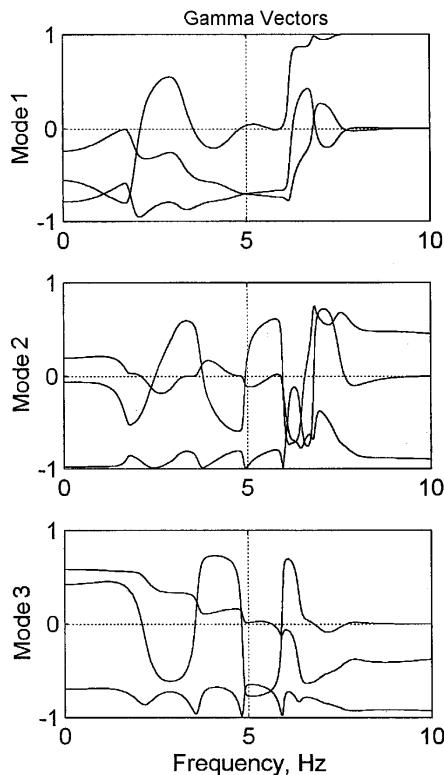
Fig. 10.30   Fig. 10.31

If six response measurement points are selected at locations 1, 3, 4, 6, 8, 10 and only three input points are chosen at locations 1, 8, 10, i.e. a subset of the output points, then a rectangular FRF matrix is obtained. In this case, six-element

phi-vectors result from equation (10.83), offering better spatial resolution. They can be used to obtain better estimates of the normal modes.

The MMIF plot from Fig. 10.27 corresponds to this selection of excitation and response measurement locations.

Once the excitation modal vectors are obtained, they can be used to enhance a response mode shape on a measured FRF by spatial filtering. Plots of the three spatially filtered receptances or modal receptances h_r are shown in Figs. 10.32 to 10.36. It can be seen that several modes are observable in each SRF.

Each SRF magnitude curve exhibits more than one peak. Only peaks corresponding to zero crossings in the RMIF plot can be analyzed to obtain estimates for the damping ratio and modal mass of normal modes.
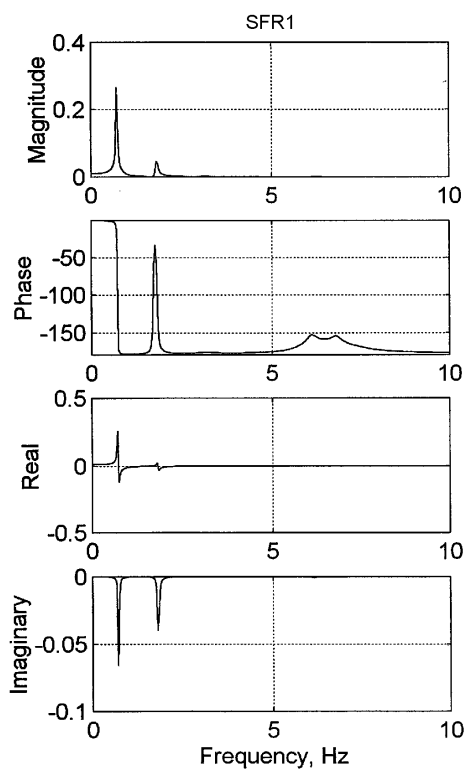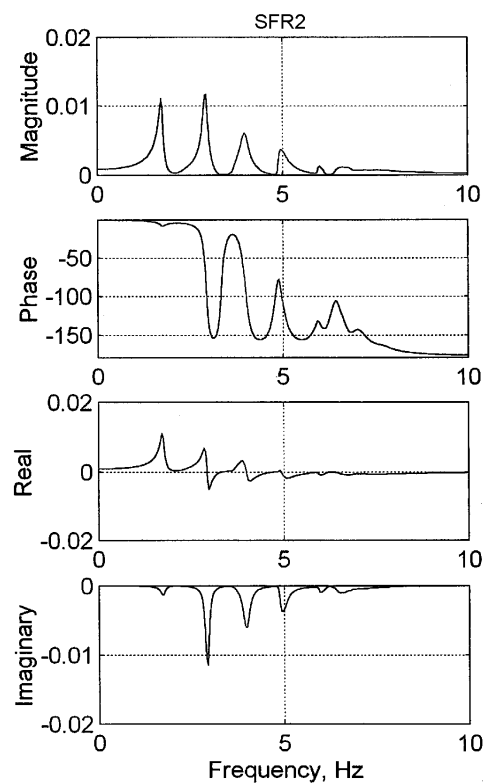
Fig. 10.32   Fig. 10.33

Modal damping ratios computed by SDOF circle fit methods are compared to analytical FEM values in Table 10.5. Values determined based on the slope of the RMIF curves at the points of frequency axis crossing (Section 9.3.2.4) are also presented.

Table 10.5. Modal damping ratios of the 10-DOF system

Mode	1	2	3	4	5	6	10
Damping ratio,%							
FEM	0.451	1.143	1.839	2.501	3.107	3.640	5.247
SDOF circle fit	0.451	1.142	1.837	2.496	3.102	3.633	5.193
RMIF slope	0.449	1.145	1.843	2.515	3.121	3.722	5.362

Single DOF analysis of SFR loops gives better results. Again, only the first three modes are relevant for the discussion, but fairly good estimates have also been obtained for other four modes.
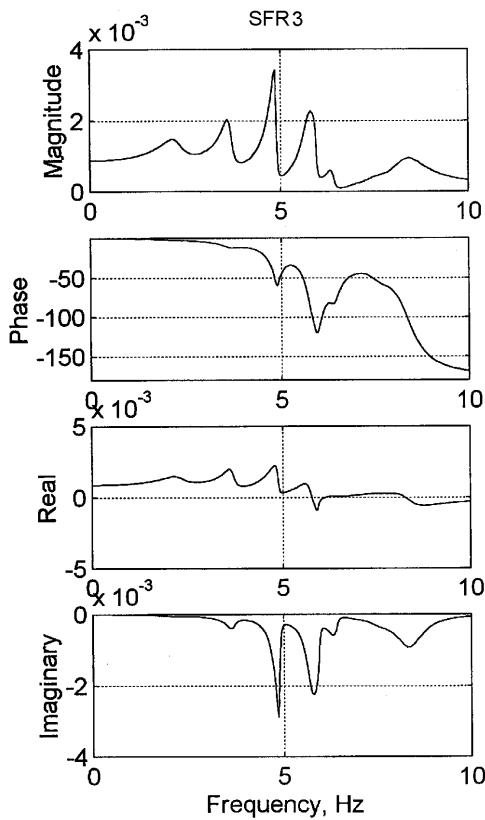
Fig. 10.34
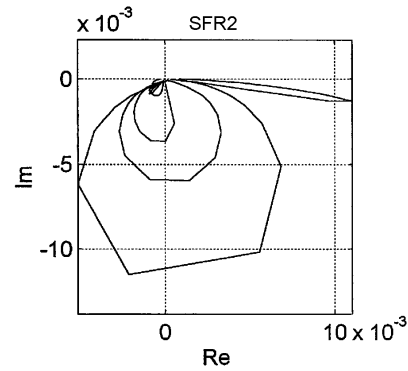
Fig. 10.35
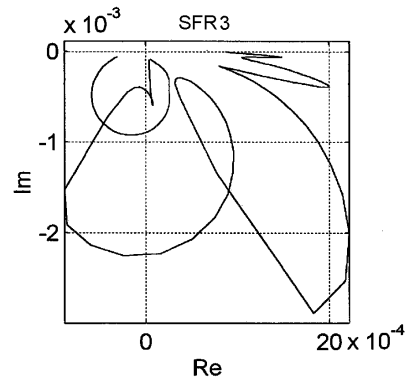
Fig. 10.36

Nyquist plots of SFRs have almost circular loops for the modes that can be analyzed using SDOF parameter estimation methods. Figure 10.35 shows the second SFR with circular loops for modes 3 and 4. Figure 10.36 is the Nyquist plot for the third SRF and has circular loops for modes 6 and 10.

10.3.7.2 Best monophase modal vectors

As mentioned in Section 9.3, test derived FRF matrices are usually rectangular, with the number of rows (response measurement coordinates), N_o, much larger than the number of columns (excitation coordinates), N_i. In equation (7.174)

$$\{\tilde{x}\} = \left[H(\mathrm{i}\omega) \right]\{\hat{f}\}, \tag{10.91}$$

$\left[H(\mathrm{i}\omega) \right]$ is an $N_o \times N_i$ matrix.

The monophase condition (7.182)

$$\{x_R\} = -\lambda\{x_I\}, \tag{10.92}$$

leads to the spectral problem of a rectangular matrix pencil

$$\left[H_R \right]\{\hat{f}\} = \lambda\left[-H_I \right]\{\hat{f}\} \tag{10.93}$$

in which the number of equations, N_o, is larger than the number of unknowns, N_i.

The (approximate) solution of (10.93) implies finding the force distribution that can produce the closest approximation to a monophase response vector, for the given number and location of excitation coordinates.

Provided that $\cos\theta \neq 0$, this can be obtained from the eigenproblem

$$\left[C \right]\{\hat{f}\}_r = \lambda_r\left[-B \right]\{\hat{f}\}_r, \tag{10.94}$$

where the square matrices

$$\left[C \right] = \left[H_I \right]^T\left[H_R \right], \qquad \left[B \right] = \left[H_I \right]^T\left[H_I \right]. \tag{10.95}$$

The characteristic phase-lag theory presented in Section 7.4.2 can be formally reformulated replacing $\left[H_R \right]$ by $\left[C \right]$, and $\left[H_I \right]$ by $\left[B \right]$.

The force vector $\{\hat{f}\}_r$ gives rise to a response

$$\{\tilde{x}\} = \{\hat{x}\}\mathrm{e}^{-\mathrm{i}\theta_r} = \left[H \right]\{\hat{f}\}_r. \tag{10.96}$$

Premultiplying by $\left[H_I \right]^T$ we obtain

$$\left[H_I \right]^T\{\hat{x}\}\mathrm{e}^{-\mathrm{i}\theta_r} = \left(\left[C \right] + \mathrm{i}\left[B \right]\right)\{\hat{f}\}_r =$$

$$= \left(-\lambda_r + \mathrm{i}\right)\left[B \right]\{\hat{f}\}_r = -\sqrt{1 + \lambda_r^2}\left[B \right]\{\hat{f}\}_r\mathrm{e}^{-\mathrm{i}\theta_r}$$

or

$$\left[H_I \right]^T\{\hat{x}\} = -\sqrt{1 + \lambda_r^2}\left[B \right]\{\hat{f}\}_r. \tag{10.97}$$

If rank $[H_I]^T = N_i$, then the smallest norm solution of (10.97) is

$$\{\hat{x}\}_r = -\sqrt{1 + \lambda_r^2}\, [H_I]\{\hat{f}\}_r,$$ (10.98)

which is the 'best' response vector.

For $\cos\theta_r = 0$,

$$[C(\omega_r)]\{\Xi\}_r = \{0\}.$$ (10.99)

The condition

$$\det[C(\omega_r)] = 0,$$

or

$$\det\left([H_I(\omega_r)]^T [H_R(\omega_r)]\right) = 0$$ (10.100)

gives the undamped natural frequencies (extended Asher's method [10.36]).

10.3.7.3 Eigenvectors of the coincident FRF matrix

A simpler modal parameter extraction method [10.37] is based on the eigenvalue problem of the real part of the FRF matrix

$$[H_R(\omega)]\{v\}_r = \mu_r\{v\}_r. \qquad (r = 1,...,n)$$ (10.101)

If the system is acted upon by the monophase force distribution $\{v\}_r e^{i\omega t}$, the eigenvalue $\mu_r(\omega)$ is a measure of the reactive energy transmitted to the system. This energy cancels at the undamped natural frequency ω_r.

The forcing vectors $\{v\}_r$ satisfy the orthogonality conditions

$$\begin{aligned} \{v\}_r^T\{v\}_s &= 0, \\ \{v\}_r^T[H_R(\omega)]\{v\}_s &= 0. \end{aligned} \qquad r \neq s$$ (10.102)

Solving equation (10.101) at discrete values ω, for which $[H_R(\omega)]$ is measured, and plotting the eigenvalues μ_r against frequency, the undamped natural frequencies ω_r can be located at the zero crossings, $\mu_r(\omega_r) = 0$.

For $\omega = \omega_r$ equation (10.101) becomes identical with equation (7.197). Thus $\{v(\omega_r)\}_r \equiv \{\Xi\}_r$ is the tuned forcing vector that can isolate the normal mode $\{u\}_r$ at ω_r. The latter is obtained from (7.200)

$$[H_I(\omega_r)]\{\Xi\}_r = -\rho_r\{u\}_r,$$ (10.103)

where ρ_r is a frequency-dependent scale factor.

Because the determinant is equal to the product of eigenvalues

$$\det\left[H_R(\omega)\right]=\prod_{r=1}^{N}\mu_r(\omega),\qquad(10.104)$$

it follows that

$$\det\left[H_R(\omega_r)\right]=0.\qquad(10.105)$$

This is the basis of Asher's method [10.35].

Denote

$$\bar{\beta}_r(\omega)=\{v\}_r^T\left[H_R(\omega)\right]\{v\}_r=\mu_r\{v\}_r^T\{v\}_r,$$
$$\bar{\alpha}_r(\omega)=-\{v\}_r^T\left[H_I(\omega)\right]\{v\}_r,\qquad(10.106)$$

to obtain

$$\bar{\beta}_r(\omega_r)=0\,,$$

$$\left(\frac{\mathrm{d}\bar{\beta}_r}{\mathrm{d}\omega}\right)_{\omega_r}=-2\rho_r^2\omega_r M_r=\{\varXi\}_r^T\{\varXi\}\left(\frac{\mathrm{d}\mu_r}{\mathrm{d}\omega}\right)_{\omega_r},\qquad(10.107)$$

$$\bar{\alpha}_r(\omega_r)=\rho_r^2\omega_r C_{rr}.$$

Values for M_r and C_{rr} can be obtained from the above equations.

The quadratic forms in equations (10.106) are proportional to the reactive and respectively the active energy transmitted to the system.

If vectors $\{\varXi\}_r$ are orthonormalized, the modal masses of normal modes given by

$$M_r=-\frac{1}{2\rho_r^2\omega_r}\left(\frac{\mathrm{d}\mu_r}{\mathrm{d}\omega}\right)_{\omega_r},\qquad(10.108)$$

are proportional to the slope of the diagram $\mu_r(\omega)$ at the points of frequency axis crossing. Non-diagonal modal damping coefficients are given by

$$C_{rs}=\frac{1}{\rho_r\omega_r}\{u\}_s^T\{\varXi\}_r.\qquad(10.109)$$

Generally, the modal damping coefficients are given by

$$C_{rs}=\frac{1}{\omega_r}\{u\}_s^T\left[Z_I(\omega_r)\right]\{u\}_r,\qquad(10.110)$$

where the matrix $\left[Z_I(\omega)\right]$ can be calculated from measured data (7.179)

$$\left[Z_I(\omega)\right] = -\left[H^*(\omega)\right]^{-1}\left[H_I(\omega)\right]\left[H(\omega)\right]^{-1}. \tag{10.111}$$

The characteristic eigenvalue plots permit a more accurate location of the UNFs than the determinantal plot used in Asher's method. The technique can be used to separate vibration modes with closely spaced UNFs and can identify modes with overcritical damping. The main drawback is the requirement to determine, in a preliminary stage, the order of the system and to use square FRF matrices.

Example 10.5

Consider the two-degree-of-freedom system with nonproportional damping from Fig. 10.37, *a,* with the following parameters: $m_1 = 10\,\text{kg}$, $m_2 = 1\,\text{kg}$, $k_1 = 10^7\,\text{N/m}$, $k_2 = 10^6\,\text{N/m}$, $c_1 = c_2 = 500\,\text{Ns/m}$.
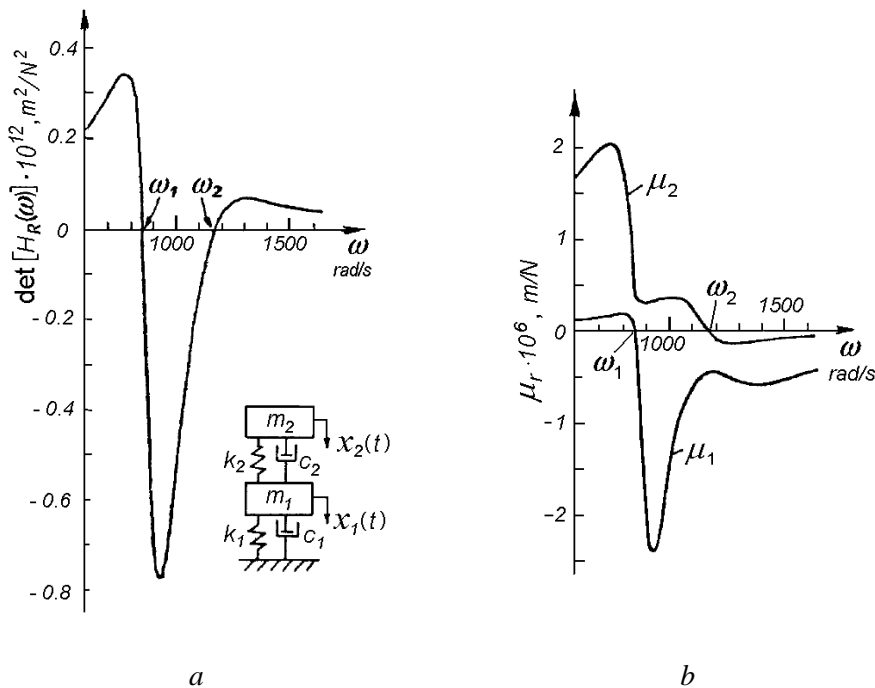
Fig. 10.37 (from [10.45])

First, the polar diagrams of the complex receptances were plotted based on analytically derived expressions of the FRFs polluted with 5% additive noise. The subsequent calculations were performed considering these as experimentally generated plots. The graph of $\det\left[H_R(\omega)\right]$ as a function of frequency is shown in Fig. 10.37, *a*. The eigenvalues of the matrix $\left[H_R(\omega)\right]$ are plotted as a function of

frequency in Fig. 10.37, *b*. The undamped natural frequencies are located at the zero crossings of this plot.

Table 10.6 shows a comparison of the values of modal characteristics determined solving the equations of motion and those estimated from the polar plots using the above presented method [10.45].

Table 10.6. Modal parameters of 2-DOF system from Fig. 10.37

Quantity	Values determined solving the equations of motion		Values estimated from the polar plots	
	Mode 1	Mode 2	Mode 1	Mode 2
ω_r	854.309	1170.5367	854.3	1170.0
$\{\varXi\}_r$	$\left\{\begin{matrix} 1 \\ -1.5877 \end{matrix}\right\}$	$\left\{\begin{matrix} 1 \\ -0.7873 \end{matrix}\right\}$	$\left\{\begin{matrix} 1 \\ -1.58768 \end{matrix}\right\}$	$\left\{\begin{matrix} 1 \\ -0.7873 \end{matrix}\right\}$
$1/\rho_r$	$-1.3758 \cdot 10^{-6}$	$0.3634 \cdot 10^{-6}$	$-1.374 \cdot 10^{-6}$	$0.391 \cdot 10^{-6}$
$\{u\}_r$	$\left\{\begin{matrix} 1 \\ 3.7015 \end{matrix}\right\}$	$\left\{\begin{matrix} 1 \\ -2.701 \end{matrix}\right\}$	$\left\{\begin{matrix} 1 \\ 3.7016 \end{matrix}\right\}$	$\left\{\begin{matrix} 1 \\ -2.7215 \end{matrix}\right\}$
$\left\| \dfrac{\mathrm{d}\mu_r}{\mathrm{d}\omega} \right\|_{\omega_r}$	$-21.77 \cdot 10^{-9}$	$-3.3 \cdot 10^{-9}$	$-22.24 \cdot 10^{-9}$	$-3.314 \cdot 10^{-9}$
M_r	23.701	17.298	21.562	16.341
$\begin{bmatrix} C_{11} & C_{12} \\ C_{21} & C_{22} \end{bmatrix}$	$\begin{bmatrix} 41492 & -4500 \\ -4500 & 735078 \end{bmatrix}$		$\begin{bmatrix} 41548 & -4533 \\ -4533 & 68696 \end{bmatrix}$	

Example 10.6

Consider the two-degree-of-freedom system from Fig. 10.38.
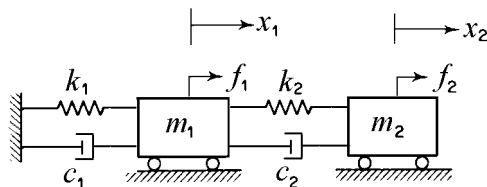
Fig. 10.38

The physical parameters are given in Table 10.7 for the following four cases: Case I: lightly damped system with relatively separated natural frequencies; Case II: lightly damped system with closely spaced natural frequencies; Case III: highly damped system with relatively separated natural frequencies; Case IV: highly damped system with closely spaced natural frequencies.

Table 10.7. Physical parameters of 2-DOF systems in Example 10.6

Case		I	II	III	IV
$m_1 = m_2$	kg	0.0259	0.0259	0.0259	0.0259
$k_1 = k_3$	N/m	100	100	100	100
k_2	N/m	50	1	50	1
c_1	Ns/m	0.3	0.3	3	3
c_2	Ns/m	0.2	0.2	2	2
c_3	Ns/m	0.1	0.1	1	1

Draw the plots of the determinant and the eigenvalues of the coincident receptance matrix versus frequency, for the four systems, and estimate the modal parameters based on these diagrams.

The Nyquist plots of the receptance FRFs are shown in Fig. 4.40. Analytical expressions of the modal parameters are given in Example 4.15.
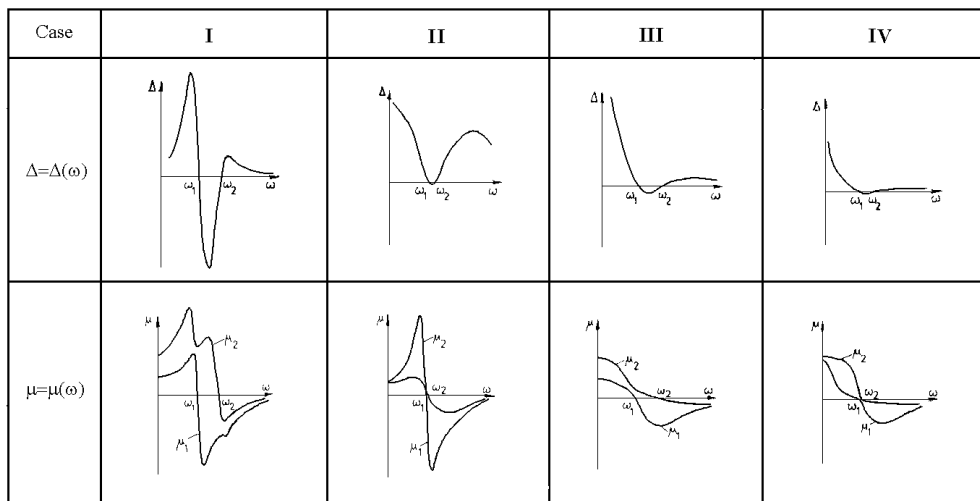
Fig. 10.39

The diagrams are shown in Fig. 10.39. The undamped natural frequencies are located at the crossings with the frequency axis. The coincident-response determinant plot has a single curve, making difficult the accurate location of close natural frequencies. In the plot of the eigenvalues of the coincident response matrix, each curve crosses only once the frequency axis, at the corresponding natural frequency. This enables a more accurate location of undamped natural frequencies, but applies only to square FRF matrices, when the number of output points is equal to the number of input points, which is hardly to achieve in a test.

The numerical values of the quantities derived from the determinantal and eigenvalue curves, as well as the modal parameters are given in Table 10.8.

Table 10.8. Modal parameters of 2-DOF systems in Example 10.6

Case		I		II	
$10^6 \left.\dfrac{d\Delta}{d\omega}\right\|_{\omega_1}$	$10^6 \left.\dfrac{d\Delta}{d\omega}\right\|_{\omega_2}$	-0.164	0.0455	-35.59	33.65
$10^6 \left.\dfrac{d\mu_1}{d\omega}\right\|_{\omega_1}$	$10^6 \left.\dfrac{d\mu_2}{d\omega}\right\|_{\omega_1}$	-166.8	-15.94	-16679	-2232
ω_1	ω_2	62.24	87.69	62.16	62.71
$\{\Xi\}_1$	$\{\Xi\}_2$	$\left\{\begin{matrix}1\\0.33\end{matrix}\right\}$	$\left\{\begin{matrix}1\\-0.71\end{matrix}\right\}$	$\left\{\begin{matrix}1\\0.33\end{matrix}\right\}$	$\left\{\begin{matrix}1\\-0.71\end{matrix}\right\}$
$\rho_1 \cdot 10^3$	$\rho_2 \cdot 10^3$	53.65	16.26	53.65	22.77
$\{u\}_1$	$\{u\}_2$	$\left\{\begin{matrix}1\\1\end{matrix}\right\}$	$\left\{\begin{matrix}1\\-1\end{matrix}\right\}$	$\left\{\begin{matrix}1\\1\end{matrix}\right\}$	$\left\{\begin{matrix}1\\-1\end{matrix}\right\}$
M_1	M_2	0.0518	0.0518	0.0518	0.0518
K_1	K_2	200	400	200	204
ζ_1	ζ_2	0.062	0.132	0.055	0.192
Case		III		IV	
$10^6 \left.\dfrac{d\Delta}{d\omega}\right\|_{\omega_1}$	$10^6 \left.\dfrac{d\Delta}{d\omega}\right\|_{\omega_2}$	-186.7	15.97	-0.00357	0.00346
$10^6 \left.\dfrac{d\mu_1}{d\omega}\right\|_{\omega_1}$	$10^6 \left.\dfrac{d\mu_2}{d\omega}\right\|_{\omega_1}$	-16679	-1594	-166.8	-22.32
ω_1	ω_2	64.28	84.92	62.16	62.71
$\{\Xi\}_1$	$\{\Xi\}_2$	$\left\{\begin{matrix}1\\0.33\end{matrix}\right\}$	$\left\{\begin{matrix}1\\-0.71\end{matrix}\right\}$	$\left\{\begin{matrix}1\\0.33\end{matrix}\right\}$	$\left\{\begin{matrix}1\\-0.71\end{matrix}\right\}$
$\rho_1 \cdot 10^3$	$\rho_2 \cdot 10^3$	5.365	1.626	5.365	2.277
$\{u\}_1$	$\{u\}_2$	$\left\{\begin{matrix}1\\1\end{matrix}\right\}$	$\left\{\begin{matrix}1\\-1\end{matrix}\right\}$	$\left\{\begin{matrix}1\\1\end{matrix}\right\}$	$\left\{\begin{matrix}1\\-1\end{matrix}\right\}$
M_1	M_2	0.0518	0.0518	0.0518	0.0518
K_1	K_2	200	400	200	204
ζ_1	ζ_2	0.540	1.409	0.547	1.919

Example 10.7

Consider the two-degree-of-freedom system with nonproportional damping from Fig. 10.38, with the following parameters: $m_1 = 100\,\text{kg}$, $m_2 = 1\,\text{kg}$, $k_1 = 9.9 \cdot 10^6\,\text{N/m}$, $k_2 = 0.1 \cdot 10^6\,\text{N/m}$, $c_1 = c_2 = 125\,\text{Ns/m}$.
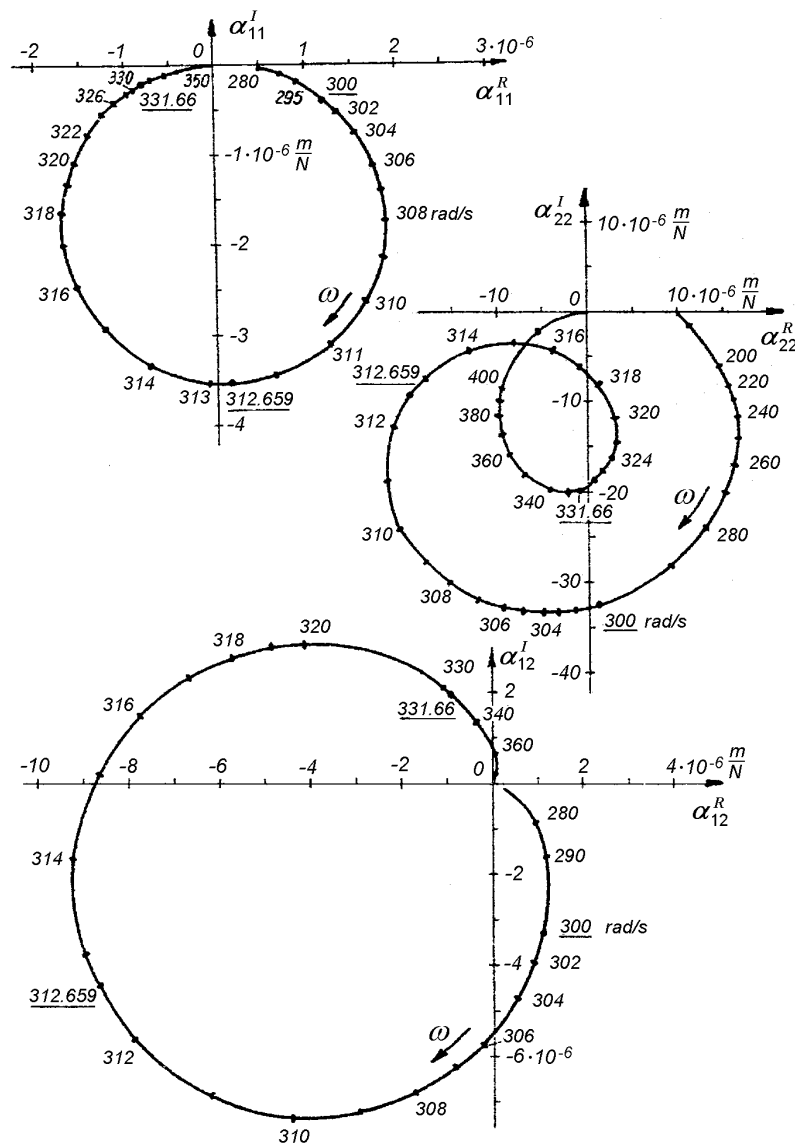

Fig. 10.40

First, the Nyquist plots of complex receptances are plotted point by point (Fig. 10.40) based on the analytical expressions. The subsequent calculations are performed considering these as noise-free experimentally generated plots. Next, the eigenvalues of the matrix $\left[H_R(\omega) \right]$ are plotted as a function of frequency as in Fig. 10.41. At the zero crossings, the undamped natural frequencies are determined as $\omega_1 = 300 \, \text{rad/s}$ and $\omega_2 = 331.6 \, \text{rad/s}$. They are marked on the polar plots in Fig. 10.40 along with the first undamped natural frequency 312.659 rad/s.
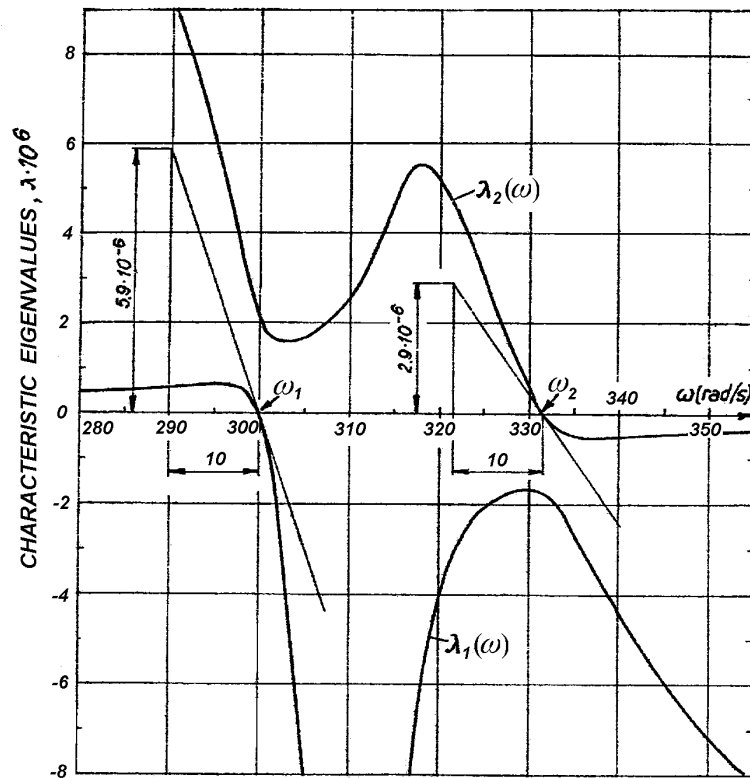
Fig. 10.41

The appropriated forcing vectors $\{ \varXi \}_r$ are determined as the latent vectors of the coincident receptance matrix calculated at the natural frequencies

$$\left[H_R(300) \right] \{ \varXi \}_1 = 10^{-6} \begin{bmatrix} 1.2 & 1.07 \\ 1.07 & 0.95 \end{bmatrix} \{ \varXi \}_1 = \begin{Bmatrix} 0 \\ 0 \end{Bmatrix}, \quad \{ \varXi \}_1 = \begin{Bmatrix} 1 \\ -1.12 \end{Bmatrix},$$

$$\left[H_R(331.6) \right] \{ \varXi \}_2 = 10^{-6} \begin{bmatrix} -0.81 & -0.9 \\ -0.9 & -1 \end{bmatrix} \{ \varXi \}_2 = \begin{Bmatrix} 0 \\ 0 \end{Bmatrix}, \quad \{ \varXi \}_2 = \begin{Bmatrix} 1 \\ -0.9 \end{Bmatrix},$$

The undamped normal modes $\{u\}_r$ and the normalization factors ρ_r in (10.103) are determined as follows

$$[H_I(300)]\{\varXi\}_1 = 10^{-6}\begin{bmatrix} -0.4 & -3.3 \\ -3.3 & -32.5 \end{bmatrix}\begin{Bmatrix} 1 \\ -1.12 \end{Bmatrix} = 3.296 \cdot 10^{-6}\begin{Bmatrix} 1 \\ 10.04 \end{Bmatrix},$$

$$[H_I(331.6)]\{\varXi\}_2 = 10^{-6}\begin{bmatrix} -0.22 & 1.95 \\ 1.95 & -19.8 \end{bmatrix}\begin{Bmatrix} 1 \\ -0.9 \end{Bmatrix} = -1.975 \cdot 10^{-6}\begin{Bmatrix} 1 \\ -10.01 \end{Bmatrix},$$

hence

$$\rho_1 = -3.296 \cdot 10^{-6}, \quad \rho_2 = -1.975 \cdot 10^{-6}, \quad \{u\}_1 = \begin{Bmatrix} 1 \\ 10.04 \end{Bmatrix}, \quad \{u\}_2 = \begin{Bmatrix} 1 \\ -10.01 \end{Bmatrix}.$$

The slopes of the tangents to the curves from Fig. 10.41 at the points of intersection with the real axis are

$$\left(-\frac{d\mu_1}{d\omega}\right)_{\omega=300} = 0.59 \cdot 10^{-6}, \qquad \left(-\frac{d\mu_2}{d\omega}\right)_{\omega=331.6} = 0.29 \cdot 10^{-6}.$$

The modal masses are given by

$$M_r = \frac{\{\varXi\}_r^T\{\varXi\}_r}{2\rho_r^2\omega_r}\left(-\frac{d\mu_r}{d\omega}\right)_{\omega_r},$$

resulting in $M_1 = 204.06$ and $M_2 = 202.9$. The modal stiffnesses $K_r = M_r\omega_r^2$ are $K_1 = 18.365 \cdot 10^6$ and $K_2 = 22.31 \cdot 10^6$.

The modal damping matrix calculated from (10.109) is

$$[C] = 250\begin{bmatrix} 41.44 & -49.02 \\ -49.02 & 61.13 \end{bmatrix}.$$

Table 10.9 shows a comparison of the values of the true modal characteristics, determined solving the equations of motion, and those estimated from the polar plots using the above presented method. The modal damping ratios are also calculated as

$$\zeta_{rr} = \frac{C_{rr}}{2\omega_r M_r}.$$

The system has nonproportional damping. Solving the eigenvalue problem (7.88) we obtain the complex eigenvalues

$$\lambda_1 = -4.785 + i\,312.659, \qquad \lambda_2 = -58.965 + i\,312.685,$$

and the complex eigenvectors

$$\{\psi\}_1 = \begin{Bmatrix} 1 \\ 1.207 - i\,2.698 \end{Bmatrix}, \quad \{\psi\}_2 = \begin{Bmatrix} 1 \\ -8.865 - i\,35.222 \end{Bmatrix}.$$

Table 10.9. Modal parameters of 2-DOF system from Fig. 10.38.

Quantity	True values		'Measured' values	
	Mode 1	Mode 2	Mode 1	Mode 2
ω_r	300	$100\sqrt{11}$	300	331.6
$\{\Xi\}_r$	$\left\{\begin{matrix}1\\-9/8\end{matrix}\right\}$	$\left\{\begin{matrix}1\\-11/12\end{matrix}\right\}$	$\left\{\begin{matrix}1\\-1.12\end{matrix}\right\}$	$\left\{\begin{matrix}1\\-0.9\end{matrix}\right\}$
$\{u\}_r$	$\left\{\begin{matrix}1\\10\end{matrix}\right\}$	$\left\{\begin{matrix}1\\-10\end{matrix}\right\}$	$\left\{\begin{matrix}1\\10.04\end{matrix}\right\}$	$\left\{\begin{matrix}1\\-10.01\end{matrix}\right\}$
M_r	200	200	204.06	202.9
K_r	$18\cdot10^6$	$22\cdot10^6$	$18.365\cdot10^6$	$22.31\cdot10^6$
ζ_{rr}	0.08541	0.11495	0.08462	0.11357
$\begin{bmatrix}C_{11} & C_{12}\\C_{21} & C_{22}\end{bmatrix}$	$250\begin{bmatrix}41 & -49\\-49 & 61\end{bmatrix}$		$250\begin{bmatrix}41.44 & -49.02\\-49.4 & 61.13\end{bmatrix}$	

The damped natural circular frequencies

$$\sigma_1 = 312\,659\,\text{rad/s}, \qquad \sigma_2 = 312\,685\,\text{rad/s},$$

are only $0.026\,\text{rad/s}$ apart, hence the damped natural frequencies are only $0.0041\,\text{Hz}$ apart. This explains the particular shape of the Nyquist plots, without clearly separated loops, which requires specific parameter estimation techniques. In comparison, the difference between the undamped natural frequencies is $(\omega_2 - \omega_1)/2\pi = 5.039\,\text{Hz}$, which makes their location much easier.
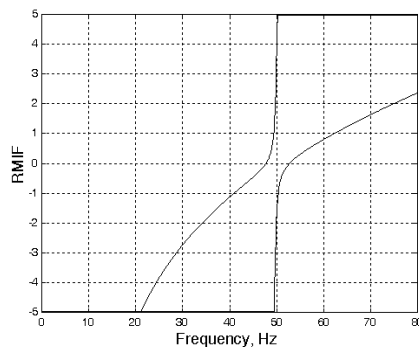
Fig. 10.42

The Real Mode Indicator Function (RMIF) is presented in Fig. 10.42. For comparison, the Multivariate Mode Indicator Function is shown in Fig. 10.43.
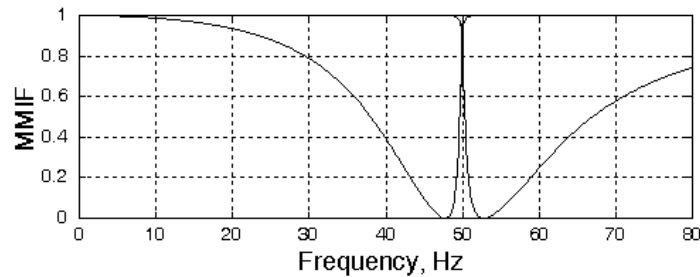
Fig. 10.43

10.4 Time domain methods

When the measurement data span a large frequency range and contain the contribution of a large number of modes, identification methods based on time domain models tend to provide the best results. However they can only estimate modes inside the range of measurements and take no account of the residual effects of the off-range modes. A detailed presentation of methods like the Complex Exponential, Least-Squares Complex Exponential, Polyreference Complex Exponential and Eigensystem Realization Algorithm is beyond the aim of this lecture course and can be found in [10.26]. In the following, only one variant of the Ibrahim Time Domain is presented and the basis of the Random Decrement technique.

10.4.1 Ibrahim time-domain method

A method for the direct identification of modal parameters from the free response is known as the Ibrahim Time Domain method [10.46].

In the early formulation, it was assumed that the number of response measurement locations N_o equals the number of degrees of freedom of the hypothetical lumped parameter system with all modes excited. This required prior knowledge of the number of equivalent degrees of freedom to be excited, in order to use the correct number of measurement locations. Later this condition was relaxed, resulting in the following identification algorithm.

The solution (7.69) of the equation of the free motion (7.68) is

$$\{x\} = \{\psi\} e^{\lambda t}, \tag{10.112}$$

so that (7.70)

$$\left(\lambda^2 [m] + \lambda [c] + [k] \right) \{\psi\} = \{0\}. \qquad (10.113)$$

The problem of modal testing is to determine, from the test data, the values of λ and $\{\psi\}$ which satisfy equation (10.113).

The measured free responses at N_o locations on a structure under test can be written as

$$\{x\} = \sum_{r=1}^{2n} \{\psi\}_r \, e^{\lambda_r t} . \qquad (10.114)$$

The response at time t_i is

$$\{x(t_i)\} = \{x\}_i = \sum_{r=1}^{2n} \{\psi\}_r \, e^{\lambda_r t_i} = \left[\{\psi\}_1 \ \{\psi\}_2 \ \cdots \ \{\psi\}_{2n} \right] \begin{Bmatrix} e^{\lambda_1 t_i} \\ \vdots \\ e^{\lambda_{2n} t_i} \end{Bmatrix}. \qquad (10.115)$$

The response vectors measured at N_t different instances of time can be written as

$$\left[\{x\}_1 \ \{x\}_2 \ \cdots \ \{x\}_{N_t} \right] = \left[\{\psi\}_1 \ \{\psi\}_2 \ \cdots \ \{\psi\}_{2n} \right] \begin{bmatrix} e^{\lambda_1 t_1} & e^{\lambda_1 t_2} & \cdots & e^{\lambda_1 t_{N_t}} \\ e^{\lambda_2 t_1} & e^{\lambda_2 t_2} & \cdots & e^{\lambda_2 t_{N_t}} \\ \vdots & \vdots & & \vdots \\ e^{\lambda_{2n} t_1} & e^{\lambda_{2n} t_2} & \cdots & e^{\lambda_{2n} t_{N_t}} \end{bmatrix}$$

$$(10.116)$$

or

$$[X] = [\psi][\Lambda]. \qquad (10.117)$$

Responses that occur at time Δt later with respect to those of equation (10.117) are

$$\left[\{\hat{x}\}_1 \ \{\hat{x}\}_2 \ \cdots \ \{\hat{x}\}_{N_t} \right] = \left[\{\psi\}_1 \ \{\psi\}_2 \ \cdots \ \{\psi\}_{2n} \right] \begin{bmatrix} e^{\lambda_1(t_1+\Delta t)} & e^{\lambda_1(t_2+\Delta t)} & \cdots & e^{\lambda_1\left(t_{N_t}+\Delta t\right)} \\ e^{\lambda_2(t_1+\Delta t)} & e^{\lambda_2(t_2+\Delta t)} & \cdots & e^{\lambda_2\left(t_{N_t}+\Delta t\right)} \\ \vdots & \vdots & & \vdots \\ e^{\lambda_{2n}(t_1+\Delta t)} & e^{\lambda_{2n}(t_2+\Delta t)} & \cdots & e^{\lambda_{2n}\left(t_{N_t}+\Delta t\right)} \end{bmatrix}$$

$$(10.118)$$

where

$$\{\hat{x}\}_i = \{x(t_i + \Delta t)\}. \qquad (10.119)$$

Equation (10.118) can be written as

$$\left[\{\hat{x}\}_1 \ \ \{\hat{x}\}_2 \ \ \cdots \ \ \{\hat{x}\}_{N_t} \right] = \left[\{\hat{\psi}\}_1 \ \ \{\hat{\psi}\}_2 \ \ \cdots \ \ \{\hat{\psi}\}_{2n} \right] [\Lambda] \tag{10.120}$$

or

$$\left[\hat{X} \right] = [\hat{\psi}][\Lambda], \tag{10.121}$$

where

$$\{\hat{\psi}\}_i = \{\psi\}_i \, e^{\lambda_i \Delta t}. \qquad i = 1, 2, ..., N_t \tag{10.122}$$

The responses given by equations (10.117) and (10.121) can be manipulated to solve for the eigenvalues and modal vectors. A square matrix $[A_s]$ of order N_o, referred to as the "system matrix", can be defined such that

$$[A_s][\psi] = [\hat{\psi}]. \tag{10.123}$$

Premultiplying (10.117) by $[A_s]$ and using equations (10.121) and (10.123) we obtain

$$[A_s][X] = \left[\hat{X} \right] \tag{10.124}$$

so that

$$[A_s] = \left[\hat{X} \right][X]^+ \tag{10.125}$$

where the pseudo-inverse

$$[X]^+ = [X]^T \left([X][X]^T \right)^{-1}. \tag{10.126}$$

Equation (10.123) relates each column $\{\psi\}_i$ of $[\psi]$ to the corresponding column $\{\hat{\psi}\}_i$ of $[\hat{\psi}]$ through

$$[A_s]\{\psi\}_i = \{\hat{\psi}\}_i. \tag{10.127}$$

But the column vectors $\{\psi\}_i$ and $\{\hat{\psi}\}_i$ are related by (10.122) so that

$$[A_s]\{\psi\}_i = e^{\lambda_i \Delta t} \{\psi\}_i \tag{10.128}$$

which is a standard eigenvalue problem. The eigenvectors $\{\psi\}_i$ are the modal vectors and the eigenvalues $\lambda_i = -\sigma_i + \mathrm{i}\, \nu_i$ can be obtained from

$$e^{\lambda_i \Delta t} = -\beta_i + \mathrm{i}\, \gamma_i$$

as

$$-\sigma_i = \frac{1}{2\Delta t} \ln \left(\beta_i^2 + \gamma_i^2 \right), \tag{10.129}$$

$$v_i = \frac{1}{\Delta t} \tan^{-1} \frac{\gamma_i}{\beta_i} . \tag{10.130}$$

Since $\left[A_s \right]$ is of order N_o, if $N_o > 2n$ there will be computational modes which have to be sorted out.

A *Modal Confidence Factor* (MCF) has been developed based on equation (10.122) calculated using different time interval shifts [10.22].

The accuracy of all mode shape identifications has been quantified by computing a *Mode Shape Correlation Constant* (MSCC) between the identified mode shapes $\{\psi\}_2$ and the input mode shapes $\{\psi\}_1$, calculated in a manner analogous to that of coherence [10.47]

$$MSSC = \frac{\left| \{\psi\}_1^T \{\psi\}_2^* \right|^2}{\left(\{\psi\}_1^T \{\psi\}_1^* \right) \left(\{\psi\}_2^T \{\psi\}_2^* \right)} \times 100 . \tag{10.131}$$

The concept is known as the *Modal Assurance Criterion* (MAC) as presented in [10.48].

10.4.2 Random decrement technique

There are cases when controlled excitation or initial excitation cannot be used. Examples are the in-flight response measurements, where a complete knowledge of the excitation is usually not available. In such cases, the *random decrement* (randomdec) technique [10.49] is often used to obtain the free responses needed in the above identification method.

Simply stated, the *randomdec* technique provides a means for obtaining damping and frequency information by performing an ensemble average of segments of a random time history of the structural response. The underlying assumption in the method is that the structural response is the linear superposition of the responses to a step force (initial displacement), an impulsive force (initial velocity), and a random force. If the segments used in the ensemble average are chosen so that the initial displacement is the same for all segments and the initial velocities of alternating segments have opposite signs, then the resulting ensemble average, called the *randomdec signature*, represents the response to a step force, since the averages of the impulse force and random force components approach zero as the number of segments used in the ensemble average increases.

To avoid averaging out the deterministic part of the signal, the samples can be taken starting always with: 1) a constant level (this will give the free decay step response), 2) positive slope and zero level (this will give the free decay positive impulse response), and 3) negative slope and zero level (this will give the free decay negative impulse response). Different randomdec signatures can be obtained by different "triggering" (selection of the starting point) of each ensemble member. Thus, for flutter prediction in linear systems constant-level triggering is not necessary. The number of segments to be averaged depends on the signal shape. Usually 400 to 500 averages are sufficient to produce a repeatable signature.

The essentials of one type of construction for this approach are shown in Fig. 10.44. Houbolt's approach [10.50] consists of triggering each time the response crosses zero with a positive slope, and triggering and inverting each time the response crosses with a negative slope (option 1).
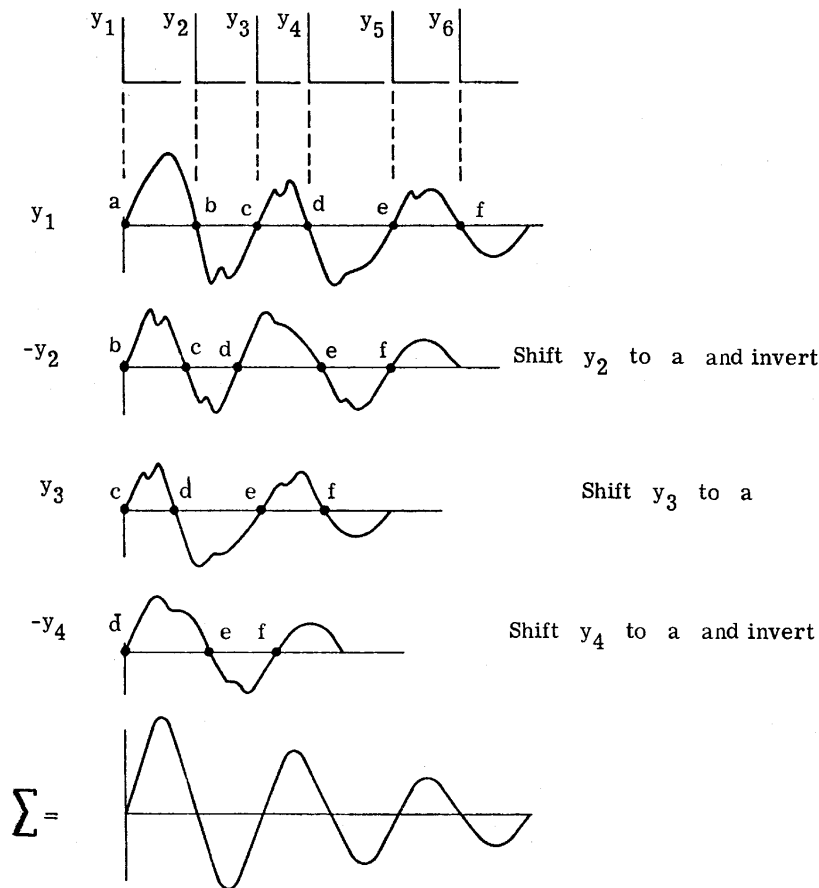
Fig. 10.44 (from [10.50])

Other variants are based either on Cole's approach [10.51] of triggering each time the response crosses a preselected level, regardless of the sign of the slope (option 2) or on Cole's approach of triggering each time the response crosses zero with a positive slope (option 3). A comparison of these three options is given in Fig. 10.45.

For a single degree of freedom system, the natural frequency and damping ratio can be calculated directly from the randomdec signature by the logarithmic decrement measurement, since the signature is a free vibration decay curve of the system. The practical decay analysis is based on the assumption that the decay time history is an exponential function. A plot of the log magnitude of the decay versus time is a straight line (Fig. 2.25). The slope of plot of the log of the successive half-cycle amplitudes versus the number of half cycles can be used to determine the damping ratio.

For multi-degree-of-freedom systems, in which modes are well separated, the natural frequency and damping ratio can be determined either by bandpass filtering the response data or using a moving-block technique.
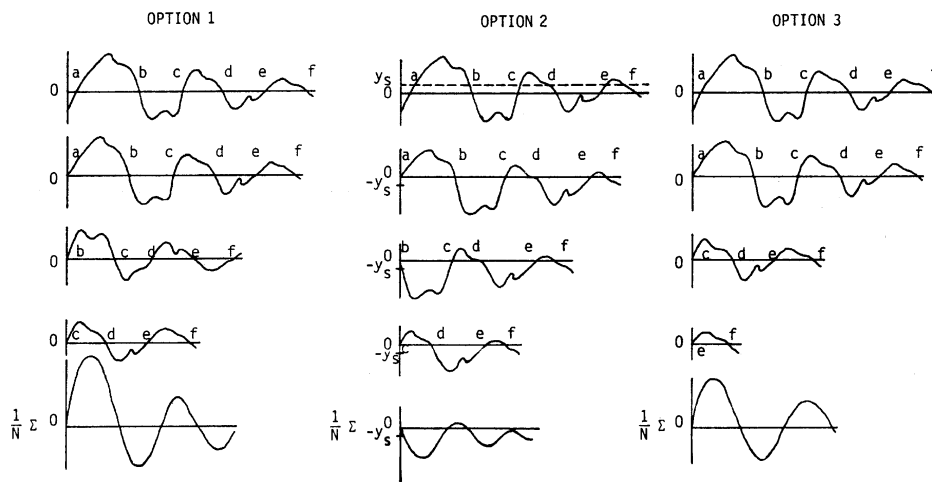
Fig. 10.45

Theoretical aspects and developments of the random decrement technique are presented in [10.52].

References

10.1   Ewins, D.J., *Whys and wherefores of modal testing,* Report No.78005, Dynamics Section, Imperial College, London, 1978.

10.2 Berman, A., *Determining structural parameters from dynamic testing*, Shock and Vibration Digest, vol.7, no.1, pp 10-17, 1975.

10.3 Radeş, M., *Metode dinamice pentru identificarea sistemelor mecanice*, Editura Academiei, Bucureşti, 1979.

10.4 Gauzy, H., *Vibration testing by harmonic excitation*, Manual of Aeroelasticity (Jones, W.P., ed), vol.1, no.4A, pp 1-21, 1960.

10.5 Mead, D. J., *The Internal Damping Due to Structural Joints and Techniques for General Damping Measurement*, ARC Report 19870, 1958.

10.6 Broadbent, E.G. and Hartley, E.V., *Vectorial Analysis of Flight Flutter Results*, RAE Technical Note Struct. No.233, 1958.

10.7 Woodcock, D.L., *On the interpretation of the vector plots of forced vibrations of a linear system with viscous damping*, Aeronautical Quarterly, vol.14, no.1, pp 45-62, 1963.

10.8 Kennedy, C.C. and Pancu, C.D.P., *Use of vectors in vibration measurement and analysis,* Journal of Aeronautical Sciences, vol.14, no.11, pp 603-625, 1947.

10.9 Marples, V., *The derivation of modal damping ratios from complex-plane response plots*, Journal of Sound and Vibration, vol.31, no.1, pp 105-117, 1973.

10.10 McCracken, D.D. and Dorn, W.S., *Numerical Methods and Fortran Programming*, Wiley, N.Y., 1964.

10.11 ∗∗∗ *MODENT Suite of Integrated Structural Dynamic Analysis Software*, ICATS, 1988-2002, www.icats.co.uk.

10.12 Radeş, M. and Ewins, D.J., *Analysis of FRF test data using the pivoted QLP decomposition*, Proc. Int. Conf. on Structural Dynamics Modelling, Funchal, Madeira, Portugal, pp 509-516, June 2002.

10.13 De Vries, G., *Beitrag zur Bestimmung der Schwingungseigenschaften von Flugzeugen im Standversuch unter besonderer Berücksichtigung eines neuen Verfahrens zur Phasenmessung*, ZWB Forschungsbericht No.1882, 1942.

10.14 Zimmermann, H., *Interpretation der Ergebnisse von Flugschwingungs-versuchen anhand einer verallgemeinerten Flatterbeziehung*, Aeroelastik-Kolloquium der T. U. Berlin, 1971.

10.15 Pendered, J.W. and Bishop, R.E.D., *A critical introduction to some industrial resonance testing techniques*, Journal of Mechanical Engineering Science, vol.5, no.4, pp 345-367, 1963.

10.16 Salter, J.P., *Steady State Vibration*, Kenneth Mason, Hampshire, 1969.

10.17 Ewins, D.J., *Measurement and application of mechanical impedance data*, Journal of the Society of Environmental Engineers, Dec.1975, June 1976.

10.18 Shoudao, Lu, and Radeş, M., *System modeling from mobility measurement data*, Buletinul Institutului Politehnic Bucureşti, Seria Mecanică, vol.43, nr.3, pp 69-76, 1981.

10.19 Radeş, M., *Methods for the analysis of structural frequency response measurement data,* Shock and Vibration Digest, vol.8, no.2, pp 73-88, 1976.

10.20 Buzdugan, Gh., Mihăilescu, E. and Radeş, M., *Vibration Measurement*, Martinus Nijhoff Publ., Dordrecht, 1986.

10.21 Stahle, C.V. Jr., *Phase separation technique for ground vibration testing*, Aerospace Engineering, vol.21, pp 56-57, 91-96, 1962.

10.22 Ibrahim, S.R., *Modal confidence factor in vibration testing*, Journal of Spacecraft and Rockets, vol.15, no.5, pp 313-316, 1978.

10.23 ∗∗∗ *User's Manual for Modal Analysis*, Version 9.0, Structural Dynamics Research Corporation, 1985.

10.24 Klosterman, A. and Zimmerman, R., *Modal survey activity via frequency response measurement data*, SAE Paper No.751068, 1975.

10.25 Natke, K.-J., *A method for computing natural vibration quantities from the results of vibration testing in one exciter configuration*, NASA TT F-12, 446, 1969.

10.26 Maia, N.M.M. and Silva, J.M.M., (eds.), *Theoretical and Experimental Modal Analysis*, Research Studies Press Ltd., Taunton, 1997.

10.27 Radeş, M., *Analysis techniques of experimental frequency response data*, Shock and Vibration Digest, vol.11, no.2, pp 15-24, 1979.

10.28 Radeş, M., *Frequency domain experimental modal analysis techniques*, Shock and Vibration Digest, vol.17, no.6, pp 3-15, 1985.

10.29 Radeş, M., *Modal analysis using frequency response measurement data*, Shock and Vibration Digest, vol.20, no.1, pp 13-21, 1988.

10.30 Radeş, M., *Linear model parameter estimation*, Shock and Vibration Digest, vol.25, no.5, pp 3-15, 1993.

10.31 Leuridan, J., *Some Direct Parameter Model Identification Methods Applicable for Multiple Input Modal Analysis*, Ph.D. Dissertation, Department of Mechanical and Industrial Engineering, University of Cincinnati, 1984.

10.32 Radeş, M., *Analysis of measured structural frequency response data*, Shock and Vibration Digest, vol.14, no.5, pp 21-32, 1982.

10.33 Bonneau, E., *Determination of the vibration characteristics of a structure from the expression of the complex power supplied*, Recherche Aérospatiale, no.130, pp 45-51, 1969.

10.34 Smith, S. and Woods, A.A. Jr., *A multiple driver admittance technique for vibration testing of complex structures*, Shock and Vibration Bulletin, vol.42, Part 3, pp 15-23, 1972.

10.35 Asher, G.W., *A method of normal mode excitation utilizing admittance measurements*, Proc. National Specialists' Meeting on Dynamics and Aeroelasticity, Inst. of Aeronautical Sci., Fort Worth, Texas, pp 69-76, 1958.

10.36 Ibáñez, P., *Force appropriation by extended Asher's method*, SAE Paper No.760873, 1976.

10.37 Radeş, M., *On modal analysis of structures with nonproportional damping*, Rev. Roum. Sci. Techn.-Mécanique Appliquée, vol.26, no.4, pp 605-622, 1981.

10.38 Traill-Nash, R.W., *Some Theoretical Aspects of Resonance Testing and Proposals for a Technique Combining Experiment and Computation*, Commonwealth of Australia, Aeronautical Research Laboratories, Report No. SM280, 1961.

10.39 Radeş, M., *Experimental modal analysis using the extended method of characteristic phase lags*, Buletinul Institutului Politehnic Bucureşti, Seria Construcţii de maşini, vol.46-47, pp 66-73, 1984-1985.

10.40 Radeş, M., *System identification using real frequency-dependent modal characteristics*, Shock and Vibration Digest, vol.18, no.8, pp 3-10, 1986.

10.41 Radeş, M., *Modal analysis of structures with frequency dependent properties*, Proceedings of 17th International Modal Analysis Conference, Kissimmee, Florida, pp 349-355, 1999.

10.42 Pickrel, C.R., *Estimating the rank of measured response data using SVD and principal response functions*, Second Int. Conf. on Structural Dynamics Modelling, Test Analysis and Correlation, Cumbria, UK, pp 89-99, 1996.

10.43 Habedank, G., *Über die Reduktion der Anzahl der Freiheitsgrade bei der Schwingungsberechnung von Strukturen*, VDI-Berichte No.221, pp 73-78, 1974.

10.44 Kammer, D.C., *Sensor placement for on-orbit modal identification and correlation of large space structures*, Journal of Guidance, Control and Dynamics, vol.14, pp 251-259, 1991.

10.45 Radeş, M., *Estimation of modal parameters of structures with nonproportional damping*, Buletinul Institutului Politehnic Bucureşti, Seria Mecanică, vol.43, pp 79-82, 1981.

10.46 Ibrahim, S.R. and Mikulcik, E.C., *The experimental determination of vibration parameters from time responses*, Shock and Vibration Bulletin, No.46, Part 5, pp 187-196, 1976.

10.47   Pappa, R.S. and Ibrahim, S.R., *A parametric study of the Ibrahim Time Domain modal identification algorithm*, Shock and Vibration Bulletin, No.51, Part 3, pp 43-71, 1981.

10.48   Allemang, R.J., *Investigation of Some Multiple Input/Output Frequency Response Function Experimental Modal Analysis Techniques*, Ph.D. Thesis, University of Cincinnati, 1980.

10.49   Ibrahim, S.R., *Random decrement technique for modal identification of structures*, J. Spacecraft and Rockets, vol.14, no.11, pp 696-700, 1977.

10.50 Houbolt, J.C., *On identifying frequencies and damping in subcritical flutter testing*, Flutter Testing Techniques, NASA-SP-415, Paper N77-21023, 1976.

10.51 Cole, H.A., *On-the-line analysis of random vibrations*, AIAA Paper No.68-288, 1968.

10.52   Asmussen, J.C., *Modal Analysis Based on the Random Decrement Technique,* Ph.D. Thesis, Aalborg University, Denmark, 1997.

11.

DYNAMIC MODEL REDUCTION

During the pre-test analysis phase, the finite element model, which contains more degrees of freedom than can be surveyed, is reduced to a condensed test/analysis model. Assuming that the original FEM is an accurate representation of the physical structure, the aim is to choose a reduced order model which represents the FEM as closely as possible.

Four methods of reducing FEM matrices are currently in use: physical coordinate reduction, modal coordinate reduction, hybrid reduction and FRF reduction. These reduction methods have shown to differ in both accuracy and robustness.

11.1 Reduced dynamic models

The importance of the dynamic reduction in a dynamic analysis is emphasized in Fig. 11.1. While the cost of assembling the dynamic equations and the cost of recovering response quantities (such as forces and stresses) are each proportional to the number of degrees of freedom N_{dof} of the model, the cost of the solution of dynamic equations is proportional to something between the square and the cube of the number of DOFs. In order to lower this cost, modal reduction is used when $N_{dof} < 300$, and non-modal reduction is recommended when $N_{dof} > 300$.

In the early days of dynamic analysis using the finite element method, the computers used were far less powerful than those of today and it was therefore necessary to reduce the number of physical DOFs to solve "large" eigenvalue problems. The Irons-Guyan reduction [11.1]-[11.3] was used as the basic static condensation technique.

Today computers are very powerful and the resources of RAM and disk space are almost unlimited. Enhanced eigenvalue solvers based on subspace iteration have been developed to solve real large eigenvalue problems (see Chapter 8). Physical coordinate reduction is no longer needed to solve large eigenvalue

problems. However, modal tests are performed with a limited number of accelerometers. To investigate the orthogonality properties of the measured real modes, a reduced mass matrix with a rank equal to the number of measured displacements (DOFs) is necessary. In general, variants of the Irons-Guyan static condensed mass matrix are used.

DYNAMIC ANALYSIS
($N_{dof} > 50$)

```
┌─────────────────┐
│  Assembly of    │        Cost ~ N_dof
│ dynamic equations│
└─────────────────┘
         │
         ▼
┌─────────────┐          N_dof <300      Modal Reduction
│   Dynamic   │
│  Reduction  │          N_dof >300      Non-Modal Reduction
└─────────────┘
         │
         ▼
┌─────────────────┐
│  Solution of    │       Cost ~ (N_dof)² .... (N_dof)³
│ dynamic equations│
└─────────────────┘
         │
         ▼
┌──────────────────┐
│   Recovery of    │
│ response quantities:│   Cost ~ N_dof
│ forces and stresses│
└──────────────────┘
```
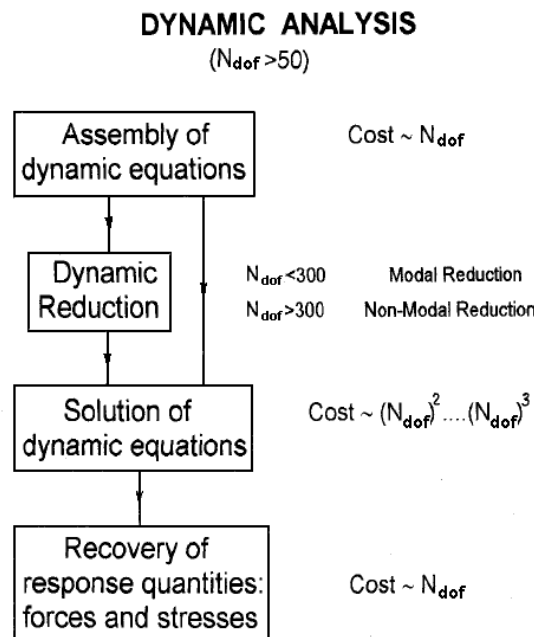
Fig. 11.1

System level FEMs must be limited in size so that dynamic analyses should not be uneconomic or impractical. In complex aerospace structures, the subsytem mass and stiffness matrices shall be condensed and delivered to the prime contractor. The reduced model must meet high requirements with respect to natural frequencies and mode shapes. Modal reduction methods have been developed, as well as hybrid methods like the Craig-Bampton technique [11.4].

11.1.1 Model reduction philosophy

In developing a reduced-order model, it is assumed that for a general, linear, time-invariant dynamic system there exists a discrete analytical model

$$\left[m\right]\{\ddot{u}\}+\left[c\right]\{\dot{u}\}+\left[k\right]\{u\}=\{f(t)\}, \qquad (11.1)$$

where $[m]$ $[c]$ and $[k]$ are, respectively, the mass, damping and stiffness matrices of order $n \times n$, $\{f\}$ is the forcing distribution and $\{u\}$ is a column vector of displacement coordinates in the configuration space.

The free vibration problem of the associate conservative system

$$[m]\{\ddot{u}\} + [k]\{u\} = \{0\},\qquad(11.2)$$

leads to the eigenvalue problem

$$[k]\{\varphi\} = \omega^2 [m]\{\varphi\}\qquad(11.3)$$

or

$$[k][\varPhi] = [m][\varPhi][\varLambda],\qquad(11.4)$$

where the modal matrix

$$[\varPhi] = \left[\ \{\varphi\}_1 \ \{\varphi\}_2 \ \cdots \{\varphi\}_n \ \right]\qquad(11.5)$$

and the spectral matrix

$$[\varLambda] \ = diag \left(\omega_r^2 \right).\qquad(11.6)$$

In order to comply with the usual notation used in test-analysis correlation studies, the notation in this chapter differs occasionally from the rest of the book.

A mathematical model such as equation (11.1) may be large enough to exceed the order of the test model, i.e. the number of available response measurement coordinates. Thus, it is important to seek the means of reducing the model order without seriously degrading the model ability to predict the dynamic response of the structure.

A reduced order model can be obtained using a coordinate transformation

$$\{u\} = [T]\{x\},\qquad(11.7)$$

where $\{x\}$ is an $\ell \times 1$ column vector $(\ell < n)$ and $[T]$ is an $n \times \ell$ rectangular transformation matrix which relates the n elements of the vector $\{u\}$ to a smaller number ℓ of the elements of $\{x\}$. Substituting (11.7) in (11.1) and pre-multiplying by the transposed transformation matrix gives

$$[T]^T [m][T]\{\ddot{x}\} + [T]^T [c][T]\{\dot{x}\} + [T]^T [k][T]\{x\} = [T]^T \{f(t)\},$$

or

$$[m_{red}]\{\ddot{x}\} + [c_{red}]\{\dot{x}\} + [k_{red}]\{x\} = \{f_{red}\},\qquad(11.8)$$

where $\left[m_{red} \right] = \left[T \right]^T \left[m \right] \left[T \right]$, $\left[c_{red} \right]$ and $\left[k_{red} \right]$ are $\ell \times \ell$ reduced-order matrices and $\left\{ f_{red} \right\} = \left[T \right]^T \left\{ f(t) \right\}$ is a reduced forcing vector.

Model reduction techniques vary in the way the matrix $\left[T \right]$ and the vector $\left\{ x \right\}$ are chosen. A proper choice of $\left[T \right]$ will drastically reduce the number of DOFs without altering the lower eigenfrequencies and the mode shapes of interest.

In the reduction, practically, the only requirement that is being imposed is that of the preservation of kinetic and strain energies

$$U = \frac{1}{2} \left\{ u \right\}^T \left[k \right] \left\{ u \right\} = \frac{1}{2} \left\{ x \right\}^T \left[T \right]^T \left[k \right] \left[T \right] \left\{ x \right\} = \frac{1}{2} \left\{ x \right\}^T \left[k_{red} \right] \left\{ x \right\},$$

$$V = \frac{1}{2} \left\{ \dot{u} \right\}^T \left[m \right] \left\{ \dot{u} \right\} = \frac{1}{2} \left\{ \dot{x} \right\}^T \left[T \right]^T \left[m \right] \left[T \right] \left\{ \dot{x} \right\} = \frac{1}{2} \left\{ \dot{x} \right\}^T \left[m_{red} \right] \left\{ \dot{x} \right\}.$$

11.1.2 Model reduction methods

There are five basic numerical procedures in common use for structural model reduction: a) physical coordinate reduction, b) modal coordinate reduction, c) combined static and modal reduction, d) Rayleigh-Ritz reduction, and e) principal component reduction.

a) *Independent coordinate method*

This method assumes that a subset of physical coordinates may be expressed as a linear combination of the remaining coordinates.

Let $\left\{ u_a \right\}$ be an $n_a \times 1$ vector of *independent* (*a*ctive) coordinates and $\left\{ u_o \right\}$ be an $n_o \times 1$ vector of *dependent* (*o*mitted) coordinates. If $\left\{ u_a \right\}$ resides in the top partition of the full $\left\{ u \right\}$ vector, and $\left\{ u_o \right\}$ in the bottom partition

$$\left\{ u \right\} = \left\{ \begin{matrix} \left\{ u_a \right\} \\ \left\{ u_o \right\} \end{matrix} \right\} = \left[T \right] \left\{ u_a \right\}. \tag{11.9}$$

If a constraint equation can be established between the two sets

$$\left\{ u_o \right\} = \left[G_{oa} \right] \left\{ u_a \right\}, \tag{11.10}$$

where $\left[G_{oa} \right]$ is an $n_o \times n_a$ matrix, then

$$\left\{ u \right\} = \left\{ \begin{matrix} \left\{ u_a \right\} \\ \left\{ u_o \right\} \end{matrix} \right\} = \left\{ \begin{matrix} \left\{ u_a \right\} \\ \left[G_{oa} \right] \left\{ u_a \right\} \end{matrix} \right\} = \left[\begin{matrix} \left[I_a \right] \\ \left[G_{oa} \right] \end{matrix} \right] \left\{ u_a \right\}, \tag{11.11}$$

where $\left[I_a \right]$ is an $n_a \times n_a$ identity matrix.

The transformation matrix is

$$[T] = \begin{bmatrix} [I_a] \\ [G_{oa}] \end{bmatrix}. \tag{11.12}$$

b) Rayleigh-Ritz method

In the Rayleigh-Ritz analysis, the vector $\{u\}$ can be expanded in a series of admissible function vectors

$$\{u\} \cong \sum_{r=1}^{L} \gamma_r \{\psi\}_r = [\Psi]\{\gamma\}, \tag{11.13}$$

where $[\Psi] = \begin{bmatrix} \{\psi\}_1 & \{\psi\}_2 & \cdots & \{\psi\}_L \end{bmatrix}$ are Ritz-basis vectors and $\{\gamma\}^T = \lfloor \gamma_1 \quad \gamma_2 \quad \cdots \quad \gamma_L \rfloor$ are Ritz coordinates.

Reduction methods based on Ritz vectors result in reduced models that do not necessarily include a subset of the DOFs of the full modes. They are not examined herein.

Comparing (11.13) with (11.9) and (11.11) it turns out that the columns of $[T]$ are Ritz-basis vectors. They are displacement patterns associated with the $\{u_a\}$ DOFs when the $\{u_o\}$ DOFs are released. They represent global shape functions. They are also referred to as "constraint modes", defined by producing a unit displacement at each active DOF in turn, with all other active DOFs blocked and all omitted DOFs unconstrained and unloaded.

c) Modal method

Let

$$[\Phi_{n\ell}] = \begin{bmatrix} \{\varphi\}_1 & \{\varphi\}_2 & \cdots & \{\varphi\}_\ell \end{bmatrix} \tag{11.14}$$

be the first ℓ modal vectors of (11.4). Then a transformation

$$\{u\} = [\Phi_{n\ell}]\{q\}, \tag{11.15}$$

where $\{q\}^T = \lfloor q_1 \quad q_2 \quad \cdots \quad q_\ell \rfloor$ are modal (principal) coordinates, is similar to (11.7).

d) Hybrid methods

In some model reduction schemes, the reduced vector is defined as a combination of physical and modal coordinates

$$\{x\} = \left\{ \begin{Bmatrix} x_a \end{Bmatrix} \\ \begin{Bmatrix} q_p \end{Bmatrix} \right\}, \tag{11.16}$$

where $\{x_a\}$ are active physical coordinates and $\{q_p\}$ are some generalized coordinates.

The transformation (11.7) becomes

$$\{u\} = \begin{bmatrix} [I_a] & [0] \\ [G_{oa}] & [G_{op}] \end{bmatrix} \left\{ \begin{Bmatrix} x_a \end{Bmatrix} \\ \begin{Bmatrix} q_p \end{Bmatrix} \right\} = [T]\{x\}, \tag{11.17}$$

where $[G_{oa}]$ and $[G_{op}]$ are defined relative to the various reduced model concepts.

11.2 Physical coordinate reduction methods

Physical coordinate reduction methods, first developed as eigenvalue economizers, were used to allow faster computation of the eigenproperties with computer storage savings. The relationship between *o*mitted (discarded) and *a*ctive (retained) DOFs is employed to reduce the size of the eigenvalue problem (before solving it), while preserving the total strain and kinetic energies in the structure.

The static or Irons-Guyan reduction [11.3] neglects the inertia terms associated with the omitted degrees of freedom (*o*-DOFs). In the Habedank reduction [11.5], currently known as the Improved Reduced System (IRS) method [11.6], the inertial effects of *o*-DOFs are taken into account. The iterative IRS method (IIRS) converges to a reduced model which reproduces a subset of the modal model of the full system [11.7].

Selection of active DOFs (*a*-DOFs) is of considerable importance. An automatic selection of *a*-DOFs was first presented by Henshell and Ong [11.8]. The automatic selection of the number and location of *a*-DOFs suggested by Shah and Raymund [11.9] complies with Kidder's guideline [11.10] and is based on small values of the ratio of the diagonal elements of the stiffness and mass matrices. Stepwise elimination of *o*-DOFs is used in [11.11].

11.2.1 Irons-Guyan reduction

11.2.1.1 Static condensation of dynamic models

The Irons-Guyan reduction (GR) technique retains as 'active' (masters) a small fraction n_a of the model DOFs. The remaining n_o omitted DOFs (slaves) are

forced to take values giving least strain energy, regardless of whatever effect this may have on the kinetic energy.

The displacement vector is partitioned as

$$\{u\} = \left\{ \begin{array}{c} \{u_a\} \\ \{u_o\} \end{array} \right\}$$ (11.18)

and the modal vector $\{\varphi\}$ is also written

$$\{\varphi\} = \left\{ \begin{array}{c} \{\varphi_a\} \\ \{\varphi_o\} \end{array} \right\}.$$ (11.19)

The strain energy is

$$U = \frac{1}{2}\{u\}^T[k]\{u\} = \frac{1}{2} \left\lfloor \{u_a\}^T \{u_o\}^T \right\rfloor \left[\begin{array}{cc} [k_{aa}] & [k_{ao}] \\ [k_{oa}] & [k_{oo}] \end{array} \right] \left\{ \begin{array}{c} \{u_a\} \\ \{u_o\} \end{array} \right\}$$ (11.20)

or

$$2U = \{u_a\}^T[k_{aa}]\{u_a\} + 2\{u_o\}^T[k_{oa}]\{u_a\} + \{u_o\}^T[k_{oo}]\{u_o\}.$$

The condition that minimizes U with respect to $\{u_o\}$ is

$$\frac{\partial U}{\partial\{u_o\}} = [k_{oa}]\{u_a\} + [k_{oo}]\{u_o\} = \{0\}.$$ (11.21)

This is a constraint equation between active and omitted DOFs

$$\{u_o\} = -[k_{oo}]^{-1}[k_{oa}]\{u_a\},$$ (11.22)

or

$$\{u_o\} = [G_{oa}]\{u_a\}, \qquad [G_{oa}] = -[k_{oo}]^{-1}[k_{oa}],$$ (11.23)

so that

$$\{u\} = \left\{ \begin{array}{c} \{u_a\} \\ \{u_o\} \end{array} \right\} = \left[\begin{array}{c} [I_a] \\ [G_{oa}] \end{array} \right]\{u_a\} = [T_S]\{u_a\},$$ (11.24)

with

$$[T_S] = \left[\begin{array}{c} [I_a] \\ [G_{oa}] \end{array} \right] = \left[\begin{array}{c} [I_a] \\ -[k_{oo}]^{-1}[k_{oa}] \end{array} \right].$$ (11.25)

Note that equation (11.21) is equivalent to the assumption that in free vibration problems there are no inertial forces at the *o*-DOFs.

The eigenvalue problem (11.3) can be written

$$\begin{bmatrix} [k_{aa}] & [k_{ao}] \\ [k_{oa}] & [k_{oo}] \end{bmatrix} \begin{Bmatrix} \{\varphi_a\} \\ \{\varphi_o\} \end{Bmatrix} = \lambda \begin{bmatrix} [m_{aa}] & [m_{ao}] \\ [m_{oa}] & [m_{oo}] \end{bmatrix} \begin{Bmatrix} \{\varphi_a\} \\ \{\varphi_o\} \end{Bmatrix}, \quad (11.26)$$

where $\lambda = \omega^2$.

The right hand side of equation (11.26) may be regarded as a load vector of inertial forces

$$\begin{bmatrix} [k_{aa}] & [k_{ao}] \\ [k_{oa}] & [k_{oo}] \end{bmatrix} \begin{Bmatrix} \{\varphi_a\} \\ \{\varphi_o\} \end{Bmatrix} = \begin{Bmatrix} \lambda[m_{aa}]\{\varphi_a\} + \lambda[m_{ao}]\{\varphi_o\} \\ \lambda[m_{oa}]\{\varphi_a\} + \lambda[m_{oo}]\{\varphi_o\} \end{Bmatrix} = \begin{Bmatrix} \{f_a\} \\ \{f_o\} \end{Bmatrix}. \quad (11.27)$$

If $\{f_o\} = \{0\}$, the lower partition yields

$$[k_{oa}]\{\varphi_a\} + [k_{oo}]\{\varphi_o\} = \{0\},$$

$$\{\varphi_o\} = -[k_{oo}]^{-1}[k_{oa}]\{\varphi_a\} = [G_{oa}]\{\varphi_a\}, \quad (11.28)$$

and

$$\{\varphi\} = \begin{Bmatrix} \{\varphi_a\} \\ \{\varphi_o\} \end{Bmatrix} = \begin{bmatrix} [I_a] \\ [G_{oa}] \end{bmatrix} \{\varphi_a\} = [T_S]\{\varphi_a\}. \quad (11.29)$$

Thus, the main assumptions in GR are: a) no external forces act on the *o*-DOFs, and b) inertia can be neglected in the determination of internal forces.

Using the reduction transformation (11.24), the strain energy is

$$U = \frac{1}{2}\{u\}^T[k]\{u\} = \frac{1}{2}\{u_a\}^T[T_S]^T[k][T_S]\{u_a\} = \frac{1}{2}\{u_a\}^T[k_a]\{u_a\}, \quad (11.30)$$

and the kinetic energy is

$$V = \frac{1}{2}\{\dot{u}\}^T[m]\{\dot{u}\} = \frac{1}{2}\{\dot{u}_a\}^T[T_S]^T[m][T_S]\{\dot{u}_a\} = \frac{1}{2}\{\dot{u}_a\}^T[m_a]\{\dot{u}_a\}, \quad (11.31)$$

where the reduced stiffness and mass matrices are

$$[k_a] = [T_S]^T[k][T_S], \quad (11.32)$$

$$[m_a] = [T_S]^T[m][T_S]. \quad (11.33)$$

The reduced stiffness matrix is

$$[k_a] = [k_{aa}] + [k_{ao}][G_{oa}] = [k_{aa}] - [k_{ao}][k_{oo}]^{-1}[k_{oa}] \quad (11.32, a)$$

and the reduced mass matrix is

$$[m_a] = [m_{aa}] + [m_{ao}][G_{oa}] + [G_{oa}]^T([m_{oa}] + [m_{oo}][G_{oa}]). \quad (11.33, a)$$

The eigenvalue problem (11.3) becomes

$$[k][T_S]\{\varphi_a\} = \lambda[m][T_S]\{\varphi_a\}$$

or, premultiplying by $[T_S]^T$, and using (11.32) and (11.33),

$$[k_a]\{\varphi_a\} = \lambda[m_a]\{\varphi_a\}. \tag{11.34}$$

After solving for eigenvalues λ and eigenvectors $\{\varphi_a\}$, the mode shapes of the full problem (11.3) are obtained by expansion from equation (11.29).

With a suitable choice of *a*-DOFs, acceptable accuracy may be obtained even with 10% of *a*-DOFs. Such success is generally attributed to Rayleigh's principle, that a first order error in modal shapes gives only a second order error in estimated frequency. It will be shown that GR can be thought of as a discrete Rayleigh-Ritz reduction method, with $[T_S]$ the matrix of the basis vectors as columns and $\{u_a\}$ the Ritz coordinates.

Because $n_a \ll n_o$, inversion of $[k_{oo}]$ approaches the inversion of $[k]$. In practice, a formal inversion of $[k_{oo}]$ is not performed. An alternative procedure is to directly use the Gauss elimination on the *o*-DOFs without partitioning $[k]$, because Gauss elimination can be performed in any order. The bandwidth of the stiffness matrix will increase during the reduction process and problems of storage need be considered.

11.2.1.2 Practical implementation of the GR method

Instead of calculating the matrix $[k_a]$, it may be preferable to evaluate the flexibility matrix $[\delta_a] = [k_a]^{-1}$. This is obtained solving the static problem for unit loads applied at each *a*-DOF in turn

$$\begin{bmatrix} [k_{aa}] & [k_{ao}] \\ [k_{oa}] & [k_{oo}] \end{bmatrix} \begin{bmatrix} [\delta_a] \\ [\delta_o] \end{bmatrix} = \begin{bmatrix} [I_a] \\ [0] \end{bmatrix}, \tag{11.35}$$

where $[I_a]$ is an identity matrix.

Equations (11.35) can be written

$$[k_{aa}][\delta_a] + [k_{ao}][\delta_o] = [I_a], \tag{11.36}$$
$$[k_{oa}][\delta_a] + [k_{oo}][\delta_o] = [0]. \tag{11.37}$$

Equation (11.37) yields

$$[\delta_o] = -[k_{oo}]^{-1}[k_{oa}][\delta_a] = [G_{oa}][\delta_a]. \tag{11.37, a}$$

This is similar with the constraint equation (11.22), which implies that the *o*-DOFs are free from inertial forces.

Substitution of (11.37, *a*) into (11.36) yields

$$[k_{aa}][\delta_a]+[k_{ao}][G_{oa}][\delta_a]=[I_a],$$

$$[\delta_a]=[[k_{aa}]+[k_{ao}][G_{oa}]]^{-1}=[k_a]^{-1},$$

so that

$$[X]=\begin{bmatrix}[\delta_a]\\[\delta_o]\end{bmatrix}=\begin{bmatrix}[I_a]\\[G_{oa}]\end{bmatrix}[\delta_a]=[T_S][k_a]^{-1}. \qquad (11.38)$$

The matrix $[X]$ can be used instead of $[T_S]$ in the reduction process. The columns of $[X]$ are linear combinations of the trial vectors $[T_S]$. Hence, the use of $[X]$ as trial vectors will give the same eigenvalues as $[T_S]$ even though they may produce different reduced matrices $[k_a]$ and $[m_a]$.

The essential steps of the GR method, as implemented in [11.12], are the following:

1. Choose the *a*-DOFs.

2. Compute the displacement vectors $[X]$ solving

$$[k][X]=[P], \qquad (11.39)$$

where $[P]^T=[[I_a]\ [0]]$ so that $\{P\}_i$ is a unit vector containing 1 in the row corresponding to the *i*-th *a*-DOF.

3. Use the trial vectors $[X]$ to form the reduced eigenproblem

$$([k_{red}]-\lambda[m_{red}])\{\psi\}=\{0\}, \qquad (11.40)$$

where

$$[k_{red}]=[X]^T[k][X],\ [m_{red}]=[X]^T[m][X]. \qquad (11.41)$$

4. Solve the reduced eigenproblem.

5. Use the vectors $\{\psi\}$ to calculate mode shapes of the full problem

$$\{\varphi\}=[T_S]\{\varphi_a\}=[T_S][\delta_a][k_a]\{\varphi_a\}=[X]\{\psi\}. \qquad (11.42)$$

The use of the matrix $[X]$ will give the same eigenvalues as $[T_S]$ but different reduced matrices. This is a drawback when a reduced mass matrix is needed for cross-orthogonality checks.

Because

$$[k_{red}]=[X]^T[k][X]=[k_a]^{-T}[T_S]^T[k][T_S][k_a]^{-1}=[\delta_a], \quad (11.43)$$

$$[m_{red}]=[X]^T[m][X]=[k_a]^{-1}[m_a][k_a]^{-1}=[\delta_a][m_a][\delta_a], \quad (11.44)$$

the reduced eigenproblem (11.40) can be written

$$\left[\delta_a \right]\{\psi\} = \lambda \left[\delta_a \right]\left[m_a \right]\left[\delta_a \right]\{\psi\}, \qquad (11.45)$$

or, premultiplying by $\left[k_a \right]$,

$$\{\psi\} = \lambda \left[m_a \right]\left[\delta_a \right]\{\psi\}. \qquad (11.46)$$

Using the transformation $\left[\psi \right] = \left[k_a \right]\left[\varphi_a \right]$ we obtain (11.34).

11.2.1.3 Selection of active DOFs

Different qualitative criteria have been used in the past for the selection of a-DOFs. We mention only a few:

"Select the active DOFs associated with large mass concentrations and which are reasonably flexible with respect to other mass concentrations and fixed constraints" [11.13].

"Select the DOFs that have the largest entries in the mass matrix. Select the DOFs that have the largest movements (components of the eigenvector) in the modes of interest" [11.14].

"Select the active DOFs in the zones of maximum strain energy and which strongly contribute to the total kinetic energy" [11.15].

"The chosen DOFs must always be translations as opposed to rotations. In the case of a complicated assembly, the a-DOFs are situated in the most flexible regions" [11.16].

Hence, good results can be obtained by eliminating the DOFs for which the inertia forces are negligible compared to the elastic forces.

The automatic selection of a-DOFs has been later suggested [11.8] based on small values of the ratio k_{ii}/m_{ii} between the diagonal elements of the stiffness and mass matrices for the i-th coordinate.

The GR method is valid for frequencies which are smaller than a cut-off value, ω_c, equal to the smallest eigenfrequency of the o-DOFs eigenvalue problem

$$\left[k_{oo} \right]\{\varphi_o\} = \omega^2 \left[m_{oo} \right]\{\varphi_o\}. \qquad (11.47)$$

Kidder's cut-off frequency ω_c should be approximately three times the highest significant frequency so that all the significant mode shapes are preserved [11.10]. Improper selection neglecting this condition may result in missing frequencies in the reduced eigenvalue problem.

The lower partition of equation (11.26) yields the constraint equation

$$\{\varphi_o\} = -\left[\left[k_{oo} \right] - \omega^2 \left[m_{oo} \right] \right]^{-1}\left[\left[k_{oa} \right] - \omega^2 \left[m_{oa} \right] \right]\{\varphi_a\}. \qquad (11.48)$$

The inverse term is expanded as

$$\left[\left[k_{oo}\right]-\omega^2\left[m_{oo}\right]\right]^{-1} \cong \left[k_{oo}\right]^{-1}+\omega^2\left[k_{oo}\right]^{-1}\left[m_{oo}\right]\left[k_{oo}\right]^{-1}+..., \qquad (11.49)$$

and the terms in ω^4 are ignored

$$\left[\left[k_{oo}\right]\left(\left[I_o\right]-\omega^2\left[k_{oo}\right]^{-1}\left[m_{oo}\right]\right)\right]^{-1} \cong \left(\left[I_o\right]+\omega^2\left[k_{oo}\right]^{-1}\left[m_{oo}\right]\right)\left[k_{oo}\right]^{-1}. \quad (11.50)$$

GR is valid for those natural frequencies for which the infinite series in equation (11.49) converges. If ω_1 is the smallest eigenfrequency of the *o*-DOF problem

$$\left(\left[I_o\right]-\omega^2\left[k_{oo}\right]^{-1}\left[m_{oo}\right]\right)\{\varphi_o\}_1 = \{0\}, \qquad (11.51)$$

then convergence is achieved for $\omega \ll \omega_1$.

The procedure to select the *a*-DOFs is the following:

1. Let ω_c be a cut-off frequency which is higher than all the significant frequencies.

2. Find a DOF for which the ratio k_{ii}/m_{ii} is the largest. If several DOFs have the same ratio, then the one with the smallest index is considered in the next step.

3. If this ratio is larger than ω_c^2, eliminate this DOF from the mass and stiffness matrices by GR.

4. Apply steps 2 and 3 to the reduced matrices obtained in step 3.

5. Repeat steps 2 to 4 until the largest ratio found in step 2 is less than or equal to ω_c^2.

The DOFs associated with the reduced matrices are the *a*-DOFs.

The main features of the algorithm are: a) elimination of one *o*-DOF at a time, b) well adapted to structures with uniform geometry and mechanical characteristics, c) yields bad results for structures with irregular mass distribution when it concentrates *a*-DOFs in regions having significant masses, and d) if several DOFs have the same k_{ii}/m_{ii} ratio, the elimination is dependent on the node numbering.

The Stepwise Guyan Reduction (SGR) is illustrated in Example 11.1.

To account for the effect of each eliminated DOF, say the *p*-th DOF, on the remaining DOFs, the diagonal elements of the stiffness and mass matrices can be modified as follows [11.17]

$$k_{ii} = k_{ii} - k_{ip}^2/k_{pp}, \qquad m_{ii} = m_{ii} - \left(k_{ip}/k_{pp}\right)^2 m_{pp}. \qquad (11.52)$$

11.2.1.4 *Iterative Guyan reduction*

Results of GR can be improved by iteration [11.12]. One can compute improved trial vectors in (11.39) using the inertial forces generated by the approximate eigenvectors computed by the original GR method as the basis for the trial vector

$$\{P\}=[m][X]\{\varphi\}. \tag{11.53}$$

They can be used in GR and steps 2 through 5 repeated until the eigenvalues have converged.

These are essentially simultaneous inverse iterations and hence should improve the eigenvectors.

11.2.2 Improved Reduced System (IRS) method

Dynamic effects can be approximately accounted for by considering the inertia forces as external forces acting on the *o*-DOFs. They can be statically reduced to the *a*-DOFs. IRS allows for the direct inclusion of the inertial effects of the omitted DOFs [11.6].

IRS is an improved static condensation [11.5], involving minimization of both the strain energy functional and the potential energy of applied forces. Like GR it does not require a solution of the full system eigenproblem. IRS is less sensitive to the number and location of *a*-DOFs. IRS only approximates the full system dynamics in the *a*-modes and necessitates extra *a*-DOFs to preserve accuracy. It produces a very robust TAM [11.18].

The equation of motion for free vibrations is

$$\begin{bmatrix} [m_{aa}] & [m_{ao}] \\ [m_{oa}] & [m_{oo}] \end{bmatrix} \begin{Bmatrix} \{\ddot{u}_a\} \\ \{\ddot{u}_o\} \end{Bmatrix} + \begin{bmatrix} [k_{aa}] & [k_{ao}] \\ [k_{oa}] & [k_{oo}] \end{bmatrix} \begin{Bmatrix} \{u_a\} \\ \{u_o\} \end{Bmatrix} = \begin{Bmatrix} \{0\} \\ \{0\} \end{Bmatrix}. \tag{11.54}$$

Expanding the upper and lower partitions

$$[m_{aa}]\{\ddot{u}_a\} + [m_{ao}]\{\ddot{u}_o\} + [k_{aa}]\{u_a\} + [k_{ao}]\{u_o\} = \{0\}, \tag{11.55}$$

$$[m_{oa}]\{\ddot{u}_a\} + [m_{oo}]\{\ddot{u}_o\} + [k_{oa}]\{u_a\} + [k_{oo}]\{u_o\} = \{0\}. \tag{11.56}$$

From equation (11.56), neglecting the inertial terms, we obtain

$$\{u_o\}=-[k_{oo}]^{-1}[k_{oa}]\{u_a\}=[G_{oa}]\{u_a\}, \tag{11.57}$$

$$[G_{oa}]=-[k_{oo}]^{-1}[k_{oa}] \quad . \tag{11.58}$$

Equations (11.54)

$$[m]\{\ddot{u}\}+[k]\{u\}=\{0\} \tag{11.59}$$

have the solution

$$\{u\} = [T_S]\{u_a\} = \begin{bmatrix} [I_a] \\ [G_{oa}] \end{bmatrix}\{u_a\}. \tag{11.60}$$

Substituting (11.60) in (11.59) and premultiplying by $[T_S]^T$ gives

$$[m_a]\{\ddot{u}_a\} + [k_a]\{u_a\} = \{0\}, \tag{11.61}$$

where

$$[m_a] = [T_S]^T[m][T_S], [k_a] = [T_S]^T[k][T_S]. \tag{11.62}$$

Substituting the acceleration vector from (11.61)

$$\{\ddot{u}_a\} = -[m_a]^{-1}[k_a]\{u_a\}, \tag{11.63}$$

and the acceleration vector calculated from (11.58)

$$\{\ddot{u}_o\} = [G_{oa}]\{\ddot{u}_a\} = -[G_{oa}][m_a]^{-1}[k_a]\{\ddot{u}_a\}, \tag{11.64}$$

into (11.56) written as

$$\{u_o\} = -[k_{oo}]^{-1}([m_{oa}]\{\ddot{u}_a\} + [m_{oo}]\{\ddot{u}_o\} + [k_{oa}]\{u_a\}), \tag{11.65}$$

a new constraint equation is obtained between the *o*-DOFs and the *a*-DOFs

$$\{u_o\} = [G_{oa}^{(1)}]\{u_a\}, \tag{11.66}$$

where

$$[G_{oa}^{(1)}] = -[k_{oo}]^{-1}[k_{oa}] + [k_{oo}]^{-1}([m_{oa}] + [m_{oo}][G_{oa}])[m_a]^{-1}[k_a].$$

The reduction to *a*-DOFs is now defined by

$$\{u\} = \begin{Bmatrix} \{u_a\} \\ \{u_o\} \end{Bmatrix} = \begin{bmatrix} [I_a] \\ [G_{oa}^{(1)}] \end{bmatrix}\{u_a\} = [T_{IRS}]\{u_a\}. \tag{11.67}$$

The IRS transformation matrix is [11.6]

$$[T_{IRS}] = \begin{bmatrix} [I_a] \\ [G_{oa}] + [k_{oo}]^{-1}([m_{oa}] + [m_{oo}][G_{oa}])[m_a]^{-1}[k_a] \end{bmatrix}. \tag{11.68}$$

where $[G_{oa}]$, $[m_a]$ and $[k_a]$ are obtained from GR.

Equation (11.68) can also be written

$$\left[T_{IRS}\right]=\left[T_S\right]+\begin{bmatrix}[0]\\ \left[k_{oo}\right]^{-1}\left(\left[m_{oa}\right]-\left[m_{oo}\right]\left[k_{oo}\right]^{-1}\left[k_{oa}\right]\right)\left[m_a\right]^{-1}\left[k_a\right]\end{bmatrix}. \quad (11.69)$$

If equation (11.56) is written

$$\left[k_{oa}\right]\{u_a\}+\left[k_{oo}\right]\{u_o\}=\{f_o\},$$

$$\{u_o\}=\left[G_{oa}\right]\{u_a\}+\left[k_{oo}\right]^{-1}\{f_o\}, \quad (11.70)$$

the inertia forces acting on *o*-DOFs are approximated as

$$\{f_o\}=\left(\left[m_{oa}\right]+\left[m_{oo}\right]\left[G_{oa}\right]\right)\left[m_a\right]^{-1}\left[k_a\right]\{u_a\}. \quad (11.71)$$

The new improved mass and stiffness matrices are

$$\left[m_a^{IRS}\right]=\left[T_{IRS}\right]^T\left[m\right]\left[T_{IRS}\right]=\left[m_a\right]+\left[\varDelta m_a\right] ,$$
$$\left[k_a^{IRS}\right]=\left[T_{IRS}\right]^T\left[k\right]\left[T_{IRS}\right]=\left[k_a\right]+\left[\varDelta k_a\right]. \quad (11.72)$$

The matrix $\left[\varDelta k_a\right]$ produces a slight adjustment of the stiffness matrix, while $\left[\varDelta m_a\right]$ produces a better mass distribution, which will produce a better set of eigenpairs, which is more accurate than that obtained using GR.

Stepwise Improved Reduction System (SIRS) method

In order to reduce the size of the eigenvalue problem, the coordinates in (11.59) can be eliminated one at a time. The DOF for which the ratio k_{ii}/m_{ii} of the diagonal elements of $\left[m\right]$ and $\left[k\right]$ is highest, is denoted u_o and moved into the bottom location for elimination [11.11].

Equation (11.59) can be written

$$\left[P\right]^T\left[m\right]\left[P\right]\left[P\right]^T\{\ddot{u}\}+\left[P\right]^T\left[k\right]\left[P\right]\left[P\right]^T\{u\}=\{0\}, \quad (11.73)$$

where $\left[P\right]$ is a permutation matrix of the form

$$\left[P\right]=\left[\{e\}_1 \quad \cdots \quad \{e\}_{j-1} \quad \{e\}_{j+1} \quad \cdots \quad \{e\}_n \quad \{e\}_j\right] ,$$

in which $\{e\}_j$'s are columns of the identity matrix.

Equation (11.73) can be partitioned as

$$\begin{bmatrix}\left[m_{aa}\right] & \left[m_{ao}\right]\\ \left[m_{oa}\right] & m_{oo}\end{bmatrix}\begin{Bmatrix}\{\ddot{u}_a\}\\ \ddot{u}_o\end{Bmatrix}+\begin{bmatrix}\left[k_{aa}\right] & \left[k_{ao}\right]\\ \left[k_{oa}\right] & k_{oo}\end{bmatrix}\begin{Bmatrix}\{u_a\}\\ u_o\end{Bmatrix}=\begin{Bmatrix}\{0\}\\ 0\end{Bmatrix}, \quad (11.74)$$

where u_o, k_{oo} and m_{oo} are scalars, and $\{u_a\}$ is the column vector of the remaining a-DOFs. If several DOFs have the same ratio k_{ii}/m_{ii}, then the one with the smallest index is considered first. If this ratio is greater than a cut-off frequency squared, ω_c^2, then the corresponding DOF is eliminated.

In the SIR method, the reduction to a-DOFs is defined by (11.67)

$$\left\{ \begin{array}{c} \{u_a\} \\ u_o \end{array} \right\} = [P]\left[\begin{array}{c} [I_a] \\ \left[G_{oa}^{(1)}\right] \end{array} \right]\{u_a\} = [P][T_1]\{u_a\}.$$

After one reduction step, the reduced homogeneous equation of motion is

$$[m_1]\{\ddot{u}_a\} + [k_1]\{u_a\} = \{0\}, \tag{11.75}$$

where

$$[m_1] = [T_1]^T[P]^T[m][P][T_1], \quad [k_1] = [T_1]^T[P]^T[k][P][T_1].$$

The SIR transformation matrix is of the form

$$[T] = ([P][T_1])_1([P][T_1])_2 \cdots ([P][T_1])_n, \tag{11.76}$$

and the full reduced system matrices are given by

$$[m_{red}] = [T]^T[m][T], \quad [k_{red}] = [T]^T[k][T]. \tag{11.77}$$

The physical coordinate reduction is defined by

$$\{u\} = [T]\{u_{red}\}, \tag{11.78}$$

where $\{u_{red}\}$ contains the selected a-DOFs of the reduced model.

At each reduction step, the effect of the removed o-DOF is redistributed to all the remaining a-DOFs, so that the next reduction will remove the o-DOF with the highest k_{ii}/m_{ii} ratio in the reduced mass and stiffness matrices. The procedure is applied until the highest ratio k_{ii}/m_{ii} is equal to or less than ω_c^2. In this way, the minimum number of a-DOFs is automatically determined, as well as their location.

Modal vector back-expansion is carried out using the *Inverse SIR* (ISIR) method based on the transformation (11.78), where $[T]$ is given by (11.76).

11.2.3 Iterative Improved Reduced System (IIRS) method

The IRS method is based on the transformation matrix $[T_{IRS}]$ which utilizes the reduced matrices $[m_a]$ and $[k_a]$ from GR.

An improvement can be made [11.7] using $\left[m_a^i \right] = \left[m_a^{IRS} \right]$ and $\left[k_a^i \right] = \left[k_a^{IRS} \right]$ from (11.72) in a new transformation matrix

$$[T_{i+1}] = \begin{bmatrix} [I_a] \\ [G_{oa}] + [k_{oo}]^{-1}([m_{oa}] + [m_{oo}][G_{oa}^{(i)}])[m_a^i]^{-1}[k_a^i] \end{bmatrix} \qquad (11.79)$$

where

$$\left[m_a^{i+1} \right] = [T_{i+1}]^T [m][T_{i+1}], \quad \left[k_a^{i+1} \right] = [T_{i+1}]^T [k][T_{i+1}], \qquad (11.80)$$

$$\left[G_{oa}^{(i+1)} \right] = -[k_{oo}]^{-1}[k_{oa}] + [k_{oo}]^{-1}([m_{oa}] + [m_{oo}][G_{oa}^{(i)}])[m_a^i]^{-1}[k_a^i].$$

The iteration process can be continued until the reduced set of equations reproduces the eigensystem to within some specified convergence criterion. The number of correctly recalculated modes is less than half the order of the reduced model.

Stepwise Iterated Improved Reduction (*SIIR*)

If substitution of accelerations (11.64) and (11.65) into equation (11.74) is repeated, for the subsequent iterations the constraint equation becomes [11.11]

$$u_o = \left[G_{oa}^{(i+1)} \right] \{ u_a \},$$

where

$$\left[G_{oa}^{(i+1)} \right] = -k_{oo}^{-1} \left[[k_{oa}] - [k_{oo}]^{-1}([m_{oa}] + m_{oo}[G_{oa}^{(i)}])[m_i]^{-1}[k_i] \right].$$

The reduction to *a*-DOFs becomes

$$\begin{Bmatrix} \{u_a\} \\ u_o \end{Bmatrix} = [P] \begin{bmatrix} [I_a] \\ [G_{oa}^{(i)}] \end{bmatrix} \{u_a\} = [P][T_i]\{u_a\},$$

where the subscript *i* denotes the *i*-th iteration.

After one reduction step, the SIIR homogeneous equation of motion is

$$[m_i]\{\ddot{u}_a\} + [k_i]\{u_a\} = \{0\},$$

where

$$[m_i] = [T_i]^T [P]^T [m][P][T_i], \quad [k_i] = [T_i]^T [P]^T [k][P][T_i].$$

Generally, the SIIR method converges monotonically to a reduced model that preserves the lower eigenvalues and the corresponding reduced eigenvectors of the full system [11.18].

After solving the reduced eigenvalue problem, equation (11.78) is used in the Inverse SIIR (ISIIR) method to expand the *a*-DOF vector to the size of the full problem, using the transformation matrix

$$[T] = ([P][T_i])_1 ([P][T_i])_2 \cdots ([P][T_i])_n ,$$

where subscript *i* is the number of iterations in the SIIR method.

A measure of the accuracy of the expanded mode shapes is given by the relative mode shape error

$$\| \{ \Delta \varphi \} \| / \| \{ \varphi \} \| = \| \{ \varphi \}_{FEM} - \{ \varphi \}_{expanded} \| / \| \{ \varphi \}_{FEM} \|.$$

Numerical simulation results obtained for two simple structural systems are presented in the following. For better comparison of results, the stepwise reduction has been applied as in [11.8], without imposing a cut-off frequency, selecting *a priori* the number of *a*-DOFs.

Example 11.1

Figure 11.2 shows the planar beam system of Example 5.11 with $\rho = 7850 \, \text{kg/m}^3$, $E = 2.1 \cdot 10^{11} \, \text{N/m}^2$, $A = 3.73 \cdot 10^{-4} \, \text{m}^2$, $I = 1.055 \cdot 10^{-7} \, \text{m}^4$. Compute the first 10 modes of vibration using SGR, SIR and SIIR.
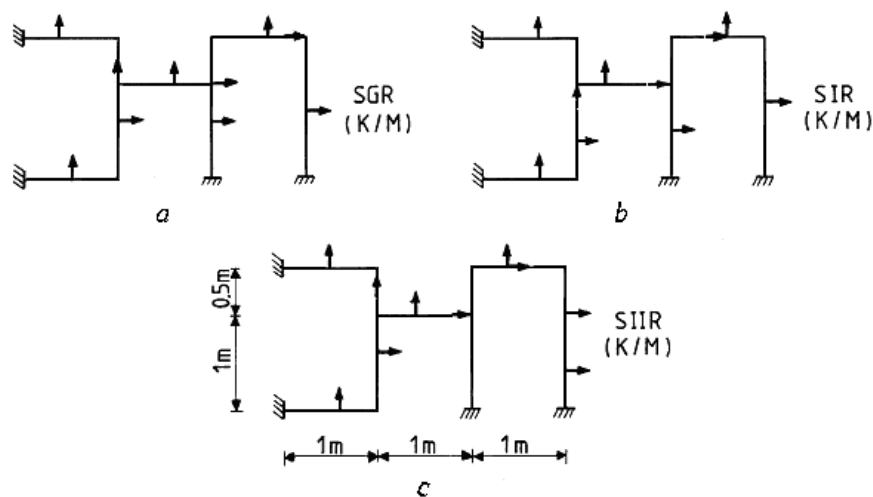
Fig. 11.2

The first 12 planar mode shapes are reproduced in Fig. 11.3.
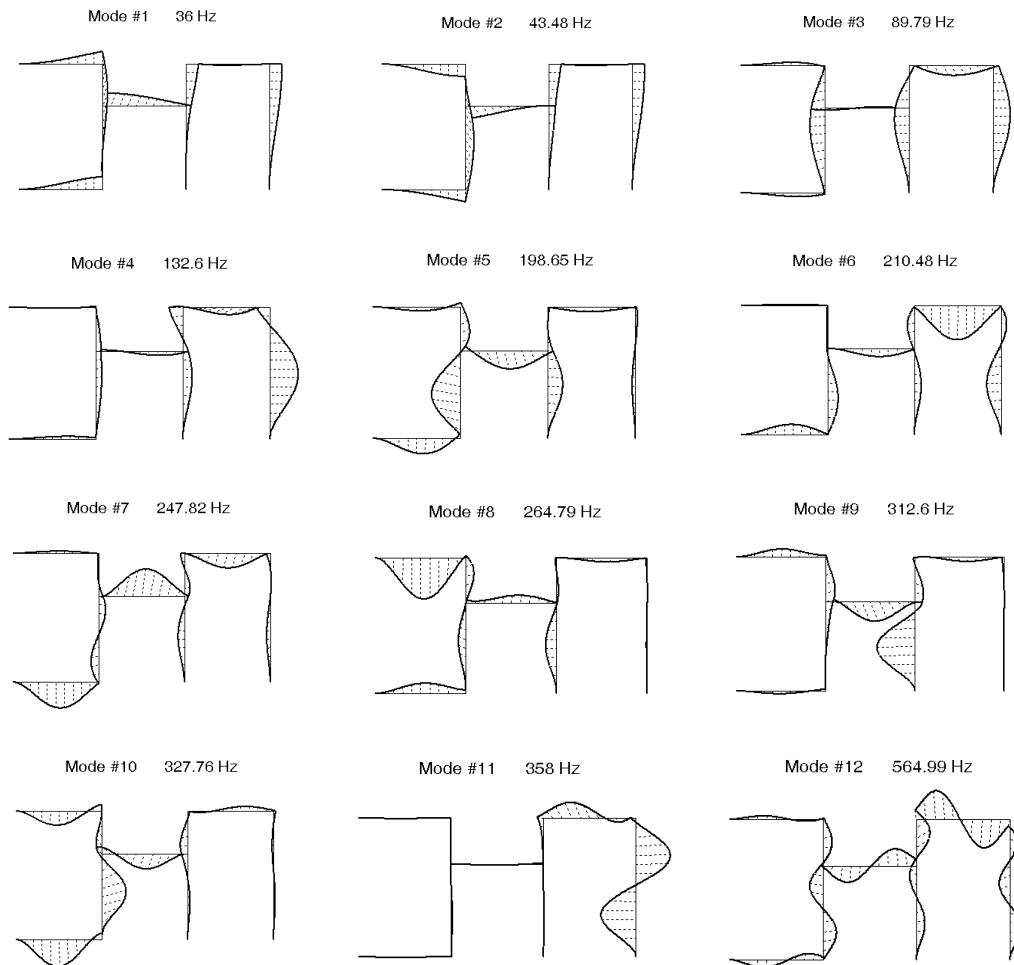
Fig. 11.3

The first ten natural frequencies are given in Table 11.1. The FEM values listed in the second column correspond to the full eigenvalue problem.

Columns three to five list natural frequencies computed using SGR, SIR and SIIR (5 iterations) for a selection of 10 *a*-DOFs using the stepwise K/M elimination criterion. The table shows a good reproduction of the low frequency spectrum.

Columns six to eight list the relative error of expanded mode shapes by Inverse Stepwise Reduction. For some modes, the iterations in SIIR (and ISIIR) do not improve on the values in SIR (and ISIR). Location of *a*-DOFs by the three methods is marked in Fig. 11.1 by arrows.

Table 11.1. Natural frequencies and mode shape errors for the planar frame of Fig. 11.2

Mode	Natural Frequency, Hz				Mode Shape Error, %		
Nr	FEM	SGR	SIR	SIIR	ISGR	ISIR	ISIIR
1	35.996	36.024	35.996	35.996	1.08	0.004	0.0000
2	43.478	43.537	43.478	43.478	1.57	0.008	0.0000
3	89.786	90.407	89.786	89.785	5.18	0.066	0.0005
4	132.60	133.98	132.61	132.60	6.78	0.69	0.0066
5	198.65	203.33	198.69	198.65	12.42	1.21	0.38
6	210.48	216.82	210.64	210.48	15.19	3.91	0.37
7	247.82	254.84	248.05	247.84	16.97	3.56	2.07
8	264.79	277.12	264.89	264.84	21.07	2.19	5.54
9	312.60	326.36	312.85	326.66	24.79	4.23	132.4
10	327.76	337.91	328.86	356.90	22.89	9.36	137.9

Example 11.2

Figure 11.4 shows a simplified FEM of a planar truss structure for which $\rho = 2800 \, \text{kg/m}^3$, $E = 0.75 \cdot 10^{11} \text{N/m}^2$, $I = 0.0756 \, \text{m}^4$, $A_{vert} = 0.006 \, \text{m}^2$, $A_{hor} = 0.004 \, \text{m}^2$, $A_{diag} = 0.003 \, \text{m}^2$. It is modelled with 48 Bernoulli-Euler beam elements with consistent mass matrices and 44 nodes with 3 DOFs per node. The structure is constrained to vibrate only in its own plane.
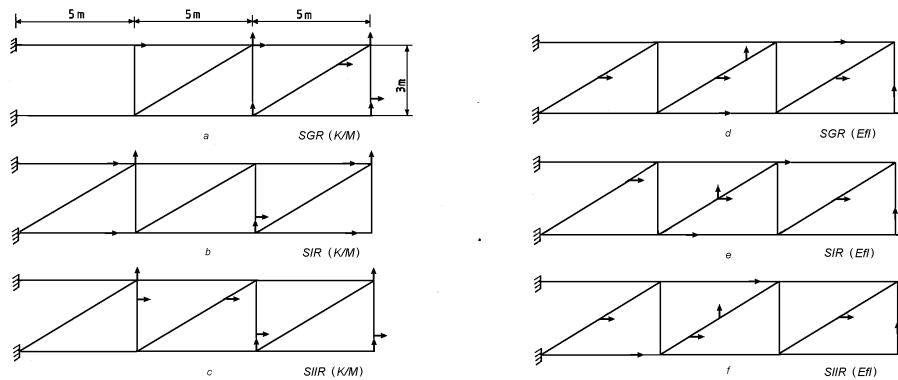
Fig. 11.4

Table 11.2 lists the natural frequencies and the full size mode shape relative errors for the first eight modes of vibration, for a selection of 8 *a*-DOFs, using the K/M elimination criterion. Again, the accuracy is very good for the SIIR method with only 5 iterations and for frequencies above the horizontal lines, which indicate

the location of the natural frequency of the last eliminated *o*-DOF system (Kidder's limit). Mode shape expansion by the ISIIR method gives excellent results. Figures 11.4, *a, b, c* show the location of *a*-DOFs by the three reduction methods [11.11].

Table 11.2. Natural frequencies and mode shape errors for the planar truss of Fig. 11.4

Mode Nr.	Natural Frequency, Hz				Mode Shape Error, %		
	FEM	SGR (K/M)	SIR (K/M)	SIIR (K/M)	ISGR (K/M)	ISIR (K/M)	ISIIR (K/M)
1	45.151	45.185	45.151	45.151	0.24	0.0019	0.0000
2	79.070	79.776	79.070	79.070	1.55	0.053	0.0001
3	227.72	243.72	228.66	227.71	19.04	4.96	0.0215
4	249.94	269.33	250.73	249.94	20.09	4.52	0.024
5	365.63	405.72	371.74	365.66	33.48	22.78	1.83
6	444.03	558.18	499.19	448.49	104.99	92.43	24.01
7	452.83	577.83	516.41	466.89	140.64	119.62	62.45
8	476.83	854.48	546.85	508.47	133.47	134.02	87.68

For comparison, Figures 11.4, *d, e, f,* show the location of *a*-DOFs by the three reduction methods, using the Effective Independence (EfI) method presented in Section 12.5.1.2.
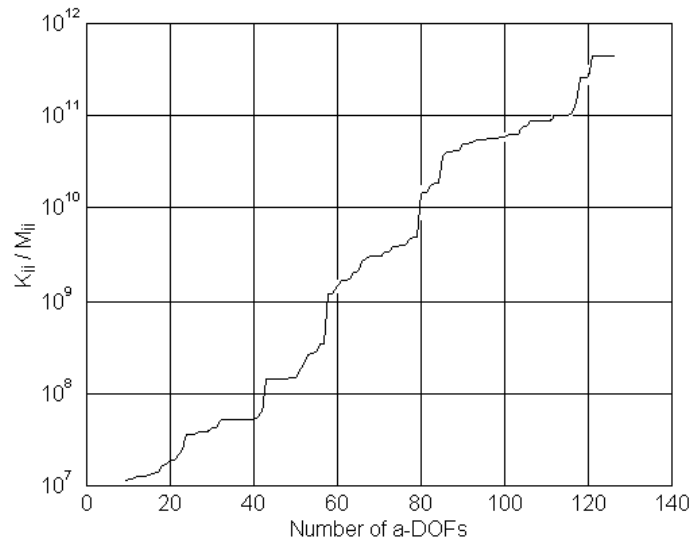
Fig. 11.5

Figure 11.5 displays the variation of the k_{ii}/m_{ii} ratio during the stepwise reduction process from 126 to 8 a-DOFs (right to left).

11.2.4 Dynamic condensation

Equation (11.26) may be written as

$$\begin{bmatrix} [k_{aa}]-\omega^2[m_{aa}] & [k_{ao}]-\omega^2[m_{ao}] \\ [k_{oa}]-\omega^2[m_{oa}] & [k_{oo}]-\omega^2[m_{oo}] \end{bmatrix} \begin{Bmatrix} \{u_a\} \\ \{u_o\} \end{Bmatrix} = \begin{Bmatrix} \{0\} \\ \{0\} \end{Bmatrix}, \qquad (11.81)$$

and may be solved for in terms of $\{u_a\}$

$$\{u_o\}=-\left[[k_{oo}]-\omega^2[m_{oo}]\right]^{-1}\left[[k_{oa}]-\omega^2[m_{oa}]\right]\{u_a\},$$

or

$$\{u_o\}=\left[[I_o]-\omega^2[d_{oo}]\right]^{-1}\left[[G_{oa}]+\omega^2[d_{oa}]\right]\{u_a\}, \qquad (11.82)$$

where

$$[d_{oo}]=[k_{oo}]^{-1}[m_{oo}], \quad [d_{oa}]=[k_{oo}]^{-1}[m_{oa}].$$

As long as $\left\|\omega^2[d_{oo}]\right\|<1$ for some valid norm, a first order binomial expansion of equation (11.82) will yield

$$\{u_o\}=\left[[I_o]+\omega^2[d_{oo}]\right]\left[[G_{oa}]+\omega^2[d_{oa}]\right]\{u_a\},$$

$$\{u_o\}\cong\left[[G_{oa}]+\omega^2\left([d_{oo}][G_{oa}]+[d_{oa}]\right)\right]\{u_a\}=\left[G_{oa}^d\right]\{u_a\}. \quad (11.83)$$

This leads to a reduced set of equations comparable to equations (11.34)

$$\left[k_a^d\right]\{\varphi_a^d\}=\omega^2\left[m_a^d\right]\{\varphi_a^d\}, \qquad (11.84)$$

where

$$\left[k_a^d\right]=[k_{aa}]+[k_{ao}]\left[G_{oa}^d\right], \quad \left[m_a^d\right]=[m_{aa}]+[m_{ao}]\left[G_{oa}^d\right] \qquad (11.85)$$

are functions of ω^2.

To reduce equation (11.84) to a simpler form, in which the eigensolution may be easily obtained, the ω^2 term in $\left[G_{oa}^d\right]$ may be set to a pre-selected value ω_f^2. The transformation matrix for the *Dynamic Condensation* method is [11.19]

$$\left[G_{oa}^d\right]=[G_{oa}]+\omega_f^2\left([d_{oo}][G_{oa}]+[d_{oa}]\right),$$

$$\left[G_{oa}^d \right] = \left[G_{oa} \right] + \omega_f^2 \left[k_{oo} \right]^{-1} \left(\left[m_{oa} \right] + \left[m_{oo} \right] \left[G_{oa} \right] \right). \quad (11.86)$$

The reduction to *a*-DOFs is defined by

$$\{u\} = \left\{ \begin{array}{c} \{u_a\} \\ \{u_o\} \end{array} \right\} = \left[\begin{array}{c} \left[I_a \right] \\ \left[G_{oa}^d \right] \end{array} \right] \{u_a\} = \left[T_D^f \right] \{u_a\}, \quad (11.87)$$

where the transformation matrix

$$\left[T_D^f \right] = \left[\begin{array}{c} \left[I_a \right] \\ \left[G_{oa}^d \right] \end{array} \right]. \quad (11.88)$$

The reduced eigensystem will produce the best approximation to the full system for modes closest to ω_f^2 and will deteriorate as the frequency moves away. Use of this method over a broad frequency range is impractical.

11.2.5 Iterative dynamic condensation

The *Iterative Dynamic Condensation* (IDC) is an extension of the GR method which requires neither matrix inversion nor series expansion.

Equation (11.81) can be written

$$\left[\begin{array}{cc} \left[k_{aa} \right] - \omega^2 \left[m_{aa} \right] & \left[k_{ao} \right] - \omega^2 \left[m_{ao} \right] \\ \left[k_{oa} \right] - \omega^2 \left[m_{oa} \right] & \left[k_{oo} \right] - \omega^2 \left[m_{oo} \right] \end{array} \right] \left\{ \begin{array}{c} \{u_a\} \\ \{u_o\} \end{array} \right\} = \left[\begin{array}{cc} \left[D_{aa} \right] & \left[D_{ao} \right] \\ \left[D_{oa} \right] & \left[D_{oo} \right] \end{array} \right] \left\{ \begin{array}{c} \{u_a\} \\ \{u_o\} \end{array} \right\} = \left\{ \begin{array}{c} \{0\} \\ \{0\} \end{array} \right\}. \quad (11.89)$$

From the lower partition

$$\{u_o\} = -\left[D_{oo} \right]^{-1} \left[D_{oa} \right] \{u_a\} = \left[\overline{G}_{oa} \right] \{u_a\}, \quad (11.90)$$

so that

$$\{u\} = \left\{ \begin{array}{c} \{u_a\} \\ \{u_o\} \end{array} \right\} = \left[\begin{array}{c} \left[I_a \right] \\ \left[\overline{G}_{oa}(\omega) \right] \end{array} \right] \{u_a\} = \left[T_D \right] \{u_a\}. \quad (11.91)$$

From conditions of energy conservation, the reduced matrices are

$$\left[\overline{m} \right] = \left[T_D \right]^T \left[m \right] \left[T_D \right], \quad \left[\overline{k} \right] = \left[T_D \right]^T \left[k \right] \left[T_D \right], \quad (11.92)$$

giving a condensed dynamic matrix

$$\left[\overline{D} \right] = \left[\overline{k} \right] - \omega^2 \left[\overline{m} \right]. \quad (11.93)$$

The algorithm proposed by Paz [11.20] starts by assigning an approximate value (e.g., zero) to the first eigenfrequency ω_1, applying the dynamic condensation to the matrix $\left[\overline{D}_1 \right] = \left[\overline{k} \right] - \omega_1^2 \left[\overline{m} \right]$ and then solving the reduced eigenproblem to

determine the first and second eigenfrequencies, ω_1 and ω_2, and the first eigenvector. Next, the dynamic condensation is applied to the matrix $\left[\bar{D}_2 \right] = \left[\bar{k} \right] - \omega_2^2 \left[\bar{m} \right]$ to reduce the problem and calculate the second the third eigenfrequencies, ω_2 and ω_3, and the second eigenvector. The process continues this way, with one virtually exact eigenfrequency and eigenvector, and an approximation of the next order eigenfrequency calculated at each step.

The following three steps are executed to calculate the *i*-th eigenfrequency ω_i and eigenvector $\{ \varphi \}_i$ as well as an approximation of the eigenvalue of the next order ω_{i+1}.

Step 1. The approximation of ω_i is introduced in equation (11.89) written with the *o*-set in the upper partition

$$\begin{bmatrix} \left[D_{oo}(\omega_i) \right] & \left[D_{oa}(\omega_i) \right] \\ \left[D_{ao}(\omega_i) \right] & \left[D_{aa}(\omega_i) \right] \end{bmatrix} \left\{ \begin{matrix} \{ u_o \} \\ \{ u_a \} \end{matrix} \right\} = \left\{ \begin{matrix} \{ 0 \} \\ \{ 0 \} \end{matrix} \right\}. \tag{11.94}$$

Applying the partial Gauss-Jordan elimination of *o*-set coordinates, equation (11.94) is transformed into

$$\begin{bmatrix} \left[I_o \right] & -\left[\bar{G}_{oa}(\omega_i) \right] \\ \left[0 \right] & \left[\bar{D}_i \right] \end{bmatrix} \left\{ \begin{matrix} \{ u_o \} \\ \{ u_a \} \end{matrix} \right\} = \left\{ \begin{matrix} \{ 0 \} \\ \{ 0 \} \end{matrix} \right\}, \tag{11.95}$$

in which

$$\left[\bar{G}_{oa}(\omega_i) \right] = -\left[D_{oo}(\omega_i) \right]^{-1} \left[D_{oa}(\omega_i) \right], \quad \left[\bar{D}_i \right] = \left[\bar{k}_i \right] - \omega_i^2 \left[\bar{m}_i \right]. \tag{11.96}$$

Step 2. The reduced mass matrix $\left[\bar{m}_i \right]$ and the reduced stiffness matrix $\left[\bar{k}_i \right]$ are calculated from equations (11.92) as

$$\left[\bar{m}_i \right] = \left[T_i \right]^T \left[m \right] \left[T_i \right], \quad \left[\bar{k}_i \right] = \left[\bar{D}_i \right] + \omega_i^2 \left[\bar{m}_i \right], \tag{11.97}$$

where

$$\left[T_i \right] = \left[\left[I_a \right] \quad \left[\bar{G}_{oa}(\omega_i) \right]^T \right]^T. \tag{11.98}$$

Step 3. The reduced eigenproblem

$$\left[\left[\bar{k}_i \right] - \omega_i^2 \left[\bar{m}_i \right] \right] \left\{ \varphi_a \right\}_i = \left\{ 0 \right\} \tag{11.99}$$

is solved to obtain an improved eigenfrequency ω_i, its corresponding eigenvector $\{\varphi_a\}_i$ and also an approximation for the next order eigenvalue ω_{i+1}.

This three-step process may be applied iteratively. The value of ω_i obtained in step 3 may be used as an improved approximate value in step 1 to obtain a further improved value of ω_i in step 3. The convergence is obtained in 2 to 3 steps.

Paz's condensation method has two drawbacks: a) when an inadequate *a*-set is used, some estimated modes will converge to higher modes, missing intermediate values; b) the procedure does not produce mass and stiffness matrices for a reduced model; for each approximate vibration mode there is another transformation matrix and therefore a different reduced model; and c) calculation of the reduced mass matrix involves the multiplication of three matrices of dimensions equal to the total number of DOFs.

In the *Modified Dynamic Condensation* method (Paz, 1989), the reduced stiffness matrix $\left[\bar{k}_i\right]$ is calculated only once, by simple elimination of n_o displacements in equation (11.89), after setting $\omega = 0$. The reduced mass matrix is calculated from

$$\left[\bar{m}_i\right] = \frac{1}{\omega_i^2}\left(\left[\bar{k}_i\right] - \left[\bar{D}_i\right]\right),$$

(11.100)

where $\left[\bar{D}_i\right]$ is given in the partitioned matrix of equation (11.95).

11.3 Modal coordinate reduction methods

Modal reduction methods use the FEM mode shapes to reduce the FEM and thus require *previous solution* of the complete eigenvalue problem. They provide exact frequencies and mode shapes for the targeted modes, and outperform the physical coordinate reduction methods which need too many sensors, even when only a small number of modes are targeted for identification and correlation. While all reduction error is eliminated from Test/TAM correlation analysis, robustness of these methods is dependent upon the fidelity of the FEM to the test article.

11.3.1 Definitions

The complete displacement vector $\{u\} = \{u_n\}$ is partitioned into two complimentary sets: $\{u_a\}$ - *active* DOFs (retained in the TAM, or instrumented) and

$\{u_o\}$- *omitted* DOFs, and in the contribution $\{u_t\}$- from the *target* modes and $\{u_r\}$- from the *residual* (not targeted) modes

$$\{u_n\}=\left\{\begin{array}{c}\{u_a\}\\\{u_o\}\end{array}\right\}=\{u_t\}+\{u_r\}=\left\{\begin{array}{c}\{u_{at}\}+\{u_{ar}\}\\\{u_{ot}\}+\{u_{or}\}\end{array}\right\}. \tag{11.101}$$

The complete coordinate transformation is

$$\{u\}=[\Phi]\{q\}, \tag{11.102}$$

where $[\Phi]$ is the full modal matrix (11.5), solution of (11.4), and $\{q\}$ is the vector of modal coordinates.

Equation (11.102) can be partitioned as

$$\{u\}=\left[\begin{array}{c}[\Phi_a]\\[\Phi_o]\end{array}\right]\{q\}=\left[[\Phi_t]\ [\Phi_r]\right]\left\{\begin{array}{c}\{q_t\}\\\{q_r\}\end{array}\right\}=\left[\begin{array}{cc}[\Phi_{at}]&[\Phi_{ar}]\\[\Phi_{ot}]&[\Phi_{or}]\end{array}\right]\left\{\begin{array}{c}\{q_t\}\\\{q_r\}\end{array}\right\} \tag{11.103}$$

and also as

$$\tag{11.104}$$

We assume that there are n_a active DOFs, n_o omitted DOFs, n_t target DOFs, n_r residual DOFs, and *n* is the order of the model

$$n = n_a + n_o = n_t + n_r. \tag{11.105}$$

11.3.2 Modal TAM and SEREP

Based on an idea from [11.21], the Modal TAM was suggested by Kammer [11.22]. Originally formulated as a global mapping technique used to develop

rotational DOFs for modal test data [11.23], a System Equivalent Reduction/Expansion Process (SEREP) was developed by O'Callahan [11.24].

The displacements corresponding to the target modes can be written

$$\{u_t\} = \left\{ \begin{array}{c} \{u_{at}\} \\ \{u_{ot}\} \end{array} \right\} = \left[\begin{array}{c} [\Phi_{at}] \\ [\Phi_{ot}] \end{array} \right] \{q_t\}. \tag{11.106}$$

From the upper partition

$$\{u_{at}\} = [\Phi_{at}]\{q_t\} . \tag{11.107, a}$$

If $n_a > n_t$

$$\{q_t\} = [\Phi_{at}]^g \{u_{at}\} , \tag{11.108}$$

where the Moore-Penrose generalized inverse is of rank n_t, $[\Phi_{at}]^g[\Phi_{at}] = [I_t]$,

$$[\Phi_{at}]^g = \left[[\Phi_{at}]^T [\Phi_{at}] \right]^{-1} [\Phi_{at}]^T . \tag{11.109}$$

Substitution of (11.109) into the lower partition

$$\{u_{ot}\} = [\Phi_{ot}]\{q_t\} \tag{11.107, b}$$

gives

$$\{u_{ot}\} = [\Phi_{ot}][\Phi_{at}]^g \{u_{at}\} . \tag{11.110}$$

The full system displacement vector (11.106) is

$$\{u_t\} = \left\{ \begin{array}{c} \{u_{at}\} \\ \{u_{ot}\} \end{array} \right\} = \left[\begin{array}{c} [\Phi_{at}][\Phi_{at}]^g \\ [\Phi_{ot}][\Phi_{at}]^g \end{array} \right] \{u_{at}\} = [T_{SEREP}]\{u_{at}\}. \tag{11.111}$$

The transformation matrix of the SEREP is

$$[T_{SEREP}] = [\Phi_t][\Phi_{at}]^g = \left[\begin{array}{c} [\Phi_{at}][\Phi_{at}]^g \\ [\Phi_{ot}][\Phi_{at}]^g \end{array} \right] .$$

If $[\Phi_{at}]$ is full rank, then $[\Phi_{at}][\Phi_{at}]^g = [I_a]$, and the transformation matrix of the Modal TAM, also referred to as SEREPa (non-smoothing SEREP), is

$$[T_m] = \left[\begin{array}{c} [I_a] \\ [\Phi_{ot}][\Phi_{at}]^g \end{array} \right] = [\Phi_t][\Phi_{at}]^{-1}. \tag{11.112}$$

The test (instrumented) DOFs are fixed as active DOFs.

Denoting *A*-analytic and *X*-experimental, equation (11.111) gives

$$\left\{ u_{at} \right\}_A = \left[\Phi_{at} \right] \left[\Phi_{at} \right]^g \left\{ u_{at} \right\}_X = \left[S_a \right] \left\{ u_{at} \right\}_X ,$$

where $\left[S_a \right] \neq \left[I_a \right]$ is a projection matrix which does the scaling of experimental vectors. The expansion of experimental vectors is defined by

$$\left\{ \varphi_{at} \right\}_A = \left[S_a \right] \left\{ \varphi_{at} \right\}_X .$$

If $n_a = n_t$ and providing that the columns of $\left[\Phi_{at} \right]$ are independent,

$$\left[S_a \right] = \left[I_a \right] , \quad \left[\Phi_{at} \right]^g = \left[\Phi_{at} \right]^{-1},$$

and the SEREP becomes the Modal TAM.

The reduced mass and stiffness matrices are

$$\left[m_{at} \right] = \left[T_m \right]^T \left[m \right] \left[T_m \right] = \left[\Phi_{at} \right]^{-T} \left[\Phi_t \right]^T \left[m \right] \left[\Phi_t \right] \left[\Phi_{at} \right]^{-1} = \left[\Phi_{at} \right]^{-T} \left[\Phi_{at} \right]^{-1},$$

$$\left[k_{at} \right] = \left[T_m \right]^T \left[k \right] \left[T_m \right] = \left[\Phi_{at} \right]^{-T} \left[\Phi_t \right]^T \left[k \right] \left[\Phi_t \right] \left[\Phi_{at} \right]^{-1} = \left[\Phi_{at} \right]^{-T} \left[\omega_t^2 \right] \left[\Phi_{at} \right]^{-1}.$$

$$(11.113)$$

The eigensystem of $\left[m_{at} \right]$ and $\left[k_{at} \right]$ has the same eigenvalues as the original system. The eigenvectors

$$\left\{ \varphi_t \right\} = \left[T_m \right] \left\{ \varphi_{at} \right\} .$$

When $n_a > n_t$ the reduced system matrices are

$$\left[m_{at} \right] = \left[\Phi_{at} \right]^{gT} \left[\Phi_{at} \right]^g ,$$

$$\left[k_{at} \right] = \left[\Phi_{at} \right]^{gT} \left[\omega_t^2 \right] \left[\Phi_{at} \right]^g .$$

It can be shown that, even though the reduced system matrices $\left[m_{at} \right]$ and $\left[k_{at} \right]$ are rank deficient (rank n_t, order n_a), the reduced eigensolution will produce the proper eigensystem once the null values have been removed [11.22].

Advantages of the SEREP are: a) the arbitrary selection of target modes (that are to be preserved in the reduced model); b) the quality of the reduced model is not dependent upon the location of the selected *a*-DOFs; c) the frequencies and mode shapes of the reduced system are exactly equal to the frequencies and mode shapes (at the selected locations and for the selected modes) of the full system model; d) the reduction/expansion process is reversible; expanding the reduced system mode shapes back to the full system space develops mode shapes that are exactly the same as the original mode shapes of the full system model; and e) the

FEM mode shapes and frequencies predicted by the Modal TAM can be precisely controlled, which is important in the case of large space structures.

Disadvantages of SEREP are: a) while the Modal TAM is numerically very accurate, it may not be robust; b) use of SEREP as a Modal TAM in test-analysis orthogonality and cross-orthogonality computations can result in larger off-diagonal terms than the corresponding values produced by a less accurate Static TAM; and c) the sensitivity to discrepancies between test and FEM mode shapes is due to the Modal TAM poor representation of residual modes (not targeted for identification and correlation).

The main differences between the SEREP and the GR can be summarized as follows. In GR the transformation matrix $[T_S]$ is based solely on the stiffness matrix so that the inertial forces of the full system are not preserved when the full system is mapped down to a reduced space. In SEREP, the matrix $[T_m]$ is based on the analytical modal vector set which inherently contains information concerning the inertial forces. In GR, the modal matrix formed from the eigensolution of the *a*-DOF system is only an approximation of the modal matrix $[\Phi_t]$ that is formed from the first n_a eigenvectors of the full system. The quality of the estimation of eigenvalues and modal matrix depends on the selection of the *a*-DOFs.

11.3.3 Improved Modal TAM

The *Improved Modal TAM* [11.25] combines the exact representation of the FEM target modes with a better representation of the residual modes. This makes it less sensitive to differences between test mode shapes (corrupted by noise and other modes) and analysis mode shapes

The full displacement vector can be explicitly expressed in terms of target and residual mode contributions

$$\{u_n\} = \{u_t\} + \{u_r\} = [\Phi_t]\{q_t\} + [\Phi_r]\{q_r\} \ . \tag{11.114}$$

The modal reduction for the target modes can be written

$$\{u_t\} = \left\{ \begin{cases} \{u_{at}\} \\ \{u_{ot}\} \end{cases} \right\} = [T_m]\{u_{at}\} = \begin{bmatrix} [I_a] \\ [R_{tm}] \end{bmatrix}\{u_{at}\} = \begin{bmatrix} [I_a] \\ [\Phi_{ot}][\Phi_{at}]^g \end{bmatrix}\{u_{at}\}. \tag{11.115}$$

Similarly, the modal reduction for the residual modes can be written

$$\{u_r\} = \left\{ \begin{cases} \{u_{ar}\} \\ \{u_{or}\} \end{cases} \right\} = [T_r]\{u_{ar}\} = \begin{bmatrix} [I_a] \\ [R_{rm}] \end{bmatrix}\{u_{ar}\} = \begin{bmatrix} [I_a] \\ [\Phi_{or}][\Phi_{ar}]^g \end{bmatrix}\{u_{ar}\}, \tag{11.116}$$

where $[T_r]$ is the modal transformation matrix for the residual modes and

$$\left[\Phi_{ar} \right]^g = \left[\left[\Phi_{ar} \right]^T \left[\Phi_{ar} \right] \right]^{-1} \left[\Phi_{ar} \right]^T .$$

Equations (11.115) and (11.116) are exact. By contrast, the *Modal TAM approximation* to the full displacement vector $\{\hat{u}\}$, in which only target modes are used in the reduction, is

$$\{\hat{u}\} = \left\{ \begin{Bmatrix} u_a \\ u_o \end{Bmatrix} \right\} = [\, T_m\,]\{u_a\} = \begin{bmatrix} [I_a] \\ [R_{tm}] \end{bmatrix} \{u_a\} = \begin{bmatrix} [I_a] \\ [\Phi_{ot}][\Phi_{at}]^g \end{bmatrix} \{u_a\}. \quad (11.117)$$

The displacement vector for the *a*-DOFs

$$\{u_a\} = \{u_{at}\} + \{u_{ar}\} \qquad\qquad (11.118)$$

can be written using the identity

$$\{u_a\} = \left[[\Phi_{at}][\Phi'_{ar}] \right] \left[[\Phi_{at}][\Phi'_{ar}] \right]^{-1} \{u_a\}. \qquad (11.119)$$

Separating $\{u_{at}\}$ and $\{u_{ar}\}$

$$\{u_a\} = \left[[\Phi_{at}][0] \right] \left[[\Phi_{at}][\Phi'_{ar}] \right]^{-1} \{u_a\} + \left[[0][\Phi'_{ar}] \right] \left[[\Phi_{at}][\Phi'_{ar}] \right]^{-1} \{u_a\}.$$
$$(11.120)$$

The target active DOF displacement vector is

$$\{u_{at}\} = \left[[\Phi_{at}][0] \right] \left[[\Phi_{at}][\Phi'_{ar}] \right]^{-1} \{u_a\} = [P_T]\{u_a\}, \qquad (11.121)$$

where

$$[P_T] = \left[[\Phi_{at}][0] \right] \left[[\Phi_{at}][\Phi'_{ar}] \right]^{-1} \qquad (11.122)$$

is a projector matrix of rank n_t.

From equation (11.122)

$$[P_T] \left[[\Phi_{at}][\Phi'_{ar}] \right] = \left[[\Phi_{at}][0] \right] \qquad (11.123)$$

so that

$$[P_T][\Phi_{at}] = [\Phi_{at}], \quad [P_T] = [\Phi_{at}][\Phi_{at}]^g, \qquad (11.124)$$

$$[P_T][\Phi'_{ar}] = [0]. \qquad (11.125)$$

From equation (11.120), the residual active DOF displacement vector is

$$\{u_{ar}\} = \left[[0][\Phi'_{ar}] \right] \left[[\Phi_{at}][\Phi'_{ar}] \right]^{-1} \{u_a\} = [P_N]\{u_a\}, \qquad (11.126)$$

where

$$\left[P_N \right] = \left[\left[0 \right] \left[\Phi'_{ar} \right] \right] \left[\left[\Phi_{at} \right] \left[\Phi'_{ar} \right] \right]^{-1} \tag{11.127}$$

is the projection onto the null space of $\left[P_T \right]$ along its column space.

From equation (11.127)

$$\left[P_N \right] \left[\left[\Phi_{at} \right] \left[\Phi'_{ar} \right] \right] = \left[\left[0 \right] \left[\Phi'_{ar} \right] \right] \tag{11.128}$$

so that

$$\left[P_N \right] \left[\Phi'_{ar} \right] = \left[\Phi'_{ar} \right], \quad \left[P_N \right] = \left[\Phi'_{ar} \right] \left[\Phi'_{ar} \right]^g, \tag{11.129}$$

$$\left[P_N \right] \left[\Phi_{at} \right] = \left[0 \right]. \tag{11.130}$$

The above equations show that the projectors $\left[P_T \right]$ and $\left[P_N \right]$ are complementary

$$\left[P_T \right] + \left[P_N \right] = \left[I_a \right], \tag{11.131}$$

where $\left[I_a \right]$ is an identity matrix.

Using equations (11.121) and (11.126), equation (11.118) becomes

$$\{ u_a \} = \{ u_{at} \} + \{ u_{ar} \} = \left[P_T \right] \{ u_a \} + \left[P_N \right] \{ u_a \}. \tag{11.132}$$

The complete *a*-set TAM *approximation* to the full FEM displacement vector is given by

$$\{ \hat{u} \} = \{ u_t \} + \{ u_r \} = \left[T_m \right] \{ u_{at} \} + \left[T_r \right] \{ u_{ar} \},$$

$$\{ \hat{u} \} = \left(\left[T_m \right] \left[P_T \right] + \left[T_r \right] \left[P_N \right] \right) \{ u_a \} = \left[T_{IM} \right] \{ u_a \}. \tag{11.133}$$

The transformation matrix of the Improved Modal TAM reduction method is

$$\left[T_{IM} \right] = \left[T_m \right] \left[P_T \right] + \left[T_r \right] \left[P_N \right]. \tag{11.134}$$

The reduced mass and stiffness matrices are

$$\left[m_m \right] = \left[T_{IM} \right]^T \left[m \right] \left[T_{IM} \right], \quad \left[k_m \right] = \left[T_{IM} \right]^T \left[k \right] \left[T_{IM} \right]. \tag{11.135}$$

Equations (11.135) can also be written

$$\begin{aligned} \left[m_m \right] = &\left[P_T \right]^T \left[m_{at} \right] \left[P_T \right] + \left[P_T \right]^T \left[T_m \right]^T \left[m \right] \left[T_r \right] \left[P_N \right] + \\ &+ \left[P_N \right]^T \left[T_r \right]^T \left[m \right] \left[T_m \right] \left[P_T \right] + \left[P_N \right]^T \left[m_r \right] \left[P_N \right], \end{aligned} \tag{11.136}$$

$$[k_m] = [P_T]^T[k_{at}][P_T] + [P_T]^T[T_m]^T[k][T_r][P_N] + $$
$$+ [P_N]^T[T_r]^T[k][T_m][P_T] + [P_N]^T[k_r][P_N],$$

(11.137)

where

$$[m_{at}] = [T_m]^T[m][T_m], \quad [k_{at}] = [T_m]^T[k][T_m]$$

(11.138)

are the Modal TAM mass and stiffness matrices, and

$$[m_r] = [T_r]^T[m][T_r], \quad [k_r] = [T_r]^T[k][T_r],$$

(11.139)

in which $[m]$ and $[k]$ are the FEM mass and stiffness matrices.

If equations (11.136) and (11.137) are pre- and post-multiplied by $[\Phi_{ta}]$, the following expressions result

$$[\Phi_{at}]^T[m_m][\Phi_{at}] = [\Phi_{at}]^T[m_{at}][\Phi_{at}] = [I_t],$$
$$[\Phi_{at}]^T[k_m][\Phi_{at}] = [\Phi_{at}]^T[k_{at}][\Phi_{at}] = [\Omega],$$

(11.140)

where $[I_t]$ is an identity matrix and $¡\,\Omega\,\ll$ is the diagonal matrix containing the target mode eigenvalues. Therefore, the Improved Modal TAM exactly predicts the target modes and frequencies as does the Modal TAM.

If equations (11.136) and (11.137) are pre- and post-multiplied by $[\Phi'_{ar}]$, we get

$$[\Phi'_{ar}]^T[m_m][\Phi'_{ar}] = [\Phi'_{ar}]^T[m_r][\Phi'_{ar}],$$
$$[\Phi'_{ar}]^T[k_m][\Phi'_{ar}] = [\Phi'_{ar}]^T[k_r][\Phi'_{ar}],$$

(11.141)

which confirm the residual dynamics. The Improved Modal TAM null space dynamics comes exclusively from the residual modes, as desired.

The residual subspace can be generated using the target subspace and the flexibility matrix of the system. Starting from the orthogonality and mass normalization condition

$$[\Phi]^T[k][\Phi] = ¡\,\omega^2\,\ll$$

and partitioning the modal vectors into target and residual sets, we get

$$[k]^{-1} = \big[[\Phi_t]\ [\Phi_r]\big] \begin{bmatrix} [\omega_t]^2 & [0] \\ [0] & [\omega_r]^2 \end{bmatrix}^{-1} \big[[\Phi_t]\ [\Phi_r]\big]^T.$$

The residual modes satisfy the equation

$$\left[\Phi_r\right] \left\lceil \omega_r^2 \right\rfloor^{-1} \left[\Phi_r\right]^T = \left[k\right]^{-1} - \left[\Phi_t\right] \left\lceil \omega_t^2 \right\rfloor^{-1} \left[\Phi_t\right]^T . \qquad (11.142)$$

11.3.4 Hybrid TAM

The first Modal TAM with residuals, referred to as the Hybrid TAM, has been introduced Kammer [11.26] based on an idea from [11.21]. The approach is based on equation (11.133) which is written

$$\left\{\hat{u}\right\} = \left[T_{Th}\right]\left\{u_a\right\} . \qquad (11.143)$$

The Hybrid TAM transformation matrix is

$$\left[T_{Th}\right] = \left[T_m\right]\left[P_T\right] + \left[T_S\right]\left[P_N\right] , \qquad (11.144)$$

where $\left[T_m\right]$ is the modal TAM transformation matrix and $\left[T_S\right]$ is the static condensation (GR) transformation matrix (replaces $\left[T_r\right]$).

Using equation (11.131), the transformation matrix can be simplified to

$$\left[T_{Th}\right] = \left[T_S\right] + \left(\left[T_m\right] - \left[T_S\right]\right)\left[P_T\right] . \qquad (11.145)$$

The Hybrid TAM considers an oblique projector

$$\left[P_T\right] = \left[\Phi_{at}\right]\left[\Phi_{at}\right]^T\left[m_{at}\right] \qquad (11.146)$$

instead of that given by equation (11.122). It requires prior generation of the Modal TAM mass matrix $\left[m_{at}\right]$.

11.3.5 Modal TAMs vs. non-modal TAMs

A comparison of the performance of the Test-Analysis Models presented so far is of interest at this stage.

In GR (Static TAM), the transformation matrix $\left[T_S\right]$ is based solely on the stiffness matrix $\left[k\right]$. Inertial forces of the full system are not preserved when the full system is mapped down to a reduced space.

The modal matrix formed from the eigensolution of the *a*-DOF system is only an approximation of $\left[\Phi_t\right]$ that is formed from the first '*a*' eigenvectors of the

full system. The quality of the estimation of eigenvalues and modal matrix depends on the selection of *a*-DOFs.

GR does capture eigenfrequencies to a good extent. The constraint modes, that are a linear combination of the eigenvectors of the $[k]$ matrix alone (inertia discarded), span the lower modes of the system rather well, with accuracy deteriorating with increasing frequency.

GR and IRS TAM are approximations of the FEM dynamics. They require a relatively large number of active (instrumented) DOFs to obtain a reasonable level of accuracy, especially when the kinetic energy is spread out over a large portion of the structure. Selection of *a*-DOFs is an important issue.

In SEREP and MODAL TAM, the transformation matrix $[T_m]$ is based on the analytical modal vector set, which inherently contains information concerning the inertial forces.

The Modal TAM represents the target modes exactly but does a poor job with the residual modes.

The Hybrid TAM, which incorporates *static modes* along with the target modes, predicts all target modes exactly and also the *residual frequencies* well.

IMTAM predicts target modes exactly and residual modes reasonably, since the linear transformation used has the residual modes represented as their linear combination. The higher modes are in error, as they are weighted very low due to the inversion $[k]^{-1}$.

Modal TAM eliminates reduction errors. IMTAM improves the robustness of Modal TAM including the residual modes $[\varPhi'_{ar}]$.

The number of residual modes that can be used in a TAM generation is $n_a - n_t$. There are two possibilities: a) use a projection matrix that divides the n_a – dimensional space, containing the *a*-set dynamics, into two complementary spaces (column space of $[\varPhi_{ta}]$ and the complementary null space); and b) stack directly some residual modes with the target modes in the modal matrix when constructing the generalized inverse. In order to ensure properly ranked matrices, $n_t + n'_r = n_a$.

The difference in performance of Hybrid TAM and IMTAM is marginal. It is reported that, in a cross-orthogonality test, half of the off-diagonal terms of the cross orthogonality matrix *XOR* calculated via IMTAM were lower, and half were larger than the corresponding terms determined via the Hybrid TAM.

The IRS-TAM performs better in cross-orthogonality tests as the Hybrid TAM.

11.3.6 Iterative Modal Dynamic Condensation

An iterative dynamic condensation method was presented in [11.27]. It starts with a trial condensation matrix to form a reduced eigenvalue problem. The eigensolution obtained in an iteration step is used to improve the condensation matrix by taking advantage of a particular form of the orthogonality conditions of the eigenvectors. No Gaussian elimination or matrix inversions are required to upgrade the condensation matrix.

The generalized eigenvalue problem (11.4)

$$[k][\varPhi] = [m][\varPhi][\varLambda], \tag{11.147}$$

can be transformed into the standard form

$$[S][\varPsi] = [\varPsi][\varLambda], \tag{11.148}$$

using the transformation

$$[\varPhi] = [Y]^{-1}[\varPsi], \tag{11.149}$$

where $[Y]$ is obtained from the Cholesky decomposition of $[m]$

$$[m] = [Y]^T[Y] \tag{11.150}$$

and the transformed stiffness matrix is

$$[S] = [Y]^{-T}[k][Y]^{-1}. \tag{11.151}$$

Equation (11.148) can be written in partitioned form

$$\begin{bmatrix} [S_{aa}] & [S_{ao}] \\ [S_{oa}] & [S_{oo}] \end{bmatrix} \begin{bmatrix} [\varPsi_{aa}] & [\varPsi_{ao}] \\ [\varPsi_{oa}] & [\varPsi_{oo}] \end{bmatrix} = \begin{bmatrix} [\varPsi_{aa}] & [\varPsi_{ao}] \\ [\varPsi_{oa}] & [\varPsi_{oo}] \end{bmatrix} \begin{bmatrix} [\varLambda_a] & [0] \\ [0] & [\varLambda_o] \end{bmatrix}. \tag{11.152}$$

Equation (11.152) is equivalent to four matrix equations

$$[S_{aa}][\varPsi_{aa}] + [S_{ao}][\varPsi_{oa}] = [\varPsi_{aa}] \; \varLambda_a \ll, \tag{11.153}$$

$$[S_{aa}][\varPsi_{ao}] + [S_{ao}][\varPsi_{oo}] = [\varPsi_{ao}] \; \varLambda_o \ll, \tag{11.154}$$

$$[S_{oa}][\varPsi_{aa}] + [S_{oo}][\varPsi_{oa}] = [\varPsi_{oa}] \; \varLambda_a \ll, \tag{11.155}$$

$$[S_{oa}][\varPsi_{ao}] + [S_{oo}][\varPsi_{oo}] = [\varPsi_{oo}] \; \varLambda_o \ll. \tag{11.156}$$

The eigenvectors in $[\varPsi]$ are normalized to have unitary Euclidean norm

$$[\varPsi]^T[\varPsi] = \begin{bmatrix} [\varPsi_{aa}]^T & [\varPsi_{ao}]^T \\ [\varPsi_{oa}]^T & [\varPsi_{oo}]^T \end{bmatrix} \begin{bmatrix} [\varPsi_{aa}] & [\varPsi_{ao}] \\ [\varPsi_{oa}] & [\varPsi_{oo}] \end{bmatrix} = \begin{bmatrix} [I_a] & [0] \\ [0] & [I_o] \end{bmatrix}. \tag{11.157}$$

Equation (11.157) is equivalent to four normality conditions

$$[\Psi_{aa}]^T [\Psi_{aa}] + [\Psi_{ao}]^T [\Psi_{oa}] = [I_a],$$

$$[\Psi_{aa}]^T [\Psi_{ao}] + [\Psi_{ao}]^T [\Psi_{oo}] = [0], \qquad (11.158)$$

$$[\Psi_{ao}]^T [\Psi_{aa}] + [\Psi_{oo}]^T [\Psi_{oa}] = [0],$$

$$[\Psi_{ao}]^T [\Psi_{ao}] + [\Psi_{oo}]^T [\Psi_{oo}] = [I_o].$$

Introduce two condensation matrices $[R]$ and $[\hat{R}]$ so that

$$[\Psi_{oa}] = [R][\Psi_{aa}], \qquad (11.159)$$

$$[\Psi_{ao}] = [\hat{R}][\Psi_{oo}], \qquad (11.160)$$

where

$$[R] = [\Psi_{oa}][\Psi_{aa}]^{-1}, \quad [\hat{R}] = [\Psi_{ao}][\Psi_{oo}]^{-1}. \qquad (11.161)$$

Substitution of (11.159) and (11.160) in (11.158) yields

$$[\Psi_{aa}]^T [\hat{R}][\Psi_{oo}] + [\Psi_{aa}]^T [R]^T [\Psi_{oo}] = [0],$$

$$[\Psi_{aa}]^T \left([\hat{R}] + [R]^T \right) [\Psi_{oo}] = [0],$$

$$[\hat{R}] = -[R]^T,$$

so that equation (11.160) can be written

$$[\Psi_{ao}] = -[R]^T [\Psi_{oo}]. \qquad (11.160, a)$$

From (11.152), the eigenvalue problem corresponding to the *a*-set is

$$\begin{bmatrix} [S_{aa}] & [S_{ao}] \\ [S_{oa}] & [S_{oo}] \end{bmatrix} \begin{bmatrix} [\Psi_{aa}] \\ [\Psi_{oa}] \end{bmatrix} = \begin{bmatrix} [\Psi_{aa}] \\ [\Psi_{oa}] \end{bmatrix} [\Lambda_a] \qquad (11.162)$$

and for the *o*-set

$$\begin{bmatrix} [S_{aa}] & [S_{ao}] \\ [S_{oa}] & [S_{oo}] \end{bmatrix} \begin{bmatrix} [\Psi_{ao}] \\ [\Psi_{oo}] \end{bmatrix} = \begin{bmatrix} [\Psi_{ao}] \\ [\Psi_{oo}] \end{bmatrix} [\Lambda_o]. \qquad (11.163)$$

If the condensation matrix $[R]$ were known, equations (11.162) and (11.163) could be reduced to their condensed forms

$$\begin{bmatrix} [\Psi_{aa}] \\ [\Psi_{oa}] \end{bmatrix} = \begin{bmatrix} [I_a] \\ [R] \end{bmatrix} [\Psi_{aa}]. \qquad (11.164)$$

Using (11.164) in (11.162) and premultiplying by $\begin{bmatrix} [I_a]^T & [R]^T \end{bmatrix}$ yields

$$\left[[I_a]^T \ [R]^T\right]\left[\begin{matrix}[S_{aa}][S_{ao}]\\ [S_{oa}][S_{oo}]\end{matrix}\right]\left[\begin{matrix}[I_a]\\ [R]\end{matrix}\right][\Psi_{aa}]=\left[[I_a]^T \ [R]^T\right]\left[\begin{matrix}[I_a]\\ [R]\end{matrix}\right][\Psi_{aa}][\Lambda_a]$$

or

$$[k^*][\Psi_{aa}]=[m^*][\Psi_{aa}][\Lambda_a] \ , \tag{11.165}$$

where the condensed stiffness and mass matrices $[k^*]$ and $[m^*]$ are

$$[k^*]=[S_{aa}]+\left([R]^T[S_{oa}]\right)^T +[R]^T[S_{oa}]+[R]^T[S_{oo}][R] \ , \tag{11.166, a}$$

$$[m^*]=[I_a]+[R]^T[R] \ . \tag{11.166, b}$$

Similarly, defining

$$\left[\begin{matrix}[\Psi_{ao}]\\ [\Psi_{oo}]\end{matrix}\right]=\left[\begin{matrix}-[R]^T\\ [I_o]\end{matrix}\right][\Psi_{oo}], \tag{11.167}$$

using (11.167) in (11.163) and premultiplying by $\left[-[R] \ [I_o]^T\right]$ yields the following condensed eigenproblem

$$[k'][\Psi_{oo}]=[m'][\Psi_{oo}][\Lambda_o] \tag{11.168}$$

where

$$[k']=[S_{oo}]-[S_{oa}][R]^T -\left([S_{oa}][R]^T\right)^T +[R][S_{aa}][R]^T \ , \tag{11.169, a}$$

$$[m']=[I_o]+[R][R]^T \ . \tag{11.169, b}$$

Equations (11.165) and (11.168) define the two condensed complementary eigenvalue problems. Solving them for $[\Psi_{aa}]$ and $[\Psi_{oo}]$, the complete eigenvector matrix $[\Psi]$ can be obtained from

$$[\Psi]=\left[\begin{matrix}[I_a]^T -[R]^T\\ [R] \ \ \ [I_o]\end{matrix}\right]\left[\begin{matrix}[\Psi_{aa}] \ [0]\\ [0] \ [\Psi_{oo}]\end{matrix}\right]. \tag{11.170}$$

For this one needs to know $[R]$. The formal definition (11.161) cannot be used since the eigenvectors are not known *a priori*. It can be calculated iteratively.

From equation (11.155), assuming the right side zero,

$$[S_{oa}][\Psi_{oa}]=-[S_{oo}][\Psi_{oa}], \tag{11.171}$$

wherefrom, comparing with (11.156), we get

$$[\Psi_{oa}^{(0)}]=\left(-[S_{oo}]^{-1} [S_{oa}]\right)[\Psi_{aa}^{(0)}]=[R^{(0)}][\Psi_{aa}^{(0)}].$$

The initial approximation for $[R]$ is obtained as

$$\left[R^{(0)}\right] = -\left[S_{oo}\right]^{-1}\left[S_{oa}\right].$$ (11.172)

Using (11.172) in (11.166) and (11.165) one obtains $\left[\Lambda_a^{(0)}\right]$ and $\left[\Psi_{oa}^{(0)}\right]$.

This approximate solution can be used to obtain an improved $\left[R\right]$, as described below by (11.178).

Consider equation (11.155) again, but now with the right side not equal to zero

$$\left[S_{oo}\right]\left[\Psi_{oa}\right] = \left[\Psi_{oa}\right]\left[\Lambda_a\right] - \left[S_{oa}\right]\left[\Psi_{aa}\right].$$ (11.173)

The first term in equation (11.173) is the correction term to be added to (11.171) to improve the original estimate. Replacing $\left[\Psi_{oa}\right] = \left[R\right]\left[\Psi_{aa}\right]$ we get

$$\left[S_{oo}\right]\left[\Psi_{oa}\right] = \left[R\right]\left[\Psi_{aa}\right]\left[\Lambda_a\right] - \left[S_{oa}\right]\left[\Psi_{aa}\right],$$

$$\left[\Psi_{oa}\right] = \left[S_{oo}\right]^{-1}\left(\left[R\right]\left[\Psi_{aa}\right]\left[\Lambda_a\right] - \left[S_{oa}\right]\left[\Psi_{aa}\right]\right).$$ (11.174)

Post-multiplying by $\left[\Psi_{aa}\right]^{-1}$

$$\left[R\right] = \left[\Psi_{oa}\right]\left[\Psi_{aa}\right]^{-1} = \left[S_{oo}\right]^{-1}\left(\left[R\right]\left[\Psi_{aa}\right]\left[\Lambda_a\right]\left[\Psi_{aa}\right]^{-1} - \left[S_{oa}\right]\right).$$ (11.175)

To avoid the inversion of $\left[\Psi_{aa}\right]$ we use the orthogonality property

$$\left[\Psi_{aa}\right]^T\left[k^*\right]\left[\Psi_{aa}\right] = \left[\Lambda_a\right],$$ (11.176)

$$\left[\Psi_{aa}\right]\left[\Psi_{aa}\right]^T\left[k^*\right] = \left[\Psi_{aa}\right]\left[\Lambda_a\right]\left[\Psi_{aa}\right]^{-1},$$

which is substituted in (11.175) yielding

$$\left[R\right] = \left[S_{oo}\right]^{-1}\left(\left[R\right]\left[\Psi_{aa}\right]\left[\Psi_{aa}\right]^T\left[k^*\right] - \left[S_{oa}\right]\right).$$ (11.177)

If the actual condensation matrix $\left[R\right]$ and the modal submatrix $\left[\Psi_{aa}\right]$ are used in (11.177), the equality is identically satisfied. One can also use (11.177) to define a recursive relationship

$$\left[R^{(\ell+1)}\right] = \left[S_{oo}\right]^{-1}\left(\left[R^{(\ell)}\right]\left[\Psi_{aa}^{(\ell)}\right]\left[\Psi_{aa}^{(\ell)}\right]^T\left[k^{*(\ell)}\right] - \left[S_{oa}\right]\right).$$ (11.178)

The iterative calculation starts with $\left[R^{(0)}\right]$, then determines $\left[\Psi_{aa}^{(0)}\right] \rightarrow \left[R^{(0)}\right] \rightarrow \left[k^{*(1)}\right]$, $\left[m^{*(1)}\right] \rightarrow \left[\Psi_{aa}^{(1)}\right]$, $\left[\Lambda_a^{(1)}\right] \rightarrow \left[R^{(2)}\right]$ until the desired convergence is achieved. The convergence criterion can be in terms of a tolerance limit on the eigenvalues $\left[\Lambda_a\right]$ calculated at two consecutive iteration steps.

From (11.168) we obtain $\left[\Psi_{oo} \right]$ and from (11.170) the full modal matrix $\left[\Psi \right]$.

Note that the Iterative Dynamic Condensation is not a TAM.

11.4 Hybrid reduction methods

Hybrid reduction methods are based on the representation of the physical DOFs on a subspace of independent base vectors. The generalized coordinates consist of a set of n_a 'active' physical coordinates, $\{u_a\}$, and a set of n_p (modal) coordinates, $\{q_p\}$.

11.4.1 The reduced model eigensystem

The full system displacement vector is

$$\{u\} = \left\{ \begin{array}{c} \{u_a\} \\ \{u_o\} \end{array} \right\} = \left[\begin{array}{cc} \left[I_a\right] & \left[0\right] \\ \left[G_{oa}\right] & \left[G_{op}\right] \end{array} \right] \left\{ \begin{array}{c} \{u_a\} \\ \{q_p\} \end{array} \right\} = \left[T_H \right] \{x\} \qquad (11.179)$$

so that the transformation matrix is

$$\left[T_H \right] = \left[\begin{array}{cc} \left[I_a\right] & \left[0\right] \\ \left[G_{oa}\right] & \left[G_{op}\right] \end{array} \right]. \qquad (11.180)$$

The reduced dynamic model is described by the equation of the undamped free motion

$$\left[m_H\right]\{\ddot{x}\} + \left[k_H\right]\{x\} = \{0\}, \qquad (11.181)$$

where

$$\left[m_H\right] = \left[T_H\right]^T \left[m\right] \left[T_H\right], \qquad \left[k_H\right] = \left[T_H\right]^T \left[k\right] \left[T_H\right], \qquad (11.182)$$

or, using (11.180),

$$\left[k_H\right] = \left[\begin{array}{cc} \left[k'_{aa}\right] & \left[k_{ap}\right] \\ \left[k_{pa}\right] & \left[k_{pp}\right] \end{array} \right], \qquad \left[m_H\right] = \left[\begin{array}{cc} \left[m'_{aa}\right] & \left[m_{ap}\right] \\ \left[m_{pa}\right] & \left[m_{pp}\right] \end{array} \right], \qquad (11.183)$$

where

$$\left[k'_{aa}\right] = \left[k_{aa}\right] + \left[k_{ao}\right]\left[G_{oa}\right] + \left[G_{oa}\right]^T \left(\left[k_{oa}\right] + \left[k_{oo}\right]\left[G_{oa}\right]\right), \qquad (11.184)$$

$$\left[k_{ap} \right]^T = \left[k_{pa} \right] = \left[G_{op} \right]^T \left(\left[k_{oa} \right] + \left[k_{oo} \right] \left[G_{oa} \right] \right), \tag{11.185}$$

$$\left[k_{pp} \right] = \left[G_{op} \right]^T \left[k_{oo} \right] \left[G_{op} \right], \tag{11.186}$$

and similarly

$$\left[m'_{aa} \right] = \left[m_{aa} \right] + \left[m_{ao} \right] \left[G_{oa} \right] + \left[G_{oa} \right]^T \left(\left[m_{oa} \right] + \left[m_{oo} \right] \left[G_{oa} \right] \right), \tag{11.187}$$

$$\left[m_{ap} \right]^T = \left[m_{pa} \right] = \left[G_{op} \right]^T \left(\left[m_{oa} \right] + \left[m_{oo} \right] \left[G_{oa} \right] \right), \tag{11.188}$$

$$\left[m_{pp} \right] = \left[G_{op} \right]^T \left[m_{oo} \right] \left[G_{op} \right]. \tag{11.189}$$

In equations (11.184)-(11.189) the partition (11.26) in *a*-set and *o*-set DOFs has been used for the full equations.

11.4.2 Exact reduced system

The equation of free undamped vibrations (11.81)

$$\begin{bmatrix} \left[k_{aa} \right] - \omega^2 \left[m_{aa} \right] & \left[k_{ao} \right] - \omega^2 \left[m_{ao} \right] \\ \left[k_{oa} \right] - \omega^2 \left[m_{oa} \right] & \left[k_{oo} \right] - \omega^2 \left[m_{oo} \right] \end{bmatrix} \begin{Bmatrix} \{ u_a \} \\ \{ u_o \} \end{Bmatrix} = \begin{Bmatrix} \{ 0 \} \\ \{ 0 \} \end{Bmatrix}, \tag{11.190}$$

can be solved for in terms of $\{ u_a \}$

$$\{ u_o \} = -\left[\left[k_{oo} \right] - \omega^2 \left[m_{oo} \right] \right]^{-1} \left[\left[k_{oa} \right] - \omega^2 \left[m_{oa} \right] \right] \{ u_a \}. \tag{11.191}$$

The displacement vectors can be written as sums

$$\{ u_a \} = \{ u_a^c \} + \{ u_a^r \}, \tag{11.192}$$

$$\{ u_o \} = \{ u_o^c \} + \{ u_o^r \}, \tag{11.193}$$

where the superscripts denote *c*-constrained, *r*-relaxed.

Step 1. When the *a*-set coordinates are constrained to zero, $\{ u_a^c \} = \{ 0 \}$, the lower partition of (11.190) yields

$$\left(\left[k_{oo} \right] - \omega^2 \left[m_{oo} \right] \right) \{ u_o^c \} = \{ 0 \}. \tag{11.194}$$

For the exact solution, the full 'o'-eigenvalue problem should be solved $\left(n_p = n_o \right)$ giving the modal matrix of "constraint modes" $\left[\Phi_{oo} \right]$ and the spectral matrix $\left[\Lambda_o \right]$ containing the eigenvalues of the complementary system

$$\{ u_o^c \} = \left[\Phi_{oo} \right] \{ q_o \}, \tag{11.195}$$

$$\left[k_{oo} \right]\left[\Phi_{oo} \right] = \left[m_{oo} \right]\left[\Phi_{oo} \right]\left[\Lambda_o \right] . \qquad (11.196)$$

From equations (11.179), (11.186) and (11.189) we get

$$\left[G_{op} \right]=\left[\Phi_{oo} \right] \ , \ \ \left[m_{pp} \right]=\left[I_o \right], \ \ \left[k_{pp} \right]=\left[\Lambda_o \right] . \qquad (11.197)$$

Step 2. Relaxing the constraints of the "complementary system", the solution is obtained setting $\omega = 0$ in equation (11.191), producing

$$\left\{ u_o^r \right\}=\left[G_{oo} \right]\left\{ u_a^r \right\}, \qquad (11.198)$$

where

$$\left[G_{oa} \right]= -\left[k_{oo} \right]^{-1}\left[k_{oa} \right] \qquad (11.199)$$

is the standard Irons-Guyan static condensation transformation.

Equation (11.179) becomes

$$\{ u \}=\left\{ \begin{Bmatrix} u_a \\ u_o \end{Bmatrix} \right\}=\begin{bmatrix} \left[I_a \right] & \left[0 \right] \\ \left[G_{oa} \right] & \left[\Phi_{oo} \right] \end{bmatrix}\begin{Bmatrix} \left\{ u_a^r \right\} \\ \left\{ q_o \right\} \end{Bmatrix}=\left[T_H \right]\begin{Bmatrix} \left\{ u_a \right\} \\ \left\{ q_o \right\} \end{Bmatrix}. \qquad (11.200)$$

Because $\left[k_{oa} \right]+\left[k_{oo} \right]\left[G_{oa} \right]=\left[0 \right]$, we obtain the standard static Irons-Guyan reduced matrices

$$\left[k'_{aa} \right]=\left[k_{aa} \right]+\left[k_{ao} \right]\left[G_{oa} \right]=\left[k_a \right], \qquad (11.201)$$

$$\left[m'_{aa} \right]=\left[m_{aa} \right]+\left[m_{ao} \right]\left[G_{oa} \right]+\left[G_{oa} \right]^T\left(\left[m_{oa} \right]+\left[m_{oo} \right]\left[G_{oa} \right] \right)=\left[m_a \right], \qquad (11.202)$$

and also

$$\left[k_{ap} \right]^T =\left[k_{pa} \right] =\left[0 \right],$$

$$\left[k_{pp} \right]=\left[\Phi_{oo} \right]^T\left[k_{oo} \right]\left[\Phi_{oo} \right]= \ ¡\ \Lambda_o \ll, \qquad (11.203)$$

$$\left[m_{pp} \right]=\left[\Phi_{oo} \right]^T\left[m_{oo} \right]\left[\Phi_{oo} \right]=\left[I_o \right],$$

$$\left[m_{pa} \right]=\left[B_{oa} \right]=\left[\Phi_{oo} \right]^T\left(\left[m_{oa} \right]+\left[m_{oo} \right]\left[G_{oa} \right] \right).$$

Equation (11.181) becomes

$$\left(\begin{bmatrix} \left[k_a \right] & \left[0 \right] \\ \left[0 \right] & \left[\Lambda_o \right] \end{bmatrix}-\omega^2\begin{bmatrix} \left[m_a \right] & \left[B_{oa} \right]^T \\ \left[B_{oa} \right] & \left[I_o \right] \end{bmatrix} \right)\begin{Bmatrix} \left\{ u_a \right\} \\ \left\{ q_o \right\} \end{Bmatrix}=\begin{Bmatrix} \left\{ 0 \right\} \\ \left\{ 0 \right\} \end{Bmatrix}, \qquad (11.204)$$

From the lower partition

$$\left(\left[\Lambda_o \right]-\omega^2\left[I_o \right] \right)\left\{ q_o \right\}= \omega^2\left[B_{oa} \right]\left\{ u_a \right\},$$

$$\left\{ q_o \right\} = \omega^2 \left(\left[\Lambda_o \right] - \omega^2 \left[I_o \right] \right)^{-1} \left[B_{oa} \right] \left\{ u_a \right\}. \qquad (11.205)$$

Substituting (11.205) into equation (11.204), the exact reduced eigenproblem is obtained as

$$\left(\left[k_a^c \right] - \omega^2 \left[m_a^c \right] \right) \left\{ u_a \right\} = \left\{ 0 \right\}, \qquad (11.206)$$

where

$$\left[k_a^c \right] = \left[k_a \right] \ ,$$

$$\left[m_a^c \right] = \left[m_a \right] + \left[B_{oa} \right]^T \omega^2 \left(\left[\Lambda_o \right] - \omega^2 \left[I_o \right] \right)^{-1} \left[B_{oa} \right] = \left[m_a \right] + \left[m_a^A \left(\omega^2 \right) \right]. \qquad (11.207)$$

The mass adjustment $\left[m_a^A \left(\omega^2 \right) \right]$ is a function of ω^2, making (11.206) a nonlinear eigenvalue problem.

"The exact constraint condition (11.191) is singular for frequencies near the modes of the dynamic system represented by the matrices of *o*-DOFs. This singularity is removed if the inertia terms are omitted as in GR. Any attempt to approximate the exact inertia terms will be poorly conditioned unless *a*-DOFs are selected so that the modes of the '*o*'-system are well above the frequency range of interest. This *instability of the reduction process* is an issue of concern for all models which seek to approximate the inertia forces missing in GR (Static TAM). This explains why a static TAM is often needed to get good orthogonality of the test modes even though the IRS-TAM or the hybrid TAM might provide a more accurate match of the FEM frequencies and mode shapes " [11.28].

11.4.3 Craig-Bampton reduction

The Craig-Bampton reduction [11.4] is a subset of the Exact Reduced System technique.

The coordinates $\left\{ u_a \right\}$ consist of interface (attachment) and other (internal) retained physical coordinates. The coordinates $\left\{ q_p \right\}$ are a *truncated* set of normal mode coordinates $\left(n_p < n_o \right)$

$$\left\{ u \right\} = \left[T_H \right] \left\{ \begin{matrix} \left\{ u_a \right\} \\ \left\{ q_p \right\} \end{matrix} \right\}, \qquad \left[T_H \right] = \begin{bmatrix} \left[I_a \right] & \left[0 \right] \\ \left[G_{oa} \right] & \left[\Phi_{pp} \right] \end{bmatrix}.$$

The normal modes are obtained with all interface and other retained physical coordinates fully restrained, hence the name "constrained normal modes".

The coordinate transformation matrix $\left[T_H \right]$ (11.180) consists of an n_a set of "statical constraint modes"

$$\begin{bmatrix} I_a \\ G_{oa} \end{bmatrix},$$

defined by statically imposing a unit displacement on one physical coordinate and zero displacements on the remaining *a*-DOFs, and a truncated set of n_p normal modes of the *o*-set eigenproblem,

$$\begin{bmatrix} \Phi_{pp} \end{bmatrix},$$

representing displacements relative to the fixed component boundaries.

The *constraint modes* represent global shape functions or Ritz vectors, i.e. displacements produced by displacing the boundaries.

Taking only $n_p < n_t$ $\left(n_t < n_o \right)$ target modes in (11.195)

$$\left\{ u_o^c \right\} = \left[\Phi_{ot} \right] \left\{ q_{ot} \right\}, \tag{11.208}$$

$$\{u\} = \begin{bmatrix} \begin{bmatrix} I_a \end{bmatrix} & \begin{bmatrix} 0 \end{bmatrix} \\ \begin{bmatrix} G_{oa} \end{bmatrix} & \begin{bmatrix} \Phi_{ot} \end{bmatrix} \end{bmatrix} \left\{ \begin{Bmatrix} u_a \end{Bmatrix} \\ \begin{Bmatrix} q_{ot} \end{Bmatrix} \right\} = \begin{bmatrix} T_{Ht} \end{bmatrix} \left\{ \begin{Bmatrix} u_a \end{Bmatrix} \\ \begin{Bmatrix} q_{ot} \end{Bmatrix} \right\}, \tag{11.209}$$

so that

$$\begin{bmatrix} k_{oo} \end{bmatrix} \begin{bmatrix} \Phi_{ot} \end{bmatrix} = \begin{bmatrix} m_{oo} \end{bmatrix} \begin{bmatrix} \Phi_{ot} \end{bmatrix} \lfloor \Lambda_{ot} \rfloor,$$

$$\begin{bmatrix} \Phi_{ot} \end{bmatrix}^T \begin{bmatrix} k_{oo} \end{bmatrix} \begin{bmatrix} \Phi_{ot} \end{bmatrix} = \lfloor \Lambda_{ot} \rfloor, \quad \begin{bmatrix} \Phi_{ot} \end{bmatrix}^T \begin{bmatrix} m_{oo} \end{bmatrix} \begin{bmatrix} \Phi_{ot} \end{bmatrix} = \begin{bmatrix} I_t \end{bmatrix}. \tag{11.210}$$

Equation (11.204) becomes

$$\left(\begin{bmatrix} \begin{bmatrix} k_a \end{bmatrix} & \begin{bmatrix} 0 \end{bmatrix} \\ \begin{bmatrix} 0 \end{bmatrix} & \begin{bmatrix} \Lambda_{ot} \end{bmatrix} \end{bmatrix} - \omega^2 \begin{bmatrix} \begin{bmatrix} m_a \end{bmatrix} & \begin{bmatrix} B_{oa} \end{bmatrix}^T \\ \begin{bmatrix} B_{oa} \end{bmatrix} & \begin{bmatrix} I_t \end{bmatrix} \end{bmatrix} \right) \left\{ \begin{Bmatrix} u_a \end{Bmatrix} \\ \begin{Bmatrix} q_{ot} \end{Bmatrix} \right\} = \left\{ \begin{Bmatrix} 0 \end{Bmatrix} \\ \begin{Bmatrix} 0 \end{Bmatrix} \right\}, \tag{11.211}$$

where the reduced stiffness and mass matrices have constant elements.

The reduction is done by truncating the number of constrained normal modes $\left(n_t < n_o \right)$.

11.4.4 General Dynamic Reduction

The *General Dynamic Reduction* (GDR) method [11.29], as the Craig-Bampton reduction [11.4], allows for the general substructuring that permits the *a*-DOFs to be subdivided into various sets of DOFs.

With the *a*-DOFs constrained, the *o*-DOFs can be expressed as

$$\{ u_o \} = [G_{oa}]\{ u_a \} + [G_{op}]\{ q_p \}. \qquad (11.212)$$

The transformation matrix relating the *o*-DOFs to the generalized coordinates is

$$[G_{op}] = [\Phi_{op}] - [G_{oa}][\Phi_{ap}], \qquad (11.213)$$

where $[\Phi_{op}]$ and $[\Phi_{ap}]$ are the modal matrices for the *o*-set and *a*-set using n_p generalized coordinates ($n_p = n_t$ target modes)

$$[\Phi_p] = \left[\begin{array}{c} [\Phi_{ap}] \\ [\Phi_{op}] \end{array} \right]$$

and constraining the $\{ u_a \}$ vector set in some reasonable fashion.

When $\{ u_a \}$ is constrained to zero, $[\Phi_{ap}] = [0]$ and equation (11.213) gives $[G_{op}] = [\Phi_{op}]$.

This way, the GDR method will follow the ERS method but would not use the full set of complementary system eigenvectors.

In MSC/NASTRAN, the truncated set of normal modes used in CBR is replaced by a subspace of independent vectors generated with the aid of a modified power method, starting the iteration process with a set of vectors filled with random numbers.

Normal modes in CBR are calculated using a time-consuming eigenvalue extraction method, while the GDR derived vectors are obtained from a matrix iteration process. In MSC/NASTRAN the run in which the system matrices are reduced is in fact the same run used to solve the eigenvalue problem of the complete reference FEM.

11.4.5 Extended Guyan Reduction

The *Extended Guyan Reduction* method [11.30] also employs generalized coordinates, but uses a different method to determine $[G_{oa}]$ and $[G_{op}]$.

Equation (11.83) is

$$\{u_o\} \cong \left[[G_{oa}] + \omega^2 \left([d_{oo}][G_{oa}] + [d_{oa}] \right) \right] \{u_a\} = [G_{oa}^d]\{u_a\}. \quad (11.214)$$

Defining a set of generalized coordinates at *a*-DOFs as

$$\{ q_a \} = \omega^2 \{ u_a \}, \tag{11.215}$$

$$\{u_o\} = [\, [G_{oa}]\,[d_{oo}]\,[G_{oa}] + [d_{oa}]\,] \begin{Bmatrix} \{u_a\} \\ \{q_a\} \end{Bmatrix}, \tag{11.216}$$

$$[G_{op}] = [d_{oo}][G_{oa}] + [d_{oa}] = [k_{oo}]^{-1}([m_{oa}] + [m_{oo}][G_{oa}]). \tag{11.217}$$

Note that $n_p = n_a$.

Equation (11.204) becomes

$$\left(\begin{bmatrix} [k_a] & [0] \\ [0] & [k_p] \end{bmatrix} - \omega^2 \begin{bmatrix} [m_a] & [B_{pa}]^T \\ [B_{pa}] & [m_p] \end{bmatrix} \right) \begin{Bmatrix} \{u_a\} \\ \{q_a\} \end{Bmatrix} = \begin{Bmatrix} \{0\} \\ \{0\} \end{Bmatrix}, \tag{11.218}$$

where

$$\begin{aligned} [k_p] &= [k_{pp}] = [G_{op}]^T [k_{oo}][G_{op}], \\ [m_p] &= [m_{pp}] = [G_{op}]^T [m_{oo}][G_{op}], \end{aligned} \tag{11.219}$$

$$[B_{pa}] = [G_{op}]^T([m_{oa}] + [m_{oo}][G_{oa}]), \tag{11.220}$$

and $[k_a]$ and $[m_a]$ are the Guyan reduced matrices.

Like in the ERS method, the model can be further reduced to the *a*-set using equations similar to (11.205) - (11.207) except for

$$\{ q_a \} = \omega^2 \left([k_p] - \omega^2 [m_p] \right)^{-1} [B_{pa}] \{u_a\}, \tag{11.221}$$

$$[k_a^c] = [k_a], \tag{11.222}$$

$$[m_a^c] = [m_a] + [B_{pa}]^T \omega^2 \left([k_p] - \omega^2 [m_p] \right)^{-1} [B_{pa}] = [m_a] + [m_a^A(\omega^2)], \tag{11.223}$$

so that the reduced problem is (11.206)

$$\left([k_a^c] - \omega^2 [m_a^c] \right) \{u_a\} = \{0\}$$

and the full system displacement vector is

$$\{u\} = \begin{Bmatrix} \{u_a\} \\ \{u_o\} \end{Bmatrix} = \begin{bmatrix} [I_a] & [0] \\ [G_{oa}] & [d_{oo}][G_{oa}] + [d_{oa}] \end{bmatrix} \begin{Bmatrix} \{u_a\} \\ \{q_a\} \end{Bmatrix}. \tag{11.224}$$

The transformation matrix has the same form as for the Craig-Bampton reduction. The only difference is the partition $[G_{op}]$. Its columns are "mass-

weighted" static shape vectors associated with the *o*-DOFs when the *a*-DOFs are constrained.

Calculation of constrained mass-weighted shape vectors requires much less computational effort than constrained mode shape vectors.

11.4.6 MacNeal's reduction

Consider $n_t = n_a$ and $n_r = n_o$ in equation (11.75) so that [11.31], [11.32]

$$\{u\} = \left[\,[\varPhi_t]\,[\varPhi_r]\,\right]\left\{\begin{array}{c}\{q_t\}\\\{q_r\}\end{array}\right\} = [\varPhi_t]\{q_t\} + [\varPhi_r]\{q_r\}, \qquad (11.225)$$

$$\left([k] - \omega^2[m]\right)\{u\} = \{f\} = \left\{\begin{array}{c}\{f_a\}\\\{0\}\end{array}\right\}, \qquad (11.226)$$

where $\{f_a\}$ are harmonic interface forces acting between substructures.

The corresponding eigenvalue problem is

$$\left([k] - \omega_r^2[m]\right)\{\varphi\}_r = \{0\}, \qquad (11.227)$$

$$[\varPhi]^T[k][\varPhi] = [\varLambda], \quad [\varPhi]^T[m][\varPhi] = [I]. \qquad (11.228)$$

Substituting in (11.226) the coordinate transformation

$$\{u\} = [\varPhi]\{q\} \qquad (11.229)$$

and premultiplying by $[\varPhi]^T$ gives

$$\left([\varLambda] - \omega^2[I]\right)\{q\} = [\varPhi]^T\{f\}, \qquad (11.230)$$

or, in partitioned form

$$\left(\left[\begin{array}{cc}[\varLambda_t] & [0]\\ [0] & [\varLambda_r]\end{array}\right] - \omega^2\left[\begin{array}{cc}[I_t] & [0]\\ [0] & [I_r]\end{array}\right]\right)\left\{\begin{array}{c}\{q_t\}\\\{q_r\}\end{array}\right\} = \left[\begin{array}{c}[\varPhi_t]^T\\ [\varPhi_r]^T\end{array}\right]\{f\}. \quad (11.231)$$

From the lower partition

$$\{q_r\} = \left([\varLambda_r] - \omega^2[I_r]\right)^{-1}[\varPhi_r]^T\{f\} \qquad (11.232)$$

which substituted in (11.225) gives

$$\{u\} = [\varPhi_t]\{q_t\} + [\varPhi_r]\left([\varLambda_r] - \omega^2[I_r]\right)^{-1}[\varPhi_r]^T\{f\},$$

or

$$\{u\} = [\Phi_t]\{q_t\} + [\delta_r]\{f\}, \tag{11.233}$$

where the "dynamic residual flexibility matrix" is

$$[\delta_r] = [\Phi_r]([\Lambda_r] - \omega^2 [I_r])^{-1}[\Phi_r]^T. \tag{11.234}$$

If the maximum natural frequency ω_r to be calculated for the structure is much less than the lower eigenfrequency of the residual (omitted) system included in $\iota \Lambda_r \ll$, then it is possible to disregard the term $-\omega^2 [I_r]$ in equation (11.184) in the sense of static condensation.

The "static residual flexibility matrix" can be approximated by

$$[\delta_r^S] \approx [\Phi_r][\Lambda_r]^{-1}[\Phi_r]^T, \tag{11.235}$$

so that the approximate displacement vector

$$\{\hat{u}\} = [\Phi_t]\{q_t\} + [\delta_r^S]\{f\} = [\Phi_t]\{q_t\} + [\Phi_r][\Lambda_r]^{-1}[\Phi_r]^T\{f\}. \tag{11.236}$$

If $n_a = n_t$ then $\{f\}$ can be determined from the upper partition of (11.231)

$$([\Lambda_t] - \omega^2 [I_t])\{q_t\} = [\Phi_t]^T\{f\} \tag{11.237}$$

as a function of $\{q_t\}$, so that $\{\hat{u}\}$ can be expressed in terms of the reduced set $\{q_t\}$ of target (active) modal coordinates

$$\{\hat{u}\} = \left[[\Phi_t] + [\Phi_r][\Lambda_r]^{-1}[\Phi_r]^T[\Phi_t]^{-T}([\Lambda_t] - \omega^2 [I_t])\right]\{q_t\}. \tag{11.238}$$

11.5 FRF reduction

Frequency Response Function matching [11.33] is based on the identity relating the FRF matrix and the dynamic stiffness matrix

$$[[Z(\omega)]\ [H(\omega)]] = \begin{bmatrix} [Z_{aa}] & [Z_{ao}] \\ [Z_{oa}] & [Z_{oo}] \end{bmatrix} \begin{bmatrix} [H_a] \\ [H_o] \end{bmatrix} = \begin{bmatrix} [I_a] \\ [0] \end{bmatrix}. \tag{11.239}$$

From the lower partition

$$[H_o] = -[Z_{oo}]^{-1}[Z_{oa}][H_a], \tag{11.240}$$

$$\left[\,H\,\right]=\begin{bmatrix}\left[\,H_a\,\right]\\\left[\,H_o\,\right]\end{bmatrix}=\begin{bmatrix}\left[\,I_a\,\right]\\-\left[\,Z_{oo}\,\right]^{-1}\left[\,Z_{oa}\,\right]\end{bmatrix}\left[\,H_a\,\right]=\left[\,T^{FRF}\left(\omega\right)\right]\left[\,H_a\,\right]. \quad (11.241)$$

The transformation matrix is

$$\left[\,T^{FRF}\,\right]=\begin{bmatrix}\left[\,I_a\,\right]\\-\left[\,Z_{oo}\,\right]^{-1}\left[\,Z_{oa}\,\right]\end{bmatrix}. \qquad (11.242)$$

The reduced dynamic stiffness matrix is

$$\left[\,Z_{red}\left(\omega\right)\right]=\left[\,T^{FRF}\,\right]^T\left[\,Z\,\right]\left[\,T^{FRF}\,\right]. \qquad (11.243)$$

The reduced FRF matrix

$$\left[\,H_{red}\left(\omega\right)\right]=\left[\,Z_{red}\left(\omega\right)\right]^{-1} \qquad (11.244)$$

is compared to the measured $\left[\,H_a\,\right]$.

Comparison of FRF matrices has some possible advantages: a) each FRF contains information about out-of-band modes, b) experimental FRFs are free from errors from modal parameter estimation, and c) is flexible to specify *a*-DOFs.

References

11.1 Irons, B.M., *Eigenvalue economizers in vibration problems*, Journal of the Aeronautical Society, vol.67, pp 526-528, 1963.

11.2 Guyan, R.J., *Reduction of stiffness and mass matrices*, AIAA Journal, vol.3, no.2, p 380, Feb 1965.

11.3 Irons, B.M., *Structural eigenvalue problems: Elimination of unwanted variables*, AIAA Journal, vol.3, no.5, pp 961-962, 1965.

11.4 Craig, R.R. and Bampton, M.C.C., *Coupling of substructures for dynamic analyses*, AIAA Journal, vol.6, no.7, pp 1313-1319, July 1968.

11.5 Habedank, G., *Über die Reduktion der Anzahl der Freiheitsgrade bei der Schwingungsberechnung von Strukturen*, VDI-Berichte Nr. 221, pp 73-78, 1974.

11.6 O'Callahan, J., *A procedure for an Improved Reduced System (IRS) model*, Proceedings of 7th International Modal Analysis Conference, Las Vegas, Nevada, pp 17-21, 1989.

11.7 Blair, M.A., Camino, T.S. and Dickens, J.M., *An iterative approach to a reduced mass matrix,* Proceedings of 9th International Modal Analysis Conference, Florence, Italy, pp 621-626, 1991.

11.8   Henshell, R.D. and Ong, J.H., *Automatic masters for eigenvalue economization*, Earthquake Engineering and Structural Dynamics, vol.3, no.4, pp 375-383, April 1975.

11.9 Shah, V.N. and Raymund, M., *Analytical selection of masters for the reduced eigenvalue problem,* International Journal for Numerical Methods in Engineering, vol.18, no.1, pp 89-98, 1982.

11.10 Kidder, R.L.: *Reply by author to A.H. Flax*, AIAA Journal, vol.13, p. 702, 1975.

11.11 Radeş, M., *Stepwise physical coordinate reduction for model correlation*, Proceedings of NATO-Advanced Study Institute "Modal Analysis and Testing", Sesimbra, Portugal, May 3-15, pp 379-388, 1998.

11.12   Razzaque, A., *The Irons-Guyan reduction method with iterations*, Proceedings of 10th International Modal Analysis Conference, San Diego, Ca., pp 137-145, 1992.

11.13 Ramsden, J.N. and Stoker, J.R., *Mass condensation: A semiautomatic method for reducing the size of vibration problems*, International Journal for Numerical Methods in Engineering, vol.1, no.4, pp 333-349, 1969.

11.14 Levy, R., *Guyan reduction solutions recicled for improved accuracy,* NASTRAN-Users Experiences, NASA, pp 201-220, Sept. 1971.

11.15 Popplewell, N., Bertels, A.W.M. and Arya, B., *A critical appraisal of the elimination technique*, Journal of Sound and Vibration, vol.31, no.2, pp 213-233, 1973.

11.16 Downs, B., *Accurate reduction of stiffness and mass matrices for vibration analysis and a rationale for selecting master degrees of freedom*, Journal of Mechanical Design, vol.102, no.2, pp 412-416, 1980.

11.17 Matta, K.W., *Selection of degrees of freedom for dynamic analysis*, Journal of Pressure Vessel Technology, vol.109, no.1, pp 65-69, 1987.

11.18   Gordis, J.H., *An analysis of the Improved Reduced System (IRS) model reduction procedure*, Modal Analysis, vol.9, no.4, pp 269-285, 1994.

11.19 O'Callahan, J.C., Chou, C.M. and Koung, R.T.F., *Improved starting vectors for subspace iteration solution using dynamic condensation,* Proceedings of 4th International Modal Analysis Conference, Los Angeles, Ca., pp 858-863, 1986.

11.20 Paz, M., *Dynamic condensation*, AIAA Journal, vol.22, no.5, pp 724-727, 1984.

11.21   Link, M., *Identification of physical system matrices using incomplete vibration test data,* Proceedings of 4th International Modal Analysis Conference, Los Angeles, Ca., pp 386-393, 1986.

11.22 Kammer, D.C., *Test-analysis-model development using an exact modal reduction*, International Journal of Analytical and Experimental Modal Analysis, pp 174-179, Oct 1987.

11.23 O'Callahan, J.C., Avitable, P., Madden, R. and Lieu, I.W., *An efficient method of determining rotational degrees of freedom from analytical and experimental data*, Proceedings of 4th International Modal Analysis Conference, Los Angeles, Ca., pp 50-58, 1986.

11.24 O'Callahan, J.C., Avitable, P.A. and Riemer, R., *System equivalent reduction expansion process (SEREP),* Proceedings of 7th International Modal Analysis Conference, Las Vegas, Nevada, pp 29-37, Feb 1989.

11.25 Bhatia, S.S. and Allemang, R., *A test-analysis-matrix (TAM) with improved dynamic characteristics*, Proceedings of 13th International Modal Analysis Conference, Nashville, Tennessee, pp 1506-1514, 1995.

11.26 Kammer, D.C., *A hybrid approach to test-analysis-model development for large space structures*, Journal of Vibration and Acoustics, vol.113, pp 325-332, July 1991.

11.27 Suarez, L.E. and Singh, M.P., *Dynamic condensation method for structural eigenvalue analysis*, AIAA Journal, vol.30, no.4, pp 1046-1054, April 1992.

11.28 Baker, M., *Review of test/analysis correlation methods and criteria for validation of finite element models for dynamic analysis*, Proceedings of 10th International Modal Analysis Conference, San Diego, Ca., pp 985-991, 1992.

11.29 Fuh, J.S., Gustavson, B. and Berman, A., *Error estimation and compensation in reduced dynamic models of large space structures*, AIAA Structural Dynamics and Materials Conference, May 1986.

11.30 Conti, P., *A higher order generalization of the Guyan reduction method*, Proceedings of 7th International Modal Analysis Conference, Las Vegas, Nevada, pp 529-532, Feb 1989.

11.31 MacNeal, R.H., *A hybrid method of component mode synthesis,* Computers and Structures, vol.1, pp 581-601, Dec 1971.

11.32 Irretier, H. and Sinapius, M., *A modal synthesis method based on analytical eigensolutions of the substructures with condensation of modal degrees of freedom*, Eurodyn90, Bochum, Germany, pp 381-388, June 1990.

11.33 Yang, M. and Brown, D., *An improved procedure of handling damping during FE model updating*, Proceedings of 14th International Modal Analysis Conference, Dearborn, Michigan, pp 576-584, 1996.

12.

TEST-ANALYSIS CORRELATION

In structural modeling, the large order analytical model is correlated with the low order experimental model, in order to validate or update the former. Test-analysis correlation studies are carried out to validate structural finite element models. Direct comparison of mode shapes requires a test-analysis model which is a reduced representation of the structure. Its degrees of freedom (DOF) correspond to sensor/exciter locations during the modal survey test and are a small sub-set of the analytical DOFs. Mass and stiffness matrices containing only test DOFs are commonly used in orthogonality and cross-orthogonality checks. This chapter presents model comparison techniques and strategies for the placement of sensors and exciters.

12.1 Dynamic structural modeling

One of the primary modeling objectives in structural dynamics is to produce reliable structural models to predict the dynamic response, to derive design loads and limit responses, to establish stability margins or to design adequate control systems for large scale structures.

Uncertainties of purely analytical modeling procedures, such as discretization, boundary conditions, joint flexibilities, and damping, require experimental verification of the predictive accuracy of the analytical (usually finite element) model. Current practice is to use models based on, or improved by, the use of measured quantities.

Purely test-based modeling may have the same level of uncertainty due to the limited capabilities of test methods, truncated temporal and spatial available information, and shortcomings of the identification approach. The solution is to use combined analytical/experimental procedures to derive structural models able to meet the performance goals of the respective dynamic mechanical system.

Complete procedures include pre-test planning and analysis, finite element (FE) modeling, test data acquisition, data reduction and analysis, model parameter identification, test/analysis correlation, model validation or updating.

12.1.1 Test-analysis requirements

Requirements of combined dynamic test/analysis procedures include use of consistent and accurate experimental data, compatibility of experimental and analytical models and model verification/updating using test data.

Current issues met in comparisons between experiment and prediction are: a) condensation (reduction) of analytical models; b) condensation of experimental data to obtain a minimum order identification model; c) expansion of measured modal vectors; d) calculation of real normal modes from identified complex or monophase forced modes of vibration; and e) identification of the spatial properties of the model. A schematic view of structural modeling is shown in Fig. 12.1.
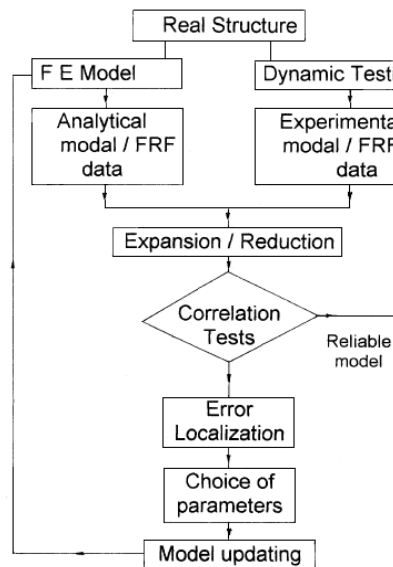
Fig. 12.1 (from [12.1])

Detailed schemes are presented in Fig. 12.2 and Annex 1. The "experimental route" (measured FRFs $\rightarrow$ modal model $\rightarrow$ spatial model) is compared to the "analytical route" (FE model $\rightarrow$ modal model $\rightarrow$ analytical FRFs), which is crossed in reverse direction. Comparisons and correlations between experiment and prediction can be made using each dynamic model (physical, modal, and response).

Considering that the structure of the model is known (or assumed), the problem is to use a noisy set of measurement data to find those parameters of the model that fit the data optimally. The optimization problem consists of the minimization of a cost function based on residuals that define the difference between measured and predicted quantities. Measured quantities are considered the most accurate. Most updating procedures are based on the sensitivity of modal parameters to changes in physical properties of the modeled system.

Direct *comparison of modal quantities* requires prior pairing of the corresponding measured and analytical modes. Some formulations introduce modal parameters in cost functions based on stress residuals. Generally, only real modal quantities are compared, requiring a real-normalization of identified complex modes or their calculation from monophase-forced modes.
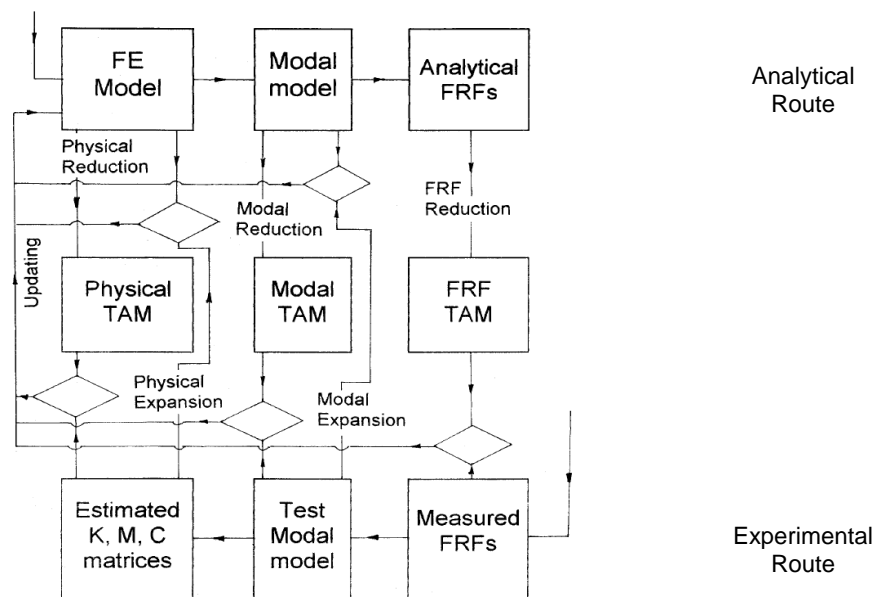
Fig. 12.2

Comparison of spatial properties implies prior condensation of analytical mass and stiffness matrices. This distributes the local errors over all matrix terms. Modal condensation, extended Guyan reduction or dynamic reduction can be used, as shown in Section 11.3. However, global updating procedures, in which elements of global matrices are adjusted by minimizing global objective functions, cannot localize error sources.

Local updating procedures based on subsystem formulations are preferred. The design parameters are proportionality constants in the relationships between global matrices and element or subsystem matrices. Combined with a

sensitivity analysis, this maintains the physical interpretation of localized errors. However, selection of correction parameters might be a difficult task.

Comparison of response properties seems the most appropriate, although frequency response functions (FRF) are the end product of the analytical route, containing all modeling uncertainties. Direct use of input/output measurement data for comparison of output residuals implies a linearity check. Otherwise a linear model will be forced to fit a nonlinear structure.

12.1.2 Sources of uncertainty

The identification of a mechanical system or structure from test data is complicated by uncertainties in system modeling. These uncertainties often lead to modeling errors.

Modeling errors are due to system properties which are not fully understood, such as nonlinearities, hysteresis, model dimensions, truncation errors, and a general lack of the full characterization of structural materials. The incompleteness of the test data set can be due to *spatial truncation* and *frequency truncation*. In the first case, the number of measurement degrees of freedom (DOF) is limited and different from the FE DOFs, and the rotational DOFs cannot be readily measured. In the second case, the number of measured mode shapes is limited, while some modes are not excited or not identified. In addition to system uncertainties, forces (such as preloads) may be acting on the system during the period of parameter identification which are not taken into account as input data.

Errors associated with *model reduction* are also associated with *modal identification*. The transformation between test DOFs and analysis DOFs is frequency dependent. It is very sensitive to the proximity of the system natural frequencies to the natural frequency of the subsystem remaining when all retained (test) DOFs are constrained.

In model updating, there are FE errors, model correction errors, connectivity errors and global correction errors.

Errors inherent to the FE technique include discretization errors (mesh quality, efficiency of shape functions), global approximation errors (integration, truncation, round-off, eigenparameter extraction), and interpolation errors (elemental). Errors introduced by the analyst include the omission of 'unimportant' details, choice of elements to represent a given geometry and uncertainties associated with boundary conditions. Issues of concern are the global errors which have not directly associated elements.

Model correction errors encompass linearization (use of design parameters to multiply elemental matrices), frequency dependence of correction factors (different modes have varying degrees of sensitivity to changes in a given element; also inclusion/exclusion of a mode makes significant differences), choice

of elements kept in analysis, the objective function to be minimized, weighting of input parameters, number and location of measurement coordinates, location of frequency points in FRFs and vector expansion errors.

As for the *global correction errors*, it must be emphasized that methods based on a least squares fit will not necessarily lead to an analytical model that is physically representative of the actual structure. All it can do is to correctly predict the measured modes. In global updating, any effect due to an update to the stiffness matrix can be accomplished by an update of the mass matrix. Also, an increase of accuracy within the frequency band of interest may be accompanied by a corresponding loss of accuracy outside the frequency band.

Having in view all these possible errors, model updating often reduces to a simple *model fitting.*

A first step in the general process of *model verification* is the *model validation*, where the basic structure of the model is verified. The next step is the *parameter estimation*. In order for parameter estimation to be successful, so that the model may be used with confidence to predict system behavior in a new environment, the basic structure of the model must be "correct", i.e. the primary load paths, mass distribution and boundary conditions must be properly represented in the equations of motion. This is a time-consuming trial and error process.

The *validation* of a theoretical model is usually done in three main steps: a) comparison of specific dynamic properties, measured vs. predicted; b) quantification of the extent of differences (or similarities) between the two sets of data; and c) adjustment or modification of one or the other set of results in order to bring them closer to each other.

Note that the concept of a verified model is different from that of a validated model. A model is said to be *verified* if it contains the correct features, most importantly the appropriate number and choice of DOFs, to represent the behavior of the structure. A model is said to be *valid* if the coefficients in that model are such as to provide an acceptable quantitative representation of the actual behavior. A model can only be validated after it has been verified. This means that comparisons and correlations can be made only after the two models to be used are compatible with each other, and with their intended roles [12.2].

12.1.3 FRF based testing

Most FRF-based modal testing procedures involve structural excitation, acquisition of frequency response data, calculation of FRFs, extraction of modal parameters, and model verification or modification. All parts of this process are connected and must be treated as interdependent.

Pre-test analysis. The first stage is exploratory and is intended to provide a general view of the dynamic properties of a structure; e.g., modal density, level of

damping, degree of nonlinearity, repeatability of data. Based on these data, the basic test parameters can be chosen; i.e., frequency range, coordinates to be included, set of FRFs that should be measured and analyzed. The test plan is a compromise between resources, test objective and know-how.

The geometry of the structure must be defined and discretized into points at which measurements will be taken. It is recommended that the number of points used be equal to or greater than the number of modes of interest. Otherwise, geometry truncation errors will affect the model. In some cases, the response at assumed stations can be analytically generated from responses at actual stations.

The main question to be answered is the following: What is the optimal set of actuator/sensor locations, input time-histories and system (structural) characterizations required for a particular structure so that errors in system modeling would have minimal effect on the identified results?

Translational as well as rotational degrees of freedom must be considered, especially at structural attachment points, for proper application of modification procedures. During preliminary tests, checks are made of the suspension of the structure and the exciter attachment site, and of reciprocity, repeatability, linearity, and instrumentation calibrations. Excitation locations and check levels are selected.

When multi-input excitation is used, the reciprocity and coherence functions at each exciter location can be plotted and compared. Those locations displaying the best reciprocity and coherence are selected as the reference coordinates in the generation of the FRF matrix. The experimental conditions affect the covariance matrix of the estimates. With a bad choice of input, some parameters of interest may not be identifiable. Theoretically, an impulse or white noise random excitation applied at appropriate locations will excite all modes of the system. But sometimes the signal energy could be insufficient to excite both the global and local modes.

Significant participation of the important modes is a necessary condition for practical identification. Selection of response measurement locations which ensure an effective relative independence of contributing modes is important. It is also desirable to select an input which maximizes the sensitivity of the system output to unknown parameters. As criteria to achieve an optimal input are not fully developed, it is good practice to choose an input that is, as far as possible, similar to the inputs the system will experience during operation. Force patterns can also be calculated that may be used to enhance FRFs to make single-degree-of-freedom identification methods applicable to high modal density situations.

A test-analysis model can also be developed in the pre-test phase. Sometimes it helps in the definition of test geometry.

Singular value ratio plots and mode indicator functions can be used to determine the effective number of modes active within a particular frequency

range. Pole Stabilization Diagrams are also used to define the optimum number of roots in the identification algorithm. Nonlinearities can be recognized from the pattern of isochrones (as shown in Chapter 2).

Data acquisition and processing. The second stage of modal tests on complex structures is the process in which all the data required to build the final model are measured and then processed. As shown in Chapter 10, two techniques are currently in widespread use for determining structural dynamic characteristics: modal tuning and frequency response. Modal tuning methods attempt to excite and isolate one particular mode through sinusoidal excitation. Frequency response methods attempt to excite modes occurring in a finite frequency range and to measure FRFs. Calculation of FRFs from simultaneous multiple force inputs has shortened measurement time and improved the consistency of data. Time response methods using free decays, impulse response functions, and random decrement signatures are also in use.

Data base validation. The third stage is verification of the accuracy of modal parameters. Comparisons of natural frequencies and damping levels are made as dispersion error checks. Before orthogonality checks for mode shapes are performed, matching the node and sensor numberings is a necessary step. The Modal Assurance Criterion (MAC) is used for mode pairing. Discrepancies between measured and identified mode shapes are made on a DOF basis using the Coordinate MAC. If the mass matrix accurately represents the mass properties of the modal model, a diagonal orthogonality error matrix is obtained. In practice, if the off-diagonal terms of the error matrix are less than a given value, the set of measured modes is orthogonal. Synthesized FRF expressions recreated from a mathematical model are then compared with experimentally measured FRF data to check the fitting accuracy.

12.2 Test-analysis models

Advanced engineering structures require *accurate* analytical (finite element) models (FEM) for structural analysis and control system design. A basic objective of a modal survey is to verify that the FEM of a structure is sufficiently accurate to predict the structure's response to operating environments. The modal surveys measure the natural frequencies and mode shapes of the structure for use in model verification.

In general, the FEM has many more degrees of freedom than the measurement points on the test structure. In order to compare the FEM with the test results directly, a reduced representation or Test-Analysis Model (TAM) must be generated. The degrees of freedom of the TAM will correspond one for one with accelerometers in the modal survey test configuration. The TAM is represented by mass and stiffness matrices containing only test DOFs.

The development of a TAM serves several major functions. The selection of TAM DOFs optimizes the test measurements and excitation locations. The reduced mass matrix provides an ability to calculate on-site orthogonality checks of the test modes. Finally, the TAM enables a quantitative comparison of the accuracy of the FEM during post-test correlation activities in the form of orthogonality and cross-orthogonality checks. All of these tasks require an accurate reduction of the FEM mass and stiffness matrices down to the TAM DOFs, or the TAM will not be able to perform its functions.

The position of the TAM between the FEM and the Test Model is schematically shown in Fig. 12.3. Apart from the FEM/TAM and TAM/Test comparison and correlation, FEM/Test comparisons are also made, either at the full FEM size or at the TAM size.

The main TAM performance criteria are accuracy and robustness [12.3]. *Accuracy* is a measure of the TAM ability to match the full FEM mode shapes and frequencies. *Robustness* is a measure of the TAM ability to provide reliable cross-orthogonality (analytical vs. test) and self-orthogonality (test vs. test) results. Robustness is of particular importance because showing orthogonal test modes is a commonly used requirement to determine the success of a modal survey. The TAM challenge is to match as closely as possible the TAM eigenpairs to those of the full FEM, providing at the same time reliable orthogonality results, especially when the FEM has inaccuracies.
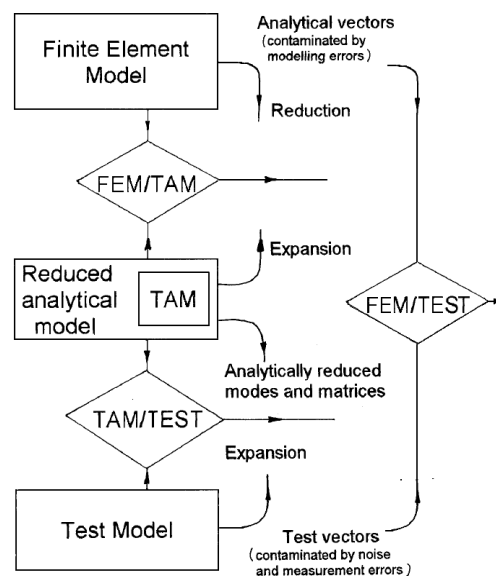

Fig. 12.3

The TAM concepts presented in Chapter 11 are based on various reduction methods.

The relationship between the FEM displacement vector and the reduced test-derived vector of *a*-DOFs or generalized coordinates is expressed as

$$\{u\}=[T]\{u_a\} \tag{12.1}$$

where the transformation matrix $[T]$ has the following expressions, in which the notations from Chapter 11 are used:

a) for the Static TAM (11.25)

$$[T_S]=\begin{bmatrix}[I_a]\\[G_{oa}]\end{bmatrix}=\begin{bmatrix}[I_a]\\-[k_{oo}]^{-1}[k_{oa}]\end{bmatrix}. \tag{12.2}$$

b) for the IRS-TAM (11.68)

$$[T_{IRS}]=\begin{bmatrix}[I_a]\\[G_{oa}]+[k_{oo}]^{-1}([m_{oa}]+[m_{oo}][G_{oa}])[m_a]^{-1}[k_a]\end{bmatrix}. \tag{12.3}$$

c) for the Modal TAM (11.112)

$$[T_m]=\begin{bmatrix}[I_a]\\[\Phi_{ot}][\Phi_{at}]^g\end{bmatrix}=[\Phi_t][\Phi_{at}]^{-1}. \tag{12.4}$$

d) for the Hybrid TAM (11.145)

$$[T_{Th}]=[T_S]+([T_m]-[T_S])[\Phi_{at}][\Phi_{at}]^T[m_{at}]. \tag{12.5}$$

The reduced mass matrices have the form

$$[m_{TAM}]=[T]^T[m_{FEM}][T]. \tag{12.6}$$

Comparisons of modal TAMs and non-modal TAMs are presented in Section 11.3.5, and in [12.3] and [12.4].

It was shown [12.5] that the Arnoldi vectors (Section 8.6.3) provide a more suitable subspace for model reduction than the eigenvector space used in the Modal TAM. Without compromising accuracy, they can ensure robustness by proper selection of the first vector and choice of the number of Arnoldi vectors used in calculation.

The transformation matrix of the Arnoldi TAM is

$$[T_A]=\begin{bmatrix}[I_a]\\[V_o][V_a]^+\end{bmatrix}, \tag{12.7}$$

where $\left[V_a \right]$ and $\left[V_o \right]$ are the top and respectively bottom partition of the matrix of "target" Arnoldi vectors and $^+$ denotes the pseudoinverse.

The Schur TAM [12.6] is a modified Modal TAM constructed with Schur vectors, resulting in reduced computational expense. Generalized Schur vectors are the columns of one of the orthogonal matrices that simultaneously transform the stiffness and mass matrices to upper triangular form (Section 8.4.4). For large and sparse matrices, they provide a basis with much better numerical properties than a set of eigenvectors and a more suitable subspace for model reduction. Schur vectors are determined *before* eigenvectors.

The transformation matrix of the Schur TAM is

$$\left[\, T_{Sch} \,\right] = \left[\begin{array}{c} \left[I_a \right] \\ \left[U_o \right]\left[U_a \right]^+ \end{array} \right], \tag{12.8}$$

where $\left[U_a \right]$ and $\left[U_o \right]$ are the upper and respectively lower partition of the matrix of "target" Schur vectors.

It is useful to compare TAM mass matrices, $\left[m_{TAM} \right]$, obtained by different model reduction methods, either on the same test modal vectors, or on reduced analytical modal vectors. The comparison is based on the orthogonality of the reduced mass matrices with respect to either the test or the analytical modal vectors.

There are three main kinds of comparison: 1) analytical-to-analytical (FEM-to-FEM, TAM-to-TAM, and TAM-to-FEM), 2) experimental-to-experimental, and 3) analytical-to-experimental [12.7].

The Test Orthogonality matrix, defined as

$$\left[TOR \right] = \left[\Phi_{TEST} \right]^T \left[m_{TAM} \right]\left[\Phi_{TEST} \right], \tag{12.9}$$

is a measure of the robustness of the TAM reduction method, i.e. the ability of the TAM to provide *TOR* matrices that resemble the identity matrix, when the FEM has inaccuracies. It is used to verify the quality of test data during modal testing. The matrix $\left[\Phi_{TEST} \right]$ contains the measured modal vectors as columns. Use of the TAM mass matrix raises problems. One must differentiate reduction errors from discrepancies between the FEM and the TEST model.

Equation (12.9) can also be written

$$\left[TOR \right] = \left[\Phi_{Xa} \right]^T \left[m_a \right]\left[\Phi_{Xa} \right]. \tag{12.9, a}$$

A normalized version, allowing different scaling of the two vector sets $\left(r,q \right)$ is

$$ORM\,(\,r,q\,) = \frac{\{\varphi_X\}_r^T\,[\,m_a\,]\{\varphi_X\}_q}{\left(\{\varphi_X\}_r^T\,[\,m_a\,]\{\varphi_X\}_r\right)^{1/2}\left(\{\varphi_X\}_q^T\,[\,m_a\,]\{\varphi_X\}_q\right)^{1/2}}\,.$$

It should be mentioned that, when correlating test with test, no procedure will diagnose a systematic fault that is present in both sets of data (e.g., calibration inaccuracies), as its effect on the mode shapes will be cancelled out by the correlation algorithm.

The Generalized Mass matrix is defined as

$$[\,GM\,] = \left[\varPhi_{FEM}^R\right]^T\,[\,m_{TAM}\,]\left[\varPhi_{FEM}^R\right]\,,\qquad(12.10)$$

where $\left[\varPhi_{FEM}^R\right]$ is the matrix of target analysis modes reduced to the measured DOFs. It is used as an indicator of the goodness of the TAM mass matrix, revealing errors in the TAM due to the reduction process. For a perfect TAM it should approximate to the identity matrix.

The Cross Orthogonality matrix

$$[\,XOR\,] = \left[\varPhi_{FEM}^R\right]^T\,[\,m_{TAM}\,][\,\varPhi_{TEST}\,]\qquad(12.11)$$

is a less stringent check of robustness, since the test modal vectors are used only once in the calculation.

Note that the TAM accuracy, i.e. its ability to predict the dynamic response of the structure to operating environments, is assessed by comparison of modal frequencies and mode shapes, i.e. of test and TAM modal properties.

Example 12.1

An indirect comparison of the TAM mass matrices, obtained by four reduction methods presented above, can be made based on the test mode shapes and the mixed orthogonality check *TOR*. A typical result is illustrated in Fig. 12.4, presenting the *TOR* matrices calculated from four different reduced mass matrices. The reference FEM of the structure, having about 45,000 DOFs, has been reduced to a 120 DOFs TAM, having 15 flexible natural modes between 5.2 and 34.3 Hz.

The largest off-diagonal terms occur in the TOR matrix of the Modal TAM (Fig. 12.4, *a*), especially for the higher residual modes. This can be an indication that the spatial resolution given by the selected response measurement points (the *a*-set) is insufficient to make the target modes linearly independent and observable – an important outcome of such a comparison process.

The Hybrid TAM shows a slight improvement on the Modal TAM, due to the inclusion of static modes with the target modes (Fig. 12.4, *b*).

Surprisingly, the Static TAM performs better than the Modal TAM, showing smaller off-diagonal terms (Fig. 12.4, *c*). The IRS TAM yields the best reduced mass matrix, producing the lowest off-diagonal elements in the TOR matrix (Fig. 12.4, *d*).
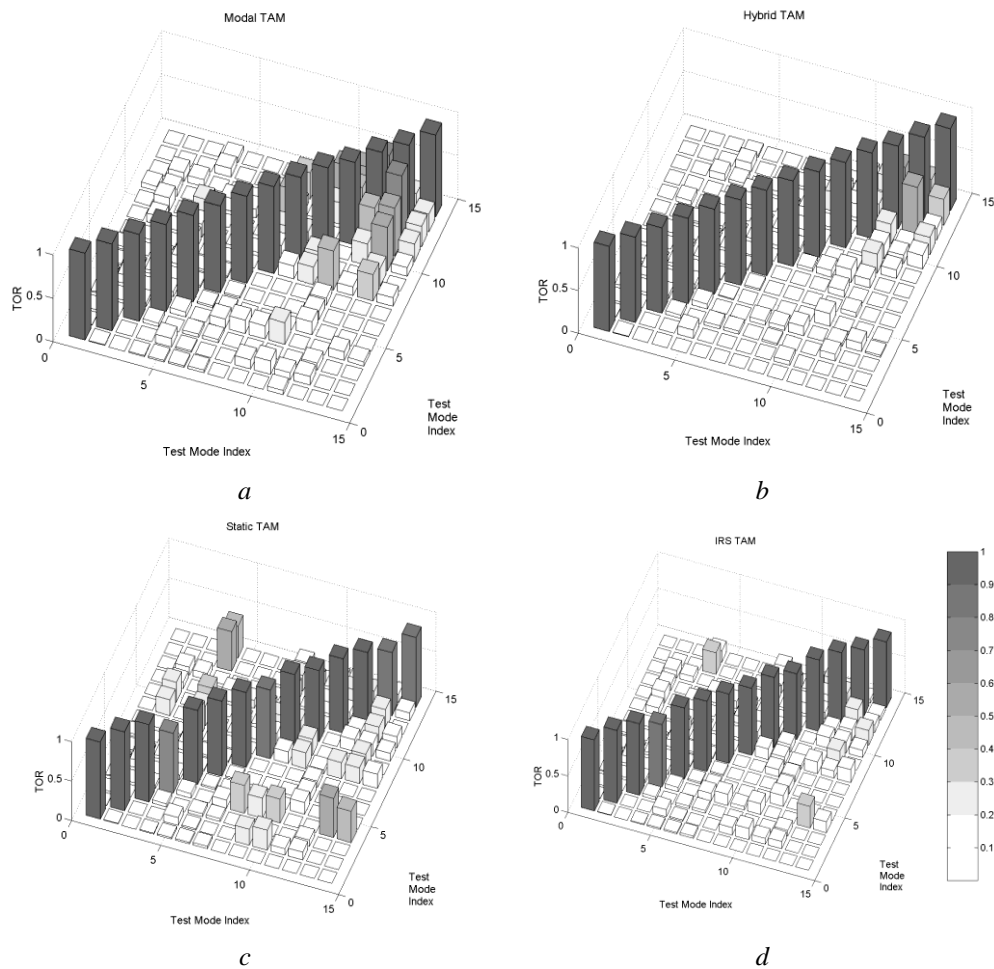
Fig. 12.4 (from [12.7])

While the Modal TAM gives the best match in frequencies and target modes, its prediction capability is low outside the frequency range spanned by the selected target modes.

The Static TAM, implemented as the Guyan Reduction in many computer programs, performs better in orthogonality checks, but is dependent on the selection of *a*-DOFs and generally requires more *a*-DOFs to give comparable accuracy. However, these types of comparisons are usually problem-dependent.

12.3 Comparison of modal properties

Modal properties that are compared usually include natural frequencies, real mode shape vectors, modal masses, modal kinetic and strain energies. For systems with complex modes of vibration one can add modal damping ratios and complex mode shapes.

Comparison of modal vectors can be done at the reduced order of TAM or at the full order of the FEM. Reduction of the physical mass matrix or expansion of test modal vectors bring inherent approximations in the comparison criteria. A test-analysis comparison is meaningful only for matched modes, i.e. for Correlated Mode Pairs (CMPs). These are estimates of the same physical mode shape and their entries correspond one-for-one with their counterparts. Mode matching (pairing) is an essential step before any comparison can be undertaken.

It is useful to compare: 1) measured mode shapes against modal vectors determined by an analytical model; 2) estimates of the same test modal vector obtained from different excitation locations; 3) estimates of the same modal vector obtained from different modal parameter identification processes using the same test data; and 4) one test mode shape before and after a change in the physical structure caused by a wanted modification, by damage or by operation over time.

12.3.1 Direct comparison of modal parameters

Scalar quantities, such as natural frequencies, modal damping ratios, norms of modal vectors, modal masses and modal energies are usually compared by simple tabulation of the relative error. If there is one-for-one correspondence between the r-th and the q-th modes, then the following discrepancy indicators are used:

- the relative modal frequency discrepancy

$$\varepsilon_f = \frac{\left| f_r - f_q \right|}{f_r} \cdot 100 \, ;$$

- the relative modal damping discrepancy

$$\varepsilon_\zeta = \frac{\left| \zeta_r - \zeta_q \right|}{\zeta_r} \cdot 100 \, ;$$

- the relative mode shape norm difference

$$\varepsilon_\psi = \mathrm{abs} \frac{\left| \{\psi\}_r^H \{\psi\}_r \right| - \left| \{\psi\}_q^H \{\psi\}_q \right|}{\left| \{\psi\}_r^H \{\psi\}_r \right|} \cdot 100.$$

For some spacecraft structures, having about twenty flexible modes up to 50 Hz, modeling accuracy criteria typically specify values $\varepsilon_f \leq 5\%$. Comparative values for mode shape and damping ratio discrepancies are $\varepsilon_\psi \leq 10\%$ and $\varepsilon_\zeta \leq 25\%$, respectively.

A straightforward way to compare two compatible sets of data is by making an *X-Y* plot of one data set against the other. The method can be used to compare natural frequencies from two different models. For well-correlated data, the points of the resulting diagram should lie close to a straight line of slope equal to 1. If the approximating straight line has a slope different from 1, this indicates a bias error due to either calibration or erroneous material property data. Large random scatter about a 45° line indicates poor correlation or bad modelling.

The procedure can be applied to the mode shapes of correlated mode pairs. Each element of a test mode shape is plotted against the corresponding element of the analytical modal vector. For consistent correspondence, the points should lie close to a straight line passing through the origin. If both modal vectors are mass-normalized, then the approximating line has a slope of ± 1.

12.3.2 Orthogonality criteria

The most relevant way to assess the validity of a set of modal vectors is the orthogonality check. For this it is necessary to compute: a) a FEM of the tested structure, b) an analytical mass matrix reduced to the test DOFs, and/or c) a set of test mode shapes expanded to the FEM DOFs.

The formulae given below assume that experimentally measured (test) quantities are labelled by *X* and theoretically predicted (analytical) quantities are labelled by *A*.

The mass-orthogonality properties of FEM real mode shapes can be written

$$\left[\, \Phi_A \,\right]^T \left[\, m_A \,\right] \left[\, \Phi_A \,\right] = \left[\, I \,\right], \tag{12.12}$$

where $\left[\, \Phi_A \,\right]$ is the modal matrix at the full FEM order, $\left[\, m_A \,\right]$ is the FEM full-order mass matrix and $\left[\, I \,\right]$ is the identity matrix of the corresponding size.

For the TAM, the mass-orthogonality condition becomes

$$\left[\, \Phi_A^R \,\right]^T \left[\, m_A^R \,\right] \left[\, \Phi_A^R \,\right] = \left[\, I \,\right], \tag{12.13}$$

where $\left[\, m_A^R \,\right]$ is the reduced TAM mass matrix (Section 12.4.1) and $\left[\, \Phi_A^R \,\right]$ contains the modal vectors reduced to the measured DOFs and mass-normalized with respect to $\left[\, m_A^R \,\right]$.

12.3.2.1 Test Orthogonality Matrix

A mixed orthogonality test of the set of measured modal vectors $[\Phi_X]$ is often done to check the quality of measurement data. The Test Orthogonality (*TOR*) matrix (12.9) can be written

$$[TOR] = [\Phi_X]^T [m_A^R][\Phi_X]. \qquad (12.14)$$

If the measured modal vectors are orthogonal and mass-normalized with respect to the reduced mass matrix $[m_A^R]$, then $[TOR]$ will be the identity matrix. Test guidelines specify $TOR_{rr} = 1$ and $|TOR_{rq}| < 0.1$.

12.3.2.2 Cross Orthogonality Matrix

A cross-orthogonality test is performed to compare paired modal vectors, measured with analytical.

A *Cross Generalized Mass* (CGM) matrix, defining a Cross Orthogonality (*XOR*) criterion, can be constructed with mass-normalized modal vectors either at the TAM size:

$$[XOR_{TAM}] = [\Phi_X]^T [m_A^R][\Phi_A^R], \qquad (12.15)$$

or at the full FEM size:

$$[XOR_{FEM}] = [\Phi_X^E]^T [m_A][\Phi_A], \qquad (12.16)$$

where $[\Phi_X^E]$ contains the test modal vectors expanded to the full FEM DOFs.

For perfect correlation, the leading diagonal elements XOR_{rr} should be larger than 0.9, while the off-diagonal entries $|XOR_{rq}|$ should be less than 0.1.

Use of the reduced mass matrix $[m_A^R]$ raises problems. One must differentiate reduction errors from discrepancies between the FEM and the test model.

When the reduced TAM mass matrix is obtained by the SEREP method (Section 11.3.2), *XOR* is referred to as a *Pseudo-Orthogonality Criterion* (POC). It is demonstrated that $POC_{TAM} = POC_{FEM}$. In this case, the full FEM mass matrix is not needed to compute either $[m_A^R]$ or POC_{TAM} because

$$[m_A^R] = ([\Phi_A^R]^+)^T [\Phi_A^R]^+, \qquad (12.17)$$

where the superscript + denotes the pseudoinverse [12.1].

Cross-orthogonality criteria cannot locate the source of discrepancy in the two sets of compared mode shapes. Large off-diagonal elements in the cross-orthogonality matrices may occur simply because they are basically small differences of large numbers. Also, modes having nearly equal frequencies may result in linear combinations of analysis modes rotated with respect to the test modes, case in which the off-diagonal elements of $[XOR]$ are skew-symmetric.

12.3.3 Modal vector correlation coefficients

This section presents global indicators for vector correlation and degree-of-freedom-based vector correlation methods.

12.3.3.1 Modal Scale Factor

If the two compared mode shape vectors have different scaling factors, it is useful to determine the slope of the best line through the data points. This is calculated as the least squares error estimate of the proportionality constant between the corresponding elements of each modal vector

$$\{\varphi_A\} = MSF(A, X) \cdot \{\varphi_X\}, \tag{12.18}$$

where $\{\varphi_X\}$ is the test vector and $\{\varphi_A\}$ is the compatible analytical vector.

For real vectors, it is a real scalar referred to as the *Modal Scale Factor* (*MSF*), defined as

$$MSF(A, X) = \frac{\{\varphi_X\}^T \{\varphi_A\}}{\{\varphi_X\}^T \{\varphi_X\}}, \tag{12.19}$$

For complex vectors, the superscript *T* is replaced by *H* (hermitian) and the MSF is a complex scalar.

The MSF gives no indication on the quality of the fit of data points to the straight line. Its function is to provide a consistent scaling factor for all entries of a modal vector. It is a normalized estimate of the modal participation factor between two excitation locations for a given modal vector.

12.3.3.2 The Modal Assurance Criterion

One of the most popular tools for the quantitative comparison of modal vectors is the *Modal Assurance Criterion* (*MAC*) [12.8].

The *MAC* was originally introduced in modal testing in connection with the *MSF*, as an additional confidence factor in the evaluation of a modal vector from different excitation locations.

When an FRF matrix is expressed in the partial fraction expansion form, the numerator of each term represents the matrix of residues or modal constants.

Each residue matrix is proportional to the outer product of one modal vector and the corresponding vector of the modal participation factors. Each column of the residue matrix is proportional to the respective modal vector. One can obtain estimates of the same modal vector from different columns of the residue matrix. *MAC* has been introduced as a measure of consistency and similarity between these estimates.

If the elements of the two vectors are used as the coordinates of points in an *X-Y* plot, the MAC represents the normalized least squares deviation or 'scatter' of corresponding vector entries from the best straight line fitted to the data, using the MSF. The concept can be applied to the comparison of any pair of compatible vectors.

The MAC is calculated as the normalized scalar product of the two sets of vectors $\{\varphi_A\}$ and $\{\varphi_X\}$. The resulting scalars are arranged into the MAC-matrix

$$MAC\left(r,q\right)=\frac{\left|\{\varphi_A\}_r^T\{\varphi_X\}_q\right|^2}{\left(\{\varphi_A\}_r^T\{\varphi_A\}_r\right)\left(\{\varphi_X\}_q^T\{\varphi_X\}_q\right)}, \qquad (12.20)$$

where the form of a coherence function can be recognized, indicating the causal relationship between $\{\varphi_A\}$ and $\{\varphi_X\}$.

Note that the modulus in the numerator is taken *after* the vector multiplication, so that the absolute value of the sum of product elements is squared. An equivalent formulation is

$$MAC\left(A,X\right)=\frac{\left|\sum_{j=1}^{n}\{\varphi_A\}_j\{\varphi_X\}_j\right|^2}{\left(\sum_{j=1}^{n}\{\varphi_A\}_j^2\right)\left(\sum_{j=1}^{n}\{\varphi_X\}_j^2\right)}. \qquad (12.21)$$

The MAC has been used as a *Mode Shape Correlation Constant*, to quantify the accuracy of identified mode shapes [12.9]. For complex modes of vibration

$$MAC\left(r,q\right)=\frac{\left|\{\psi_A\}_r^T\{\psi_X\}_q^*\right|^2}{\left(\{\psi_A\}_r^T\{\psi_A\}_r^*\right)\left(\{\psi_X\}_q^T\{\psi_X\}_q^*\right)}, \qquad (12.22)$$

and is clearly a real quantity, even if the mode shape data are complex.

The *MAC* takes values between 0 and 1. Values larger than 0.9 indicate consistent correspondence, whereas small values indicate poor resemblance of the

two shapes. The MAC does not require a mass matrix and the two sets of vectors can be normalized differently. The division cancels out any scaling of the vectors.

If $\{\varphi\}_r$ and $\{\varphi\}_q$ are the *r*-th and *q*-th columns of the real modal matrix $[\Phi]$, then, using the cross-product (Gram) matrix $[G] = [\Phi]^T[\Phi]$, the *MAC* can be written

$$MAC(r,q) = \frac{G_{rq}^2}{G_{rr}\,G_{qq}} = \cos^2\theta_{rq}\,, \qquad (12.23)$$

where $G_{rq} = \{\varphi\}_r^T\{\varphi\}_q$ is the inner product and θ_{rq} is the angle between the two vectors. *MAC* is measure of the squared cosine of the angle between the two vectors. It shows to what extent the two vectors point in the same direction.

If $MAC \cong 0$, the two modal vectors are *not consistent*. This can be due to: a) non-stationarity (mass or stiffness change during test), b) non-linearity (whose influence appears differently in FRFs generated from different exciter and sensor locations), c) noise on the reference modal vector $\{\varphi_X\}$, d) use of invalid parameter estimation algorithm (e.g.: real instead of complex modes), and e) orthogonal vectors.

If $MAC \cong 1$, the modal vectors are *consistent*, but *not* necessarily *correct*. This can result when: a) measured vectors are incomplete (too few response stations – spatial truncation), b) modal vectors are the result of a forced excitation other than the desired input (e.g.: unbalance), c) modal vectors are primarily coherent noise ($\{\varphi_X\}$ should be a true modal vector), and d) modal vectors represent the same modal vector with different arbitrary scaling (given by the *MFS*).
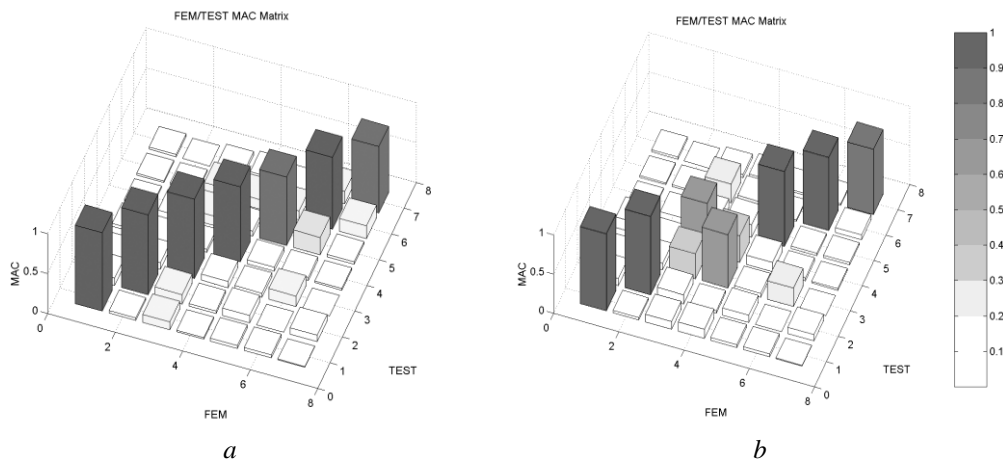

Fig. 12.5 (from [12.7])

The ideal *MAC* matrix cannot be a unit matrix because the modal vectors are not directly orthogonal, but mass-orthogonal (Fig. 12.5, *a*). However, the *MAC* matrix indicates which individual modes from the two sets relate to each other. If two vectors are switched in one set, then the largest entries of the *MAC* matrix are no more on the leading diagonal and it resembles a permutation matrix. The two large off-diagonal elements show the indices of the switched vectors, as illustrated in Fig. 12.5, *b*. Figure 12.6 is the more often used form of Fig. 12.5, *b*.
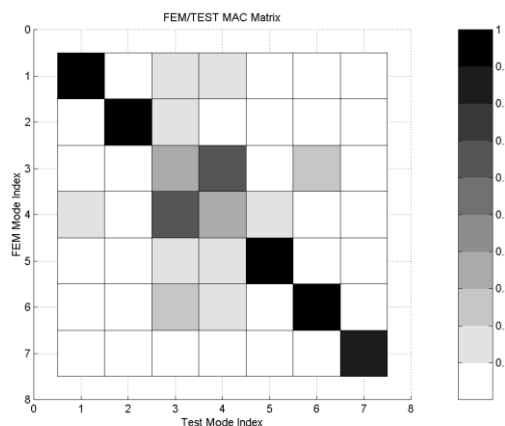

Fig. 12.6 (from [12.7])

The *MAC* can only indicate consistency, not validity, so it is mainly used in pre-test mode pairing. The *MAC* is incapable of distinguishing between systematic errors and local discrepancies. It cannot identify whether the vectors are orthogonal or incomplete.

For axisymmetric structures, that exhibit spatial phase shifts between test and analysis mode shapes, improved *MAC* values can be obtained by the rotation of mode shapes prior to correlation. For test mode shapes that contain multiple diametral orders, a special *Fourier MAC* criterion has been developed, using the first two primary Fourier indices.

The *MAC* is often used to assess the experimental vectors obtained by modal testing, especially when an analytical mass matrix is not available, and to compare test modal vectors with those calculated from FEM or TAM. The success of this apparent misuse is explained by two factors: First, test modal vectors usually contain only translational DOFs because rotational DOFs are not easily measured. If rotational DOFs were included in the modal vectors, the *MAC* would yield incorrect results. In this case it will be based on summations over vector elements of incoherent units, having different orders of magnitude. Second, for uniform structures, the modal mass matrix is predominantly diagonal and with not too different diagonal entries. In these cases, the *MAC* matrix is a good approximation for a genuine orthogonality matrix.

12.3.3.3 Normalized cross-orthogonality

A *Modified MAC* (*ModMAC*), weighted by the mass or the stiffness matrix, referred to as the *Normalized Cross-Orthogonality* (*NCO*) is defined as [12.10]:

$$NCO\left(r,q\right)=\frac{\left|\left\{\varphi_{A}\right\}_{r}^{T}\left[W\right]\left\{\varphi_{X}\right\}_{q}\right|^{2}}{\left(\left\{\varphi_{A}\right\}_{r}^{T}\left[W\right]\left\{\varphi_{A}\right\}_{r}\right)\left(\left\{\varphi_{X}\right\}_{q}^{T}\left[W\right]\left\{\varphi_{X}\right\}_{q}\right)}. \qquad (12.24)$$

The weighting matrix $\left[W\right]$ can be either the mass or the stiffness matrix. In the first case, it is sensitive to local modes with high kinetic energy (rather than just the global low order mode shapes), in the second case - to regions of high strain energy. Applying the *NCO* separately, using the analytical mass and stiffness matrices, it is possible to locate sources of inadequate modeling. However one must be careful to differentiate inherent reduction errors from discrepancies between the FEM and test data.

The *NCO* is able to use two arbitrarily scaled modal vectors. It defines the CMPs more clearly than the MAC. The square root version of *NCO* is being also used as a cross-orthogonality check based on mass-normalized modal vectors.

12.3.3.4 The AutoMAC

The *AutoMAC* addresses the spatial (or DOF) incompleteness problem.

The *MAC* can show correlation of actually independent vectors. If the number of DOFs is insufficient to discriminate between different mode shapes, it is possible that one analytical modal vector to appear as being well correlated with several experimental vectors.

It is necessary to check if the number of DOFs included in the model is sufficient to define all linearly independent mode shapes of interest. This check can be done using the *AutoMAC*, which correlates a vector with itself based on different reduced DOF sets. Spatial aliasing is shown by larger than usual off-diagonal elements of the *AutoMAC* matrix.

12.3.3.5 The FMAC

The *FMAC* is an efficient way of displaying the MAC, the AutoMAC and the natural frequency comparison in a single plot [12.11], such that the mode shape correlation, the degree of spatial aliasing and the natural frequency comparison can be plotted simultaneously. This is obtained by drawing a circle with a radius proportional to the MAC or AutoMAC value at the coordinates of each modal frequency pair, as shown in Fig. 12.7.
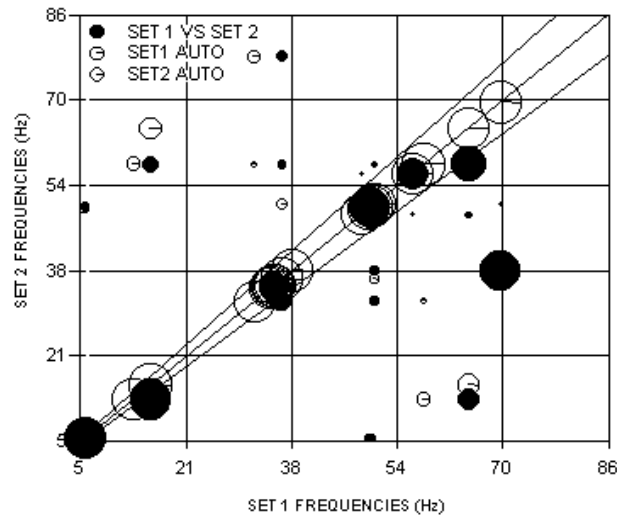
Fig. 12.7 (from [12.11])

Example 12.2

The experimental data used in this example have been obtained for the GARTEUR SM-AG-19 testbed (Fig. 9.66) as described in Section 9.4.5 and Example 10.2. Natural frequencies are listed in Table 10.2 for the unmodified structure, referred to as UNMOD, and in Table 9.3 for the structure modified by a mass added to the tail, referred to as MOD1.
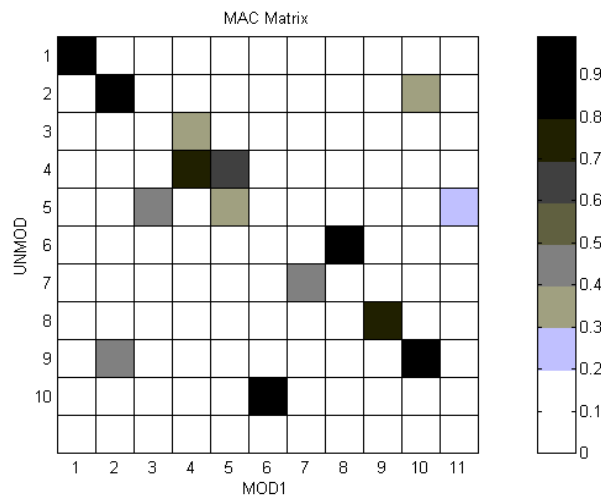

Fig. 12.8 (from [12.12])

As can be seen from the mode description in the two tables, there are changes in the mode ordering as a result of the mass modification. One of the ways to track these changes is via the modal assurance criteria.

Table 12.1. MAC matrix between UNMOD and MOD1

		MOD1 Mode Index										
		1	2	3	4	5	6	7	8	9	10	11
U N M O D I n d e x	1	**99.05**	0.28	0.05	0.34	0.01	0	0.43	18.76	0	0.28	0.04
	2	0	**98.23**	2.20	0.10	0.14	0	1.97	0	0.11	**36.62**	0.71
	3	0	0.15	13.55	**30.66**	16.41	0.02	0.10	0.50	0.97	0.55	0.21
	4	0.57	0.19	7.40	**70.00**	66.76	0.33	0.63	3.67	0.96	0.24	0.03
	5	0	0	**45.13**	1.75	**31.98**	0.51	0.87	0.02	0.63	17.98	**24.43**
	6	19.05	0.09	0	3.01	2.15	0.03	5.81	**94.51**	0.03	0.61	0
	7	0.43	1.03	18.87	0.42	5.38	18.44	**43.76**	3.84	0.17	11.99	7.04
	8	0	0	0.14	0.38	0.13	0.29	0	0.14	**75.82**	0.10	0.38
	9	0	**47.38**	2.76	0.03	3.46	2.64	13.90	0.15	0.61	**81.99**	1.23
	10	0	0.46	0.17	0.30	0.55	**94.34**	4.16	0.04	3.06	1.11	0

Figure 12.8 and Table 12.1 show the MAC matrix between the 10 identified modes of UNMOD and the 11 modes of MOD1. It is evident that modes 1, 2, 4 and 7 keep the same index in both sets. Modes 3, 5, 6, 8, 9 and 10 of UNMOD became modes 5, 3, 8, 9, 10 and 6 of MOD1. The swapping of modes 3 and 5 has been established by animation of the respective mode shapes and it is not so evident in Fig. 12.8. In fact, mode 5 of MOD1 is a linear combination of two modes of UNMOD.
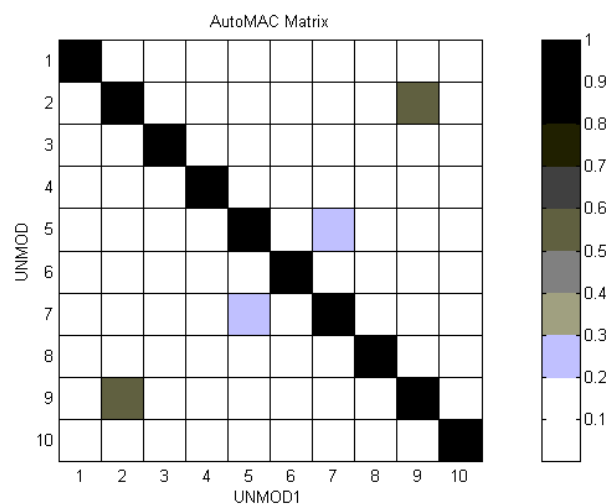

Fig. 12.9 (from [12.12])

Table 12.2. AutoMAC matrix of UNMOD

		UNMOD Mode Index									
		1	2	3	4	5	6	7	8	9	10
U	1	100	0.15	0	0	0	19.69	0.70	0.04	0.05	0
N	2	0.15	100	0.06	0	0	0.16	0.74	0.03	52.42	0.33
M	3	0	0	100	0.15	8.58	0.23	0.39	0.36	0.70	0
O	4	0	0	0.15	100	1.09	3.49	0.20	0.17	0.50	0
D	5	0	0.16	8.58	1.09	100	0	22.65	0.19	4.54	0.08
I	6	19.69	0.09	0.23	3.49	0	100	7.53	0.20	0	0.07
n	7	0.70	1.03	0.39	0.20	22.65	7.53	100	1.69	0	7.51
d	8	0.04	0	0.36	0.17	0.19	0.20	1.69	100	0.65	0.96
e	9	0.05	52.42	0.70	0.50	4.54	0	0	0.65	100	4.92
x	10	0	0.33	0	0	0.08	0.07	7.51	0.96	4.92	100

An explanation for the off-diagonal entries with relatively high value in the MAC matrix can be given using the AutoMAC plots. Figure 12.9 and Table 12.2 show the AutoMAC matrix of UNMOD. The existence of non-negligible off-diagonal correlation terms in the AutoMAC is an indication of spatial aliasing. This occurs when the number and location of the chosen response measurement coordinates are inadequate to distinguish the modes from each other.
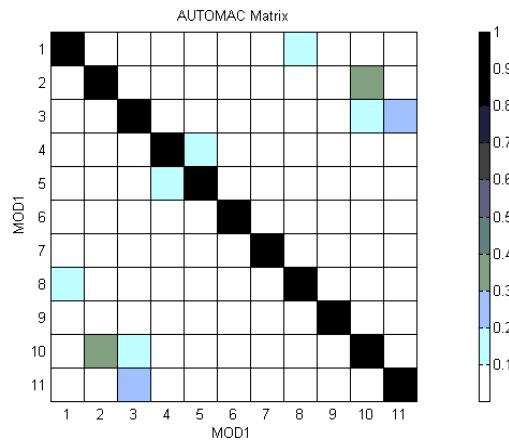

Fig. 12.10 (from [12.12])

Figure 12.10 and Table 12.3 show the AutoMAC matrix of MOD1. It is evident that entries (9,2), (6,1) and (7,5) in the AutoMAC matrix of UNMOD correspond to entries (9,2), (6,1) and (7,3) in the MAC matrix. Entries (1, 8), (2, 10) and (3, 11) in the AutoMAC matrix of MOD1 correspond to entries (1, 8), (2, 10) and (5, 11) in the MAC matrix. Subtracting the large off-diagonal terms of the AutoMAC matrix from the corresponding lower or upper triangle of the original MAC matrix would result in a sort of deflated MAC matrix with better mode-pairing properties.

Table 12.3. AutoMAC matrix of MOD1

|		MOD1 Mode Index										
		1	2	3	4	5	6	7	8	9	10	11
M O D 1 I n d e x	1	100	0.06	0.01	1.22	0.50	0	0.40	18.07	0.03	0.11	0.08
	2	0.06	100	1.33	0	0.54	0	1.01	0	0.03	32.56	0.54
	3	0.01	1.33	100	0.83	0.41	0.17	1.04	0	0.23	13.29	27.99
	4	1.22	0	0.83	100	18.78	0.01	0.29	3.42	2.16	0.29	0.09
	5	0.50	0.54	0.41	18.78	100	0.01	1.60	1.87	0.07	5.78	2.69
	6	0	0	0.17	0.01	0.01	100	0.65	0	0.78	0	0.49
	7	0.40	1.01	1.04	0.29	1.60	0.65	100	1.38	9.64	3.07	3.50
	8	18.07	0	0	3.42	1.87	0	1.38	100	0.25	0.70	0
	9	0.03	0.03	0.23	2.16	0.07	0.78	9.64	0.25	100	0.35	0.24
	10	0.11	32.56	13.29	0.29	5.78	0	3.07	0.70	0.35	100	0.45
	11	0.08	0.54	27.99	0.09	2.69	0.49	3.50	0	0.24	0.45	100
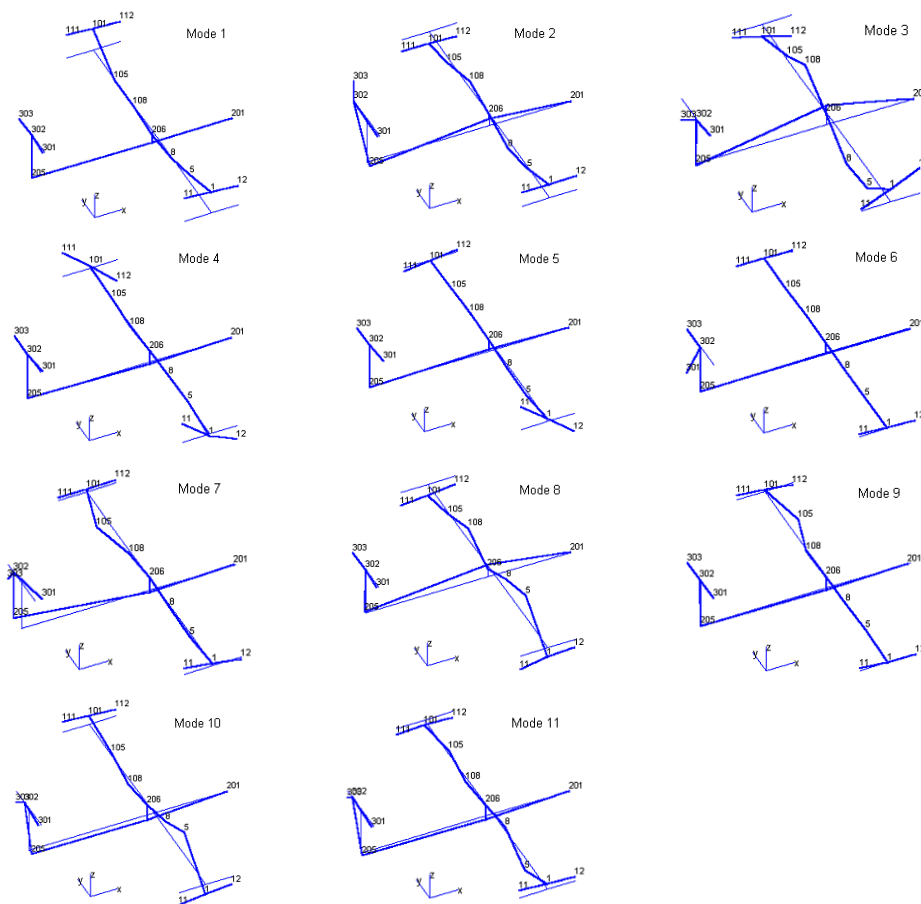
Fig. 12.11

The mode shapes for MOD1 are shown in Fig. 12.11.

12.3.4 Degree of freedom correlation

In the comparison of two sets of modal vectors, one of the issues of interest is the influence of individual DOFs on the vector resemblance. The spatial dependence of the previously-presented correlation criteria can be misleading. On one side, unacceptable large off-diagonal terms in cross-orthogonality matrices can correspond to large errors in points of very small shape amplitude. On the other hand, very small off-diagonal elements of the *XOR* matrix do not necessarily indicate unrelated vectors.

A series of criteria have been developed to reveal the DOF dependence of the discrepancy between modal vectors. Their interpretation is not obvious and caution must be taken in their use as indicators of modeling accuracy [12.12].

12.3.4.1 Coordinate Modal Assurance Criterion

The *Coordinate MAC* (*COMAC*) is used to detect differences at the DOF level between two modal vectors [12.13]. The *COMAC* is basically a row-wise correlation of two sets of compatible vectors, which in *MAC* is done column-wise.

The *COMAC* for the *j*-th DOF is formulated as

$$COMAC\,(j) = \frac{\left(\displaystyle\sum_{\ell=1}^{L} \left| (\varphi_A)_{j\ell}\,(\varphi_X)_{j\ell} \right| \right)^2}{\displaystyle\sum_{\ell=1}^{L} (\varphi_A)_{j\ell}^2 \cdot \sum_{\ell=1}^{L} (\varphi_X)_{j\ell}^2} \,, \tag{12.25}$$

where ℓ is the index of the CMP, $(\varphi_A)_{j\ell}$ is the *j*-th element of the ℓ-th paired analytical modal vector, and $(\varphi_X)_{j\ell}$ is the *j*-th element of the ℓ-th paired experimental modal vector. Both sets of modal vectors must have the same normalization.

The *COMAC* is applied only to CMPs after a mode pairing using the *MAC*. It is a calculation of correlation values at each DOF, *j*, over all CMPs, *L*, suitably normalized to present a value between 0 and 1. The summation is performed on rows of the matrix of modal vectors, in a manner similar to the column-wise summation in the MAC. However, at the numerator, the modulus sign is inside the summation, because it is the relative magnitude at each DOF over all CMPs that matters.

The only thing the *COMAC* does, is to detect local differences between two sets of modal vectors. It does not identify modeling errors, because their location can be different from the areas where their consequences are felt. Another

limitation is the fact that *COMAC* weights all DOFs equally, irrespective of their magnitude in the modal vector.
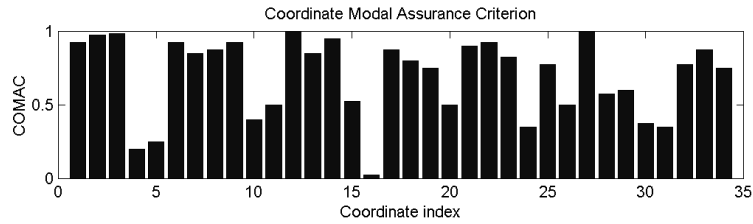

Fig. 12.12 (from [12.7])

The simplest output of the computation is a list of *COMAC* values between 0 and 1, which help locating the DOFs for which the correlation is low. These DOFs are also responsible for a low value of *MAC*. The *COMAC* can be displayed as a bar graph of its magnitude against the DOF index (Fig. 12.12).

12.3.4.2 Enhanced Coordinate Modal Assurance Criterion

A different formulation, loosely called also COMAC, is

$$COMAC(j) = 1 - ECOMAC(j), \qquad (12.26)$$

where the *Enhanced Coordinate Modal Assurance Criterion* (ECOMAC) is defined as [12.14]

$$ECOMAC(j) = \frac{\sum_{\ell=1}^{L} \left| (\varphi_A)_{j\ell} - (\varphi_X)_{j\ell} \right|}{2L}. \qquad (12.27)$$

The *ECOMAC* is the average difference between the elements of the modal vectors. It has low values for correlated vectors. It is sensitive to calibration and phase shifting errors in test data. The ECOMAC is dominated by differences at DOFs with relatively large amplitudes.

12.3.4.3 Normalized cross-orthogonality location

A different criterion that avoids the phase sensitivity is the *Normalized Cross-Orthogonality Location* (*NCOL*), defined as [12.10]

$$NCOL(j) = \frac{\sum_{\ell=1}^{L} \left((\varphi_X)_{j\ell} \, (\varphi_A)_{j\ell} - (\varphi_A)_{j\ell}^2 \right)}{\sum_{\ell=1}^{L} (\varphi_A)_{j\ell}^2}. \qquad (12.28)$$

NCOL is a DOF-based normalized cross-orthogonality check which does not contain mass or stiffness terms. It allows the inclusion of phase inversions (there is not a modulus under the sum in the numerator) that are important near nodal lines.

12.3.4.4 Modulus difference

The *Modulus Difference* (MD) is defined as the column vector formed by the differences between the absolute values of the corresponding elements of two paired modal vectors [12.13]:

$$MD(\ell) = \left| \{\varphi_A\}_\ell \right| - \left| \{\varphi_X\}_\ell \right|. \tag{12.29}$$

The Modulus Difference Matrix:

$$\left[MDM \right] = \left[MD(1) \quad MD(2) \quad .... \quad MD(L) \right] \tag{12.30}$$

can be displayed as a 3D graph showing the locations of low correlation between two sets of modal vectors. An alternative implementation exists for complex modes.

12.3.4.5 Coordinate Orthogonality Check

The *Coordinate Orthogonality Check* (*CORTHOG*) determines the individual contribution of each DOF to the magnitude of the elements of the cross-orthogonality matrix [12.15].

If the XOR_{TAM} for the *r-q* mode pair and the *j-k* DOF pair is written in the double sum form:

$$XOR\ _{rq}^{jk} = \sum_{j=1}^{L} \sum_{k=1}^{L} \left((\varphi_X)_{jr}\ m_{jk}\ (\varphi_A)_{kq} \right), \tag{12.31}$$

where m_{jk} are elements of the analytical mass matrix, it can be seen that each off-diagonal element results from a summation of contributions from all DOFs.

For an off-diagonal term to become zero, the vectors need not be correlated. Each product $(\varphi_X) m (\varphi_A)$ is not zero, only their summation. Inspection of $(\varphi_X) m (\varphi_A)$ products is not sufficient to assess discrepant DOFs. A comparison is imposed of expected $(\varphi_A) m (\varphi_A)$ products to actual values $(\varphi_X) m (\varphi_A)$. The best approach is to compute the difference $(\varphi_X)_j\ m_{jk}\ (\varphi_A)_k - (\varphi_A)_j\ m_{jk}\ (\varphi_A)_k$ for each *j-k* DOF pair and to normalize it by division with the maximum difference [12.15].

If (φ_X) is replaced by (φ_A), then the double sum represents elements of the analytical orthogonality matrix. The CORTHOG is the simple difference of the

corresponding triple product terms in the two matrices, summed for the column index of DOFs:

$$CORTHOG\ (j)_{rq} = \sum_{\ell=1}^{L} \left(\left(\varphi_X \right)_{jr} m_{j\ell} \left(\varphi_A \right)_{\ell q} - \left(\varphi_A \right)_{jr} m_{j\ell} \left(\varphi_A \right)_{\ell q} \right). \quad (12.32)$$

The *CORTHOG* can also be displayed as a bar graph of its magnitude against the DOF index. It identifies which DOFs are most likely discrepant with respect to the FEM DOFs, on a weighted base.

12.3.5 Modal kinetic energy

Modal kinetic energy and modal strain energy comparisons are being used to assess the TAM validity or to locate dynamically important DOFs. Modal effective mass distributions are also used for comparison of important modes.

The modal mass matrix

$$\left[GM \right] = \left[\varPhi_{FEM}^{R} \right]^{T} \left[m_{TAM} \right] \left[\varPhi_{FEM}^{R} \right] \quad (12.33)$$

has elements

$$GM_{ij} = \sum_{k} \left(\left(\varphi_{Ak} \right)_i \sum_{\ell} m_{k\ell} \left(\varphi_{A\ell} \right)_j \right), \quad (12.34)$$

with i, j over target mode shapes and k, ℓ over TAM DOFs.

For $i = j$, the term within the bracket

$$KE_{kj} = \left(\varphi_{Ak} \right)_j \sum_{\ell} m_{k\ell} \left(\varphi_{A\ell} \right)_j \quad (12.35)$$

is the kinetic energy associated with the *k*-th DOF for the *j*-th mode.

Kinetic energy computations are performed for the FEM modes to determine which DOFs within any mode are dynamically important. This helps in the selection of sensor locations. The distribution of KE within the TAM modes can be compared to the FEM to assess TAM validity.

A Modal Strain Energy criterion can be developed is a similar way based on the modal stiffness matrix.

12.4 Comparison of FRFs

Compared response functions usually include Frequency Response Functions (FRFs), Operating Deflection Shapes (ODSs) and Principal Response

Functions (PRFs). In the following, the presentation will be focused on the comparison of FRFs. ODSs can be compared as mode shape vectors.

There are three main kinds of comparison: 1) analytical-to-analytical, 2) experimental-to-experimental, and 3) analytical-to-experimental. The latter is of interest in structural modification and updating procedures and will be considered as default.

12.4.1 Comparison of individual FRFs

A typical FRF contains hundreds of values so that a graphical format is the most appropriate for comparisons. Diagrams of the FRF magnitude as a function of frequency are satisfactory for most applications. Bode diagrams, showing both the magnitude and the phase variation with frequency, are often used. Nyquist plots for selected parts of the frequency response are preferred only for highly damped systems, or when detailed information around a resonance is required. A visual inspection is usually sufficient to determine similarities or lack of agreement of two FRFs.

The simplest comparisons may include: 1) FRFs measured using different excitation levels, as a linearity check; 2) FRFs measured or calculated switching the input and output points, as a reciprocity check; 3) FRFs measured or calculated before and after a structural modification, to show its effect on the system response; 4) FRFs calculated for different models and levels of damping; 5) FRFs calculated before and after a data reduction intended to eliminate the noise and the linearly-related redundant information.

It is customary to use an overlay of all the FRFs, measured from all combinations of input and output coordinates, and to count the resonance peaks as a preliminary estimation of the model order.

Comparisons of measured and predicted FRFs may include: 1) FRFs calculated with different terms included in the summation, to check the effect of residual terms and whether a sufficient number of modes have been included; 2) a measured FRF and the corresponding regenerated analytical curve, calculated from an identified modal model; 3) an initially unmeasured FRF curve, synthesized from a set of test data, and the corresponding FRF curve obtained from a later measured set of data, to check the prediction capability of the analytical model.

Three factors must be borne in mind when analytically-generated FRF curves are used in the comparison. First, the way the damping has been accounted for in the theoretical model; second, the fact that the analytical FRFs are usually synthesized from the modal vectors of the structure and depend on the degree of modal truncation, and third, when the compared FRFs originate from two models, one model being obtained by a structural modification of the other, the comparison must take into account the frequency shift and the change of the scale factor in the

FRF magnitude. For instance, if the reference stiffness matrix is modified by a factor of α, the frequencies in the modified model increase by a factor of $\sqrt{\alpha}$, while the FRF magnitudes of an undamped model decrease by a factor of α.
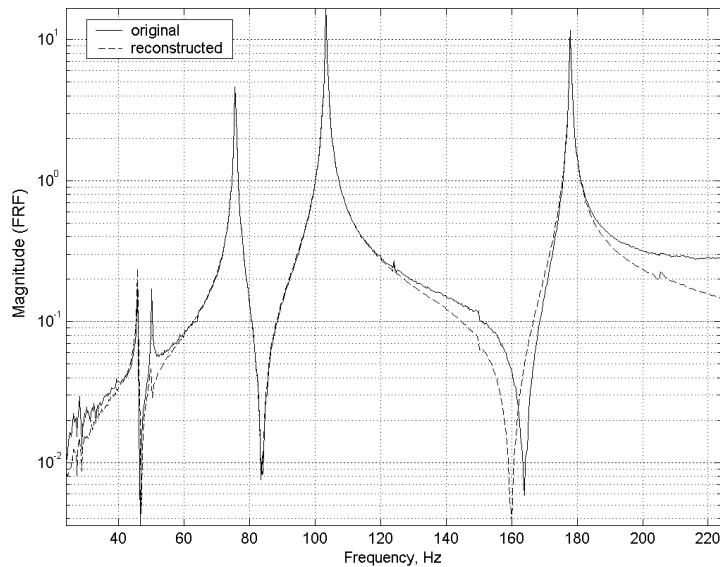

Fig. 12.13 (from [12.7])

Generally, in the correlation of measured and synthesized FRFs in an updating process, pairing of FRFs at the same frequency has no physical meaning. As several physical parameters at the element level are modified, an average frequency shifting exists at each frequency line, so that an experimental frequency ω_X will correspond to a different analytical frequency ω_A.

A global error indicator, calculated as the ratio of the Euclidean norm of the difference of two FRF vectors measured at discrete frequencies and the norm of a reference FRF vector, is of limited practical use. Visual inspection of two overlaid FRF curves can be more effective in localizing discrepancies (Fig. 12.13).

12.4.2 Comparison of sets of FRFs

An FRF data set is usually measured at a larger number of response measurement points, N_o, than the number of input (reference) points, N_i. The measured FRF matrix $\left[H(\omega) \right]_{N_o x N_i}$ contains values measured at a single frequency, ω. If measurements are taken at N_f frequencies, then a complete set

of FRF data is made of N_f matrices, of row dimension N_o and column dimension N_i. In a typical modal test, at least one column of the FRF matrix is measured. For structures with close or coincident natural frequencies, FRF elements from several such columns are measured. In order to compare several FRFs simultaneously it is necessary to use some frequency response correlation coefficients.

12.4.2.1 Frequency Response Assurance Criterion

Consider a complete set of N_oN_i FRFs, measured at N_o response locations and N_i excitation locations, each containing values measured at N_f frequencies.

A Compound FRF (CFRF) matrix, of size $N_f \times N_oN_i$ can be constructed such that each row corresponds to different individual FRF values at a specific frequency, and each column corresponds to a different input/output location combination for all frequencies (9.8)

$$\left[A \right]_{N_f x N_o N_i} = \left[\left\{ H_{11} \right\} \left\{ H_{21} \right\} \ldots \left\{ H_{j\ell} \right\} \ldots \right], \qquad (12.36)$$

where $\left\{ H_{j\ell} \right\}$ is an N_f dimensional FRF column vector, with response at location j due to excitation at ℓ.

Each column of the CFRF matrix is an FRF. If the magnitude of its entries is plotted as a function of frequency, then an FRF curve is obtained. The columns of the CFRF matrix are (temporal) vectors that can be compared using the MAC approach, i.e. calculating a correlation coefficient equal to the squared cosine of the angle between the two vectors.

The *Frequency Response Assurance Criterion* (*FRAC*), defined as [12.16]

$$FRAC \ (j,\ell) = \frac{\left| \left\{ H_{X j\ell} \right\}^H \left\{ H_{A j\ell} \right\} \right|^2}{\left(\left\{ H_{X j\ell} \right\}^H \left\{ H_{X j\ell} \right\} \right) \left(\left\{ H_{A j\ell} \right\}^H \left\{ H_{A j\ell} \right\} \right)}, \qquad (12.37)$$

is used to assess the degree of similarity between measured $\left\{ H_X \right\}$ and synthesized $\left\{ H_A \right\}$ FRFs, or any compatible pair of FRFs, across the frequency range of interest.

The *FRAC* is a spatial correlation coefficient, similar to the *COMAC*, but calculated like the *MAC*. It is a measure of the shape correlation of two FRFs at each *j,* ℓ input/output location combination. The *FRAC* can take values between 0 (no correlation) and 1 (perfect correlation).

The *FRAC* coefficients can be displayed in a *FRAC* matrix, of size $N_o x N_i$, which looks different from the usual *MAC* matrix, the diagram of each column resembling a *COMAC* plot.

12.4.2.2 Response Vector Assurance Criterion

The transposed CFRF matrix can be written

$$\left([A]^T \right)_{N_o N_i x N_f} = \left[\{ H(\omega_1) \} \ \{ H(\omega_2) \} \ ... \ \{ H(\omega_f) \} \ ... \right], \quad (12.38)$$

where each column contains all $N_o N_i$ FRFs, measured at a certain frequency ω_f $(f = 1, 2, ..., N_f)$ for N_o output locations and N_i input locations.

A temporal vector correlation coefficient can be defined using the columns of the $[A]^T$ matrix. If the column vector $\{ H(\omega_f) \}$ contains only the N_o entries from the ℓ-th input point, then the *Response Vector Assurance Criterion* (*RVAC*) is defined as [12.17]

$$RVAC \ (\omega_f, \ell) = \frac{\left| \{ H(\omega_f) \}_\ell^H \{ H(\omega_f) \}_\ell \right|^2}{\left(\{ H(\omega_f) \}_\ell^H \{ H(\omega_f) \}_\ell \right) \left(\{ H(\omega_f) \}_\ell^H \{ H(\omega_f) \}_\ell \right)}. \quad (12.39)$$

It contains information from all response DOFs simultaneously and for one reference point, at a specific frequency. The *RVAC* is analogous to the *MAC* and takes values between 0 (no correlation) and 1 (perfect correlation). Each N_o dimensional column is a *response vector*, i.e. the vector of displacements at all N_o response measurement points, calculated or measured at a given frequency, so that the *RVAC* can also be applied to the correlation of operating deflection shapes.

When the analytical model is undamped, the complex values of the measured FRFs should be converted into real ones, using an approximation of the type

$$\{ H_{real} \} = \text{abs} \left(\{ H_{complex} \} \right) \text{sign} \left(\text{Re} \{ H_{complex} \} \right). \quad (12.40)$$

The *RVAC* coefficients can be displayed in a plot of the type used for the MAC.

However, the *RVAC* matrix, of size $N_f \times N_f$, yields a much denser diagram, plotted at several hundred frequency values, hence more difficult to interpret. It helps in the selection of frequencies for correlation, within the intervals with high values of *RVAC*, where the FEM data are close to the test data.

12.4.2.3 Frequency Domain Assurance Criterion

If the analytical FRF is calculated at N_f analytical frequencies ω_A, and the test FRF is measured at N_f experimental frequencies ω_X, then a *Frequency Domain Assurance Criterion* (*FDAC*) can be defined [12.18], whose real version is

$$FDAC\ (\omega_A,\omega_X,\ell\ )=\frac{\{H_X(\omega_X)\}_\ell^T\,\{H_A(\omega_A)\}_\ell}{\left|\{H_X(\omega_X)\}_\ell^T\,\{H_X(\omega_X)\}_\ell\right|\,\left|\{H_A(\omega_A)\}_\ell^T\,\{H_A(\omega_A)\}_\ell\right|},$$

(12.41)

where $\{H_A(\omega_A)\}$ is the analytical FRF at any analytical frequency, ω_A, and $\{H_X(\omega_X)\}$ is the experimental FRF at any experimental frequency, ω_X.

Using experimental FRFs converted to real values, the *FDAC* is calculated as the cosine of the angle between the FRF column vectors, with values between -1 and 1, to take into account the phase relation between the FRF vectors. Note that the original version of *FDAC*, still used in many publications, had the numerator squared, like the MAC, being insensitive to the phase lag between the FRFs.

While the *FRAC* is a *coordinate* correlation measure across all frequencies, the *RVAC* and *FDAC* coefficients represent the correlation between two sets of FRFs at specific *frequencies* across the full spatial domain. The *RVAC* cross-correlates each frequency line with every other measured frequency line, across the spatial domain. In a way, the *MAC* can be considered as the *RVAC* evaluated only at the natural frequencies.

The *FRAC* is sometimes compared to the *COMAC*, but the calculation is different. The modulus in the numerator is taken *after* the vector multiplication, like in the *MAC*, and *not inside* the summation, for each term of the scalar product, as it is taken in the *COMAC*.

Frequency response correlation coefficients must be applied with great care, using stiffness factors to adjust for frequency shifts and being aware of the approximations introduced by the inclusion of an arbitrary damping model in the analysis. A global frequency shift between the experimental and predicted FRFs leads to a biased correlation coefficient even if the FRFs are otherwise identical. Selection of frequency points is a key factor in any FRF-based correlation.

Using magnitudes or logarithm values instead of complex values gives better results, especially for lightly-damped structures whose FRFs exhibit large differences in the order of magnitude and the phase angles. When the damping updating is not of interest, it is useful to choose the frequency points away from resonances and anti-resonances, though the largest discrepancies noticed visually occur in these regions. The FRAC coefficients are more sensitive to resonances and less sensitive to anti-resonances heavily affected by modal truncation.

The *FRAC* and *RVAC* are useful tools for examining the level of correlation of FRF data used in frequency-based model updating procedures.

12.5 Sensor-exciter placement

Selection of the number and location of measurement coordinates is an important part of the pre-test planning activity. Optimal selection of sensor and exciter locations is influenced by the number of modes of interest in the analysis.

The efficiency of all model reduction methods and modal indicators (as the MIFs) is fully dependent on the selection of active DOFs. Decisions to make are the following: a) number and index of target modes, b) number of sensor locations, c) where to place sensors, d) number of exciter locations, e) where and on what direction to apply the excitation, and f) best exciter/sensor combination.

12.5.1 Selection of active DOFs / Sensor placement

Different model reduction methods are presented in Chapter 11. Non-modal condensation techniques, like the Irons-Guyan reduction, are used to generate a reduced model that accurately maintains the characteristics of the original model at the lower frequencies. The sensor placement aims to measure the lower frequency modes accurately. It is postulated that the active DOFs of the FEM can also serve as response measurement locations for modal testing, i.e. as sensor locations.

In control dynamics and health monitoring applications the objective is to track only a preselected sub-set of target modes, discarding some low-frequency, non-observable or non-important modes. This makes modal reduction methods best adequate.

12.5.1.1 Small stiffness / large inertia criterion

The strategy for the automatic selection of dynamic DOFs based on concepts developed in connection to the Irons-Guyan reduction (GR) is presented in Section 11.2.1.3. As originally conceived, the aim of GR was to reduce the model order *before* solving the eigenvalue problem, using only the physical matrices of the FEM. The reduction of the size of the eigenvalue problem uses a transformation matrix based on the spatial distribution of the mass and stiffness properties.

The automatic selection of *a*-DOFs is based on small values of the ratio k_{ii}/m_{ii} between the diagonal elements of the stiffness and mass matrices for the *i*-th coordinate. The GR method is valid for frequencies which are smaller than a cut-off value, ω_c, equal to the smallest eigenfrequency of the *o*-DOFs eigenvalue

problem (11.47). Stepwise elimination of o-DOFs improves the accuracy of non-modal reduction techniques.

12.5.1.2 Effective independence method (EfI)

Test/analysis correlation techniques require linearly independent test modes; otherwise the cross-orthogonality matrix check fails. The requirement of absolute identifiability is more stringent than that of observability demanded by most identification and control techniques. Active DOFs must be located so that the resulting modal vectors can be spatially differentiated. In the Effective Independence (EfI) method [12.19], candidate a-DOF locations are ranked according to their contribution to the linear independence of the FEM target modes. This implies solution of the FEM full size eigenvalue problem.

Starting with the full modal matrix $[\Phi]$ of the FEM, the first step is to remove all coordinates which cannot be measured (e.g.: rotations) or which are considered of little significance. Next, the target modes are determined using a modal selection procedure [12.20] which orders the modes in terms of their contribution to the input/output dynamics of the model. Let $[\Phi_{st}]$ be the reduced matrix of n_t target modes truncated to the n_s candidate active DOF locations.

The cross-product (Gram) matrix $[A_o]$ is then formed

$$[A_o] = [\Phi_{st}]^T [\Phi_{st}] = \sum_{i=1}^{n_s} \lfloor \varphi_i \rfloor^T \lfloor \varphi_i \rfloor \qquad (12.42)$$

which will be referred to as the *Fisher information matrix* (FIM).

The problem is to search for the best set of n_a active (master) locations from the n_s candidate locations so that $\det[A_o] = \det(FIM)$ is maximized.

The matrix

$$[P_\Phi] = [\Phi_{st}][\Phi_{st}]^+ = [\Phi_{st}][A_o]^{-1}[\Phi_{st}]^T \qquad (12.43)$$

is computed, where $^+$ denotes the pseudo-inverse.

This is the orthogonal projector onto the column space of $[\Phi_{st}]$, with *trace* equal to its *rank* and to the number of target modes n_t (idempotent matrix)

$$\text{trace}\,[P_\Phi] = \sum_{i=1}^{n_t} P_{ii} = \sum_{i=1}^{n_t} \lambda_i = \text{rank}\,[P_\Phi] = n_t\,.$$

Each diagonal element P_{ii} represents the fractional contribution of the *i*-th DOF to the rank of $[P_\Phi]$, and hence to the linear independence of the target modes.

If $P_{ii} = 0$, the *i*-th row of $[\Phi_{st}]$ is null and the modes are not observable from the *i*-th sensor location. If $P_{ii} = 1$, the *i*-th sensor location is vital to the linear independence.

Elements P_{ii} are sorted based on magnitude. The DOF location with minimum contribution to the rank of $[P_\Phi]$, indicated by the smallest element, is removed from the candidate set. The matrix $[P_\Phi]$ is then recomputed, and the process is repeated, DOFs being deleted one at a time, until the number n_a is attained or until eliminating one additional DOF creates a rank deficiency.

It is useful to track the P_{ii} values. If several DOFs have the same P_{ii} value, then they are deleted simultaneously [12.21].

The initial candidate DOF set is iteratively (suboptimally) reduced to the desired number n_a. Removing a DOF location, i.e. discarding the corresponding row from the reduced matrix of modal vectors $[\Phi_{st}]$, resumes to subtracting the respective dyadic product from the sum, setting a deflated matrix

$$[B] = [A_o] - \lfloor \varphi_i \rfloor^T \lfloor \varphi_i \rfloor. \tag{12.44}$$

Because

$$[B] = [A_o]\left([I_t] - [A_o]^{-1} \lfloor \varphi_i \rfloor^T \lfloor \varphi_i \rfloor\right),$$

$$\det[B] = \det[A_o] \cdot \det\left([I_t] - [A_o]^{-1} \lfloor \varphi_i \rfloor^T \lfloor \varphi_i \rfloor\right),$$

$$\det[B] = \det[A_o] \cdot \det\left([I_t] - \lfloor \varphi_i \rfloor [A_o]^{-1} \lfloor \varphi_i \rfloor^T\right),$$

$$\det[B] = \det[A_o](1 - P_{ii}), \qquad 0 \le P_{ii} \le 1 \tag{12.45}$$

the EfI method tends to maintain $\det(FIM)$ that quantifies the total amount of information retained.

The value of $\det(FIM)$ varies with the number of DOFs, so it cannot give an absolute assessment of the quality of a set of locations. However, plots of $\det(FIM)$ versus the number of retained DOFs are useful to determine both the quality of the elimination process and a lower limit when the *FIM* becomes rank deficient.

Another useful information is obtained tracking the elimination process on the diagram of $\text{cond}(FIM)$ vs. the number of retained DOFs. The smallest the condition number, the best the choice of locations. Minima on these plots show optimal values for the number of retained DOFs, while a sudden increase denotes the lower limit set by the rank deficiency of the *FIM* matrix.

Several other criteria have been investigated [12.22] to assess the quality of any set of *a*-DOF locations. The 2-norm condition number of the eigenvector matrix, defined as the ratio of the largest singular value to the smallest, was considered the best.

For the calculation of $[P_\Phi]$, the n_t columns in $[\Phi_{st}]$ are assumed to be linearly independent. As the matrix $[A_o]$ is symmetric and positive definite, its eigenvalues are real and positive. Solving the eigenvalue problem

$$\left([A_o] - \lambda [I] \right) \{\psi\} = \{0\}, \tag{12.46}$$

for orthonormal eigenvectors

$$[\Psi]^T [A_o] [\Psi] = [\Lambda], \quad [\Psi]^T [\Psi] = [I],$$

and the spectral decomposition of $[A_o]$ is

$$[A_o] = [\Psi][\Lambda][\Psi]^T = \sum_{r=1}^{n_t} \lambda_r \{\psi\}_r \{\psi\}_r^T, \tag{12.47}$$

so that its inverse is

$$[A_o]^{-1} = \sum_{r=1}^{n_t} \frac{1}{\lambda_r} \{\psi\}_r \{\psi\}_r^T.$$

The orthogonal projector (12.43) becomes

$$[P_\Phi] = [\Phi_{st}][\Psi][\Lambda]^{-1}[\Psi]^T[\Phi_{st}]^T,$$

$$[P_\Phi] = \left([\Phi_{st}][\Psi][\Lambda]^{-1/2} \right) \left([\Phi_{st}][\Psi][\Lambda]^{-1/2} \right)^T,$$

$$[P_\Phi] = \sum_{r=1}^{n_t} \left(\frac{1}{\sqrt{\lambda_r}}[\Phi_{st}]\{\psi\}_r \right) \left(\frac{1}{\sqrt{\lambda_r}}[\Phi_{st}]\{\psi\}_r \right)^T. \tag{12.48}$$

Example 12.3

Figure 12.14 shows half of a rigid-jointed plane frame for which $\rho = 7810 \,\text{kg/m}^3$, $E = 2.1 \cdot 10^{11} \,\text{N/m}^2$, $I = 271 \,\text{mm}^4$, $A = 80.6 \,\text{mm}^2$, $\ell = 0.2032 \,\text{m}$.

The columns are built into the ground and the extensions of cross-members are simply supported at the right end. The frame was modelled with 51 DOFs, using 21 beam elements neglecting shear deformations and rotatory inertia.

The model was first reduced by eliminating 12 axial displacements along the vertical members and 18 rotations. The remaining 21 translations have been used to select a reduced number of *a*-DOF locations. If the first six modes of vibration are selected as target modes, the location of 6, 9 and respectively 12 *a*-DOF positions chosen by EfI is shown in Fig. 12.14, *a*. For comparison, the location of the same number of *a*-DOFs by the K/M method is illustrated in Fig. 12.14, *b*.

6 masters   9 masters   12 masters

Location by EfI method

a

6 masters   9 masters   12 masters

Location by K/M method

b
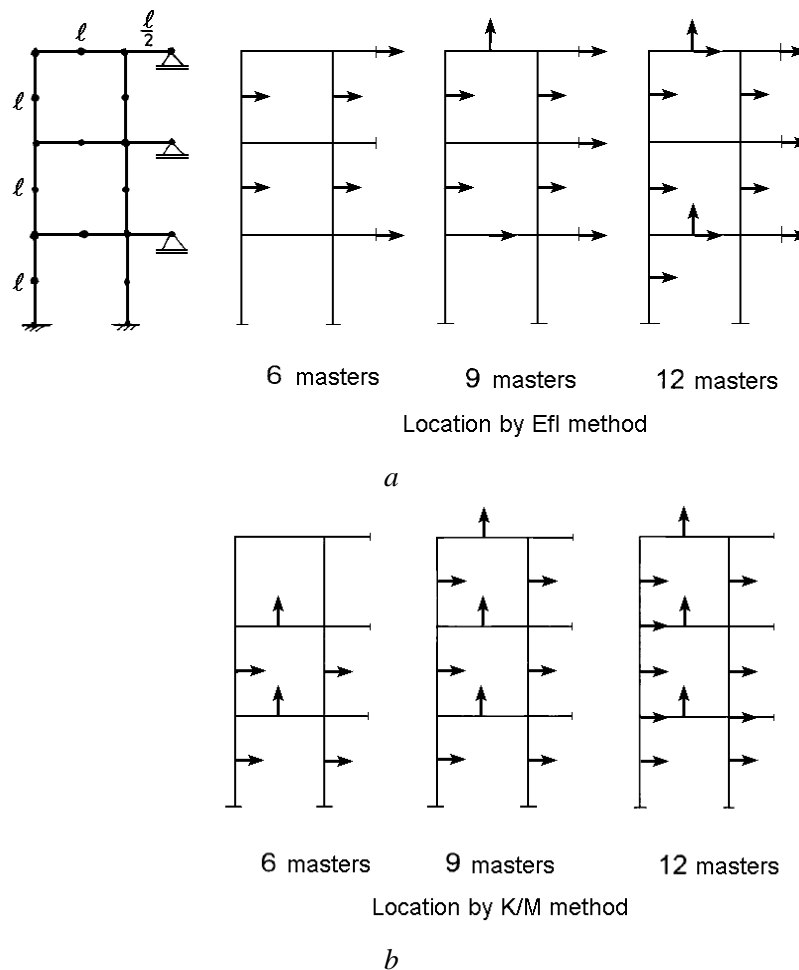
Fig. 12.14

Eigenfrequencies calculated with the Irons-Guyan reduction method using 12 and 6 DOFs, respectively, selected by EfI and K/M are given in Table 12.4. It is

seen that EfI method performs better and by proper selection of *a*-DOFs has a higher cut-off frequency.

The poor selection of 6 DOFs by the K/M method is explained partly by the existence of 9 identical k_{ii}/m_{ii} values, from which only six with the lowest indices are chosen.

Table 12.4. Natural frequencies of the planar frame from Fig. 12.14

Mode no.	Full FE model	Reduced FE model			
	51 DOFs	12 DOFs	12 DOFs	6 DOFs	6 DOFs
		EfI method	K/M method	EfI method	K/M method
	Natural frequency, Hz				
1	34.039	33.7457	33.9	33.792	36.672
2	108.568	108.519	112.6	108.989	198.483
3	187.317	187.561	198.8	200.030	458.955
4	423.479	425.483	427.0	460.657	604.325
5	520.839	524.707	524.8	638.479	824.552
6	605.249	611.349	629.4	641.248	827.047
7	624.523	630.552	660.4		
8	767.527	779.801	-		
9	823.296	823.571	823.4		
10	826.027	826.122	826.1		
11	827.175	827.184	827.2		
12	962.435	975.250	916.3		
Cut-off frequency		1608.7	232.1	358.5	70.8

Figure 12.15, *a* shows the evolution of $\det(FIM)$ and $\text{cond}(FIM)$ for six *a*-DOFs. Because the target modes are the lowest 6 modes, there is no rank deficiency. The index $\det(FIM)$ decreases monotonically, but $\text{cond}(FIM)$ is lowest for 12 *a*-DOFs.

Figure 12.15, *b* shows the same plots when the four target modes are the modes 4, 5, 6, 7. If four *a*-DOFs are selected, the plots indicate rank deficiency for values lower than 9. Figure 12.15, *c* shows the same tendency for three target modes 9, 10, 11, and six selected *a*-DOFs. The minimum number of 9 *a*-DOFs corresponds to the nine identical lowest k_{ii}/m_{ii} values.

a

b

c
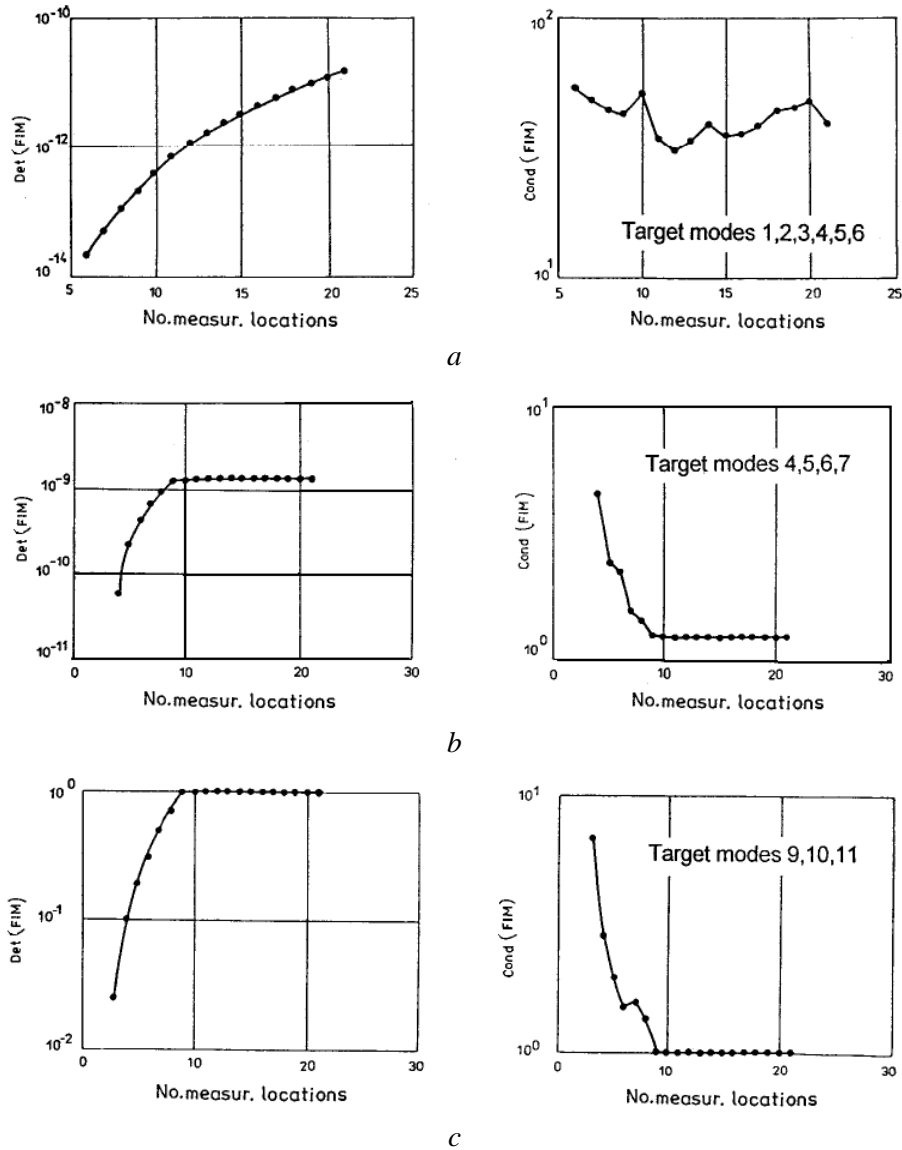
Fig. 12.15

12.5.1.3 Sensor location with Arnoldi and Schur vectors

S̲ensor L̲ocation with A̲rnoldi V̲ectors (SLAVE) is a variant of the Effective Independence method [12.6], using Arnoldi vectors instead of eigenvectors. It is used with the Arnoldi TAM, which is the Modal TAM calculated based on Arnoldi vectors instead of modal vectors.

Using the Rayleigh-Ritz approximation (8.48), the eigenvectors $\left[\Phi_{st}\right]$ can be expressed as linear combinations of Arnoldi vectors $\left[V_s\right]$. The matrix $\left[V_s\right]$ is obtained by truncating $\left[V_m\right]$ in (8.48) to n_t columns.

The orthogonal projector onto the column space of $\left[\Phi_{st}\right]$ is the matrix

$$\left[P_\Phi\right] = \left[\Phi_{st}\right]\left[\Phi_{st}\right]^+ = \left[V_s\right]\left[V_s\right]^+, \tag{12.49}$$

where $^+$ denotes the Moore-Penrose pseudoinverse.

The diagonal element

$$P_{ii} = \mathrm{diag}\left(\left[V_s\right]\left[V_s\right]^+\right), \tag{12.50}$$

is the *Effective Independence value* corresponding to the *i*-th sensor. It represents the fractional contribution of the *i*-th DOF to the rank of $\left[P_\Phi\right]$, and hence to the independence of the target modes.

The EfI strategy is to sort the elements P_{ii} serially, based on magnitude. At each step, the smallest element P_{ii} is eliminated from the candidate set. The corresponding row is discarded from the matrix $\left[V_s\right]$, recomputing the matrix $\left[P_\Phi\right]$ with the deflated matrix $\left[V_s\right]$ until the desired number of sensors is attained.

Example 12.4

Consider the grounded planar frame structure used in the third GARTEUR updating exercise (Fig. 11.4). The structure is constrained to vibrate only in its own plane. Here it is modelled with 78 Bernoulli-Euler beam elements (instead of 48 in Example 11.2) with consistent mass matrices. The model consists of 72 free nodes resulting in 144 translational and 72 rotational DOFs. The horizontal beams, of 5m length, and the diagonal beams are modelled with 7 elements each. The vertical beams, of 3m length, are modelled with 5 elements each.
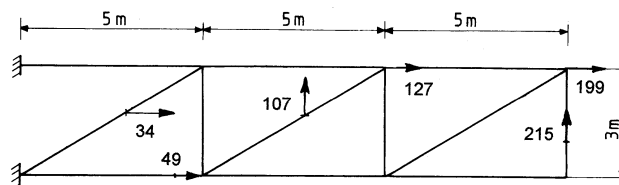
Fig. 12.16 (from [12.5])

The first six natural frequencies are given in Table 12.5. The FEM values, listed in the second column, correspond to the full eigenvalue problem $\left(n = 216\right)$,

being obtained after 32 iterations for a convergence tolerance of 10^{-10} and 12 Arnoldi vectors. A starting vector of ones has been used.

Table 12.5. Modal data from the Modal TAM

| No | FEM natural frequency, Hz | Number of Arnoldi vectors | | | | | |
| | | 8 | | 9 | | 10 | |
		Frequency error, %	Mode shape error, %	Frequency error, %	Mode shape error, %	Frequency error, %	Mode shape error, %
1	45.15	0	0	0	0	0	0
2	79.04	0	0	0	0	0	0
3	227.18	0	0.01	0	0	0	0
4	249.67	0	0.06	0	0	0	0
5	363.56	0.18	5.42	0.02	1.11	0	0
6	437.88	5.94	125.1	3.20	122.6	0	0

Columns 3, 5 and 7 list the discrepancies of frequencies computed with the Arnoldi algorithm, using 8, 9 and 10 Arnoldi vectors, respectively, 6 target modes, for a selection of 6 master DOFs by the EfI elimination technique. The relative frequency discrepancy shows a very good reproduction of the low frequency spectrum. In fact, for $n_a \geq 10$, all the first six Modal TAM eigenfrequencies have zero error.

Table 12.6. Modal data from the Arnoldi TAM

| No | FEM | Arnoldi TAM | Frequency error, % | Mode shape error, % | Diag MAC x 100 |
	Natural frequency, Hz				
1	45.15	45.15	0	0	100
2	79.04	79.04	0	0	100
3	227.18	227.18	0	0	100
4	249.67	249.67	0	0	100
5	363.56	363.56	0	0.3	100
6	437.88	446.64	1.97	108.13	17.3

Columns 4, 6 and 8 list the relative discrepancy of the expanded mode shapes, calculated as $\left\| \{\varphi\}_{FEM} - \{\varphi\}_{expanded} \right\| / \left\| \{\varphi\}_{FEM} \right\| \cdot 100$.

For comparison, Table 12.6 shows the data computed using the Arnoldi TAM, for a selection of 6 eigenvectors, 12 Arnoldi vectors and the same convergence tolerance. The six active DOFs selected by EfI are shown in Figure 12.16. Column 6 lists the diagonal entries of the MAC matrix between the FEM and the expanded mode shapes. It shows perfect matching for the first five modes.

The robustness of the Arnoldi TAM is assessed with a global figure of merit, based on the Normalized Cross-Orthogonality (*NCO*) matrix. The *NCO rms* error is calculated as

$$rms1 = \text{rms}\left([NCO] - \text{diag}(NCO) \right). \tag{12.51}$$

It is a measure of the lack of orthogonality between the two sets of modal vectors. For $n_a = 6$, one obtains *rms*1=0.084. The low value indicates the good performance of the Arnoldi TAM.
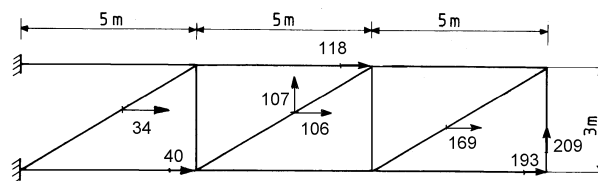
Fig. 12.17 (from [12.6])

For the same structure, the Schur TAM has been constructed using the active DOFs shown in Fig. 12.17, selected by the EfI technique, using only translational DOFs and based on the orthogonal projector onto the column space of Schur vectors.

The FEM eigenfrequencies have been determined using the JDQR algorithm and its MATLAB implementation *jdqr.m* [8.23]. The natural frequencies calculated using the Schur TAM are exactly the same as those computed using the full FEM.

The Schur vectors are very similar to the modal vectors. Figure 12.18 illustrates the first six Schur modes. If overlaid, at the scale of the drawing the eigenmodes could hardly be distinguished from the Schur modes.

A comparison of the first eight eigenvectors and the expanded Schur vectors based on (12.8) is presented in Table 12.7. Column 3 lists the relative discrepancy between the two sets of eigenvectors, calculated as $\left\| \{\varphi\}_{FEM} - \{\varphi\}_{Schur} \right\| / \left\| \{\varphi\}_{FEM} \right\| \cdot 100$. Figure 12.19 is a plot of the relative discrepancy between the first 16 eigenmodes and the Schur vectors. Column 4 lists the diagonal entries of the MAC matrix between the FEM modal vectors and the matched Schur vectors.
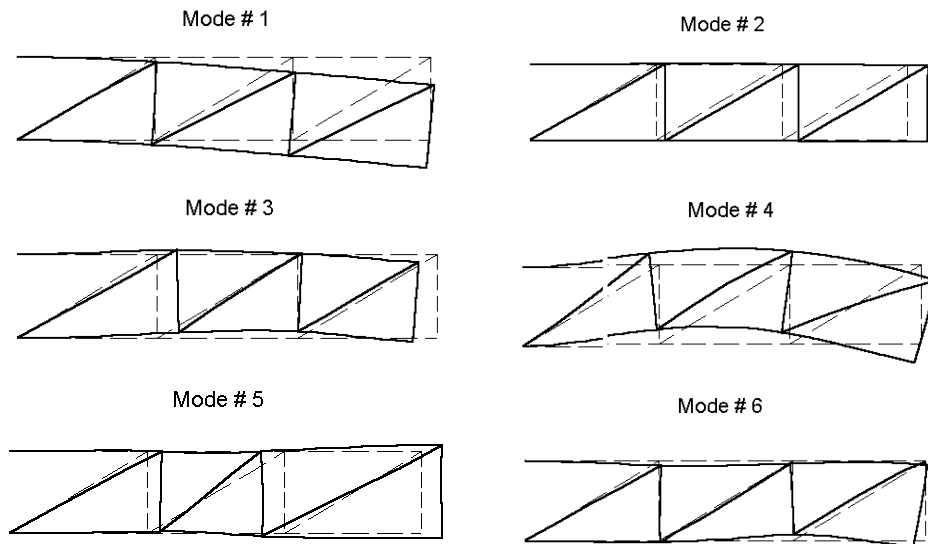
Fig. 12:18 (from [12.6])

The robustness of the Schur TAM is assessed with the *NCOrms* error (12.51). In this case *rms*1 = 0.136. The low value indicates relatively good performance. However this value is higher than that calculated for the Arnoldi TAM and near that calculated for the Modal TAM. The Schur TAM preserves the exact reduction features of the Modal TAM but has intrinsic reduced robustness, being based on a limited number of Schur vectors which very closely resemble the target eigenmodes.

Table 12.7. Comparison of Schur vectors and eigenvectors

No	Natural frequency, Hz	Relative vector discrepancy, %	diag(MAC) x 100
1	45.15	0	100
2	79.04	0.11	100
3	227.18	0.52	100
4	249.67	2.63	99.9
5	363.56	0.94	100
6	437.88	5.77	99.7
7	446.07	7.95	99.4
8	469.42	7.7	99.4

The use of Schur vectors in model reduction and correlation is justified by the fact that Schur vectors are obtained *before* eigenvectors and with less computational effort. Eigenvectors are obtained from an eigendecomposition to

diagonal form, while Schur vectors are obtained from an eigendecomposition to upper triangular form, which is computationally cheaper. Moreover, Schur vectors are known to provide a basis with much better numerical properties than a set of eigenvectors.
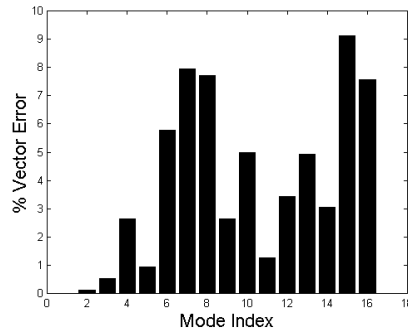
Fig. 12.19 (from [12.6])

For large order systems, eigenvectors are computed as linear combinations of Schur vectors. Because the Schur matrix is dominantly diagonal and the number of elements of its eigenvectors is equal to the vector index, the first several eigenvectors of the system matrix are combinations of only a few Schur vectors. Moreover, the largest contribution in the summation of each system eigenvector comes from the Schur vector with the same index.

Example 12.5

Consider the planar frame from Example 11.1 (Fig. 12.20). The first ten FEM natural frequencies are listed in the second column of Table 12.8. The third column lists frequencies computed with the Arnoldi TAM, using 20 Arnoldi vectors and 10 target modes, for a selection of 10 a-DOFs by the SLAVE elimination technique shown in Fig. 12.20. A starting vector of ones has been used. The relative frequency error shows a very good reproduction of the low frequency spectrum. In fact, for $n_a = 12$, all the first ten TAM eigenfrequencies have zero error.

After solving the reduced eigenvalue problem using the Arnoldi TAM matrices, the a-DOF vectors have been expanded to the size of the full problem (246 DOFs), using the transformation matrix (12.7). Column five lists the relative error of the expanded mode shapes, calculated as $\left\| \{\varphi\}_{FEM} - \{\varphi\}_{exp\,anded} \right\| / \left\| \{\varphi\}_{FEM} \right\| \cdot 100$.

The last column in Table 12.8 lists the diagonal entries of the MAC matrix between the FEM mode shapes and the expanded mode shapes. It shows perfect matching for the first eight modes.
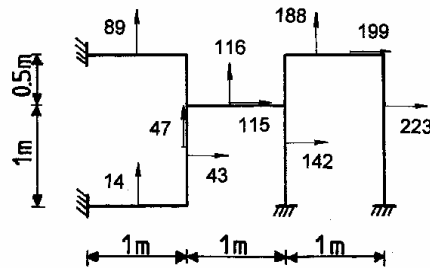
Fig. 12.20

Table 12.8. Comparison of modal data from FEM and Arnoldi TAM

No	FEM	Arnoldi TAM	Frequency error,	Mode shape error,	diag(MAC) × 100
	Eigenfrequency, Hz		%	%	
1	35.996	35.996	0	0	100
2	43.478	43.478	0	0	100
3	89.786	89.786	0	0	100
4	132.60	132.60	0	0	100
5	198.65	198.65	0	0	100
6	210.48	210.48	0	0.01	100
7	247.82	246.82	0	0.46	100
8	264.79	264.80	0.01	1.05	100
9	312.60	313.64	0.33	19.81	96.1
10	327.76	337.24	2.89	42.21	83

The robustness of the Arnoldi TAM is assessed with two global figures of merit, based on the Normalized Cross-Orthogonality (*NCO*) matrix. The *NCO rms* error *rms*1 (12.51) and the rms error difference between the NCO matrix and the identity matrix

$$rms2 = \text{rms}\big(\text{abs}(NCO) \text{-} [I]\big). \qquad (12.52)$$

Both differences are measures of the lack of orthogonality between the two sets of modal vectors.

For $n_a = 10$, $rms1 = 0.952$ and $rms2 = 1.347$. For $n_a = 12$, $rms1 = 0.947$ and $rms2 = 0.899$. The low values indicate the good performance of the Arnoldi TAM.

12.5.1.4 Selection of the candidate set of sensors

Initially, a candidate set of sensor locations should be selected. This candidate set should be large enough to include all of the important dynamics within the target modes that are to be identified by the experiment. In a modal survey of a large space structure it might include as many as 500 candidate locations.

A possible procedure is to select the candidate set based on the modal kinetic energy distribution, that gives a measure of the dynamic contribution of each FEM physical degree of freedom to each of the target mode shapes.

This distribution is computed using the relation

$$KE_{kj} = \left(\varphi_{Ak} \right)_j \sum_{\ell} m_{k\ell} \left(\varphi_{A\ell} \right)_j \tag{12.53}$$

which defines the kinetic energy associated with the *k*-th DOF for the *j*-th target mode.

If the values of KE_{kj} are added over all degrees of freedom, the generalized mass is

$$GM_{jj} = \sum_k KE_{kj} = \sum_k \left(\varphi_{Ak} \right)_j \sum_{\ell} m_{k\ell} \left(\varphi_{A\ell} \right)_j \; . \tag{12.54}$$

If the target modes are normalized to unit mass, $GM_{jj} = 1.0$.

The candidate set of sensor locations should result in a total kinetic energy of sufficient value for each of the target modes. In [12.19] it is considered that as little as 40-50% would be sufficient.

In the EfI method it is assumed that the initial candidate set of sensor locations renders the modal partitions $\left[\varPhi_{st} \right]$ linearly independent.

Attention should be paid to *directional modes*. Certain DOFs are measured with more accuracy than other DOFs. This will pose problems for orthogonality checks. Modal TAM and SEREP are independent of the *a*-DOFs and the *t*-set of target modes. For GR and IRS, the selection of the *a*-DOFs is important.

The *small* value DOF of a given modal vector may contribute equally to an orthogonality check when compared to *large* value DOFs of the same modal vector. Small value DOFs may contain more error than large value DOFs; they will contaminate the orthogonality check at the TAM size or will contaminate the experimental mode expansion.

For structures that contain directional modes it is hard to find a good *a*-set for all target modes. One possible solution is to use different sets of target directional modes, especially in correlation studies with expanded modes.

12.5.2 Exciter placement

The problem of finding the optimum exciter configuration for the n_t target modes was defined as one of combinatorial optimization [12.23], [12.24]. Most algorithms describe either actuator placement for given sensor locations, or sensor placement for given actuator locations. Tentative algorithms for the *simultaneous* selection of sensor and actuator locations have also been developed [12.25].

Suboptimal selection procedures are based on the assumption that the n_a response measurement locations are chosen as potential locations for the n_i exciters $(n_i < n_a)$.

12.5.2.1 Preselection by EfI method

Optimal selection of excitation locations using the EfI method has been considered in [12.26]. Though the basic assumption - linear independence of the forcing vectors - is of questionable physical significance, use of the method in a first stage of selection may be helpful. Considerations regarding the energy input from the exciter locations yield similar results.

Introducing proportional damping as a good first approximation, a matrix of forcing vectors $[F_a]$ is computed premultiplying the modal matrix $[\Phi_{at}]$ by either the corresponding reduced stiffness or the mass matrix. Assume that

$$[F_a] = [k_a]\,[\Phi_{at}].\tag{12.55}$$

The EfI method is then applied to the cross-product matrix

$$[C_F] = [F_a]^T\,[F_a].\tag{12.56}$$

The number of rows n_a is reduced to n_i, when the process is stopped to avoid rank deficiency of the force matrix.

12.5.2.2 Use of synthesized FRF data

Adding damping to the FEM modal data set, a proportionally damped system is created, from which the FRF matrix $[H]$ can be calculated either for the frequency range spanned by the target modes or only at the undamped natural frequencies.

Writing the covariance of the FRF matrix as a sum of dyadic products

$$[H][H]^H = \sum_{\ell=1}^{n_i} \{H\}_\ell \{H\}_\ell^H = \sum_{\ell=1}^{n_i} [G_\ell], \qquad (12.57)$$

the information from the ℓ-th exciter is given by the $[G_\ell]$ matrix.

While $[H]$ is complex, $[H][H]^H$ is hermitian, hence with real diagonal elements. The trace of the rank one matrix $[G_\ell]$ can be used as a measure of the ℓ-th exciter contribution to the FRF information. Plots of $\text{trace}[G_\ell]$ versus frequency help to rank exciter locations.

12.5.2.3 Final selection using MMIF

The final selection of exciters is based on the analysis of the multivariate mode indicator function (MMIF) calculated from synthesized FRF matrices. MMIF curves are plotted using one, two and three excitation DOFs (columns in the FRF matrix) in turn, and n_a response measurement DOFs (rows in the FRF matrix). The minimum number of exciters is determined by the pseudo-multiplicity of eigenfrequencies and is increased if supplementary important local modes have to be excited. Controllability and local impedance characteristics (to avoid large nonlinearities) have to be taken into account, as well as coupling of excitation DOFs by skew mounting of exciters.

A measure of how effective the exciter configuration is at exciting the target modes is obtained by calculating the average mode purity index

$$\Delta_m = \frac{1}{n_m} \sum_{j=1}^{n_m} \left[1 - MMIF(\omega_j) \right], \qquad (12.58)$$

where $MMIF(\omega_j)$ is calculated at the j-th undamped natural frequency located by MMIF. Values $\Delta_m > 0.95$ indicate good location.

Example 12.6

Consider the 11-DOF system from Fig. 9.19. Physical parameters and natural frequencies are given in Table 9.2.

Assuming that the first two modes have to be identified using four sensors, the EfI method selects locations 1, 2, 10, 11. If we want to identify modes 3, 4, 5, and 6, EfI locates four sensors at 1, 5, 8, 11. If the target modes are the first six modes, the EfI method locates four sensors at 1, 4, 8 and 11. However plots of $\det(FIM)$ and $\text{cond}(FIM)$ show rank deficiency for a number of sensors less than the number of target modes (Fig. 12.21). Location of six sensors results in 1, 2, 4, 8, 10, and 11.
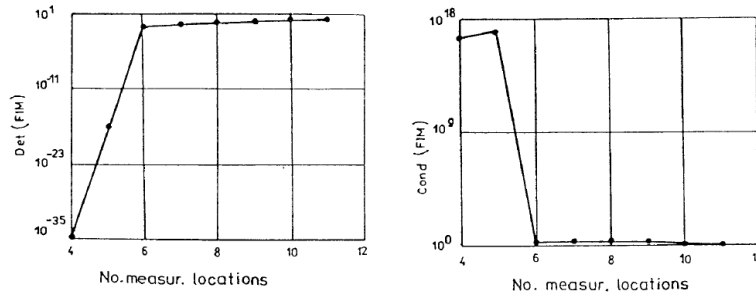
Fig. 12.21 (from [12.21])

For exciter location by EfI, the matrix of undamped eigenvectors is replaced by the matrix of forces calculated by premultiplying the modal matrix by the hysteretic damping matrix reduced to the coordinates selected as sensor locations.
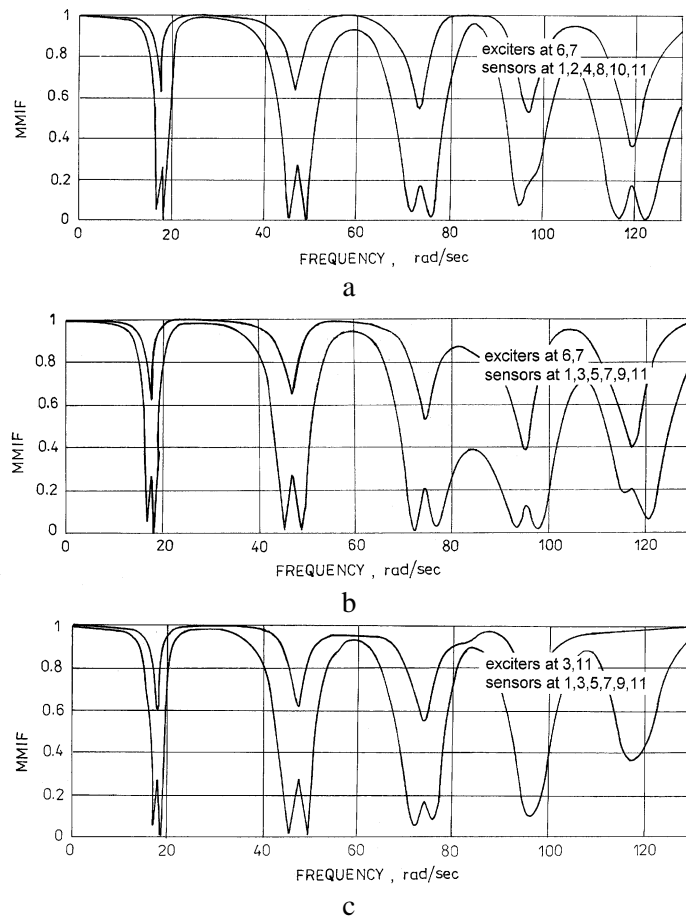
Fig. 12.22 (from [12.21])

If the first two modes are target modes, the extension of EfI method places two exciters at locations 3 and 11. If the target modes are 3, 4, 5, 6, trying to locate only two exciters, EfI yields locations 8 and 11. This is wrong, because a minimum of four exciters have to be located to avoid rank degeneracy, and both exciters are here on the same half of the system.

If a 6×11 FRF matrix is set up for coordinates 1, 2, 4, 8, 10, and 11 selected by EfI for sensors, and the traces of the eleven dyadic product components are calculated and plotted against frequency, two exciters are located at 6 and 7. Figure 12.22, *a* shows the tracked MMIF constructed using a 6×2 FRF matrix with forces at 6 and 7, and responses at 1, 2, 4, 8, 10, and 11. For comparison, Fig. 12.22, *b* shows the MMIF for forces at 6, 7 and responses at 1, 3, 5, 7, 9, and 11, where the undamped mode shapes have large values. The second location performs better, which confirms the sub-optimal character of the suggested procedure. The MMIF for forces at 3 and 11 (Fig. 12.22, *c*) shows that the extended EfI yields the worst results.

12.5.3 Input/output test matrix

A procedure for the simultaneous placement of sensors and exciters, using data from an *a priori* finite element model or from pre-test measurements, is based on the subset selection of linearly independent columns of a Compound Frequency Response Function (CFRF) matrix [12.27]. The first step is the SVD of the CFRF matrix. In a second step, the Effective Independence method is applied to the rank-limited matrix of right singular vectors of the CFRF matrix. The rows selected by stepwise elimination determine a sufficiently independent subset of FRFs whose output/input indices show the optimum sensor/actuator location.

The coordinate combinations for excitation/response measurement can be presented in an I/O Matrix [12.28], with the index of the input coordinate displayed on the abscissa axis and the index of the output coordinate displayed on the ordinate axis.

Example 12.7

Consider the 15 DOF lumped parameter system shown in Fig. 9.6 of Example 9.1. The system has 10 modes of vibration between 10-80 Hz and 5 (local) modes between 120-160 Hz.

Receptance FRFs were first computed at 256 frequencies between 50-80 Hz, for excitation and response at coordinates 1, 2, 4, 5, 7, 8, 10, 11, 13, and 14 (the large masses), then polluted with 5% multiplicative noise. The plot of left singular vectors (UMIF) from Fig. 12.23 shows the location of the natural frequencies of the first ten modes in the range 10-80 Hz.

The problem was to select, from the 100 columns of the CFRF matrix, a minimum set of sufficiently independent columns, able to describe the system response between 50-80 Hz. Their number was set by the effective rank of the CFRF matrix. Based on the PRF plot, a value $N_r = 6$ was considered, which corresponds to the six resonant modes within the considered frequency range.
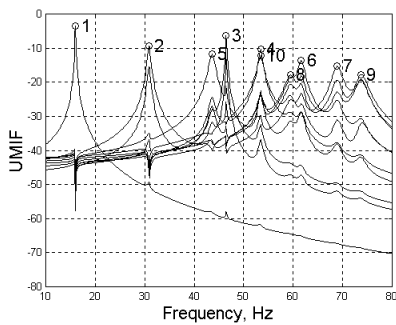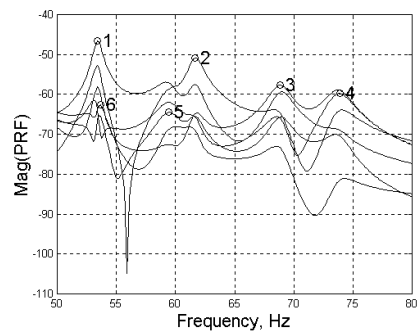
Fig. 12.23   Fig. 12.24

To determine the location of the six FRFs in the CFRF matrix, the Effective Independence method was applied to the 100×6 submatrix of right singular vectors. The selected matrix contained the columns with indices 38 (11/5), 20 (14/2), 100 (14/14), 68 (11/10), 37 (10/5), 14 (5/2) of the CFRF matrix. Numbers in parentheses indicate the actual output/input coordinate index (different from figure).
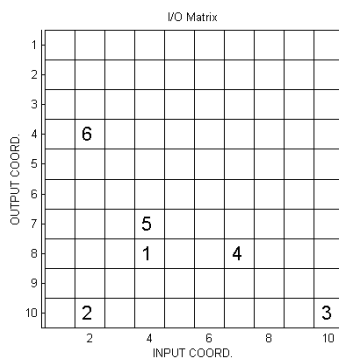
Fig. 12.25

The PRF plot for the reduced FRF matrix is shown in Fig. 12.24, where all 6 initial PRFs are represented. This is an indication that the six selected FRFs can successfully replace the 100 functions considered initially. The I/O Test Matrix (Fig. 12.25) shows the coordinate combinations for excitation/response measurement.

Annex 1
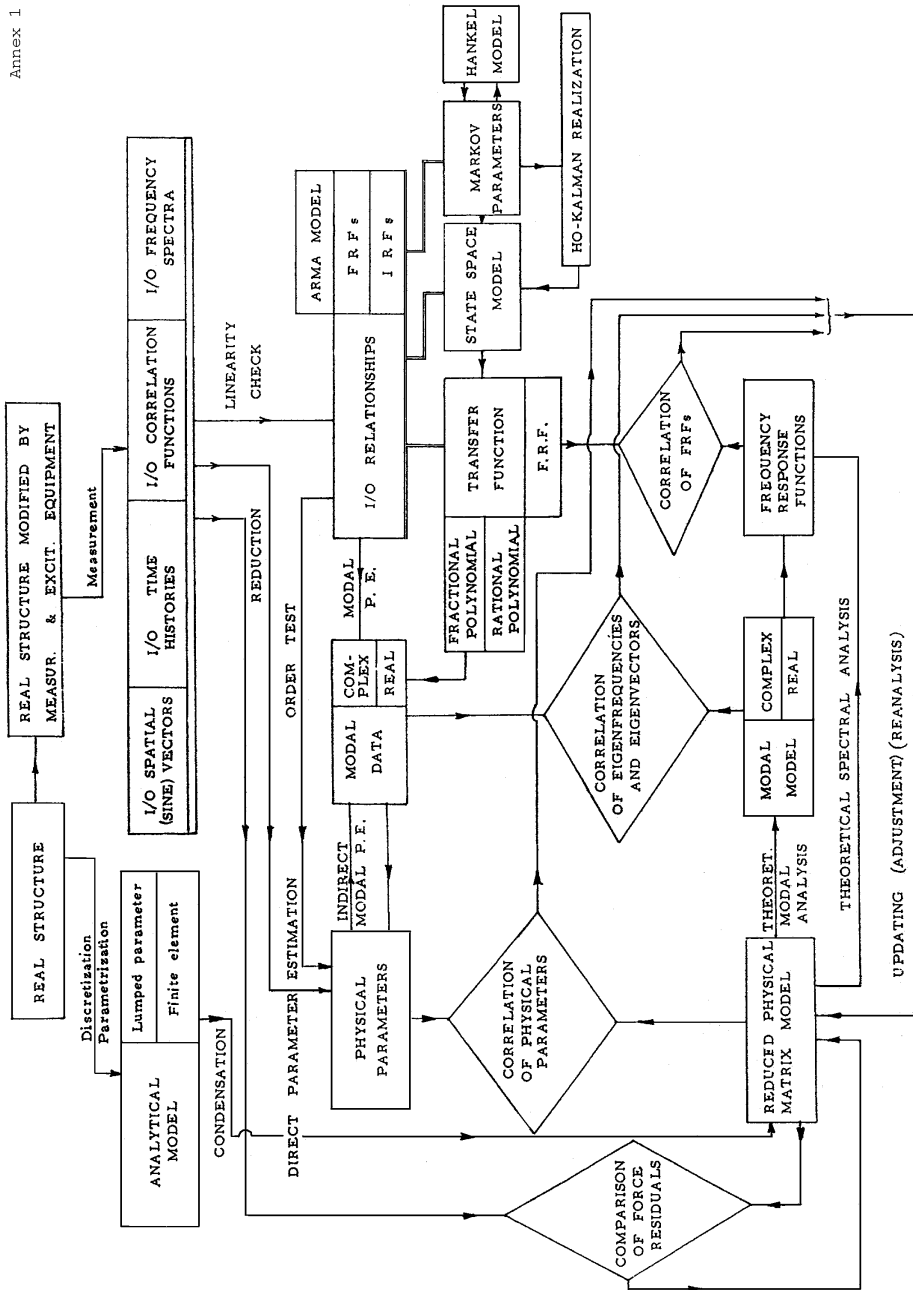
References

12.1   Radeş, M., *Test-Analysis Correlation in Dynamic Structural Modeling*, Institut für Mechanik, Universität Gh Kassel, Germany, Feb 1997.

12.2   Ewins, D.J., *Model validation: Correlation for updating*, IUTAM-IITD International Winter School on Optimum Dynamic Design using Modal Testing and Structural Dynamic Modification, pp 115-130, Dec 1997.

12.3   Freed, A.M. and Flanigan, C.C., *A comparison of test-analysis model reduction methods*, Proceedings of 8th International Modal Analysis Conference, Kissimmee, Florida, pp 1344-1350, 1990.

12.4   Baker, M., *Review of test/analysis correlation methods and criteria for validation of finite element models for dynamic analysis*, Proceedings of 10th International Modal Analysis Conference, San Diego, Ca., pp 985-991, 1992.

12.5   Radeş, M. and Ewins, D.J., *Some Applications of Arnoldi Vectors in Modal Testing*, Proceedings of 21st International Modal Analysis Conference, Kissimmee, Florida, Paper S11P06, Feb. 2003.

12.6   Radeş, M., *Test-analysis correlation using Schur vectors*, , Proceedings of International Conference on Noise and Vibration Engineering ISMA-2004, Leuven, Belgium, pp 1917-1924, Sept 2004.

12.7   Radeş, M., *Comparison of vibration properties,* in 'Encyclopedia of Vibration' (S. Braun, D. Ewins, S. S. Rao, eds), Academic Press, London, pp 256-277, 2002.

12.8   Allemang, R.J., *Investigation of Some Multiple Input/Output Frequency Response Function Experimental Modal Analysis Techniques*, Ph.D. Thesis, Univ. of Cincinnati, 1980.

12.9   Pappa, R.S. and Ibrahim, S.R., *A parametric study of the Ibrahim Time Domain modal identification algorithm*, Shock and Vibration Bulletin, no.51, Part 3, pp 43-71, 1981.

12.10   Lieven, N.A.J. and Waters, T.P., *Error location using normalised orthogonality*, Proceedings of 12th International Modal Analysis Conference, Honolulu, Hawaii, pp 761-764, 1994.

12.11   Fotsch, D. and Ewins, D.J., *Application of MAC in the frequency domain*, Proceedings of 18th International Modal Analysis Conference, San Antonio, Texas, pp 1225-1231, 2000.

12.12   Heylen, W. and Avitable, P., *Correlation considerations – Part 5 (Degree of freedom correlation techniques)*, Proceedings of 16th International Modal Analysis Conference, Santa Barbara, Ca., pp 207-214, 1998.

12.13   Lieven, N.A.J. and Ewins, D.J., *Spatial correlation of mode shapes, The Coordinate Modal Assurance Criterion (COMAC)*, Proceedings of 6th

International Modal Analysis Conference, Kissimmee, Florida, pp 605-609, 1988.

12.14   Hunt, D.L., *Application of an enhanced Coordinate Modal Assurance Criterion,* Proceedings of 10th International Modal Analysis Conference, San Diego, Ca., pp 66-71, 1992.

12.15   Avitable, P. and Pechinsky, F., *Coordinate Orthogonality Check (COORTHOG)*, Proceedings of 12th International Modal Analysis Conference, Honolulu, Hawaii, pp 753-760, Feb 1994.

12.16   Heylen, W. and Lammens, S., *FRAC: A consistent way of comparing frequency response functions*, Proceedings of Conference 'Identification in Engineering Systems', Swansea, pp 48-57, March 1996.

12.17   Avitable, P., *Modal Handbook*, 17th International Modal Analysis Conference, Orlando, Florida, 1999.

12.18   Pascual, R., Golinval, J.C. and Razeto, M., *Testing of FRF based model updating methods using a general finite element program*, Proceedings of International Conference on Noise and Vibration Engineering ISMA 21, Leuven, Belgium, vol.3, pp 1933-1945, 1996.

12.19   Kammer, D.C., *Sensor Placement for On-Orbit Modal Identification and Correlation of Large Space Structures*, Journal of Guidance, Control and Dynamics, vol.14, pp 251-259, 1991.

12.20   Blelloch, P.A. and Carney, K.S., *Modal selection in structural dynamics*, Proceedings of 7th International Modal Analysis Conference, Las Vegas, Nevada, pp 742-749, 1989.

12.21   Radeş, M., *Sensor and exciter location for structural identification and control*, Interaction between Dynamics and Control in Advanced Mechanical Systems (ed. D.H. van Campen), Kluwer Academic Publ., Dordrecht, pp 329-336, 1997.

12.22   Penny, J.E.T., Friswell, M.I. and Garvey, S.D., *Automatic choice of measurement locations for dynamic testing*, AIAA Journal, vol.32, pp 407-414, 1994.

12.23   Niedbal, N. and Klusowski, E., *Optimal exciter placement and force vector tuning required for experimental modal analysis*, Proceedings of 15th International Seminar on Modal Analysis, Leuven, Belgium, pp 1195-1222, 1990.

12.24   Lallement, G., Cogan, S. and Andriambololona, H., *Optimal selection of the measured degrees of freedom and application to a method of parametric correction*, Proceedings of 9th International Modal Analysis Conference, Florence, Italy, pp 369-375, 1991.

12.25   Gawronski, W., *Simultaneous placement of actuators and sensors*, Journal of Sound and Vibration, vol.228, no.4, pp 915-922, 1999.

12.26 Lim, T.W., *Actuator/sensor placement for modal parameter identification of flexible structures*, Journal of Modal Analysis, vol.8, pp 1-14, 1993.

12.27   Radeş, M., *Sensor/actuator location using principal response functions*, Proceedings of ICED2007, International Conference on Engineering Dynamics, Carvoeiro, Portugal, Paper 9A-1064, April 2007.

12.28   Radeş, M., *Condensation of frequency response test data by the QR decomposition*, Proceedings of International Conference on Noise and Vibration Engineering ISMA25, Leuven, Belgium, vol.3, pp 1241-1246, 2000.

Index